Sonobactericide

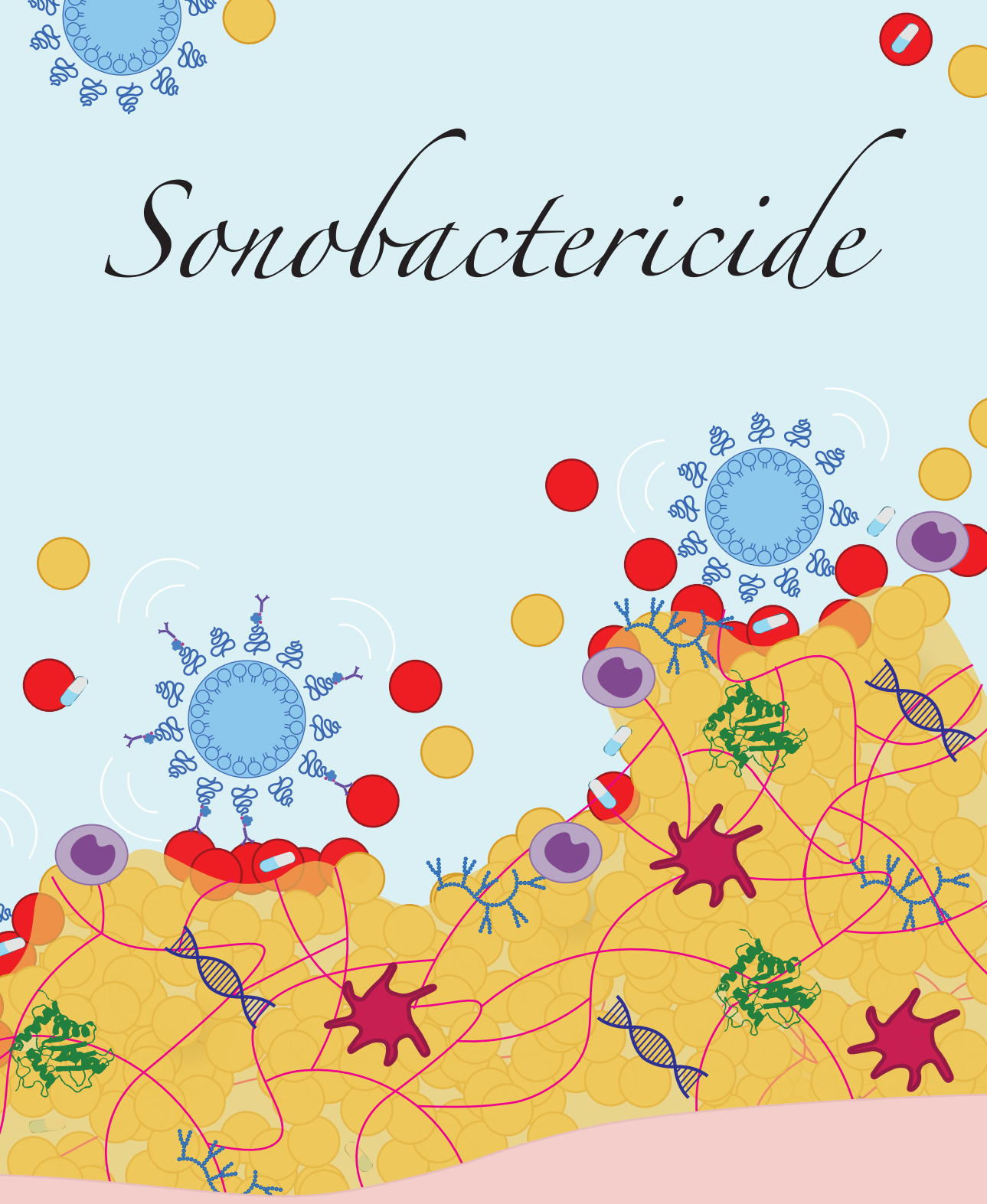

Kirby Lattwein

Sonobactericide

Kirby Renee Lattwein

Colophon

ISBN: 978-94-6421-182-5

Cover design: Kirby Lattwein, Blossom Baksh
Layout design: Kirby Lattwein

Printed by: Ipskamp Printing, Enschede, the Netherlands

For a printed version please contact:
Secretary Biomedical Engineering
Erasmus MC, Rotterdam, the Netherlands

An electronic version is available at:
http://hdl.handle.net/1765/131894

Sonobactericide

Thesis

to obtain the degree of Doctor from the
Erasmus University Rotterdam
by command of the
rector magnificus

Prof. dr. F.A. van der Duijn Schouten

and in accordance with the decision of the Doctorate Board

The public defence shall be held on
Wednesday 14th of April 2021 at 15.30 hours

by

Kirby Renee Lattwein

born in Charlotte, North Carolina, the United States of America

Erasmus University Rotterdam

Doctoral Committee:

Promoters:	Prof. dr. ir. N. de Jong
	Prof. dr. ir. A.F.W. van der Steen
Other members:	Prof. dr. T. Coenye
	Prof. dr. C.K. Holland
	Prof. dr. M.P.M. de Maat
	Prof. dr. E. Stride
	Prof. dr. P. Verhamme
Co-promoters:	Dr. K. Kooiman
	Dr. W.J.B. van Wamel

This work was supported by the Erasmus Medical Center Foundation. Additional financial support for the printing of this thesis was kindly provided by Erasmus University Rotterdam.

Financial support by the Dutch Heart Foundation for the publication of this thesis is gratefully acknowledged. The research described in this thesis was supported by a grant of the Dutch Heart Foundation (DHF *2016SB001*).

This work was performed in the framework of the Medical Delta UltraHB program. Medical Delta is gratefully acknowledged for financial support for the printing costs of this thesis.

- For my darling Julia -

Even when we are apart, I am always with you,

to the sun and back, and beyond the stars…I love you so.

- For Dixie -

May everyone in the world have someone in their life

as loving as you. Thank you, truly, for always being there for me.

Contents

Non-targeted microbubbles

Non-targeted and targeted microbubbles 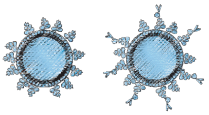

Targeted microbubbles 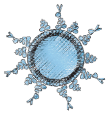

“It is the possibility of having a dream come true that makes life interesting.

- The Alchemist,
  Paulo Coelho

1

Introduction

Bacteria are in and on all of us from the moment we are born. In fact, it is estimated that we host more bacterial cells than our own human cells (39:30 trillion cells)[1]. These bacteria are limited to the areas of the body with contact to the outside world, to include the gastrointestinal tract, and exist in a commensalistic or mutualistic relationship. The closed cardiovascular system is a sterile environment, which is crucial to maintain since a pathogenic bacterium gaining access would be able to travel anywhere in the body. Most people, if not all, reading this thesis actually have had at least one point in their lives when bacteria entered their blood stream, such as from a scraped knee, paper cut, or vigorous tooth brushing. With a healthy immune system these bacteria are often easily cleared from the body. However, when the immunological triggered response is ineffective at neutralizing the invading bacteria, a life-threatening situation can quickly develop. Since the 1940s, there are prescribed medications, i.e. antibiotics, that can specifically kill these bacteria or slow the growth to give the body enough time to overcome the infection. The advent of antibiotics significantly changed the uncertain course of bacterial infections, where a simple cut or scrape becoming infected no longer meant life or death depending only on how the body could manage. Finally, after being plagued by bacteria since our existence, an effective new tool that dramatically reduced mortality was added to our arsenal. Unfortunately, this relief was to be short-lived.

Although initially most people viewed antibiotics as a cure-all, and some may still do, it is not. Soon after Alexander Fleming discovered the fungus-produced antibacterial substance named penicillin, resistance was already identified before the first prescription[3] and became a clinical problem by the 1950s[4]. **Ever since then, scientists have been in a perpetual, quick-pace race against bacteria developing resistance to each new antibiotic (over 150)**. Resistance generally refers to when bacteria can render an antibiotic ineffective, such as by producing new degrading enzymes or altering the physical structure of the target binding site[5]. Despite general resistance development, with the continued antibiotic and vaccine development, dramatically less people died from acute infections caused by planktonic, i.e. free-floating, bacteria. This is when chronic (persistent) infections took center-stage, further challenging the prowess of antibiotics as an effective weapon against pathogenic bacteria.

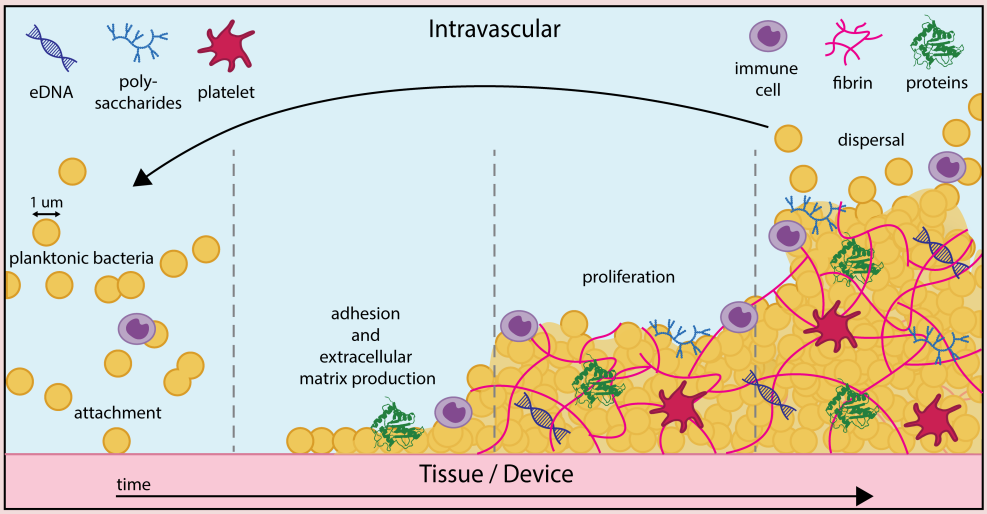

Figure 1.1. Illustration depicting biofilm formation and maturation (not drawn to scale).

Chronic bacterial infections occur when bacteria aggregate or (~80%)[6] form a biofilm. Bacterial aggregates have similar characteristics to biofilms, albeit not surface-associated. Although the bacterial findings presented in this thesis could potentially be extrapolated to aggregates, the research focus is on biofilm. **Biofilms begin with the successful attachment of at least one bacterium to a surface, which then proliferates into a dense, heterogenous community protected by a continually constructed extracellular polymeric matrix consisting of microbial and host components (Fig. 1.1)[7].** Bacteria residing in biofilms were first observed in dental plaque and described as "an innumerable quantity of Animals" by the Dutch microbiology and microscopy pioneer Antoni van Leeuwenhoek in 1683[8]. However, biofilms were only formerly recognized as the source of chronic infections some 300 years later and the name 'biofilm' introduced into medical microbiology in 1985[9]. This time-lag was largely due initially to both van Leeuwenhoek's secrecy over his intellectual property (i.e., the design and methods for his single-lens microscopes) and the ensuing skepticism which led many to believe these tiny animals were either imaginative or relatively unimportant[10]. Fast-forward to the first decades of the antibiotic era, and people were perplexed as to the cause of these infections because bacteria were often not detected using culture-based clinical sampling and antibiotic therapy, the star of the show, was delivering a lackluster performance.

Today, we now understand that the characteristic nature of biofilms was responsible for the baffling results. Certain phenotypic trade-offs that bacteria make to thrive in biofilms, and thus the human body, can give rise to viable, yet planktonically growth-impaired populations that are nonculturable and thus, escape laboratory detection[11]. **Bacteria embedded within a biofilm matrix are extremely well-protected against the multitude of potential assaults aimed at their removal.** In this setting, host defenses, such as phagocytosis and free radical production, are rendered inconsequential and the immune response itself can be skewed to one that does not favor clearance[12]. Biofilm formation additionally confers a decreased susceptibility to antimicrobials, which was also first observed by van Leeuwenhoek with the use of a strong wine-vinegar[8]. **Antibiotics are found to be 10-1000x less effective against bacteria in biofilms versus in a planktonic state[13,14].** To clarify, this is also due to antimicrobial tolerance, meaning bacteria liberated from a biofilm will become susceptible again if not resistant to the compound[15]. Furthermore, resistance development is facilitated within the densely packed biofilms by enhancing the cell-to-cell exchange of both plasmids carrying resistance genes and communication signals controlling gene expression (i.e., quorum sensing)[16,17].

Around 100 formerly known bacterial species have so far been identified as pathogenic to humans[18]. Many use the same bacterial protective mechanisms, however they can be used differently. For example, *Pseudomonas aeruginosa* skews the immune response towards anti-inflammatory, whereas *Staphylococcus aureus* (*S. aureus*) towards proinflammatory[12]. These can also be species-specific, including the secreted toxins and immune evasion factors. The microbial focus of this thesis is on *S. aureus*, a common commensal residing either permanently or transiently in ~50% of the population. **The clinical impact of *S. aureus* biofilms is high, for it is implicated in and the predominate infecting agent of many chronic infections, associated with higher mortality rates and twice as long hospital stays, and the majority require surgical removal for infection resolution[7,19].**

The biofilm matrix composition and micromilieu within can vary between species and strains, and also the environment surrounding the biofilm has a strong influential role. In the cardiovascular system, certain *S. aureus* strains releases coagulases that converts fibrinogen in the blood into fibrin that is incorporated throughout the developing

matrix to provide further cover and concealment from antimicrobials and the immune system[20]. Therefore, thesis chapters that focus on cardiovascular biofilms use strains isolated from patients with *S. aureus* infective endocarditis, a life-threatening (22-66% mortality[19]) biofilm infection of the heart valves, surrounding endocardial tissue, or indwelling cardiac device. The environment is also taken into consideration, such as by growing biofilms under turbulent conditions and using mammalian cell culture media or human plasma for fibrin strand development. **Despite the rapid expansion of biofilm research and new technologies, these infections have increasing morbidity rates and mortality rates that have not improved over the last decades[19,21,22].** Now untreatable bacterial infections threaten us once again, driving the necessity to direct focus on the discovery of not only new "traditional" antibiotics, but also towards novel or repurposed diagnostic and therapeutic strategies.

Sound is amazingly influential. **Both heard and unheard frequencies can induce a vast array of effects.** If you can take a moment, close your eyes and open up to the sound around you. What do you hear? Perhaps it's waves crashing against the shore line, possibly it's rain hitting against the roof, or maybe it's the sound of an engine humming on your way to a thesis defense. The sound you heard (20 - 20,000 Hz) began as mechanical energy transmitted as a pressure wave in air that vibrated across the intricate auditory system within your ear, transforming it into an electrical nerve impulse resulting in a physiological and emotional response, such as a decreased heart rate and calmness. Using sound as a healing tool can be traced back to the Aboriginal Australians with the didgeridoo estimated at least 40,000 years ago[23]. Today, we use medical ultrasonography, which uses electrical energy converted into inaudible sound waves (> 20,000 Hz) for a variety of applications in diagnostics, procedural guidance, and therapeutics.

Figure 1.2. Ultrasound image of a 10-week old fetus.

One of the best-known applications of ultrasound is in fetal monitoring (See Fig. 1.2). As a clinical diagnostic, this modality is portable, inexpensive, and harmless. When ultrasound comes into contact with echogenic tissue, it is reflected back, which can be processed into an electrical signal to allow for visualization inside the human body. The tissue type and the boundaries between tissues with different densities determines the amount of ultrasound reflected. The acoustical parameters can be tuned to the application, such as high-intensity (10^3-10^5 W/m^2), focused ultrasound with short microsecond pulses to mechanically break-up tissue or long millisecond pulses for thermal ablation, or low-intensity (1-10 mW/cm^2), unfocused ultrasound for diagnostic imaging[24,25]. **Ultrasound is instrumental for the diagnosis and assessment of many diseases, including infective endocarditis.** However, often the infection is missed in the early stages of disease, where the patient then presents weeks later with a dangerously large biofilm, as seen in Figure 1.3.

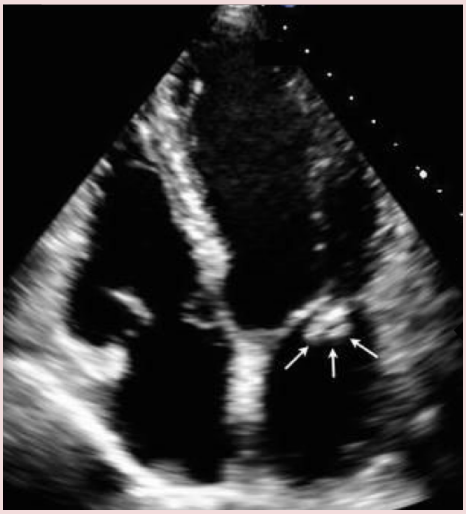

Figure 1.3. Ultrasound image of an infective endocarditis vegetation, i.e. biofilm, attached to the mitral valve indicated by the white arrows. Image reprinted, with permission from [2] © 2015, Springer-Verlag London.

Over the last decades, ultrasound has been investigated as a possible addition or alternative in the treatment of bacterial infectious diseases. The first experiments investigating ultrasound as a therapeutic tool were inspired by the observation of small fish killed when swimming into a high frequency, high intensity beam during the development of submarine SONAR in 1917[26]. Bacteria were the only organisms, out of a variety tested ranging from frogs to unicellular eukaryotes, to survive all exposures[27]. Depending on the acoustical parameters, it can induce various bio-effects in mammalian cells, both thermal and non-thermal related, such as ultrastructural changes (e.g., plasma membrane disruption, lysosome damage, and cytoplasmic vacuolation), protein synthesis stimulation, and intracellular calcium ion elevation[28]. **Ultrasound-induced bioeffects have also been observed in bacteria,**

to include non-lethal enhanced membrane permeability, lethal physical destruction of both inner and outer cell structures, and biochemical triggered apoptosis[29,30]. For the last 26 years, research has been further directed towards combining ultrasound and antimicrobials[31-33]. The majority of these studies demonstrated a synergistic response against biofilms, thus advocating for the use of ultrasound as an adjunct to antibiotic therapy. However, it is yet to be seen in the clinical setting, and several ultrasound studies observed no change or enhancement in bacterial viability[30,31]. Increasing the footprint of ultrasound-induced bactericidal effects and antibiotic synergy could improve therapeutic efficacy for clinical consideration.

Bubbles are a natural enigma that exist in almost all facets of life, beguiling us and perplexing some of the greatest minds for thousands of years. This holds true for bubbles used in medical ultrasound contrast imagining, albeit for a shorter time frame (decades). These bubbles, called microbubbles, are smaller than 1/10th the thickness of this sheet of paper (<10 micrometers) and consist of a gas encapsulated by a shell commonly composed of phospholipids. This gas core responds to ultrasound waves by volumetrically expanding when the pressure is low and compressing when high. For cardiac diagnostic imaging, a frequency of 2 MHz is often used, which means microbubbles in this field expand and compress 2 million times a second. These oscillating microbubbles scatter the ultrasound allowing for visualization. The mechanical power of these oscillations is known to induce mammalian cellular responses that can be used for drug delivery enhancement beyond that of ultrasound alone[34]. The addition of biomarkers to the shells of microbubbles, known as targeted microbubbles, can allow for the molecular guidance of both disease diagnosis and therapy enhancement[35]. For the experiments investigating the ultrasound-induced effects of bacteria/biofilm, acoustic cavitation is often acknowledged as the main driver[30]. Therefore, the addition of exogenous cavitation nuclei to an acoustic field, specifically microbubbles for this thesis, could increase the therapeutic effect against bacteria beyond preexisting microscopic gas bubbles as seen with mammalian cells[34]. This thesis proposes ***sonobactericide***, which is the use of ultrasound and exogenous cavitation nuclei, either alone or as a therapeutic complement, for biofilm eradication or as a theranostic for bacterial infections. The current research, concepts, and considerations concerning Sonobactericide are extensively discussed in Chapter 2.

Aim and Thesis Outline

This thesis is primarily focused on ***sonobactericide***. The overarching aim is to investigate its potential as a therapeutic tool for combatting life-threatening chronic bacterial infections, with a particular focus on cardiovascular biofilms and infective endocarditis. In addition to the chapters directly addressing the aim, there are supportive chapters that provide insight separately into important aspects on biofilm and microbubbles that have potential to negatively or positively impact the effectiveness of sonobactericide.

Sonobactericide is a multidisciplinary approach, and thus, not only an understanding of the inflicted organ system(s) is critical, but also that of the bacteria, ultrasonic waves, and microbubbles. In **Chapter 2**, a comprehensive overview of the relevant literature (up to August 2019) on sonobactericide is provided, with additional attention directed at how the various aspects of the different disciplines, such as bacterial structure, acoustic frequency, and microbubble composition, could impact therapeutic success.

Intriguingly, the 'Father' of both microscopy and microbiology, van Leeuwenhoek, was a Dutchman from Delft (~17 km from Erasmus MC), and so it seems appropriate that this thesis also includes chapters specifically on these two areas, **Chapter 3** and **4** respectively. **Chapter 3** describes in detail the state-of-the-art imaging system, a custom-built Nikon A1R+ confocal microscope (nanometer spatial resolution) coupled to the Brandaris-128 ultra-high-speed camera (nanosecond temporal resolution), that was used, either together or apart, in Chapters 4-6 and 8-11 for cellular and microbubble response visualization. **Chapter 4** highlights the capability of drugs commonly taken during an infection, in this case paracetamol (acetaminophen), to possibly induce more resilient forms of biofilm, which may necessitate the tuning of Sonobactericide to these drug-induced changes to be most effective.

In **Chapters 5-7**, non-targeted microbubbles are used to explore their potential to induce biofilm therapeutic effects. Each of these chapters builds towards a more *in vivo*-like cardiovascular *S. aureus* biofilm model. **Chapter 5** investigates in real-time, and at high resolution, the displacement and cell membrane permeabilization

(i.e., sonoporation) of bacteria within biofilms as a result of microbubble oscillation. **Chapter 6** expands upon this with focus on the structural effects ultrasound-activated microbubbles have on both the bacteria and fibrin matrix of more cardiovascular-like biofilms. **Chapter 7** uses infected human blood clots to emulate infective endocarditis pathophysiology and with flow, treats these using sonobactericide.

Targeting microbubbles directly to biofilms could enhance sonobactericide's theranostic potential. However, it is then crucial to understand how they differ from non-targeted microbubbles in both acoustic signal and induced cellular effects. In **Chapter 8,** various acoustical parameters are investigated to determine if key distinguishable differences exist between bound and unbound microbubbles alone. **Chapter 9** then varies acoustic pressure and cycles to examine both the targeted and non-targeted microbubble response and the influence it has on endothelial cells.

Chapters 10 and **11** are both targeted microbubble studies. **Chapter 10** furthers mechanistic research on the cellular responses to insonified microbubbles using $\alpha_V\beta_3$ as the target to endothelial cells, and focusing on both the microbubble and the ensuing sonoporation and cell-cell contact opening. In **Chapter 11**, a new targeted MB is developed using the antibiotic vancomycin to target *S. aureus* biofilms and tested *in vitro* under flow, along with providing a therapeutic proof-of-concept. Lastly, all of the chapters are placed into a larger context in **Chapter 12,** which provides a discussion on several key topics central to Sonobactericide and an outlook into the future.

Together, these chapters aim to provide more depth and breadth into the understanding of ultrasound-activated microbubble therapy, with a specific interest towards sonobactericide. Finally, I hope you, the reader of this thesis, never lose an insatiable curiosity in the midst of a society full of black and white boundaries; at least for the duration of the unfolding journey of black lines on white pages that lies before you.

“Not all those who wander are lost.

- The Lord of the Rings,
J.R.R. Tolkien

2

Sonobactericide: an emerging treatment strategy for bacterial infections

Kirby R. Lattwein, Himanshu Shekhar,
Joop J.P. Kouijzer, Willem J.B. van Wamel,
Christy K. Holland, and Klazina Kooiman

Based on:
Ultrasound in Medicine & Biology, vol. 45, no. 2, pp. 193-215, 2020

Abstract

Ultrasound has been developed as both a diagnostic tool and a potent promoter of beneficial bioeffects for the treatment of chronic bacterial infections. Bacterial infections, especially those involving biofilm on implants, indwelling catheters and heart valves, affect millions of people each year, and many deaths occur as a consequence. Exposure of microbubbles or droplets to ultrasound can directly affect bacteria and enhance the efficacy of antibiotics or other therapeutics, which we have termed *sonobactericide*. This review summarizes investigations that have provided evidence for ultrasound-activated microbubble or droplet treatment of bacteria and biofilm. In particular, we review the types of bacteria and therapeutics used for treatment and the *in vitro* and pre-clinical experimental setups employed in sonobactericide research. Mechanisms for ultrasound enhancement of sonobactericide, with a special emphasis on acoustic cavitation and radiation force, are reviewed, and the potential for clinical translation is discussed.

Introduction

In recent decades, the combination of ultrasound and cavitation nuclei has been investigated as an alternative approach to treatment of several life-threatening diseases. Ultrasound is a common diagnostic tool and offers several advantages: it is non-invasive and inexpensive, available at the point-of-care, and is a safe medical application. Many different types of cavitation nuclei exist, including gas or liquid filled and coated or non-coated. These include micro- and nanobubbles, nanocups, droplets and echogenic liposomes. When exposed to ultrasound pressure waves, gas-filled nuclei respond by expanding and contracting volumetrically, and droplets vaporize into microbubbles. Microbubble oscillations and acoustic droplet vaporization impart theragnostic potential because this characteristic response can both be detected by clinical diagnostic ultrasound scanners and locally enhance treatment by inducing cellular responses[36-38]. "Sonobactericide" describes the enhancement of bactericidal action aided by ultrasound and the presence of cavitation nuclei, both endogenous and exogenous. This terminology is consistent with the nomenclature of other therapeutic applications of ultrasound-activated cavitation nuclei such as sonoporation—the formation of micropores within cell membranes[36], sonothrombolysis—the lysis of thrombi[37], sonoreperfusion—the restoration of perfusion after microvascular obstruction[39] and sonodynamic therapy—the treatment of neoplastic cells using a sonosensitizer[40]. Sonobactericide, like the other approaches, can be used either alone or in combination with other drugs, such as antimicrobials.

Sonobactericide arrives at a time when traditional microbial therapy is limited by the increasing prevalence of multidrug-resistant bacteria. There are several resistance mechanisms and a large contributing factor is the development of biofilms, bacterial communities encased in a complex extracellular polymeric matrix consisting of variable amounts of numerous constituents, such as polysaccharides and proteins. This matrix provides both a scaffold for antibiotic binding and an anoxic and acidic environment that can deactivate antibiotics and decrease bacterial susceptibility *via* a reduced metabolism[41]. In addition to the presence of a protective extracellular matrix, the large heterogeneity and general 3-D structure of a biofilm hinder antibiotic delivery, penetration and effectiveness. Additionally, it is difficult to diagnose bacterial infections before they become extensively established[42,43]. Sonobactericide, as illustrated in

Figure 2.1, may increase the "footprint" of antibiotic bactericidal action, directly kill bacteria, and reduce treatment time.

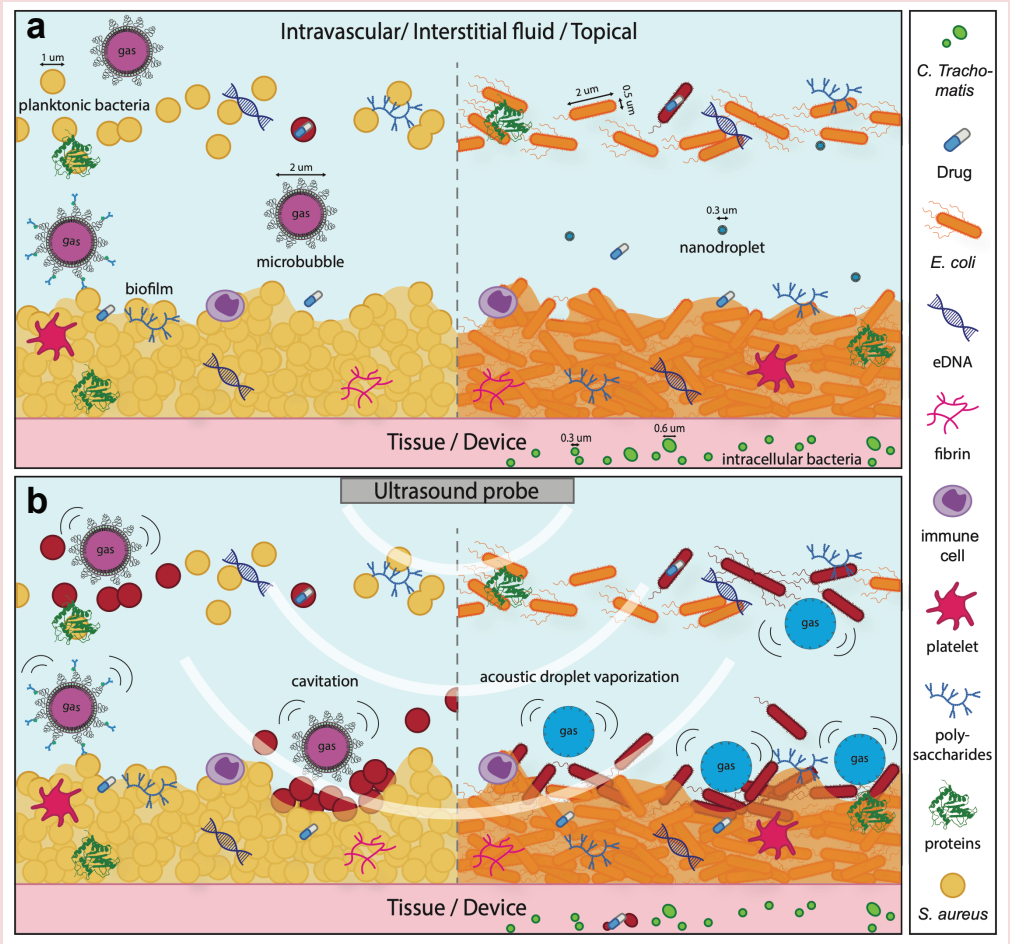

Figure 2.1. Concept of sonobactericide (not drawn to scale). (a) Potential infection environments before ultrasound. Sizing of bacteria and cavitation nuclei is denoted with a *double-headed arrow*. (b) Ultrasound application in which cavitating microbubbles and activated nanodroplets disrupt bacteria and biofilm composition. Bacteria that have become red in (b) are considered dead or to have compromised membranes because of the effects from ultrasound and cavitating nuclei.

This review focuses specifically on the principles of sonobactericide using exogenous cavitation nuclei for potential clinical translation. As this new line of research gains ground, it is pertinent to establish important considerations for future work. Main concepts of the variability of bacteria, microbubble composition and acoustic behavior and ultrasound parameters are addressed, and the experimental setups and measured outcomes are evaluated. Articles on sonobactericide published before August 2019 were identified using PubMed, Web of Science and Google Scholar search engines with the keywords "ultrasound," "microbubble" (or "bubble" or "contrast") and "bacteria" or "biofilm." Sonobactericide articles referenced by those found in our search were also included. Articles were excluded if they were not written in English or if ultrasound alone, that is, without added cavitation nuclei (i.e., microbubbles or droplets), was investigated as a potential application for treatment. For treatment with ultrasound alone, the reader is referred to other excellent reviews[30,31,44]. Twenty-seven sonobactericide articles were selected for this review (Table 2.1). One article that investigated microbubbles targeted to biofilm for diagnostic application[45] and six articles that studied the effect of cavitation nuclei on bacteria without ultrasound[46-51] were excluded from Table 1 because these studies did not meet our definition of sonobactericide.

Table 2.1. Overview of sonobactericide papers

Pathogen Type	Pathogen	Culture type	in vitro	In vivo	Model set-up	Antimicrobial	Cavitation nuclei	US frequency (MHz)	Pressure / Intensity or calculated pressure	Cycles/ PRF/ Treatment time	Ref
Gram+	*E. faecalis*	biofilm	x	-	root canals of single-rooted polymer and human teeth	5.25% NaOCl	custom-made	0.032 ±0.004	N.D.	N.D., 1 min	(Halford, et al. 2012)
		intracellular	x	-	Infected human bladder cell organoid model	gentamicin	custom-made	1.1	2.5MPa	25% duty cycle, PRF 50 Hz, 20 s	(Horsley, et al. 2019)
	P. acnes	planktonic; *in vivo*: N.D.	x	x	eppendorf tube; intradermally into mouse ears	lysozyme	custom-made	1	*in vitro*: 1, 2, 3 W/cm^2 *in vivo*: 3 W/cm^2	50% duty cycle, *in vitro*: 1 min; *in vivo*: 1 min, q.d. for 13 d	(Liao, et al. 2017)
	S. aureus	planktonic	x	x	tissue culture plate; bone cement in rabbit tibiae	vancomycin	SonoVue	1	0.3 W/cm^2	30% duty cycle, 24 h	(Lin, et al. 2015)
		biofilm	x	-	tissue culture plate/ coverslip	vancomycin	custom-made	1	0.3 W/cm^2	50% duty cycle, 5 min	(Guo, et al. 2017)
		biofilm	x	-	infected clot on a suture in glass capillaries	oxacillin	Definity	0.12	0.44 MPa (PTP)	continuous wave, 50 s on 30 s off, 30 min	(Lattwein, et al. 2018)
		biofilm	-	x	subcutaneously implanted titanium plate in mice	human β-defensin 3	custom-made /SonoVue	0.08	0.2 W/cm^2	50% duty cycle, 20 min, t.i.d. for 7, 14, 28 d	(Zhou, et al. 2018)
	S. epidermidis	biofilm	x	x	tissue culture plate; subcutaneously implanted disk in rabbits	vancomycin	SonoVue	0.08	*in vitro*: 1 W/cm^2 *in vivo*: 0.5 W/cm^2	50% duty cycle, *in vitro*: 10 min; *in vivo*: 20 min, t.i.d. for 72 h	(He, et al. 2011)
		biofilm	x	-	OptiCell	vancomycin	custom-made	0.3	0.5 W/cm^2 or 0.12 MPa*	50% duty cycle, 5 min	(Dong, et al. 2013)
		biofilm	x	-	OptiCell	vancomycin	custom-made	1	0.5 W/cm^2 or 0.12 MPa*	50% duty cycle, 5 min	(Dong, et al. 2017)

Table 2.1. Continued

Gram+		biofilm	x	-	OptiCell	vancomycin	custom-made	1	0.5 W/cm^2 or 0.12 MPa*	50% duty cycle, 5 min	(Dong, et al. 2017)
		biofilm	-	x	subcutaneously implanted catheter in rabbits	vancomycin	custom-made	0.3	0.5 W/cm^2 or 0.12 MPa*	50% duty cycle, 5 min, b.i.d. for 48 h	(Dong, et al. 2018)
		biofilm	x	-	tissue culture plate; glass FluoroDish	vancomycin	SonoVue	1	1 W/cm^2 or 0.24 MPa*	50% duty cycle, 10 min	(Hu, et al. 2018)
	S. aureus & *S. epidermidis*	biofilm	x	-	tissue culture plate with titanium plate	human β-defensin 3	SonoVue	0.08	1 W/cm^2	50% duty cycle, 10 min	(Zhu, et al. 2013)
		biofilm	-	x	subcutaneously implanted titanium plate in mice	human β-defensin 3	SonoVue	0.08	0.2 W/cm^2	50% duty cycle, 20 min, t.i.d. for 48 h	(Li, et al. 2015)
	S. mutans	biofilm	x	-	tissue culture plate with disk	none	Sonazoid	0.28	N.D.	0-90% duty cycle, 1 min	(Nishikawa, et al. 2010)
Gram–	A. *baumannii*	biofilm	x	-	tissue culture plate/ coverslip	polymyxin B	custom-made	1	3 W/cm^2	continuous wave, 5 min	(Fu, et al. 2019)
	C. trachohmatis	intracellular	x	-	infected HeLa cells in tissue plate with gas permeable bottom	doxycycline; ceftizoxime	custom-made	1.011	0.15, 0.44 W/cm^2 or 0.13, 0.23 MPa#	25% duty cycle, 20 sec	(Ikeda-Dantsuji, et al. 2011)
	E. coli	planktonic	x	-	centrifuge tubes	none	Albunex; ST68 custom-made	1	500 W/cm2	1 ms pulse, PRF 20 Hz, 5 min	(Vollmer, et al. 1998)
		planktonic	x	-	tubes	gentamicin	SonoVue	0.0465	0.01 W/cm^2	33% duty cycle, 12 h	(Zhu, et al. 2014)
		N.D.	-	x	direct injection into rat prostates	none	custom-made	1	0.5 MPa / 0.023 W/cm^2	1% duty cycle, 5 min	(Yi, et al. 2016)
		N.D.	-	x	intratracheally infected mice	gentamicin	Definity	1.3	0.9 – 1.2 MPa (PNP)	pulse every 5 s, 5 min	(Sugiyama, et al. 2018)

Table 2.1. Continued

Gram-	*F. nucleatum*	planktonic	x	-	tissue culture plate	none	Optison	0.96	0.5 MPa (PPP)	50% duty cycle, PRF 1 Hz, 90 s	(Han, et al. 2005)
		planktonic	x	-	tissue culture plate	none	Definity	1	0.25, 0.5, >0.9 MPa (PPP)	0 -50% duty cycle, PRF 1-100 Hz, 10, 90, 450 s	(Han, et al. 2007)
	P. aeruginosa	biofilm	x	-	glass coverslip in flow cell	gentamicin; streptomycin	Definity	0.5	1.1 MPa (PNP)	16 cycle tone burst, PRF 1 kHz, 5 min	(Ronan, et al. 2016)
	P. putida	biofilm	x	-	glass coverslip in acetate film chamber	none	SonoVue	0.25, 1	0.1, 0.5, 0.7 MPa (PNP)	50 µs pulse	(Goh, et al. 2015)
	E. coli & *P. pastoris* - (yeast)	planktonic	x	-	microfluidic system	none	custom-made	0.13	10 bar (~1 MPa)	500-50,000 cycles, ms – s, every 5 s	(Tandiono, et al. 2012)
Mixed	N.D.	biofilm	x	-	nylon membrane surface	none	custom-made	0.042	N.D.	2 sec pulse, every 2 min, 15 min	(Agarwal, et al. 2014)

US = ultrasound; PRF = pulse repetition frequency; N.D. = not defined; PTP = peak-to-peak pressure; PPP = peak positive pressure; PNP = peak negative pressure; q.d. = once a day; b.i.d. = twice a day; t.i.d. = thrice a day; * = calculated peak pressure from spatial pulse-average intensity (I_{SPTA}) values obtained by personal communication with author(s); # = calculated peak pressure from spatial-average temporal-average intensity (I_{SATA}) values obtained by personal communication with author(s). Calculations were performed using the formulae (Kinsler, et al. 2000):

$I_{SATA} = P^2/2\rho c$, where P denotes the peak pressure, and ρ and c denote the density and speed of sound, and

$I_{SPTA} = I_{SATA}$/Duty factor

Bacteria

There exists a vast diversity among bacteria; even closely related bacteria can have different morphologies, metabolisms and defenses. Considering shape morphology, besides the familiar rod (bacillus), spherical (coccus) and spiral (twisted) types, at least six other general shapes exist[52]. Though current sonobactericide research into pathogenic bacteria is dominated by bacillus- and coccus-shaped bacteria, infectious diseases are also caused by bacteria with other morphologies. Microbubbles may oscillate differently when paired with similarly spherical-shaped *Staphylococcus aureus*, versus rod-shaped *Escherichia coli* or the junction of the kidney-shaped diplococcus *Neisseria meningitidi*s because of total surface area contact, tension and rigidity. These shape differences along with variation in cell surface could influence treatment success. For example, fimbriae are bristle-like external filamentous structures protruding from some bacterial cell surfaces which may create a stand-off distance between the cavitation nuclei and cell wall. It has been observed that as the initial stand-off distance increases, biofilm disruption, sonoporation and cytoskeleton disassembly decrease[53,54]. Moreover, microbubble dynamics also depend on the distance from and material properties of a surface[55,56].

Based on the cell envelope (a multilayered structure on the outside of the cell), almost all bacteria can be subdivided into two main groups: Gram+ or Gram–. The cell envelope of Gram+ bacteria consists of a thick (20–80 nm) peptidoglycan layer, which is threaded with teichoic acid, but lacks an outer membrane, as illustrated in Figure 2.2a. Peptidoglycan is made up of repeating units of muramic acid, which are cross-linked by peptide side chains. Gram– bacteria are covered by a thin peptidoglycan cell wall (<10 nm), surrounded by an outer lipid bilayer membrane containing pores, lipoproteins and lipopolysaccharide[57], as illustrated in Figure 2.2b. It is possible that these structural differences between Gram+ and Gram– bacteria will also result in dissimilar responses to sonobactericide. Several studies have compared treatment efficacy on both bacteria types[58], including ultrasound (67 and 20 kHz) paired with antibiotics without exogenous cavitation nuclei[59,60], and observed a markedly different response. Furthermore, the size of the bacteria (~0.5–5 μm), whether a single bacterium, dividing bacterium or aggregates of several bacteria, and its location (in a suspension, on a surface, or intracellular) could have an impact on the therapeutic effectiveness of sonobactericide.

Seemingly subtle differences within a group of eukaryote cells can affect the differential reaction to oscillating microbubbles. This variable cell response to microbubbles is supported by sonoporation studies that have reported differences in drug delivery efficiency in two different cancer cell lines[61]. The top three types of bacteria on which sonobactericide has been evaluated are (i) *Staphylococcus epidermidis* (Gram+, 7 studies, 26%); (ii) *S. aureus* (Gram+, 6 studies, 22%); and (iii) *E. coli* (Gram–, 4 studies, 15%) (Table 2.1). Methicillin-resistant *S. epidermidis* was employed in the majority of the studies (6 out of 7), whereas methicillin-resistant *S. aureus* (MRSA) was used in 4 of the 6 studies. Two research teams used a green fluorescent protein containing Gram– strain (*E. coli, Pseudomonas aeruginosa*)[62,63]. The majority of the studies used only one type of bacteria. Only one study used mixed types of bacteria[64]. Two articles compared two different types of bacteria[65,66], and another compared a bacterium and a fungus[63]. Only four studies used patient-derived clinical isolates originating from a central venous catheter[67], infective endocarditis blood culture[68], pneumonia-induced sputum[69], and urine from a patient with lower urinary tract symptoms[70]. With the exception of Agarwal et al.[64], who used bacteria from a wastewater reclamation plant to investigate membrane biofouling removal, the other groups used lab-derived strains, which may limit clinical applicability. Though a laboratory strain may be deemed wild type, the preparation and (worldwide) dissemination can lead to genetic changes that cause both disruption of virulence regulatory pathways, which often imparts loss of typical *in vivo* virulence potential, and phenotypic variation among an entire strain pedigree[71]. Also, typing clinical isolates, such as staphylococcal protein A (*spa*) typing performed by Lattwein et al.[68] or core-genome multi-locus sequence typing, would aid in the verification of disease association.

Three modes of growth exist for bacteria: planktonic, associated with a surface and intracellular. Bacteria in different growth modes have distinctly different characteristics. Planktonic refers to free living bacterial cells, which can occur in two forms: as single bacterial cells or in clusters known as planktonic aggregates[72]. Clinically, this planktonic mode generally refers to bacteria that gain entrance to the human body in the bloodstream and cause bacteremia, which results in acute infections often effectively treated by the host immune system and antibiotics[73,74]. Seven sonobactericide studies (26%) focused on planktonic bacteria (Table 2.1).

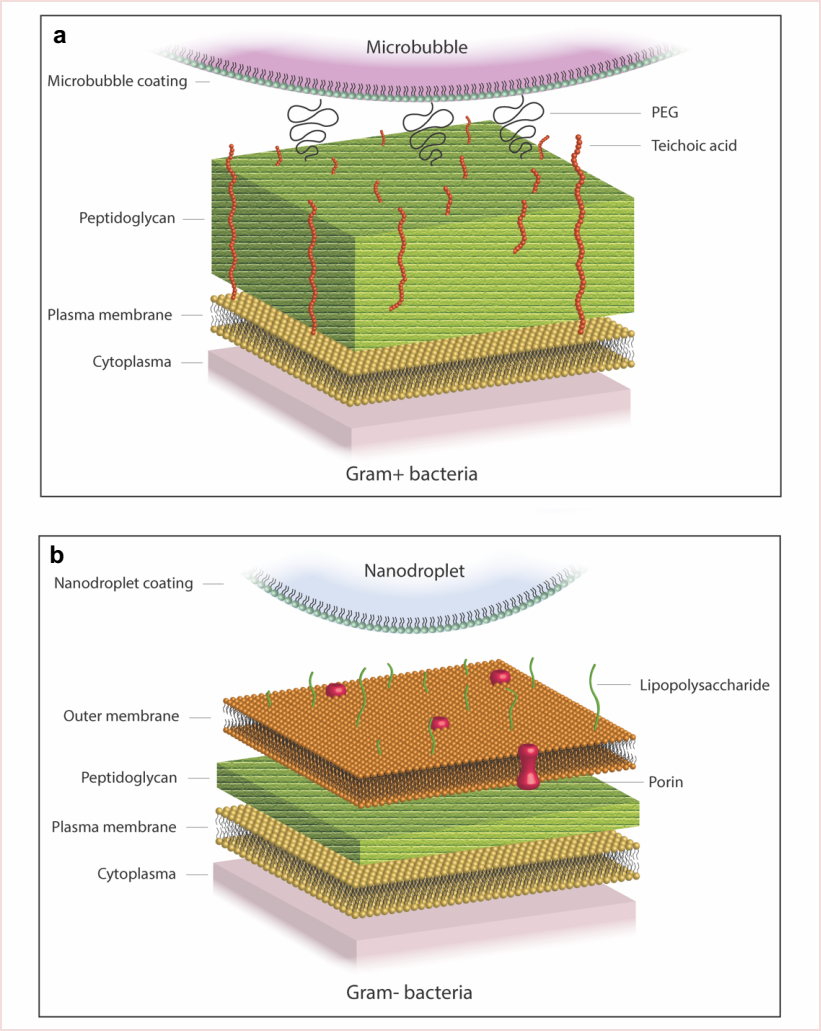

Figure 2.2. Interaction of cavitation nuclei with bacteria: (a) interaction between phospholipid-coated microbubbles and Gram+ bacteria, (b) interaction between phospholipid-coated nanodroplets and Gram– bacteria. PEG = polyethylene glycol.

In contrast, bacteria adhering to living (biotic) and non-living (abiotic) surfaces cover themselves with a protective matrix, classically known as a biofilm. Bacteria in a biofilm are protected against attacks from the immune system and are up to 1000 times more

resistant to antimicrobial therapy than planktonic bacteria[75]. Biofilm formation is abundant, and an estimated 60% of human bacterial infections are biofilm related[76,77]. Correspondingly, 63% (17/27) of the sonobactericide studies focused on treatments for biofilm infections. Biofilm can occur on teeth; native and prosthetic heart valves; medical implants, such as prosthetic joints, surgical mesh and screws; pacemakers; and indwelling catheters[78]. These biofilms consist of surface aggregates of bacteria imbedded in an extracellular matrix of sugars of bacterial origin, extracellular DNA and proteins, both originating from either the host or the bacteria. For instance, when *S. aureus* is exposed to blood, the coagulation cascade is activated by coagulase produced by the bacterium. The fibrin forms a scaffold to which the bacteria bind, facilitating the formation of a biofilm[79]. Other biofilm composition examples include *Pseudomonas aeruginosa* forming sputum-encased biofilms surrounded by immune cells in lungs affected by cystic fibrosis[80], and *Proteus mirabilis* forming crystalline biofilms by inducing urinary salt precipitation in the catharized urinary tract[81]. Biofilm extracellular matrix composition and architecture are complex and highly influenced by species/strain/lineage, developmental conditions, nutrient availability, cell–cell signaling and interactions with the (host) environment[82]. Moreover, most biofilm infections are polymicrobial[83], which adds to the microenvironment complexity. The various processes driving bacterial responses are not completely understood. Thus simulating human *in vivo* biofilms remains highly challenging[84,85].

There are indications that bacteria in a single biofilm do not behave *en groupe*. Archer et al.[7] found that *S. aureus* biofilms contain cells in at least four distinct metabolic states: aerobic, fermentative, dormant (including very slow growing cells and persisters) or dead. It is likely that bacterial cells in different metabolic states, stages of cell division or growth phases will respond differently to sonobactericide. This hypothesis is supported by the observation that planktonic bacteria in stationary growth phase are more resistant to ultrasound alone or combined with cavitation nuclei[86].

Bacteria can be dispersed from mature biofilms and become planktonic again[87]. Dispersal agents, including chemical, enzymatic and mechanical methods, can also be used to make biofilm bacteria more susceptible to therapeutics. Recent literature on *P. aeruginosa* suggests that bacteria dispersed from biofilms have a physiology different

from those of both planktonic and biofilm growth modes[88]. This difference suggests a possible transitional growth mode for bacteria acclimating to the planktonic state. These researchers found that the dispersed cell phenotype was highly virulent and remained for at least 2 h. This finding is supported further by studies that manipulated biofilm dispersal, which led to increased disease severity and progression in mice and a transition from asymptomatic colonization to active infection, respectively[89,90]. Chua et al.[88] discovered that dispersed cells exhibited lower iron uptake gene expression and paired the dispersal agent with an iron chelator, which led to significant reduced viability. Other work revealed that dispersed bacteria exhibited increased antibiotic susceptibility and, only after lag phase (≥3 h), were more active[91]. Thus, biofilm dispersal should be considered and investigated for sonobactericide development.

Experimental Approaches

The first to report sonobactericide in combination with an antimicrobial was Ikeda-Dantsuji et al. in 2011. Since then, 18 articles on sonobactericide using antimicrobials have been published (Table 2.1). The most studied clinical antibiotic was vancomycin (7 studies, 26%). Six other antibiotics were investigated, with different ones for Gram+ and Gram– bacteria except gentamicin. Two groups investigated two antibiotics separately on the same bacterial strain. Ikeda-Dantsuji et al.[92] investigated one antibiotic to which the *Chlamydia trachomatis* strain was susceptible (doxycycline) and one to which this bacterial strain was resistant (ceftizoxime). Ronan et al.[62] used two aminoglycosides (gentamicin and streptomycin) to which the *P. aeruginosa* PAO1 strain was susceptible as determined by CO_2 metabolic production.

In addition to the antibiotics, three other antimicrobials were investigated: sodium hypochlorite (NaOCl), lysozyme and human β-defensin 3 (Table 2.1). The studies included either clinically appropriate antimicrobials (dental, NaOCl[93]) or antimicrobials testing a new approach (lysozyme[94]; human β-defensin 3[65,66,95]). Sodium hypochlorite is a disinfectant used widely in endodontic irrigation and health care facilities[96]. Human β-defensin 3, an endogenous broad-spectrum antimicrobial peptide produced by various cells in the human body[97], was administered in free form or encapsulated in liposomes[95]. The aim was to load the liposomes onto SonoVue microbubbles, but proof thereof was not provided. Lysozyme is a naturally occurring antimicrobial protein and was used in five (non-sonobactericide) papers as the microbubble coating material[46-49,51].

All sonobactericide studies used an appropriate antibiotic targeting a specific microbe, according to therapeutic guidelines[98-103], excluding 2 studies that could not be linked to guidelines because of nondisclosure of microbe information beyond species[104] and no disease aim[65]. Two examples of correct antibiotic and microbe pairings are found in Sugiyama et al.[105], who aimed to treat severe Gram– bacterial pneumonia and used an *E. coli* strain for which the Canadian guideline recommends gentamicin[99], and Lattwein et al.[68], who aimed to treat infective endocarditis and used a methicillin-susceptible *S. aureus* isolate for which both the European[102] and American[101] guidelines recommend oxacillin. Additionally, of the studies using an antibiotic, 2 of 9 focusing on Gram+

bacteria used strains already resistant to first-line antibiotics. Many infections are not dominated by resistant microbes, and Gram– bacteria can have higher resistance profiles than Gram+ bacteria[106]. This choice could be influenced by media coverage, strain access or geographic location. All articles using vancomycin and methicillin-resistant microbes originated from China, which has high levels of reported antimicrobial resistance[106].

A few groups performed sonobactericide using non-antimicrobial therapeutics. One paper used recombinant tissue plasminogen activator (rt-PA), a clinically approved fibrinolytic agent, in combination with the antibiotic oxacillin[68]. Two articles investigated gene transfection of plasmid DNA into planktonic bacteria[107,108]. The microbubble-mediated accumulation of bone marrow mesenchymal stem cells, which can suppress inflammation, was investigated as a treatment for chronic bacterial prostatitis[109]. Although the majority of sonobactericide studies paired their treatments with therapeutics, 5 (19%) focused directly on the mechanical and biological effects resulting from ultrasound and microbubbles alone[53,63,64,86,110].

Many of the *in vitro* studies were performed in polystyrene tissue culture well-plates, ranging from 96- to 6-well plates, for both planktonic and biofilm studies (10 studies, 37%; Table 2.1). To the well-plates, Zhu et al.[65] added a 10-mm diameter titanium plate (1 mm thick); Guo et al.[111] a 13-mm glass coverslip; Fu et al.[69] a 12-mm glass coverslip; and Nishikawa et al.[110] a polystyrene disk (dimensions not provided). Two studies also cultured biofilm in a FluoroDish, a 35-mm dish containing a 23.5-mm glass window[67,112]. The geometry of both these containers could result in the reflection of ultrasound at the bottom of the well and at the medium–air interface. As a result, constructive and deconstructive interference leading to standing waves could have occurred[113]. Standing waves may also form within the body, especially in the presence of bone[114]. Microbubbles may aggregate at the nodes of a standing wave[115]. Increases in *in situ* acoustic pressure caused by constructive interference can cause unwanted bio-effects mediated by inertial cavitation[116,117]. The presence of standing waves produces acoustic field variations that are sensitive to changes in transducer position, excitation frequency or temperature[118]. The acoustic intensity of the ultrasound field is proportional to the square of the pressure amplitude when the ultrasound wavelength is much smaller than the

transducer aperture[119]. Under the plane wave approximation, the acoustic pressure is related to the intensity as follows: $I = P^2/2pc$, where P is the peak acoustic pressure, p is the density and c is the speed of sound[120]. For traveling waves, the intensity is a function of time; that is, once the wave has passed a given spatial location, the intensity drops to zero. However, for standing waves, the peak intensity at a spatial location remains constant over time. Effects of standing wave formation during insonation of cells in different holders have previously been investigated in detail[121].

Measurement of *in situ* acoustic parameters is critical to understanding treatment effects, correlating the treatment effects to specific outcomes and translating these to an *in vivo* setting[122]. Only 5 sonobactericide studies reported calibrating the output *in situ*[53,62,63,68,70]. The lack of standardization of exposure setups makes it difficult to compare the results in the literature. Reporting spatial maps of the acoustic field *in situ* could help improve the reproducibility and interpretation of *in vitro* studies between groups[122].

In the well-plates and FluorDishes, cavitation nuclei were administered once for treatment times varying from 20 s to 10 min (see Table 2.1), with the exception of one study in which fresh microbubbles were administered every 4 h for 24 h[104]. It is unclear whether microbubbles were still present beyond a few minutes during insonification because of destruction or dissolution. For example, Mannaris and Averkiou[123] reported that SonoVue microbubbles, insonified *in vitro* for 20 ms at 1 MHz using 10 cycle pulses at a pulse repetition frequency (PRF) of 100 Hz, were destroyed and/or dissolved after only a few pulses at 400 kPa acoustic pressure, whereas microbubbles were still present after all pulses at an acoustic pressure of 100 kPa. In addition, pulses longer than 100 cycles at acoustic pressures >0.4 did not give any added benefit in terms of microbubble oscillation. One group used the OptiCell cell culture system for their biofilm experiments[124,125], which consists of two gas-permeable, thin (75 μm) polystyrene membranes, spaced parallel and 2 mm apart, providing 50 cm^2 area of cell culture. Microbubbles were administered once for a 5 min treatment (0.3 or 1 MHz, 0.12 MPa, 50% duty cycle) period.

Several groups used a less commercial *in vitro* setup. Goh et al.[53] used an acetate film square chamber with the top and right sides each consisting each of a coverslip and the

ultrasound (250 kHz or 1 MHz, 0.1–1 MPa, 50-μs pulse) transducer positioned below. One coverslip had a biofilm, such that the microbubbles were either floating beneath the biofilm or optically trapped at varying distances from the side. Lattwein et al.[68] performed sonobactericide under plasma flow (0.65 mL/min) on biofilms grown statically on human whole blood clots placed in glass capillaries (2.15-mm inner diameter). Microbubbles were continuously infused, and ultrasound (120 kHz, 0.44 MPa, continuous wave, 50 s on 30 s off) was applied intermittently for 30 min. Ronan et al.[62] grew biofilms in a cylindrical flow cell (17 mL/h) with an acoustically transparent membrane on one side and a glass coverslip on the other, and flow was halted to perform sonobactericide (0.5 MHz, 1.1 MPa, 16-cycle tone burst, PRF = 1 kHz) for 5 min, with microbubbles administered once. Flow was also used by Tandiono et al.[63] to treat planktonic bacteria in a microfluidic system composed of polydimethylsiloxane-made channels. In humans, biofilms can develop in variable fluid flow environments depending on the location or under static conditions. Biofilms are highly sensitive to these different conditions[126]. Thus, selection of the appropriate static or flow condition setting should be tailored to the specific aimed application, such as superficial skin wound or intravascular device infections.

For dental application, Halford et al.[93] grew biofilms in the root canal (12 mm length) of single-rooted extracted human teeth under constant agitation (120 rpm). Microbubbles were delivered into canals and insonified with a P5 Newtron dental ultrasonic hand piece (28 to 36 kHz ultrasound) for 1 min. Horsley et al.[70] employed a bladder organoid model using a modified acoustically compatible chamber[127]. Briefly, a polycarbonate filter insert (12 mm diameter) cultured with infected human bladder cells was fixed between an Ibidi culture dish (35 mm) and a polydimethylsiloxane lid. Cavitation nuclei were added, and the dish and lid were coupled and then insonified (1.1 MHz, 2.5 MPa, 5500 cycles, 20 ms pulse duration) for 20 s. Other *in vitro* experimental setups were on nylon membranes (47 mm diameter, pore size = 0.2 μm) and in centrifuge tubes (2 and 5 mL) (Table 2.1). Nylon membrane biofilms were treated in a beaker placed in a sonicator (0.042 MHz, on for 2 s every 2 min) while microbubbles were continuously introduced for 15 min[64]. The planktonic bacteria in tubes were treated (1 MHz, 500 W/cm^2, 2% duty cycle) for 5 min[86] or 12 h (0.0465 MHz, 0.01 W/cm^2, 33% duty cycle)[128] and in Eppendorf tubes (1 MHz, 1–3 W/cm^2, 50% duty cycle) for 1 min[94], all with a one-time administration of microbubbles.

Three *in vitro* studies were followed up with a corresponding *in vivo* study in the same article[94,104,112]. Thirty percent of the articles on sonobactericide (8/27) have investigated therapeutic efficacy in pre-clinical animal models (Table 2.1). Four groups chose to emulate implanted medical device infections using subcutaneous implants, near the spine, with biofilm grown on catheter pieces or polyethylene disks in rabbits[112,129] and titanium plates in mice[66,95]. Microbubbles were injected subcutaneously into the implant area before ultrasound. For each of the three ultrasound exposures (20 min) per day, He et al.[112] injected 200 μL of microbubbles (2×10^8 to 5×10^8/mL) every 5 min, and both Li et al.[66] and Zhou et al.[95] injected 30 μL once, 2×10^8 to 5×10^8/mL and concentration not disclosed, respectively. Dong et al.[129] applied ultrasound twice a day for 5 min, and injected 500 μl (1.2×10^9/mL diluted to 1% v/v) each time. All studies used a 50% duty cycle. However, acoustic parameters, treatment intervals and duration times varied (Table 2.1).

Lin et al.[104] investigated the ability of sonobactericide to increase the elution rate of antibiotics from vancomycin-loaded bone cement in a periprosthetic infection rabbit tibia model. Ultrasound (1 MHz, 0.3 W/cm^2, 30% duty cycle) was applied transcutaneously for 24 h, and microbubbles (2×10^8 to 5×10^8/mL) were injected into the same space as the *S. aureus* bacteria at four time points. Surrounding tissues were evaluated directly after treatment. For chronic bacterial prostatitis modeled in rats, Yi et al.[109] used sonobactericide to induce accumulation of bone marrow mesenchymal stem cells to reduce inflammatory reactions and resolve infection. After 4 wk of infection induction with *E. coli*, microbubbles (0.1 mL/kg) were directly injected into prostates and insonified (1 MHz, 0.5 MPa, 1% duty cycle) for 5 min. Afterward, stems cells (1×10^7) were administered intravenously, and therapeutic effectiveness was evaluated after 24 h and 2 wk.

Another study focused on harnessing sonobactericide in a model of severe bacterial pneumonia with the goal of enhancing antibiotic delivery to infected lung tissue in mice[105]. *E. coli* were administered intratracheally, and 6 h later gentamicin was injected intraperitoneally. After 30 min, microbubbles (1×10^9) were intravenously administered and ultrasound (1.3 MHz, 0.9–1.2 MPa, pulse every 5 s; pulse duration not specified) was transmitted thoracically for 5 min. Lavage and tissues samples were

evaluated at 30 min and 2 h, respectively, after ultrasound application. Liao et al.[94] also used mice and aimed to improve acne vulgaris treatment using transdermal sonobactericide with lysozyme-shelled microbubbles. Ears were infected intradermally with *Propionibacterium acnes*. Gel loaded with lysozyme microbubbles was placed on top of the infected area and insonified (1 MHz, 3 W/cm^2, 50% duty cycle) daily for 1 min. Effectiveness was assessed at several time points during the 13 d of treatment.

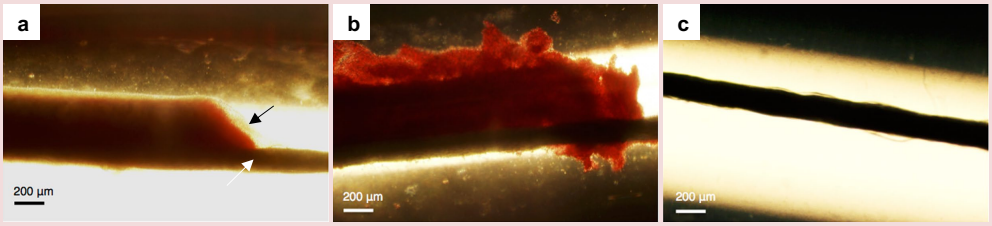

Figure 2.3. Bright-field micrographs of *in vitro*-produced *Staphylococcus aureus*-infected clots after 30-min treatment with (a) plasma alone; (b) plasma, recombinant tissue plasminogen activator (rt-PA, thrombolytic) and oxacillin (antibiotic); and (c) plasma, rt-PA, oxacillin, ultrasound and Definity (microbubble). The *black arrow* in image (a) indicates the biofilm (beige). The *thick black line*, seen in all images and denoted by a *white arrow* in image (a), is the suture to which the respective infected clots were adhered. Ultrasound parameters were 0.12 MHz and 0.44 MPa peak-to-peak pressure, intermittent (50 s on, 30 s off) continuous waves for 30 minutes. Adapted, with permission, from Lattwein et al.[68].

Various techniques were used for assessing sonobactericide efficacy. The colony-forming unit plate-counting method was utilized to determine antimicrobial efficacy (14/27, 52%), for some *in vitro* and all except one *in vivo* study[109]. Bacterial plating is relatively easy to perform and considered the "gold standard" for determining viable bacteria counts. This technique, however, is widely known to underestimate the absolute number of bacteria. Another potential limitation is that often to obtain post-treatment samples, biofilms have been mechanically disrupted, scraped, centrifuged, digested, vortexed or sonicated, which might have induced microbial alterations. Several articles employed histopathologic staining, either crystal violet or hematoxylin and xeosin, to observe bacterial morphology (macroscopy and light microscopy), quantify biofilm

density by absorbance levels in a microplate reader or compare inflammatory effects over time. This method can be used for high-throughput screening, but it does not discriminate between live and dead cells. Immunohistochemistry was used by Yi et al.[109] to quantify inflammatory cytokine expression and distribution. Agarwal et al.[64] desiccated their mixed species biofilms to determine fixed biomass for overall density quantification and also, albeit with additional steps, for extracellular protein and polysaccharide content.

Several microscopic techniques were utilized for visualization of treatment, including light, epifluorescence, confocal laser scanning and transmission and scanning electron microscopy. Light microscopy was combined with or without time-lapse and high-speed camera observations[53,63,68,93]; see Figure 2.3 for a light microscopy example. Fluorescence detection, with either a widefield or a confocal microscope, was the most frequently utilized optical imaging modality for qualitative and quantitative visualization of live and fixed cell populations (16/27, 59%). These images can provide information not only on viability, but also biomass, average biofilm thickness and structural heterogeneity. Live/dead nucleic acid staining with Syto 9 (viable cells) and propidium iodide (dead or membrane-disrupted cells) were often used and the cells were observed with confocal microscopy (Fig. 2.4) to assess biofilm populations. Note that biofilm nucleic acid fluorescence signals might not only indicate a single bacterium, but also extracellular DNA found throughout many biofilms[130]. To investigate biofilm compositional changes, extracellular proteins were stained with fluorescein isothiocyanate (FITC), lipids with Nile red and α- and β-polysaccharides with lectin concanavalin A conjugated with tetramethyl rhodamine and fluorescence brightener, respectively[64]. These polysaccharides (α, β) can also be visualized with FITC-conjugated lectin concanavalin A and wheat germ agglutinin[45]. Scanning and transmission electron microscopy was used for post-treatment ultrastructural observations of planktonic bacteria and biofilm morphology (10/27; 37%). Scanning electron microscopy (Fig. 2.5) was also used to complement confocal findings[65,66,95,111,124,129]. For transmission microscopy, sample preparation of biofilms required removal from culture plate; thus, the biofilms were mechanically scraped, which could alter cellular structure[67].

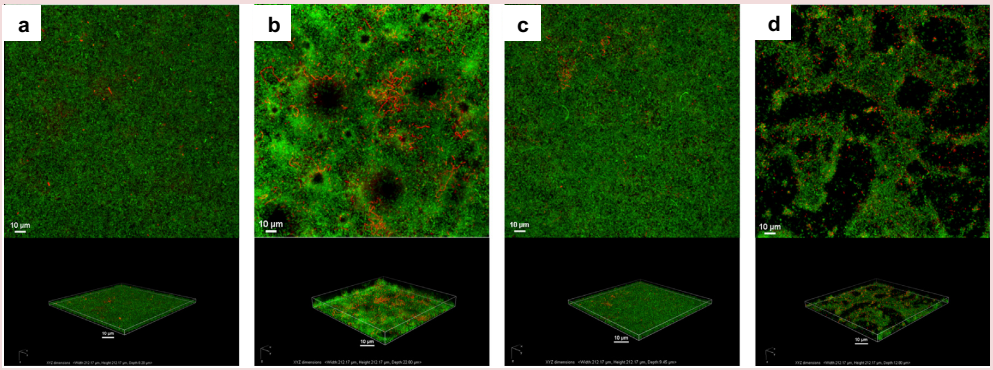

Figure 2.4. Confocal laser scanning micrographs of *in vitro*, propidium iodide (red)-stained, *Pseudomonas aeruginosa* PAO1:gfp-2 biofilms after treatment with (a) nothing (control); (b) ultrasound and Definity (microbubbles); (c) gentamicin (antibiotic) alone; and (d) gentamicin, ultrasound and Definity. Top: Top-down maximum intensity projection. Bottom: Corresponding 3-SD volume rendering. Ultrasound parameters were 0.5 MHz at 1.1 MPa peak negative pressure with a 16-cycle tone burst and pulse repetition frequency of 1 kHz for 5 min. Reprinted, with permission, from Ronan et al.[62].

Genetic testing was performed in 7 studies, using the polymerase chain reaction (PCR) method6[3,65,66,95,96,107-109,125]. PCR was used to investigate the impact of sonobactericide on (i) the expression of genes[65,66,95,125] and mRNA[109]; (ii) the successful incorporation of a gene[107,108]; and (iii) the status of genes up- and downstream after incorporation[108]. PCR was also used to quantify intracellular DNA released into the supernatant after treatment, which provided an indication of disrupted (lysed) cells[63]. With respect to its advantages, PCR is not technically demanding and is fast and highly sensitive. High sensitivity is also a disadvantage concerning contamination; in addition, the specific target of interest must already be known, and caution should be taken in interpreting the results because of the potential for extracellular DNA released from bacteria not triggered by lysis. Two studies investigating intracellularly infected mammalian cells evaluated cytotoxicity in response to therapy using a trypan blue exclusion test[92] and a lactate dehydrogenase assay[70].

Changes in biofilm metabolism, in response to different treatments, were measured by confocal imaging with 5-cyano-2,3-ditolyltetrazolium chloride dye[67], a CO_2-evolution monitoring system[62] or an absorbance-based resazurin assay[69,111]. Although investigation of cellular metabolism provides an indication of the overall bio-effect, the growth rate, biomass, cell viability and persister development could not be specified. Vollmer et al.[86] and Yi et al.[109] used bioluminescence as an indicator of bacterial cell stress responses and the distribution of stem cells in rats, respectively. Besides using fluorophore internalization, one group used a fluorescence polarization immunoassay to determine the amount of vancomycin eluted from bone cement after *in vitro* treatments[104]. An enzyme-linked immunosorbent assay was also used after treatments to determine levels of gentamicin[105] and inflammatory cytokines[109] in tissue. Both immunoassays are highly specific, even in samples with protein content such as serum[131,132], and are commercially available for various antibiotics on the market.

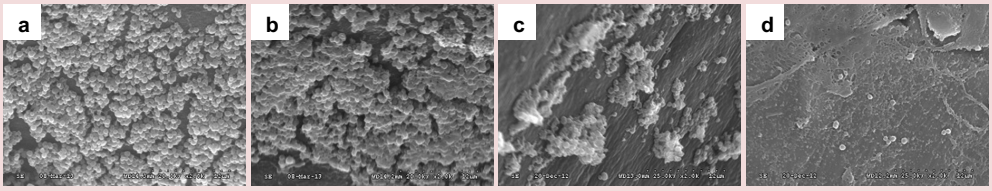

Figure 2.5. Scanning electron micrographs of *Staphylococcus epidermidis* biofilms from catheters subcutaneously implanted in rabbits following treatment with (a) nothing (control); (b) ultrasound and custom-made microbubbles; (c) vancomycin (antibiotic) alone; and (d) vancomycin, ultrasound and custom-made microbubbles. Original magnification: × 2000. Ultrasound parameters were 0.3 MHz and 0.5 W/cm2 (or 0.12 MPa) with a 50% duty cycle for a total of 20 min (5 min twice daily). Adapted, with permission, from Dong et al.[129].

Cavitation Nuclei for Sonobactericide

Cavitation nuclei are a key part of sonobactericide because their volumetric changes in response to an ultrasound field induce bio-effects. From the commercially available cavitation nuclei, SonoVue was used most often (8 studies, 30%). SonoVue (available as Lumason in the United States, approved by the U.S. Food and Drug Administration [FDA] in 2016) consists of SF_6 gas microbubbles (mean diameter: 1.5–2.5 μm, ≥99% of microbubbles ≤10 μm) stabilized by a lipid coating[133]. SonoVue/Lumason is approved for clinical diagnostic use in several countries worldwide[134]. Other commercially available lipid-coated microbubbles have also been used for sonobactericide studies, namely, Definity (4 studies, 15%, (octafluoropropane (C_3F_8) gas core; mean diameter 1.1–3.3 μm; 98% of microbubbles <10 μm) (Definity 2011) and Sonazoid (1 study, 4%, C_4F_{10} gas core; mean diameter 2.1 μm± 0.1; <0.1% of microbubbles larger than 7 μm)[135]. Definity and Sonazoid are approved for clinical diagnostic use in several countries worldwide[134]. Note that Albunex, used by Vollmer et al.[86], was the first commercially available ultrasound contrast agent (in 1992), with a mean microbubble diameter of 3.8 μm (98.8% of microbubbles <10 μm), an air core and a human albumin coating[136]. However, Albunex is no longer available[137]. Optison is another human albumin-coated microbubble (C_3F_8 gas core, mean diameter: 3.0–4.5 μm; 95% of microbubbles <10 μm; FDA approved in 2012) and approved for clinical use in the United States and Europe. Vollmer et al.[86] also used custom-made microbubbles (ST68, mean diameter: 3.8 μm, air core, coating mixture of surfactants Span 60 and Tween 80[138]) in their study.

The advantage of using commercially available cavitation nuclei is that their response to ultrasound has been thoroughly characterized[139-145]. In addition, these cavitation nuclei are sterile with minimal batch-to-batch variability. On the other hand, custom-made cavitation nuclei as used in 11 of the sonobactericide studies can offer advantages, such as targeting by incorporating a ligand in the coating and drug loading.

Although there are several types of targeted microbubbles for ultrasound molecular imaging and drug-loaded microbubbles for ultrasound-mediated drug delivery, or a combination thereof[35-37], so far only one study has employed microbubbles targeted to *S. aureus* biofilms *in vitro* using a monoclonal immunoglobulin antibody to protein A or

a lectin from *P. aeruginosa* for ultrasound molecular imaging[45]. These targeted microbubbles were found to bind to the biofilm matrix in proportion to the surface area.

A few studies have reported on drug-loaded microbubbles or droplets for treatment of bacterial biofilms. Horsley et al.[70] conjugated custom-made gentamicin-loaded liposomes onto microbubbles (ratio 1:5) using biotin–avidin bridging (mean diameter: 5.79 ± 1.53 μm). The microbubbles had a gas core of SF_6 and the lipid coating consisted of 1,2-distearoyl-*sn*-glycero-3-phosphocholine (DSPC), 1,2-distearoyl-*sn*-glycero-3-phosphoethanolamine-*N*-carboxy(poly-ethylene glycol) (DSPE-PEG(2000)), DSPE-PEG-biotin and 1,2-dipalmitoyl-*sn*-glycero-3-phosphoethanolamine-*N*-(lissamine rhodamine B sulfonyl) (ammonium salt) (Rod-PE) in a molar ratio of 79.5:10:10:0.5. The protein lysozyme was used as the drug and also formed the coating of microbubbles. One study custom-made these microbubbles with an air gas core (mean diameter of 4 ± 1 or 6 ± 2 μm, depending on the duration of protein denaturation: 15 and 2 min, respectively)[46,48], and another used C_3F_8 (mean diameter: 2.5–2.9 μm, depending on the sonication power)[94]. Lysozyme-coated microbubbles loaded with either spherical bovine serum albumin-coated gold nanoparticles (4.5 nm in diameter) or polyvinylpyrrolidone-coated gold nanoparticles (15 nm in diameter) were also produced by Cavalieri et al.[47]. Both types of gold nanoparticles had no effect on microbubble size distribution or stability. Mahalingam et al.[49] produced poly(vinyl alcohol)-lysozyme-coated microbubbles (10–250 μm, nitrogen gas core) loaded with gold nanoparticles (average diameter: ~10 nm). These microbubbles were more stable when they contained gold nanoparticles than without them, which is in contrast to what Cavalieri et al.[47] found. The difference in the type of coating or microbubble size could be the reason for the difference in stability.

Nanodroplets that can be phase-transitioned into microbubbles using ultrasound, a phenomenon known as acoustic droplet vaporization[146,147], have been loaded with the antibiotic vancomycin by Argenziano et al.[50]. The nanodroplets (average diameter ~300 nm) had a core of perfluoropentane and shell of lipid and dextran sulfate to which the vancomycin was coupled by electrostatic interaction. The authors sterilized their formulation using ultraviolet light. The nanodroplets (mean diameter: 309 nm) made by Guo et al.[111] consisted of a core of perfluoropentane and a coating of lipids. Microbubbles (mean diameter: 1.5 μm) containing a C_3F_8 gas core and coating of the same lipids were also produced.

Four groups produced custom microbubbles for co-administration with an antibiotic[92,124,125,129], an antibiotic encapsulated in a liposome[69] or stem cells[109,124,125,129] produced lipid-coated microbubbles with a gas core of C_3F_8 and diameter of 4–6 μm. The coating consisted of the lipids DSPC and 1,2-dipalmitoyl-*sn*-glycerol-3-phosphate-ethanolamine at a molar ratio of 66:34. The microbubbles were sterilized by ^{60}Co irradiation. Ikeda-Dantsuji et al.[92] produced microbubbles (~1 μm) encapsulating C_3F_8 gas and coated with DSPC and DSPE-PEG(2000), at a molar ratio of 94:6. Microbubbles (mean diameter: 2.39 ± 0.05 μm) with a coating of 1,2-dipalmitoyl-*sn*-glycero-3-phosphocholine, DSPE and cholesterol, mass ratio of 10:4:1 and a C_3F_8 gas core were produced by Fu et al.[69]. A thorough characterization of the response of these microbubbles to ultrasound was not reported in these publications. The lipid-coated microbubbles (1,2-dipalmitoyl-*sn*-glycero-3-phosphoglycerol, DSPC and PEG4000 at a mass ratio of 30:30:3000 w/w) with a C_3F_8 gas core (mean: 2 μm) made by Yi et al.[109] were compared with SonoVue for liver imaging[148]. Enhancement was similar but persisted longer (still present 6 min 30 s after injection) for these custom-made microbubbles.

In the study by Halford et al.[93], microbubbles were produced during ultrasound treatment (28–36 kHz) from a solution containing perfluorodecahydronaphthalene as oxygen carrier; 30% hydrogen peroxide, or H_2O_2, as oxidizer; and the non-ionic detergent surfactant Triton X-100 as shell stabilizer. The figure of the formed microbubbles indicates microbubble diameters on the order of 200 μm. Non-coated microbubbles were also produced during ultrasound treatment (130 kHz) in the study by Tandiono et al.[63]. In another study, non-coated microbubbles with a mean size of 5–10 μm were produced with a microbubble generator[64]. No specifics on the gas core and microbubble coating were provided.

The synergy between microbubbles and ultrasound exposure parameters is important for sonobactericide because the radial pulsation of microbubbles may increase the "footprint" of bactericidal action and reduce treatment times. The oscillation of each microbubble depends highly on its resonance behavior, that is, the ultrasound frequency at which the amplitude of oscillation is largest. In general, the resonance frequency is inversely related to the microbubble diameter, but the properties of the microbubble coating also play a role as rigid microbubble coatings increase the resonance frequency[36,149].

Interestingly, 78% (21/27) of sonobactericide studies used lipid-coated microbubbles (see Table 2.1). A small fraction of the commercially available microbubbles are resonant for a particular insonification scheme because of the polydisperse population[150]. Different ultrasound center frequencies were used for sonobactericide, including frequencies used in clinical diagnostic imaging (1 MHz, 13 studies, and 1.3 MHz, 1 study; see Table 2.1). At these frequencies, only a subpopulation of the microbubbles are expected to oscillate in resonant modes. The ultrasound frequency employed in the other studies was lower, namely, 500 kHz (1 study), on the order of 300 kHz (4 studies), 120–130 kHz (2 studies) or between 28 and 80 kHz (7 studies). For these very low ultrasound frequencies, only microbubbles substantially larger than 10 μm in diameter would have been at resonance. Gas from the microbubbles was likely liberated and coalesced and grew by rectified diffusion in the acoustic field until the microbubbles reached resonant size[151,152]. Another important consideration for microbubble oscillation is the viscosity of the surrounding medium and confinement because oscillations are damped when the viscosity increases or when microbubbles are confined[36]. For the *in vivo* studies, the microbubbles were confined in tissue as a result of injection into the area of the implanted catheter[129], dish[112], titanium plate[66] or tibial canal[104]. It appears that these studies did not consider the effect of attenuation of ultrasound by overlying tissue.

Experimental Outcomes

All sonobactericide studies have reported an enhanced effect beyond that of antibiotics alone. The goal of all of these studies was proof-of-principle and the approaches used generally differed. Directly comparing these 27 articles is difficult because of the large variability between them. Differences between the groups include the bacteria used and the different growth conditions, ultrasound parameters, cavitation nuclei and experimental setups. Nevertheless, this section aims to provide a discussion and make general comparisons between the experimental outcomes.

Ultrasound interacts with tissue by heating[153], radiation force[154] and cavitation-based mechanism[155,156]. Heating and radiation force could enhance the effect of antibiotics[157], increasing membrane permeability[158] and cell detachment, respectively. Cavitation is an important mechanism for sonobactericide. Stable cavitation involves gentle oscillations of microbubbles[159], and inertial cavitation denotes the rapid growth and rapid collapse of microbubbles[160]. The acoustic pressure required to initiate inertial cavitation can be higher than the pressure required for stable cavitation[159] and also depends on fluid properties and the cavitation nuclei[161]. Inertial cavitation forms microjets that can damage or deform the biofilms[53]. Administration of cavitation nuclei can reduce the cavitation threshold[159].

When microbubbles oscillate in an ultrasound field, fluid flow is generated around the microbubbles[149,162]. This phenomenon is known as microstreaming. The effects of microstreaming are prominent when the oscillating bubble is located near a boundary and when it is excited at resonance[149]. Microstreaming can cause bio-effects by promoting fluid transport and producing shear stresses on cells[163]. Microbubble destruction in response to ultrasound can occur through either acoustically driven diffusion or microbubble fragmentation[164]. Fragmentation in response to ultrasound exposure is typically associated with inertial cavitation[165] and can produce mechanical bio-effects.

Table 2.1 indicates that the majority of sonobactericide studies used one pressure amplitude, or acoustic intensity, and one center ultrasound frequency. Four studies tested multiple pressures/intensities[53,92,94,107], and one employed two frequencies[53].

Ikeda-Dantsuji et al.[92] reported that a higher ultrasound intensity (0.44 W/cm^2) further increased sonobactericide efficacy above that of doxycycline alone by approximately three times that of the lower intensity setting (0.15 W/cm^2). However, when another antibiotic (ceftizoxime), to which *C. trachomatis* is resistant, was employed, they found that the higher ultrasound intensity only slightly improved the therapeutic efficacy further. Liao et al.[94] found that higher-intensity insonification (2 and 3 W/cm^2) beyond 1 W/cm^2 did not further enhance sonobactericide. Han et al.[107] also found that as the acoustic pressure increased (0.25, 0.5, >0.9 MPa), delivery of their model drug into bacteria correspondingly increased.

Other ultrasound parameters were explored, such as PRF (0–100 Hz), duty cycle (5 and 50%), concentration of cavitation nuclei (0, 3.3, 10, 33% v/v) and exposure duration (0, 10, 90, 450 s)[107]. An increase in efficacy was seen with corresponding increased parameters, except PRF, which had no increased effect. As desired, bacterial viability was not affected among the parameters tested by Han et al.[107] for the creation of an recA-positive strain of *Fusobacterium nucleatum*. recA renders bacteria more sensitive to ultraviolet light and reportedly repairable sonoporation[107]. By using similar sonobactericide conditions also on planktonic, exponential growth phase, Gram–bacteria, albeit with *E. coli*, Vollmer et al.[86] observed bacterial death (up to 49.7 ± 6.2%) and activation of stress-response genes.

Goh et al.[53] used high-speed optical imaging to investigate the impact of cavitating microbubbles on biofilm surfaces. At 0.1 MPa (1 MHz, 50-μs pulse), microbubble oscillation was reported to be small, and caused minimal biofilm disruption. At a higher pressure (0.7 MPa, 1 MHz, 50-μs pulse), a 7.4-μm SonoVue microbubble had an extremely large radial excursion (R_{max} = 27.3 μm) with a liquid jet within that led to mechanical dislodgement of the bacteria from the biofilm. The direction of a jet with respect to the surface of the biofilm depends on the elasticity of the surface[166]. Accordingly, jet formation can create substantial shear force leading to either an indentation or an invagination of the surface[167,168]. Although Goh et al.[53] used two ultrasound frequencies (0.25 and 1 MHz), they applied each frequency in a different setup (biofilm horizontally or vertically positioned). Therefore, the effects of the different frequencies could not be compared. They found that ultrasound parameters

and the distance between the biofilm surface and the cavitating microbubbles affected the efficacy of biofilm disruption. Ultrasound alone did not disrupt the biofilm structure. As the initial distance between the microbubble and the biofilm increased, the disruption efficacy decreased. This observation provides support for the use of biofilm-targeted microbubbles to increase the efficacy of sonobactericide.

Ronan et al.[62] also described biofilm disruption, in the form of craters, after ultrasound and microbubble exposure without antibiotics (Fig. 2.4). If bacteria are forcibly released from biofilms by microbubble oscillations, as suggested by several studies including Ronan et al.[62] and Goh et al.[53], then the viability and status of these dispersed cells after treatment need to be assessed. Sonobactericide could be combined with current "traditional" or other new antimicrobials to reduce the spread of or eliminate altogether transitional dispersed cells that may be more virulent. Planktonic bacteria are often sensitive to antibiotics at much lower concentrations than are the same bacteria in biofilms[169]. Thus, liberation of bacteria into the bloodstream after sonobactericide is not necessarily anticipated to pose additional risks.

Inertial cavitation caused by ultrasound-mediated microbubble destruction can produce defects in the biofilm matrix, aiding the penetration of antibiotics[112]. Microbubbles and ultrasound exposure have been reported to increase the elution of an antibiotic from polymethylmethacrylate cement and increase the efficacy of bactericidal treatment *in vitro* and *in vivo*[104]. Ultrasound-mediated microbubble destruction can also increase the metabolic activity of the bacteria in the biofilm, making it responsive to treatment with antibiotics[67]. However, Ronan et al.[62] reported a decrease in biofilm metabolism, by analyzing carbon dioxide production, after either antibiotic alone or antibiotic combined with ultrasound and microbubbles. Because of the experimental setup, it could not be definitively determined if the decrease was from growth rate or biofilm mass reduction, and is speculated to be both. Although bacteria can develop resistance to antimicrobials over time through genetic alterations, ultrasound acts without allowing these organisms to adapt to the physical stresses[86]. Additionally, Zhou et al.[95] found *in vivo* that expression of the MecA gene responsible for encoding resistance to β-lactam antibiotics in MRSA was significantly reduced in the sonobactericide group with human β-defensin 3, more than twice that of the antimicrobial alone.

It has been postulated that bacterial cells could be more susceptible to sonobactericide because of their rigid cell membranes, which contrasts with the compliant phospholipid bilayers of mammalian cells that may resist rupture owing to ultrasound exposure[170]. When ultrasound is combined with cavitation nuclei and an antibiotic, sonobactericide efficacy can be enhanced, as illustrated by the *in vitro* and *in vivo* studies in this review. For example, *in vitro* studies reported by Dong et al.[124] utilized Sonovue and reduced colony-forming units of *S. epidermidis* eightfold relative to treatment with vancomycin and ultrasound (1-MHz frequency, 0.5-W/cm^2 intensity, 50% duty cycle, 5 min). In *in vivo* studies, findings of enhanced bacterial killing when sonobactericide included an antimicrobial were also reported; for example, Sugiyama et al.[105] observed an almost 1-log reduction in colony-forming units compared with all controls. Sonobactericide could produce equivalent therapeutic effects at a lower antibiotic dose, which may reduce complications associated with systemic toxicity, especially renal and liver complications. Sonobactericide may increase antibiotic (and other therapeutics) cytotoxicity; Horsley et al.[70] reported higher toxicity in human urothelial cells with ultrasound-exposed solutions of microbubbles coated with liposomes containing gentamicin at 2.64 and 5.28 μg/mL than free gentamicin at the much higher clinically approved dosage (200 μg/mL). This finding highlights that cytotoxicity should be more widely considered as a sonobactericide test parameter in future studies.

In addition to Han et al.[107], the microbubble dose dependence of sonobactericide has been investigated by three other groups that found an increase in the efficacy of sonobactericide with increasing concentration of microbubbles [92,124,125], indicating dose-dependent synergy. Only Han et al.[107] used more than two concentrations, with which a near-linear trend between microbubble concentration and treatment efficacy could be observed. A similar increase in bio-effects with increasing microbubble concentration has been reported for sonoporation of eukaryotic cells[171] and blood–brain barrier disruption[172]. Increasing the antibiotic concentration also resulted in an increasing dose–effect relationship for all treatments of *Acinetobacter baumannii*, including microbubbles combined with free polymyxin B and microbubbles combined with free chitosan-modified polymyxin B-loaded liposomes[69]. Horsley et al.[70] increased both antibiotic and microbubble concentrations, because gentamicin was encapsulated on liposomes bound to the microbubbles, which led to an enhanced reduction of bacterial load in infected urothelial cells.

The "in vial" concentration of Definity is 4.2×10^9 microbubbles/mL, that of Albunex 7×10^8 microbubbles/mL[173] and that of SonoVue/Lumason 3.0×10^8 to 1.1×10^9 microbubbles/mL. Assuming a blood volume of 5 L in an average human, the *in vivo* concentrations for Definity, Albunex and Lumason correspond to 8.4×10^5/mL, 1.4×10^5/mL and 6×10^4 to 2.2×10^5/mL, respectively. Several sonobactericide studies reported thus far have used high concentrations of microbubbles (10^7 to 10^8/mL) both *in vitro*[67,86,124,125] and *in vivo*[66,112,129], relative to the concentrations currently used in clinical diagnostic imaging. This approach could potentially be employed in non-vascular applications such as dental, skin wound and implant biofilms[66,112,129]. Furthermore, pre-clinical studies in both small animal and rodent models suggest that high concentrations of microbubbles administered intravenously, up to 250 times higher than the clinical dose, may be well tolerated[133]. Although *in vitro* studies have indicated that large microbubbles (~0.3 mm) can destroy biofilms under flow by microbubble collision[174,175], this mechanism is unlikely to occur for microbubbles of clinically relevant sizes for vascular applications (*i.e.,* 1–10 μm).

Five studies used custom-made lysozyme-coated microbubbles in the absence of ultrasound[46-49,51]. These exhibited antimicrobial properties on *Micrococcus lysodeikticus, S. aureus* and *E. coli.* Lysozyme-coated microbubbles, or poly(vinyl alcohol)-lysozyme-coated microbubbles, loaded with gold nanoparticles were found to have a stronger antimicrobial effect than non-loaded microbubbles on planktonic *Micrococcus lysodeikticus*[47] and *E. coli*[49]. The coated gold nanoparticles alone lacked lytic activity in the Cavalieri study, and thus the authors attributed the enhanced antimicrobial effect of the gold nanoparticles loaded on the lysozyme microbubbles to improved binding and, consequently, increased interaction of the bacteria with the surface of the lysozyme-microbubbles. Contrarily, gold nanoparticles alone had an antibacterial rate of ~50% at 3 h in the Mahalingam et al.[49] study. The difference in antibacterial activity of gold nanoparticles could be explained by the different bacteria employed. Combining these lysozyme-coated microbubbles with ultrasound could have further enhanced the antimicrobial properties as Liao et al.[94] observed when using them in their *in vitro* and *in vivo* study. Sonobactericide used against *P. acnes* had an enhanced antibacterial effect and resulted in a 1.45-fold reduction in inflammatory reactions relative to lysozyme-coated microbubbles alone. Furthermore, after 13 d of treatment, inflammation was no longer observed.

Vancomycin-loaded nanodroplets[50], in the absence of ultrasound, were significantly more effective at an earlier time point than vancomycin alone or non-loaded nanodroplets alone in killing planktonic MRSA (isolated from human ulcerated wounds). The authors attributed their findings to the time-sustained release of vancomycin from the loaded nanodroplets. However, the altered charge could also have played a role as vancomycin is positively charged and the vancomycin-loaded nanodroplets are negatively charged. Ultrasound exposure significantly enhanced vancomycin delivery from the loaded nanodroplets *ex vivo* through non-infected porcine skin, indicating the potential to treat skin infections[50].

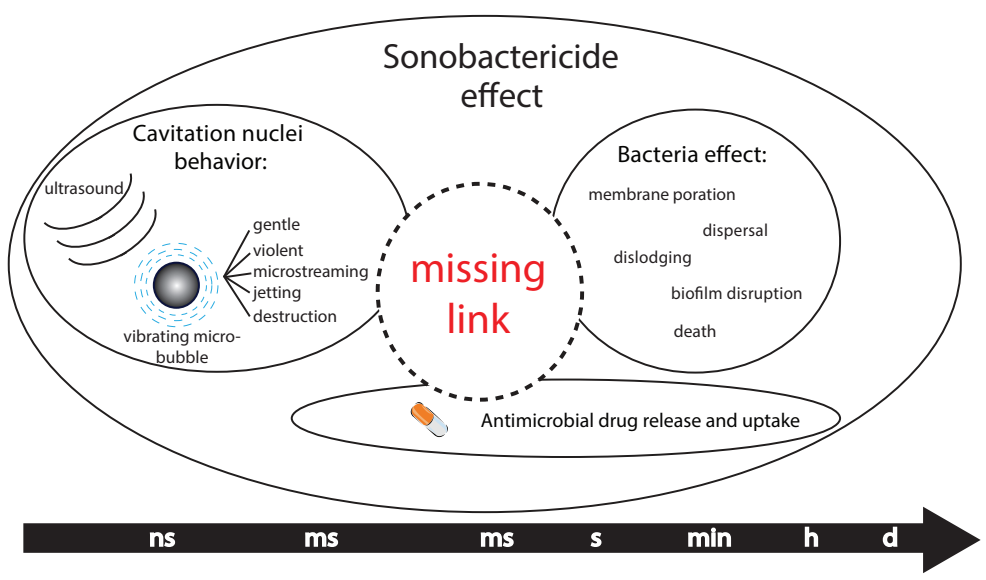

Figure 2.6. Different time scales of the therapeutic effects of sonobactericide.

Clinical Translation of Sonobactericide

Diagnostic ultrasound contrast examinations are performed worldwide[134, 176-178], including for the detection of the metastatic spread of bacterial infective endocarditis[179,180]. Fifteen of the 27 sonobactericide studies (56%) used microbubbles that are clinically approved, by the FDA and European Medicines Agency, which could help with the translation of sonobactericide into the clinic. Contrarily, sonobactericide with custom-made microbubbles containing Triton[93] is not translatable because this surfactant is toxic to cells[181,182]. The ideal characteristics of a clinically relevant treatment can be broadly described as improved patient outcomes, reduction in treatment times and practical implementation in the clinic. More specifically, broad-spectrum bactericidal activity, low risk for inducing resistance and minimal mammalian cell cytotoxicity could be considered. The reader is referred to two review articles that provide conceptional discussions on the ideal antibiotic that could aid sonobactericide strategies[183,184]. The use of clinically relevant animal models of biofilm would help translate the development of sonobactericide. For example, Lin et al.[104] used a periprosthetic infection rabbit tibia model. However, periprosthetic joint infection models have limited translational value as described in the review by Carli et al.[185]. While proposing criteria for an optimal animal model, this review stresses the critical importance of animal, pathogen, implant and outcome measurement selection and a method that replicates the "human" periprosthetic environment, wherein at least one of these areas current models fall short.

The choice of ultrasound insonification parameters is important for the clinical translation of sonobactericide. A wide frequency range (tens of kilohertz to 1.3 MHz) has been reported for sonobactericide (see Table 2.1), along with pulsed[70,86,104], continuous wave[65,69] or intermittent[64,68] ultrasound in sonification. More studies directly investigating different ultrasound parameters should be performed to better understand the effect they have on sonobactericide. The choice of frequency and exposure parameters needs to focus on safety, efficacy and compatibility with existing clinical workflows for rapid clinical translation. Several *in vitro* studies have been conducted in sonication baths at frequencies ranging from 20–80 kHz[65,128], which are likely not directly suitable for *in vivo* applications. Physiotherapy probes[66,67,112] and gene transfer equipment[69,124,125] have also been adapted for sonobactericide studies. Development of

of specialized probes may be necessary for treating biofilms that are not easily accessible or where a small geometric footprint may be needed. Ultrasonic energy may be delivered to infected areas either extracorporeally or using catheter-based ultrasound probes. Catheters have been reported previously for sonothrombolysis[186,187], and could be investigated for sonobactericide in vascular organs.

Microbubble concentration, type and route depend on the location of the biofilm being treated. Microbubbles can be delivered intravenously, intra-arterially or by direct injection into the site of interest[188]. When necessary, high concentrations can be achieved site-specifically by local infusion of microbubbles. On the other hand, delivering microbubbles to biofilm infections associated with prosthetic joints may be challenging because the biofilm is typically located within the joint space[189]. In the case of bacterial infective endocarditis, contact between the microbubbles and the biofilm may be hampered by rapid pulsatile blood flow. Targeting the microbubbles to the biofilm could further aid in therapeutic efficacy. Clinical phase 0 trials have successfully been completed for ultrasound molecular imaging of prostate, ovarian and breast cancer using targeted microbubbles[190,191], thereby paving the way for clinical use of targeted microbubbles. The *S. aureus* biofilm-targeted microbubbles developed by Anastasiadis et al.[45] lack clinical translation because the *P. aeruginosa* lectin used as ligand causes red blood cell agglutination[192], and the protein A antibody used as ligand must compete with host antibodies that cover protein A[193]. For other potential targeting possibilities, the reader is referred to the reviews by van Oosten et al.[194] and Koo et al.[195].

Conclusions and Future Perspectives

Therapeutic effects of sonobactericide can include direct bacterial killing, biofilm degradation and dispersal and increased or synergistic therapeutic effectiveness of antimicrobials or other drugs, all resulting from the physical phenomena of ultrasound combined with cavitation nuclei aided by the addition of an antimicrobial agent. It is the different time scales at which these actions occur that makes sonobactericide challenging, as illustrated in Figure 2.6. The time scale of the microbubble vibration is on the order of microseconds in a megahertz ultrasound field, which is many orders of magnitude smaller than the time scale of physiologic effects (milliseconds), let alone that of biological effects (seconds to minutes) and clinical relevance (days to months). The link between, and the mechanistic aspects of, cavitation nucleation, the effect on (intracellular) bacteria/biofilms and antimicrobial drug release and uptake need to be elucidated in future studies to efficiently treat bacterial infections.

The effect of the biofilm type on sonobactericide efficacy has received limited attention. For example, the age and composition of the biofilm[196] may contribute to its resilience to sonobactericide. The antibiotic penetration through biofilm decreases appreciably with the age of the biofilm[197]. Additionally, biofilms formed *in vivo* may differ in composition and morphology from *in vitro* biofilm models[84]. For example, recent research has indicated that infective endocarditis can be a polymicrobial infection[198]. These effects should be elucidated in future pre-clinical and clinical studies, as also addressed in other reviews[199,200].

Nanoscale cavitation nucleating agents such as nanodroplets and polymeric nanocups[201] could be interesting for sonobactericide as they could penetrate the biofilm and help nucleate cavitation throughout the biofilm. In particular, the process of droplet vaporization may exert mechanical forces on the biofilm in addition to antibiotic activity [111]. Nanodroplets can nucleate sustained cavitation in closed fluid spaces[202]. Polymeric nanocups nucleate inertial cavitation activity with thresholds inversely proportional to size. For example, nanocups with mean sizes of 180 and 600 nm have been reported to nucleate inertial cavitation at peak rarefactional pressures of 3 and 0.5 MPa, respectively[201]. These agents have not yet been investigated for treating biofilms. Despite the potential advantages offered by nanodroplets and nanocups, these agents are not

yet clinically approved or readily available. Therefore, sonobactericide using these agents may not be clinically feasible in the near future.

Recalcitrant biofilms may be treated with shock waves[203,204] or histotripsy[205,206]. Jetting from shock waves has been used in the clinic to destroy kidney stones and gallstones with lithotripsy[207]. Highly focused image-guided ultrasound beams can help concentrate acoustic energy at the biofilm site, while avoiding collateral damage. Histotripsy can be combined with a cavitation nucleation agent, such as phase-shift nanodroplets[208] and echogenic liposomes[209], to lower the acoustic pressure thresholds for ablation, which could potentially improve the safety profile of treatment. Another potential application to treat biofilm infections harnessing sound is an ultrasonically activated stream. Birkin et al.[210] reported that by applying low-amplitude ultrasound (135 kHz, 120–250 kPa) through a liquid stream directed at a surface, endogenous cavitation nuclei can be sufficiently activated at the solid/liquid interface to disrupt biofilm.

Combining ultrasound, cavitation nuclei and antibiotic therapy with matrix-degrading enzymes implicated in biofilm dispersal, such as glycosidases, proteases and deoxyribonucleases[65,66211], is a promising strategy for treating biofilms. Our group has recently reported the use of rtPA, a clinically approved fibrinolytic agent, along with Definity microbubbles, an antibiotic and 120-kHz intermittent ultrasound for sonobactericide in an *in vitro* flow model[68]. This strategy could be promising for treating biofilms that have fibrin as a primary structural component. The microstreaming produced by cavitation nuclei[36] can help remove biofilm degradation products and enhance the delivery of drugs, similar to sonothrombolysis studies[212]. Although the feasibility of biofilm dispersal has been reported in previous studies[211], more work needs to be done to elucidate the efficacy of combination therapy with matrix-degrading enzymes, ultrasound and microbubbles. Future research could also include the interference of quorum sensing, which is bacterial communication that regulates several virulence pathways through signaling molecules and increases with cell density[213]. Because of the high potential of this approach, many compounds are under development that could be combined with sonobactericide to enhance efficacy[214]. In addition, it is unknown if sonobactericide has an effect on quorum sensing without these agents.

The safety and efficacy of sonobactericide are paramount. Accurate characterization of the acoustic fields[122] and parameters used, standardization of protocols for the assessment of treatment efficacy and development of *in vitro* and pre-clinical models that mimic the *in vivo* milieu will help accelerate the transition of sonobactericide to the clinic. In addition, enabling image guidance methods, such as active[215] or passive cavitation imaging[216] and real-time feedback[217], may help monitor treatment progress, standardize the acoustic dose and aid in improving the safety and efficacy of *in situ* destruction of biofilms.

Acknowledgements

Financial support from the Erasmus MC Foundation (fellowship to K.K.) and U.S. National Institutes of Health, National Institute of Neurologic Disorders and Stroke, Grant R01 NS047603 (PI: C.K.H.) is gratefully acknowledged. The Erasmus MC Foundation is the funding agency for the fellowship to Klazina Kooiman.

“It’s not what you look at that matters, it’s what you see.

- Walden (Life in the Woods), Henry David Thoreau

3

Combined confocal microscope and Brandaris 128 ultra-high-speed camera

Inés Beekers, Kirby R. Lattwein, Joop J.P. Kouijzer, Simone A.G. Langeveld, Merel Vegter, Robert Beurskens, Frits Mastik, Rogier Verduyn Lunel, Emma Verver, Antonius F.W. van der Steen, Nico de Jong, and Klazina Kooiman

Based on:
Ultrasound in Medicine & Biology, vol. 45, no. 9, pp. 2575-2582, 2019

Abstract

Controlling microbubble-mediated drug delivery requires the underlying biological and physical mechanisms to be unraveled. To image both microbubble oscillation upon ultrasound insonification and the resulting cellular response, we developed an optical imaging system that can achieve the necessary nanosecond temporal and nanometer spatial resolutions. We coupled the Brandaris 128 ultra-high-speed camera (up to 25 million frames per second) to a custom-built Nikon A1R+ confocal microscope. The unique capabilities of this combined system are demonstrated with three experiments showing microbubble oscillation leading to either endothelial drug delivery, bacterial biofilm disruption, or structural changes in the microbubble coating. In conclusion, using this state-of-the-art optical imaging system, microbubble-mediated drug delivery can be studied with high temporal resolution to resolve microbubble oscillation and high spatial resolution and detector sensitivity to discern cellular response. Combining these two imaging technologies will substantially advance our knowledge on microbubble behavior and its role in drug delivery.

Introduction

To successfully treat diseases, administered drugs need to overcome barriers in the human body that hinder efficient delivery. Currently, high dosages are required because only a fraction of the therapeutic actually reaches the target site. This leads to high toxicity levels in healthy tissue, causing undesirable side effects[218,219]. However, lipid-coated gas microbubbles (1–10 μm) in combination with ultrasound can locally enhance drug delivery, allowing for therapeutics to be delivered efficiently and only to the intended target site. When ultrasound is applied, microbubbles oscillate and thereby permeabilize cell membranes (sonoporation), open intercellular junctions, and stimulate endocytosis[36,220,221]. The underlying physical and biological mechanisms enhancing these different pathways are poorly understood. Elucidating the microbubble–cell interaction is fundamentally important for controlling and optimizing drug delivery, and therefore, microbubble oscillation behavior and the cellular response should be studied simultaneously.

To resolve the microbubble oscillation in an ultrasound field of clinically relevant frequencies (MHz), a system with nanosecond temporal resolution is required. Currently, there are two ultra-high-speed cameras that can achieve such high frame rates, up to 25 million frames per second (Mfps) with sufficient consecutive frames: the Brandaris 128[222] and the UPMC Cam[223]. Both cameras have been coupled to an upright microscope (BXFM, Olympus, Tokyo, Japan) for brightfield and widefield fluorescence microscopy. This enables the concurrent visualization of microbubble oscillation and cellular response. Although these systems have been used to study vascular drug delivery[224-227], imaging resolution showing the cellular response was very poor. Microbubble oscillation leading to bacterial biofilm disruption has been observed at a lower temporal resolution using a 3 Mfps camera[53]. With the use of high-speed cameras, it has been possible to study the microbubble–cell interaction; however, the cellular response was still imaged with poor sensitivity and at a low optical and temporal resolution.

Confocal microscopy allows us to better unravel cellular response, as it provides nanometer spatial resolution, 3-D imaging with high axial resolution, and good detector sensitivity for different fluorescent cell labeling. Live confocal microscopy imaging of

microbubble-mediated drug delivery has revealed a wide-range of cellular effects: pore formation[228] and recovery[229], opening of intercellular junctions[224], endocytosis[230], lipoplex[231] and doxorubicin[232] delivery, changes in reactive oxygen species levels[233], increased bacterial metabolism[67], sonoprinting[234], cytoskeleton disruption[235], and intercalation of model drugs[236]. However, all these studies lack information on the specific microbubble behavior that was responsible for the observed cellular effect, because of the relatively low frame rates of confocal microscopy imaging (<500 fps).

Microbubble response to ultrasound varies a lot, and even equal-sized microbubbles in the same ultrasound field do not respond identically[237-239]. We need to gain more insight into microbubble behavior to achieve a more predicable response to ultrasound. To understand how the response is affected by microbubble composition, we want to image both the microbubble oscillation behavior and the coating microstructure[240]. In the past, it has only been possible to image coating microstructure in a static setup, without ultrasound, using, for example, 4Pi high-resolution confocal microscopy[241].

To date, the technological gap has made it impossible to image microbubble oscillation (high temporal resolution) and detailed cellular response (high spatial resolution) in the same field of view of a single sample. To overcome this challenge, we developed a novel optical imaging system by coupling an upright custom-built Nikon confocal microscope to the Brandaris 128 ultra-high-speed camera (Fig. 3.1), which is described in this technical note.

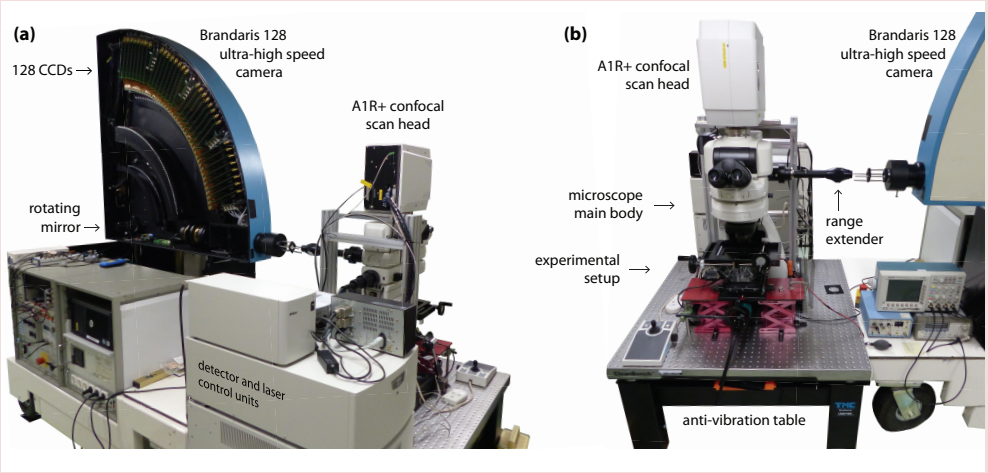

Figure 3.1. Combined confocal microscope and Brandaris 128 ultra-high-speed camera. (a) From the back of the system, the inside of the Brandaris 128 casing with the rotating mirror and 128 charge-coupled devices (CCDs) is seen. (b) At the front of the system are the confocal microscope and the experimental setup. The range extender facilitates the coupling of the Brandaris 128 to the confocal microscope.

Materials and Methods

The Brandaris 128 ultra-high-speed camera is a programmable camera with 128 sensitive charge-coupled devices (CCDs) and a fast rotating mirror that sweeps the image over the CCDs, resulting in a minimum interframe time of 40 ns (25 Mfps)[222]. Consecutive 128-frame recordings can be done at an 80 ms interval, with a maximum of 50 consecutive recordings[242]. The brightfield image is 500 × 292 pixels with 8-bit gray-scale values and a typical resolution of 400 nm[222].

The main body of the confocal microscope is a custom-built upright Eclipse Ni-E microscope (Nikon Instruments, Amsterdam, The Netherlands). By physically removing the conventional base of the main body, the microscope was customized to accommodate the water bath for ultrasound insonification. Microscope modules were chosen to meet our requirements such that the light path (Fig. 3.2) could be directed toward the four different output ports: (i) a binocular (NI-TT-E Motorized Quadrocular Tilting Tube, Nikon Instruments), (ii) a color camera (DS-Fi3, Nikon Instruments) for digital acquisition of brightfield and widefield fluorescence images, (iii) the A1R+ confocal scan head, and (iv) the Brandaris 128 ultra-high-speed camera.

Two motorized turret modules (NI-FLT6-E Mot Epi-fluorescent turret, Nikon Instruments) were incorporated to rotate the desired filters or mirrors into the light path. One turret holds a full mirror to direct the light path toward the Brandaris 128 camera (Fig. 3.2, *turret A*). The other turret is used for switching between filter cubes for widefield fluorescence imaging (Fig. 3.2, *turret B*). The four installed filter cubes have the following excitation (Ex), dichroic mirror (DM), and emission (Em) filters: BFP-A with Ex390/18, DM416, and Em460/60; GFP-A with Ex469/35, DM497, and Em525/39; TRITC-A with Ex542/20, DM570, and Em620/52; and Cy5-4040 C with Ex628/40, DM660, and Em692/40 (center wavelength/bandwidth in nanometers; Semrock Inc., Rochester, NY, USA). Widefield fluorescence is performed with a metal halide light source with motorized shutters and neutral density filters (C-HGFIE, Fiber Illuminator Intensilight, Nikon Instruments). During confocal imaging, excitation is achieved with a laser unit (LU-N4, Nikon Instruments) equipped with four lasers (405, 488, 561, and 640 nm; all 15 mW at the output of the fiber tip). The system has a hybrid detector unit (A1-DUG, GaAsP Multi Detector Unit, Nikon Instruments) that includes

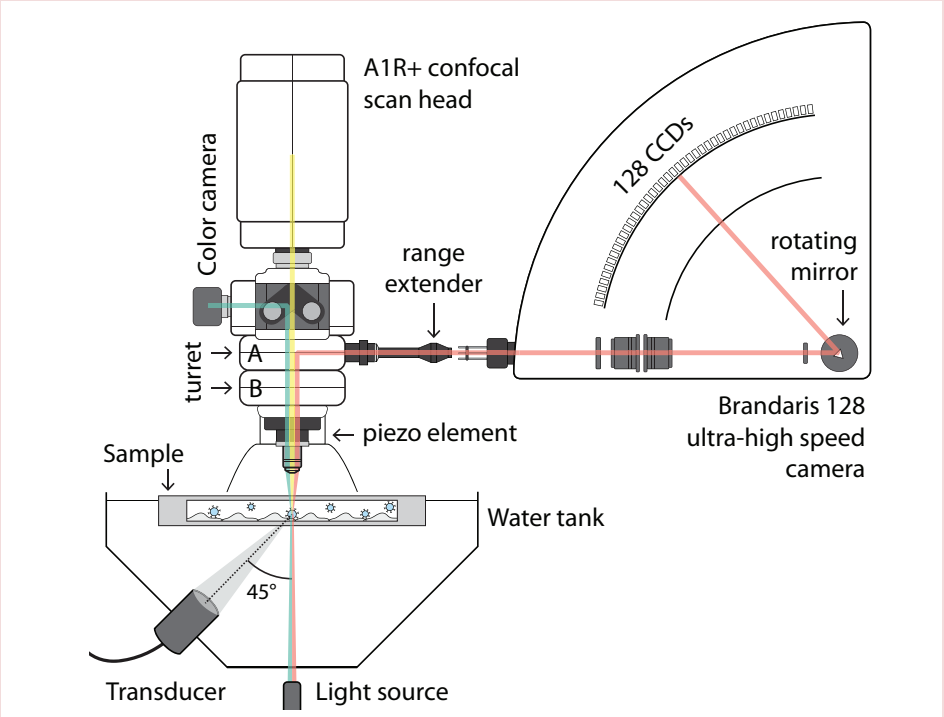

Figure 3.2. Schematic of the light paths to the different imaging output ports (not to scale). The light path goes through the sample, the objective, and the main body of the microscope toward either the color camera (*green*), the confocal scan head (*yellow*) or the Brandaris 128 ultra-high-speed camera (*red*). The light source is used for brightfield and Brandaris 128 imaging. The motorized turret A can place the full mirror in the light path for Brandaris 128 imaging, while turret B can insert the desired filter cubes for widefield fluorescence imaging. The sample can be insonified from below under a 45° angle in a water tank, which can be heated to 37°C. CCDs = charge-coupled devices.

two gallium arsenide phosphide (GaAsP) photomultiplier tubes (PMTs) and two standard multi-alkali PMTs. The GaAsP PMTs are highly efficient in detecting the 525/50 and 595/50 nm ranges in comparison to the standard multi-alkali PMTs. To create four detection channels, the emitted light is split using three filter cubes. The first filter cube (DM FF495-Di03, Semrock Inc.; Em filter ET450/50 m, Chroma, Bellows Falls, VT, USA) delimits the 450/50 nm channel which is detected by a standard multi-alkali PMT. The second filter cube (DM T560 LPXR, Chroma; Em filter ET525/50 m,

Chroma) delimits the 525/50 nm channel, which is detected by a GaAsP PMT. The third filter cube (DM T640 LPXR, Chroma; Em filter ET595/50 m, Chroma; Em ET700/75 m, Chroma) delimits the 595/50 and 700/75 nm channels, which are detected with a GaAsP PMT and a standard multi-alkali PMT, respectively.

For high-precision focusing and 3-D z-stack imaging, the microscope's main body combines two z-scanning devices. First, long ranges (12 mm) can be scanned with the main body's motorized z functionality, which was retained despite the customization. Next, with a piezo element (MCL NANO-F200 N, Mad City Labs Inc., Madison, WI, USA), faster and more precise z-focusing can be performed in a 200 μm range, resulting in improved z-stack imaging. To isolate vibration, the confocal microscope was installed on an active anti-vibration optical table (74-9090 M Cleanbench top and 12M-424-88 micro-g modular post mount support, Physik Instrumente, Karlsruhe, Germany).

The field of view of the Brandaris 128 camera had to overlap with that of the microscope. Therefore, the Brandaris 128 camera's casing had to be aligned and coupled to the output port of the microscope's main body. This was achieved by fixing a laser pointer on the casing of the Brandaris 128 to project onto a target on the microscope body. Further, to reproduce alignment, the position of both systems with respect to the room was documented using a laser distance measuring tool (GLM 40, Bosch, Stuttgart, Germany). A second requirement was parfocality; that is, the Brandaris 128 and the confocal need to have the same focal plane. To that end, a range extender (XT2 Collimating Emission-Port Adaptor, Photometrics, Tucson, AZ, USA) was inserted in the light path between the output port of the microscope and the Brandaris 128 input port.

When fast switching between confocal imaging and Brandaris 128 acquisition is desired, a Multifunction I/O Device (USB-6000, National Instruments, Austin, TX, USA) can trigger the motorized turret to rotate the full mirror into the light path, temporarily intercepting time-lapse confocal imaging to acquire with the Brandaris 128 camera instead. The trigger is given when the rotating mirror in the Brandaris 128 reaches a desired rotation speed. Once the Brandaris 128 acquisition is complete, another trigger is given to remove the mirror from the light path, such that confocal imaging is restored. The confocal recording is intercepted at least for the duration of consecutive Brandaris

128 recordings and the mechanical turret rotation time of 300 ms. The trigger events and turbine speeds are registered in the confocal recording for correct data registration.

The capabilities of the combined Brandaris 128 and confocal microscopy imaging system are demonstrated with three *in vitro* experiments: endothelial drug delivery, bacterial biofilm disruption, and microbubble coating microstructure alterations. The microbubbles used in the experiments were all in-house produced by probe sonication as previously described[241]. Briefly, the main lipid of the coating was 1,2-distearoyl-*sn*-glycero-3-phosphocholine and the microbubbles had a C_4F_{10} gas core. All images were acquired with a 100 × objective (CFI Plan 100XC W, Nikon Instruments) that is chromatic aberration-free infinity (CFI), corrected for field curvature (Plan) and water dipping (W). This objective has a numerical aperture of 1.10; therefore, the resolution achieved with confocal microscopy is 250 nm. The confocal scan speed varies from 0.03–1 fps per acquisition channel, depending on the chosen pixel dwell time. By decreasing the field of view, we can image up to 5 fps. From the Brandaris 128 ultra-high-speed recordings, the microbubble radius as function of time was determined using custom-designed image analysis software[243]. During the endothelial drug delivery and biofilm disruption experiments, the sample was inserted in the water tank at 37°C (Fig. 3.2) and insonified with a single-element focused transducer (2.25 MHz center frequency, 76.2 mm focal length, –6 dB beam width at 2 MHz of 3 mm; V305, Panametrics-NDT, Olympus, Waltham, MA, USA). When the microbubble coating was studied, the sample was inserted in the water tank at room temperature and insonified with a single-element broadband transducer (1 to 9 MHz bandwidth, 25 mm focal distance, –6 dB beam width at 1 MHz of 1.3 mm; PA275, Precision Acoustics, Dorchester, U.K.).

Results

In the first experiment, the response of human umbilical vein endothelial cells to $\alpha_v\beta_3$-targeted microbubbles upon ultrasound insonification was imaged. Acquisition started with confocal microscopy time-lapse imaging (0.65 fps, CFI Plan 100 × W objective), revealing the initial state of the cells and the location of the microbubble (Fig. 3.3a). Next, the light path was automatically switched toward the Brandaris 128 to record microbubble oscillation during ultrasound insonification (2 MHz, 250 kPa peak-negative-pressure [PNP], single 10-cycle burst) (Fig. 3.3b). This temporarily intercepted confocal microscopy imaging until the Brandaris 128 recording finished and the light path was switched back. Confocal microscopy imaging proceeded for 3.5 min after ultrasound, monitoring the cellular response (Fig. 3.3c). Uptake of propidium iodide was observed locally around the microbubble (Fig. 3.3c, 00:30–00:44), followed by diffusion throughout the cytoplasm and into the nucleus (Fig. 3.3c, 02:25). Moreover, confocal microscopy imaging revealed opening of the intercellular junctions (Fig. 3.3c, 02:25–03:50, *arrows*).

The second experiment started with confocal microscopy time-lapse imaging (0.32 fps, CFI Plan 100 × W objective) of a *Staphylococcus aureus* biofilm. This revealed vancomycin-targeted microbubbles adhered to bacteria (Fig. 3.4a). Confocal time-lapse imaging was temporarily intercepted to record microbubble oscillation with the Brandaris 128 upon ultrasound insonification (2 MHz, 250 kPa PNP, single 10,000-cycle burst). After the Brandaris 128 recording, the light path was switched back and confocal imaging continued for 40 s. Confocal microscopy imaging after insonification revealed microbubbles had clustered (Fig. 3.4c). Moreover, bacteria detached in the area where microbubbles were originally located, revealing microbubble-mediated disruption of the biofilm (Fig. 3.4c, 0:22, *arrows*). Toward the end of the confocal recording, partial redisposition of bacteria was observed (Fig. 3.4c, 00:57).

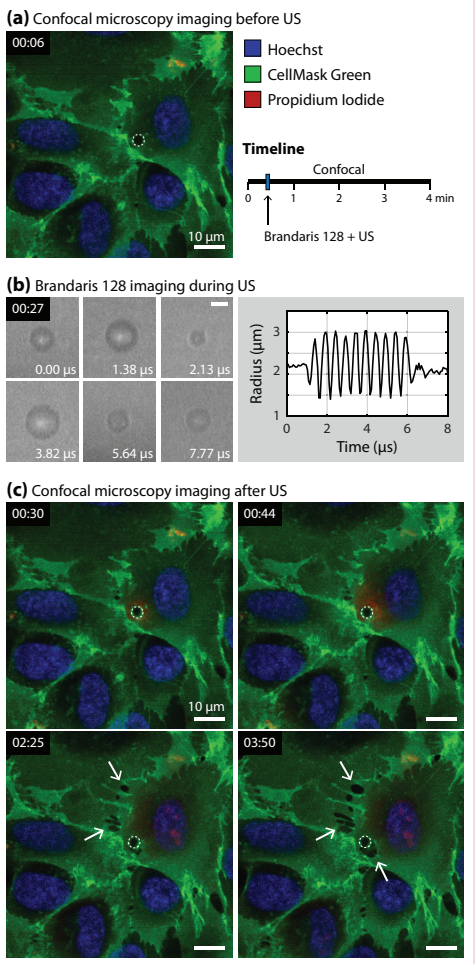

Figure 3.3. Selected frames from time-lapse imaging of microbubble-mediated endothelial drug delivery. Human umbilical vein endothelial cells (Lonza, Verviers, Belgium) were grown in MV2 medium (PromoCell GmbH, Heidelberg, Germany) to confluency for 2 d in a CLINIcell (50 μm membrane; Mabio, Turcoing, France). The cell nuclei were stained with Hoechst (5 µg/mL; Thermo Fisher Scientific, Waltham, MA, USA), cell membranes with CellMask Green (4 μg/ml; Thermo Fisher Scientific), and sonoporation with propidium iodide (25 μg/ml; Sigma-Aldrich, St. Louis, MO, USA). The *dashed line* delineates the microbubble. (a) Confocal microscopy before ultrasound (US) to image initial cell state. (b) Microbubble oscillation recorded with the Brandaris 128 ultra-high-speed camera (bar=3 μm) and the microbubble radius as a function of time determined from this recording. (c) Confocal microscopy after US to image cellular response. The *arrows* indicate opening of intercellular junctions.

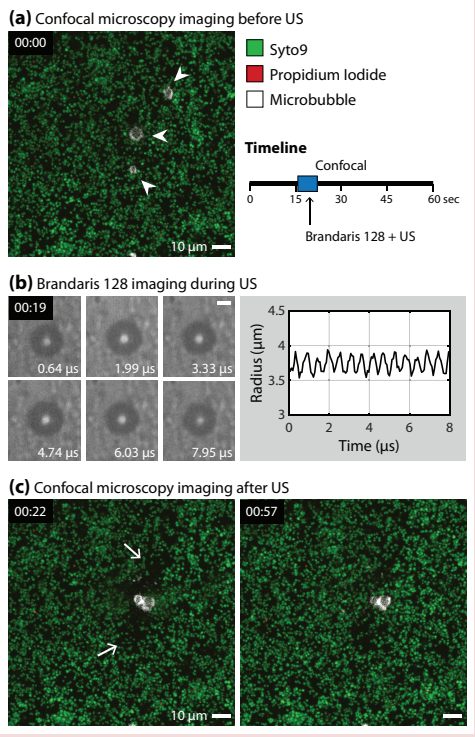

Figure 3.4. Selected frames from time-lapse imaging of microbubble-mediated biofilm disruption. A clinical isolate of *Staphylococcus aureus* (SA25268) was grown in IMDM medium (Thermo Fisher Scientific) for 24 h in an ibiTreat μ-slide (0.8 mm channel height; I Luer; Ibidi GmbH, Martinsried, Germany). The live bacteria were stained with Syto9 (4 µg/ml; Thermo Fisher Scientific), the dead bacteria with propidium iodide (25 µg/ml; Sigma-Aldrich), and the microbubble shell with DiD (Thermo Fisher Scientific). (a) Confocal microscopy before ultrasound (US) to image the initial biofilm and microbubbles (*arrowheads*). (b) The oscillation of the microbubble located in the center of (a) was recorded with the Brandaris 128 ultra-high-speed camera (bar=3 μm). The microbubble radius as a function of time was extracted from this recording. (c) Confocal microscopy after US to image biofilm disruption (*arrows*).

The third experiment aimed to image the microbubble coating microstructures before and after ultrasound insonification. Before ultrasound, a *z*-stack was acquired (0.4 μm step size, 31 slices, CFI Plan 100 × W objective) of a microbubble that also contained rhodamine-B-1,2-dihexadecanoyl-*sn*-glycero-3-phosphoethanolamine, triethylammonium salt (rhodamine-DHPE). The 3-D image (Fig. 3.5a) revealed that the lipid expanded phase, as stained by the rhodamine-DHPE[244], was distributed in a characteristic honeycomb pattern. Next, Brandaris 128 ultra-high-speed imaging revealed microbubble oscillation (Fig. 3.5b) upon ultrasound insonification (1.4 MHz, 50 kPa PNP, single 8-cycle burst). After ultrasound, another *z*-stack was acquired revealing structural changes in the microbubble coating (Fig. 3.5c, *arrows*).

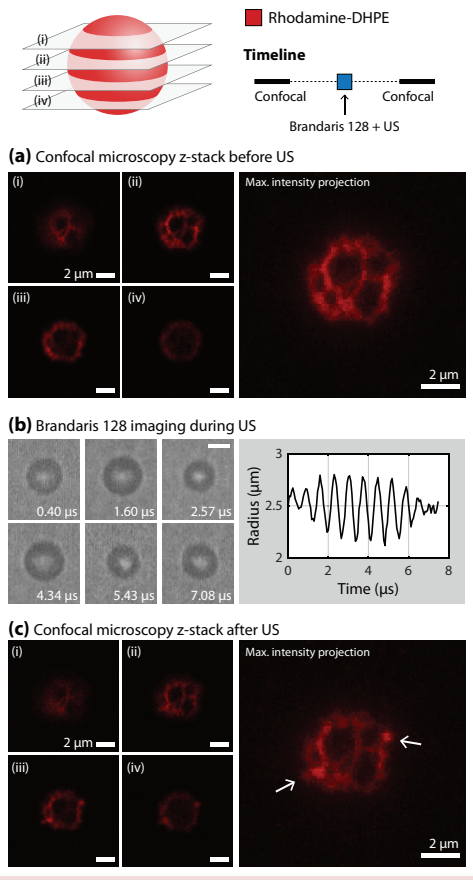

Figure 3.5. Imaging of structural changes in microbubble coating. The lipid-expanded phase was stained with rhodamine-DHPE (0.01 mol%; Thermo Fisher Scientific). Microbubbles were studied in a CLINIcell (50 μm membrane; Mabio). (a) Selected z-slices from 3-D confocal microscopy (i-iv) and the maximum intensity projection before ultrasound (US). (b) Selected frames of the Brandaris 128 ultra-high-speed recording revealing microbubble oscillation (bar=3 μm) and the resulting microbubble radius as a function of time. (c) Selected z-slices (i-iv) and maximum intensity projection after US. The *arrows* indicate a focal area of increased fluorescence intensity (*i.e.*, hot spot) suggestive of local microbubble shell buckling.

Discussion

The novel combined confocal microscope and Brandaris 128 ultra-high-speed camera make it possible to study both the cell and microbubble structures with nanometer spatial resolution and the microbubble oscillation with nanosecond temporal resolution, as demonstrated with the three experiments. With this unique device we were able for the first time to relate microbubble oscillation behavior to alterations in cell integrity and microbubble coating microstructures.

Microbubble-mediated endothelial drug delivery (Fig. 3.3) monitored with confocal microscopy provides better detector sensitivity and higher frame rates than the widefield microscope originally coupled to the Brandaris 128. As a result, low and fast changes of local propidium iodide uptake caused by sonoporation can now be detected. This is essential when studying safe drug delivery because low uptakes have been associated with reversible sonoporation and cell viability[245]. Moreover, specific fluorescent cell dyes can now be imaged with high resolution, revealing previously concealed cellular responses. For example, we were able to observe the opening of intercellular junctions using a cell membrane dye (Fig. 3.3c).

The advantage of high-resolution confocal microscopy is also demonstrated when imaging biofilm disruption by oscillating microbubbles (Fig. 3.4). Because of the small size of bacteria (~1 μm in diameter), they cannot be well resolved with widefield microscopy. The added value of this new optical system is that we can now distinguish individual bacteria and observe effects on biofilms caused by oscillating microbubbles, while also gaining insight into how microbubbles vibrate nearby a biofilm. Furthermore, the light path switching is quick enough to observe the disruption of the biofilm before redisposition of bacteria occurs (Fig. 3.4c). However, this data set also reveals a drawback of the Brandaris 128 ultra-high-speed camera recordings. Because a maximum of 128 frames can be acquired, it is only possible to partially image the 10,000-cycle microbubble oscillation. Therefore, in this Brandaris 128 acquisition, the microbubble clustering was not observed (Fig. 3.4b) and could only be inferred from the confocal microscopy after ultrasound (Fig. 3.4c).

The developed optical imaging system will be essential not only in understanding ultrasound-mediated drug delivery, but also in designing ultrasound contrast agents. We can finally image how microbubble oscillation behavior affects the structural organization of the coating and vice versa. Although 4Pi microscopy has higher axial resolution and overcomes the signal loss toward the part of the microbubble furthest away from the objective (Fig. 3.5, iv), because of the laser diffraction by the microbubble's gas core, we were able to discern the coating microstructures with the confocal microscope (Fig. 3.5). To date, lipid shedding and buckling of the phospholipid shell caused by microbubble oscillation has been observed only using widefield fluorescence microscopy, at 150,000 fps[246] or 5 Mfps[247]. However, because of the poor axial resolution of widefield microscopy, structural details of the phospholipid shell could not be resolved.

Simultaneous Brandaris 128 and confocal microscopy imaging is not possible with the combined system. This technical limitation remains as the Brandaris 128 requires 100% of the light path to overcome the CCD detection limits. Automatic switching between confocal and Brandaris 128 imaging minimizes the time during which confocal microscopy imaging is interrupted. It is difficult to precisely predict the start of a Brandaris 128 acquisition, as the acceleration of the turbine is variable. Therefore, confocal microscopy is often interrupted about 2 s before the Brandaris 128 recording starts. During this time no change is expected in the confocal image, because insonification has not taken place yet. As soon as the Brandaris 128 acquisition has completed, during which ultrasound was applied, the full mirror is rotated out of the light path. As a result, the confocal microscope can restore imaging to detect rapid cellular effects with a maximum delay of 300 ms plus the time to scan a confocal frame (which depends on the confocal scan speed chosen). For the endothelial drug delivery example, this corresponded to <1.8 s, and for the biofilm disruption example, this was <3.4 s.

The confocal microscope can image a larger field of view than the Brandaris 128 ultra-high-speed camera. For instance, with the CFI Plan 100 × W objective, the field of view of the confocal microscope is 128×128 μm and that of the Brandaris 128 is 45×32 μm. Hence, as seen in Figure 3.4, sometimes microbubbles are observed in the field of view

of the confocal microscope, but their oscillation cannot be recorded with the Brandaris 128. Finally, adapting the microscope's main body by removing the conventional base disabled the automatic refocusing capability. Regardless, a desired focus depth can be manually restored because the software is still able to read out the *z*-position of the objective.

Conclusion

A state-of-the-art optical imaging system was developed by coupling a custom-built confocal microscope to the Brandaris 128 ultra-high-speed camera. Microbubble-mediated drug delivery can now be studied at both high spatial and temporal resolution to evaluate cellular response upon microbubble oscillation. Additionally, changes in microbubble coating structure caused by oscillation behavior can be discerned. With this novel optical imaging system we expect to further elucidate microbubble-mediated drug delivery and advance the development of ultrasound contrast agents.

Acknowledgements

This work was supported in part by the Applied and Engineering Sciences TTW (Veni-Project 13669), a part of NWO; the Erasmus MC Foundation; the Phospholipid Research Center, Heidelberg, Germany; and the Thoraxcenter of Erasmus MC. The authors thank Gert van Cappellen and Adriaan Houtsmuller from the Erasmus MC Optical Imaging Center; Willem J. B. van Wamel from the Department of Medical Microbiology and Infectious Diseases, Erasmus MC; and Alessandra Scarpellini from Nikon Instruments Europe for the fruitful discussions.

“ *Try not.*

Do. Or do not.

There is no try.

- Star Wars Episode V,
  Yoda (George Lucas)

4

Paracetamol modulates biofilm formation in Staphylococcus aureus clonal complex 8 strains

Kirby R. Lattwein*, Andi R. Sultan*, Nicole A. Lemmens-den Toom, Susan V. Snijders, Klazina Kooiman, Annelies Verbon, and Willem J.B. van Wamel

*Both authors contributed equally

Scientific Reports, vol. 11, 5114, 2021

Abstract

Staphylococcus aureus biofilms are a major problem in modern healthcare due to their resistance to immune system defenses and antibiotic treatments. Certain analgesic agents are able to modulate *S. aureus* biofilm formation, but currently no evidence exists if paracetamol, often combined with antibiotic treatment, also has this effect. Therefore, we aimed to investigate if paracetamol can modulate *S. aureus* biofilm formation. Considering that certain regulatory pathways for biofilm formation and virulence factor production by *S. aureus* are linked, we further investigated the effect of paracetamol on immune modulator production. The *in vitro* biofilm mass of 21 *S. aureus* strains from 9 genetic backgrounds was measured in the presence of paracetamol. Based on biofilm mass quantity, we further investigated paracetamol-induced biofilm alterations using a bacterial viability assay combined with N-Acetylglucosamine staining. Isothermal microcalorimetry was used to monitor the effect of paracetamol on bacterial metabolism within biofilms and green fluorescent protein (GFP) promoter fusion technology for transcription of staphylococcal complement inhibitor (SCIN). Clinically relevant concentrations of paracetamol enhanced biofilm formation particularly among strains belonging to clonal complex 8 (CC8), but had minimal effect on *S. aureus* planktonic growth. The increase of biofilm mass can be attributed to the marked increase of N-Acetylglucosamine containing components of the extracellular matrix, presumably polysaccharide intercellular adhesion. Biofilms of RN6390A (CC8) showed a significant increase in the immune modulator SCIN transcription during co-incubation with low concentrations of paracetamol. Our data indicate that paracetamol can enhance biofilm formation. The clinical relevance needs to be further investigated.

Introduction

Healthcare-related infections caused by biofilms formed by *Staphylococcus aureus* have a high mortality (up to 66%) and includes severe chronic infections, such as osteomyelitis and infective endocarditis, and those related to in-dwelling medical devices[7,248-251]. The unfavorable outcome of biofilm-associated infections has been attributed to the decreased susceptibility of *S. aureus* to antibiotics and host defenses[7,252-256]. Furthermore, it is known that mature *S. aureus* biofilms produce numerous virulence factors that enhance pathogenicity[7,248], such as staphylococcal complement inhibitor (SCIN), Protein A, and thermonuclease, already during the early stages of biofilm formation[257,258]. Biofilm development of *S. aureus* depends on its genetic background[259] and is highly affected by environmental conditions, including the substrate to which the biofilm is attached to[7,248,259-261] and growth media composition[257,261,262].

It has been shown that some compounds and drugs that are often paired with antibiotics can modulate *S. aureus* responses that further reduces antibiotic susceptibility[263,264]. Nonsteroidal anti-inflammatory drugs, like acetylsalicylic acid (aspirin) and ibuprofen, can increase the inhibitory concentration of fusidic acid, an anti-staphylococcal drug[263]. Many other antibiotics used to treat *S. aureus* infections, such as beta-lactams and vancomycin, may actually promote biofilm formation[252-255]. Furthermore, non-antibiotic drugs like acetylsalicylic acid can even modulate biofilm generation[264-265]. Paracetamol, another antipyretic drug, is frequently used before and during early infection symptoms and is often given concomitantly with antibiotic treatment once infection has been confirmed. The mechanism of paracetamol remains uncertain on the molecular level and is different from acetylsalicylic acid in that it does not induce anti-inflammatory effects. Until now, it has not been investigated if paracetamol has an influence on biofilm formation and development.

Clinical isolates of *S. aureus* consist of various genetic backgrounds with an unequal worldwide distribution[266]. One of the prominent clonal clusters, clonal complex 8 (CC8), causes a significant proportion of *S. aureus* infections in certain regions[266]. For example, methicillin-resistant USA300 is the most prevalent strain in the United states, while ST-239 is mainly found in Asia, Australia, Eastern Europe, and South America[266]. Considering that the *S. aureus* regulator pathway for biofilm formation and virulence

factor production are correlated[267,268], we also studied the impact of paracetamol on the transcription of staphylococcal complement inhibitor (SCIN) protein. SCIN is a potent immune modulator which is able to inhibit host complement activation pathways during the early stages of biofilm formation[257]. Since paracetamol is frequently being used in the early stages of infection when biofilms are formed[257], we studied the effect of paracetamol exposure on *S. aureus* biofilm formation using 21 strains from 9 genetic backgrounds, which includes the clinically relevant CC8 strains ST239 and USA300. In addition, the impact of paracetamol on the transcription of SCIN protein was determined.

Materials and Methods

Bacterial strains and growth conditions

The *S. aureus* strains used in this study are listed in Table 4.1. Strains were plated on blood agar (5% sheep blood; BD, Trypticase™, Thermo Fisher Scientific, Bleiswijk, the Netherlands) and incubated overnight at 37 °C. The green fluorescent protein (GFP) construct containing strains were plated on tryptic soy agar (TSA) supplemented with 10 μg/mL chloramphenicol (Oxoid Limited, Basingstoke, UK).

The effect of paracetamol on planktonic bacteria

To determine the effect of paracetamol (Sigma Aldrich, Zwijndrecht, the Netherlands) on bacterial growth, a broth microdilution method was performed for all strains[269,270]. One hundred microliter of a 1:100 dilution (optical density (OD) of0.50 (±0.05) at 600 nm in NaCl 0.9%) of each strain in Iscove's Modified Dulbecco's Medium (IMDM) (Gibco®, Thermo Fisher Scientific) was added to 100 μL of culture media containing paracetamol for final concentrations of 0.5, 1, 2, 4, 8, 16, and 32 μg/mL. After 24 h incubation at 37 °C in sterile round-bottom 96-well polystyrene tissue culture plates (Costar no. 3799; Corning Inc., Corning, NY), the optical densities (OD_{600nm}) were read in a microplate reader (Epoch 2 Microplate reader, BioTek Instruments, Inc., Winooski, VT, USA).

Biofilm formation mass assessment

In vitro biofilms were generated from both wild type and GFP-containing strains (Table 4.1) by the method described previously[257]. Biofilm formation was assessed using a dynamic, microtiter plate biofilm formation assay as previously described by Christensen *et al.*[248,257,271,272], with slight modifications. Briefly, for each strain or isolate, 5 mL of NaCl 0.9% was inoculated with overnight grown *S. aureus* (at 37 °C on blood agar) until an OD_{600nm} of 0.50 (±0.05) was reached. Thereafter, 10 μL was dispensed into a sterile flat-bottom 96-well polystyrene tissue culture plates (Costar no. 3596; Corning Inc., Corning, NY) containing a serial dilution (0.5, 1, 2, 4, 8, 16, and 32 μg/mL) of paracetamol in 190 μL of IMDM. The plates were incubated at 37°C for 24 h with continuous shaking at 150 rpm. Bacterial growth was then measured using a microplate reader (BMG technologies, Ortenberg, Germany) at OD_{600nm}. Afterwards, the visible

Table 4.1. *S. aureus* strains used in this study

Strain	Genetic background	Description	Source / Ref
Mup903	CC1	Commensal strain	[291]
Mup3648	CC1	Commensal strain	[291]
Mup2778	CC5	Clinical strain	[291]
Mup3904	CC5	Clinical strain	[291]
Mup568	CC15	Clinical strain	[291]
Mup1675	CC15	Clinical strain	[291]
M82	CC20	Clinical strain	[257]
Mup2091	CC30	Clinical strain	[291]
Mup3534	CC30	Clinical strain	[291]
Mup1173	CC45	Clinical strain	[291]
Mup2396	CC45	Clinical strain	[291]
B-DYK 25337	CC223	Clinical strain	Erasmus MC
Mup2704	CC8, ST72	Clinical strain	[291]
Mup4423	CC8, ST72	Commensal strain	[291]
M116	CC8, ST239	Clinical strain	[257]
RWW337	CC8, ST239	Clinical strain	[292]
RWW338	CC8, ST239	Clinical strain	[292]
SAC042W	CC8, USA300	SAC042W, Clinical strain	[293]
8325-4	CC8	Laboratory strain	[294]
RN6390	CC8	Laboratory strain	[295]
Newman	CC8	Laboratory strain	[296]
scn-GFP (+)	CC8	scn promoter (pSK236GFP in RN6390)	[297]
PrP-GFP (+)	CC8	Page repressor promoter (pACL1484 in RN6390)	[274]

biofilms which had formed in the wells were washed once with 200 μL of sterile phosphate-buffered saline (PBS) containing 1% BSA and 0.05% azide. Biofilms were then air dried and stained with 50 μL of 1% crystal violet in distilled water for 2 min. Excess crystal violet was removed by washing the plates with distilled water for five times. The stained biofilm was then dissolved in 200 μL of extraction solution (50% dH_2O, 40% EtOH, 10% acetyl acid) and the absorbance of crystal violet measured at OD_{490nm} in the Epoch 2 microplate reader.

Fluorescence staining of biofilm

For visualization of the cellular and extracellular matrix components, biofilms were stained using a LIVE/DEAD® BacLight Bacterial Viability Kit (Thermo Fisher Scientific) and Wheat Germ Agglutinin (WGA) - Alexa Fluor® 350 conjugate (Invitrogen BV, Breda, the Netherlands), according to the manufacturer's protocol with slight modification. Biofilms grown for 4 h were washed once with 200 μL of IMDM. Then 50 μL of IMDM, 50 μL of 15 µM propidium iodide (PI), 50 μL of 2.5 µM SYTO9, and 0.5 μL of 1 mg/mL WGA-Alexa fluor® 350 conjugate was added to each well and the plate incubated at 22 °C on an orbital shaker (300 rpm) in the dark for 35 min. The biofilms were then imaged using an Olympus IX51 fluorescence microscope (Olympus Nederland B.V., Zoeterwoude, the Netherlands) with 20- and 40-times magnification. For confocal microscopy, a custom-built Nikon A1R + confocal microscope[273] (Nikon Instruments Europe, Amsterdam, the Netherlands) was used with a 60-times water immersion lens (CFI NIR Apo 60X W, Nikon Instruments). For imaging, WGA-Alexa fluor® 350 conjugate was excited at 405 nm, detected at 450/50 nm (center wavelength/bandwidth), SYTO 9 was excited at 488 nm, detected at 525/50 nm, and PI was excited at 561 nm, detected at 595/50 nm. Biofilms imaged with the confocal microscope were grown in CLINIcell culture chambers (CLINIcell25–50-T, REF 00106, MABIO, Tourcoing, France) in 12 mL using the same biofilm formation and fluorescence staining methods with volumes proportionally adjusted according to manufacturer protocol.

Bacterial metabolism rate measurement

The effect of paracetamol on bacterial metabolism was monitored with a microcalorimeter according to the previously described protocol[258]. Briefly, overnight

cultures of *S. aureus* on blood agar at 37 °C were suspended in 5 mL NaCl 0.9% until OD_{600nm} of 0.50 (±0.5) was reached. Then 10 μL of this suspension was mixed with 9990 μL IMDM to create a 1:1000 dilution. Ten μL of the diluted suspension was added into sterile plastic "insert" tubes (designed for the microcalorimeter) containing 190 μL of different concentrations (0.5 – 32 mg/mL) of paracetamol in IMDM. These tubes were then placed into sealed platinum tubes and placed inside a multi-channel microcalorimeter (calScreener™SymCel, Sverige AB, Sweden) for 24 h at 37 °C to determine real-time bacterial metabolic activity.

Measurement of immune modulator SCIN transcription

To study the effect of paracetamol on the transcription of the immune modulator SCIN during biofilm formation, RN6390 carrying a *scn* (SCIN) promotor GFP construct and RN6390 carrying a plasmid that constitutively produces GFP as a positive control (phage repressor promoter-GFP fusion construct) were used as previously described by Rooijakkers *et al.*[274] (Table 4.1). *In vitro* biofilms were generated from both GFP-containing strains (Table 4.1) by the method described previously[257]. After an hour of incubation at 37 °C, the growth medium was replaced with 200 μL of fresh IMDM medium containing paracetamol (serial dilution 0.5 – 32 μg/μL). The biofilms were then incubated in a FLUOstar Optima microplate fluorescence reader (BMG Lab Technologies, Chicago, IL, USA) at 37 °C with 150 rpm periodic rotational shaking. The accumulation of fluorescence, used as a measure for gene transcription, was determined (excitation at 485nm, emission at 520nm, and gain setting 1738) automatically every five min during the 4th and 5th hours of biofilm formation. Median fluorescence intensities (MFI) of the *scn* promoter-GFP strain co-incubated with paracetamol were compared to the MFI of the strain incubated without paracetamol.

Data analysis

Statistical analysis was performed with GraphPad Prism (GraphPad Software Inc., Version 5.01, San Diego, CA, USA) and Microsoft Excel 2010. Data were analyzed with an unpaired t-test or one-way ANOVA; a P-value ≤ 0.05 was considered as statistically significant. All experiments were independently repeated at least three times and data are presented as mean (SEM) or as median with range.

Results

Clinically relevant doses of paracetamol have limited effect on *S. aureus* planktonic growth

Since the concentration of paracetamol in human serum is normally below 30 μg/mL[275,276], we overnight co-incubated *S. aureus* with 0.5, 1, 2, 4, 8, 16, and 32 μg/mL of paracetamol. We found that these clinically relevant concentrations of paracetamol had no significant effect on planktonic growth of *S. aureus* strains, except for some of the strains having a CC8 genetic background (Fig. 4.1). Results in these CC8 strains were variable: the growth rate of strain 8325-4 was higher in the presence of higher doses of paracetamol, while RN6390 and Newman had lower growth rates at higher concentrations.

Low doses of paracetamol increase biofilm formation of CC8 genetic cluster strains

To study the effect of paracetamol on biofilm formation, a biofilm quantification assay was performed on all strains following overnight incubation with paracetamol using the same concentrations as used in the planktonic growth experiments. In 15 of the 21 strains, an increase in biofilm mass could be demonstrated (Fig. 4.2). Of particular note, this phenomenon was primarily observed in *S. aureus* strains belonging to CC8 (2774 (ST72), M116 (ST239), RWW337 (ST239), RWW338 (ST239), SAC042W (USA300), 8325-4, RN6390, and Newman), and less visible in non-CC8 strains (CC1 (903), CC5 (2778, 3904), CC15 (1675), CC30 (2091, 3534), and CC223) when exposed to doses of paracetamol less than 32 μg/mL. Not every paracetamol concentration below 32 μg/mL always led to a clear increase in biofilm mass. For example, the mean value of strain M116 (ST239) indicates biofilm mass increased at 0.5 – 4 µg/mL and 16 µg/mL, whereas at 8 µg/mL biofilm mass was unaffected.Conversely at these doses, other strains of various backgrounds were observed with mainly reductions in biofilm and as low as obtaining only 63% (mean) of the control biofilm mass for 8 μg/mL paracetamol (strain 3648 (CC1); Fig. 4.2e).

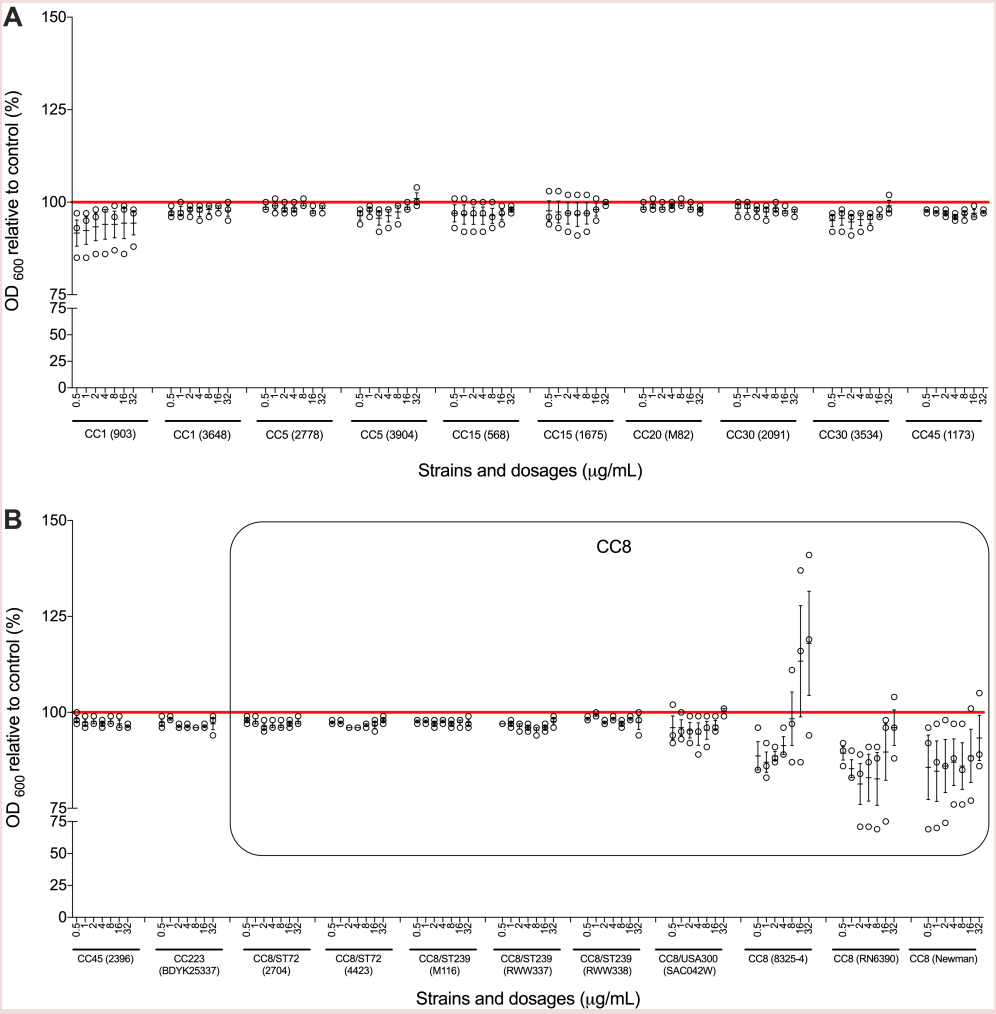

Figure 4.1. Broth microdilution susceptibility tests were performed on all study strains. (A) Strains with genetic backgrounds of CC1, CC5, CC15, CC20, CC30 and CC45. (B) Strains with genetic backgrounds of CC45, CC72, CC223 and CC8. The results are depicted as the percentage of paracetamol treated *S. aureus* MICs relative to its control (untreated). The red horizontal line represents the control. The black box outlines CC8 strains. Each black circle represents one experiment. Data points are presented with SEM of all three separate experiments performed for each dilution.

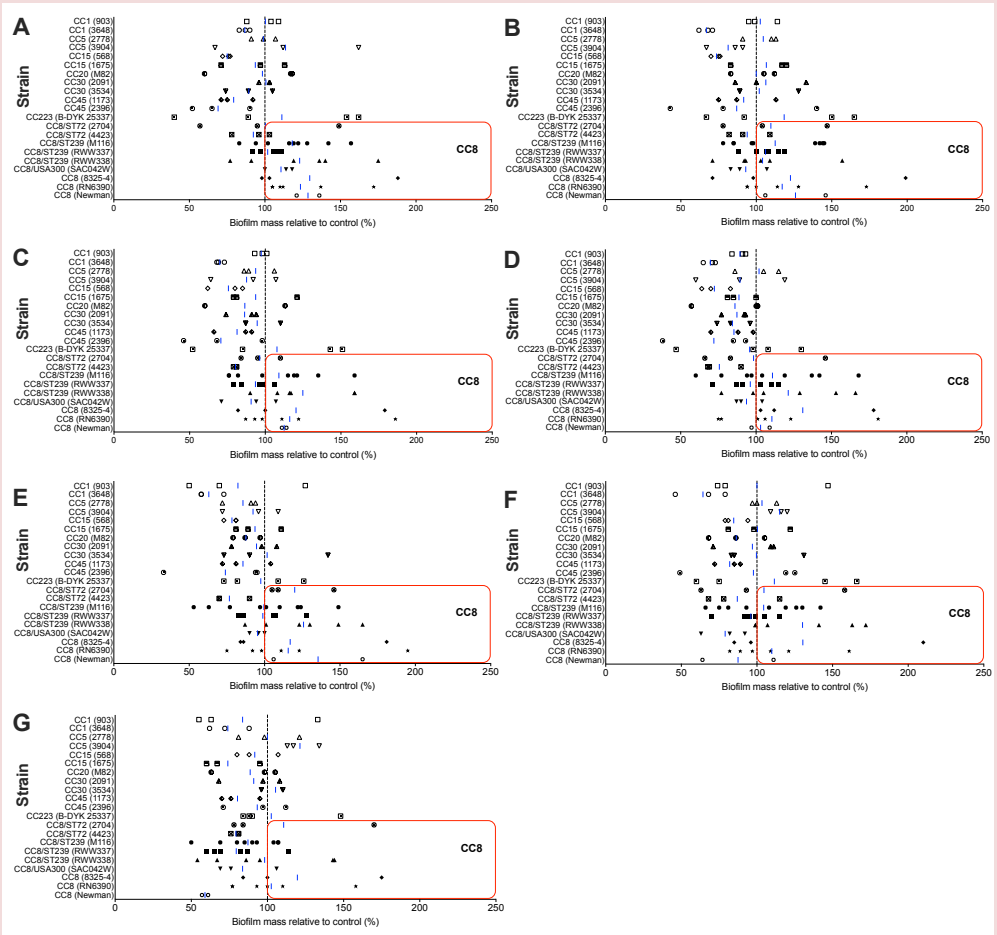

Figure 4.2. *Staphylococcus aureus* biofilm mass changes in response to various concentrations of paracetamol. Paracetamol stimulates and reduces biofilm formation at clinical doses in strains with different genetic backgrounds, most notably those belonging to CC8 including ST239. Biofilms were grown and co-incubated with 0.5 (A), 1 (B), 2 (C), 4 (D), 8 (E), 16 (F), and 32 (G) µg/mL of paracetamol. Red boxes outline the biofilm mass increase of CC8 strains above control mass. Data from at least three separate experiments are presented as aligned dot plots with a blue line indicating the mean value.

Paracetamol did not significantly alter the metabolism rate of biofilm-associated *S. aureus*

To determine if the paracetamol-associated increase in biofilm formation was only due to an increase in the number of bacterial cells, we studied the metabolic rate of *S. aureus* biofilms (CC20 strain M82 and CC8 strains: M116, RN6390, and Newman) when exposed to different concentrations of paracetamol. The addition of paracetamol did not change the heat flow by *S. aureus* during 24 h biofilm formation for all strains tested (Fig. 4.3). Some minor, non-significant deviations included a delayed heat curve at 4 μg/mL in strain M82 (CC20) (Fig. 4.3a) and reduced heat flow at the highest therapeutic concentration (32 μg/mL) in strain RN6390 (CC8) (Fig. 4.3c). These data indicate that although the biomass of biofilms of CC8 strains generally increased when exposed to paracetamol, an increase of bacterial cells is unlikely to be the cause.

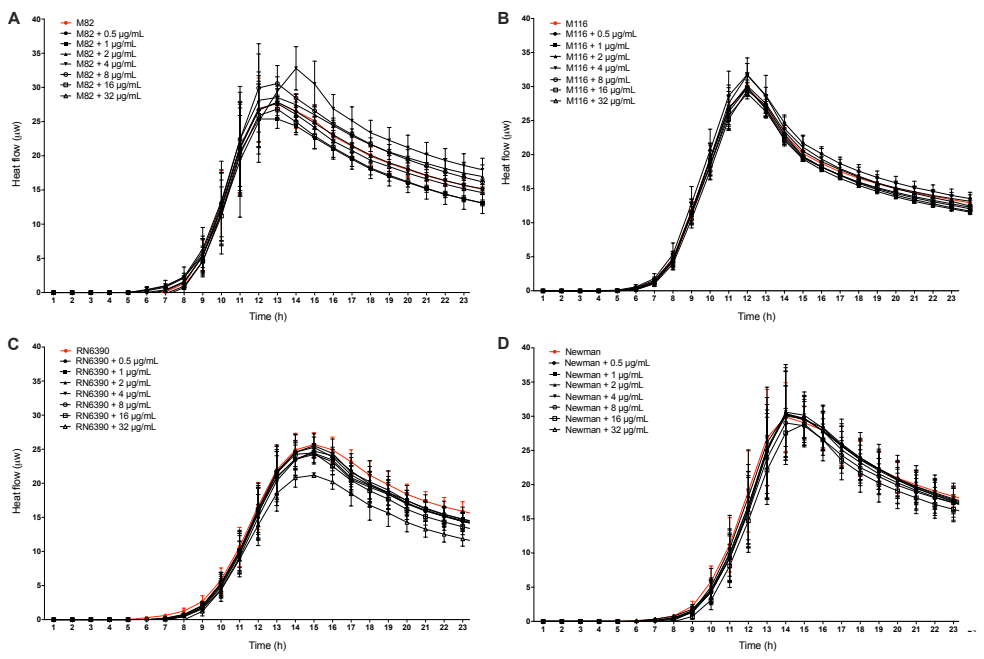

Figure 4.3. The metabolic rate of biofilms in the presence of different dosages of paracetamol. Metabolic heat flow generated during overnight biofilm formation at 37°C and co-incubation without (red line) or with 0.5-32 μg/mL paracetamol of *S. aureus* CC20 strain M82 (A) and CC8 strains; M116 (B), RN6390 (C), and Newman (D) were monitored with isothermal microcalorimetry in real-time. Data from three separate experiments are presented as mean value and SEM.

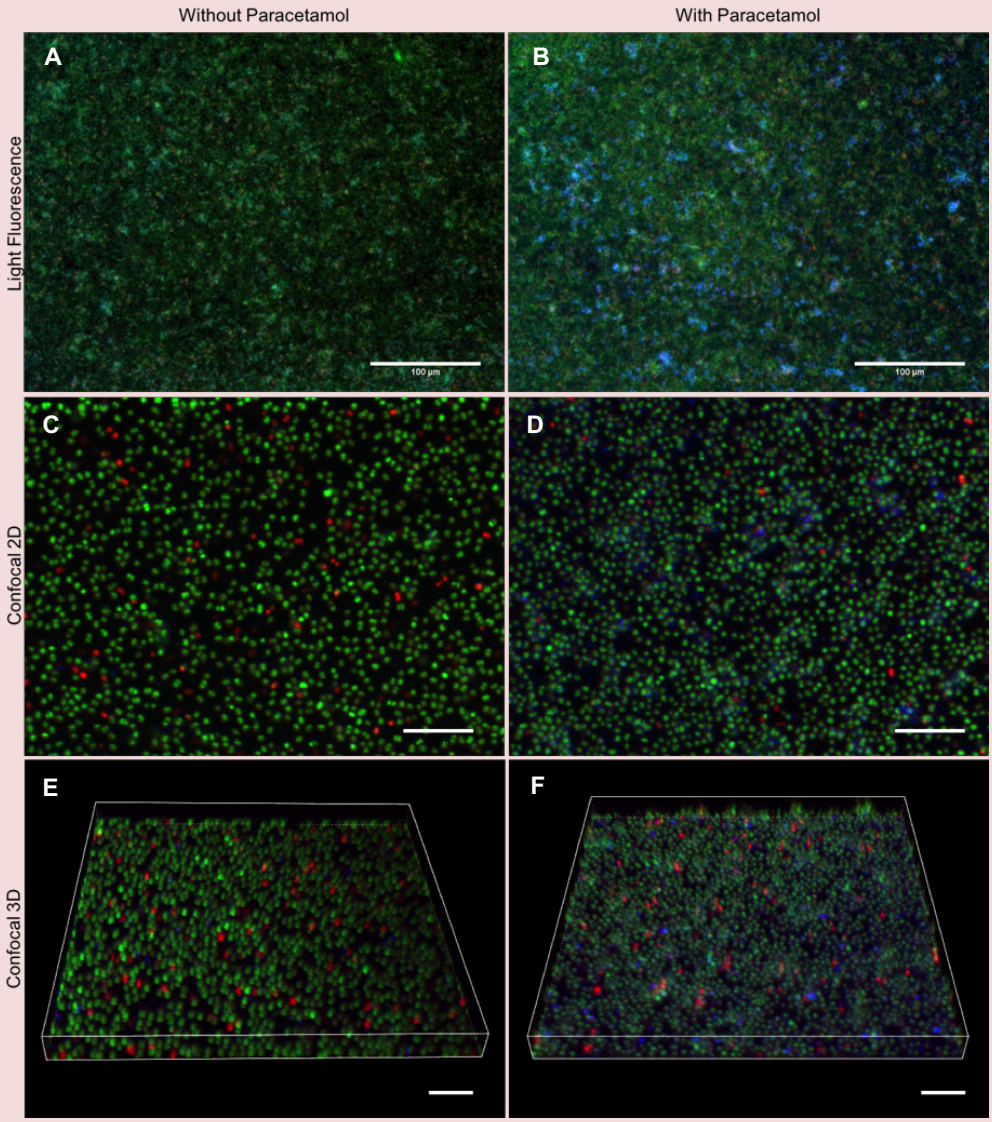

Figure 4.4. The effect of paracetamol on staphylococcal biofilm matrix composition. Biofilms of *S. aureus* strain M116 (CC8, ST239) were grown 37°C without (A, C, E) and with (B, D, F) paracetamol (2 µg/ml). Fluorescent images of stained biofilms were captured using inverted light fluorescence microscopy (A, B) and confocal laser scanning microscopy (C-F) with corresponding three-dimensional volume rendering (E,F). For all images, green fluorescence (SYTO 9 stained) are live bacteria, red fluorescence (PI stained) are dead bacteria and/or eDNA, and blue fluorescence (WGA stained) are N-Acetylglucosamine. All images are representative of three separate experiments.

Paracetamol modulates polysaccharide expression during biofilm formation

An explanation for the increase of biofilm mass could be an increase in non-cellular components, such as extracellular DNA (eDNA), proteins and/or polysaccharides7,277-281. To investigate this hypothesis, we co-incubated *S. aureus* strain M116 (CC8) biofilms with 2 µg/mL of paracetamol overnight and studied the biofilms using light fluorescence and confocal microscopy (Fig. 4.4). Paracetamol-exposed biofilms had an increase of N-Acetyl glucosamine content in their extracellular matrix (Fig. 4.4).

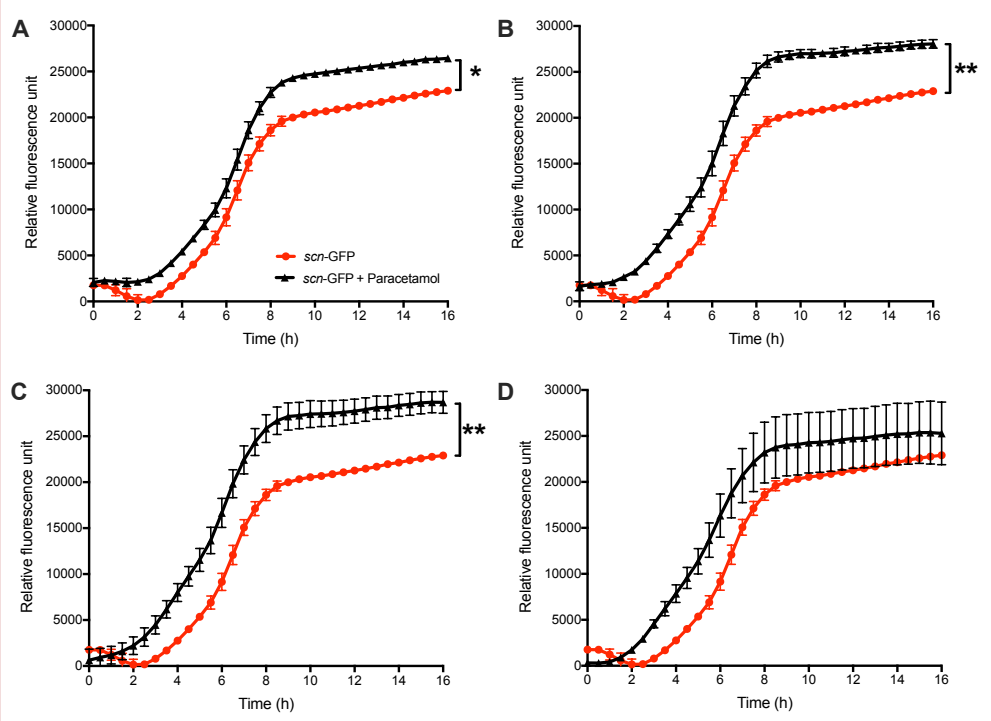

Figure 4.5. Transcription of the SCIN promoter following paracetamol incubation. Transcription of the SCIN gene promoter – GFP (*scn*-GFP+) in strain RN6390 (CC8) was monitored during overnight incubation at 37°C without and with 0.5 (A), 1 (B), 2 (C) or 4 (D) µg/mL of paracetamol. A single asterisk ($p < 0.05$) and two asterisks ($p < 0.01$) represent a statistically significant difference between without and with paracetamol treatment. Data from three separate experiments are presented as mean value and SEM.

Small doses of paracetamol increase immune-modulator transcription

RN6390 (CC8) containing a SCIN promoter-green fluorescence protein fusion was used to study the effect of paracetamol exposure on the transcription of the immune modulator SCIN protein. During overnight co-incubation with paracetamol, the biofilms had a significant upregulation of *scn* promoter transcription ($p = 0.009$) when lower doses (< 4 μg/mL) of paracetamol were added during biofilm formation (Fig. 4.5A-C). No difference was observed with a higher dose of 4 μg/mL (Fig. 4.5D).

Discussion

In this study, we show that paracetamol exposure can lead to an increase in biofilm mass of *S. aureus* strains, particularly from the CC8 genetic background which includes the highly prevalent ST239 and USA300 strains. Bacterial metabolism during biofilm formation did not significantly increase as a consequence of adding paracetamol. It could be that the total number of biofilm-associated bacteria exposed to paracetamol is less than the untreated bacteria, but those fewer exposed cells are producing more heat due to the increased production of polysaccharides and secreted proteins. However, the heat production due to polysaccharide and secreted protein generation might be negligible in comparison to the heat produced due to cellular growth. Regardless, in both cases there is no increase in the number of biofilm-associated bacteria due to paracetamol treatment and thus, the observed increases of biofilm mass due to paracetamol exposure seems to be best explained by an increase of non-cellular components.

Furthermore, the increase in biofilm mass was associated with an increase in the part of the biofilm rich in N-Acetyl glucosamine, presumably polysaccharide intercellular adhesin (PIA). PIA is a positively charged poly-β(1-6)-*N*-acetylglucosamine (PNAG) and the predominant exopolysaccharide component of the extracellular polymeric matrix of staphylococcal biofilms encapsulating bacteria[281,282]. Additionally, PIA mechanically and chemically prevents the killing of *S. aureus* by phagocytizing leukocytes, antimicrobial peptides, and antibiotics[281-283]. No previous data regarding PIA modulation by paracetamol exists to our knowledge. However, a study by Dotto, *et al.*[264] showed that

acetylsalicylic acid promotes biofilm formation of *S. aureus* in a PIA-dependent manner. These data suggest that use of both paracetamol and acetylsalicylic acid during *S. aureus* infections may be potentially harmful due to increasing biofilm formation.

Bacterial secreted proteins were another consideration in our study. Since the regulator pathway for biofilm formation and toxin production, including immune modulators, are correlated[267,268], we expected to find that immune modulator production by *S. aureus* could be affected by paracetamol as well. Our data indeed showed that SCIN production can be stimulated significantly by low doses of paracetamol. This finding mimics the

data from Price *et al.*[284], which demonstrated that acetylsalicylic acid could modulate *S. aureus* virulence factor production. SCIN is a potent immune modulator, which is able to inhibit the release of chemoattractant C5a and therefore blocking the host complement activation pathways[285,286]. Previously, we showed that *S. aureus* produced SCIN already during the early stages of biofilm formation[257]. The observed increase in SCIN production, along with PIA and potentially other virulence factors yet to be investigated, in response to paracetamol would aid invading staphylococci to evade the innate immune system and potentiate infection.

Currently, the mechanism of biofilm modulation by paracetamol has not been elucidated, but there are indications that an impaired iron regulation within cells may influence this phenomenon[287,288], probably via iron chelation by paracetamol[289]. In an iron-restricted condition, biofilm and virulence factor production is increased[264,290]. Paracetamol has been demonstrated *in vivo* to reduce excess hepatic iron after administration[289]. In addition, a previous study on acetylsalicylic acid and biofilm showed that free Fe^{2+} reduction in culture media by acetylsalicylic acid, via iron chelation, could promote biofilm formation of *S. aureus* CC5 and CC8 strains, including Newman and USA300[264]. This observation suggests that iron-modulation by paracetamol may enhance *S. aureus* biofilm formation.

Conclusion

In summary, this study indicates that current clinical concentrations of an analgesic-antipyretic like paracetamol may have a role in the development and persistence of *S. aureus* biofilm-related infections, especially, but not limited to, strains belonging to CC8. For clinical practice our data suggest that in patients with a suspected *S. aureus* infection, the indication for paracetamol administration should be carefully weighed against the risk of increased biofilm formation. The mechanism of action and the effect on an established, mature biofilm by paracetamol need to be investigated in future studies.

Acknowledgements

This study was partly funded by a DIKTI scholarship 2014, grant number 3340/E4.4/K/2014, of the Republic of Indonesia (to A.R.S.) and the Erasmus MC Foundation (fellowship to K.K).

Love is the one thing we're capable of perceiving that transcends dimensions of time and space.

- Interstellar,
Christopher Nolan

5

Dispersing and sonoporating biofilm-associated bacteria with sonobactericide

Kirby R. Lattwein, Inés Beekers,
Joop J.P. Kouijzer, Mariël Leon-Grooters,
Tom van Rooij, Antonius F.W. van der Steen,
Nico de Jong, Willem J.B. van Wamel,
and Klazina Kooiman

In preparation for submission

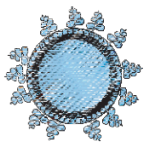

Abstract

Biofilm infections compromise approximately 65% of all microbial infections. Bacteria encased in a biofilm pose significant challenges to successful treatment because antibiotics are often ineffective. *Staphylococcus aureus* (*S. aureus*) infections are associated with higher morbidity and mortality than most other pathogenic bacteria. Sonobactericide, which uses ultrasound and cavitation nuclei, is a potential strategy to increase antimicrobial effectiveness or directly kill bacteria. Several studies suggest that sonobactericide can lead to bacterial dispersion or sonoporation. However, real-time observations during and directly after insonification and/or high-resolution imaging to distinguish individual bacteria are missing. Therefore, in this *in vitro* study we investigated in real-time and high-resolution the effects of ultrasound-induced microbubble oscillation on *S. aureus* biofilms, with and without an antibiotic. Biofilms were exposed to ultrasound (2 MHz, 100-400 kPa, 100-1000 cycles, every second for 30 seconds) with either an antibiotic (oxacillin, 1 µg/mL) alone, microbubbles (10^7/mL) alone, or both antibiotic and microbubbles. Time-lapse confocal microscopy recordings of 10 min were performed to detect bacterial responses with post-hoc image analysis for particle counting to quantify dispersion and sonoporation. This study observed bacterial dispersion as the dominant effect over sonoporation resulting from oscillating microbubbles at these acoustical settings. Increasing pressure or cycles both led to significantly more dispersion, with up to 83.7% biofilm removal. Antibiotic presence did enhance some treatments above oscillating microbubbles alone. These findings help elucidate the direct effects induced by sonobactericide to better understand its potential as a biofilm treatment strategy.

Introduction

Life-threatening biofilm infections pose a major challenge to healthcare systems, leading to substantial increases in mortality and expenses (12 million people are affected and 400,000 die in the USA alone every year[298]). In addition to being community-acquired, 5-10% of all acute-care hospital patients develop a bacterial infection[299], and an estimated 65% of all and 80% of recurrent and chronic infections are associated with biofilms[6,300,301]. Biofilm infections occur when bacteria adhere to tissue and/or devices, and subsequently encase themselves in a protective matrix as they grow. In addition to increasing rates of bacteria with antibiotic resistance, biofilms hinder antibiotic effectiveness up to 1000-fold compared to bacteria in a planktonic (free-floating) state[302]. Therefore, these patients often require long duration, high-dose combination antibiotic therapy. When antibiotic failure occurs, local and systemic complications can quickly develop, often requiring surgery without a guarantee of eradication[301,303]. A therapeutic strategy either as an adjunct to enhance antibiotic efficacy, or as an alternative to directly kill bacteria or breakup biofilms would be a major breakthrough for biofilm-associated infections.

One potential antibacterial strategy emerging in preclinical studies is sonobactericide[304]. It uses ultrasound and cavitation nuclei, such as lipid-coated microbubbles, combined with or without antibiotics and/or other therapeutics, for bacterial infection management. The ability for ultrasound and microbubbles to induce a bactericidal effect stems from microbubble oscillation, i.e. expansion and contraction of the gas core, induced by each ultrasonic wave. These oscillations can exert a mechanical pressure directly on nearby cells and lead to other cell affecting phenomena, such as microbubble displacement, jetting, microstreaming, and reactive oxygen species creation[36,305,306]. Microbubble-induced cellular effects have been extensively studied in mammalian cells, and continue to be as mechanistic pathways and microbubble behavior are not fully understood[306]. One such microbubble-cell effect is the enhancement of drug uptake pathways by stimulating endocytosis, opening cellular junctions, and increasing membrane permeability by membrane perforation called sonoporation[36,306]. Sonoporation can be transient or permanent, causing cellular responses (ion in- and outflux, structural modifications, etc.) that alter cells and can result in cell death [306,307]. This and other mammalian cellular effects due to ultrasound driven cavitation may

also occur in bacterial cells, though most likely to different extents given the many distinctive differences between eukaryotic and prokaryotic cells.

Sonobactericide has been demonstrated in at least 27 scientific papers[304]. Five of these papers were on *Staphylococcus aureus* (*S. aureus*) biofilms, which is the predominate infecting microbe for many types of infections and associated with more severe disease, higher mortality, and longer hospital stays[7,19]. A range of cellular effects as a result of sonobactericide have been observed and suggested, including biofilm disruption/dispersal[53,62,68], sonoporation[107,124,125], and antibiotic synergy[62,65,68,70,124]. However, these studies did not provide real-time observations during and directly following insonification and/or high-resolution imaging to distinguish individual bacteria. Combining both real-time and high-resolution live-cell fluorescence imaging would provide valuable information to better understand how sonobactericide works and can succeed as a therapeutic infection intervention.

Therefore, in this *in vitro* study, real-time responses of *S. aureus* in biofilms to ultrasound-induced microbubble oscillations were investigated at high-resolution with a focus on sonoporation and cell dispersion. Ultrasound at a frequency of 2 MHz was used to insonify biofilms with and without non-targeted microbubbles and the corresponding clinically relevant antibiotic oxacillin. Ultrasound pressures and cycles were varied to determine if changes in either parameter affected the treatment outcome. Continuous confocal microscopy recordings of 10 min combined with subsequent fluorescent particle counting analysis were used to assess the direct effects of sonobactericide on *S. aureus* biofilms.

Materials and Methods

Bacterial isolate handling and characterization

The clinical *S. aureus* strain used in this study was isolated from a patient with confirmed infective endocarditis at the Erasmus University Medical Center Rotterdam, the Netherlands. The isolate was de-identified and anonymized according to institutional policy and stored at -80 °C. All overnight cultures were grown on blood agar plates (tryptic soy agar with 5% sheep blood; BD, Trypticase™, Thermo Fisher Scientific, Waltham, MA, USA) at 37 °C.

The antibiotic sensitivity profile of the isolate and bacterial species identification was determined using the VITEK 2 system (bioMérieux, Marcy-l'Étoile, France). The profile testing included the following antibiotics: benzylpenicillin, oxacillin, gentamicin, kanamycin, tobramycin, ciprofloxacin, levofloxacin, erythromycin, clindamycin, linezolid, teicoplanin, vancomycin, tetracycline, fosfomycin, fusidic acid, mupirocin, chloramphenicol, rifampicin, and trimethoprim/sulfamethoxazole.

The isolates were sent to the University Medical Center Groningen, Genome Analysis Facility (Groningen, the Netherlands) for whole-genome sequencing. The obtained genome data was analyzed to identify known *S. aureus* genes using the core-genome multi-locus sequence typing (MLST+) scheme in the BioNumerics 7.6.3 software (Applied Maths, Sint-Martens-Latem, Belgium)[308]. Additional genetic characterization with Staphylococcal protein A (*spa*)-typing was done as previously described by Harmsen et al.[309]. The raw sequencing data was then analyzed with the BioNumerics software using the *spa*-typing plugin (Applied Maths). The *spa* repeat plot is provided in Supplemental Figure 1. Both sequencing type results were used in PubMed to search for disease association and other related information already published in scientific literature.

Biofilm formation

Biofilms were formed *in vitro* as previously described[257,310] with minor modifications. Briefly, single bacterial colonies from overnight *S. aureus* cultures were suspended in 4 mL of saline solution (0.9% NaCl) to reach an optical density of 0.5 (±0.05) at 600 nm

in a cell density meter (Ultraspec 10, Amersham Biosciences, Little Chalfont, UK). The suspension (0.5 mL) was then used to inoculate 9.5 mL of sterile Iscove's Modified Dulbecco's Medium (IMDM; Gibco, Bleiswijk, the Netherlands) in an OptiCell™ cell culture chamber (Nunc™, Thermo Fisher Scientific, Wiesbaden, Germany). Inoculated OptiCells were placed in an incubator at 37 °C for 24 h, first statically for 3 h to allow for bacterial adherence to the gas-permeable, polystyrene film bottom membrane, and then dynamically on a rotary platform shaker at 150 rpm (Rotamax 120, Heidolph Instruments, Schwabach, Germany).

Biofilm formation was visually assessed using a crystal violet staining, which dyes both the gram-positive bacterial cells and polysaccharide matrix[311]. Biofilms were carefully washed three times with sterile phosphate-buffered saline and then stained using 1% crystal violet (V5265; Sigma-Aldrich, Zwijndrecht, the Netherlands) for 2 min. Unbound crystal violet was removed by washing OptiCells (n=3) five times with sterile deionized water and air dried at room temperature by leaving the in- and outlet ports open.

Biofilm antibiotic response assay

To further minimize the uncertainty of whether the result of treatments with an antibiotic were in fact due to ultrasound and microbubble effects and not due to the antibiotic alone, a time-lapse antibiotic killing curve experiment was performed. Biofilms were formed following the same protocol for the OptiCell, but volume scaled for black, 96-well, clear flat-bottom plates (Costar no. 3904; Corning Inc., Corning, NY, USA) by adding 10 µL of inoculate (0.5 optical density) to 190 µL IMDM in each well.

Following 24 h incubation, biofilms were gently washed thrice with 200 µL IMDM to remove planktonic cells. Propidium iodide (PI) was used as a fluorescence indicator of cell viability, since it is impermeable to living cells and can only bind to nucleic acids if the cell membrane is compromised, either from death or extrinsic factors[312]. Triton X-100 is a potent detergent that disrupts bacterial cell membranes leading to cell lysis, and thus used for the positive control[313]. After washing, 200 µL containing IMDM and PI (25 µg/mL; P4864, Sigma-Aldrich) was added to the wells either alone, with the antibiotic oxacillin (28221; Sigma-Aldrich) at concentrations ranging serially from 0.016 to

256 µg/mL, or with 0.1% Triton X-100 (X100, Sigma-Aldrich). The plates were then directly placed in a temperature-regulated microplate reader (FLUOstar Optima, BMG Labtech, Ortenberg, Germany) maintained at 37 °C and with shaking (150 rpm) between the automated plate fluorescence readings (excitation 541 nm, emission 612 nm) done every 15 min for 12 h.

Microbubble preparation

Non-targeted microbubbles consisting of a lipid monolayer shell and a C_4F_{10} (F2 Chemicals, Preston, UK) gas core were made using a 20-kHz ultrasonic probe (1 min sonication) as previously published[56,245,314]. The lipid shell was comprised of the following: 1,2-distearoyl-*sn*-glycero-3-phosphocholine (DSPC; 84.8 mol %; P6517; Sigma-Aldrich), polyoxyethylene-(40)-stearate (PEG-40 stearate; 8.2 mol %; P3440; Sigma-Aldrich), and 1,2-distearoyl-*sn*-glycero-3-phosphoethanolamine-N-carboxy (polyethylene glycol) (DSPE-PEG(2000); MW 2000; 7.0 mol %; PEG6175.0001; Iris Biotech GmbH, Marktredwitz, Germany). Prior to sonication, 1,1'-diocta-decyl-3,3,3',3'-tetramethylindodicarbocyanine perchlorate (DiD; D307, Thermo Fisher Scientific), a lipophilic, far-red fluorescent dye, was added to fluorescently label the microbubble shells. Microbubbles were washed three times by centrifugation (400 *g*) for 1 min in C_4F_{10}-saturated phosphate-buffered saline to remove excess dye and lipid debris before experiments. A Coulter Counter Multisizer 3 (Beckman Coulter, Mijdrecht, the Netherlands) with a 20 µm aperture tube was then used (n=3) to determine microbubble size distribution and concentration at the start of each experimental day using microbubbles (n=9). The mean microbubble size was found to be 4.0 ± 0.3 µm, which is a known to be a diameter (~3.9 – 4.5 µm) resonant at 2 MHz[498].

Experimental sonobactericide set-up

To allow for the high spatial resolution necessary to capture the micrometer cellular responses of *S. aureus*, a custom-built upright Nikon A1R+ confocal microscope with the same specifications as described previously[273] was used. An OptiCell was placed, with the biofilm on the upper membrane, into a temperature-controlled (37 °C) water bath situated directly beneath the microscope as depicted in Figure 5.1A. A single-element, focused ultrasound transducer (a 2.25 MHz center frequency used at 2 MHz, 76.2 mm focal distance, -6 dB beam width of 3 mm; V305 Panametrics-NDT, Olympus,

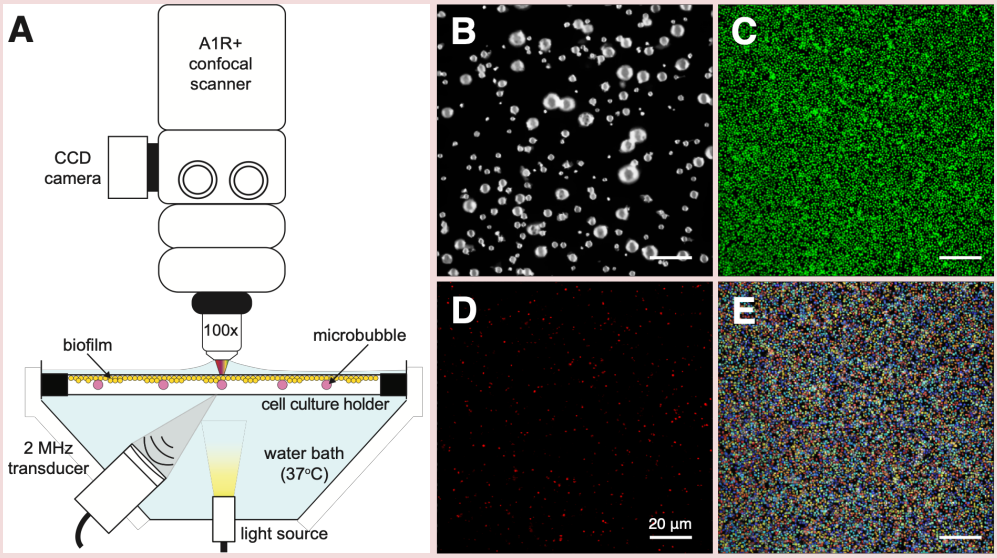

Figure 5.1. Experimental set-up and imaging example. (A) Schematic of the experimental set-up allowing for simultaneous optical imaging and ultrasound insonification (not drawn to scale). Confocal image example of all three channels, where (B) microbubbles are fluorescently-labelled with DiD lipid dye (pseudo-colored white), (C) living bacteria stained with SYTO 9 (pseudo-colored green), and (D) dead/membrane-compromised bacteria stained with propidium iodide (pseudo-colored red). (E) Image output of cells segmented in different colors used for quantitative analysis.

Waltham, MA, USA), which the output had been previously calibrated using a 1 mm needle hydrophone (PA2293; Precision Acoustics, Dorchester, UK), was situated below the OptiCell at a 45° angle to minimize standing wave formation and buildup. The acoustical focus was aligned with the optical focus for simultaneous ultrasound insonification and visualization[223]. The insonification protocol consisted of a 2-MHz acoustic pulse with either a 100 or 1000 cycle burst at a pulse repetition frequency (PRF) of 1 Hz for 30 s generated by an arbitrary waveform generator (DG1032Z; RIGOL Technologies Inc., Beijing, China). A 2 MHz frequency is within the frequency range used by diagnostic scanners and transthoracic echocardiography [409,499]. The signal was amplified (ENI A-500 broadband amplifier; Electronics & Innovation, Rochester, NY, USA) to obtain peak-negative pressures of 100, 200, and 400 kPa for an overall MI < 0.3. The confocal microscope was equipped with a 100× water dipping objective (CFI Plan 100XC W, 2.5 mm working distance, Nikon Instruments, Amsterdam, the Netherlands) for all optical imaging.

Experimental sonobactericide protocol

For biofilms, five different experimental ultrasound insonifications were used: no ultrasound; 100 kPa, 100 cycles; 100 kPa, 1000 cycles; 200 kPa, 100 cycles; and 400 kPa, 100 cycles. This was performed without microbubbles, with microbubbles, and also without and with microbubbles with oxacillin on a total of 21 biofilms over 10 experimental days (total of 114 experimental exposures). If the experimental arm included oxacillin, a concentration of 1 µg/mL was used because it is above the minimal inhibitory concentration of ≤0.25 µg/mL and below the peak serum concentration of 43 µg/mL reported for 500 mg slow IV administration, taking into consideration 94% protein binding[315]. Oxacillin was added to biofilms 3.5 h before experiments based on the antibiotic response assay results (data not shown) showing PI uptake due to oxacillin minimized after this time point.

Before each OptiCell was placed into the water bath, the *S. aureus* within the biofilm were fluorescently stained to visualize both living and dead/membrane-compromised bacteria with fluorophores SYTO 9 (final concentration of 2 µg/mL; S34854; Thermo Fisher Scientific) and PI (final concentration of 25 µg/mL), respectively. Depending on the treatment group, microbubbles (final concentration of 10^7 microbubbles/mL) were added at the same time. The OptiCell was orientated with the biofilm on the upper membrane and mixed to achieve homogenous distribution. For microbubbles to float up to the biofilm and any planktonic bacteria to fall down, 5 min were allowed to elapse for every biofilm before experiments. Each OptiCell was moved along the X and Y directions, while taking care that each new area was not acoustically overlapping with at least 1 cm margins. Ten min time-lapse confocal laser scanning microscopy was performed using three channels: (1) SYTO 9 excited at 488 nm, detected at 525/50 nm (center wavelength/bandwidth), (2) PI excited at 561 nm, detected at 595/50 nm, and (3) DiD excited at 640 nm, detected at 700/75 nm. Each field-of-view consisted of 512 × 512 pixels (128 × 128 µm) and was imaged at 1.29 frames per second using bi-directional, resonant scanning. Optical image recordings began 15 s prior to insonification to establish initial cell state, and continued for 585 s to detect bacterial responses to the different exposure conditions. Any focus drift that occurred was manually corrected during the imaging procedure.

Fluorescence image analysis

Post-hoc image analysis was performed in MATLAB (The MathWorks, Matick, MA, USA) on time-lapse images acquired with the confocal microscope. The fluorescence intensity was monitored in the control groups to ensure time-lapse imaging did not lead to phototoxicity or bleaching. Particle counting was performed using custom-designed analysis software to determine the total number of cells in a field-of-view as a quantitative measure of dispersion and sonoporation using the channels for SYTO9 and PI imaging (Fig. 5.1 C, D). Images were first converted to binary by thresholding (threshold for SYTO9 at 600 and PI at 800; image intensity ranging from 0-4095). Next, all connected components were identified through the *bwconncomp* function in MATLAB. All connected components with an area between 0.5 and 5 μm^2 were counted as individual particles and those larger than 5 μm^2 were subsequently watershed, for proper image segmentation of the constituent particles. The output of the image segmentation was visualized with a color-coded map of the counted particles (Fig. 5.1E).

The initial number of cells was defined as those counted before ultrasound (the first 15 s of recording). The number of particles after treatment was defined as the mean number of particles counted in three frames recorded after ultrasound, selected in intervals between 1-2 min, 5-6 min, and 9-10 min where focus change was negligible to account for focus drift. For sonoporation, two measures were used to assess changes in PI as a response to treatment. First, the increase in number of PI cells was considered in the context of all cells in a field-of view by using the following formula:

$$Sonoporation\ (\%) = \left(\left(\frac{[PI]}{[SYTO9]}\right)_{after} - \left(\frac{[PI]}{[SYTO9]}\right)_{initial}\right) \times 100$$

Secondly, the change in PI relative to only the initial PI amount was calculated:

$$PI\ Change\ (\%) = PI\frac{after}{initial} \times 100$$

For dispersion, removal of all cells from the field-of-view was calculated with:

$$Dispersion\ (\%) = \left(\frac{(PI + SYTO9)_{after}}{(PI + SYTO9)_{initial}}\right) \times 100$$

Statistics

All quantifiable data are graphically displayed in boxplots showing the median and interquartile ranges. Statistical analysis of the acquired data was performed using MATLAB and GraphPad Prism 8 (GraphPad Software Inc., San Diego, CA, USA). To determine significant differences among the various acoustical settings, with and without microbubbles, the Mann-Whitney U nonparametric test was used. For determining if the addition of oxacillin to the same treatment group had significance, parametric testing was used. First, the test of equality of variances was ran for each data comparison. If it was not significant then a Student's t-test was performed and if significant a Welch's t-test for unequal variances was performed. Outliers from the data are indicated with a black dot based on if the data point was above or below 1.5× the interquartile range. A result was considered significant when the P value was found to be <0.05.

Data Availability

Whole genome sequencing data will be submitted to the open public database European Nucleotide Archive. The assigned accession number will be disclosed once approved. All other data that support the findings of this study are available from the authors upon reasonable request.

Results

Isolate characterization and biofilm confirmation

The clinical isolate was identified as a *S. aureus* strain with a genetic background belonging to sequence-type(ST) 398 and *spa*-type t571. The isolate used in this study was found to be methicillin sensitive, with a minimal inhibitory concentration of ≤0.25 µg/mL for oxacillin. Further susceptibility was found for all other antibiotics tested, except for erythromycin and clindamycin. The biofilm antibiotic (oxacillin) response assay revealed the first 30 min with minimal effects, followed by a linear PI uptake for the next 3 h, and then rounding off to a stable level for the remaining time. Sequencing established biofilm-producing capability and the presence of various virulence factor genes, which can be found in Supplemental Table 5.1. Crystal violet and live/dead staining confirmed viable biofilm mass covering the entire OptiCell membranes. Less growth was observed in the areas directly around the injection ports and were therefore excluded in all optical and acoustical experiments.

Sonobactericide

Confocal microscopy using live/dead staining confirmed a bacterial population within the biofilms composed of predominately viable bacterial cells (Fig. 5.2, 5.3), with less than 0.5% dead cells (Fig. 5.7). The total amount of bacterial cells on average in a single field-of-view was 6967±1682. Minimal photobleaching and phototoxicity was observed over the full time-lapse imaging procedure for all three fluorophores, and subsequently confirmed with fluorescence intensity monitoring of the imaging control experiments (no ultrasound insonification and with or without microbubbles). The imaging controls had no significant differences in dispersion or PI uptake from all ultrasound alone control treatment groups (Fig. 5.5-7).

Figure 5.2 shows an example of a biofilm treated with sonobactericide at 200 kPa and 100 cycles. Bacteria with noticeable PI uptake were observed over the entire field-of-view, and occurred during and throughout the 555 s following the 30 s insonification. This is highlighted by the purple squares, showing instances where a cell became PI positive at 47 s (i.e. 17 s after insonification) seen in the bottom square; at 105 s (i.e. 75 s after insonification) in the top square; at 458 s (i.e. 428 s after insonification) in

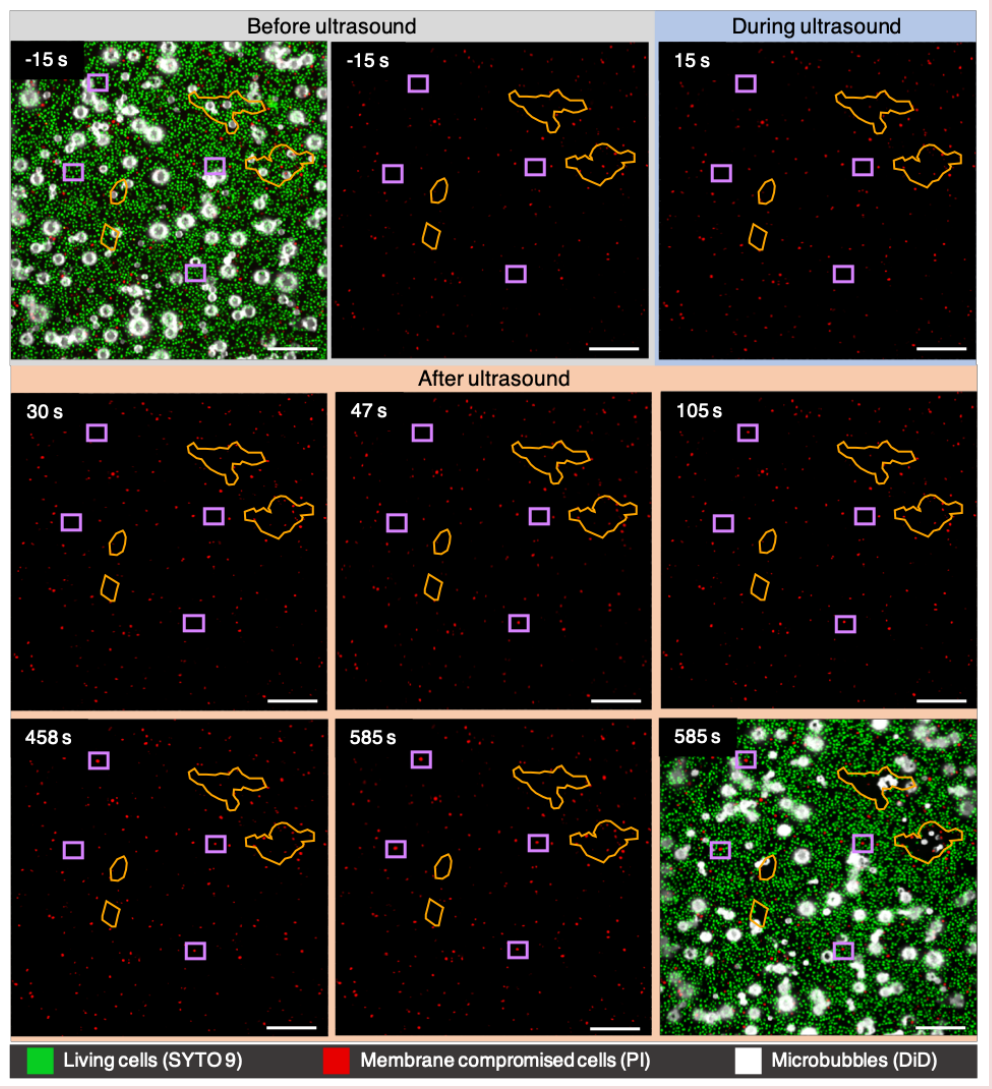

Figure 5.2. Sonobactericide of *S. aureus* biofilm at ultrasound settings of 2 MHz, 200 kPa, 100 cycles, PRF 1 Hz, 30 s. Selected confocal microscopy frames during a 10 min time-lapse recording where the first and last frame are a composite of all three channels, and all others are the PI channel only. Time 0 s is the start of insonification. Purple squares highlight example cells with PI uptake at different timepoints and orange outlines mark regions of dispersion. Scale bars represent 20 µm.

the right square; and 585 s (i.e. 555 s after insonification) in the left square in Figure 5.2. At this setting, bacteria dispersal was minimal (main areas outlined in orange). During dispersion, it appeared that living bacteria were dispersed more easily and readily than PI positive cells. Most ultrasound-induced microbubble displacement led to dispersion. Some cells in the near vicinity (≤ ~3 µm) of a microbubble were dispersed, but not due to displacement. The attractive movements of microbubbles toward each other to form clusters (and the cluster as a whole moving led to the most noticeable dispersion. All outlined dispersion areas involved microbubbles < 4 um, and the two largest areas had the most microbubbles clustering together (5, uppermost outline; 6, second uppermost). Lipid shedding was observed directly with cluster formation and microbubble movement, and occurred only in the four outlined areas of dispersion.

PI uptake also occurred during and throughout the recording following insonification at the higher pressure setting of 400 kPa with the same number of cycles, namely 100 (Fig. 5.3). By the first imaging frame after ultrasound began, ~500 ms, microbubble clustering could already be seen, and lipid shedding and fragmentation by the second frame (~800 ms). All bacteria, SYTO 9 and PI positive cells, were seen to be displaced and/or dispersed by microbubble movements. Most microbubbles in the field-of-view clustered, which occurred faster and led to far more dispersion than what was observed at lower pressures, as seen in Figure 5.2. The large cluster in the bottom three frames of Figure 5.3 consisted of more than 20 microbubbles, and altogether a width of 33.8 µm at the largest point. Microbubbles touching or sized 4.5 ± 0.5 µm (average ± SD; min 3.8 µm - max 5.4 µm; n=9) prior to insonification were seen to be the drivers of clustering. The majority of solitary ≤ 2 µm microbubbles did not displace to form clusters, but remained non-displaced, fragmented, or were swept up by cluster movement. By 5 min of imaging, if not sooner, most liberated bacterial movement due to dispersal events had settled and lipid debris levels stabilized. Some lipid debris remained throughout the entirety of the recording after having been formed by microbubble lipid shedding and fragmentation as early as ~800 ms into ultrasound insonification.

The biofilm responses to the two different ultrasound settings seen in the confocal microscopy examples (Fig. 5.2 and 5.3) can be further understood when quantifying the bacterial population based on fluorescence of cell-state separately, as shown in Figure. 5.4.

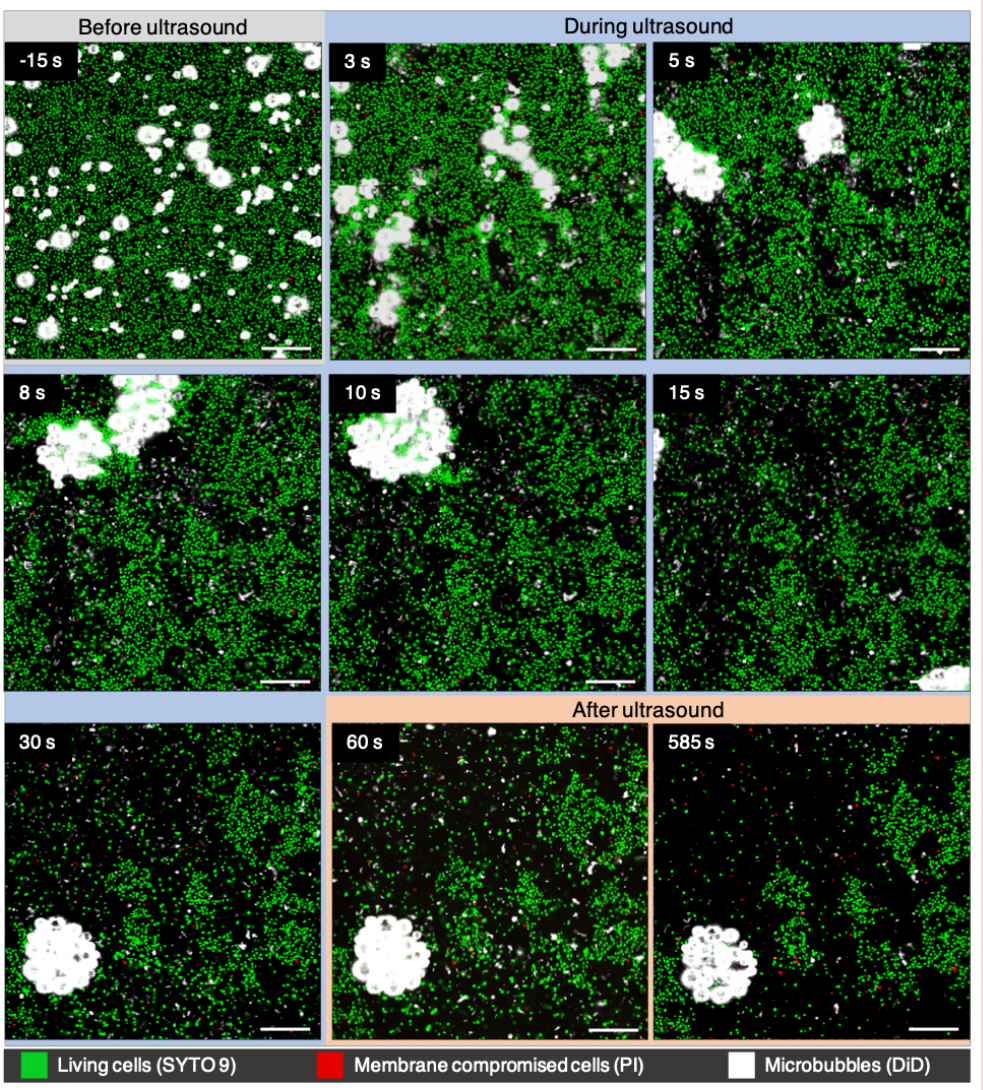

Figure 5.3. Sonobactericide of *S. aureus* biofilm at ultrasound settings of 2 MHz, 400 kPa, 100 cycles, PRF 1 Hz, 30 s. Selected confocal microscopy frames during a 10 min time-lapse recording of all three channels together. Scale bars represent 20 µm.

For the lower pressure setting (Fig. 5.4A), the number of PI positive cells increased by 26.4% while the living cells stained with SYTO9 decreased by 6.4%. By doubling the pressure but keeping the cycles the same, a dramatically different outcome transpired that can be seen in Fig. 5.4B. PI uptake initially shows a spike in PI positive cells followed by a sharp decrease of 52.0%, and then continues to stay along that threshold. The number of SYTO9 cells experienced a more dramatic decrease of 77.5%, which took 3 min to stabilize due to dispersed cell movements still ongoing after microbubble-induced dispersion as seen in Figure 5.3. Both graphs show higher rates of dispersal for SYTO9 cells than PI positive cells, even when considering true PI positive cell counts dispersed is slightly offset by PI uptake that occurred at the same time.

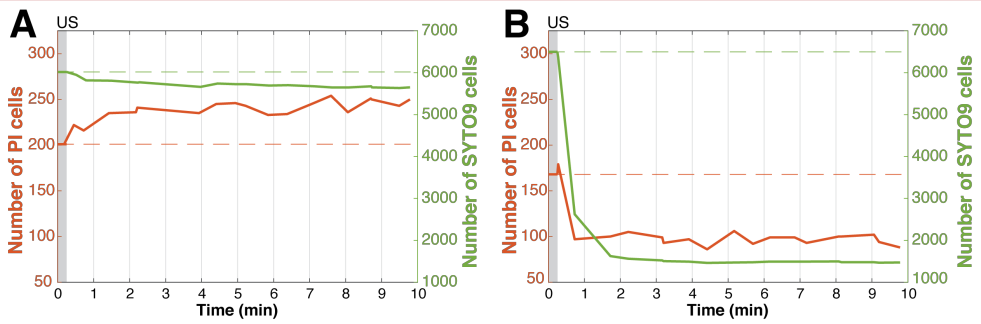

Figure 5.4. Different rates of dispersion and sonoporation of bacteria within biofilms. Example time-lapse line graphs during and after ultrasound with microbubbles treatment indicating (A) minimal dispersion and increasing PI (ultrasound: 2 MHz, 200 kPa, 100 cycles, PRF 1 Hz, 30 s), corresponding to Fig. 5.2, and (B) high dispersion with minimal PI uptake (ultrasound: 2 MHz, 400 kPa, 100 cycles, PRF 1 Hz, 30 s), corresponding to Fig. 5.3. The grey bar at time point 0 indicates ultrasound insonification.

Figure 5.5 focuses on sonoporation by examining only the PI uptake independent of dispersion and from all experimental data beyond the two examples. Without an antibiotic (Fig. 5.5A), all ultrasound settings without microbubbles were not significantly different from the imaging alone, i.e. no ultrasound, even though some variability can be seen. With microbubbles, the lower pressure settings (100 and 200 kPa) with 100 cycles were not different from all treatment groups without microbubbles or without ultrasound. The number of PI positive cells decreased for the two higher settings when compared to the majority of the other experimental arms, including the

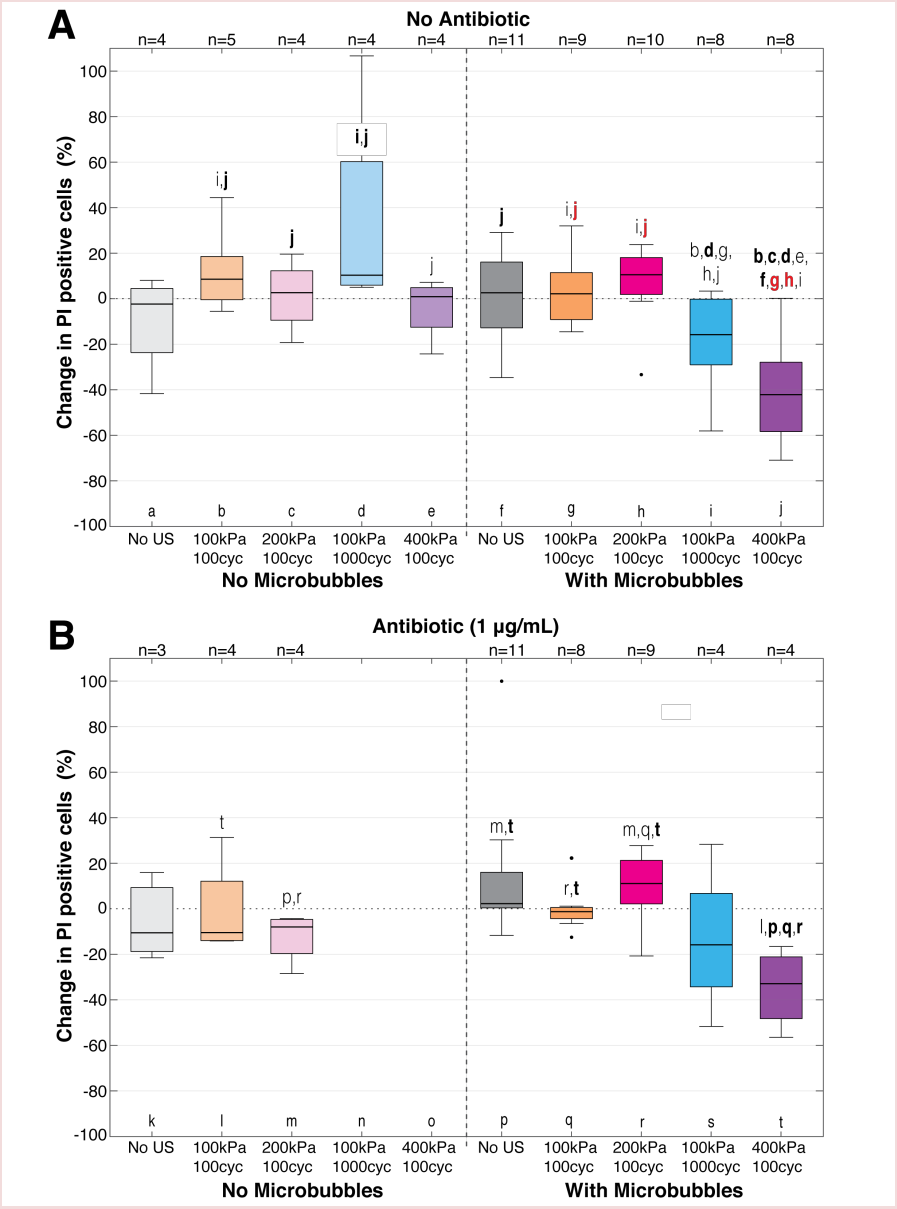

Figure 5.5. Sonoporation considering change in propidium iodide positive cells only. Statistically significant differences from other treatment groups are indicated with letters above the box plots either in a non-bolded typeface for $p<0.05$, a bolded typeface for $p<0.01$, or bolded red letters for $p<0.001$. Black circles denote outliers.

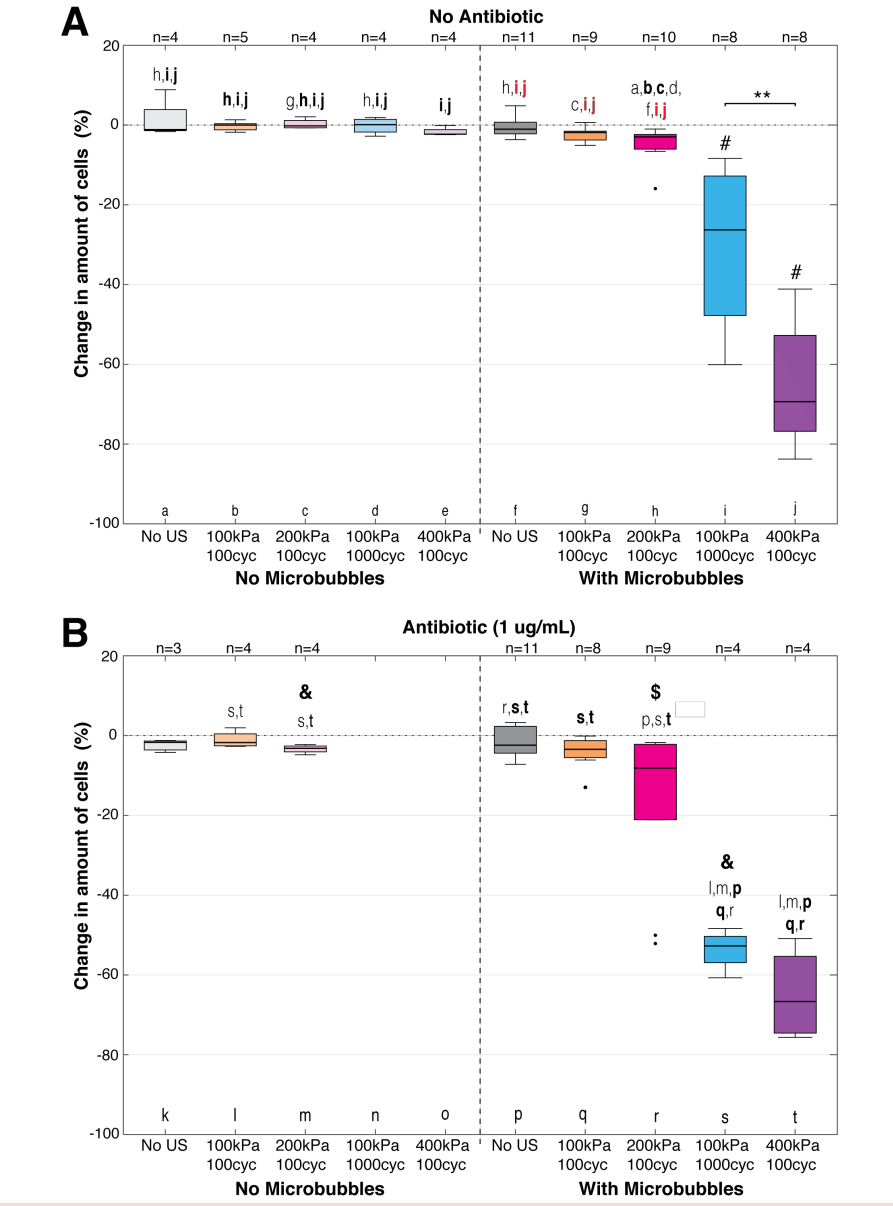

Figure 5.6. Dispersion of bacteria within biofilms. Statistically significant differences are indicated with letters in non-bolded typeface for $p<0.05$, bolded typeface or (**) for $p<0.01$, and bolded red letters for $p<0.001$. Black circles denote outliers. Treatment groups statistically different from all other groups within the same graph are marked by a (#). If adding an antibiotic (B) was different from the same treatment without (A), that is denoted with (&) for $p<0.05$ and ($) for $p<0.09$.

ultrasound alone settings of 100 kPa, 1000 cycles, and 400 kPa, 100 cycles, i.e. the same settings without microbubbles. With the addition of an antibiotic (Fig. 5.5B), similar trends are seen, and for most groups the variability decreased with the exception of 200 kPa, 100 cycles and 100 kPa, 1000 cycles. This altered the significance patterns in such that 100 kPa, 1000 cycles loses its significant difference from all other experimental groups; as well as 200 kPa, 100 cycles becoming significant to the same setting without microbubbles and to the same number of cycles but double the pressure with microbubbles (i.e. 100 kPa, 100 cycles). The two higher ultrasound settings with antibiotic also showed decreases in overall PI uptake as seen without antibiotic (Fig. 5.5A), where all four decreases can largely be attributed to dispersion.

Figure 5.6 takes both cell populations (SYTO 9 for living and PI for membrane-compromised) into account to determine total amount of dispersion. For all settings without microbubbles and no antibiotic, minimal dispersion (≤2.8%) occurred with little variability (Figure 5.6A). This was similar with microbubbles and no ultrasound (≤3.7%). With ultrasound and microbubbles and each successive parameter increase the amount of dispersed cells increased, and dramatically so for the two higher ultrasound settings with up to a maximum of 83.7% biofilm removal. At 100 cycles, the difference between 100 and 200 kPa was not significant, but the addition of microbubbles was significant at 200 kPa, 100 cycles compared to its ultrasound only control without microbubbles. This significance was also found for the higher ultrasound settings against their no microbubble controls, which also extended to all other experimental groups (Fig 5.6A), and with a much higher level of variability in dispersal response. This variability decreased for these two settings when an antibiotic was added, but led to a wider range of values for the other microbubble treatment groups (Fig. 5.6B). Antibiotic presence led to more dispersed cells for all groups (with and without microbubbles), except for 400 kPa, 100 cycles with microbubbles which had 0.3% less dispersal. The cell dispersal increased when an antibiotic was added and was statistically significant at 200 kPa, 100 cycles no microbubbles and 100 kPa, 1000 cycles with microbubbles, and approaching $p<0.05$ significance at 200 kPa, 100 cycles with microbubbles ($p = 0.0776$).

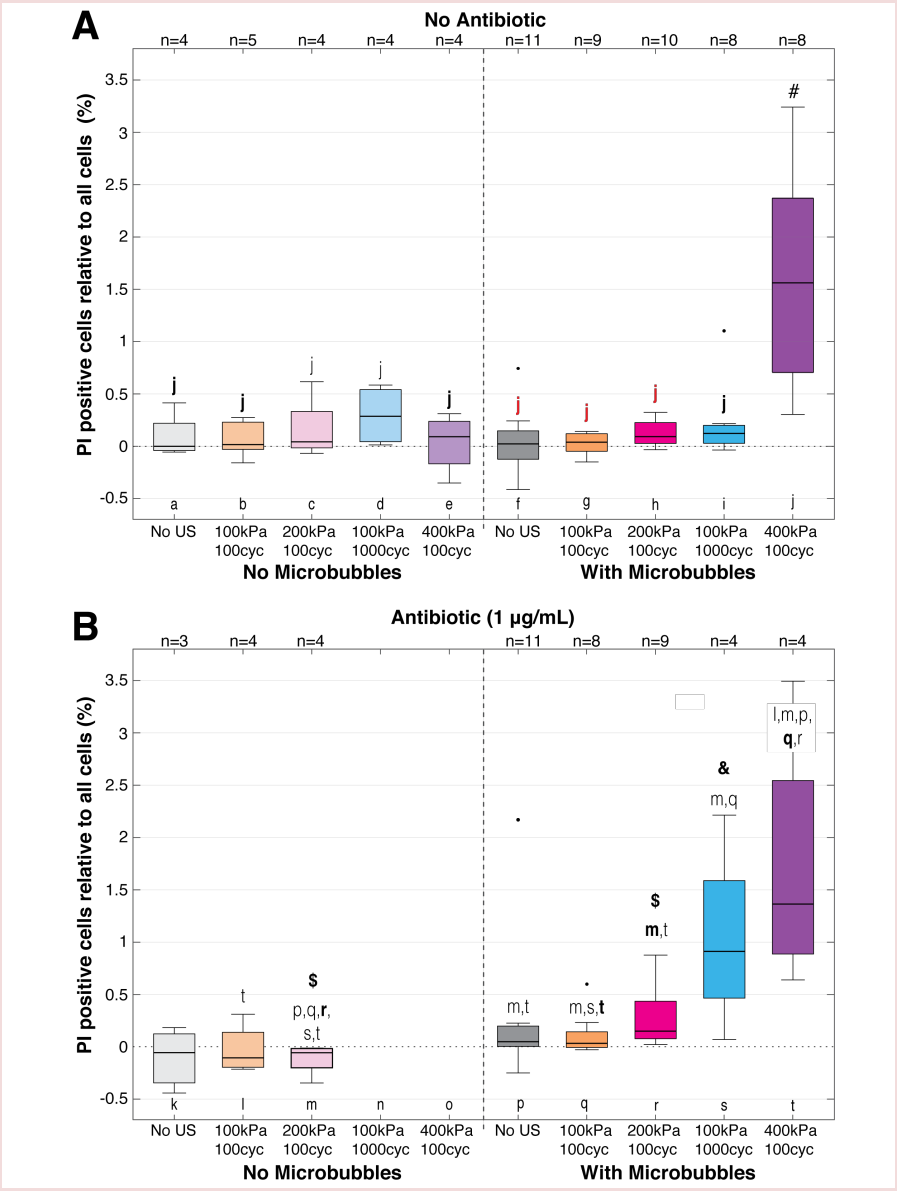

Figure 5.7 Sonoporation relative to all cells in field-of-view. Statistically significant differences are indicated with letters in non-bolded typeface for $p<0.05$, bolded typeface for $p<0.01$, and bolded red letters for $p<0.001$. Black circles denote outliers. Treatment groups statistically different from all others in the same graph are marked by a(#). If adding an antibiotic (B) was different from the same treatment without (A), that is denoted with a (&) for $p<0.05$ and ($) for $p<0.09$.

In order to understand the complete story, the total PI uptake was placed in the context of the ~7000 cells present in a field-of-view and accounting for dispersion (Fig. 5.7). The higher acoustic pressure of 400 kPa, 100 cycles showed a significantly higher, more variable response with an increase of PI uptake up to 3.2% despite having the highest percentage of biofilm removal (Fig. 5.6). For the other settings, the overall change in PI positive cells was close to negligible, with <1% for all treatment groups without an antibiotic (Fig. 5.7A). When antibiotic was included in the experiments (Fig. 5.7B), the outcome was also negligible at <1% for tested groups without microbubbles, with microbubbles without ultrasound, and for microbubbles with ultrasound at 100 kPa, 100 cycles. Increases in acoustic pressure or cycles with microbubbles and antibiotic resulted in more PI positive cells overall (Fig. 5.7B). At 200 kPa, 100 cycles, the addition of microbubbles results in a significant increase in PI uptake, as well as approaching significance ($p=0.0819$) when compared to the same settings without an antibiotic. Half the pressure but 10× the cycles (100 kPa, 1000 cycles) led to significantly more PI uptake (up to a maximum of 2.2%) with a wider value range than without an antibiotic, despite the significantly higher rate of dispersion seen with an antibiotic at this setting (Fig. 5.6). The highest pressure of 400 kPa, 100 cycles with microbubbles and an antibiotic was similar to without an antibiotic, both exhibiting a larger amount of PI positive cells (up to 3.5%) and more variability than all other experimental groups.

Discussion

The direct effects of sonobactericide in terms of dispersion and sonoporation were investigated in real-time and at high-resolution for the first time in this *in vitro* study. A *S. aureus* clinical isolate was used to produce biofilms that were subsequently exposed to ultrasound with or without microbubbles. The addition of an antibiotic was also used to evaluate synergism in response to sonobactericide. During continuous high-resolution fluorescence microscopy over 10 min, dispersion was quantified by bacterial cells leaving the field-of-view and sonoporation by cellular PI uptake.

Based on published literature, both the 398 sequence- and t571 *spa*-type of the clinical isolate used in this study have been implicated in several types of invasive infections, including blood stream, intravascular device-associated, and post-cardiac surgery infections, and found in other countries outside of the Netherlands and Europe[316-323]. The t571 *spa*-type designation with human-associated ST398 has been observed repeatedly and sometimes disproportionally more common than other *spa*-types[316,319,320]. Additionally, the methicillin sensitive ST398 variant (including with t571) is suggested to be more virulent than both methicillin resistant ST398 and sensitive non-ST398 strains and associated with a higher 30-day mortality[316,317].

Sonoporation, defined as membrane permeabilization as a result of ultrasound and oscillating microbubbles, was observed by PI fluorescence upon and after treatment[306]. The bacteria that showed immediate PI uptake were most likely more susceptible to and/or experienced more microbubble-induced effects. This could be location dependent in relation to the microbubble, or enhanced due to the physiological state of the cell, or other endo- or exogenous processes. For cells that took longer to become PI positive, the damage and stress experienced was most likely not enough to cause direct cell membrane impairment and the activated repair mechanisms were sufficient at preventing immediate lysis. Though this can readily be seen in mammalian cells as transient and increasing PI influx lasting over minutes[245,324], this may not occur in bacteria or a certain resolution or fluorophore binding threshold needs to be met for visualization. The latter seems plausible given the optical set-up in this study having a lateral and axial resolution up to 200 nm and 600 nm[325], respectively. The pore size necessary for a single bacterium to not immediately lyse would need to be in the

magnitude of 1-10s nm, since a 100 nm pore is already a tenth of the cell size. In mammalian cells, membrane pores as small as 1 nm have been observed with electron microscopy following microbubble-induced sonoporation[36,307]. Since a pore would need to just be at least the diameter of a PI molecule, which is 1.3 nm[326], the limitation to conclusively know if transient PI uptake can occur in *S. aureus* then lies with the optical detection limit.

The chance that PI uptake is due to spontaneous cellular responses not driven by sonobactericide cannot be fully negated. However, spontaneous bacterial cell death has been reported to occur only at a frequency of <0.01%[327]. Ultrasound alone did not induce significant cell death, and is supported by studies that found only microbubble cavitation to induce significant stress responses[86] and microstructure damage seen either only on bacteria exposed to ultrasound with cavitating microbubbles[124] or the most devastating effects by sonobactericide plus antibiotic[67]. It is possible that the effects of sonoporation may take more than 585 s to induce cell death, and a longer imaging protocol might have detected more PI positive cells similar to other sonobactericide papers which waited 24 h after ultrasound before optical imaging[124,125]. Identification of delayed cell death may be missed when assessing viability at one specific timepoint or time-window, thus underestimating the true impact of sonobactericide. Though this is outside the scope of this study, it remains an important consideration for future investigations since the complete cell response pathway to microbubble-induced damage/stress is unknown, along with if a bacterium can survive once triggered.

Sonoporation at higher pressures and cycles is challenging to track on a single cell level because of the high rates of dispersion observed in this study. In the confocal recordings, it appeared that living cells dispersed more easily than dead cells, and following dispersion more cells that remained in the field-of-view became PI positive by the end (Fig. 5.2-3). However, this only reveals part of the story since the cellular responses of the bacteria that were dispersed or fell off are unknown. There exists evidence that bacteria released from biofilms using chemical dispersal agents may be more virulent than the typical planktonic cells for a few hours before becoming highly susceptible again[88-90,328]. It is possible that the mechanical microbubble-induced disruption of the biofilm does not lead to this more virulent profile and/or that many are damaged in the

process that leads to immediate or delayed cell lysis. Thus, cells dispersed by sonobactericide should be fully characterized to determine and address potential safety issues and challenges that these cells, whether more virulent or not, could pose.

The polydisperse microbubbles employed in this study had an average diameter of 4 µm, which is slightly larger than current commercially available lipid-shelled contrast agents (ranging from 1.1 to 3.3 µm[304]). However, other sonobactericide studies used similarly sized microbubbles[124,125,129] and the mean diameter is in range of the clinically approved human albumin-coated microbubbles (Optison, mean diameter of 3 – 4.5 µm[304]). Of potential importance is that this larger size is closer to resonance frequency at 2 MHz[56], which could translate to a more efficacious sonobactericide treatment since a larger microbubble population would achieve maximum excursion amplitude.

The microbubble concentration used in this study was chosen to maximize sonoporation potential because of the sheer number of cells (~7000), and is supported by Dong *et al*.[124] who observed that a higher microbubble concentration led to enhanced bacterial PI uptake in biofilms. On the one hand, a lower concentration may enhance dispersal by minimizing the shielding effect that can happen with higher concentrations, and larger bubble sizes at higher pressures[329,330]. Shielding was sometimes observed and most likely contributed to the heterogenous responses seen at some settings (Fig. 5.5-7). On the other hand, enhanced microbubble displacement may result in less cell death as reported in endothelial cells where non-displacing microbubbles were more lethal[245], although it should be noted that mammalian cells and *S. aureus* are very different cell types. Dispersal was a direct consequence of microbubble displacement and subsequent clustering possibly due to secondary Bjerknes forces. Our data is in agreement with the current knowledge that clustering happens quickly (ms) and occurred at a faster rate with a larger number of microbubbles at higher acoustic parameters[331]. The range of microbubble sizes (3.8 - 5.4 µm) leading to clustering were both within and slightly outside of resonance (~3.9 – 4.5 µm)[412], however that was determined for free bubbles and at 50 kPa. Increasing pressure is known to (linearly) dampen resonance frequency[500].

The resulting microbubble dynamics leading to dispersal observed in this study explain previous high-resolution sonobactericide paper findings of biofilm disruption and craters, since these were not observed in real-time and only after sonobactericide

(> 5 min – 24 h)[62,65,124,125]. Craters and cell detachment have been described in confluent cervical cancer cell monolayers, but such phenomena required high-pressure, (4 MPa peak-negative pressure) shock-wave bubble cluster generation[332]. Around the detachment area Ohl *et al.*[332] observed a rim of dead cells (how much time after ultrasound and observational imaging was not provided). In our study, the PI positive cells were found throughout the entire field-of-view and a higher number was not observed particularly around the rim of the detachment areas.

Antibiotic synergism was observed in this study by enhanced dispersion and a higher percentage of PI positive cells when considering the whole field-of-view (Fig. 5.6-7). This effect was not as sharply observed as in other sonobactericide studies looking into therapeutic synergism[62,65,68,124], which could be due to the different ultrasound parameters, such as a shorter insonification time, or limited by the experimental design. One such considerations is that the recordings may be too short to capture the full effect, as previously discussed for PI uptake. Future studies could include real-time imaging followed by hourly sampling points to address this. Additionally, two ultrasound only insonifications are missing in the antibiotic group, which when performed may further reveal synergistic effects. Another possibility is that the 3.5 h waiting step after adding oxacillin may also lead to an underestimation. This step was done to better understand the effects which were microbubble induced and not directly from the antibiotic alone. It is possible that performing the experiments 0.5 h after antibiotic addition in the 3 h window during linear PI uptake could better represent the true synergistic effects of sonobactericide. This further highlights the importance of experimental design and should be explored and considered in future studies while taking into account the *in vivo* situation to prevent effect under or overestimation.

Conclusion

Both dispersion and sonoporation were observed in this investigative study on sonobactericide. Bacterial dispersion was significantly more prominent than sonoporation as a result of oscillating non-targeted microbubbles for these *S. aureus* biofilms and acoustical settings of 2 MHz, 100-400 kPa, 100-1000 cycles, every s for 30 s. Antibiotic synergism was observed for some exposure settings. These findings provide informative details for the first time on how sonobactericide in real-time and at high-resolution can aid in biofilm infection treatment. At the same time further investigations are necessary to establish dispersion of bacteria as a safe therapeutic strategy.

Acknowledgements

The authors would like to thank Robert Beurskens, Frits Mastik, Simone A.G. Langeveld from the Department of Biomedical Engineering and Andi R. Sultan, Susan V. Snijders, and Corné H. Klassen from the Department of Medical Microbiology and Infectious Diseases, both from Erasmus University Medical Center Rotterdam, for their skillful technical assistance. The authors also thank the other members of the Therapeutic Ultrasound Contrast Agent group (Biomedical Engineering Dept.) and the *S. aureus* working group (Medical Microbiology and Infectious Diseases Dept.) for their useful discussions. This study was financially supported by the Erasmus MC Foundation (fellowship to K.K.).

Supplemental Information

Supplemental Table 5.1. Genes present in the infective endocarditis *S. aureus* isolate.

Gene (clonal complex-associated)		Gene (biofilm-associated)	
arc	carbamate kinase	agrB	transmembrane endopeptidase; quorum sensing regulator
aroE	shikimate dehydrogenase	fnbA	fibronectin binding proteins; high biofilm production association
glpF	glycerol kinase	fnbB	
gmk	guanylate kinase	clfA	clumping factors; cell surface-associated protein responsible for fibrinogen binding and human platelet aggregation
pta	phosphate acetyltransferase	clfB	
tpi	triosephosphate isomerase	fib	extracellular fibrinogen binding protein
yqil	acetyl coenzyme A acetyltransferase	ebps	elastin binding protein
Gene (biofilm-associated)		eno	laminin binding protein
icaA	intercellular adhesions; biofilm producing ability, PIA synthesizer	cna	collagen binding protein
icaD		RNAIII	detergent-like peptides; PSMs
icaB		sarA	transcription regulator of biofilm formation, development, and several virulence factors
icaC			

PSMs = phenol-soluble modulins, PIA = polysaccharide intercellular adhesion

“Did you ever stop to think,

and forget to start again?

- Author unknown,
attributed to A.A. Milne

6

Ultrasound-activated microbubble effects on fibrin-based biofilms

Kirby R. Lattwein, Margot E. Starrenburg, Joop J.P. Kouijzer, Simone A.G. Langeveld, Mariël Leon-Grooters, Antonius F.W. van der Steen, Nico de Jong, Moniek P.M. de Maat, Willem J.B. van Wamel, and Klazina Kooiman

In preparation for submission

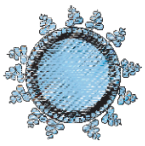

Abstract

Infective endocarditis is a life-threatening bacterial infection of the heart valves. Often both the immune system and antibiotics are ineffective against the fibrin-based biofilms (i.e., surface-associated, matrix-enclosed microbial communities). Ultrasound-mediated microbubble oscillations can induce various mechanical effects and enhance thrombolytic fibrin degradation in clots. This study investigated the interaction of ultrasound-activated microbubbles with fibrin-based biofilms by assessing real-time responses with high resolution microscopy. *Staphylococcus aureus* biofilms were grown 24 h in human plasma inside ibiTreat μ-slides. Microbubbles had a C_4F_{10} gas core encapsulated in a DSPC-based fluorescently-labelled coating. For visualization of bacteria, SYTO 9 and propidium iodide were used, and for fibrin, fibrinogen conjugates Oregon Green 488 or Alexa Fluor 647 were used. Biofilms were exposed to multiple pulses of ultrasound (2 MHz, 400 kPa, 100 or 1000 cycles, every second for 30 s and 1 s continuous wave) either alone or with a thrombolytic (rt-PA; 158 ng/mL), MBs, or rt-PA and MBs. Time-lapse confocal microscopy recordings up to 10 min were performed. Bacterial dispersion from fibrin encasement and fibrin strand displacement, breaking, and elasticity were observed and found to be ultrasound-activated microbubble response dependent. Fibrin strands displaced ~1–5.2 μm from their original position. The majority of bending fibrin strands exhibited recovery, with the longest bent strand (27.7 μm) recovering from a 3.7 μm displacement in 25.6 s. Ultrasound and microbubbles with rt-PA led to fibrin strand breaking, a different fibrin degradation pattern which led to complete liberation of bacteria at a faster rate (322 ± 161 s) than rt-PA alone (518 ± 86 s). Harnessing these ultrasound-activated microbubble-induced phenomena has potential to aid in the treatment of cardiovascular biofilm infections.

Introduction

Pathogenic bacteria can lead to life-threatening biofilm infections of foreign material and native tissue anywhere in the body. A biofilm is composed of multilayered bacterial aggregates in a matrix, composed of bacterial and host extracellular substances and local environmental components, that provides protection against the immune system and antibiotics (up to a 1000-fold less susceptible)[7,75,333]. There are several biofilm infections related to the cardiovascular system, such as those related to devices/prosthetics like vascular grafts and catheters, with infective endocarditis (IE) being one of the most well-known as it involves the heart. IE is a severe infection of the heart valves, surrounding endocardial tissue, and/or intracardiac medical devices[22,334]. The infection is fatal when left untreated, and with treatment there is an in-hospital mortality of 18-47.5%[335-338] and a 5-year mortality of 40-69%[339-341]. The challenging infection milieu necessitates the need of prolonged antibacterial treatment for all patients[342] and heart surgery for ~50%[335,336,338,342]. Over the last years, *Staphylococcus aureus* (*S. aureus*) has become the predominant pathogen causing IE (~30% of cases)[22,335,336,338,340,342-344] and is associated with more severe infection with larger biofilms, longer hospital stays, and a higher mortality[7,343,345]. Unfortunately, overall mortality numbers have hardly improved over the last twenty years[22,335,343] and thus, new strategies to treat IE, preferably less invasive, remain urgently needed.

One potential treatment strategy emerging in pre-clinical studies is called sonobactericide, which combines the use of ultrasound contrast agents and ultrasonic waves, with or without other therapeutics, to directly or synergistically treat bacterial infections[304]. Ultrasound contrast agents dispersed within a solution include microbubbles, which are between 1 and 10 µm and composed of gas nuclei encased in a shell that is generally lipid-based[36]. Upon insonification, these microbubbles compress and expand (i.e., oscillate) in accordance with the encased gas core responding to the pressure wave changes of ultrasound. Currently, microbubbles are widely used clinically in the context of diagnostic ultrasound imaging. Investigation into their ultrasound-mediated capacity as an enhancer of current therapies and directly for drug delivery involving mammalian cells has been ongoing for over 20 years[34,36], with some applications in ongoing clinical trials[34]. Only recently have potential microbubble applications expanded into the field of bacterial infections[304]. Several different infection

infection applications have been investigated thus far, with one of our previous studies focused on IE[68]. The model was developed to follow the pathogenesis by growing biofilms in plasma on human whole-blood retracted clots, albeit under static conditions to keep the clot intact. The *S. aureus* infected blood clots were then treated under flow for 30 min using sonobactericide and we found that the combination microbubbles, ultrasound, oxacillin, and a thrombolytic agent proved the most efficient treatment[68]. However, these infected clots were large (~440 um) and thus were imaged with lower magnification/resolution brightfield to allow for viewing a larger treatment area[68]. To elucidate the detailed mechanisms of how sonobactericide can be an effective infection management tool, a higher magnification and resolution is needed.

To determine how sonobactericide can be advantageous for cardiovascular bacterial infection treatment, a biofilm model was developed by growing *in vitro* biofilms in 100% human plasma using a *S. aureus* clinical isolate obtained from an IE patient. The fibrinogen in the plasma is essential to this model. It is known that cardiovascular biofilms, such as IE, have fibrin incorporated throughout the extracellular matrix due to various mechanisms, one of which includes *S. aureus* secreted coagulases leading to fibrinogen conversion to fibrin[346]. Optimal growth parameters and fibrinogen conversion to fibrin in Ibidi microchannels were determined, and visualized using brightfield and high-resolution confocal fluorescence microscopy. For sonobactericide treatment, real-time responses of *in vitro* cardiovascular replicated biofilms to ultrasound-induced microbubble behavior were qualitatively investigated for up to 10 min. Biofilms were insonified with and without microbubbles and thrombolytics (rt-PA, 20× less than the clinical dose) to assess the impact on the fibrin matrix, encased bacteria, and overall degradation.

Materials and Methods

Bacterial isolate handling and biofilm formation

A *S. aureus* strain isolated from a patient diagnosed with IE at Erasmus MC University Medical Center Rotterdam was stored at -80 °C (same isolate characterized in Chapter 5). This isolate was anonymized and de-identified per institutional policy. For each biofilm experiment, bacteria were taken from the -80 °C freezer and grown on a 5% sheep blood agar plate (tryptic soy agar; BD, Trypticase™, Thermo Fisher Scientific, Waltham, MA, USA) for 24 h at 37 °C.

All biofilms were grown in tissue culture-treated µ-Slide mono-channels (80196; ibiTreat µ-Slide $I^{0.8}$ Luer; Ibidi GmbH, Martinsried, Germany). Two different growth mediums were used for biofilm formation, either Iscove's Modified Dulbecco's Medium (IMDM; Gibco, Bleiswijk, the Netherlands) typically used in mammalian cell culture or fresh human plasma (with anti-coagulant citrate phosphate double dextrose; Sanquin, Rotterdam, the Netherlands) that had been pooled from 5 healthy donors with blood type O and directly stored at -80 °C.

Human plasma was defrosted at and IMDM warmed to 37 °C just before bacterial inoculation. To inoculate culture media, single colonies were taken from the agar plate with an inoculation loop and placed in 0.9% sodium chloride solution, which was then vortexed (Vortex genie 2; Scientific Industries Inc., NY, USA) until homogeneous. A target optical density of 0.5 (±0.05) at 600 nm (Ultrospec 10 cell density meter, Amersham Biosciences, Little Chalfront, UK) was used as the initial bacterial inoculate concentration to make subsequent dilutions representing 10^3-10^8 colony forming units per mL (CFU/mL) in the cell culture media.

A 200 μL aliquot of inoculated IMDM or plasma alone (i.e., no supplementary thrombin) was added to each Ibidi slide, filling the entire channel. To prevent the channel from being exposed to air and drying out, 60 μL of sterile IMDM or plasma was added to the in-/outlet reservoir located on each side of the channel. The Ibidi slides were then situated in a humidified chamber within a 37 °C incubator for 24, 48, and 72 h with media refreshed with new sterile media every 24 h. To find the optimal growth conditions not

only were incubation times and bacterial concentration varied, but also the growth conditions which consisted of: static, on a rotary platform shaker (150 rpm; Rotamax 120; Heidolph Instruments, Schwabach, Germany), or 3h statically and then the remaining time on the shaker. Every 24 h, biofilms were viewed using brightfield microscopy at 100× magnification (CFI Plan 100XC W, 2.5 mm working distance, Nikon Instruments, Amsterdam, the Netherlands) with a custom-built upright Eclipse Ni-E microscope (Nikon Instruments)[273]. This provided sufficient overview for assessment of the bacterial growth responses to the different parameters used for biofilm formation. Every Ibidi channel was scanned from inlet to outlet with at least two images acquired (DS-Fi3 camera; Nikon Instruments) at different positions on the slide. For all biofilm experiments described further in the material and methods, only human plasma was used as bacterial growth medium.

Bacteria and fibrin visualization

To fluorescently observe the fibrin strands in the biofilms, either the Oregon Green 488 (F7496; Thermo Fisher Scientific) or Alexa Fluor 647 fluorescently-labeled human fibrinogen conjugate (F35200; Thermo Fisher Scientific) was added to the inoculated plasma right before being added to the Ibidi channel. The fibrinogen conjugates were added to the plasma at a 4% concentration (final concentration 0.1 mg/mL in plasma containing ~ 2.5 mg fibrinogen/mL). Biofilms were grown using the different growth conditions as described in the previous section. After the desired incubation time, the plasma in which the biofilms had grown was replaced by a mix of sterile plasma, SYTO™ 9 green fluorescent nucleic acid stain (2 µl/ml; S34854; Thermo Fisher Scientific) to stain live bacteria, and propidium iodide (PI; 150 µl/ml; P4864-10ML; Sigma-Aldrich, Zwijndrecht, the Netherlands) to stain dead bacteria for subsequent imaging. The Nikon A1R+ confocal scan head with the microscope and 100× objective used for brightfield imaging were used together to visualize the different fluorescent elements of the biofilms[273]. Excitation of the fluorophores was achieved with three lasers: 488, 561, and 640 nm, where live bacteria stained with SYTO 9 or fibrin strands with Oregon Green, reflect light emitted by the 488nm laser and was detected at 525/50 nm (center wavelength/bandwidth) using a hybrid detector unit; dead bacteria, stained red with PI, reflect light emitted by the 561 nm laser and was detected at 595/50 nm; and fibrin strands stained far-red with Alexa Fluor 647, reflect light emitted by the 640 nm laser

and was detected at 700/75 nm. Confocal images were obtained at three different positions in each slide. Based on the visual results, all subsequent experiments used the optimal fibrin-biofilm formation parameters of human plasma inoculated with 10^6 bacteria, followed by 3 h static and 21 h on the shaker (150 rpm) at 37 °C.

Fibrin strand thickness

For the measurement of the fibrin strand thickness, three confocal microscopy fields-of-view of only the obtained fibrin signal in gray-scale were analyzed for a total of 15 strands. The thickness of the fibrin strands in the biofilms was measured using the ImageJ[347] *plot profile function* by drawing lines perpendicularly over the fibrin strand width in the obtained confocal images. For each image, 5 strands were measured at random and the intensity of the fluorescent signal over the 5 lines was plotted and converted into Gaussian curves. Of these 5 curves, the Full Width at Half Maximum (FWHM) was determined using the following equation, in which σ stands for the standard deviation:

$$\mathrm{FWHM} = 2\sqrt{2\ln(2)} * \sigma$$

Fibrinogen concentration

Fibrinogen concentration (g/L) was determined according to Clauss with the Sysmex CS-5100 system (Siemens, Den Haag, the Netherlands). The concentration of fibrinogen was calculated from the clotting time by using a calibration curve. Fibrinogen concentrations in plasma were determined on two different days after defrosting to 37°C, and after 24 h at 37°C in an Ibidi slide without bacteria and with biofilm.

Microbubble preparation

Non-targeted microbubbles consisting of a lipid monolayer shell and a C_4F_{10} (F2 Chemicals, Preston, UK) gas core were made using a 20-kHz ultrasonic probe (1 min sonication) as previously published[56,245,314]. The lipid shell was comprised of the following: 1,2-distearoyl-*sn*-glycero-3-phosphocholine (DSPC; 84.8 mol %; P6517; Sigma-Aldrich), polyoxyethylene-(40)-stearate (PEG-40 stearate; 8.2 mol %; P3440; Sigma-Aldrich), and 1,2-distearoyl-*sn*-glycero-3-phosphoethanolamine-N-carboxy (polyethylene glycol) (DSPE-PEG(2000); MW 2000; 7.0 mol %; PEG6175.0001; Iris

Biotech GmbH, Marktredwitz, Germany). Prior to sonication, either 1,1'-dioctadecyl-3,3,3',3'-tetramethylindodicarbocyanine perchlorate (DiD; D307, Thermo Fisher Scientific), a lipophilic, far-red fluorescent dye, or 1,1'-dioctadecyl-3,3,3',3'-tetramethylindocarbocyanine perchlorate (DiI; D282; Thermo Fisher Scientific), a lipophilic, orange-red fluorescent dye, was added to fluorescently label the microbubble shells. Microbubbles were washed three times by centrifugation (400 *g*) for 1 min in C_4F_{10}-saturated phosphate-buffered saline to remove excess dye and lipid debris before experiments. A Coulter Counter Multisizer 3 (Beckman Coulter, Mijdrecht, the Netherlands) with a 50 µm aperture tube was then used (n=3) to determine microbubble size distribution and concentration at the start of each experimental day.

Experimental sonobactericide set-up

The custom-built upright Nikon A1R+ confocal microscope described in the previous sections and equipped with the same 100× water dipping objective was used to obtain the high spatial resolution necessary to capture the micrometer responses of *S. aureus* and fibrin. Every experimental Ibidi slide was flipped upside down, such as if there was a biofilm it was on the upper side, and placed into a temperature-controlled (37°C) water bath situated directly beneath the microscope (similarly depicted in thesis Chapter 5, Fig. 5.1A, but in an Ibidi slide; and Chapter 11, Fig. 11.2C, but without a fluidic unit). A single-element, focused ultrasound transducer (a 2.25 MHz center frequency used at 2 MHz, 76.2 mm focal distance, -6 dB beam width of 3 mm; V305 Panametrics-NDT, Olympus, Waltham, MA, USA), which the output had been previously calibrated using a 1 mm needle hydrophone (PA2293; Precision Acoustics, Dorchester, UK), was situated below the Ibidi slide at a 45° angle to minimize standing wave formation and buildup. The acoustical focus was aligned with the optical focus for simultaneous ultrasound insonification and visualization[223]. A 2-MHz acoustic pulse with either a 100 or 1000 cycle burst was generated by an arbitrary waveform generator (DG1032Z; RIGOL Technologies Inc., Beijing, China), which was also used to generate the signal automatically for 30 s at a pulse repetition frequency (PRF) of 1 Hz. The signal was amplified (ENI A-500 broadband amplifier; Electronics & Innovation, Rochester, NY, USA) to obtain a peak-negative pressure of 400 kPa.

Experimental sonobactericide protocol

For the fibrin-based biofilms, different experimental ultrasound insonifications were used: no ultrasound; 400 kPa, 100 cycles; or 400 kPa, 1000 cycles. This was performed without microbubbles, with microbubbles, and also without and with microbubbles with recombinant tissue plasminogen activator (rt-PA; Alteplase; RV 12247; Actilyse®, Boehringer Ingelheim, Alkmaar, the Netherlands) on a total of 22 biofilms over 8 experimental days. If the experimental arm included rt-PA, a concentration of 158 ng/mL was used, which is 20× lower than the clinical dose. Before each Ibidi slide was placed into the water bath, the plasma in which the biofilms had grown was replaced by a mix of sterile plasma, fluorophores, microbubbles (final concentration of 10^7 microbubbles/mL), and rt-PA depending on the treatment group. SYTO 9, PI, and DiD microbubbles were added if Oregon Green fibrinogen had been used, and SYTO 9 and DiI microbubbles for biofilms formed with Alexa Flour 647 fibrinogen. The Ibidi slide was then orientated with the biofilm on the upper membrane by flipping upside down which allowed the microbubbles to float up to the biofilm and any planktonic bacteria to fall down. Five min were allowed to elapse for every biofilm before experiments. Each Ibidi slide was moved along the X and Y directions, while taking care that each new area was not acoustically overlapping. Up to ten min time-lapse confocal laser scanning microscopy was performed using the three channels with the 488, 561, and 640 nm lasers. Each field-of-view consisted of 512 × 512 pixels (128 × 128 µm) and was imaged at 1.29 frames per second using bi-directional, resonant scanning. Optical image recordings began 15 s prior to insonification to establish initial cell state, and continued for 585 s to detect bacterial responses to the different exposure conditions. Any focus drift that occurred was manually corrected during the imaging procedure.

Statistics

All quantifiable data with multiple data points are reported as mean ± standard error of the mean (SEM) or mean ± standard deviation (SD).

Results

Fibrin biofilm optimization

Bright field microscopy revealed different growth patterns dependent on the starting bacterial inoculum concentration, the type of growth medium used, and the conditions biofilms were grown under (Figure 6.1). There was a stark difference between *S. aureus* biofilms grown in a mammalian cell culture medium (IMDM; Fig. 6.1A) and plasma (Fig. 6.1B), where under the same settings IMDM resulted in an abundance of bacteria and plasma only in sparse colonies with fibrin fibers projecting outwards connecting only to nearby colonies. Combining IMDM and plasma instantly induced clot formation

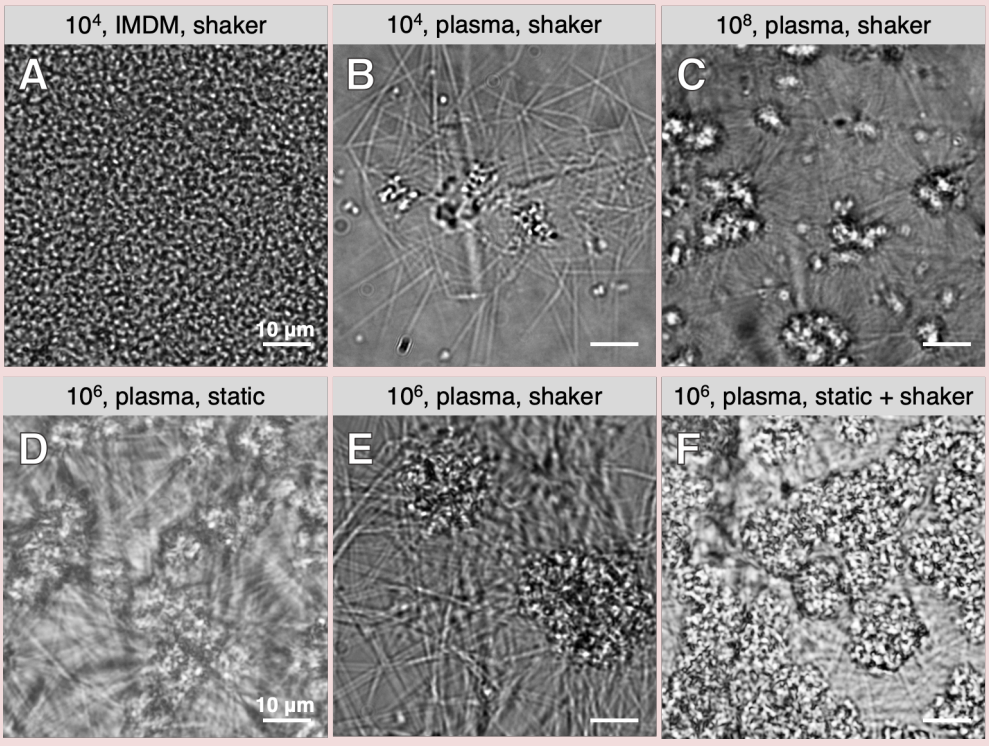

Figure 6.1. Representative examples of different tested growing conditions used for *S. aureus* fibrin biofilm model developement. Indicated at the top of each picture: bacterial starting concentration, growth medium, and growth condition for 24 h at 37°C.

throughout the whole channel. This was not a viable option as it not only led to no observable biofilm formation after 24 h, but also prevented medium refreshment in this set-up meaning follow-up sonobactericide experiments that required the adding of fluorescent dyes, microbubbles, and/or therapeutics would not be possible. If biofilms were initially formed with IMDM (24 h), then washed thoroughly and refreshed with plasma, no fibrin was detected in follow-up imaging. Increasing the starting inoculum from 10^4 to 10^8 bacteria (CFU/mL) in plasma resulted in more colonies and fibrinogen conversion to fibrin (Fig. 6.1C), though still at a much lower bacterial density than seen in Figure 6.1A. At all starting concentrations, the static growth condition facilitated more fibrin production, but did not enhance bacterial density. This can be seen in Figure 6.1D, where the static fibrin production was dense enough to slightly obscure the observation of the bacteria in brightfield. The optimal starting concentration was found to be 10^6 CFU/mL, having much denser bacterial aggregates than the lower and higher concentrations (Fig. 6.1E). Further optimization of a 3h initial static step to allow bacteria to adhere to the Ibidi slide, which was then followed by 21h of continuous orbital shaking led to an increased area of bacteria within a more robust, semi organized biofilm (Fig. 6.1F). Even though plasma was refreshed and biofilms were imaged every 24 h up to 72 h, none of the varying conditions showed enhanced growth beyond 24 h. The conditions for biofilm formation in Figure 6.1F were determined to produce biofilms better resembling the *in vivo* samples found in literature, and thus were used for all subsequent biofilm experiments. The initial fibrinogen concentration in plasma right after thawing was on average 2.35 g/L. The supernatants after 24 h biofilm growth at 37°C (Fig. 6.1F conditions) contained less than half the fibrinogen that was originally present at 1.10 g/L. (N=4). Plasma incubated for 24 h at 37°C without bacteria possessed an even lower average concentration of 0.75 g/L.

Fibrin biofilm confocal imaging

Confocal microscopy, as seen in Figure 6.2, revealed plasma grown *S. aureus* biofilms consisting of bacteria aggregates (pseudo-colored yellow; Fig. 6.2B) encased thoroughly in fibrin and within a network of connecting fibrin strands (pseudo-colored blue; Fig. 6.2C). Bacteria and fibrin fibers were not homogenously distributed throughout the biofilm. The bacteria were clumped together in dense aggregates with fibrin intertwined, in a less strand-like assembly, throughout the different layers of bacteria (Fig. 6.2D).

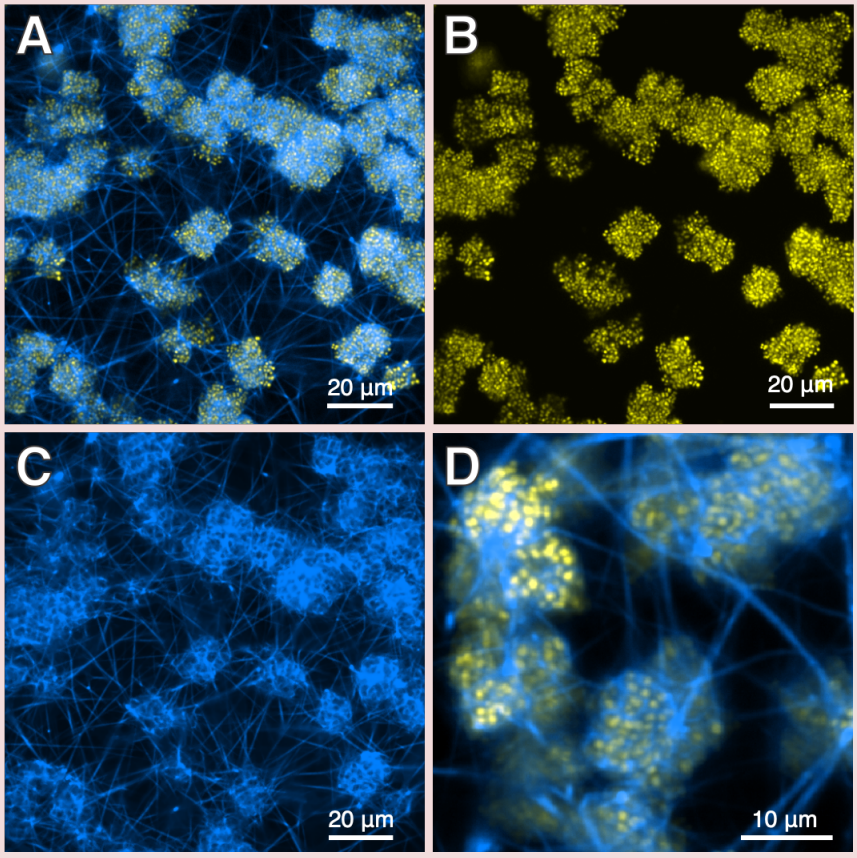

Figure 6.2. Confocal microscopy images of 24 h plasma grown *S. aureus* biofilms before treatment. (A) Composite of (B) bacteria imaged in the SYTO 9 (488nm) channel and pseudo-colored yellow; and (C) fibrin imaged in the Alexa 647 (640 nm) channel and pseudo-colored blue. (D) Composite zoomed-in image from a different biofilm.

Most of the aggregates were situated in the bottom half of the biofilm and appeared to have originated from bacteria that had adhered to the Ibidi slide. There were aggerates that were formed higher up, with some starting at 30 - 50 µm above the bottom of the biofilm (Ibidi slide). Fibrin strands seemed to originate from the aggregates, protruding outwards connecting to other strands and bacterial aggregates. This fibrin network, together with the encased bacteria, formed thick biofilms. For example, the biofilm in Figure 6.2 was 45.75 µm thick, and the thickest biofilm observed was ~60 µm. It should be noted that the complete thickness was not measured for every biofilm. The initial cell

status of bacteria within the biofilms were found to be predominantly living when propidium iodide was used as a dead cell marker. Slides with only plasma and the fluorescently-labeled fibrinogen consistently exhibited no fluorescence, indicating no auto or aspecific fluorescence signal or contamination. Fifteen fibrin fibers were measured in biofilms grown in human plasma with a mean ± SEM thickness found to be 0.81 ± 0.07 µm.

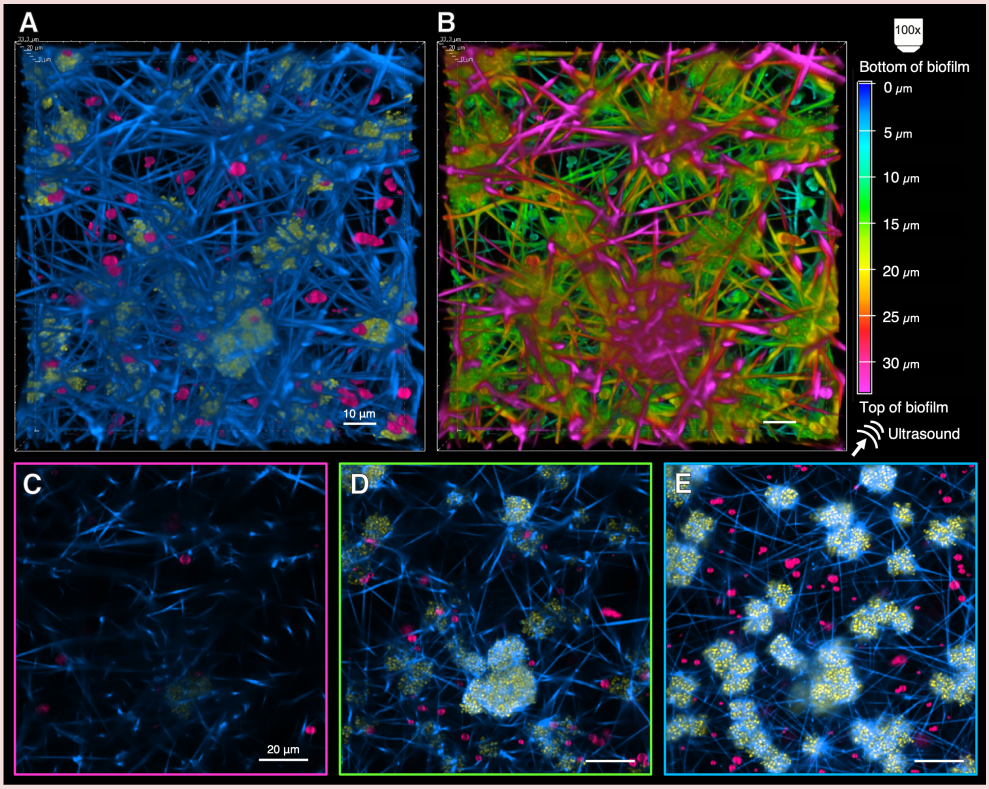

Figure 6.3. Three-dimensional volume rendering of confocal microscopy imaging of a plasma grown *S. aureus* biofilm with microbubbles before treatment. (A) Alpha-blended 3-channel composite of bacteria (psuedo-colored yellow; STYO 9), fibrin (psuedo-colored blue; Alexa 647), and microbubbles (psuedo-colored pink; DiI). (B) Same composite with depth color-coded with corresponding scale and orientation to the right. 2D image slices from the 3D volume rendering (C) at the top, (D) in the middle, and (E) at the bottom of the biofilm where the image borders are colored corresponding to the color depth scale in (B).

When microbubbles were added to the fibrin biofilms, a heterogeneous distribution was observed throughout the slide and biofilm (Figure 6.3). Microbubbles were present at every height within the fibrin biofilm network, which is highlighted with the depth coloring of Figure 6.3A seen in Figure 6.3B. Since the biofilms were flipped upside down (180°) so the buoyant microbubbles would float up against the sample, there were generally a higher number of microbubbles towards and at the highest point within the Ibidi slide, which was also the bottom of the biofilm (Fig. 6.3C-E).

Sonobactericide without a thrombolytic

Several phenomena were observed in the real-time recordings in response to sonobactericide treatment (Fig. 6.4), and did not occur with ultrasound alone. Firstly, the fibrin matrix was altered in direct response to microbubble oscillatory movements and displacement. Fibrin strands bent with a displacement of ~1-5.2 μm from their original position. Often these strands exhibited recovery, with the longest bent strand

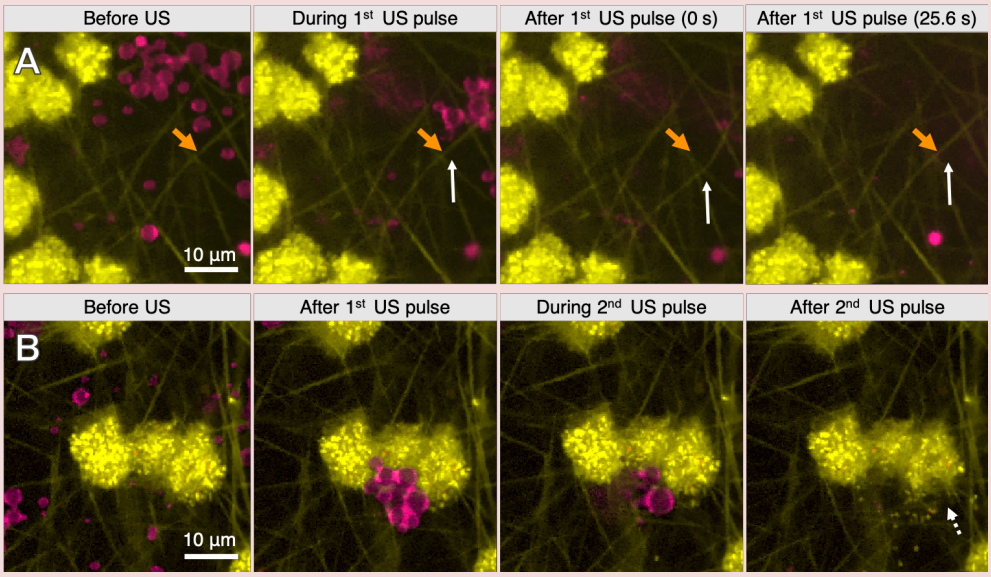

Figure 6.4. Confocal microscopy images of *S. aureus* fibrin-based biofilms (yellow, fibrin Oregon Green 488 and living bacteria SYTO 9; red, dead bacteria, propidium iodide) and microbubbles (pink, DiD) exposed to ultrasound (US; 2 MHz, 400 kPa, 100 cycles, every 1 s for 30 s, and 1 s continuous wave). (A) The white solid arrow indicates a fibrin strand that bent and recovered and the orange arrowhead indicates the original strand position. (B) The white dashed arrow points towards bacterial dispersion.

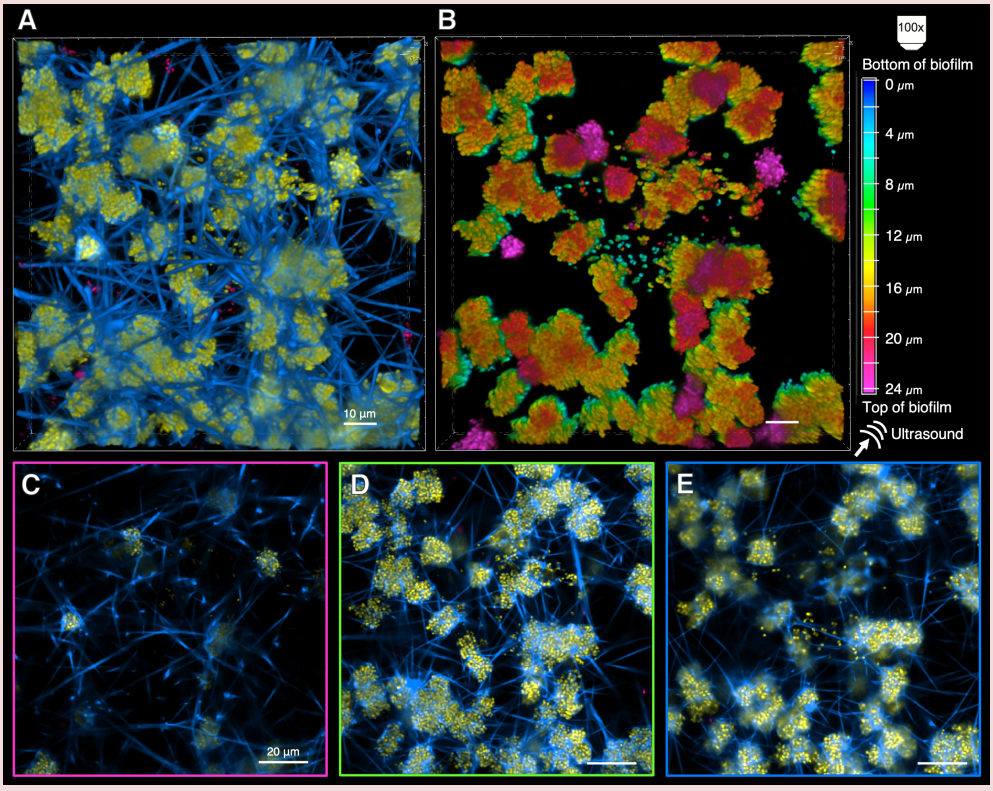

Figure 6.5. Three-dimensional volume rendering of confocal microscopy imaging of a 10 min sonobactericide-treated (2 MHz, 400 kPa, 100 cycles, every 1 s for 30 s, and 1 s continuous wave repeated every minute) *S. aureus* fibrin-based biofilm. (A) Alpha-blended 3-channel composite of bacteria (yellow; STYO 9), fibrin (blue; Alexa 647), and microbubbles (pink; DiI). (B) Only the bacteria channel with depth color-coded with corresponding scale and orientation to the right. 2D image slices from the 3D volume rendering (C)towards the top, (D) in the middle, and (E) at the bottom of the biofilm where the image borders are colored corresponding to the color depth scale in B.

(27.7 μm) recovering from a 3.7 μm displacement in 25.6 s (Fig. 6.4A). Secondly, bacterial dispersion and dislodgement from fibrin encasement was observed (Fig. 6.4B, Fig. 6.5) at varying degrees. Bacteria were dispersed, as single cells or small cell aggerates, not only in the 2D time-lapse recorded imaging plane but in all directions throughout the biofilm, as highlighted in Figure 6.5. Appreciated in the 3D volume rendering (Fig. 6.5A), the vast majority of dispersed bacteria are located in the immediate vicinity of fibrin strands. With the biofilms orientated upside down in the

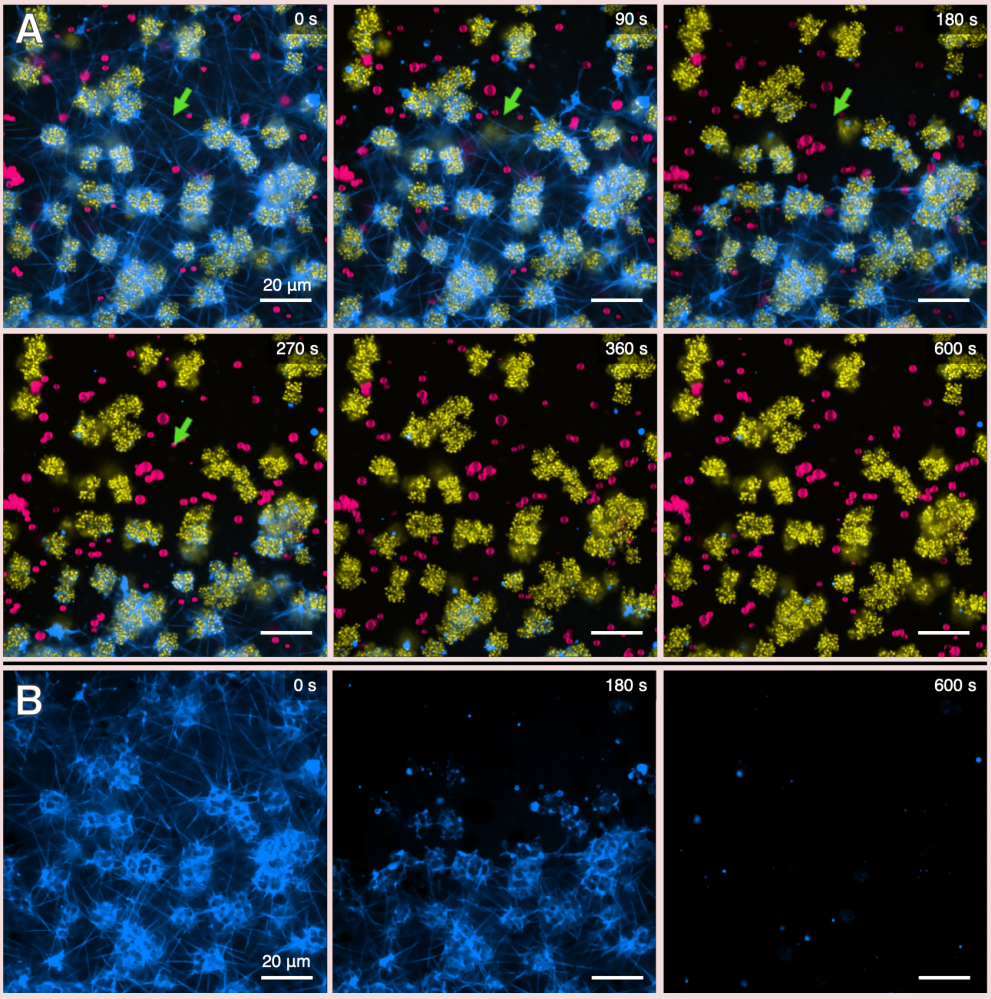

Figure 6.6. Time-lapse confocal microscopy recording of a *S. aureus* (yellow) fibrin-based biofilm with microbubbles (pink; DiI) exposed to rt-PA without ultrasound. (A) Selected composite images showing fibrin degradation and microbubbles rising up once liberated from the fibrin network. The green arrow indicates an aggregate pulled up and sinking down. (B) Fibrin (blue) channel time-lapse images only.

set-up, fewer cells were still observed at the top of the biofilm (i.e. below) despite gravity (Fig. 6.5C) than the middle or bottom (i.e. near the wall of the Ibidi channel) (Fig. 6.5D,E). Both fibrin strand bending and/or bacterial dispersion were observed in all MB with ultrasound treatment groups (2 MHz, 400 kPA, 100 or 1000 cycles; every 1 s for

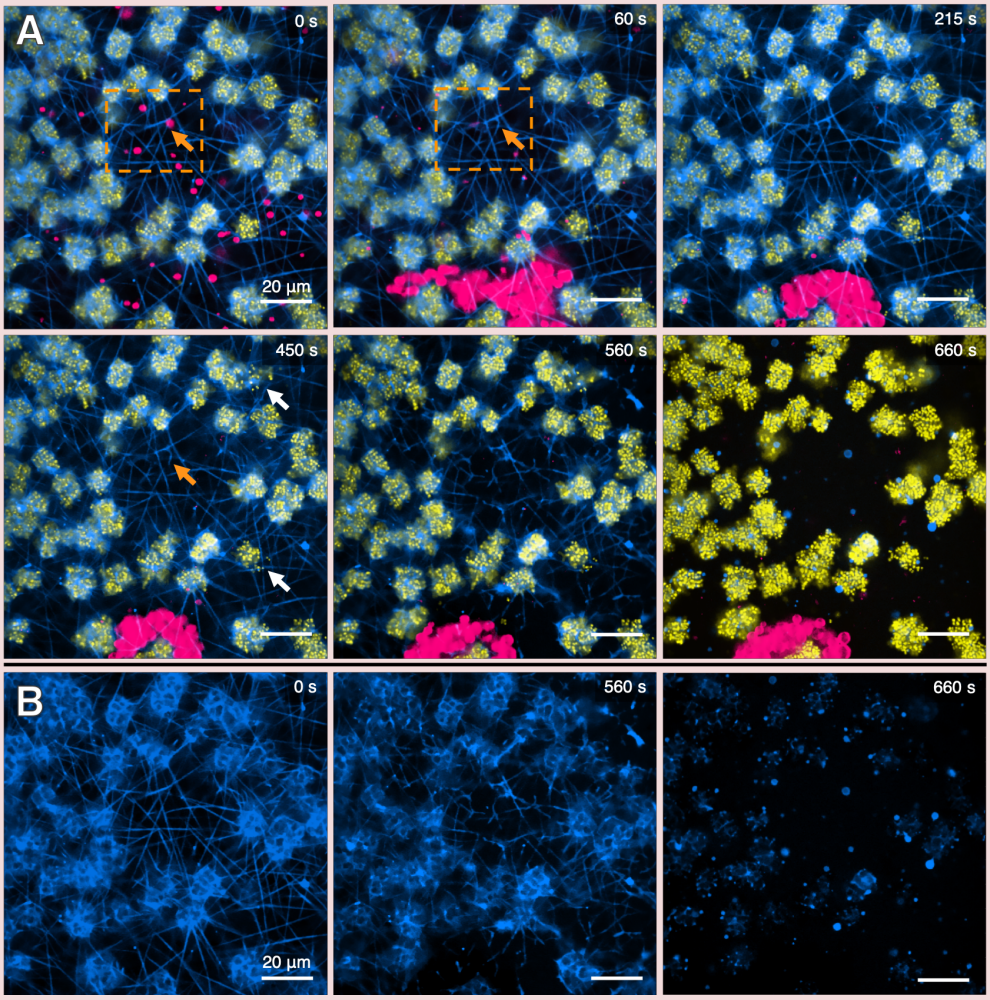

Figure 6.7. Time-lapse confocal microscopy recording of a fibrin-based biofilm with microbubbles (pink, DiI) exposed to rt-PA and ultrasound (US; 2 MHz, 400 kPa, 1000 cycles, every 1 s for 30 s, and 1 s continuous wave, every 1 min for 10 min). (A) Composite images showing fibrin bending and breaking (example indicated by orange box and arrow) and bacterial dispersion (white arrow), and ultimately all over fibrin degradation. (B) Fibrin (blue) channel time-lapse images only.

30 s, 1 s continuous wave). These effects were not always observed at or only with the first ultrasound scheme, and started or detected in subsequent ultrasound pulses throughout the recordings. Additionally, these phenomena occurred in response to single microbubble behavior and microbubble clustering, with clustered microbubble

behaviors to ultrasound often exerting a more sizable effect. If microbubble clustering occurred, this was usually in concordance with the continuous wave pulse that aided microbubble movement towards each other around the fibrin network.

Sonobactericide with a thrombolytic

The addition of the thrombolytic rt-PA to fibrin-based biofilms ultimately led to complete fibrin degradation. The pattern of degradation for rt-PA alone, as seen in Figure 6.6, showed a consistent wash-over effect that lasted 518 ± 86 s (mean ± SD; N=3). Degrading strands were seen to retract towards the bacterial aggregates, and once at the aggregate formed circular blebs. Most blebs dissolved away, but some remained throughout the duration of the recordings and at least up to 9.2 min after formation. The fibrin inside the bacterial aggregates degraded slower than the strands (Fig. 6.6B).

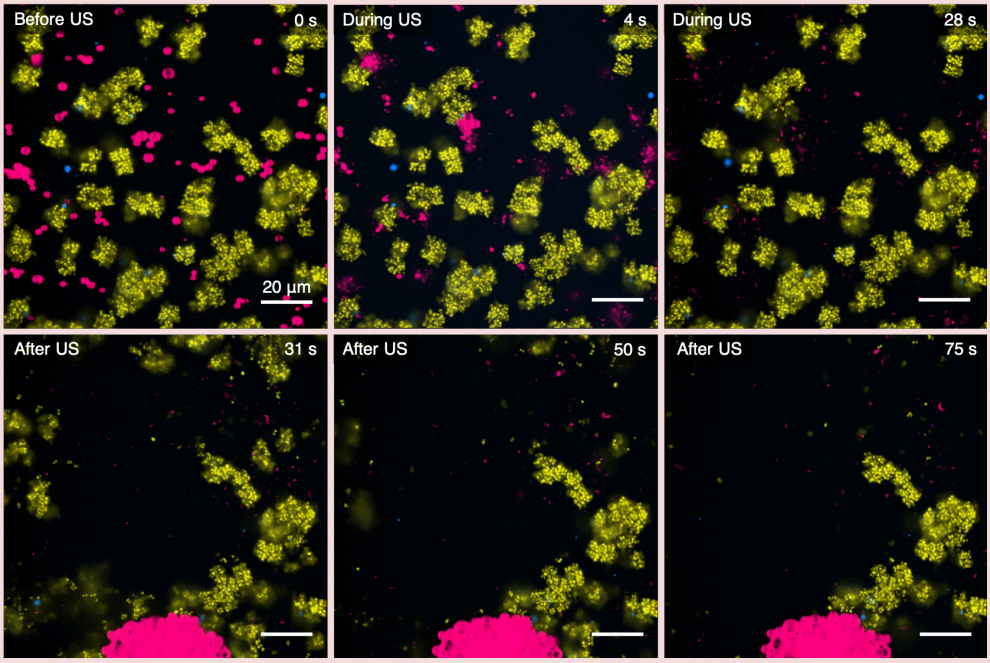

Figure 6.8. Time-lapse confocal microscopy recording of ultrasound insonification (2 MHz, 400 kPa, 1000 cycles, pulse repetition frequency 1 Hz for 30 s, and 1 s continuous wave) of the fibrin-degraded biofilm in Figure 6.6 by rt-PA only. Composite image frames of bacteria pushed and dispersed by ultrasound-mediated microbubble behavior, and subsequently falling out of the field-of-view.

The bacterial aggregates higher in the biofilm, i.e. not at the bottom potentially attached to the Ibidi chanel, were pulled up into the field-of-view by the fibrin strands retracting towards the attached aggregates. Once the fibrin strands that were connected to the higher aggregates degraded, those aggrgates were seen at first as bouyant, floating up and sinking, but ultimately sank out of the field-of-view after ~60 s (Figure 6.6, green arrow).

Bacterial dispersion and fibrin strand bending and recovery also occurred for ultrasound-activated microbubbles with rt-PA present (Fig.6.7A). Ultrasound alone with rt-PA still did not result in any dispersion or strand bending as without rt-PA. In addition to these described effects, fibrin strand breaking was now seen where fibrin had been previously bent, irregardless if the strand recovered to its original position or not (Fig. 6.7A). With ultrasound insonification, a different pattern of fibrin matrix degradation could also be observed (Fig. 6.7). Instead of a wash-over effect, the degradation began perfuse in the strand areas between the aggregates. Further it appeared to begin at the sites where fibrin strands experienced microbubble movements (e.g., Fig. 6.7A, orange arrow). Time to complete fibrin degradation once begun happened quicker at 322 ± 161 s (mean ± SD; N=7) for the sonobactericide treatment with rt-PA. Despite the different degradation pattern, circular fibrin strand blebbing and slower breakdown within the aggregates was similary observed, as seen in the last frame of Figure 6.7A and 6.7B.

When ultrasound was applied to the biofilm after fibrin degradation by rt-PA only, without other treatment conditions, the remaining bacterial aggregates that were possibly adhered to the Ibidi channel were more susceptible to sonobactericide effects (Fig. 6.8). Dispersion by ultrasound-induced microbubble movements before the 1 s continuous wave could be observed. However, the abrupt displacement and strong clustering of microbubbles in response to the continuous wave ultrasound pulse led to much more dispersion and aggregate displacement from the field-of-view.

Discussion

S. aureus fibrin-based biofilms were successfully grown *in vitro* in 100% human plasma, using Ibidi monochannel slides. Confocal microscopy revealed the formation of a 3D fibrin network of strands and an accumulation of fibrin encasing and within the bacteria aggerates. The fibrin-based biofilm appeared similar to what has been found in an *in vitro* infected blood clot model[68], an *in vivo* rabbit IE model[348], and infected IE patient tissue[334]. For example, the transmission electron microscopy of rabbit IE biofilms revealed fibrin forming pockets containing bacterial colonies with fibrin also within them[348], which seems comparable to the plasma grown bacteria in this model. Since there was no fibrin present in the plasma alone controls, it can be safely suggested that *S. aureus* induced the conversion of plasma fibrinogen into fibrin. It has been established that *S. aureus* secretes two types of extracellular coagulases, staphylocoagulase and von Willebrand factor binding protein[346], and has surface expressed coagulase (clumping factor) attached to the cell wall[349], which are all thought to contribute to infective endocarditis disease formation/progression. The difference in fibrin structure seen around the bacterial aggregates versus the distinct fibrin strands between them could perhaps then be due to the bound coagulase (and possibly others (e.g., fibronectin-binding proteins)), a higher free coagulase concentration that is closer to the bacterial aggerates, or a combination of the two.

It was also observed that within the biofilm the bacteria aggregates were situated predominately below a fibrin network layer. This upper layer of fibrin strands is seen *in vivo* and thought to be both a protective function against outside threats (such as the immune system) for microbes and host defense against secondary infection by preventing bacteria from disseminating[346]. This *in vitro* model lacks other cells that can contribute to the formation of fibrin, so in this case it is solely the microbial function. *S. aureus* produces coagulase at the moment it is inoculated, so initially at a rate faster than growth but then rapidly terminates at the first sign exponential growth rate headed towards stationary phase[350]. This could explain why maximally only about half of the fibrinogen in the plasma was found to be converted to fibrin by bacteria in this study. From a microbiological pathogenic stand point, it makes sense that bacteria only want to protect themselves to a certain extent only until they are established. If coagulases were continually produced, then too much shielding could prevent the

dispersal of biofilm cells that is naturally microbially triggered upon maturity. If other cells were to be introduced into this model, it does indicate that there is enough fibrinogen in human plasma to not necessarily be the limiting factor in replicating a more representative IE scenario but perhaps the anticoagulant presenting more of a challenge. It should be noted that the control samples, to which no bacteria are added, consistently showed a stronger decline in fibrinogen concentrations than the biofilm samples after 24 h. An explanation is hard to contrive from this, because without one it eludes that the presence of *S. aureus* somehow, for example, stabilizes fibrinogen so that it does not degrade (as much) or aspecifically bind to the Ibidi channel. More experiments need to be done to properly discern the reason for this finding before a definitive conclusion can be drawn.

The fibrin-based biofilms were found to be more robust, stiffer, and less susceptible to sonobactericide than the *in vitro* biofilms grown in IMDM medium as seen in Chapter 5 of this thesis. When looking at the same scheme of ultrasound (400 kPa, 100 cycles, pulse repetition frequency 1 Hz, for 30 s) without the continuous wave pulse and microbubbles without other therapeutics present, large amounts of dispersion were observed (up to 83.7%) in the biofilms grown in IMDM which was not observed to that degree in this study, or in the infected clots treated with ultrasound (albeit different settings) and microbubbles alone in Chapter 7[68]. This was most likely due to the restricted movements of the microbubbles situated within the fibrin mesh. Although bacterial dispersal and fibrin bending were observed without the continuous wave pulse, it was largely beneficial to get the microbubbles to move more within the fibrin network. In this study and in Chapter 5, microbubble induced effects were observed without microbubble displacement, but the degree of the effect was largely enhanced when microbubbles displaced and clustering occurred. Clustering was limited in this study unless the continuous-wave pulse was applied. Microbubble displacement and clustering may happen more readily in a fibrin-based biofilm experiencing flow like the infected clots, however rt-PA was still necessary to enhance sonobactericide treatment in that study[68] as it was here, ultimately leading to fibrin breaking and degradation. Another factor to consider was that the bacteria dislodged and dispersed due to sonobactericide appeared to stick to the fibrin strands (see Fig. 6.5). This was hard to appreciate until the biofilm was viewed in its three-dimensional structure. It is possible

that these bacteria are expressing fibrin binding surface proteins and bind to the fibrin strands[349,351]. If these cells are not binding to the strands, then alternatively the fibrin matrix may serve as a physical blockade or these bacteria are exhibiting buoyancy in the plasma counteracting gravity.

Although plasma as the media led to a much better mimic of cardiovascular biofilms than bacteria grown in traditional bacterial/mammalian cell growth media, the *in vitro* conditions of the disease model are naturally a limitation. Without being able to fully represent the varying circumstances found within the human body, such as the presence of immune cells, anatomical structure, whole blood components, and (pulsatile) flow, this model may likely underrepresent the biofilm composition compared to the *in vivo* situation. Although there are pathological reports of IE biofilms composed almost exclusively of fibrin and bacteria, which is typically not the case for *S. aureus*[345], immune and endothelial cells do play a role in pathogenesis[346] and should be considered in model development. It is possible that adding an antibiotic could have led to synergistic effects as seen in other sonobactericide studies[304], along with different ultrasound parameters having different degrees of effect, which both should be investigated in future studies *in vitro* and *in vivo*.

Conclusion

This study developed an *in vitro* cardiovascular *S. aureus* biofilm model in human plasma to investigate sonobactericide in real-time and at high resolution. Ultrasound-activated microbubble effects were observed leading to the bending and breaking of fibrin strands and releasement of bacteria from fibrin encasement, and enhancement of thrombolytic efficiency. The developed biofilm model and sonobactericide treatment settings together provide valuable insight into how fibrin is structured within a biofilm formed by *S. aureus* and the capabilities of microbubbles to directly alter fibrin structure and disperse encased bacteria, that both, to the best of our knowledge, have never been observed before in this manner. Harnessing these microbubble-induced effects could aid in the treatment of cardiovascular biofilm infections.

Acknowledgements

The authors would like to thank Robert Beurskens and Frits Mastik from the Department of Biomedical Engineering and Judith de Vries from the Department of Hematology, from the Erasmus MC University Medical Center Rotterdam, for their skillful technical assistance. The authors also thank the members of the Therapeutic Ultrasound Contrast Agent group (Biomedical Engineering Dept.) and the *S. aureus* working group (Medical Microbiology and Infectious Diseases Dept.) for their useful discussions. This study was financially supported by the Erasmus MC Foundation (fellowship to K.K.).

"It is the same with people as it is riding a bike. Only when moving can one comfortably maintain balance.

- Albert Einstein

7

An in vitro proof-of-principle study of sonobactericide

Kirby R. Lattwein, Himanshu Shekhar, Willem J.B. van Wamel, Tammy Gonzalez, Andrew B. Herr, Christy K. Holland, and Klazina Kooiman

Based on:
Scientific Reports, vol. 8, 34111, 2018

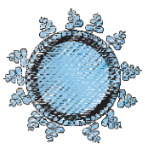

Abstract

Infective endocarditis (IE) is associated with high morbidity and mortality rates. The predominant bacteria causing IE is *Staphylococcus aureus* (*S. aureus*), which can bind to existing thrombi on heart valves and generate vegetations (biofilms). In this in vitro flow study, we evaluated sonobactericide as a novel strategy to treat IE, using ultrasound and an ultrasound contrast agent with or without other therapeutics. We developed a model of IE biofilm using human whole-blood clots infected with patient-derived *S. aureus* (infected clots). Histology and live-cell imaging revealed a biofilm layer of fibrin-embedded living Staphylococci around a dense erythrocyte core. Infected clots were treated under flow for 30 minutes and degradation was assessed by time-lapse microscopy imaging. Treatments consisted of either continuous plasma flow alone or with different combinations of therapeutics: oxacillin (antibiotic), recombinant tissue plasminogen activator (rt-PA; thrombolytic), intermittent continuous-wave low-frequency ultrasound (120-kHz, 0.44 MPa peak-to-peak pressure), and an ultrasound contrast agent (Definity). Infected clots exposed to the combination of oxacillin, rt-PA, ultrasound, and Definity achieved 99.3 ± 1.7% loss, which was greater than the other treatment arms. Effluent size measurements suggested low likelihood of emboli formation. These results support the continued investigation of sonobactericide as a therapeutic strategy for IE.

Introduction

Infective endocarditis (IE) is a life-threatening microbial infection of the heart valves and surrounding tissue, including endocardial prosthetic material. IE is associated with high morbidity and mortality (15-40% in-hospital and 40-69% 5-year mortality)[21,43,341,342]. Current standard treatment for IE consists of prolonged, intensive intravenous antibiotic therapy[21].

IE is characterized by valvular vegetations (biofilms) composed primarily of a thrombus-like mesh consisting of platelets, fibrin, extracellular polymeric substance, and bacteria at different stages of replication[334,7]. Staphylococcal, streptococcal, and enterococcal species of bacteria have been implicated as the primary cause of IE[21,43]. *Staphylococcus aureus* has been reported to have the single highest prevalence (30-31%) in IE[43] and is associated with the highest mortality and worst prognosis. These bacteria initiate colonization by adhering to microthrombi present on valves, caused either by endothelial inflammation, mechanical damage, or spontaneous formation on intact valvular surfaces[43,334,352].

High-risk surgical procedures may be required to treat IE, but this treatment is contraindicated in a large population of patients[341]. The presence of bacterial biofilm makes treatment challenging due to increased resistance to antibiotic action and the presence of bacteria in a dormant metabolic state. Bacteria situated within biofilms can be 100 - 1,000-fold less susceptible to antibiotics than the planktonic bacteria released from biofilms[75,353]. Furthermore, prolonged, high-dose antibiotic therapy paradoxically preserves persister cells within a biofilm that are tolerant to antibiotics[75]. When antibiotic therapy has concluded, persisters can switch phenotype and produce new biofilm, thereby reinitiating infection[75]. Adjuvant therapies for IE are desperately needed.

To treat various bacteria, both planktonic and residing in biofilms, other groups have successfully used low-frequency ultrasound (US) [≤1 MHz] combined with antibiotics[32,354-357]. Acoustic cavitation and streaming have been identified as the dominant mechanisms for what appears as an increase in antibiotic efficacy and penetration into biofilms. However, these studies have employed high acoustic pressures to induce inertial

cavitation, which could induce undesirable bioeffects[358]. Using ultrasound contrast agents (UCAs) as cavitation nuclei reduces the acoustic pressure threshold for producing cavitation[359], which could help translate this therapy to the clinic. UCAs are composed of encapsulated gas microbubbles (MBs; 1 – 10 µm in diameter) that oscillate volumetrically in response to US pressure variations, a phenomenon known as acoustic cavitation[36]. Cavitation of MBs has been shown to enhance US-induced bioeffects, which include drug delivery, cell death, and dissolution of thrombi (sonothrombolysis), by mechanisms such as enhanced fluid transport, sonoporation, and stimulated endocytosis[36,37,245,360]. Other investigators have tested the use of US in combination with MBs for enhancing biofilm degradation[62,65,112,124]. However, these studies have not evaluated the potential to enhance treatment of IE biofilms either by US, or US with UCAs.

In this paper, we report the results of a translatable, proof-of-principle study for treating *S. aureus* IE biofilms in an *in vitro* flow model. This treatment strategy that we have termed *sonobactericide*, combines US exposure and an UCA, with or without antibiotics or other therapeutics, to treat IE infections. A therapeutic of interest could be recombinant tissue plasminogen activator (rt-PA), a thrombolytic agent, because successful treatment of paediatric patients with IE has been reported previously[361-364]. We hypothesized that combination treatment with an antibiotic and a thrombolytic, in the presence of US and UCAs, will enhance the efficacy of *S. aureus* IE biofilm treatment. To test this hypothesis *in vitro*, we developed an infected clot model using *S. aureus* from an IE patient and human whole blood to replicate the *in vivo* early pathogenesis of IE. Infected clots were treated over a 30-minute period using an *in vitro* flow model equipped with time-lapse microscopy[152,365]. Infected clots were exposed to continuous human plasma flow either alone or with different combinations of the following: oxacillin (the antibiotic used clinically for the treatment of staphylococcal IE infections[101,102]), rt-PA, UCA Definity, and intermittent continuous-wave US. The cavitation activity nucleated by UCA was monitored using a passive detector. Treatment efficacy was assessed by measuring the infected clot width loss by bright-field microscopy. In addition, the particle size profile of the effluent produced by treatment was characterized to assess the likelihood of emboli formation.

Materials and Methods

Bacterial isolate

The *S. aureus* (JC01-2016) used in this study was an anonymized, de-identified strain isolated from an IE patient at Cincinnati Children's Hospital Medical Center, collected in accordance with guidance from the Institutional Review Board. According to institutional review board policy, anonymized, de-identified bacterial isolates such as JC01-2016 are considered Non-Human Subject Research and do not require informed consent. All experimental protocols in this study were approved by the University of Cincinnati institutional review board, and all methods were carried out in accordance with relevant guidelines and regulations. Overnight cultures of the isolate in tryptic soy broth (MP Biomedicals, USA) were added to DMSO (15%; Fisher Chemical, USA) and stored at -80°C. All overnight cultures from frozen stocks were streaked on tryptic soy agar (TSA; MP Biomedicals, USA) and incubated at 37°C.

Bacterial chromosomal DNA was isolated from a single colony using DNeasy Ultraclean Microbial kit (MoBio Laboratories, California, USA). Amplification and sequencing of the polymorphic X region of the Protein A gene was performed using spa1095F (5'-AGACGATCCTTCGGTGAGC-3') and spa1517R (5'-GCTTTTGCAATGTCATTTACTG-3') (Integrated DNA Technologies Inc., Iowa, USA)[366-368]. Amplification and sequencing was verified using primers spa1113F (5'-TAAAGACGATCCTTCGGTGAGC-3') and spa1514R (5'-CAGCAGTAGTGCCGTTTGCTT-3')[366]. PCR amplification (Mastercycler pro S, Eppendorf, New York, USA) was accomplished using 22 μl of sterile water, 1 μl of forward primer, 1 μl of reverse primer, 2 μl of isolated chromosomal DNA, and 24 μl of MidSci Taq Plus Mastermix with red tracer dye (Midsci, Missouri, USA). Thermocycler parameters were set as previously described[368]. Sequences were analysed for polymorphic X region repeats and matched to repeat succession sequences provided by Ridom SpaServer Database (http://spa.ridom.de) to determine the *spa*-type[367].

Antibiotic susceptibility testing and growth curve assessment

Oxacillin (28221; Sigma-Aldrich, Missouri, USA) susceptibility was determined (n=3) using the agar dilution method on Mueller-Hinton agar (Sigma-Aldrich, Missouri, USA), supplemented with 2% NaCl[36]. *S. epidermidis* ATCC 35984 (RP62a) was used only as

a quality control for antibiotic susceptibility testing. Bacterial growth curves (n=3) with an initial OD_{600nm} of 0.05 were produced as described by Harris et al.[370] with the exceptions of IMDM (containing no phenol red; Gibco, USA) instead of brain heart infusion medium, and samples of 3 mL were measured every 30 min for 9 h and a final sample measured at 24 h.

S. aureus inoculum preparation for infected blood clot formation

To prepare the *S. aureus* isolate for inoculation of blood clots, early exponential growth phase grown bacteria were generated following the same protocol for determining growth curves. Cultures with a starting OD_{600nm} of 0.05 were incubated at 37°C in IMDM. After 3.5 - 4 h of growth the *S. aureus* isolate was in the mid-exponential growth phase, and a 1.5 mL sample at an OD_{600nm} of 1 (approximately 1 x 10^9 CFU/mL) was obtained. The bacteria were grown to mid-exponential phase because this is when the expression of surface-associated adhesins generally occurs to facilitate initial colonization[371]. This bacterial suspension was kept at 37°C and subsequently used for inoculation within fifteen minutes of preparation.

Infected clot formation as model for IE

To produce the infected clots to resemble the *in vivo* early pathogenesis of IE, first human whole blood clots were created around silk sutures as previously described by Bader et al.[152] with the exceptions of complete experimental sterility and suture brand and size. Specifically, 9 cm sections of 6-0 silk sutures (1639G; PERMA-HAND, Ethicon Inc., USA) were threaded into 2.5 cm long borosilicate glass capillaries (1.12 mm inner diameter, World Precision Instruments Inc., USA). These capillaries were subsequently placed inside borosilicate glass culture tubes (10 mm diameter x 75 mm height, VWR International, USA). With University of Cincinnati institutional review board approval and written informed consent, venous whole blood was drawn from five healthy volunteers. Five hundred µL aliquots were transferred into each tube, and by capillary action blood was drawn into the capillaries. The glass tubes were incubated for 3 h at 37°C to allow the blood to clot around the suture, followed by refrigeration at 4°C for a minimum of three days to promote clot retraction. These retracted clots are stable and resistant to complete rt-PA thrombolysis[372].

After retraction, the clots were incubated at 37°C for 30 min. Aliquots of 30 minutes pre-warmed sterile human fresh-frozen plasma (3.325 mL; hFFP; Hoxworth Blood Centre, Cincinnati, Ohio, USA) were placed into borosilicate glass culture tubes, and inoculated with 175 µL of the prepared bacterial inoculum. The retracted clots were removed from the glass capillaries and carefully placed in the inoculated hFFP. To ensure the bacterial inoculate had reached all surfaces of the clot, the glass tubes were gently inverted approximately 8 times. Subsequently, the glass tubes were incubated for 24-30 h at 37°C, and reinverted every hour for approximately the first five hours.

Before placement in the *in vitro* flow system, infected clots were washed three times with PBS to remove any planktonic bacteria. Additionally, for histological analysis, two additional clot controls were used: sterile retracted clots alone; and sterile retracted clots following the infected clot protocol, with the exception of using no bacteria and thus incubating for 24-30 h in hFFP.

Histology

Clots were fixated in 10% neutral buffered formalin. Following fixation, clots were transferred to a tissue cassette containing a foam biopsy pad (first set specimens), or without a foam pad (2nd set specimens). These specimens were processed, embedded in paraffin, sliced (4 µm), mounted on a microscopy slide, and stained with either H&E or CV for cross-sectional analysis. Images were either captured using a camera (Digital Sight DS-Ri1, Nikon, Japan) mounted on a microscope (BX51, Olympus Inc., USA) with imaging software (NIS-Elements Basic Research, Nikon) for the first set of clot specimens, or with a virtual microscope digital slide scanner (C9600; NanoZoomer 2.0HT, Hamamatsu Photonics, Japan) and corresponding digital pathology viewing software (U12388-01; NDP.view2, Hamamatasu, Japan) for the second set of specimens.

CLSM

Individual infected clots were placed in a sterile chambered #1.5 polymer coverslip (80286; µ-slide 2 Well, ibiTreat, ibidi GmbH, Germany). Following the manufacturer's instructions, the LIVE/DEAD BacLight bacterial viability fluorescence kit (L7012, Molecular Probes, Oregon, USA) was used. After incubation, the chamber was flooded

with PBS, and then placed in the CLSM holder, where it was observed with an upright Nikon FN1 microscope attached to a Nikon A1R confocal system. A 25× long working distance objective (CFI Apo LWD NA 1.10 water-immersion) was used.

Experimental set-up

An *in vitro* flow model, depicted in Supplementary Fig. S7.1 online was used, which has been described in detail previously[152]**.** Using a syringe pump in withdrawal mode (Model 44, Harvard Apparatus, Massachusetts, USA), the perfusate flow rate was maintained at 0.65 mL/min (0.3 cm/s), consistent with previously reported sonothrombolysis studies using the same *in vitro* flow set-up[152] and coinciding with slow blood flow eddies experienced by IE biofilms[373,374].

The infected clots, along with the perfusate, were insonated with a custom-designed, unfocused, 120-kHz US transducer (60 mm diameter aperture; 5 cm distance to clot; Sonic Concepts, Washinton, USA). Distances for both the passive cavitation detector and the 120-kHz transducers to the clot was 5 cm[375]. Using a function generator (33250A; Agilent Technologies Inc., California, USA) and power amplifier (1040L; ENI, New York, USA), the transducer was excited at its resonant frequency (120-kHz). A custom-built impedance matching network (Sonic Concepts Inc., Washington, USA) was used to maximize power transfer to the transducer[152]. The acoustic field was measured and *in situ* acoustic pressure calibrated along the clot using a 0.5 mm hydrophone (TC 4038; Teledyne Reason Inc, California, USA) mounted on a computer-controlled three-axis positioner (NF-90; Velmex Inc., New York, USA)[152].

A single element acoustic passive cavitation detector (PCD; circular aperture diameter 19 mm; 5 cm distance to clot; 2.25-MHz centre frequency; -6 dB two-way bandwidth of 0.98-MHz; 595516 C; Picker Roentgen GmbH, Espelkamp, Germany) was aligned with the infected clot and used to monitor cavitation activity. As reported previously, ultraharmonic (UH) and broadband (BB) emissions were employed to detect stable and inertial cavitation, respectively[152]. To remove any noise from radiofrequency interference, the received signal from the PCD was filtered by a 10-MHz low-pass filter (J73 E, TTE, California, USA), and amplified with a wideband low-noise amplifier (CLC100, Cadeka Microcircuits, Colorado, USA). The signal was digitized (10 ms

duration, 31.25-MHz sampling frequency), and the power spectrum computed in MATLAB (The Mathworks, Massachusetts, USA). To compute the UH energy, UH bands of the power spectrum between 250-kHz and 1-MHz were summed over a 2-kHz bandwidth centred around each UH frequency[152]. The BB energy was computed by summing BB emissions between 250-kHz and 1-MHz in 4-kHz bands centred at each UH band, ± 10-kHz and ± 30-kHz respectively[152].

Experimental procedure

For each *in vitro* flow experiment, 30 mL of hFFP was placed in a 500 mL beaker for 2 h to reach gas equilibrium at 37°C. An infected clot was carefully mounted inside the glass capillary, connected to the flow system, and placed at the bottom of the 37°C water tank over the microscope objective. The focus of the PCD was aligned with the capillary and the 120-kHz therapeutic acoustic beam, and infected clots were treated for 30 min, which is the half-life of oxacillin in the body[376]. This time has also been reported for sonothrombolysis experiments[152,377]. A pulsed US exposure scheme, shown to promote UH emissions, was used as described by Bader et al.[152]. Definity and perfusate were insonated for a period of 50 s at a peak-to-peak pressure of 0.44 MPa. This was directly followed by a 30 s quiescent period to allow a fresh influx of UCA to fill the glass capillary. Acoustic emissions recorded by the PCD were acquired at a rate of 2.33-Hz (0.43 s inter-frame time)[152]. This scheme was repeated in intermittent fashion over the 30 min treatment time.

For infected clots, 9 different experimental flow exposures were included: (1) plasma alone; (2) plasma and the US exposure scheme; (3) plasma, US exposure, and Definity; (4) plasma and rt-PA; (5) plasma, rt-PA, and US exposure; and (6) plasma, rt-PA, US exposure, and Definity; (7) plasma, oxacillin, and rt-PA; (8) plasma, oxacillin, rt-PA, and US exposure; and (9) plasma, oxacillin, rt-PA, US exposure, and Definity. Definity (Lantheus Medical Imaging, North Billerica, Massachusetts, USA)[378] vials were activated according to the instructions of the manufacture and diluted to a concentration of 2 µL/mL (2×10^6 MBs/mL), the infusion dose previously used for sonothrombolysis[152]. For oxacillin, 172 µg/mL was chosen because this is the peak serum concentration of the antibiotic therapeutic dose in humans treated with IE[379,380]. For all experiments with rt-PA, 3.15 µg/mL was used, which is within the therapeutic dose range for

thrombolysis interventions[381,382]. At least 9 experiments were performed for a given treatment, using blood from 5 donors (total of 82 experimental infected clots).

Calculations of infected clot degradation metrics

To quantify instantaneous infected clot degradation from the images recorded with the CCD camera, an edge-detection and tracking analysis script in MATLAB was used as described previously[152,377]. Briefly, the initial infected clot width (ICW_i) at 0 min and the final infected clot width (ICW_f) at the completion of the 30 min experiment were used to determine FICL using the following equation:

$$\text{FICL} = \frac{\text{ICW}_\text{i} - \text{ICW}_\text{f}}{\text{ICW}_\text{i}} \times 100\%$$

The width of the infected clot was defined as the distance between the edges for each row of the image, minus the width of the suture.

Post-experiment bright-field light microscopy

Following *in vitro* flow experiments of plasma alone and the combination of plasma, thrombolytic, and antibiotic, the flow system was left intact and placed on top of an inverted microscope (IX71, Olympus Inc.). Images were obtained using a 12-bit CCD camera (Retiga-EXi, Q-imaging, British Columbia, Canada) equipped to the microscope in order to obtain additional qualitative information (e.g. colour, larger field-of-view) about clots than that inferred from time-lapse imaging.

Calculations of infected clot degradation metrics

Effluent samples from the *in vitro* flow experiments were measured directly following the 30 min protocol using a Coulter Counter (Multisizer 4, 30-µm aperture, Beckman Coulter, California, USA) to quantify the size distribution (600 nm – 18 µm) of debris, cells, and cell aggregates. This measurement was completed three times for each experimental type, with five replicates per treatment.

Statistics

Data were statistically analysed using GraphPad Prism 7 (GraphPad Software Inc, California, USA) with a significance level of $p < 0.05$. To analyse the FICL difference of means among the experimental exposures for infected clots, the Kruskal-Wallis test was used. Additionally, post-hoc testing was performed using Dunn's non-parametric pairwise multiple comparison test. The UH and BB cavitation energy difference of means was analysed using a two-way ANOVA with post-hoc analysis using Tukey's multiple comparisons test. For both the cavitation energy and FICL analyses, the Tukey method was used to calculate and report medians and interquartile ranges.

Data Availability

The data generated during and/or analysed during the current study are available from the corresponding author upon reasonable request.

Results

Bacteria isolate characterization

The *S. aureus* IE clinical isolate used in this study was found to have the *spa*-type t021. Oxacillin susceptibility was determined to be less than 2 ug/mL, thereby classifying it as methicillin-susceptible. The *S. epidermidis* quality control strain was resistant to all oxacillin concentrations, which is in accordance to its already well-known methicillin-resistant status. A growth curve indicating the lag, exponential, and stationary phase was completed for the *S. aureus* IE isolate in Iscove's Modified Dulbecco's Medium (IMDM). Based on this curve, all inoculums were prepared for experiments when bacteria were in the mid-exponential growth phase, around an optical density at 600 nm (OD_{600nm}) of 1.

Histological analysis and confocal viability assay of infected clots

Close inspection of the infected clots at high magnification showed a biofilm outer layer consisting of fibrin-embedded *Staphylococci* (Fig. 7.1a, b). Directly below the dense matrix of large quantities of bacteria within the fibrin mesh was a layer of fibrin. The inner portions of the clots were comprised of fibrin, sporadic immune cells, and predominately erythrocytes. Additionally, locations further from the clot core contained fewer erythrocytes, and an increasing amount of fibrin, seen in both the haematoxylin-eosin (H&E) and crystal violet (CV) staining (Fig. 7.1a, b). CV staining confirmed the location and presence of staphylococcal bacteria, because on a cellular level only gram-positive bacteria are stained purple (Fig. 7.1b). Of additional note, the iodine in the CV resulted in the staining of the erythrocytes brown and the fibrin yellow.

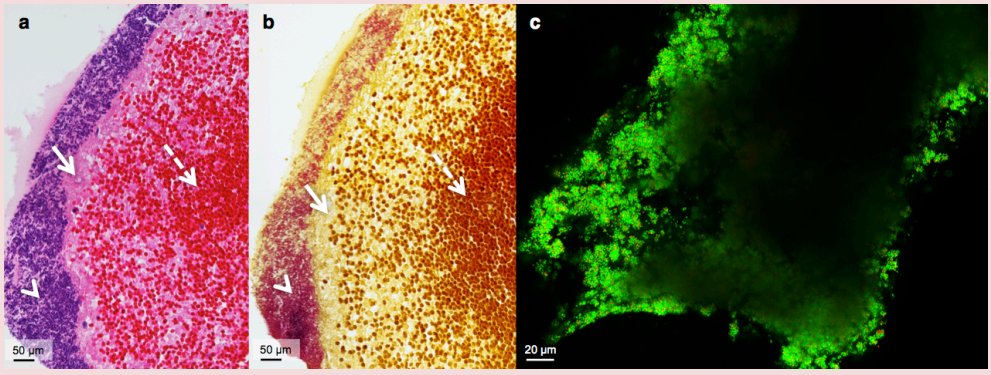

Figure. 7.1. Cross-sectional histological staining and confocal laser scanning microscopy of the infected clot model. Both A and B are each composed of two combined microscope images acquired at 40x magnification. (a) Image of H&E staining of an infected clot cross-section. The arrowhead indicates bacteria (purple), the arrow points at fibrin (pink), and a dashed-line arrow at erythrocytes (red). (b) Crystal violet staining, where an arrowhead indicates bacteria (purple), an arrow for fibrin (yellow), and a dashed-line arrow for erythrocytes (brown). (c) Image J maximum intensity projection of live (green, SYTO 9 stained) and dead (red, PI stained) *S. aureus* comprising the outer layer of a representative infected clot.

The interpretation of the living status of the infected clot bacteria could not be obtained from H&E and CV histological staining. Therefore, confocal laser scanning microscopy (CLSM) with two fluorescent markers was used to determine if bacteria were viable before flow experiments. In each case, the biofilms lining the clots were made up of predominately viable bacteria of 0.5-1 μm spheres (-cocci) (see Fig. 7.1c; fluorescently labelled green by Syto 9). Dead bacteria (fluorescently labelled red by propidium iodide) were present, however at substantially lower numbers than viable bacteria. Corresponding to the histology, the thickness of the biofilms was not homogeneous. Additionally, the biofilm structure did not appear completely intact in some places (e.g. bottom left corner, Fig. 7.1c). Occasionally observed, most likely due to green auto-fluorescence, were rod-shaped fibre-like chains, suggesting fibrin, and round objects larger than bacteria, suggesting erythrocytes, immune cells, or possibly platelets.

Histological comparison of infected and control clots

When examining the H&E staining that was performed at the same time for all infected and control clots, the infected clots, though from a different batch, had similar morphology (Fig. 7.2a1-a3) to the previous stained specimens (Fig. 7.1a). Briefly, a biofilm composed of bacteria encased the fibrin mesh on the outer layer of the clots. Directly below the biofilm was a thick fibrin layer; and below the biofilm layer, the number of erythrocytes present increased towards the predominately erythrocyte core (Fig. 7.2). The suture (top right in Fig. 7.2a1 and 7.2a3) supporting the infected clot was also lined in a fibrin layer and biofilm (Fig. 7.2a3). The biofilm was heterogeneous with varying thickness. The control clots (Fig. 7.2b1, 7.2c1) were structurally and morphologically different from the infected clots. The sterile retracted clots consisted of a porous perimeter surrounding a dense erythrocyte core (Fig. 7.2b1). The outer most layer of the perimeter appears to be less porous than the rest of the inner region (Fig. 7.2b2). This less porous outer layer is more prominent in the sterile retracted clots incubated 24 h in human fresh-frozen plasma (hFFP; Fig. 7.2c2). This clot was also devoid of the dense core seen in the sterile retracted clot not incubated with plasma. The sutures are eccentric in the infected clot compared to the controls (Fig. 7.2a3-c3). Additionally, both the infected clot core and the sterile, retracted clot have tear streaks; with multiple found in the infected clot core (Fig. 7.2a1) and two streaks, one from the left side of the suture to the outside and the other to the right of the suture, of the sterile clot (at 12 o'clock in Fig. 7.2b1).

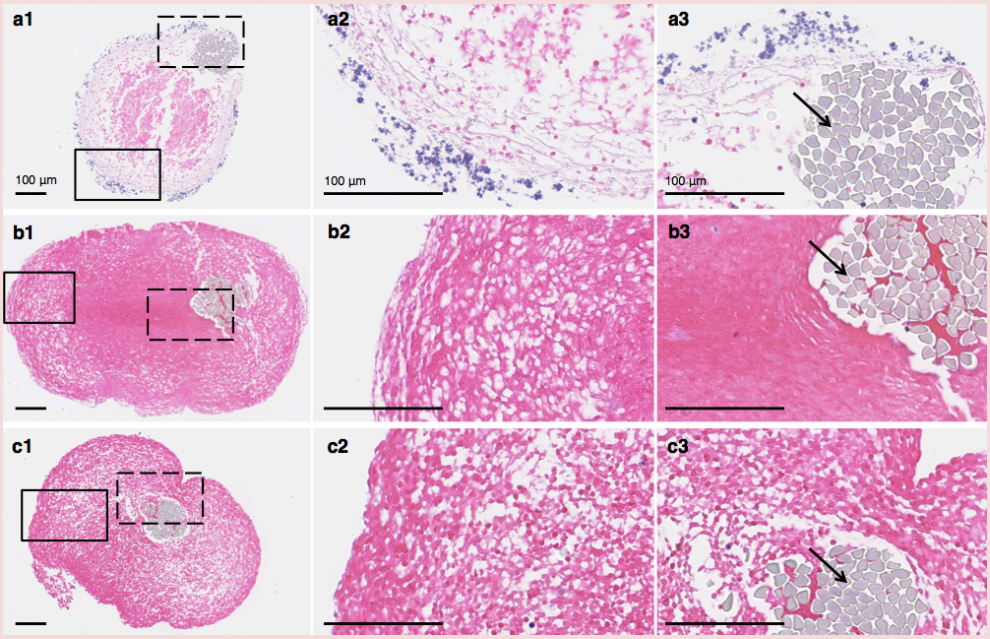

Figure 7.2 H&E histology of infected and control clot cross-sections. (a1-3) Infected clot, (b1-3) sterile, retracted clot, and (c1-3) sterile, retracted clot incubated 24 hr in sterile hFFP. The boxes with a solid black line in a1, b1, c1, represent the border region of zoomed-in focus for the images to the right (a2, b2, c2). The dashed line boxes represent the zoomed-in area of the clot by the suture for the corresponding images to the far right (a3, b3, c3). Black arrows indicate a suture thread (light grey). Images (a1, b1, c1) are at 10x magnification, and the rest (a2-3, b2-3, c2-3) are at 40x magnification.

Infected clot degradation as determined by width loss

In this study, infected clots were subjected to different combinations of therapeutics (oxacillin, rt-PA, intermittent continuous-wave 120-kHz US, and UCA Definity), while subjected to plasma flow under controlled conditions. The infected clots had an average diameter of 442.2 μm ± 47.6 SD with no significant differences between the treatment groups. The fractional infected clot width loss (FICL) over 30 min treatment was used to quantify the extent of degradation, and was computed using custom automated computer image analysis of the time-lapse microscopy images. As seen in Figure 7.3, infected clot degradation is reported as the percentage decrease in infected clot diameter

at 30 min. A perfusate flow rate of 0.65 mL/min provided minimal degradation of infected clots due to mechanical shear stress and endogenous tissue plasminogen activator from plasma flow alone, thus providing us with a stable, reproducible control. When rt-PA and oxacillin were added to the plasma, infected clot width loss appeared highly variable, ranging from minimal (6.2%) to full clot width loss, i.e. 100% FICL. Similar amounts of degradation as the plasma alone group were seen when US alone under plasma flow was used as treatment. The addition of rt-PA and oxacillin to the perfusate of the US group demonstrated a high level of variability (-14.8 – 99.9%), similar to the rt-PA and oxacillin without US treatment. The addition of Definity to the plasma and US did not result in large amounts of infected clot degradation (< 20%). However, Definity added to the plasma, rt-PA, oxacillin, and US perfusate treatment group resulted in an almost complete loss for all infected clots (99.3 ± 1.7%). This was statistically significantly different than the plasma, US, and Definity treated clots without the rt-PA and oxacillin addition.

Post-experimental light microscopy

In addition to the transverse visualization of the clots during the 30 min time-lapse imaging, a longitudinal perspective was also obtained directly after experiments using light microscopy and a colour camera. Following experiments with plasma alone, the structure of the infected clots appeared intact and adherent to the suture (Fig. 7.4a). At a higher magnification, the biofilm was visible and observed to be surrounding both the clot (red) and suture (horizontal black line) (Fig. 7.4b). The images of infected clots treated with plasma alone were consistent with histological findings. Infected clots were composed of a somewhat dense core becoming less dense towards the outer perimeter, and the biofilm as the outermost layer. When infected clots were treated with rt-PA and oxacillin in combination with the plasma, the border of the clot was no longer smooth, but irregular in shape and also appeared less dense (Fig. 7.4c). This border was also observed with the monochromatic camera during time-lapse imaging appearing as a rolling-adhesion type motion of fibrin degradation products down the length of the clot. However, the camera and experimental set-up did not allow for capturing the complete length of the clot. After treatment with all therapeutics combined, US exposure, Definity, rt-PA, and oxacillin, revealed a visibly bare suture (Fig. 7.4d).

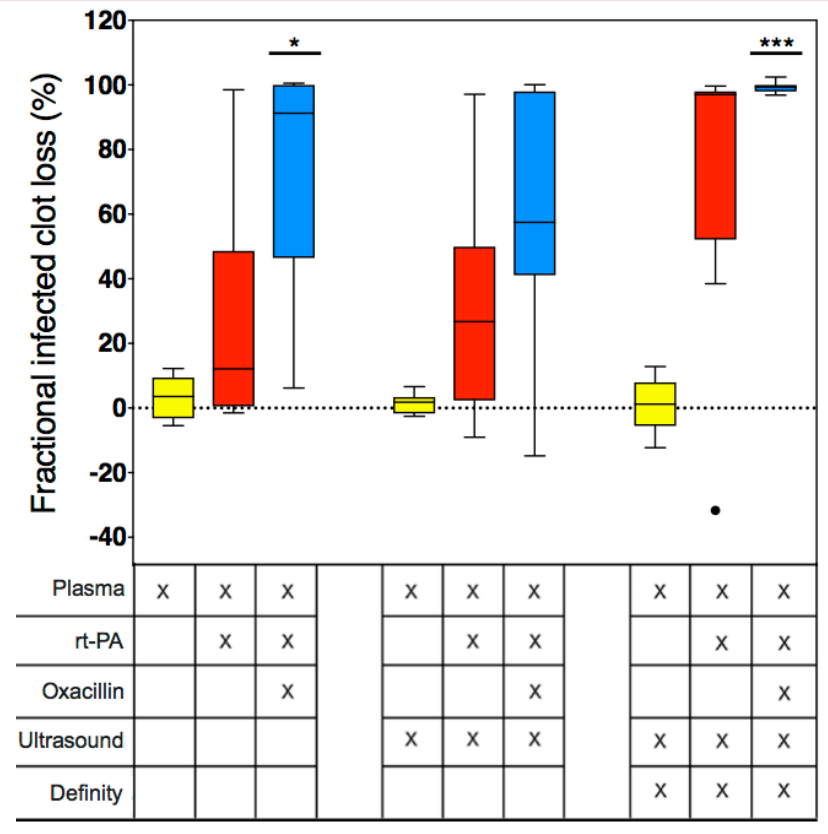

Figure 7.3. Fractional infected clot loss following different treatments. Boxes represent the interquartile range. The lines within the boxes represent the median and the whiskers indicate 1.5 times the interquartile range. The dot depicts an outlier as determined using the Tukey method. A single asterisk ($p<0.05$) or three asterisks ($p<0.001$) with a solid line above the boxes represent a statistically significant difference with the plasma alone, the plasma with ultrasound, and the plasma, ultrasound, and Definity treatment groups. The different treatment conditions are given in the table below the graph. N=9 for all treatments, with the exception of the plasma and ultrasound treated group (n=10).

Cavitation detection

Two different types of cavitation energies, ultraharmonic (UH) and broadband (BB), were detected with the passive cavitation detector (PCD), demonstrating the presence of both stable and inertial cavitation. When US without Definity was used in treatment

groups, very low levels of cavitation were detected for both types of energy (Fig. 5a, 5b). The addition of Definity resulted in significant higher levels of UH energy (Fig. 5a), indicating stable cavitation. Additionally, these three treatment groups with Definity exhibited significantly higher UH energy than BB (Fig 5a, 5b), which indicates more stable than inertial cavitation. Both UH and BB cavitation was observed to be higher in the Definity, rt-PA and oxacillin treated infected clots, albeit not a significant difference from the other two treatment groups which included Definity.

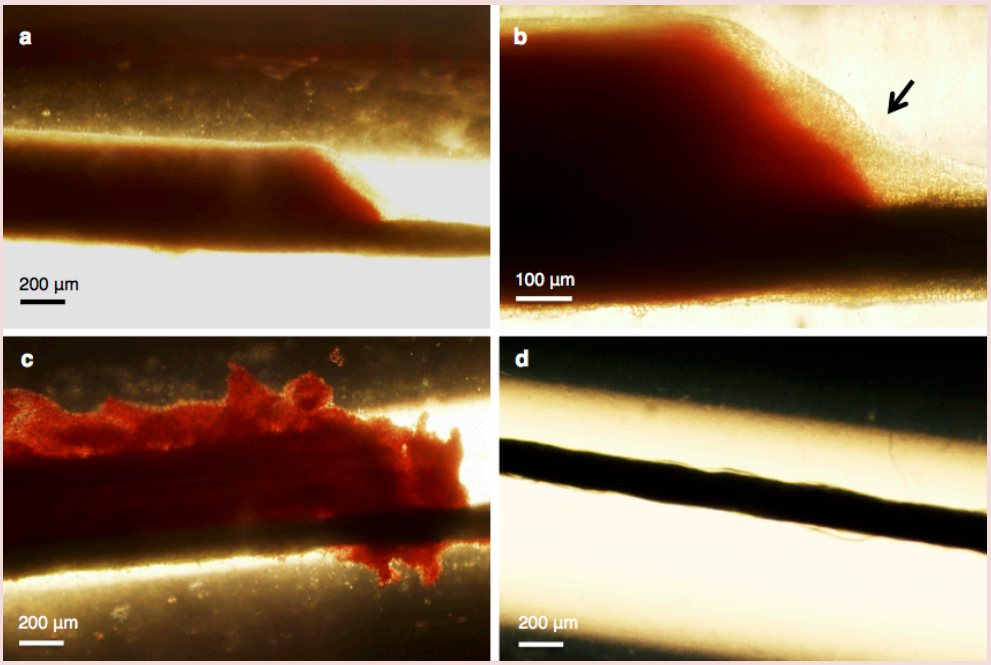

Figure 7.4. Bright-field light microscopy imaging of infected clots acquired directly following treatment. Infected clot treated only with plasma at 4x (a) and at 10x magnification (b). The black arrow in image b points out the biofilm (beige). (c) A plasma, rt-PA, and oxacillin treated infected clot at 4x magnification. (d) A plasma, rt-PA, oxacillin, ultrasound, and Definity treated infected clot at 4x magnification. The sutures (black line) are situated at the bottom of the clots, which can be observed to the right of the clot in images a-c.

Effluent particle size detection

The number-weighted size distribution of effluent particles, measured directly following treatment, is shown in Figure 6. The largest particle size detected was 10.4 µm, and 99.6% of the particles were smaller than 5 µm. The plasma treatment alone had the lowest number of particle counts, and the infected clots treated with US, Definity, rt-PA, and oxacillin had the largest amount of counts. Note that the smallest particle-sizing bin of the Coulter counter had a diameter of 0.6 µm.

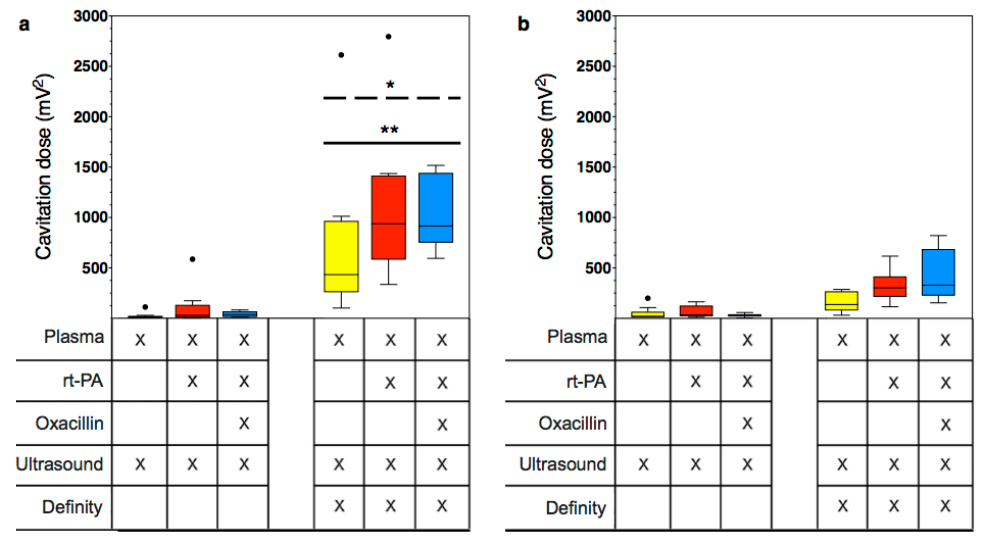

Figure 7.5. The ultraharmonic (a) and broadband (b) cavitation energy detected by the passive cavitation detector in response to 120-kHZ ultrasound insonification. Boxes represent the interquartile range. The lines within the boxes represent the median and the whiskers indicate 1.5 times the interquartile range. Black circles depict outliers as determined using the Tukey method. A single asterisk ($p<0.05$) above a dashed line represents a statistically significant difference between the ultraharmonic and broadband energies of the same treatment group. Two asterisks ($p<0.01$) represent a statistically significant difference of ultraharmonic energy between the group and the ultrasound without Definity groups. The different treatment conditions are given in the table below the graphs.

Discussion

This proof-of-principle study reports the potential efficacy of sonobactericide, combined with antibiotics and rt-PA, to enhance the treatment of bacterial infected clots in an *in vitro* flow model. In addition, this study also reports on the methods used to create a translatable *in vitro* infected clot model using human and bacterial products, on the basis of the IE isolate, methodology of infected clot, histology, and flow media, to mimic the known early pathogenesis of IE.

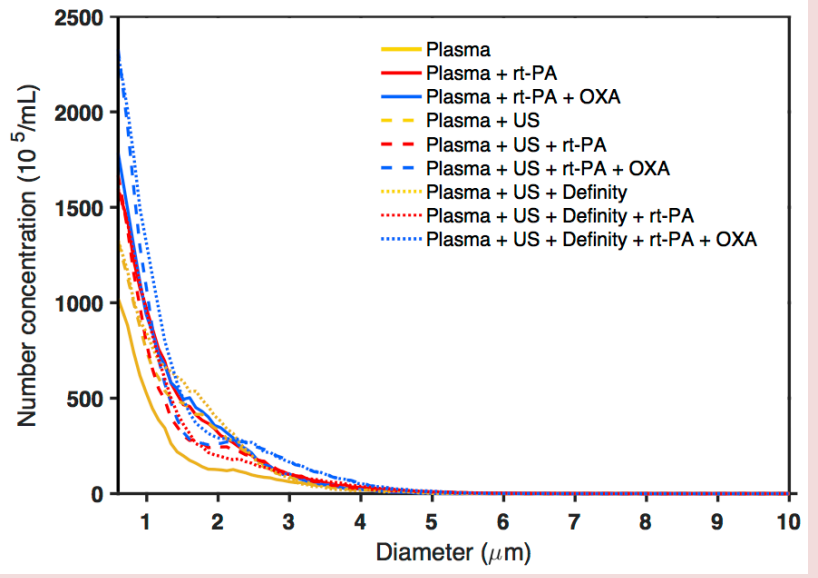

Figure 7.6. Effluent characterization using particle size measurement with the Coulter counter. Colours and line style represent different treatment groups with yellow indicating no rt-PA or oxacillin, red indicating rt-PA without oxacillin, and blue indicating oxacillin addition (n=3 per group; line represents the average). Dashed lines indicate treatment with ultrasound; dotted lines indicate treatment with ultrasound and Definity. The number-weighted particle size distribution is shown with the background subtracted. US = ultrasound and OXA = oxacillin.

To model the *in vivo* situation, a methicillin-susceptible *S. aureus* isolate that originated from an IE patient was used. A clinical IE isolate was chosen for translatability by ensuring the bacteria had the necessary factors to induce IE in a patient, because non-IE

originating isolates may lack the bacterial characteristics necessary for proper adherence (e.g. adhesins, fibronectin-, and fibrinogen-binding proteins) to host micro-thrombi to induce IE[383,384]. The isolate's *spa*-type t021 has previously been isolated from IE[385]. Although we did not directly perform an in-depth virulence factor analysis of this isolate, it has been demonstrated previously that isolates (N=105) originating from IE patients from different countries all contained the same surface-associated adhesins shown to be important for the invasiveness and development of IE (clfA, clfB, fnbA, and sdrC)[386,387]. Additionally, these factors important for IE development are highly conserved[388]. *S. aureus* is a known producer of coagulase, an enzyme that converts soluble fibrinogen into fibrin[349]. This fibrin scaffold allows the bacteria to encase themselves in a protective structure, consisting of bacterial and host components[389,390]. A marked presence of gram-positive bacterial colonies encapsulated in fibrin is seen in our histology (Fig. 7.1 and 7.2), which is consistent with that of IE in *in vivo* animal models and human surgically excised valves[334,348,390-393].

The progression of the presence of microthrombi on heart valves into IE biofilms is dependent on bacterial adherence to these initial clots[352,390]. Two previous studies developed infected clots as an *in vitro* model of IE, using a mix of human, animal, and synthetic products[394,395]. McGarth et al.[394] suspended bacteria in an eppendorf tube with a fibrin glue recipe consisting of human cryoprecipitate, bovine thrombin, monofilament line, and calcium chloride to create infected clots. Another study reported by Palmer, et al.[395] modified the previous method to include platelets and aprotinin (bovine) solution. Our study used infected retracted human blood clots, and the only synthetic media used was IMDM, which both may allow for bacterial adherence that better mimics the human situation *in vivo*. Additionally, this methodology resembles the early pathogenesis of IE, in which micro-thrombi are formed on heart valves first and then bacteria adhere and subsequently grow into an IE biofilm[43,334,352]. Human cell culture media for growing bacteria have previously been used[396,397]. IMDM was chosen because it emulates the iron-restricted environment *in vivo*. Iron restriction leads to the upregulation of virulence factors which would not be present if grown in a traditional iron rich bacterial growth media[398].

Histology and live cell imaging revealed that the morphology of infected clots reported in our study (Fig. 7.1a, b, Fig. 7.2) were consistent with the pattern of biofilm growth[7]

and resembled the structure of IE biofilms found in animal and patient samples[334]. Though limited polymorphonuclear (PMN) leukocytes are seen in our histology, neutrophilic inflammation is commonly mentioned in histopathologic findings *in vivo*. However, this inflammation is seen with regards to the valve tissue itself, resulting from endocardial injury[43]. Furthermore, it is well established *in vivo* that biofilm in IE represents a zone of localized agranulocytosis and that it would be rare that PMNs would be able to come into direct contact with the fibrin embedded bacteria[392,393]. This is supported by the clear separation of bacterial colonies and PMNs seen in histologic studies of animal and human IE biofilms[334,348,390,391]. Heterogeneous accumulation of bacteria is evident in the confocal microscopy images of the biofilm (e.g. bottom left corner, Fig. 7.1c) which is not contiguous in some places. This irregularity could also be due to the friable nature of infected clots after thin sample preparation, which could have been damaged during transport from fluorescent staining to the CLSM system or during the image capturing process.

It is widely known that the efficiency of a drug given intravenously can be affected by binding of the drug to plasma proteins[399]. Our flow model included the interaction of oxacillin with plasma proteins and inhibition of fibrinolysis with plasminogen activator inhibitor (e.g. PAI-1) and antiplasmin[400] since we used human plasma as our flow media. Additionally, MB oscillations can be affected by the viscosity of the surrounding medium, with damping occurring with increased viscosity[401]. Thus, inclusion of human plasma in our flow studies provided a test of the therapeutic effect of sonobactericide in the presence of a higher viscosity fluid approximating whole blood.

It has been demonstrated that IE biofilms *in vivo* form and generally exist on the low-pressure chamber side of valves[373]. This side of the valves are exposed to normal and regurgitant jet flow, however early IE biofilms are located beside the jet flows where low velocities exist[374]. Additionally, a range of velocities (0 to 45 cm/s over one cardiac cycle) have been reported across the mitral valve[402], which is a common site of IE. We chose 0.3 cm/s for all experiments in the *in vitro* set-up because 1) this is within range of flow speeds experienced by IE biofilms; and 2) this presents the worst-case scenario for the therapeutic outcome[403-405]. Additionally, the rate of penetration of therapeutics (both rt-PA and the antibiotic), replenishment of microbubbles as cavitation nuclei, and the removal of fibrin degradation products occurs is proportional to the flow conditions[403-405],

meaning the rate is slow under low flow conditions and fast under high flow conditions.

In this study, US and Definity alone did not enhance infected clot size reduction (Fig. 7.3). There were some clots that showed negative values for infected clot width loss. The response of clots to the thrombolytic and antibiotic may appear as growth, when the infected clot is in the early stages of degradation (Fig. 7.4c). It is likely that these infected clots could have been effectively lysed provided the treatment time was longer than the 30 min period employed in this study.

Sustained stable cavitation was harnessed in this study, monitored using a PCD detecting UH and BB emissions during 30 min flow experiments. In all cases, we observed significantly more UH than BB cavitation (Fig. 7.5), indicating more stable than inertial cavitation[152], which suggests that unwanted bioeffects may be minimized[358]. Paradoxically, stable cavitation, which occurs at a lower acoustic pressure amplitude, has been reported to correlate with enhanced thrombolysis to a greater degree than inertial cavitation in the presence of rt-PA[360]. Although UH was observed when Definity was combined with US, the addition of oxacillin and rt-PA was necessary to achieve infected clot width loss.

The inclusion of rt-PA in combination with oxacillin in our treatment regime likely benefited from this particular lytic's ability to target fibrin, which is the backbone of IE biofilm[334,406,407]. The absence of large fibrin degradation products liberated during treatment in our study (Fig. 7.6) suggests minimal risk of embolization from sonobactericide. Nonetheless, filters such as those deployed in vessels downstream of the heart valve during transcatheter aortic valve replacement procedures[408] could be used with sonobactericide to prevent embolism.

In this study, a 120-kHz frequency was chosen considering that the majority of previous studies for treating bacterial biofilms and clots in the presence of rt-PA have been performed with low frequency US[32,62,65,112,124,128,354-357]. The intermittent exposure scheme has been reported previously for sonothrombolysis[152,377]. However, diagnostic cardiac imaging is typically performed using a 2-MHz centre frequency[409]. Further studies should investigate the feasibility of using dual diagnostic and therapeutic 2-MHz cardiac imaging probes for image-guided treatment of IE. Microbubbles at 1-2 μm in diameter

are closer to resonance at 2-MHz than at 120-kHz, therefore lower acoustic pressures could be used to produce sustained stable cavitation, and therefore reduce the likelihood for any negative bioeffects to surrounding tissues.

The host immune system response, which includes inflammatory processes, is not adequately represented in our *in vitro* IE biofilm model. Another limitation is that dynamic flow was not present during the formation of the infected clot. Biofilms developed in a mostly static condition *vs*. a dynamic condition can lack robustness[410]. Additionally, only one isolate was tested in this study. More isolates must be tested in future studies to determine the ability of sonobactericide to treat other species or other isolates of *S. aureus* causing IE. Finally, this study did not investigate the direct bactericidal capability of sonobactericide in combination with antibiotics and thrombolytics, which is important in understanding the true potential of this treatment. However, it is known that bacteria released from mature biofilms become metabolically active and are thus susceptible to antibiotic treatment in the blood stream[7,353]. Freed bacteria as a result of sonobactericide should be evaluated in future studies.

Traditionally, IE is considered a contraindication for thrombolytic treatment in adults[101,102]. However, it has been shown to be effective in paediatric patients[361-364]. Unlike other thrombolytics, rt-PA has a high affinity to fibrin and thus provides a more local activation of fibrin-bound plasminogen, therefore decreasing the risk of negative effects due to systemic plasminogen cleavage[406,407]. Localized delivery of rt-PA to IE biofilms using echogenic liposomes loaded with rt-PA in combination with an antibiotic could also be a promising strategy to reduce off-target effects[377].

Lastly, studies in an IE animal model will be necessary to assess the efficacy of sonobactericide *in vivo*. Nonetheless, the work reported in this paper represents the first time that sonobactericide has been investigated as a possible therapeutic option for infective endocarditis. Accordingly, our primary goal was to determine suitable treatment conditions and to understand if this approach has potential in a tightly controlled setting. The rationale for using the *in vitro* model was to allow for precise cavitation monitoring, complete dose control, and to minimize human and microbiological variability in the infected clot. Further advantage of an *in vitro* model such as ours is constant visibility of the infected clot throughout treatment with time-

lapse microscopy. Nevertheless, it has been previously demonstrated that the results of *in vitro* simulated endocarditis biofilms (infected clots) are comparable to the *in vivo* rabbit model of endocarditis for the study of fluoroquinolone efficacy, to include pharmacokinetics[411].

Conclusion

In this proof-of-principle study, infected clots were developed as a translatable model of IE biofilm and the efficacy of sonobactericide, the use of US and an UCA in combination with or without an antibiotic and thrombolytic was evaluated *in vitro* under flow. Histology and confocal imaging revealed that the infected clot model resembled a clinical IE biofilm, especially for early pathogenesis. Infected clots exposed to the combination of oxacillin, rt-PA, ultrasound, and Definity achieved 99.3±1.7% fractional infected clot loss, which was greater than the other treatment arms. These results suggest that sonobactericide may have potential as an adjunctive therapy for IE.

Acknowledgements

The authors thank members of the Image-guided Ultrasound Therapeutics Laboratories (University of Cincinnati) and the Therapeutic Ultrasound Contrast Agent Group (Erasmus MC) for useful discussions. The authors are grateful to Prof. Joel Mortensen (Cincinnati Children's Hospital) for providing the clinical bacterial isolate, Dr. Seetharam Chadalavada (University of Cincinnati MC) for a large portion of the sterile sutures, Dr. David Witte (Cincinnati Children's Hospital) and Dr. King Lam (Erasmus MC) for interpretation of histology, and Prof. Matthew Kofron and Mike Muntifering (both from Cincinnati Children's Hospital) for assistance and training with the confocal microscopy. This work was financially supported by the Netherlands Heart Foundation (student grant 2016SB001 to K.R.L., E. Dekker program), the I & I Fund (Infection and Immunity Program, Molecular Medicine Postgraduate School, Erasmus MC; grant to K.R.L.), the National Institutes of Health (R01 GM094363 to A.B.H. and R01 NS047603 to C.K.H.), and the Erasmus MC Foundation (fellowship to K.K.).

Supplemental Information

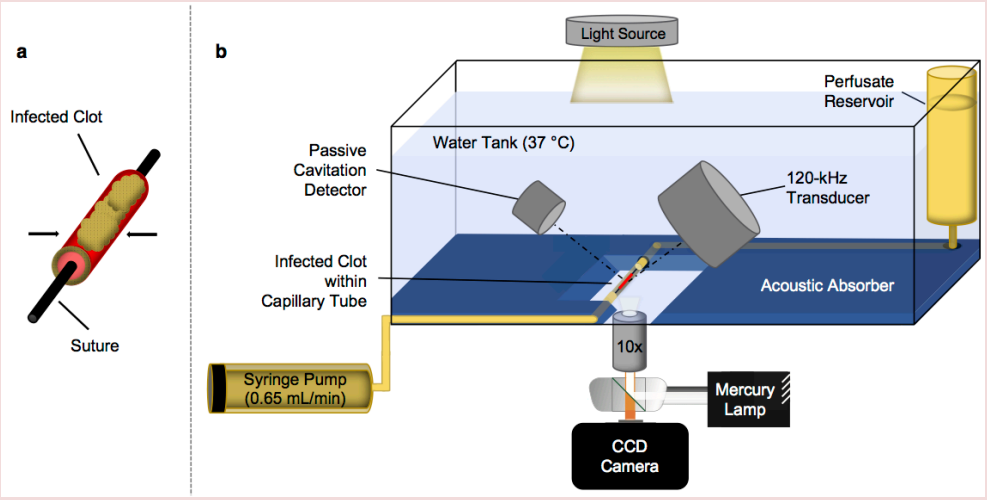

Figure S7.1. Experimental set-up. (a) Illustration of the infected clot model (442.2 µm ± 47.6 SD in width), where the infected clot composed of bacteria (yellow) and clot (red) is produced on a suture (black). (b) Schematic depicting the combined time-lapse microscopy, acoustical field set-up, and flow system to study the treatment of infected clot on a suture *in vitro* (not drawn to scale). For clarity purposes, only the bottom wall of the tank in the schematic is lined with acoustic absorber, while in reality all walls were lined. Distances for both the passive cavitation detector and the 120-kHz transducers to the clot was 5 cm. The perfusate reservoir contained plasma alone, or plasma and therapeutics.

“Our lives begin to end the day we become silent about things that matter.

- Martin Luther King, Jr.

8

Vibrational responses of bound and non-bound targeted lipid-coated single microbubbles

Tom van Rooij, Inés Beekers, Kirby R. Lattwein, Antonius F.W. van der Steen, Nico de Jong, and Klazina Kooiman

Based on:
IEEE Trans Ultrason Ferroelectr Freq Control, vol. 64, no. 5, 785-797, 2018

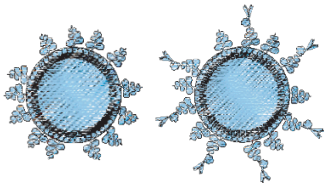

Abstract

One of the main challenges for ultrasound molecular imaging is acoustically distinguishing non-bound microbubbles from those bound to their molecular target. In this *in vitro* study, we compared two types of in-house produced targeted lipid-coated microbubbles, either consisting of DPPC or DSPC lipid as the main lipid, using the Brandaris 128 ultra-high-speed camera to determine vibrational response differences between bound and non-bound biotinylated microbubbles. In contrast to previous studies that studied vibrational differences upon binding, we used a covalently bound model biomarker (i.e., streptavidin) rather than physisorption, to ensure binding of the biomarker to the membrane. The microbubbles were insonified at frequencies between 1 and 4 MHz at pressures of 50 and 150 kPa. This study shows lower acoustic stability of bound microbubbles, of which DPPC-based microbubbles deflated most. For DPPC microbubbles with diameters between 2 and 4 μm driven at 50 kPa, resonance frequencies of bound microbubbles were all higher than 1.8 MHz, whereas those of non-bound microbubbles were significantly lower. In addition, the relative radial excursions at resonance were also higher for bound DPPC microbubbles. These differences did not persist when the pressure was increased to 150 kPa, except for the acoustic stability which further decreased. No differences in resonance frequencies were observed between bound and non-bound DSPC microbubbles. Nonlinear responses in terms of emissions at the subharmonic and second harmonic frequencies were similar for bound and non-bound microbubbles at both pressures. In conclusion, we identified differences in vibrational responses of bound DPPC microbubbles with diameters between 2 and 4 μm that distinguish them from non-bound ones.

Introduction

Ultrasound contrast agents that consist of targeted microbubbles are emerging in their applications for ultrasound molecular imaging[412-414]. These microbubbles have a ligand attached to their shell by which they can be targeted to a specific biomarker, for example $\alpha_v\beta_3$ that is expressed on the cellular membrane of endothelial cells in neovasculature[415,416]. For successful translation of ultrasound molecular imaging to the clinic, two major problems still need to be tackled: 1) producing microbubbles of the same size that also behave identical in an ultrasound field, and 2) distinguishing the response of a single targeted microbubble bound to a specific biomarker from a non-bound targeted microbubble. Since microbubbles of the same size can still have different acoustic properties[237,243,417-419], producing monodisperse microbubbles may not necessarily result in microbubbles that have, for example, the same resonance frequency. But if it is possible to determine the acoustic parameters that are specific for bound targeted microbubbles, they may be distinguished from non-bound targeted microbubbles based on their acoustic signal. Several studies investigated the difference in acoustic properties of bound and non-bound microbubbles, but these studies reported conflicting results. In the low frequency range (2 - 4 MHz) a shift in resonance frequency was found for microbubbles after binding[55,420], whereas at 11 MHz and 25 MHz no shift was observed[421]. For the responses at the subharmonic frequency either a change in frequency[421] or no change in amplitude and frequency[422] was reported upon binding. In contrast, for the response at the second harmonic frequency the results reported by Zhao et al.[422] and Casey et al.[423] were in agreement with each other: the amplitude increased for bound microbubbles. Finally, both Zhao et al. and Overvelde et al. found a decrease in the vibrational response at the fundamental frequency for bound microbubbles[55,422].

All acoustic studies on bound versus non-bound targeted microbubbles used either physisorption as a method to attach a model biomarker to an artificial surface (membrane or capillary)[55,420,422,423] or had the model biomarker embedded in agarose[421]. Physisorption of a model biomarker can result in detachment of the biomarker from the membrane or capillary which then can cover the whole targeted microbubble, including the area that is not directly in contact with the membrane. This was reported by Kooiman et al. for the model biomarker streptavidin that was physisorbed to an Opticell

membrane[424]. Functionalization of lipid-coated microbubbles with streptavidin changes the properties, such as elasticity[35,425,426] and acoustic stability[35]. Consequently, the comparisons made in previous studies between bound microbubbles and non-bound microbubbles are in fact a comparison between bound lipid-coated microbubbles covered by streptavidin and non-bound lipid-coated microbubbles, which did not have streptavidin on their shell. In addition, both physisorption and embedding a model biomarker in agarose are far from the *in vivo* situation, where biomarkers are incorporated into the cellular membrane.

We covalently linked a model biomarker to an artificial surface to study the vibrational responses of single bound targeted microbubbles and non-bound targeted microbubbles aiming to find parameters to discriminate them acoustically. Super-resolution confocal laser scanning fluorescence microscopy showed that covalent coupling of the model biomarker streptavidin to a hydrogel prevented the streptavidin to bind to the biotinylated lipid-shell of the microbubble outside the binding area[241]. That study compared the lipid distribution and binding area of two types of targeted lipid-coated microbubbles that were either coated with mainly DPPC (1,2-dipalmitoyl-*sn*-glycero-3-phosphocholine, C16:0) which is the main shell component of Definity® (Lantheus Medical Imaging, North Billerica, MA, USA) or mainly DSPC (1,2-distearoyl-*sn*-glycero-3-phosphocholine, C18:0) which is the main lipid component of SonoVue, Lumason, and BR14 (Bracco Imaging S.p.A., Milan, Italy)[133,241,378,419,427,428]. It was shown that the lipid distribution was more homogeneous for DPPC-based microbubbles than for DSPC-based microbubbles and that the binding area for DPPC-based microbubbles was significantly larger than for DSPC-based microbubbles[241]. We previously determined the acoustic properties of these DPPC and DSPC-based microbubbles in a set-up where the microbubbles were floating against an OptiCell wall (non-bound)[419] and hypothesized that the difference in ligand-distribution and binding area could alter the acoustic response after adherence of the microbubble to its molecular target. In the present study we investigated the vibrational response of in-house produced targeted DPPC-based and DSPC-based microbubbles using the Brandaris 128 ultra-high-speed optical camera[222] when they had bound to a streptavidin-coated hydrogel and compared their responses to those of non-bound microbubbles floating against the hydrogel. We aimed to identify differences in vibrational responses that may be used to discriminate bound from non-bound microbubbles.

Materials and Methods

Microbubble preparation

Biotinylated lipid-coated microbubbles with a C_4F_{10} gas core (F2 Chemicals Ltd, Preston, UK) were made as previously described[241,314] by sonication for 1 min. The coating was composed of 84.8 mol% DSPC (P6517, Sigma-Aldrich, Zwijndrecht, the Netherlands) or DPPC (850355, Avanti Polar Lipids, Alabaster, AL, USA), 8.2 mol% polyoxyethylene-40-stearate (PEG-40 stearate, P3440, Sigma-Aldrich), 5.9 mol% 1,2-distearoyl-*sn*-glycero-3-phosphoethanolamine-N-[carboxy(polyethylene glycol)-2000] (DSPE-PEG(2000), 880125, Avanti Polar Lipids); and 1.1 mol% 1,2-distearoyl-*sn*-glycero-3-phosphoethanolamine-N-[biotinyl(polyethylene glycol)-2000] (DSPE-PEG(2000)-biotin, 880129, Avanti Polar Lipids).

A 25 µm thick polyester membrane was mounted on a custom-made rectangular polyvinylchloride holder (same size as a microscope objective glass) and was custom coated with a 1-2 µm thick polycarboxylate hydrogel (XanTec bioanalytics GmbH, Düsseldorf, Germany). For the bound targeted microbubbles, the hydrogel was activated and streptavidin (S4762, Sigma-Aldrich) was subsequently covalently attached to the hydrogel using the amine coupling kit (K AN-50, XanTec bioanalytics GmbH) according to the instructions of the manufacturer as previously described[241]. Briefly, streptavidin was dissolved in acetate buffer (2 mM, pH 5.4) (1 mg/mL). After desalting the streptavidin by use of a PD-10 desalting column (GE Healthcare Bio-Sciences), the concentration was determined spectrophotometrically at 570 nm using a Pierce™ BCA Protein Assay kit (Thermo Scientific) and Thermo Multiskan EX. Three polyester membranes were placed in a 5-Slidemailer (Heathrow Scientific, Northgate, UK) with 18 mL of 1 M NaCl + 0.1 M NaB (pH 10) elution buffer (K AN-50, XanTec bioanalytics GmbH), followed by an incubation with 18 mL of 1.6 % (w/v) EDC·HCL (K AN-50, XanTec bioanalytics GmbH) in activation NHS/MES buffer (K AN-50, XanTec bioanalytics GmbH), and 18 mL of 33 µg/mL desalted streptavidin in 2 mM acetate buffer at pH 5.2-5.4. Finally, 18 mL of 1 M ethanolamine hydrochloride (pH 8.5) quenching buffer (K AN-50, XanTec bioanalytics GmbH) was used to terminate the reaction. The targeted microbubbles were allowed to adhere to the streptavidin-coated membrane in air-equilibrated phosphate buffered saline (PBS) containing calcium and magnesium (DPBS, 14080, Invitrogen, Thermo Fischer Scientific, Landsmeer, the

Netherlands) by flotation for 5 min. Then, the membrane was gently washed with air-equilibrated PBS containing calcium and magnesium three times using a 3 mL plastic Pasteur pipet. For the non-bound targeted microbubbles the hydrogel was treated in the same way, except for the addition of streptavidin. The targeted microbubbles were added below the hydrogel-coated polyester membrane of the custom-made holder and floated up due to buoyancy. The hydrogels with the non-bound targeted microbubbles and bound targeted microbubbles were orientated in the set-up as shown in Figure 8.1.

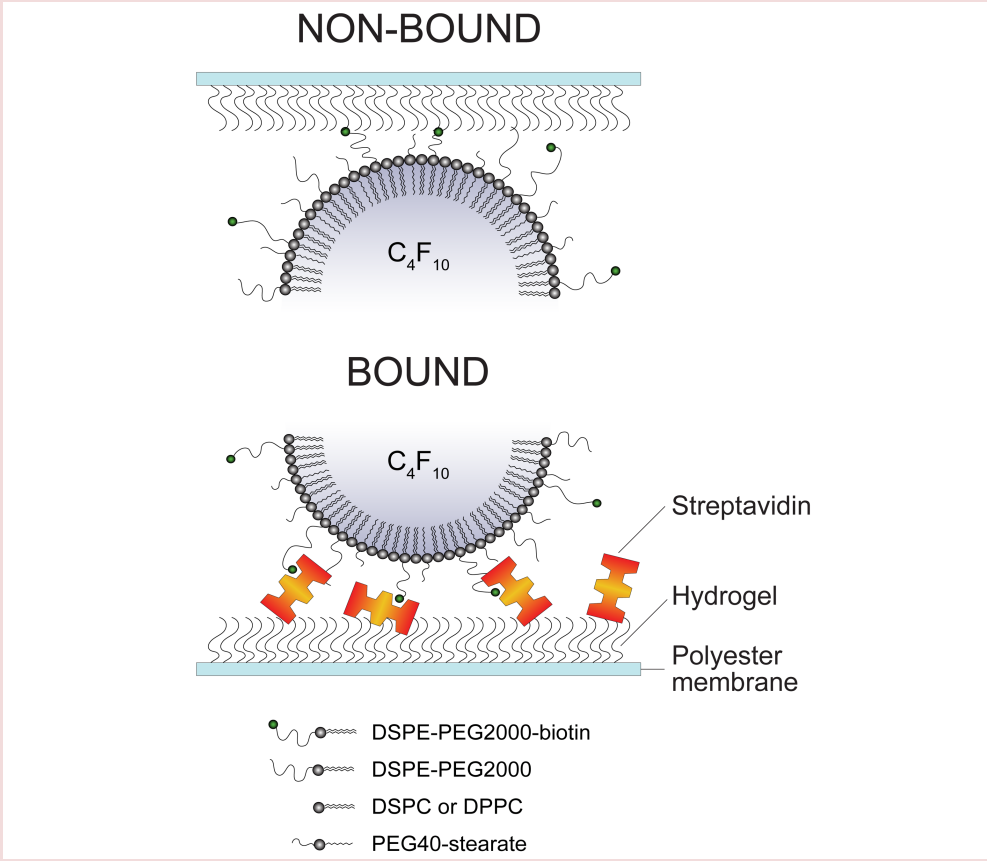

Figure 8.1. Configuration and composition of non-bound targeted microbubbles (top) floating against a streptavidin-coated membrane and targeted microbubbles bound to this membrane in the experimental set up (not to scale).

Microbubble spectroscopy

The vibrational responses of the bound and non-bound targeted microbubbles were captured using the Brandaris 128 ultra-high-speed camera operated at ~15 million frames per second[222]. Single microbubbles were investigated in ROI mode[242] using the microbubble spectroscopy technique[243] in combination with the exact same set-up as in our previous study[419], except for a higher magnification microscope objective (60×, NA = 0.9, Olympus, Tokyo, Japan). Briefly, a broadband single element polyvinyl difluoride (PVDF) transducer (25 mm focal distance, f-number 1.1, center frequency 5 MHz, PA275, Precision Acoustics Ltd, Dorchester, UK) transmitted a Gaussian tapered 8-cycle sine wave burst at transmit frequencies swept from 1 to 4 MHz (increment steps of 200 kHz) at a peak-negative pressure (P_A) of 50 or 150 kPa at the focus. The pressures were calibrated with two calibrated PVDF needle hydrophones in a separate measurement beforehand (0.2-mm diameter PA2030 and 1-mm-diameter PA1875, Precision Acoustics). The optic focus was aligned with the acoustic focus, to ensure that the microbubble received the intended pressure. The ultrasound was triggered on the second recording of each microbubble to obtain the initial resting diameter and the noise level with our contour tracking algorithm in the first recording. The experiments were conducted at room temperature and the sample was submersed in air-equilibrated PBS containing calcium and magnesium. All microbubbles were exposed to ultrasound within 2 h after addition to the custom-made holder.

Data analysis

Diameter-time (D-t) curves were obtained using custom-designed image analysis software[243] that determines the vibrational responses as described elsewhere [10]. Briefly, the acoustic stability of the microbubbles was quantified as the difference between the mean diameter of the microbubble in the initial D-t curve (D_0) and the final D-t curve (D_{end}). Next, the asymmetry of the D-t curves was measured as the ratio E/C between the relative expansion E, defined as $(D_{max} - D_0)/D_0$, and the relative compression C, defined as $(D_0 - D_{min})/D_0$, of the microbubble. Where D_{max} is the maximum diameter, D_{min} the minimum diameter in the D-t curve, and D_0 the resting diameter before vibration. The E/C ratios were used to classify the asymmetry as: compression-only behavior ($E/C < 0.5$); normal excursion ($0.5 \leq E/C \leq 2$); or expansion-only behavior ($E/C > 2$)[429].

Using the fast Fourier transformation (FFT) the frequency content of the D-t curves was analyzed in terms of the amplitude at the transmit frequency (f_T). These amplitudes were fitted to a resonance curve of a linear oscillator by a least-mean-squares method[243,419] to determine the resonance frequency (f_{res}) of the microbubble. At f_{res}, the diameter of the microbubble is referred to as D_{res}. The maximum relative radial excursions (i.e. at f_{res}) were defined as the maximum amplitude of the FFT divided by the corresponding resting diameter of the microbubble[419]. The same approach was used to determine the subharmonic resonance frequencies (f_{sub}) and the second harmonic resonance frequencies and the corresponding maximum relative radial excursions. Next, the maximum relative radial excursions were transformed into pressures as described by Emmer et al.[237,419]. All calculations were performed in MATLAB (The MathWorks Inc., Natick, MA, USA).

Statistics

Shapiro-Wilk tests for normality showed that the data was not normally distributed, so we used nonparametric testing. For comparing the acoustic stability of the microbubbles we used Wilcoxon signed-rank tests. When comparing groups, e.g. bound DSPC and non-bound DSPC, we used Mann-Whitney U tests. Medians and interquartile ranges (IQR) are reported and were calculated using Tukey's Hinges method. Statistical analyses were performed using SPSS (Statistics 21, IBM Corp., Armonk, NY, USA) and a p-value < 0.05 was regarded as significant.

Results

In total, 143 single microbubbles having a D_0 between 1.5 and 10 µm were analyzed. At 50 kPa, 46 bound DPPC microbubbles were insonified; 18 of which were also insonified at 150 kPa. For bound DSPC microbubbles, 43 were insonified at 50 kPa; 15 of which were also insonified at 150 kPa. None of the bound microbubbles detached during the experiments since every microbubble remained within the optic focus. For the non-bound microbubbles we included 26 DPPC and 28 DSPC microbubbles, which were all insonified at both 50 and 150 kPa.

Acoustic stability

At P_A = 50 kPa, both bound DPPC and DSPC-based microbubbles deflated significantly more than when they were non-bound ($p = 0.0001$), as shown in Figure 8.2. The median size for the bound DPPC microbubbles after insonification was 83% of D_0, while this was 98% for the non-bound DPPC microbubbles. The median size of bound DSPC microbubbles was 93% of D_0 after insonification, whereas non-bound DSPC microbubbles maintained their original size (100% of D_0). At a pressure of 150 kPa, the size difference between bound DPPC and non-bound DPPC microbubbles was not significant. The median diameter after insonification decreased to 53% of D_0 for bound DPPC microbubbles and to 56% for non-bound DPPC microbubbles. In case of DSPC microbubbles those that had bound deflated more than those that had not ($p = 0.004$). For the DSPC microbubbles this was 76% for the bound ones and hardly any shrinkage (98% of their initial size) for the non-bound ones. In addition, for both bound and non-bound microbubbles, those based on DPPC deflated more than those based on DSPC at 50 kPa (bound: $p = 0.001$, non-bound: $p = 0.031$) and also at 150 kPa (both $p = 0.0001$).

Linear oscillation behavior

The resonance frequencies in relation to D_{res} are shown in Figure 8.3. First of all, at a pressure of 50 kPa the resonance frequencies of bound DSPC microbubbles were similar to those of non-bound DSPC microbubbles. For DPPC-based microbubbles, the resonance frequencies of bound microbubbles were significantly higher than for non-bound DPPC microbubbles ($p = 0.045$). To further highlight the differences in resonance

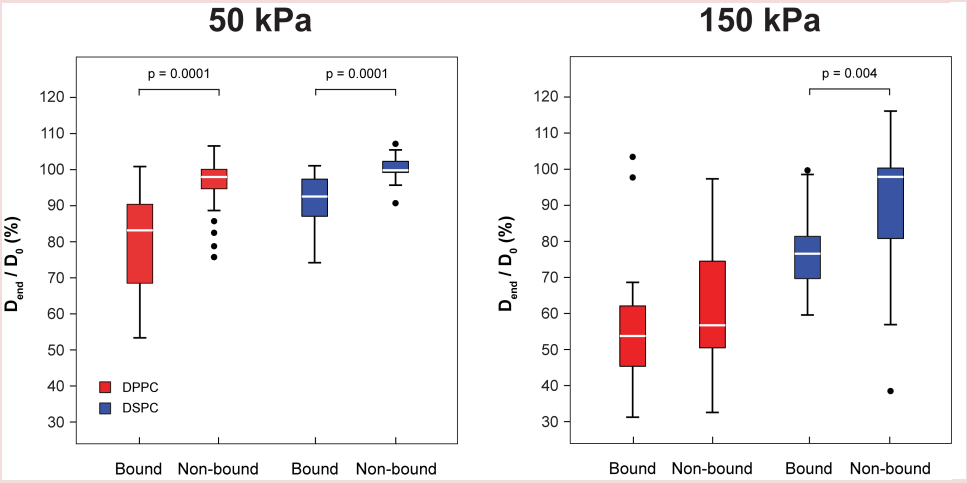

Figure 8.2. Diameter change during ultrasound exposure expressed as D_0/D_{end} for bound DPPC (50 kPa: n = 46, 150 kPa: n = 18), non-bound DPPC (50 kPa: n = 28, 150 kPa: n = 28), bound DSPC (50 kPa: n = 43, 150 kPa: n = 15) and non-bound DSPC microbubbles (50 kPa: n = 26, 150 kPa: n = 26). The filled black circles are outliers.

frequencies between bound and non-bound DPPC microbubbles, we compared the resonance frequencies of those having $D_{res} < 4$ µm. For larger microbubbles all resonance frequencies were similar, but for microbubbles having a $D_{res} < 4$ µm, the resonance frequencies of bound DPPC microbubbles were significantly higher than for non-bound DPPC microbubbles ($p = 0.002$). In addition, no overlap was found between the median (IQR) resonance frequencies of bound DPPC microbubbles and non-bound DPPC microbubbles: 1.94 (1.83 – 2.25) versus 1.59 (1.40 – 1.77). In contrast, the resonance frequencies of bound and non-bound DSPC microbubbles were similar for all studied sizes ($p = 0.494$). Median (IQR) resonance frequencies were 2.39 (1.98 – 2.78) for bound DSPC and 2.63 (2.25 – 3.11) for non-bound DSPC microbubbles. The resonance frequencies of bound DSPC microbubbles were significantly higher than those of bound DPPC-based microbubbles at $P_A = 50$ kPa ($p = 0.001$), for the non-bound DSPC and DPPC microbubbles no difference was found. The resonance frequencies at a pressure of 150 kPa were all similar. The number of microbubbles included in these graphs is lower than the total number of studied microbubbles, since some resonance peaks were below or above the measuring range (< 1 MHz or > 4 MHz); the resonance frequency

could therefore not be determined.

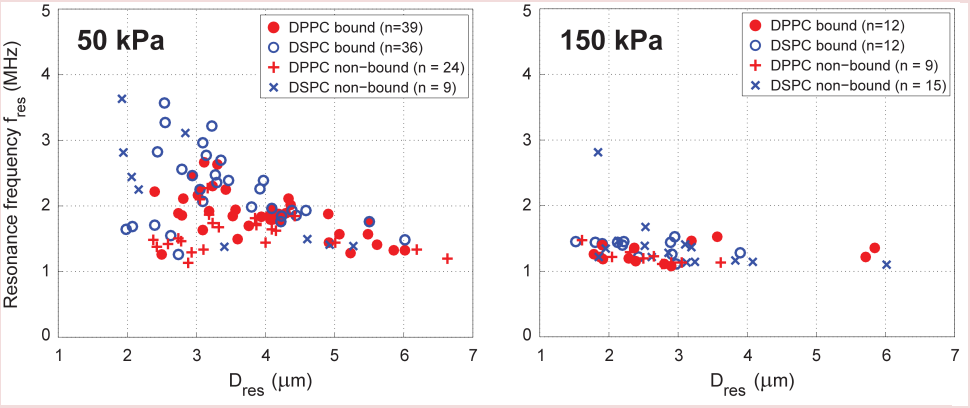

Figure 8.3. Resonance frequencies (f_{res}) of bound DPPC (filled red circles), non-bound DPPC (red crosses), bound DSPC (blue open circles), and non-bound DSPC (blue crosses) microbubbles plotted versus the diameter at resonance (D_{res}) at P_A = 50 kPa (top panel) and P_A = 150 kPa (bottom panel).

For bound DPPC microbubbles, the median maximum relative radial excursions (median (IQR) of 0.14 (0.11 – 0.18)) at the resonance frequency at a pressure of 50 kPa was significantly higher than for the non-bound DPPC microbubbles (0.09 (0.06 – 0.13), p = 0.002, Fig. 8.4,). Although the median maximum relative radial excursions of bound DSPC microbubbles 0.11 (0.08 – 0.12) were not significantly different from non-bound DSPC microbubbles 0.05 (0.03 – 0.13, p = 0.157) over the whole resonance frequency range, the maximum relative radial excursions for bound DSPC microbubbles were significantly higher for resonance frequencies > 2 MHz (bound: 0.11 (0.08 – 0.12), non-bound: 0.03 (0.02 – 0.04), p = 0.001). In addition, the maximum relative radial excursions of bound DSPC microbubbles were significantly lower than of bound DPPC microbubbles (p = 0.0001), but similar for the non-bound DSPC and DPPC microbubbles. At a driving pressure of 150 kPa the median maximum relative radial excursions of bound and non-bound DPPC microbubbles at f_{res} were similar, but significantly higher for bound DSPC than non-bound DSPC microbubbles (p = 0.001). The median (IQR) of the maximum relative radial excursions was similar for the bound microbubbles: 0.28 (0.22 – 0.33) for DPPC and 0.28 (0.23 – 0.35) for DSPC-based

microbubbles (Fig. 8.4). For non-bound microbubbles the maximum relative radial excursions were significantly higher ($p = 0.03$) for DPPC microbubbles than for DSPC microbubbles: 0.25 (0.18 – 0.28) versus 0.11 (0.09 – 0.23).

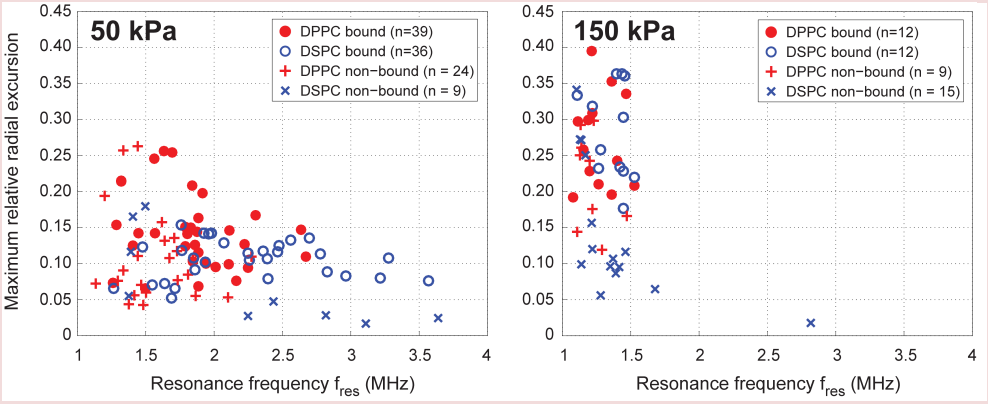

Figure 8.4. Maximum relative radial excursions at the resonance frequency of bound DPPC (filled red circles) non-bound DPPC (red crosses), bound DSPC (blue open circles), and non-bound DSPC (blue crosses) microbubbles plotted versus the resonance frequency (f_{res}) at P_A = 50 kPa (top panel) and P_A = 150 kPa (bottom panel).

Nonlinear oscillation behavior

The asymmetry of the radial excursions at each transmit frequency was expressed as the ratio between the relative expansion *E* and relative compression *C*. At 50 kPa the median of the radial excursions was compression-dominated with $0.5 < E/C < 1$ for bound targeted microbubbles of both types (Fig. 8.5) at all frequencies. For the non-bound microbubbles the oscillations were mostly symmetric, except for the frequencies between 1 and 1.6 MHz for which the radial excursions of DPPC microbubbles were compression-dominated. At P_A = 150 kPa the excursion behavior of bound microbubbles at frequencies between 1 and 1.8 MHz ranged from symmetric to expansion-dominated, whereas at higher frequencies the behavior of both microbubble types was compression-dominated. The non-bound microbubbles showed mostly symmetric oscillations.

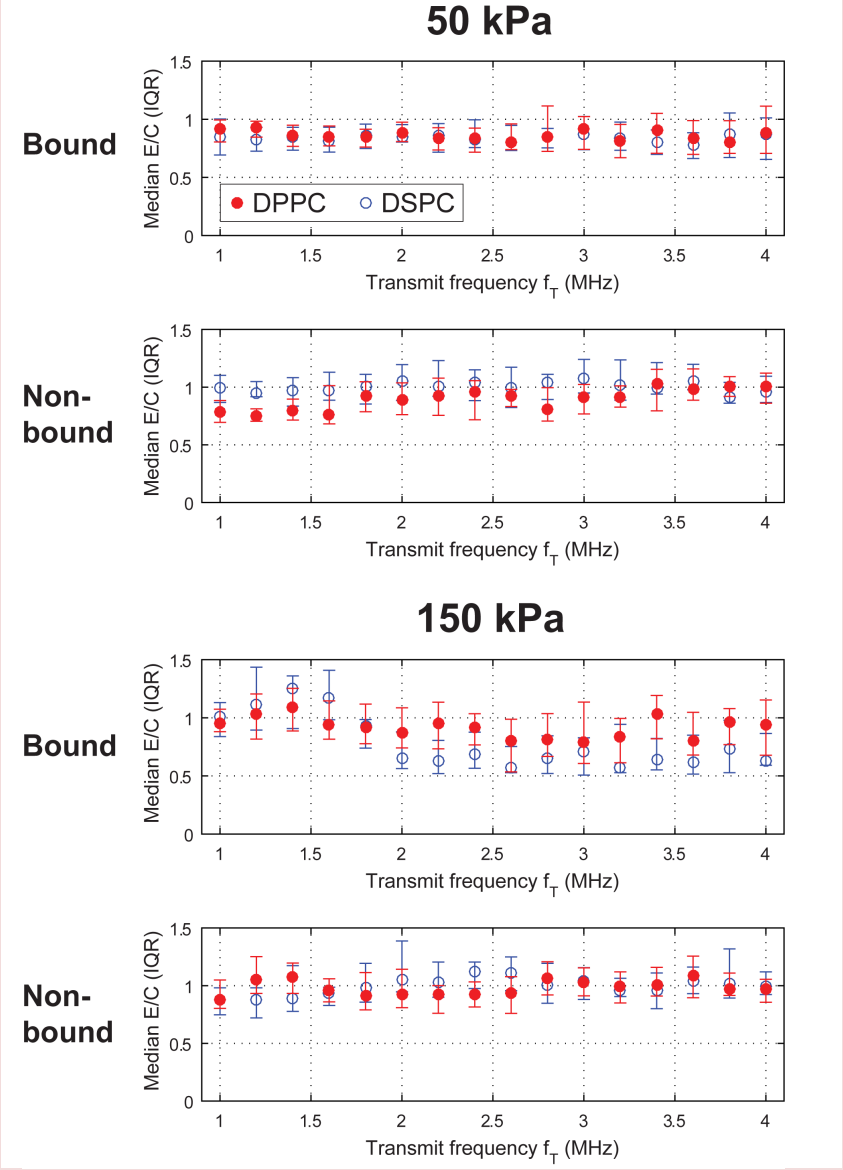

Figure 8.5. Median (IQR) ratio between the relative expansion *E* and the relative compression *C* of bound DPPC (50 kPa: n = 37, 150 kPa: n = 18) and bound DSPC (50 kPa: n = 43, 150 kPa: n = 15) microbubbles, and non-bound DPPC (50 kPa: n = 28, 150 kPa: n = 28) and non-bound DSPC (50 kPa: n = 26, 150 kPa: n = 26) microbubbles plotted versus the transmit frequency at P_A = 50 kPa (top panels) and P_A = 150 kPa (bottom panels).

Responses at the subharmonic frequency at a driving pressure of 50 kPa were present in 22 out of 46 (48%) bound DPPC microbubbles and in 7 out of 43 (16%) bound DSPC microbubbles. For both non-bound DPPC and DSPC microbubbles only one (4%) responded at the subharmonic frequency. At the higher pressure of 150 kPa, the number of bound DPPC microbubbles responsive at the subharmonic frequency was similar to that at 50 kPa: 8 out of 18 (44%), but increased to 9 out of 15 (60%) for DSPC-based microbubbles. The number of non-bound microbubbles that responded at the subharmonic frequency increased to 12 out of 28 (43%) for DPPC and 6 out of 26 (23%) for DSPC microbubbles.

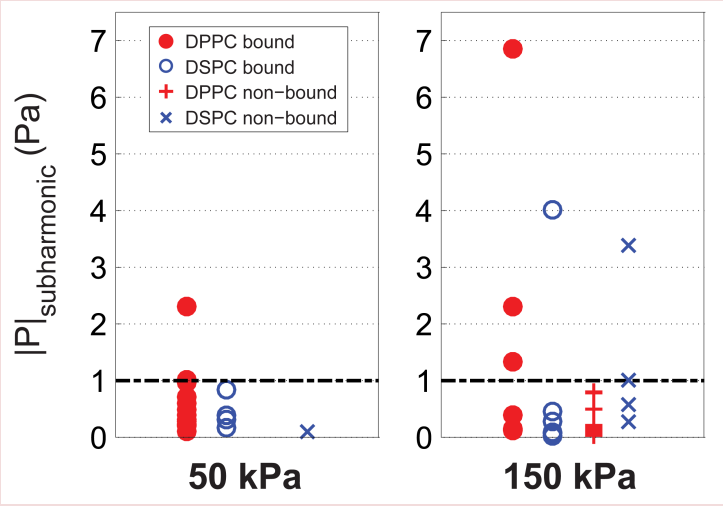

Figure 8.6. Absolute pressures emitted at the subharmonic frequency of bound DPPC (50 kPa: n = 17, 150 kPa: n = 8), bound DSPC microbubbles (50 kPa: n = 7, 150 kPa: n = 7), non-bound DPPC (50 kPa: n = 0, 150 kPa: n = 10), and non-bound DSPC microbubbles (50 kPa: n = 1, 150 kPa: n = 4).

Although quite some microbubbles had a response at the subharmonic frequency, only for the ones shown in Figure 8.6 a subharmonic resonance curve could be determined. Reasons for not being able to determine the subharmonic resonance curve were not enough points for a fit or the peak was below or above the measuring range. Emitted

subharmonic pressures were similar irrespective of binding and the type of lipid coating at each acoustic pressure (Fig. 8.6). At 50 kPa, of the 17 bound DPPC microbubbles shown in Figure 8.6, nine had a response at T2R (transmit at twice the resonance frequency with $f_{sub} = f_{res}$)[430,431] and four at TR (transmit at the resonance frequency, $f_{sub} = \frac{1}{2}f_{res}$)[418,430]. Of the seven bound DSPC microbubbles, three had a clear response at T2R and none had a response at TR. At 150 kPa, of the eight bound DPPC microbubbles seven had a response at T2R and one at TR. Of the seven bound DSPC microbubbles four had a response at T2R and none at TR. In the case of non-bound microbubbles at 50 kPa the only microbubble responsive at f_{sub} was a DSPC microbubble with a response at T2R. At 150 kPa, one out of the ten DPPC microbubbles had a response at T2R and two out of ten at TR. For the four non-bound DSPC microbubbles two had a response at T2R and none at TR. For the other microbubbles responding at f_{sub}, the relation between TR or T2R could not be determined; either because no clear relation was found between the subharmonic and fundamental frequency, or because the fundamental frequency had not been determined since the peak was located outside the measuring range. We assumed a detection limit of 1 Pa (black dashed line in Fig. 8.6) for diagnostic ultrasound scanners, achievable with a typical high-quality transducer for harm harmonic imaging[432]. The emitted pressures of the subharmonic responses will therefore be difficult to detect.

At P_A = 50 kPa, about half of both bound DPPC (53%) and bound DSPC (57%) microbubbles responded at the second harmonic frequency. The number of responding non-bound microbubbles based on DPPC was similar (50%), but for non-bound DSPC microbubbles only 1 out of 26 (4%) was responsive at the second harmonic frequency. The number of responsive microbubbles at a driving pressure of 150 kPa increased in all cases: to 14 out of 15 (93%) for bound DPPC microbubbles, 13 out of 18 (72%) for bound DSPC microbubbles, 17 out of 28 (61%) for non-bound DPPC microbubbles, and 8 out of 26 (31%) for non-bound DSPC microbubbles. The median (IQR) pressures emitted at the second harmonic frequency when insonified at 50 kPa were 2.0 (1.0 – 2.6) Pa for bound DSPC microbubbles, hence in the same order as the only non-bound DSPC microbubble (3.1 Pa, Fig. 8.7). For bound DPPC microbubbles, the emitted pressures were 4.1 (2.1 – 12.9) Pa and 2.4 (2.0 – 2.8) Pa for non-bound DPPC microbubbles, which was not significantly different ($p = 0.351$). In addition, the emitted

pressures at the second harmonic frequency of bound DPPC microbubbles were higher than those of bound DSPC microbubbles ($p = 0.004$). At the higher driving pressure of 150 kPa, the emitted pressures were significantly higher ($p = 0.017$) for non-bound than bound DSPC microbubbles, with median pressures of 28.5 (14.0 – 38.1) Pa for non-bound and 3.2 (2.4 – 8.4) Pa for bound DSPC microbubbles. The median pressures of the other groups were all similar.

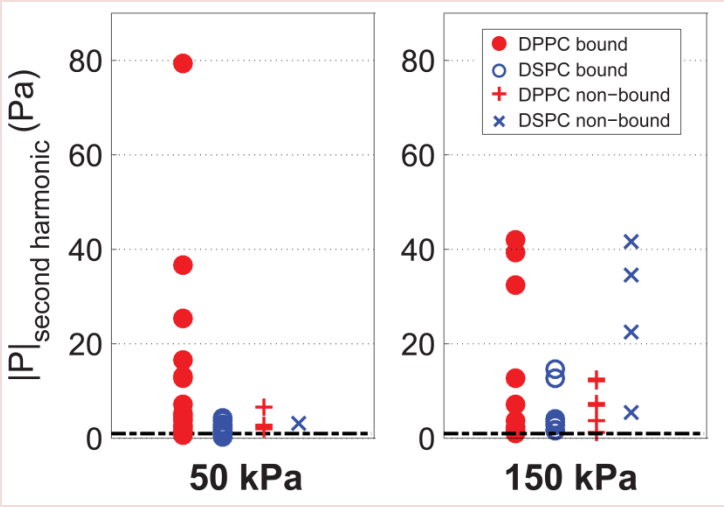

Figure 8.7. Absolute pressures emitted at the second harmonic frequency of bound DPPC (50 kPa: n = 21, 150 kPa: n = 10), bound DSPC microbubbles (50 kPa: n = 19, 150 kPa: n = 8), non-bound DPPC (50 kPa: n = 6, 150 kPa: n = 6), and non-bound DSPC microbubbles (50 kPa: n = 1, 150 kPa: n = 4).

Discussion

This study investigated vibrational responses of bound and non-bound microbubbles to identify differences to acoustically discriminate them. For DPPC-based microbubbles with diameters between 2 and 4 µm the resonance frequencies and relative radial excursions were higher than for non-bound DPPC-based microbubbles (P_A = 50 kPa). In contrast, at an insonifying pressure of 150 kPa the relative radial excursions for bound and non-bound DPPC-based microbubbles were similar. Interestingly, at this higher pressure the radial excursions for bound DSPC-based microbubbles were higher than for non-bound DSPC microbubbles, whereas these were similar at 50 kPa. We also found compression-dominated behavior and a higher number of responsive microbubbles at the second harmonic frequency for bound microbubbles, irrespective of the main coating lipid.

Acoustic stability

Bound microbubbles were acoustically less stable than non-bound microbubbles, irrespective of their main coating component. Further we found that the acoustic stability for DPPC-based microbubbles was lower than that for DSPC-based microbubbles. This was previously attributed to the shorter acyl chain length of the DPPC lipid than that of the DSPC lipid[419]. This shorter chain results in lower intermolecular van der Waals forces between the different lipids and results in less attraction and cohesion of the microbubble shell[419,433]. The maximum relative radial excursions of bound microbubbles were higher at the resonance frequency than those of non-bound microbubbles (for DPPC at 50 kPa and DSPC at 150 kPa). This means that the radial excursions after binding were more prominent, which resulted in more shrinkage and therefore a lower acoustic stability. Others have reported lower radial excursions after binding for DSPC-based microbubbles[55,422], but those studies had not covalently linked their model biomarker to their membrane. As a result, the biomarker that attached to the microbubble shell increased the stiffness[35] and therefore limits the radial oscillations.

Some non-bound DSPC microbubbles appeared to increase in diameter after insonification at 150 kPa. The microbubbles in which this was observed were all relatively small (< 2.5 µm). This apparent increase may be due to small changes in

optical focus due to radiation forces, in combination with the error in the tracking algorithm which was previously estimated to be approximately 10%[243].

Linear oscillation behavior

The resonance frequencies for bound DPPC microbubbles were higher than for non-bound DPPC microbubbles at a pressure of 50 kPa for microbubbles with diameters between 2 and 4 μm at resonance. Based on the IQRs, the resonance frequencies of most bound DPPC microbubbles of this size were higher than 1.8 MHz, whereas those of non-bound DPPC microbubbles were lower than 1.8 MHz. In terms of shell properties, a higher resonance frequency is related to an increase in elasticity (i.e., a stiffer shell) by the Marmottant model[434]. It is not likely that the elasticity changes upon binding, but the apparent stiffness may increase due to binding of the microbubble to the biomarker. We may not have found a change in apparent stiffness for DSPC-based microbubbles, because their surface binding area is smaller than for DPPC-based microbubbles as previously determined by our group for the same type of microbubbles and same streptavidin biomarker[241]. Next, the initial elasticity of DSPC microbubbles is already higher than for DPPC microbubbles[419], and it has been shown that the resonance frequencies for DSPC microbubbles did not change after conjugating the relatively heavy molecule streptavidin to the lipid shell, whereas for DPPC microbubbles the resonance frequencies increased[35]. In addition, the resonance frequency exponentially decreases for increasing microbubble size[435]. As a consequence, the difference in resonance frequencies for microbubbles with diameters between 2 and 4 μm is larger than for microbubbles with diameters between 5 and 7 μm[419]. An increase in resonance frequency for bound microbubbles will therefore be more pronounced for smaller than for larger microbubbles. This may explain why the apparent increase in stiffness was only present for bound DPPC microbubbles having diameters between 2 and 4, and not for DSPC microbubbles or larger DPPC microbubbles. At 150 kPa, however, all resonance frequencies appeared the same. The microbubble oscillations at this pressure start of very violently in the first insonifications between 1 and 1.5 MHz, thereby largely decreasing the microbubble size and shifting its original resonance frequency towards higher frequencies. Since the mechanical index (MI) was ~2× lower for the insonifications at the end of the frequency sweep, the resulting relative radial excursions were lower at the new resonant microbubble size. Therefore, the oscillations of the first

insonifcations dominated the resonance behavior, leading to an apparent resonance frequency between 1 and 1.5 MHz before shrinkage.

Others have also reported differences in resonance frequencies between bound and non-bound microbubbles. Casey et al.[423] reported an increase in resonance frequency for their bound in-house produced biotinylated microbubbles, but for DSPC microbubbles (C_3F_8 gas core and same components as our DSPC-based microbubbles, but unknown ratios) instead of for DPPC-based microbubbles as we report here. Overvelde et al.[55] found 30% lower frequencies of maximum response for targeted BG-6438 microbubbles bound to an OptiCell wall than for non-targeted BG-6437 microbubbles floating against the wall at pressures < 40 kPa (both bubble types are from Bracco Research S.A., Geneva, Switzerland). The BG-6438 microbubbles were targeted to FITC-BSA using an anti-FITC antibody attached to the microbubble shell using streptavidin-biotin bridging. The main limitation of both studies is the method of attaching the model biomarker streptavidin to the cellulose tube[423] or FITC-BSA to the OptiCell wall[55], namely by physisorption. As mentioned before, this physisorbed biomarker is likely to bind to the microbubble shell creating a lipid-coated microbubble covered with the model biomarker. These very large and heavy complexes are expected to behave completely different in an ultrasound field than a bare lipid-coated targeted microbubble, as has been shown for microbubbles that were functionalized with streptavidin depending on the initial stiffness of the microbubble coating[35]. In addition to this, Overvelde et al.[55] did not block the OptiCells to prevent unspecific binding in their experiments that compared free BG-6437 microbubbles and BG-6437 microbubbles close to the wall: the latter may have actually bound to the wall. Next to that, the BG-6437 microbubbles did not have anti-FITC antibody attached to their shell, which is not a fair comparison between microbubbles that have bound to the wall and that are floating against the wall. In our present study the covalent coupling of streptavidin to the hydrogel, and thus the membrane, was established and it was confirmed that no streptavidin was present on the microbubble shell[241].

Nonlinear oscillation behavior

For nonlinear contrast-enhanced ultrasound imaging the responses at the subharmonic and second harmonic frequencies are usually exploited[436]. At 50 kPa more bound than

non-bound microbubbles responded at the subharmonic frequency, for both the DPPC and DSPC-based coatings. At 150 kPa more microbubbles—both bound and non-bound—were responsive at the subharmonic frequency, but the emitted pressures were close to or below the assumed detection limit for clinical use of 1 Pa[432]. The subharmonic emissions seem therefore of limited use for nonlinear contrast-enhanced imaging and discrimination of bound from non-bound microbubble based on our experimental conditions.

We found similar amplitudes at the subharmonic frequency for bound and non-bound microbubbles, in line with findings of Zhao et al.[422] for microbubbles with a coating of 82 mol% DSPC, 9 mol% DSPEPEG2000, and 9 mol% DSPE-PEG2000-biotin[437]. Helfield et al.[421] reported similar amounts of bound and non-bound Target-Ready MicroMarker microbubbles that were responsive at the subharmonic frequency, whereas we found more bound microbubbles that responded. The different composition and gas core of Target-Ready MicroMarker likely contributed to these differences. As suggested by Helfield et al.[421], the membrane material could have frequency-dependent effects and their results might be biased due to aggregation of microbubbles that may have changed the echogenicity[438]. We previously performed the exact same experiments as described here for non-bound microbubbles in an OptiCell[439]. Indeed, a membrane dependent effect was observed, but was not found to be frequency related. The maximum relative radial excursions of non-bound microbubbles in an OptiCell (both DPPC and DSPC) were 2-2.5 times higher than for non-bound microbubbles floating against the hydrogel. Because the microbubbles may be partly embedded in the polymer-based hydrogel, this can damp the microbubble oscillations and therefore result in lower maximum relative radial excursions.

Another difference between our study and that of Helfield et al.[421], is that they coated their cellulose tube with streptavidin using physisorption, with the disadvantage of streptavidin covering the microbubble shell, which may have influenced the amplitude of the subharmonic signal. Indeed, their acoustic measurements showed a 20% higher subharmonic signal of Target-ready MicroMarker, a streptavidin-functionalized lipid-coated microbubble, when bound to a biotinylated agarose phantom. The difference between the results of Helfield et al. and our results presented in this study might also be due to the used techniques: ultra-high-speed optical imaging versus acoustic

measurements. In our set-up we were only able to image the top-view of the microbubble oscillations, whereas acoustic measurements can detect out-of-plane signals as well. If a larger portion of the subharmonic excursions were generated in the perpendicular plane, we might have missed those vibrations with our set-up.

Numerical simulations have shown that the subharmonic signal is optimal when the microbubble is insonified at T2R[440]. Experimental validation showed that the threshold for generating TR subharmonic responses is higher than that for T2R subharmonic responses in lipid-coated microbubbles[430,441]. The absence of DSPC responders at TR may suggest that the threshold for generating TR subharmonic responses is lower for DPPC microbubbles than for DSPC microbubbles, irrespective of them being bound or not. On the other hand, due to the applied frequency range and studied microbubble sizes the majority of the resonance frequencies were between 1.5 and 3.5 MHz, which limits the possibility to insonify microbubbles at T2R within the frequency range we applied.

The higher second harmonic amplitudes we measured for non-bound DSPC-based microbubbles at 150 kPa are in contrast with results reported by others[420,423]. The study by Casey et al.[423] used microbubbles similar to our DSPC microbubbles, but with a C_3F_8 core and attachment to a capillary wall using the physisorbed streptavidin as biomarker (f_T = 2 MHz, P_A = 90 kPa). The study by Zhao et al.[420] also used DSPC-based microbubbles, with a set-up and parameters comparable to those of Casey et al.[423]. Both studies used somewhat lower pressures, but may also have effectively studied bound targeted DSPC-based microbubbles coated with a streptavidin layer, which may explain the different findings. In our study, the emitted pressure amplitudes of bound microbubbles were similar or lower than for non-bound microbubbles and acoustic discrimination based on the second harmonic pressures does therefore not seem feasible.

DSPC vs DPPC for ultrasound molecular imaging applications

The differences between bound targeted DPPC and DSPC-based microbubbles were not as pronounced as we expected from the differences in shape change upon adherence and their surface binding areas, as previously determined by our group for the same type of

microbubbles and same streptavidin biomarker[241]. The most prominent differences we did find were higher acoustic stability for non-bound microbubbles, higher resonance frequencies (for DPPC microbubbles with diameters between 2 and 4 μm) and radial excursions for bound DPPC microbubbles at 50 kPa, and higher amplitudes at the second harmonic frequency for non-bound DSPC microbubbles than for bound DSPC microbubbles at 150 kPa. The lower resonance frequencies for DPPC microbubbles than for DSPC microbubbles were already observed for non-bound DPPC microbubbles[419], and were thus maintained upon binding.

For *in vivo* ultrasound molecular imaging the ideal targeted microbubble: 1) can effectively bind to the biomarker of interest; 2) persists binding to the biomarker after initial binding, i.e. the binding strength is larger than the shear stress induced by the flowing blood; 3) is stable during the course of the ultrasound examination; 4) nonlinearly scatters ultrasound that is microbubble specific; 5) can be discriminated acoustically from non-bound microbubbles; 6) has the same resonance frequency as the other microbubbles that are injected, i.e., all microbubbles in the population respond in the same way to ultrasound. Concerning the first two points, Kooiman et al.[241] favored targeted DPPC microbubbles over DSPC microbubbles because of their larger surface binding area to a streptavidin-coated membrane, their dome shape after binding, and a more homogeneous distribution of fluorescently labeled ligands attached to DSPE-PEG(2000). The more homogeneous lipid distribution might aid the initial attachment, whereas the larger binding area and difference in shape might be able to better sustain blood shear forces. However, binding of the microbubbles was performed under static conditions and experiments in the presence of flow are needed to verify which of the two microbubble types binds best under flow. Based on the acoustic stability (point 3), DSPC-based microbubbles are favored over DPPC-based microbubbles. This also means that the size is better maintained during insonification and the resonance frequency will therefore be more consistent throughout the investigation. In terms of nonlinear scattering of ultrasound (point 4), the maximum relative radial excursions at the subharmonic frequency for both our DPPC and DSPC microbubbles resulted in ~20 dB lower scattered pressures than the second harmonic responses. The subharmonic responses were too low and unpredictable to discriminate bound from non-bound microbubbles. In contrast, the responses at the second harmonic frequency were sufficiently high to be detected, but amplitudes were similar for bound and non-bound

microbubbles, or higher for the non-bound ones in terms of DSPC-based microbubbles (point 5). At 50 kPa, bound and non-bound DPPC microbubbles with diameters between 2 and 4 µm at resonance could be separated based on their resonance frequencies: bound DPPC microbubbles had resonance frequencies above 1.8 MHz, whereas those were significantly lower for non-bound DPPC microbubbles. Lastly (point 6), as mentioned in the introduction one of the main challenges for successful translation of ultrasound molecular imaging to the clinic is the production of microbubble populations that have the same acoustic signature. Both the DPPC and DSPC-based microbubbles can have different resonance frequencies and radial excursions although their sizes are similar. Several studies showed that monodisperse lipid-coated microbubble distributions can be produced using flow-focusing devices[150,442-444]. Talu et al.[444] and Kaya et al.[442] studied the difference between echo amplitudes of these monodisperse single microbubbles when insonified at a frequency close to resonance, and found a lower standard deviation than for polydisperse microbubbles. Segers and Versluis[445] developed an acoustic sorting chip that separated monodisperse microbubbles based on the radiation force they experienced, which resulted in an overall contrast enrichment of more than 10 dB. This is an important step towards improving the quality of *in vivo* ultrasound molecular imaging, especially if microbubbles with low shell elasticity and a diameter between 2 and 4 µm can be produced to distinguish bound from non-bound microbubbles, as shown in our study. However, this approach is still limited to specific microbubble compositions that can be produced monodispersely by means of flow-focusing devices.

Summing up all the aforementioned similarities, differences, advantages, and disadvantages of DPPC and DSPC-based microbubbles, this results in a favor for DSPC-based microbubbles for ultrasound molecular imaging solely based on a higher acoustic stability. Studying the adherence of the microbubbles under flow should reveal whether the heterogeneous lipid distribution in the DSPC shell hinders binding. On the other hand, bound DPPC microbubbles (diameters between 2 and 4 µm) at 50 kPa had resonance frequencies higher than 1.8 MHz, whereas those of non-bound DPPC microbubbles were lower than 1.8 MHz. In addition, the relative radial excursions of bound DPPC microbubbles were also higher. When monodisperse DPPC microbubbles with a diameter between 2 and 4 µm are produced, these could acoustically be discriminated based on their resonance frequency.

Limitations and outlook

Although we aimed to create a more *in vivo*-like set-up using covalent biomarker binding versus physisorption, the membrane we used in our experiments was still artificial. The 1-2 µm thick hydrogel created a softer layer between the microbubble and the polyester membrane, but to have a real *in vivo*-like membrane one would need to develop a material with exactly the same stiffness, viscosity, etc. to an actual cell layer or perform *in vivo* experiments. In addition, *in vivo* one can also study microbubble vibration when microbubbles are in contact with cells and under flow, for which the chorioallantoic membrane model could be used. This model has proven to be useful to study non-targeted microbubble vibration using ultra-high-speed imaging and targeted-microbubble mediated drug delivery[446,447].

For *in vivo* ultrasound molecular imaging multiple microbubbles may bind in closer range with each other than investigated in the present study. However, the binding range actually depends on the availability of the biomarker on the cell surface, which depends both on the cell type and the biomarker of interest. When the interbubble distance is ≤ 10 µm, this will cause interaction of the bubbles in terms of secondary Bjerknes forces, and due to the secondary Bjerknes forces a bubble will deform in the direction of their neighboring bubble[448]. Next to that, two similar sized bubbles that are close to each other result in a shift in resonance frequency and therefore a decrease in maximum relative radial excursions[449]. As a consequence, for abundant biomarkers on the cell membrane these observations may counteract the increase in resonance frequency and maximum relative radial excursions we observed for DPPC microbubbles between 2 and 4 µm at 50 kPa. This, however, should first be experimentally verified using a setup comprising of a biomarker distribution that is comparable to the *in vivo* situation. The chorioallantoic model would be a good approach to study this.

Conclusion

This study shows that binding of in-house produced DPPC-based microbubbles to a streptavidin-coated surface increased the resonance frequencies (for microbubbles with diameters between 2 and 4 µm) and the corresponding relative radial excursions at relatively low pressure (50 kPa). At this pressure, the bound 2 to 4 µm microbubbles resonated above 1.8 MHz, whereas the non-bound 2 to 4 µm DPPC microbubbles were resonant below this frequency. At higher pressure (150 kPa) this difference did not persist. No differences in resonance frequency were observed between bound and non-bound DSPC microbubbles. In terms of non-linear responses, only the responses at the second harmonic frequency of bound DSPC microbubbles at 150 kPa were lower than of non-bound DSPC microbubbles. Our in-house produced DPPC-based microbubbles were acoustically less stable than our DSPC-based microbubbles, which is the major advantage of this type of microbubble for ultrasound molecular imaging applications.

Acknowledgements

The authors thank Robert Beurskens, Frits Mastik, Michiel Manten, and Geert Springeling for technical assistance, Dr. Tom Kokhuis for valuable discussions (all from the Dept. of Biomedical Engineering, Thorax Center, Erasmus MC), and Dr. Jason L. Raymond for experimental assistance (visiting fellow Whitaker program). We also thank Ihsan Chrifi from the Dept. of Experimental Cardiology, Thorax Center, Erasmus MC, for the spectrophotometer measurements, and Dr. E. Gedig from XanTec bioanalytics GmbH, Germany, for discussions about the covalent coating of streptavidin to the polyester membranes. The authors are grateful to Prof. Dr. A.L. Klibanov from the University of Virginia, Cardiovascular Division, Charlottesville, Virginia, USA for discussions about the microbubble preparation.

"In the end, it's not the years in your life that count. It's the life in your years.

- Abraham Lincoln

9

Viability of endothelial cells after ultrasound-mediated sonoporation

Tom van Rooij, Ilya Skachkov, Inés Beekers, Kirby R. Lattwein, Jason D. Voorneveld, Tom J.A. Kokhuis, Deep Bera, Ying Laun, Antonius F.W. van der Steen, Nico de Jong, and Klazina Kooiman

Based on:
Journal of Controlled Release, vol. 238, pp. 197-211, 2016

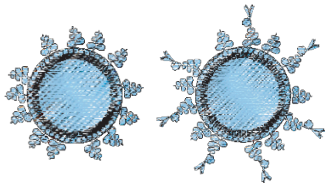

Abstract

Microbubbles (MBs) have been shown to create transient or lethal pores in cell membranes under the influence of ultrasound, known as ultrasound-mediated sonoporation. Several studies have reported enhanced drug delivery or local cell death induced by MBs that are either targeted to a specific biomarker (targeted microbubbles, tMBs) or that are not targeted (non-targeted microbubbles, ntMBs). However, both the exact mechanism and the optimal acoustic settings for sonoporation are still unknown. In this study we used real-time uptake patterns of propidium iodide, a fluorescent cell impermeable model drug, as a measure for sonoporation. Combined with high-speed optical recordings of MB displacement and ultra-high-speed recordings of MB oscillation, we aimed to identify differences in MB behavior responsible for either viable sonoporation or cell death. We compared ntMBs and tMBs with identical shell compositions exposed to long acoustic pulses (500-50,000 cycles) at various pressures (150-500 kPa). Propidium iodide uptake highly correlated with cell viability; when the fluorescence intensity still increased 120 s after opening of the pore, this resulted in cell death. Higher acoustic pressures and longer cycles resulted in more displacing MBs and enhanced sonoporation. Non-displacing MBs were found to be the main contributor to cell death, while displacement of tMBs enhanced reversible sonoporation and preserved cell viability. Consequently, each therapeutic application requires different settings: non-displacing ntMBs or tMBs are advantageous for therapies requiring cell death, especially at 500 kPa and 50,000 cycles, whereas short acoustic pulses causing limited displacement should be used for drug delivery.

Introduction

Microbubbles (MBs) are ultrasound (US) contrast agents that consist of gas bubbles with diameters between 1 and 10 µm, which are encapsulated by a stabilizing coating. Non-targeted microbubbles (ntMBs) are clinically used as blood pool agents for contrast-enhanced US imaging in cardiology and radiology[450,451] and also have therapeutic potential[36,37]. Targeted microbubbles (tMBs) are promising agents for US molecular imaging and therapy; in particular for diseases that can alter the endothelium, such as cancer and inflammation. The tMBs can adhere to specific disease-associated intravascular biomarkers by the addition of targeting ligands to the MB coating[35,452].

When MBs are insonified by US, they oscillate due to the acoustic pressure wave[36]. Oscillating MBs can increase cell membrane permeability to facilitate intracellular drug uptake (sonoporation), stimulate endocytosis, and open cell-cell junctions[36,220]. Although the exact mechanisms of MB-mediated drug uptake still remain unknown, many studies have attempted to pinpoint the US settings that best stimulate intracellular drug uptake[36,453]. So far the key findings are: 1) cell membrane pores induced by oscillating MBs can be reversible or irreversible[229]; 2) a MB has to oscillate with sufficient amplitude to induce sonoporation[454]; 3) tMBs stimulate drug uptake better than ntMBs both *in vitro*[455-459] and *in vivo*[460-463]. Recently, it has also been shown that the cell membrane pore size and pore resealing coefficient can be mathematically obtained from real-time observed MB-mediated intracellular drug uptake[228].

While reversible sonoporation likely facilitates cellular drug uptake without causing lethal damage to the cell, irreversible sonoporation is thought to lead to significant cell damage and eventually cell death. Different therapeutic approaches may require reversible or irreversible sonoporation, and a balance is expected between therapeutic effectiveness and cell damage. Hu et al.[229] revealed the size of the created cell membrane pore to be a predictor for reversible or irreversible sonoporation: pores < 30 µm^2 successfully resealed within 1 min after insonification, while pores > 100 µm^2 had not resealed within 30 min. An established method to study drug uptake by sonoporation relies on the intracellular uptake of the model drug propidium iodide (PI)[227,228,447,454,464], because this molecule can only pass the cell membrane of a live cell when it has been disrupted. After entering the cell it binds to DNA and RNA and becomes fluorescent[465].

Fan et al.[228] showed that intracellular PI fluorescence intensity directly relates to the amount of PI-DNA and PI-RNA complexes that have formed in the cell. They proposed a model to relate intracellular fluorescence intensity to the size of the created pore and its resealing time, which corresponded well with their experimental *in vitro* results on kidney[228] and endothelial cells[466].

For MB-mediated drug uptake, MB dynamics also have to be considered. The frequency generally used for MB-mediated drug delivery is 1 MHz[36], which means that the MBs oscillate one million times per second. These MB oscillations can only be resolved using an ultra-high-speed camera, capable of recording at least two million frames per second (Mfps) to satisfy the Nyquist sampling criterion[467]. While our group used ultra-high-speed recordings to determine that the relative oscillation amplitude of tMBs had to be above 50% to successfully sonoporate a cell[454] (6× 10 cycles at 1 MHz and 80-200 kPa peak negative acoustic pressure), others used high-speed cameras (in the order of a few thousand fps) to reveal that MB displacement is an important contributor to sonoporation-mediated cell death (1.25 MHz, 60-600 kPa, pulse repetition frequency (PRF) 10-1000 kHz, duty cycles 0.016-20%)[468]. MBs displace due to acoustic radiation forces, especially when longer acoustic pulses are used[469,470]. Long acoustic pulses have sparsely been used in MB-mediated drug delivery studies[471-474], even though one of these studies reported that 7,000 cycles resulted in significantly more luciferase activity than 1,000 and 5,000 cycles in endothelial cells *in vitro* (2.25 MHz, 330 kPa, PRF 20 Hz, 120 s treatment)[474]. On the other hand, no significant differences between 1,000, 5,000, and 10,000 cycles were observed; different US pulse lengths thus affected luciferase activity. So far, in depth sonoporation studies on the effect of longer acoustic pulses at different acoustic pressures are lacking, as is the relation between MB oscillation and sonoporation efficiency. In addition, the effect of the same type of ntMBs and tMBs on endothelial cells has never been directly compared *in vitro*. All prior studies comparing ntMBs and tMBs were performed on cancer[455,457-459] and smooth muscle cells[456], despite that MBs are primarily in contact with endothelial cells when injected intravenously[36,452].

In this study we used long US pulses (500-50,000 cycles) at various pressures (150-500 kPa) to investigate how these settings affect US-mediated endothelial cell membrane permeability and cell death. In order to properly compare ntMBs and tMBs, we used

home-made MBs with identical shell compositions to investigate their effect. The real-time observed PI uptake patterns were fit to the previously proposed diffusion model of Fan et al.[228] and additional Principal Component Analysis was used to determine whether cells were reversibly or irreversibly damaged. In combination with high-speed optical recordings of MB displacement and ultra-high-speed recordings of MB oscillation, we aimed to identify MB behavior responsible for viable sonoporation or cell death.

Materials and Methods

Microbubble preparation

Lipid-coated MBs with a C_4F_{10} gas core (F2 Chemicals, Preston, UK) were made by sonication as described previously[314,447]. The coating of the non-targeted MBs (ntMBs) consisted of 1,2-distearoyl-*sn*-glycero-3-phosphocholine (DSPC; 84.8 mol%; P6517; Sigma-Aldrich, Zwijndrecht, the Netherlands), polyoxyethylene-(40)-stearate (PEG-40 stearate; 8.2 mol%; P3440; Sigma-Aldrich), and 1,2-distearoyl-*sn*-glycero-3-phosphoethanolamine-N-carboxy(polyethylene glycol) (DSPE-PEG(2000); MW 2000; 7.0 mol%; 880125P; Avanti Polar Lipids, Alabaster, AL, USA). Before the experiment, the ntMBs were washed three times using centrifugation for 1 min at 400 *g*. After washing the ntMBs, the size distribution and concentration were measured using a Coulter Counter (n = 3; Multisizer 3; Beckman Coulter, Mijdrecht, the Netherlands). The mean (± standard deviation, SD) diameter of the ntMB was 2.54 (± 0.02) μm.

The same components were used for the targeted MBs (tMBs), except 1.1% of DSPE-PEG(2000) was replaced with DSPE-PEG(2000)-biotin (MW2000; 880129C; Avanti Polar Lipids). This allows for adding targeting moieties to the MBs via biotin-streptavidin bridging as previously described[447,475]. Briefly, after three washing steps by centrifugation at 400 *g* for 1 min, the concentration of the MBs was measured using a Coulter Counter (n = 3) and 1 x 10^9 biotinylated MBs were incubated with 20 µg of streptavidin (S4762; Sigma-Aldrich) on ice for 30 min. Following incubation, the streptavidin-conjugated MBs were washed once to remove non-bound streptavidin. Next, 5 µg of biotinylated anti-human CD31-antibody (BAM3567; R&D Systems, Abingdon, United Kingdom) were conjugated to the MB shell, during incubation for 30 min on ice. Following this, tMBs were washed once to remove non-bound antibodies. Directly afterwards the size distribution and concentrations were measured using a Coulter Counter (n = 3) and mean (± SD) diameter for the tMBs was 2.82 (± 0.09) μm.

Endothelial cell culture

Human umbilical vein endothelial cells (HUVECs; C2519A; Lonza, Verviers, Belgium) were cultured in EGM-2 medium (CC-3162; Lonza) in T-75 flasks (353136; BD Falcon

Fisher Scientific, Breda, the Netherlands), and maintained in a humidified incubator under standard conditions (37°C, 5% CO_2). Thereafter the cells were trypsinized using trypsin in EDTA (CC-5012; Lonza) and replated on one side of an OptiCell™ (Thermo Scientific, NUNC GmbH & Co, Wiesbaden, Germany). Experiments were performed two days later with 100% confluence of HUVECs in the OptiCell.

Experimental set-up

For visualization of the MBs and HUVECs, the microscopic set-up consisted of a fluorescence microscope (Olympus, Zoeterwoude, the Netherlands) equipped with a 5× objective (LMPlanFl 5X, NA 0.13, Olympus) for the sonoporation and cell viability assays or a 40× objective (LUMPlanFl 40XW, NA 0.80, water immersion, Olympus) to capture MB behavior. For bright-field imaging the sample was illuminated from below via a light fiber using a continuous light source and for fluorescence imaging a mercury lamp and a suitable set of fluorescent filters were used for the detection of propidium iodide (U-MWG2 filter, Olympus), Hoechst 33342 (U-MWU2 filter, Olympus), and calcein (U-MWIB2, Olympus). On top of the microscope three different cameras were mounted: 1) a high sensitivity CCD camera (AxioCam MRc, Carl Zeiss, Germany) for fluorescence imaging, 2) a high-speed Redlake Motion Pro Camera (10K, San Diego, CA, USA), and 3) the ultra-high-speed Brandaris 128 camera [36]. The experimental set-up is illustrated in Figure 9.1.

For the acoustical set-up, a 1 MHz single-element, focused transducer (focal distance 75 mm; V303; Panametrics-NDTTM, Olympus NDT, Waltham, MA, USA) was mounted in the water bath at a 45° angle below the sample (Fig. 9.1). Each OptiCell was divided into eight equally sized, acoustically non-overlapping sections (19 x 33 mm each; for schematic see Fig. 9.1), which covered the beam area (-6 dB beam width of 6.5 mm) at the focus of the transducer, as verified in advance with a calibrated 0.2 mm PVDF needle hydrophone (Precision Acoustics Ltd, Dorchester, UK). The acoustic focus was aligned with the optic focus.

During the experiment, the position of the OptiCell was adjusted to place the center of each subsection in the focal zone. The sample was insonified by a single Gaussian tapered sine wave burst generated by an arbitrary waveform generator (33220A, Agilent,

Palo Alto, CA, USA) and amplified using a broadband amplifier (ENI A-500, Electronics & Innovation, Rochester, NY, USA). The peak negative acoustic pressure of the US burst (150, 300, or 500 kPa) was kept constant for the entire OptiCell, whereas the number of cycles in the single US burst (500; 1,000; 2,000; 5,000; 10,000; 20,000; and 50,000) varied per OptiCell subsection (Fig. 9.1). For each Opticell one of the subsections was used as a control where no US was applied.

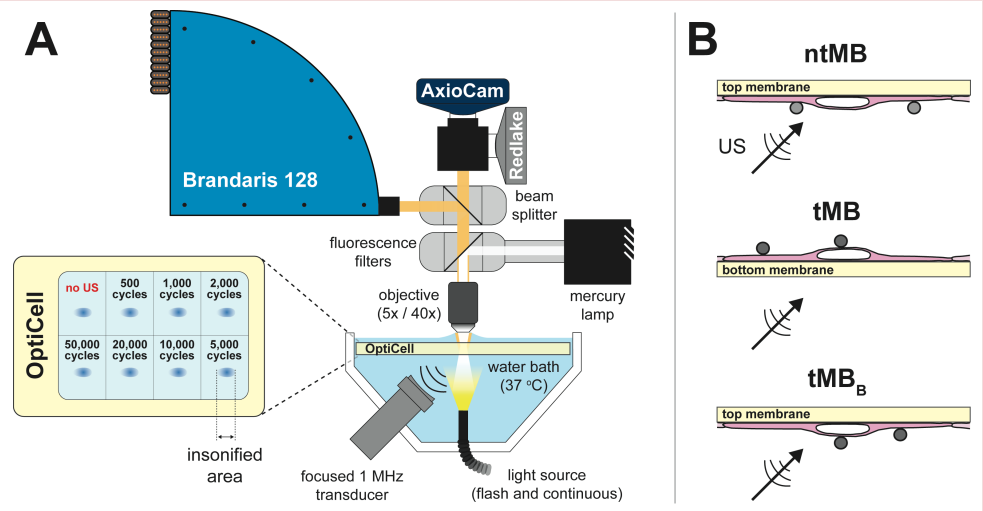

Figure 9.1. Experimental set-up. (A) Illustration of the optical imaging systems combined with the acoustical set-up. Brandaris 128 is the ultra-high-speed camera, Redlake the high-speed camera, and AxioCam the fluorescence and bright-field CCD camera. The enlarged OptiCell shows the insonification scheme. (B) Orientation of the microbubbles (MBs) with respect to the cells and the direction of ultrasound (US) insonification. Non-targeted MBs (ntMBs) were floating against the cells, targeted MBs (tMBs) were adhered on top of the cells, or tMBs adhered below the cells (tMB_B), similar to the ntMB orientation.

Time-lapse sonoporation assay

The time-lapse sonoporation assay was used to monitor sonoporation over time for the different US pressures and number of cycles and is illustrated in Figure 9.2. First, calcein-AM (C3100MP; Invitrogen; prepared in DMSO (Sigma-Aldrich)) was added to the HUVECs in the OptiCell in a final concentration of 0.25 µg/mL. We used calcein-AM

as a live-cell stain as it passively crosses into cellular membranes, has high cell retention, and is only converted to fluorescent calcein in living cells[476]. After 30 minutes of incubation (37°C, 5% CO_2) of the HUVECs with calcein-AM, we added propidium iodide (PI; final concentration 25 μg/mL; P-4864; Sigma-Aldrich) and Hoechst 33342 (final concentration 5 μg/mL; H3570; Invitrogen, Breda, the Netherlands) to the OptiCell. PI, which is live cell-impermeable, was used to determine the presence and intensity of sonoporation, or disruption of cell membranes, since it only becomes fluorescent when bound to DNA and RNA inside cells[465]. The Hoechst 33342 fluorescent dye was used to stain the nuclei of living and dead HUVECs, as it rapidly diffuses into all cells, binds specifically and quantitatively to DNA, and has low toxicity to viable cells[477]. Since Hoechst is a non-intercalating dye which binds to the minor groove of DNA[478] and PI binds to DNA and RNA by intercalating between the bases[479], no competition between both dyes is expected.

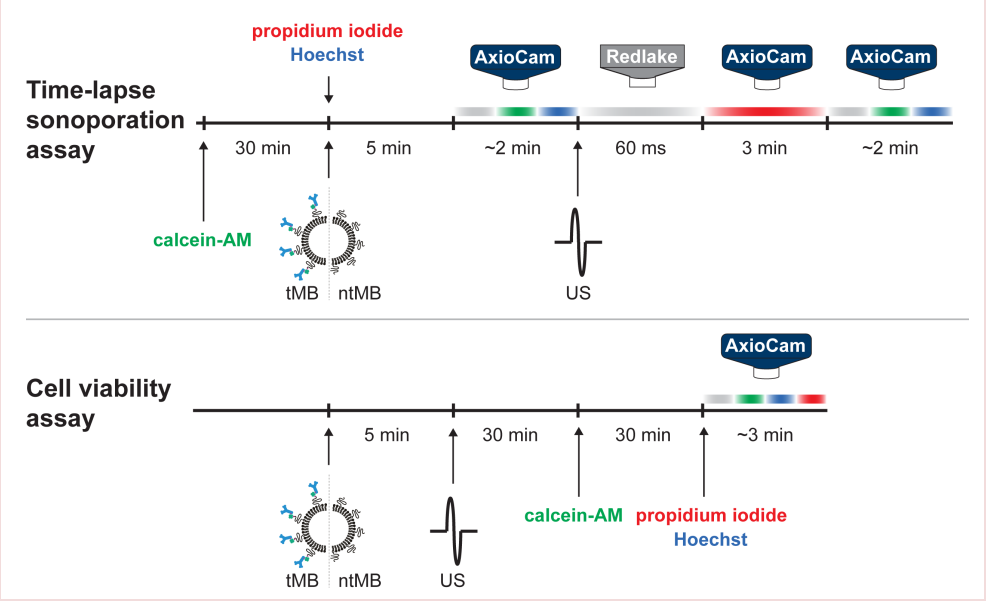

Figure 9.2. Procedural time line (not to scale) for the time-lapse sonoporation and cell viability assays. Arrows indicate when fluorescence dyes or MBs were added, or when US was applied. The cameras show which imaging system was used and the colored bars indicate the type of imaging: bright-field (grey), calcein (green), Hoechst (blue), or propidium iodide (red).

At the same time as PI and Hoechst, ~10^7 MBs were added to the OptiCell to obtain a ratio of 1-2 MBs per cell. After mixing, we incubated the OptiCell for 5 minutes at 37°C, with the cells on the top membrane. This allowed for the MBs to float up and the tMBs to adhere to the cells. The OptiCell was then placed in a 37°C water bath (Fig. 9.1). For the experiments using tMBs, the OptiCell was placed with the cells on the bottom membrane, so any non-adhered MBs would float away from the cell surface, whereas the OptiCell for the ntMB experiments was placed with the cells on the top membrane to ensure that the ntMBs were floating against the cell membranes. To investigate whether the difference in orientation of tMBs influenced sonoporation outcome, we also performed experiments on tMBs located below the cells (tMB_B, see Supplementary Material). The AxioCam was used to take snapshots in bright-field (indicated by the gray bar in Fig. 9.2), and of the fluorescent signals of calcein (green) and Hoechst (blue). Just before US exposure, the Redlake camera was started and ran for 60 ms to completely cover the full US exposure. Consequently, this camera recorded more frames after insonification for the shorter pulses than for the longest pulse. The Redlake camera recorded the MB displacement and clustering at 2,000 frames per second (fps). After these 60 ms, the AxioCam recorded the fluorescence intensity change over time for 3 min (1.5 s exposure and 5 s time intervals) caused by cellular PI uptake after US application. At the end of the protocol, snapshots in bright-field and of calcein and Hoechst signal were taken for comparison with the initial situation. This procedure was repeated for each subsection and the experiment was performed in triplicate.

Cell viability assay

For each US setting, cell viability was determined as shown in Figure 9.2. The same amount of MBs as described in the previous section (~10^7) were added to the OptiCell and left in the incubator (37°C) for 5 min. Within 3 to 4 min after the US treatment of all eight subsections of the OptiCell, HUVECs were incubated at 37°C, 5% CO_2. Thirty minutes after the US treatment, calcein-AM was added to the OptiCell and incubated for another 30 minutes under the same conditions. After the final incubation, PI and Hoechst were added to the Opticell. This procedure was followed directly with bright-field and fluorescent (calcein, Hoechst, and PI) microscopic examination using the AxioCam (Fig. 9.2). For each condition, five different fields of view were acquired within a 6 mm circle around the center of the insonified area. All experiments were done in triplicate.

Oscillatory behavior of microbubbles

To relate MB behavior to sonoporation, high imaging speeds in the range of a few million frames per second (Mfps) are required. Since these high speeds cannot be achieved using the Redlake camera, we used the Brandaris 128 ultra-high-speed camera [36] in segmented mode[242]. The protocol was similar to the time-lapse sonoporation assay, but the Redlake camera was replaced by the Brandaris 128 camera. The segmented mode of the Brandaris 128 allows for optical recording of long US pulses by dividing the CCD sensor arc into four segments. During each exposure all four segments were illuminated, however only one segment was triggered to transfer the data to the buffer channel. These triggered transfers from the consecutive segments were equally spaced over the time span of the applied US pulse. The start of the acquisition was triggered at a frame rate of 3.85 Mfps, resulting in a corresponding intersegment time of ~328 μs. During one US pulse a full recording then captured four equally spaced movies of ~8 μs in bright-field using a Xenon flash source (MVS-7010, Perkin-Elmer Optoelectronics, Wiesbaden, Germany). These settings resulted in a total acquisition time of 1017 μs. The recording time of the ultra-high-speed movies was a few µs longer than the US pulse to ensure that the start and end of the MB oscillations were fully captured. MB behavior was recorded for both tMBs and ntMBs, at 1,000 cycles for pressures of 150 and 300 kPa. The number of cycles was limited to 1,000 cycles (i.e. 1 ms duration), because the Xenon flash duration could not be extended.

Analysis of fluorescence images

All images acquired with the Axiocam (bright-field and fluorescence) were analyzed using a custom-built plugin for ImageJ[480]. To segment the nuclei, first a composite image of the Hoechst image after insonification and the final PI image was produced, to ensure clear visibility of all nuclei. We chose to use the Hoechst image after insonification, since less cell displacement was expected between this image and the first PI image. The composite image was thresholded using the method of Otsu[481], resulting in a binary image with white nuclei on a black background. A mask of this image was created and watershedding was applied to separate overlapping nuclei. The watershedding algorithm calculates the centers of the nuclei and dilates them until touching another dilated boundary or a white pixel. At the meeting point, a watershed line is drawn. Using the

Analyze Particles function, the nuclei and the area of the nuclei were located and stored in the ROI manager. The center of the nuclei was found using the Find Maxima function, added to the ROI manager, and copied to a blank image. Next, the cell borders were automatically segmented using Voronoi tessellation[482] which is a built-in option in the Find Maxima function. Voronoi tessellation is based on the theory that every point *p* has a distance to another point *q* that is less than or equal to its distance to any other point *r*. The lines in a Voronoi diagram are thus equidistant to two points in space (i.e., the cell nuclei) and correspond to the most likely position of the cell boundaries. The resulting Voronoi segmentation was transformed into a mask and stored in the ROI manager. The ROI manager now contained the center of each nucleus, the area of each nucleus, and the cell borders.

For assessing cell death using the cell viability assay, the number of cells that showed PI uptake on the images without the application of US was analyzed as described above. Next, the number of cells that had taken up PI after receiving US was normalized to the number of cells that had taken up PI in the control sections, to correct for cells that were already dead when the experiment started.

For assessing the dynamic uptake of PI after sonoporation the segmented nuclei and cell borders were overlaid on every frame of the PI fluorescence time-lapse recording after the application of US. The mean signal intensity of PI for each nucleus and each cell was obtained frame by frame. The nuclear PI uptake was used for further analysis because the segmentation of the nuclei was based on intensity thresholding of Hoechst stained nuclei, which is more accurate than the segmentation of cell borders that is based on the highest probability of a cell border being present.

PI model fit and data classification

The temporal PI intensity values in the nuclei were loaded into RStudio (RStudio, Inc., Boston, MA, USA) for further quantification of sonoporation. Fan et al.[228] derived an equation (Eq. 1) to model sonoporation dynamics of a single cell, based on the resealing of the created pore and the diffusion rate of PI into the cell.

$$F(t) = \alpha \cdot \pi D C_0 \cdot r_0 \cdot \frac{1}{\beta}\left(1 - e^{-\beta t}\right) \tag{9.1}$$

In Equation (9.1), $F(t)$ is the fluorescence intensity as a function of time, a is a coefficient that relates the amount of PI molecules to the fluorescence intensity of PI-DNA and PI-RNA. This coefficient is determined by the sensitivity of the fluorescence imaging system. The other parameters are the diffusion coefficient of PI, D, the extracellular PI concentration, C_0, the initial radius of the pore, r_0, the pore resealing coefficient, β, and time, t. The pore size coefficient, $a \cdot \pi \cdot D \cdot C_0 \cdot r_0$, determines the initial slope of the PI uptake pattern and is the scaling factor for the exponential increase. Therefore, a steep initial slope corresponds to a larger pore size. The overall slope follows $F(t) = (\alpha \cdot \pi D C_0 \cdot r_o) \cdot e^{-\beta t}$, in which the pore resealing coefficient β is the time constant that determines the time to reach the asymptotic value of the maximum PI intensity. This asymptotic maximal PI intensity value is given by the inverse relationship between the pore size and pore resealing coefficients (Eq. (9.2)). Therefore a cell with a high pore resealing coefficient quickly reaches the asymptotic value, resulting from quick resealing of the pore.

$$F(\infty) = \frac{\alpha \cdot \pi D C_o \cdot r_o}{\beta} \tag{9.2}$$

To obtain the pore size coefficient, $a \cdot \pi \cdot D \cdot C_0 \cdot r_0$, and the pore resealing coefficient, β, the PI intensities recorded in the time-lapse sonoporation assay were fit to Equation (9.1) using a nonlinear least-squares approach. Classification, based on the distributions of both coefficients, was performed using Principal Component Analysis (PCA) [45, 46] on the complete data set (all settings, both ntMB and tMB). We chose PCA because this method captures as much of the variation in the data as possible by computing eigenvectors (for determining the direction in which the data has largest variance) and corresponding eigenvalues (to determine how much variance there is in the data in that direction). The principal components (PCs) are uncorrelated with each other since the eigenvectors are perpendicular to each other. In this data set we chose two PCs because we only used the pore size coefficients and pore resealing coefficients to fit the data to Equation (9.1). Classification thresholding was applied on the PC with the largest variance, separating the complete data set in two groups. Using these PCs, the cell populations at each different setting were classified. Based on Equation (9.1), two additional thresholds were chosen to classify the cells that were most likely irreversibly damaged based on very low pore resealing coefficients. In these cells, PI intensities still

increased at the end of the time-lapse sonoporation assay (i.e. at 180 s), or > 120 s. Because pores remaining open for more than 1 min would not close[229], we assumed these pores to most likely result in cell death.

Displacement of microbubbles

Tracking of displacing MBs was implemented in Python™ (v2.7, Python Software Foundation). The recordings on which the tracking was performed were obtained with the Redlake camera and had an isotropic spatial resolution of 0.63 μm/pixel. Gaussian Mixture-based background subtraction[485] was applied to remove all but the displacing MBs from each frame. This was required to correct for illumination fluctuations among the frames and in different regions of the image, which hindered accurate MB tracking. The remaining MBs were tracked using Trackpy[486], an open source blob tracking algorithm, to obtain the trajectory of each displacing MB.

To differentiate between sonoporation due to displacing or non-displacing MBs, the latter were segmented from the AxioCam bright-field images before US application. Since the FOV of the Redlake camera was smaller than that of the AxioCam, only the part of the FOV that overlapped was analyzed. We used the Laplacian of Gaussian (LoG) blob detection algorithm (scikit-image[487]); this algorithm convolves Gaussian kernels of a range of standard deviations with an image. In this way it determines the centroid and diameter of non-displacing MBs, approximated by the standard deviation of the corresponding Gaussian kernel. In order to detect most MBs, their diameters were limited to a range between 1.7 and 5.0 μm, and a 20% overlap was allowed to properly deal with clusters and focal differences.

After locating the displacing and non-displacing MBs, their effect on cellular PI uptake was assessed. For segmentation of the nuclei from the Hoechst images, we also used the LoG blob detection algorithm, which performed best when the range to detect nuclei was limited between 5.0 and 6.7 μm in diameter, and overlapping at most 20%, to separate nuclei with seemingly overlapping borders. Centroids of the segmented cell nuclei were used as seeding points for cell border segmentation using Voronoi tessellation. For segmenting regions with PI uptake in the initial and final frame of the PI stained image sequences, the LoG blob detection algorithm was limited to diameters

between 5.0 and 8.3 μm, and allowed 25% overlap. More overlap and larger regions were allowed than for nuclei segmentation since PI can also stain the cytoplasm by binding to RNA. Regions in which PI uptake was detected in both the first and last frame were neglected, because these cells had already taken up PI before US application. Cells were defined as sonoporated when 70% of their equivalent circular diameter overlapped with a region showing PI uptake. This percentage was used to compensate for the overestimation of cellular diameters due to odd shaped cells, e.g. rectangular shaped cells. If a cell's equivalent diameter intersected with 1.25 times a MB diameter (to account for MB expansion) it was considered to be in contact with a non-displacing MB. Similarly, contact with displacing MBs occurred when the cell's full equivalent diameter intersected with a MB's trajectory (the lines connecting a MB between frames, as determined by Trackpy).

The relations between MB displacement and sonoporation outcome at all acoustic settings were visualized using scatter plots and linear fits through these data using a least-squares approach in MATLAB (The MathWorks, Natick, MA, USA).

Statistics

To compare the various acoustical settings, we performed statistical testing using Student's t-tests to identify significantly different outcomes. All statistics were performed using Student's t-tests for independent samples, where a p-value of 0.05 was regarded as significant.

For both sonoporation and cell death, different insonifying pressures were compared at the same number of cycles for both ntMBs and tMBs. One-sided t-tests were used to reveal whether higher pressures at the same number of cycles resulted in more sonoporation and cell death. The same t-tests were performed to verify whether the experimental acoustic settings resulted in more sonoporation than in the control experiments. For comparing sonoporation with cell death, we used 2-sided t-tests to verify whether the percentage of sonoporated cells was different from the percentage of cell death. The effect of ntMBs, tMBs, and tMB_B on the amount of sonoporated cells and on cell death were tested using 2-sided t-tests.

The cells that were classified as non-resealing within 120 s were compared to the cells that were determined as dead by the cell viability assay. We used 2-sided t-tests to verify whether the assumption that both populations were equal was true.

Results

Sonoporation and cell-death

The influence of various acoustic settings on cellular responses, for both ntMBs and tMBs, was evaluated by the amount of sonoporated cells and cell death, as illustrated in Figure 9.3. The sonoporation and cell death data are presented as the mean of three experiments at the same settings, with a mean (± SD) of 1,727 (± 338) cells in the FOV for ntMBs and 3,104 (± 130) cells for tMBs. The amount of injected microbubbles was adjusted accordingly, resulting in 1.9 (± 0.8) ntMBs per cell and 1.6 (± 0.3) tMBs per cell. No controls are shown for the cell death data, since these were already subtracted at all settings to correct for natural, non-US related, cell death (6.7 ± 1.1%).

The data show that applying higher acoustic pressures and more cycles increased both the number of sonoporated cells (Fig. 9.3A, C) and the number of dead cells (Fig. 9.3B, D). This trend was seen for both ntMBs (Fig. 9.3A, B) and tMBs (Fig. 9.3C, D). However, when statistically comparing the same number of cycles at increasing pressures, the increase in sonoporation at higher acoustic pressure was only significant ($p < 0.05$) for ntMBs with at least 2,000 cycles. For tMBs sonoporation at 500 kPa was always higher than at 300 kPa, whereas at 300 kPa at least 10,000 cycles had to be applied to sonoporate more cells than at 150 kPa. Cell death for the same number of cycles at increasing pressures was significantly higher when using ntMBs, in all cases. For tMBs, cell death at 500 kPa was always significantly higher than at 300 kPa. Conversely, when comparing 300 kPa and 150 kPa, cell death was not significantly different between 1,000 and 5,000 cycles.

The amount of sonoporated cells, in the presence of ntMBs at 150 kPa, only resulted in significantly more sonoporation than in control experiments (0.4% sonoporation) when applying 10,000 or 50,000 cycles (2.0% or 4.7%, respectively). At 300 kPa, at least 2,000 cycles were required to significantly yield more PI uptake than in the control experiments, whereas at 500 kPa pressure, 1,000 cycles were already sufficient. For tMBs, 150 kPa did not result in significantly more sonoporation than in the experiments without US. However, application of 300 or 500 kPa sonoporated significantly more cells than in the control experiments for all cycles considered.

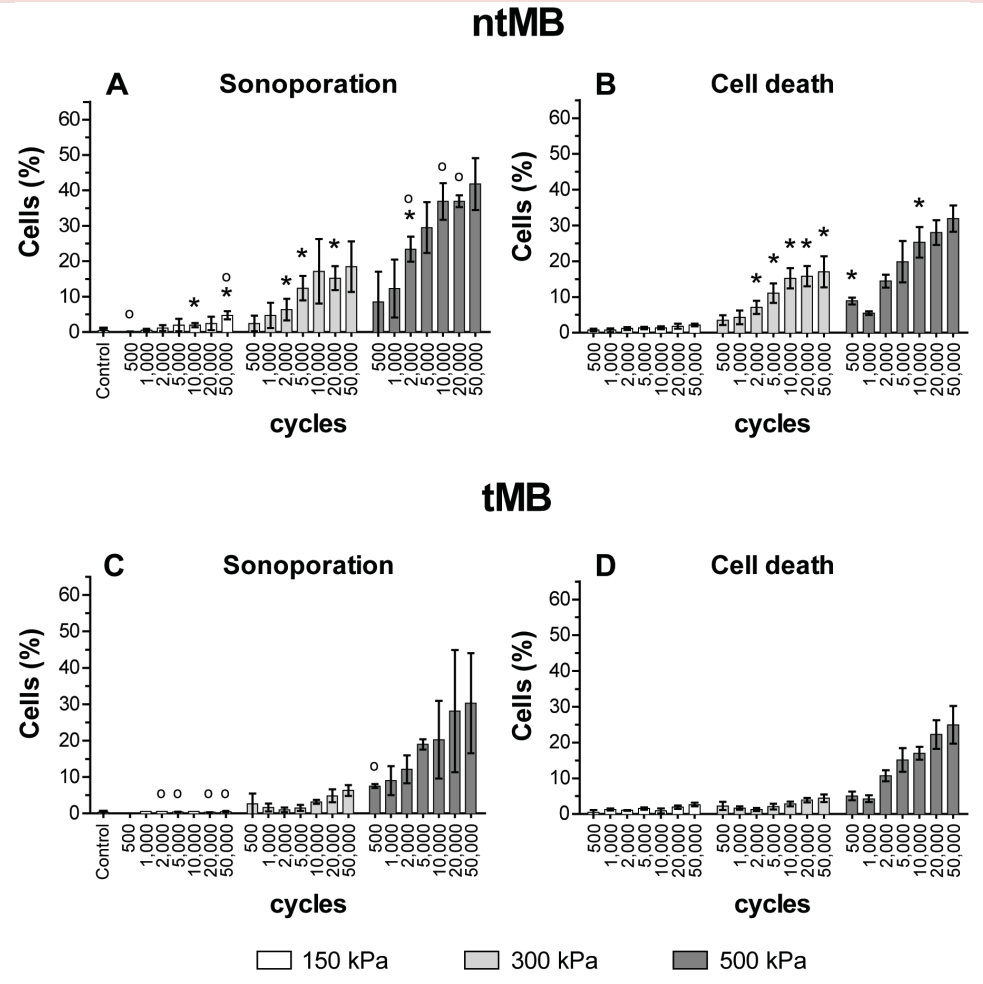

Figure 9.3. Targeted and non-targeted microbubble-mediated sonoporation and cell death after ultrasound exposure at different acoustic pressures (150, 300, and 500 kPa) and number of cycles (500 – 50,000). (A) Mean (± SD) percentage of sonoporated cells and (B) cell death after insonification of ntMBs. (C) Mean (± SD) percentage of sonoporated cells and (D) cell death after insonification of tMBs. Results were based on n = 3 repetitions of each experiment. Significant differences ($p < 0.05$) between sonoporation and cell death after US insonification in the presence of ntMB or tMB are indicated by (*). Significantly more sonoporation than cell death is indicated by (o).

The amount of sonoporated cells was expected to be higher than the amount of dead cells, because cells that are sonoporated can also remain viable. However, for most of the settings we applied, cell death was similar to the amount of sonoporated cells. The settings for which the difference between cell death and sonoporation was significant are indicated by (o) in Figure 9.3A and C. Since cell death was assessed from the viability assays—which were performed separately from the sonoporation assays—cell death could even be higher than the amount of sonoporated cells. This was the case for the 150 kPa experiments in the presence of tMBs.

To validate whether ntMBs or tMBs were more efficient in inducing sonoporation and cell death, we statistically compared them for significance. The asterisks (∗) in Figure 9.3 indicate significant differences between ntMB and tMB for sonoporation (A) and cell death (B). Although Figure 9.3A and C may suggest that ntMB more efficiently sonoporated cells than tMB at 500 kPa using long US pulses, this difference was not significant, probably due to the high standard deviations in the tMB sonoporation experiments. Cell death due to ntMBs was significantly higher for almost all number of cycles at a pressure of 300 kPa, and comparable for all settings at 150 kPa and for most settings at 500 kPa.

Sonoporation-induced PI uptake over time

Before US exposure, bright field imaging was used to discern MB locations (Fig. 9.4A); the black dots in this figure are the MBs, examples indicated by white arrows. The grey background of the image shows spherical structures; these are the nuclei of the endothelial cells in the monolayer. Fluorescence microscopy established individual cell nuclei locations by Hoechst staining (Fig. 9.4B), cell membrane integrity by the absence of PI fluorescence (Fig. 9.4C), and live cells by the presence of calcein (Fig. 9.4D). After US insonification, less MBs were present because they had dissolved, coalesced, or displaced (Fig. 9.4E). Intracellular PI uptake was observed by increase of fluorescence signal, thus indicating sonoporation (Fig. 9.4G).

Interestingly, when increasing PI signal was observed, Hoechst signal decreased (Fig. 9.4F). Because the segmentation was done on the image after US application, the segmented cell nuclei did not always exactly match the nuclei in the Hoechst image

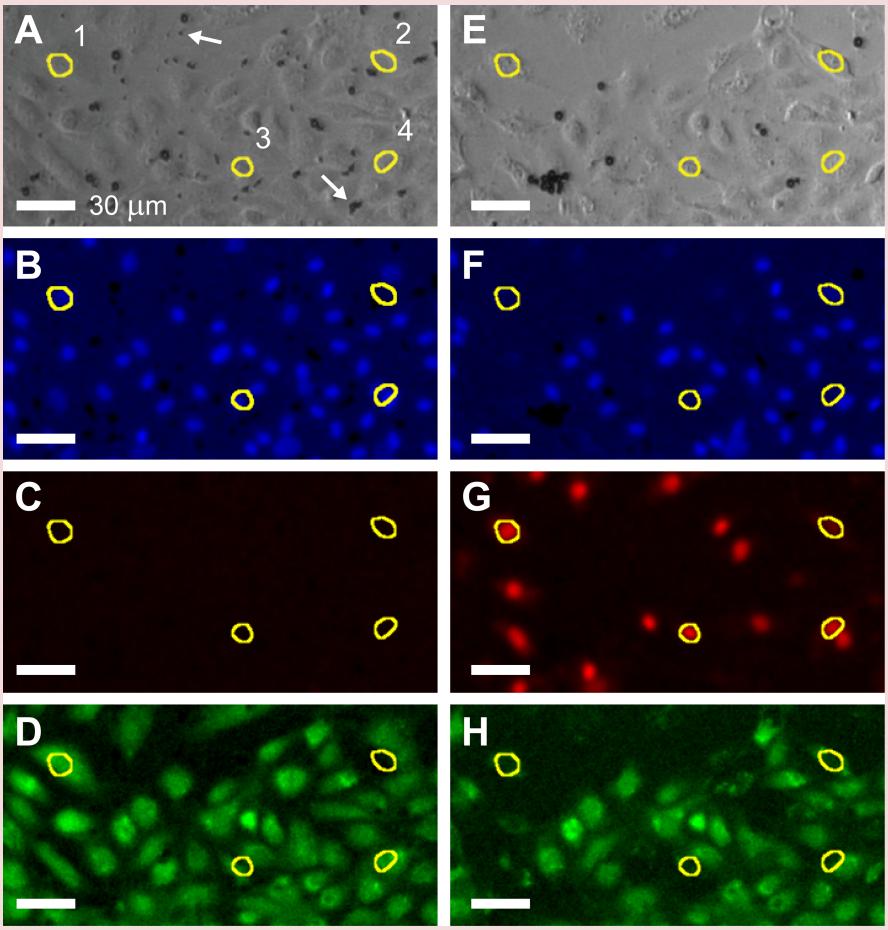

Figure 9.4. Optical recordings of microbubbles and the HUVEC monolayer. (A) Bright-field image of ntMB locations (black dots) before US exposure; an example of a single ntMB and a ntMB cluster are indicated by a white arrow. Yellow circles indicate highlighted sonoporated cells. (B) Hoechst fluorescence imaging of HUVEC nuclei before US application. (C) Fluorescence image of PI uptake before insonification; no uptake was present in the field of view. (D) Calcein stained image of live cells before US application. (E) Bright-field image after US treatment; ntMBs dissolved, displaced, and clustered. (F) Hoechst stained image of nuclei after US application; signal in sonoporated cells was lower than before US application. (G) Fluorescence image of PI signal after US application; red stained nuclei indicate sonoporated cells. (H) Calcein stained image after US application; calcein leaked out of some sonoporated cells. (I) PI fluorescence intensity as a function of time up to 180 s after US treatment (colored circles) and fit to the Fan model (Eq. 1, solid lines); black circles indicate 90% of theoretical maximum PI intensity that could be reached with the fit parameters. Cells 1 to 4 are marked with yellow circles in panels A-H, and the numbers correspond to those in panel A. US settings: 500 kPa acoustic pressure, 10,000 cycles. Scale bar 30 µm.

before US (compare panel B and F). In between the recording of these images, there can be small displacements of cells due to the radiation force of the applied US, movement of the MBs, or retraction of cells because of cell-cell contact opening. In cells that had taken up PI, calcein signal was found to decrease (Fig. 9.4H), which has previously been described as an additional measure for sonoporation[228].

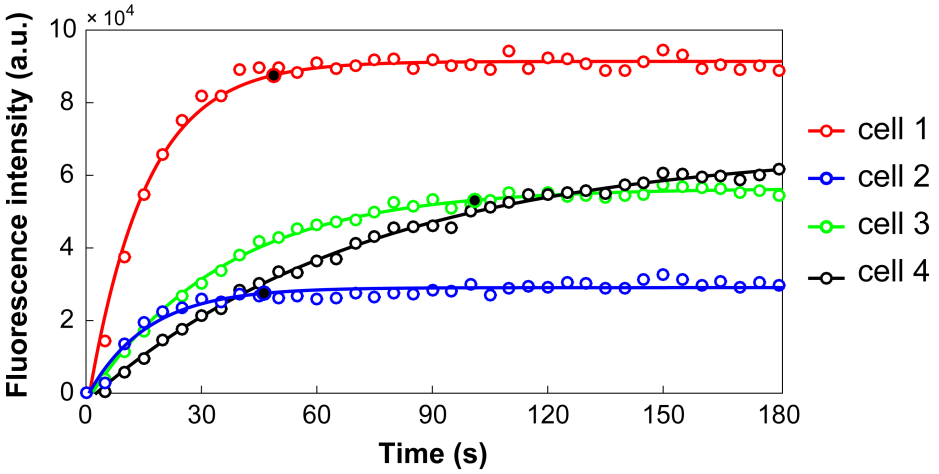

Figure 9.5. PI fluorescence intensity as a function of time up to 180 s after US treatment (colored circles) and fit to the Fan model (Eq. 1, solid lines); black circles indicate 90% of theoretical maximum PI intensity that could be reached with the fit parameters. Cells 1 to 4 are marked with yellow circles in Fig. 9.4A-H, and the numbers correspond to those in Fig 9.4A. US settings: 500 kPa acoustic pressure, 10,000 cycles. Scale bar 30 µm.

The PI time-lapse images (example shown in Fig. 9.4G) were analyzed for all acoustic settings, resulting in time-intensity curves showing the dynamic PI uptake from just after US application, up to 180 s later. The time-intensity curves were fit to the Fan model (Eq. 1) and revealed a variety of uptake dynamics. Because PI signal intensity could fluctuate between frames, we chose a robust method that only considered cells as actually sonoporated when the time-intensity curve could be fit to the model with an $R^2 > 0.8$. For $R^2 < 0.8$ the fit was regarded as less reliable, because already dead cells at the start of the experiment without clear increase in PI uptake would also be marked as sonoporated. In Figure 9.5, four different types of uptake curves are shown corresponding

to the numbered cells in Figure 9.4A. The curves obtained for ntMB insonified at 500 kPa for 10,000 cycles illustrate the general differences in PI uptake rates found at all other acoustic settings. The red and blue curve reach 90% of the maximum intensity value predicted by the model within 50 s, whereas the green curve reached this 90% value after more than 90 s, and the black one did not reach this 90% value within 180 s.

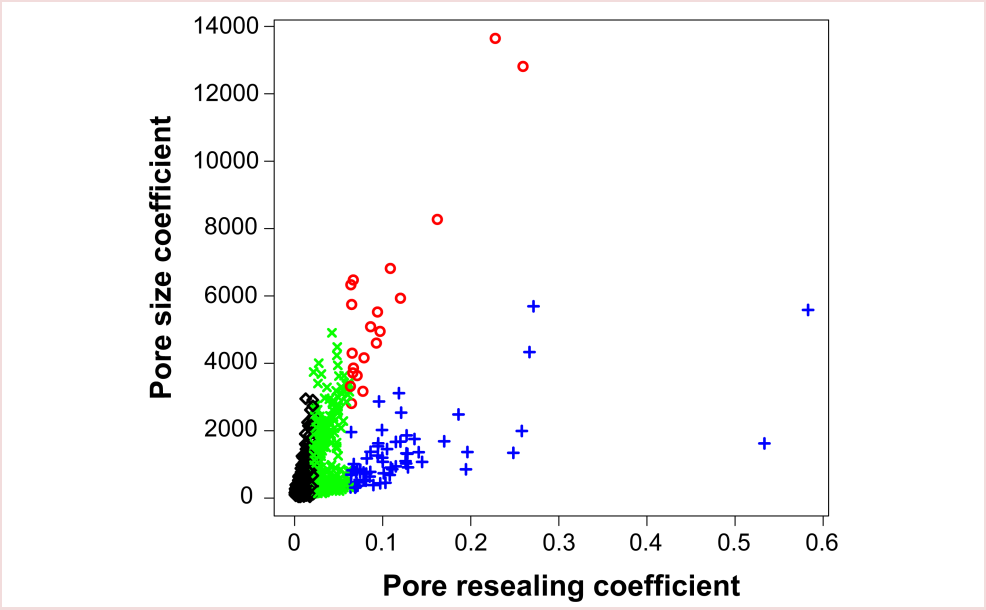

Figure 9.6. Classification of cell populations based on pore size and pore resealing coefficients. This graph originates from the same data set as Fig. 4 and shows cells with high PI uptake (red), low PI uptake (blue), cells with pores that resealed within 120 – 180 s (green), and cells with pores that did not reseal within 180 s (black). US settings: 500 kPa acoustic pressure, 10,000 cycles.

PI uptake as a function of pore size and pore resealing coefficients

The pore size and pore resealing coefficients of the cells that resulted in a reliable fit to Equation (9.1) ($R^2 > 0.8$) were used to classify those cells into groups using PCA. This approach divided the total population of cells into two groups: one with relatively high pore resealing coefficients and relatively low pore size coefficients (Fig. 9.6, blue), and one with relatively low pore resealing coefficient and relatively large pore size coefficients

(Fig. 9.6, red). The cells in the blue population had low PI uptake suggesting small pores that sealed quickly, whereas the cells classified as red had high PI uptake suggestive of large pores that sealed slower, but within 120 s. By applying the additional thresholds (based on Eq. 1, as described in the Materials and Methods section), the cells that were likely to be irreversibly damaged were identified and classified into two separate populations: cells with pores that did reseal, but only after 120 s (Fig. 9.6, green), and cell with pores that did not reseal within 180 s (Fig. 9.6, black).

Influence of acoustic settings on sonoporation-induced uptake and cell death

The impact of the acoustic pressure and the number of cycles in a single burst sine wave on sonoporation-induced PI uptake is illustrated in Figure 9.7. These graphs show the populations of the time-lapse sonoporation assays classified as high PI uptake cells (red), low PI uptake cells (blue), cells with pores that had not resealed within 120 s (grey, this is the sum of the cells previously classified as green or black), and cell death (yellow) determined from the cell viability assays for each corresponding treatment. The cells with pores that did not reseal within 120 s were expected to be dead, and statistical comparison with cell death indeed confirmed that these two populations were not significantly different except for a few settings, mainly those with very low amounts of sonoporated cells (indicated by (∗) in Fig. 9.7). The proportion of cells with low and high PI uptake (blue and red, respectively) significantly increased with increasing pressure, but did not significantly increase when only more cycles were applied. These cells were determined to be reversibly sonoporated and viable. On the other hand, the amount of cells with slow resealing pores (> 120 s, grey) and cell death (yellow), continued to increase with increasing pressure and cycles. Only increasing the number of cycles resulted in more cell death, but not necessarily in more cells that were viably sonoporated.

Oscillatory behavior of microbubbles

The ultra-high-speed movies recorded by the Brandaris 128 camera were qualitatively analyzed per segment. For each segment the number of single MBs and the number of MB clusters were counted and classified into four categories: 1) non-oscillating (white), 2) oscillating (dark grey), 3) oscillating with coalescence of MBs (black), and 4) oscillating with separation of MBs (light grey), as illustrated in Figure 9.8.

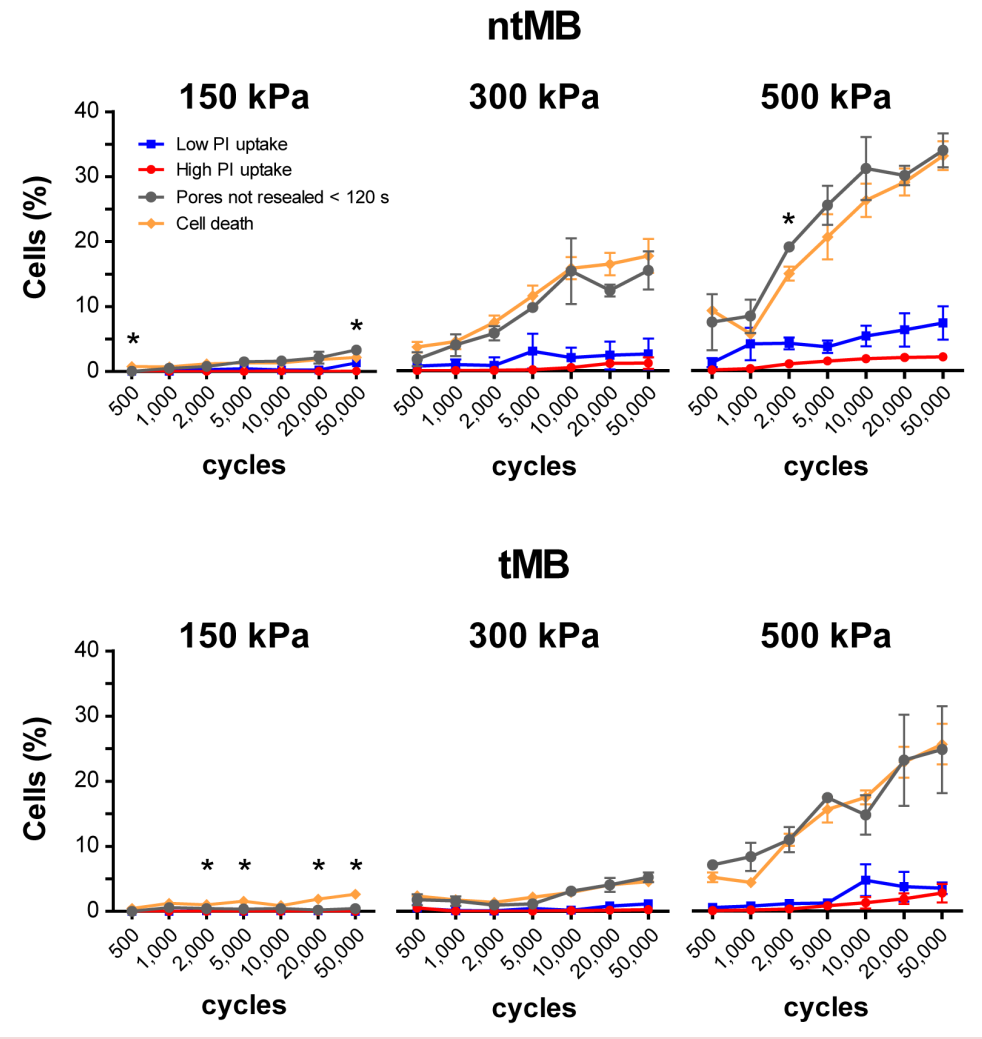

Figure 9.7. Percentage of cell death and cells classified per category by PCA and additional thresholding under various experimental acoustic pressures and cycles. The amount of cells with pores that did not reseal within 120 s (grey line) correlated well with cell death (yellow line) and was only significantly different ($p < 0.05$) at the acoustic settings marked by (*).

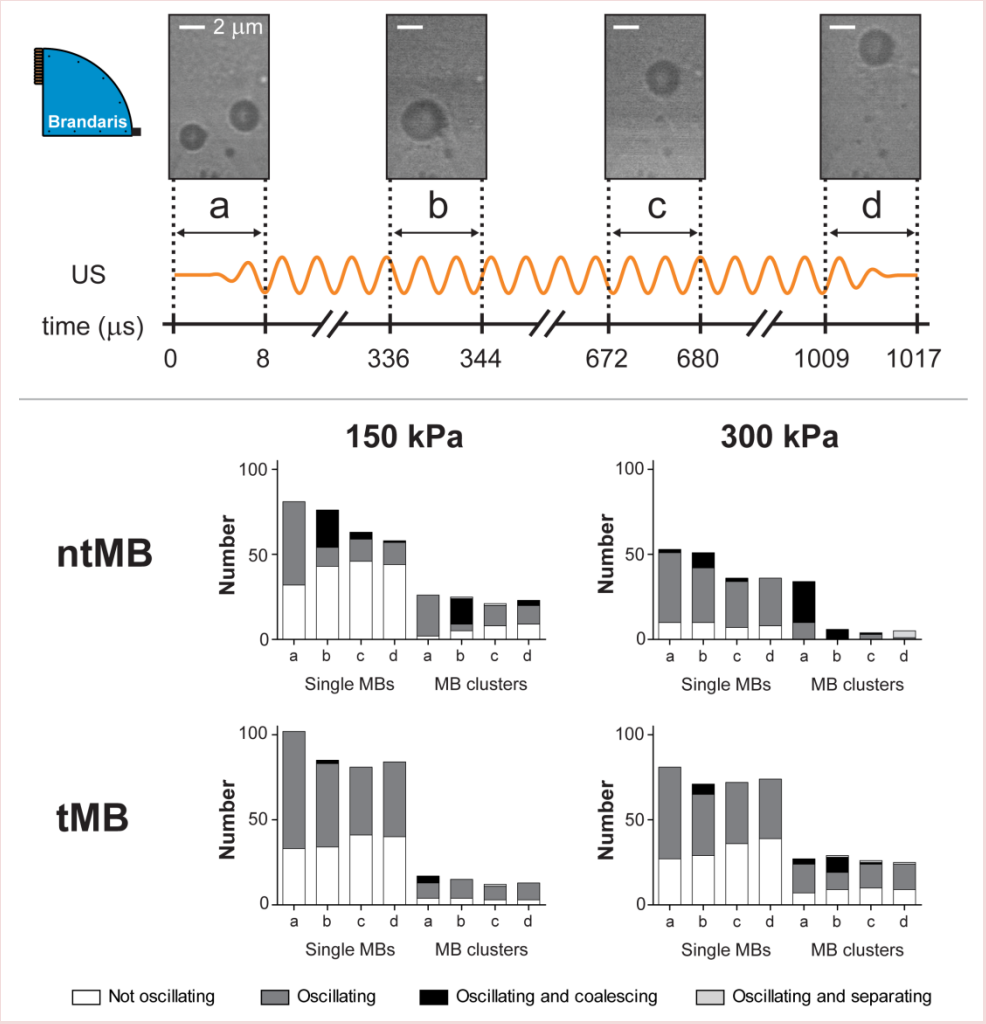

Figure 9.8. Ultra-high-speed imaging of microbubble oscillation behavior. Top: illustration of the segments at which microbubble oscillation was captured and still frames of a recording of tMBs insonified at 300 kPa and 1,000 cycles. Bottom: ntMBs and tMBs oscillation behavior categorized into single MBs and clusters at 150 and 300 kPa insonifying pressure.

The time line shows the US signal (for visualization purposes, only 20 cycles are shown in the schematic instead of the 1,000 cycles that were actually applied) and the segments of the US pulse at which the ultra-high-speed movies were recorded. The FOV of

Brandaris is smaller than that of the AxioCam or Redlake camera, therefore we could only study oscillatory behavior of a subset of MBs.

When ntMBs were insonified at 150 kPa and 1,000 cycles, more single MBs were counted than MB clusters. In the first segment about 60% of single MBs oscillated, whereas > 90% of MB clusters were oscillating. Towards the end of the US burst, only 25% of single MBs and 60% of MB clusters were still oscillating. From segment a to segment b most coalescence occurred (black). At a pressure of 300 kPa, more ntMBs oscillated: 75% of single MBs and all MB clusters (see Supplemental Video 1). The higher pressure ensured that MBs below resonance, i.e. smaller MBs, also started oscillating. In segment a and b, most clusters coalesced into larger clusters that kept oscillating until the end of the US pulse. This higher degree of clustering was probably caused by more displacement of MBs, due to higher acoustic radiation forces. At the end of the pulse, in segment 4, the large clusters split into smaller clusters or single MBs.

At 150 kPa less tMBs coalesced than ntMBs. This was hypothesized to be due to less displacement of tMBs, as tMBs were attached and higher forces are needed to dislocate them [50]. Fewer clusters were present for tMBs, but more of them were oscillating (~75% in all segments). At a higher pressure of 300 kPa, the overall trend of oscillating single tMBs and clusters was not very different than that at 150 kPa. This has already been shown in Figures 9.3 and 9.7 in terms of sonoporation efficiency. However, at 300 kPa more clusters were present and more coalescence occurred.

Displacement of microbubbles

As described in the previous section, more coalescence and clustering were observed for ntMBs, which was hypothesized to be caused by more displacing ntMBs. For each sonoporated cell, in a subset of the original image (ntMB: ~1100 cells, tMB: ~ 1700 cells), we determined it to be either in contact with: 1) both non-displacing and displacing MBs (dark grey), 2) a MB that displaced (black), 3) a MB that had not displaced (light grey), or 4) when no MB could be detected nearby the cell (white), as shown by the stacked bars in Figure 9.9 as percentages of the total amount of sonoporated cells. The red solid line illustrates the amount of sonoporated cells as a percentage of the total amount of cells in the FOV. This amount was, on average, 2.7%

higher than the amount of sonoporated cells shown in Figures 9.3 and 9.7. This was expected, since the data for those figures only accounted for the cells that fitted properly to the model. Both methods showed the same trends, thus the determination of PI uptake was performed on a representative subset of the full-size AxioCam images.

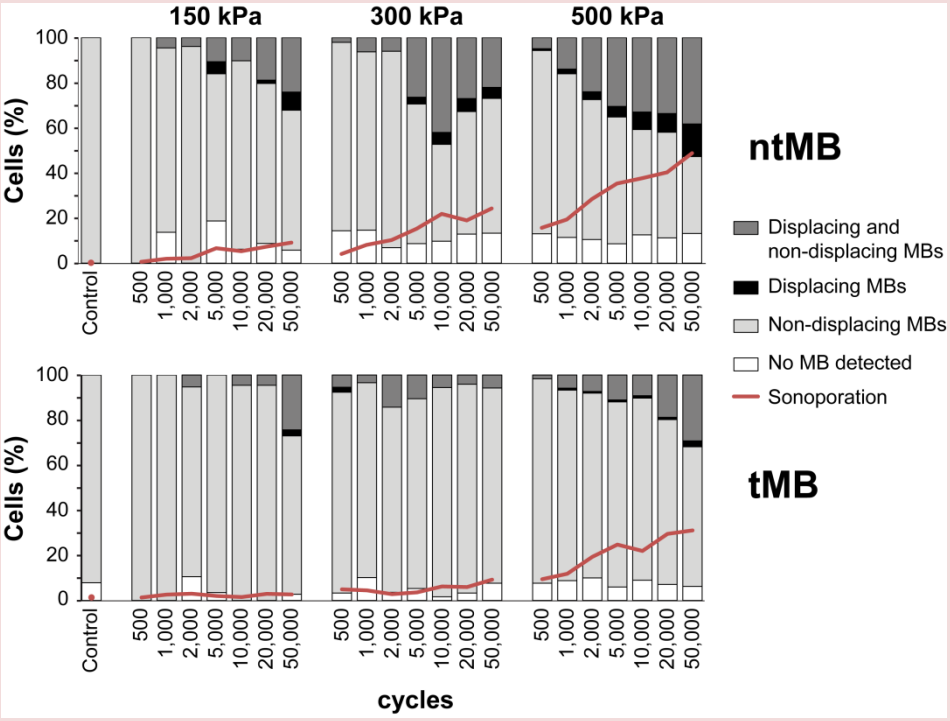

Figure 9.9. Displacement of ntMBs and tMBs under varying experimental acoustic pressures and cycles. For each acoustic setting, the stacked bar graph indicates the percentage of sonoporation caused by displacing MBs, non-displacing MBs, both, or when no MB could be detected. The red line shows the percentage of cells that were sonoporated.

Most sonoporation was induced by non-displacing MBs (light grey, Fig. 9.9), whereas for ntMBs at 500 kPa and 50,000 cycles both displacing and non-displacing MBs accounted for similar amounts of sonoporation. The use of ntMBs resulted in the highest amount of displacing MBs, which supports the previously stated hypothesis that the higher degree of clustering was due to more displacing MBs. Overall, when comparing the contribution of displacing MBs (dark grey and black in Fig. 9.9) to the amount of sonoporated cells (red

line in Fig. 9.9), they followed the same trend.

To relate MB displacement to sonoporation outcome, we compared the two cell classifications: 1) reversibly sonoporated cells that had resealing pores < 120 s (Fig. 9.7, blue and red lines) and 2) irreversibly sonoporated cells (Fig. 9.7, grey line) with A) cells that were sonoporated by displacing MBs (Fig. 9.9, dark grey and black) and B) those that were sonoporated by non-displacing MBs (Fig. 9.9, dark grey and light grey as shown in Fig. 9.10). The slope of the linear fit shows the ratio of increase between two groups; a ratio of 1 implies that the values are identical and increase proportionally (data follows the line $y = x$).

A proportional increase was found for the amount of irreversibly sonoporated cells and the amount of cells that were sonoporated by non-displacing MBs (slope 1.0 for ntMB in Fig. 9.10A; slope 1.1 for tMB in Fig. 9.10B, both $R^2 = 0.99$). In addition, the amount of sonoporated cells that was in contact with non-displacing MBs (Fig. 9.10C and D) increased four times faster than the amount of reversibly sonoporated cells (slope of 3.7 and 4.1, respectively). This strongly suggest that cells in contact with non-displacing MBs were irreversibly damaged.

On the other hand, the amount of sonoporation for cells in contact with displacing ntMBs increased twice as fast as the amount of reversibly sonoporated cells (Fig. 9.10G, slope of 2.1), while still contributing to irreversible sonoporation (Fig. 9.10E, slope of 0.57). This suggest that displacing ntMBs can both induce reversible and irreversible sonoporation. For cells in contact with displacing tMBs the amount of reversibly sonoporated cells increased proportionally (Fig. 9.10H, slope of 1.0). Further, displacing tMBs minimally contributed to irreversible sonoporation (Fig. 9.10F, slope of 0.27). This suggests that displacing tMBs mainly resulted in reversible sonoporation.

The relation between the presence of displacing and non-displacing MBs and the classification of cells was confirmed on a single cell basis, as shown in Figure 9.11 and Figure 9.5. Cells 1 and 2 were both reversibly sonoporated due to MBs displacing over their cell membranes, of which cell 1 had high PI uptake and cell 2 low uptake. Cell 1 also had non-displacing MBs in its vicinity, which might be the reason for the higher uptake o PI. Cells 3 and 4 had slow resealing pores (> 120 s) and only non-displacing MBs nearby their cell membranes.

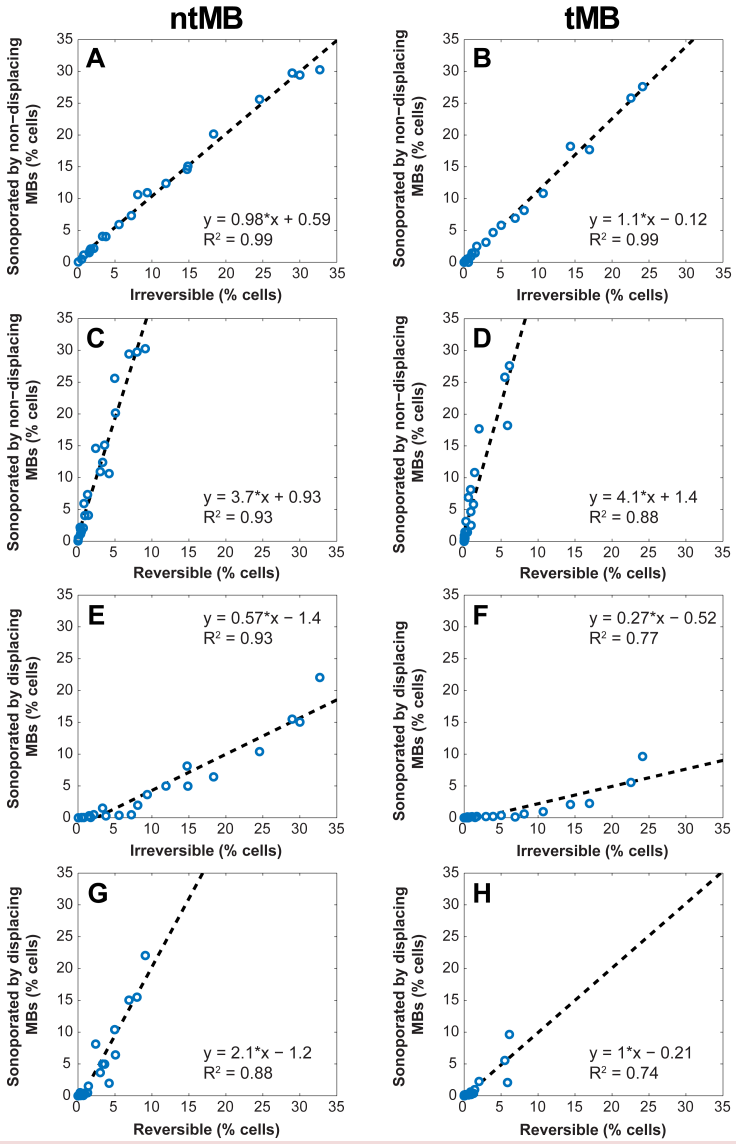

Figure 9.10. Scatter plots visualizing the relation between MB displacement and sonoporation outcome. The slope of the linear fit shows the ratio of increase between each two groups. Blue circles are the experimental data points at all 21 acoustic settings, the black dashed line the linear fit. Irreversible sonoporation is the grey data set from Fig. 6; reversible sonoporation is the sum of the red and blue data sets from Fig. 6.

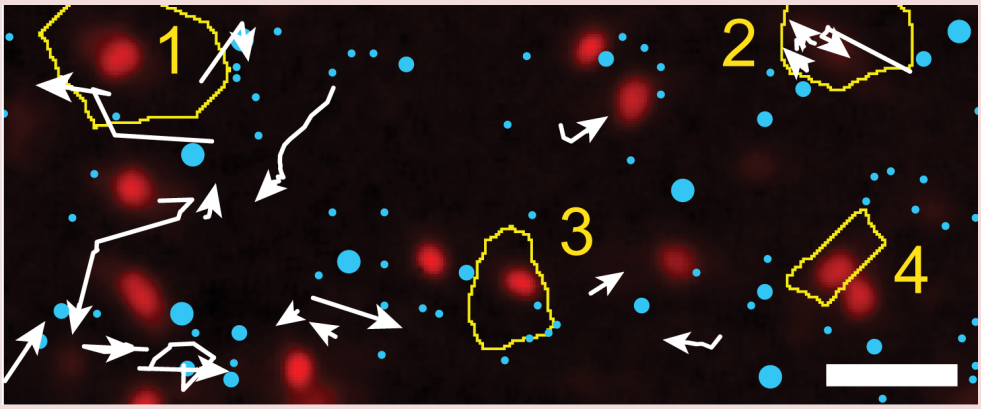

Figure 9.11. Microbubble displacement. White arrows indicate displacing ntMBs and blue filled circles indicate non-displacing ntMBs, overlaid on the same PI stained image as shown in Fig. 4G. Cells 1-4 (yellow lines) are the same ones as shown in Fig. 4. MB displacement was not correlated to the direction of US application. US settings: 500 kPa acoustic pressure, 10,000 cycles. Scale bar indicates 30 µm.

Orientation of targeted microbubbles

For all experiments concerning ntMBs, the cells were on the upper membrane of the OptiCell with the MBs floating against the cells. For the tMB experiments described so far, the cells were on the bottom membrane with the tMBs adhered on top of the cells. In addition to the comparison between ntMBs and tMBs, we also investigated the effect of the orientation of tMBs with respect to the cells and US application. We therefore placed the OptiCell containing tMBs in the same orientation as the experiments on ntMBs, so the cells were on the upper membrane with the tMBs below the cells (tMB_B). These experiments were repeated two times at 500 kPa for all investigated number of cycles with on average 3,106 (± 139) cells in the FOV.

The amount of US-induced sonoporated cells with tMB_B was higher than for the control experiments for the four settings with the smallest error bars: 1,000; 2,000; 10,000; and 50,000 cycles. Although, especially for the longer pulses, tMB_B seemed to more efficiently sonoporate cells than both tMBs and ntMBs, this was not statistically significant for most cycles. Only with 10,000 cycles were tMB_B more efficient than ntMBs (*); and only with 500 cycles were tMB_B more efficient than tMB (o) (Fig. 9.12A, $p < 0.05$).

Cell death for tMB_B was significantly higher than for the tMB_B controls after applying 2,000; 5,000; 20,000; and 50,000 cycles. In addition, cell death and the total amount of sonoporated cells were significantly different for all experimental settings. For most settings cell death of tMB_B was similar to ntMBs or tMBs, except for 1,000 cycles with ntMBs (*) and 1,000 and 2,000 cycles with tMBs (o) as shown in Figure. 9.12B. Cell death controls are not shown, since these were subtracted from cell death at the other settings to correct for natural cell death.

Cell classification based on PI uptake patterns showed similar trends for tMB_B as for ntMBs and tMBs, in terms of the amount of cells in each group. However, the cells with non-resealing pores within 120 s (Fig. 9.12C, grey) did not correlate with the amount of cell death (Fig. 9.12C, yellow), since they were significantly different for all applied settings, possibly of lower statistical power (only n = 2). As expected, displacement of tMB_B was very similar to the displacement of tMBs (Fig. 9.12D and Fig. 9.9), since the binding strength that has to be overcome to displace them is identical.

Discussion

This is the first study that directly compares ntMB and tMB-mediated sonoporation in primary endothelial cells *in vitro* using long acoustic pulses (500 – 50,000 cycles). At 1 MHz and three different acoustic pressures (150-500 kPa), we aimed to identify differences in MB behavior responsible for either viable sonoporation or cell death. The real-time observed uptake of PI upon sonoporation was fit using a previously reported diffusion model[228] and subsequently classified using PCA. Cell viability highly correlated with the four different PI uptake patterns derived from this classification. Further, displacing tMBs resulted in viably sonoporated cells, whereas non-displacing tMBs and ntMBs accounted for more cell death.

Cellular response dynamics

Four cell populations with different PI uptake profiles were found for ntMB and tMB-mediated sonoporation at each US setting. The cells that had non-resealing pores within 120 s after US application were irreversibly damaged (Fig. 9.7, grey) as this correlated well with cell death (Fig. 9.7, yellow). Further, cells having low PI uptake (Fig. 9.7, blue) and high PI uptake (Fig. 9.7, red) had pores that resealed within 120 s. Other researchers

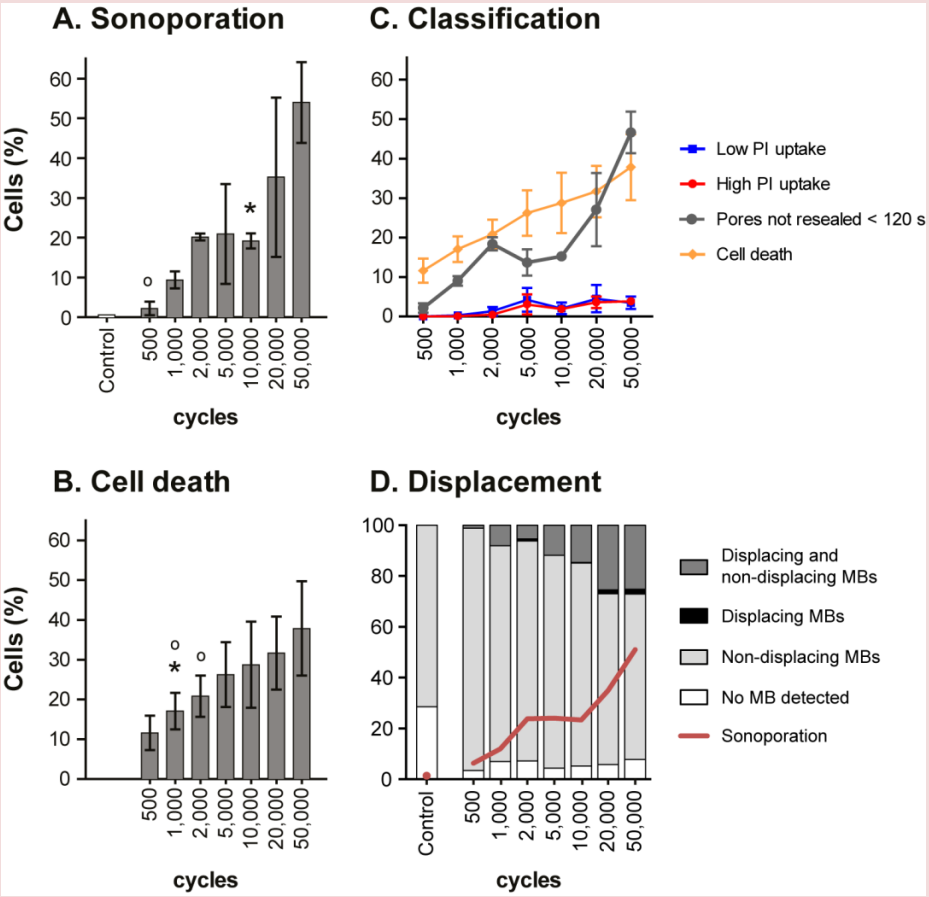

Figure 9.12. tMBs adhered below the cells (tMB_B) insonified at 500 kPa. **(A)** Mean (± SD) percentage of sonoporated cells and **(B)** cell death after insonification of tMB_B. Asterisks (*) indicate significant differences between tMB_B and ntMBs, and (o) between tMB_B and tMBs. **(C)** Classification of cells based on their pore size and pore resealing coefficient. The amount of cells with non-resealing pores within 120 s (grey) was significantly different from the amount of dead cells (yellow) for all settings. **(D)** Displacement of tMB_B. For each acoustic setting, the bar graph indicates the percentage of cells that were sonoporated by displacing MBs, non-displacing MBs, both, or when no MB could be detected. The red line shows the percentage of cells that were sonoporated.

have shown that cells remained viable when pores resealed within a few seconds up to 60 s[227,229,488]. However, these studies were not performed on human endothelial cells, but on human fibroblasts[229], bovine endothelial cell[227], and Xenopus oocytes[488]. Enhanced drug uptake up to several hours has also been reported[489,490], but cells having non-resealed pores for such long periods are not expected to be viable. We therefore believe that the route of model drug uptake in their experiments was most likely not due to pore formation, but possibly stimulated endocytosis. Our results suggest that human endothelial cells showing increasing nuclear PI signal up to 120 s were also viably sonoporated. This may imply that pores open for longer than 60 s can still result in viably sonoporated cells.

Cells that had taken up PI also showed an efflux of calcein, which is another indicator of sonoporation[228]. Next to calcein efflux, those cells also revealed lower Hoechst signals in the fluorescence images taken after US treatment than in those taken before (Fig. 9.4). Since the literature agrees upon non-competitive binding of PI and Hoechst[478,479], we believe this decrease in signal was caused by Förster resonance energy transfer (also known as FRET)[491]. The emission spectrum of Hoechst (maximum intensity at 461 nm) overlaps with the excitation spectrum of PI (491 - 495 nm); the presence of PI can therefore result in considerable quenching of the Hoechst signal[492]. Hoechst signal intensity was therefore lower in cells that had taken up PI. In addition, the amount of PI uptake was found to be related to the level of quenching; cells 1, 3, and 4 had high PI uptake (Fig. 9.4G) and Hoechst signal was almost completely quenched (Fig. 9.4F), whereas cell 2 had low PI uptake and less quenching of Hoechst signal.

Influence of oscillation and displacement of microbubbles

Quantitative assessment of the displacement of MBs revealed more PI uptake when more tMBs or ntMBs displaced (Fig. 9.9). We studied the relation between MB displacement and reversibility of sonoporation and found a clear relation between non-displacing MBs and irreversible sonoporation (Fig. 9.10A and 9.10B); an increase in sonoporation by non-displacing MBs coincides with a similar increase in irreversible sonoporation. We therefore concluded that irreversible sonoporation was mainly caused by non-displacing MBs, explained by prolonged MB oscillation at the same location on the cell membrane. The relation between displacing MBs and sonoporation is less straightforward. For ntMBs (Fig. 9.10G) the amount of cells sonoporated by displacing

ntMBs increased twice as fast as those that were reversibly sonoporated (slope of 2.1), which implies that displacing ntMBs did not only induce reversible sonoporation, but also irreversible sonoporation (Fig. 9.10E). Because longer pulses at higher acoustic pressure cause more displacement, the ntMBs can affect multiple cells or multiple displacing ntMBs can affect a single cell.

For tMBs we found an increase in reversible sonoporation that coincides with a similar increase in sonoporation caused by displacing tMBs (Fig. 9.10H). We therefore conclude that displacing tMBs mainly resulted in reversible sonoporation. The amount of irreversibly sonoporated cells by displacing tMBs is much smaller than for ntMBs (compare Fig. 9.10E and 9.10F). When tMBs detach and displace, they float away from the cells and will not contribute to more sonoporation.

Displacing tMBs resulted mainly in reversible sonoporation, whereas the much larger amount of displacing ntMBs also induced irreversible sonoporation. This may imply that reversibility is only achieved with limited displacement of MBs. Fan et al.[466,468] concluded that displacement of both ntMBs and tMBs correlated with irreversible sonoporation, while we related displacement to reversibility. This difference may be explained by larger MB displacements in their study because they used pulsed US (1.25 MHz, 60-600 kPa, PRF 10-1,000 Hz, duty cycles 0.016-20%), whereas the single US burst we used resulted in less and slower displacement for the second half of the pulse (Fig. 9.8).

In the high-speed and ultra-high-speed recordings we observed clustering of MBs. Higher pressures enhanced cluster formation, and ntMBs formed more clusters because they displaced more than tMBs. Since the amount of sonoporated cells was similar for ntMBs and tMBs (Fig. 9.3), clustering did thus not result in more sonoporation.

Mannaris and Averkiou[123] were the first to show acoustically that MBs remained oscillating during 1,000 acoustic cycles at 100 kPa. Our ultra-high-speed recordings revealed the presence and oscillation of both single MBs and MB clusters at the end of the 1,000-cycle US burst at 150 and 300 kPa, albeit that we observed more oscillating MB clusters at the end of the US pulse than single MBs. Chen et al.[493] reported contrasting observations. After 1,000 cycles their ultra-high-speed recordings only showed oscillating clusters; no single MBs were present anymore. The most likely cause

for these different findings is the high pressure (up to 1.5 MPa) they applied, which resulted in more displacement due to acoustic radiation force[437,469] and more clustering.

Sonoporation efficiency: ntMB versus tMB

The sonoporation efficiency of ntMB and tMB showed the same trend: higher pressures and more cycles resulted in more sonoporation (Fig. 9.3), as also shown by others[230,474]. However, for tMBs the amounts of sonoporated and dead cells at 300 kPa were lower than for ntMBs, which is most likely caused by MB displacement or oscillation behavior. Increasing the pressure from 150 to 300 kPa resulted in more displacing ntMBs, but the number of displacing tMBs did not increase (Fig. 9.9). In addition, the ultra-high-speed recordings showed more oscillating ntMBs for increasing pressure, while no change was observed for tMBs (Fig. 9.8). This is caused by functionalization of our tMBs with CD31 antibodies via streptavidin-biotin binding, but we did not add streptavidin nor control-antibodies to our ntMBs, as clinical ntMBs would not have this either. Functionalization of MBs alters shell properties[35] and therefore oscillation behavior[419]. Since our tMBs and ntMBs had identical lipid shells with DSPC as the main lipid, the targeting moieties would result in a higher elasticity and thus a stiffer shell of our tMBs[35]. As a consequence, higher pressures are required for tMBs to obtain the same oscillation amplitude as for ntMBs[36], which likely influences sonoporation efficiency.

The sonoporation experiments with tMBs at 500 kPa and 10,000 to 50,000 cycles showed very large error bars (Fig. 9.3C). Two of the OptiCells in which the experiments were done showed similar uptake percentages, but the amount of sonoporated cells in the third OptiCell was almost twice as high. The underlying cause for this observation is unclear; all cell layers were confluent, the total amount of cells and MB concentration was similar, as well as the average number of MBs per cell. Hence, we can only conclude that sonoporation caused by tMBs is less predictable than by ntMBs.

Our findings, that in general tMBs did not induce higher PI uptake than ntMBs, contradict other *in vitro* studies that report tMBs to be more efficient for drug delivery than ntMBs in a direct comparison. The five reported *in vitro* studies[455-459] all show that the lipid-shell tMBs are 1.1[459] to 7.7[455] fold more efficient for drug delivery than ntMBs. Four out of these five studies describe drug-loaded MBs (with paclitaxel or plasmid

DNA), the other one describes co-administration of PI[458]. A direct comparison between our study and the five reported studies is difficult, due to the differences in experimental conditions. None of these studies assessed MB-mediated drug delivery in endothelial cells. Instead, smooth muscle[456] or cancer cells were used. The study that reported the largest difference between ntMBs and tMBs, rinsed the cells to remove free MBs that had not adhered[455]. As a result, the ntMBs would almost all have been washed away, which could explain the large difference. Another study treated cancer cells in suspension[457], whereas we treated a fully confluent monolayer of endothelial cells. Two studies[457,459] used ntMBs with a different shell composition and smaller mean diameter than their tMBs, which without doubt results in differences in MB behavior[36,238,419]. In addition, one study reported that the 5.5 fold higher uptake could only be achieved with 70% confluent cells[456]. Consequently, our results are not supported by other studies, since none directly compared ntMB and tMB-mediated drug delivery in endothelial cells *in vitro*. Several studies reported more efficient drug delivery or transfection *in vivo* for tMBs than for ntMBs[460-463]. Due to blood flow, ntMBs flow by and thus have shorter contact with tissue, thereby making ntMBs less efficient. Inclusion of flow in the *in vitro* experiments is thought to result in more efficient sonoporation for tMB than for ntMB and will be subject for future studies.

Microbubble orientation

We used a different orientation of MBs relative to the cells and US direction for tMBs and ntMBs (Fig. 9.1B and Fig. 9.12). Therefore, the ntMBs could have been pushed towards the cells by the US, while the tMBs could have been pushed away from the cells. To study whether this influenced sonoporation efficiency, we performed experiments with tMBs in the same orientation as the ntMBs, which we referred to as tMB_B (tMB below cells). Because tMB_B adhered below the cells, non-adhered tMB_B would also be in contact with the cells and could have contributed to sonoporation as well. Higher amounts of non-adhered tMB_B would results in more displacing tMB_B and thus enhance sonoporation. However, since the amounts of tMB_B and tMBs in the FOV were the same (~3,100 cells), we can assume that all tMB_B had adhered and that non-adhered tMB_B did not account for the variation in PI uptake.

Sonoporation efficiency for tMB_B seemed higher than for tMBs (compare Fig. 9.3C and Fig. 9.12A), possibly caused by MBs that detached during insonification and remained in contact with the cells. In contrast, the configuration for tMBs allowed them to float away after detachment. The sonoporation efficiency, however, was not significantly different to conclude that tMB_B were more efficient than tMBs. To the best of our knowledge, no previously published studies investigated the orientation of MBs relative to the cells and US direction. Others that directly compared the effect of ntMBs and tMBs either did not mention the orientation[457,459], had the MBs on top of the cells with US applied from the MB-side[455], or had the MBs below the cells and applied US from below[456,458].

Experimental considerations

To obtain the amount of sonoporation from the nuclear PI uptake and the associated model fit, we used algorithms implemented in ImageJ and RStudio, whereas a different algorithm in Python was used to obtain sonoporation from PI uptake in the entire cell and its relation to displacing and non-displacing MBs. Although this is not ideal, we chose this approach to optimally utilize the strengths of each method: segmentation (ImageJ) and tracking of moving particles (Python). Since both methods relied heavily on correct detection of cell nuclei, we manually counted the nuclei on the Hoechst images and compared this to the outcomes of the ImageJ and Python algorithms: both detected, on average, only 6% of the nuclei incorrectly (n = 6 images). Since the errors were small, the additional analyses were expected to be comparable as well. Indeed, the segmented cell borders by Voronoi tessellation closely overlapped between the two methods. As already mentioned, sonoporation was slightly higher (2.7% on average) for the tracking method in Python, than for the more robust fitting method using RStudio. This was caused by additional detection of cytoplasmic PI uptake and by cells of which the model could not be fit ($R^2 < 0.8$) to the nuclear uptake profile.

In contrast to the paper by Fan et al.[228], we did not calculate the size of the pores, since not all parameters of our system were known. However, if we would have done this, possible multiple pores in a single cell could still have been detected as one larger pore. In addition, we only included PI uptake in the nucleus because determination of the cell borders was based on probability, whereas the nucleus could be more precisely segmented from the Hoechst images.

On average, 7.4% of sonoporated cells that were found using the tracking algorithm were classified as being sonoporated without the presence of a MB nearby (Fig. 9.9, white). Since control experiments with only MBs showed sonoporation of < 0.9% of all cells, this was not caused by spontaneous uptake of PI, but most likely due to the size of the MBs—only a few pixels in diameter—and the quality of the images. Accurately detecting ntMBs was more difficult due to the optical focus in the corresponding bright-field images; the cells were better in focus, resulting in lower discriminative power between cell structures and MBs. The error for ntMB detection was therefore higher. Manual counting of the number of MBs that was not counted by the algorithm resulted in an average of 9% more MBs per image (n = 9). This is slightly higher than the average amount of sonoporated cells without MBs nearby, because MBs that were in contact with non-sonoporated cells could have also been missed.

Limitations of this study

A limitation to our study is the use of CD31 as the ligand on our tMBs, because this is a constitutively expressed adhesion molecule on endothelial cells[494]. It can therefore not be used *in vivo*, since CD31-tMBs would adhere to the entire vasculature. Also, the MBs circulate within the vasculature *in vivo*, while we performed our studies under static conditions. Flow is expected to have an influence on the sonoporation efficiency, as ntMBs will be taken away by the flow, while tMBs will still adhere to the cells under flow[495]. A higher sonoporation efficiency for tMBs is therefore expected and shown[460,461,463] under flow and *in vivo* conditions.

Therapeutic applications

Based on our results, ntMBs exposed to an acoustic pressure of 500 kPa and a pulse length of 1,000 cycles would be most beneficial for drug delivery. These settings resulted in relatively high amounts of viably sonoporated cells (Fig. 9.7, blue) and minimal cell death (Fig. 9.7, grey/yellow). For drug delivery, high drug uptake would be most beneficial since higher doses of therapeutics can be delivered (Fig. 9.7, red). Nevertheless, we always observed equal or lower red uptake patterns in comparison to the blue uptake patterns of lower PI uptake, implying there is not one US setting that favors one over the other. On the other hand, for therapeutic applications where high cell death is desired, e.g. cancer therapies, high pressures and long pulses should be

applied (e.g., 500 kPa and 50,000 cycles). Both tMBs and ntMBs were shown to effectively kill cells, but ntMBs were more efficient. For therapies requiring sonoporation of specific cells under flow, ntMBs would need to be replaced with tMBs. ntMBs could sonoporate cells as they move along the cells, or when pressed against a thrombus occluding a blood vessel, as in the case of sonothrombolysis[37,496]. On the other hand, for locally enhanced drug delivery in tumors tMBs are required, since the MBs need to be close to the cell membrane[227,497]. Hence, the choice of using either ntMBs or tMBs highly depends on the desired therapeutic application.

Conclusion

In depth sonoporation studies on the effect of longer acoustic pulses at 1 MHz at different acoustic pressures revealed a clear relation between sonoporation efficiency and MB behavior. Different patterns of PI uptake derived from the diffusion model and subsequent classification using PCA highly correlated with cell viability. Limited displacement of the MBs enhanced drug delivery and preserved cell viability, while non-displacing MBs were the main contributor to cell death. Longer pulses resulted in more dead cells, but did not result in significant increase in viably sonoporated cells. In addition, the effect of the same type of ntMBs and tMBs to sonoporate endothelial cells was similar *in vitro* under static conditions.

Acknowledgements

The authors thank Robert Beurskens, Frits Mastik, Michiel Manten, and Geert Springeling from the department of Biomedical Engineering, Thoraxcenter, Erasmus MC, the Netherlands for technical assistance. This work is financially supported by NanoNextNL, a micro- and nanotechnology consortium of the Government of the Netherlands and 130 partners and by the Dutch Technology Foundation STW (Veni-project 13669), which is part of the Netherlands Organization for Scientific Research (NWO), and which is partly funded by the Ministry of Economic Affairs.

"What day is it?" asked Pooh.

"It's today," squeaked Piglet.

"My favourite day," said Pooh.

- Winnie-the-Pooh
A.A. Milne

10

Opening of endothelial cell-cell contacts due to sonoporation

Inés Beekers, Merel Vegter, Kirby R. Lattwein, Frits Mastik, Robert Beurskens, Antonius F.W. van der Steen, Nico de Jong, Martin D. Verweij, and Klazina Kooiman

Based on:
Journal of Controlled Release, vol. 322, pp. 426-438, 2020

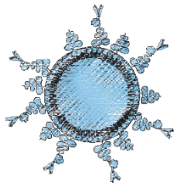

Abstract

Ultrasound insonification of microbubbles can locally increase vascular permeability to enhance drug delivery. To control and optimize the therapeutic potential, we need to better understand the underlying biological mechanisms of the drug delivery pathways. The aim of this *in vitro* study was to elucidate the microbubble-endothelial cell interaction using the Brandaris 128 ultra-high-speed camera (up to 25 Mfps) coupled to a custom-built Nikon confocal microscope, to visualize both microbubble oscillation and the cellular response. Sonoporation and opening of cell-cell contacts by single αVβ3-targeted microbubbles (n = 152) was monitored up to 4 min after ultrasound insonification (2 MHz, 100–400 kPa, 10 cycles). Sonoporation occurred when microbubble excursion amplitudes exceeded 0.7 μm. Quantification of the influx of the fluorescent model drug propidium iodide upon sonoporation showed that the size of the created pore increased for larger microbubble excursion amplitudes. Microbubble-mediated opening of cell-cell contacts occurred as a cellular response upon sonoporation and did not correlate with the microbubble excursion amplitude itself. The initial integrity of the cell-cell contacts affected the susceptibly to drug delivery, since cell-cell contacts opened more often when cells were only partially attached to their neighbors (48%) than when fully attached (14%). The drug delivery outcomes were independent of nonlinear microbubble behavior, microbubble location, and cell size. In conclusion, by studying the microbubble–cell interaction at nanosecond and nanometer resolution the relationship between drug delivery pathways and their underlying mechanisms was further unraveled. These novel insights will aid the development of safe and efficient microbubble-mediated drug delivery.

Introduction

Life-threatening diseased tissue often lies beyond the vasculature. This means that intravenously administered drugs need to extravasate from the vasculature to reach their intracellular and extravascular targets. The endothelial cells that line the vessel wall are barriers that severely limit local and effective drug delivery necessary for successful treatment. To overcome the challenges these barriers present, drug delivery can be locally enhanced using lipid-coated gas microbubbles (1–10 μm) in combination with ultrasound[36,220]. These microbubbles are widely used in the clinic to improve contrast in diagnostic ultrasound imaging. When ultrasound is applied, microbubbles will oscillate, which can permeabilize cell membranes (sonoporation), open cell-cell contacts, and stimulate endocytosis[36,220,307]. However, the underlying physical and biological mechanisms of the microbubble–cell interaction need to be elucidated. If we can control and predict the different drug delivery pathways, microbubble-mediated drug delivery can be tuned to the requirements of a therapeutic application.

To unravel the underlying mechanisms of the microbubble–cell interaction, one needs to know which microbubble behavior is responsible for which cellular response. Therefore, we need to image both the microbubble oscillation at nanosecond temporal resolution and the ensuing detailed cellular response at nanometer spatial resolution. Until now, concurrent visualization of microbubble oscillation and endothelial cell response has only been possible using an ultra-high-speed camera coupled to a widefield microscope[224,225,226,227]. In these studies, focusing on sonoporation, the microbubble behavior was known but the cellular response was imaged at low resolution and sensitivity. Helfield et al.[224] performed an additional experiment in which they only used confocal microscopy to show sonoporation and opening of cell-cell contacts in a single example. Confocal microscopy has also been used by others to visualize the cellular response at high spatial resolution and detector sensitivity. They investigated sonoporation[229,230,231,235,501], membrane perforation and recovery dynamics[229], endocytosis[230], sonoprinting[501,234], lipoplex delivery[231], and cytoskeleton reorganization[235]. However, the studies using confocal microscopy lacked information on the microbubble oscillation behavior that was responsible for the cellular effect. Since single microbubble response to ultrasound is variable[237,239] even for known acoustic pressures, the underlying mechanisms of the microbubble–cell interaction could not be fully resolved.

Sonoporation has been investigated *in vitro* and in real-time, demonstrating the capability of an oscillating microbubble to create a pore in the endothelial cell membrane[224,226,227,245,502]. The transient behavior of pore formation and recovery dynamics have been studied with live cell microscopy[228,229]. Reversible sonoporation can temporarily enhance intracellular drug delivery without cell death. However, when cell membrane integrity is not restored after pore formation, sonoporation is irreversible and will eventually lead to cell death. Pore resealing times from a few seconds up to 120 s have been reported[229,245,488,502]. Fan et al.[228] showed that upon sonoporation, the amount of fluorescent marker propidium iodide (PI) uptake can be related to the size of the pore and its resealing time. This has been used to quantify the pore dynamics of kidney[228] and endothelial cells[245,466]. Nevertheless, it remained unknown how microbubble oscillation behavior correlates with the severity of sonoporation, in terms of the pore size and its resealing characteristics. When the microbubble excursion amplitude required for sonoporation was investigated, the cellular response could only be studied at low sensitivity and spatial resolution using widefield microscopy[224,226].

Opening of cell-cell contacts has been previously observed using live cell microscopy within minutes after ultrasound insonification of a non-targeted microbubble for a single example[224]. The opened cell-cell contacts remained open for tens of minutes, suggesting a prolonged enhanced drug delivery effect of this pathway. In addition, extravasation of drug compounds from the vasculature has been shown, for instance to overcome the blood-brain barrier[503,504]. It is hypothesized that this cellular response of opening the intercellular junctions is caused by the shear stress from the oscillating microbubbles, the microbubble forces on the cytoskeleton of the cell, and/or the changes in cell morphology due to sonoporation[221]. However, there is still a lack of understanding on how microbubble oscillation behavior causes the opening of cell-cell contacts and whether this is an independent drug delivery pathway or induced upon sonoporation[221].

In this study we aimed to elucidate the missing link between microbubble oscillation behavior and the occurrence of sonoporation and opening of cell-cell contacts in cultured endothelial cells. Microbubbles were targeted to the integrin $\alpha_v\beta_3$ (alpha-v-beta-3), also known as CD51/61, expressed by endothelial cells during angiogenesis[505], which is clinically relevant for cancer and atherosclerosis therapy. Ultrasound at a 2 MHz frequency was applied, commonly used in transthoracic ultrasound[409]. A unique optical imaging

system was used consisting of the Brandaris 128 ultra-high-speed camera, to record the microbubble oscillation, coupled to a custom-built Nikon A1R+ confocal microscope, to visualize the cellular response. The cellular response upon insonification of a single targeted microbubble was studied by monitoring uptake of the model drug PI and by assessing opening of cell-cell contacts between adjacent cells. As a result, the microbubble–cell interaction was studied at both nanosecond and nanometer resolution (17 Mfps and 200 nm, respectively).

Materials and Methods

Endothelial cell culture

Primary human umbilical vein endothelial cells (HUVECs) from pooled donors (C2519A, LOT 437550, Lonza, Verviers, Belgium) were cultured in MV2 medium (C22121, PromoCell, Heidelberg, Germany), supplemented with 1% Penicillin-Streptomycin (15140122, Gibco, Thermo Fisher Scientific, Waltham, MA, USA). The HUVECs were grown (at 37 °C and 5% CO_2) in a humidified incubator to full confluency in T75 flasks. Next, they were detached using Accutase solution (A6964, Sigma-Aldrich, St. Louis, MO, USA) and replated on the bottom membrane of a CLINIcell (CLINIcell25–50-T, REF 00106, MABIO, Tourcoing, France) in 12 mL MV2. The CLINIcell is an acoustic compatible cell culture chamber with two gas permeable parallel membranes (thickness 50 µm, surface area 25 cm^2)[506]. The CLINIcells were incubated (at 37 °C and 5% CO_2) for two days to achieve a fully confluent cell monolayer. The HUVECs used in the experiments were between passage numbers 4 and 6.

Targeted microbubble preparation

For lipid-coated microbubbles with a C_4F_{10} gas core were produced in-house by probe sonication for 1 min, as previously described[241,314,419]. The coating consisted of 1,2-distearoyl-sn-glycero-3-phosphocholine (DSPC; 84.8 mol%; P6517, Sigma-Aldrich), polyoxyethylene-40-stearate (PEG-40 stearate; 8.2 mol%; P3440, Sigma-Aldrich), 1,2-distearoylsn-glycero-3-phosphoethanolamine-N-[carboxy(polyethylene glycol)-2000] (DSPE-PEG(2000); 5.9 mol%; 880125P, Avanti Polar Lipids, Alabaster, AL, USA), and

1,2-distearoyl-sn-glycero-3-phosphoethanolamine-N-[biotinyl(polyethylene glycol)-2000] (DSPE-PEG(2000)-biotin; 1.1 mol%; 880129C, Avanti Polar Lipids). Finally, to fluorescently label the microbubble coating, the lipid dye DiD (1,1'-dioctadecyl-3,3,3',3'-tetramethylindodicarbocyanine perchlorate; D307, Thermo Fisher Scientific) was added before sonication. The microbubbles were targeted to the $\alpha_v\beta_3$ integrin using biotinstreptavidin bridging, as previously described by others[447,454,475,507-509] with the exception of the type of ligand. Briefly, after washing three times by centrifugation (400*g*, 1 min) using PBS saturated with C_4F_{10}, the microbubble concentration was determined with a Coulter Counter Multisizer 3 (n = 3) (20 µm aperture tube, Beckman Coulter, Mijdrecht, the Netherlands). Next, 6×10^8 microbubbles were incubated on ice for 30 min with 60 µg of streptavidin (2 mg/mL stock concentration in PBS, S4762, Sigma-Aldrich) and washed. These streptavidin-conjugated microbubbles were incubated on ice for 30 min with 6 µg of biotinylated anti-human CD51/61 antibody (304412, BioLegend, San Diego, CA, USA), followed by a final washing step.

Experimental set-up

To study the microbubble-cell interaction, a unique optical imaging system was used consisting of the Brandaris 128 ultra-high-speed camera (up to 25 million frames per second, Mfps)[222] coupled to a custom-built Nikon A1R+ confocal microscope (Fig. 10.1A)[273]. With this system high temporal and spatial resolutions can be achieved, required to resolve the microbubble oscillation and cellular response, as explained in more detail by Beekers et al.[273]. For simultaneous imaging and ultrasound insonification, the CLINIcell was inserted into a 37 °C water tank positioned beneath the microscope. A single element focused transducer (a 2.25 MHz center frequency used at 2 MHz; 76.2 mm focal length; −6 dB beam width of 3 mm at 2 MHz; V305; Panametrics-NDT, Olympus, Waltham, MA, USA) was mounted in the water tank at a 45° angle, after having been calibrated using a needle hydrophone. The ultrasound and optical foci were aligned such that the cells in the CLINIcell could be both imaged and insonified (Fig. 1A). A single 2 MHz and 10-cycle burst was generated by an arbitrary waveform generator (33220A, Agilent, Palo Alto, CA, USA). A broadband amplifier (ENI A-500, Electronics & Innovation, Rochester, NY, USA) was used to obtain peak negative pressures (PNP) of 100, 200, 250, 300, and 400 kPa at the focus.

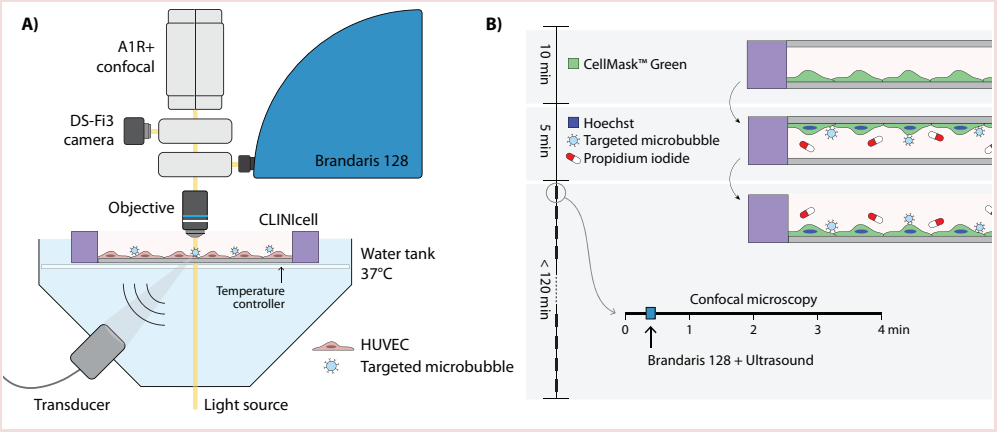

Figure 10.1. Schematic representation of the experimental procedure (not drawn to scale). (A) Experimental setup to insonify a CLINIcell under a 45° angle. The optical imaging system combines an A1R+ confocal scan head (Nikon Instruments), with a DS-Fi3 colour camera (Nikon Instruments) for widefield imaging, and the Brandaris 128 ultra-high-speed camera. (B) Timeline starting with the incubation of HUVECs with fluorescent dyes and targeted microbubbles, followed by time-lapse imaging with the combined optical imaging system.

Experimental protocol

To The HUVECs were stained with fluorescent dyes for live confocal microscopy imaging (Fig. 10.1B). They were incubated with CellMask™ Green Plasma Membrane Stain (4 µg/mL final concentration; C37608; Thermo Fisher Scientific) for 10 min inside the cell incubator to stain the cell membranes. Next, Hoechst 33342 (5 µg/mL final concentration; H3570, Thermo Fisher Scientific) was added to stain the cell nuclei and PI (25 µg/mL final concentration; P4864, Sigma-Aldrich) was added as a marker for sonoporation. The cell membrane of viable cells is impermeable for PI. When the cell membrane is compromised, PI enters the cell, binds to DNA and RNA, and becomes fluorescent[465]. Therefore, PI is often used as a marker for sonoporation to evaluate membrane perforation[54,224,227,228,510]. Additionally, CD51/61 targeted microbubbles (2×10^5 microbubbles/mL final concentration) were added and the CLINIcell was incubated during 5 min inside the cell incubator, while turned upside down to allow the targeted microbubbles to float towards the cells to achieve binding (Fig. 10.1B). The CLINIcell was then turned upright again such that only bound targeted microbubbles remained in

the focal plane of the cells. Finally, the top membrane without cells was cut from the CLINIcell, making it feasible to image with an objective with a working distance smaller than the 5 mm spacing between the CLINIcell membranes. The same incubation timeline was used for control CLINIcells without microbubbles.

To monitor the cellular response with confocal microscopy, imaging was performed with the following four channels: (1) Hoechst excited at 405 nm, detected at 450/50 nm (center wavelength/bandwidth), (2) CellMask Green excited at 488 nm, detected at 525/50 nm, (3) PI excited at 561 nm, detected at 595/50 nm, and (4) DiD excited at 640 nm, detected at 700/70 nm. Channel 1 and 4 were excited and detected simultaneously because there is no spectral overlap between Hoechst and DiD. Using a 100× water dipping objective (CFI Plan 100XC W, 2.5 mm working distance, Nikon Instruments), a field of view (FOV) of 74.2 × 74.2 µm (256 × 256 pixels) was scanned at 0.65 frames per second (fps). At each location, time-lapse imaging was performed for 4 min in total (Fig. 10.1B). This 100× objective has a high numerical aperture of 1.10; therefore, we achieve a lateral resolution up to 200 nm and an axial resolution up to 600 nm[325]. To visualize the initial cellular state, confocal microscopy time-lapse imaging started before ultrasound. Within the first minute, the light path was automatically switched from the confocal scanning head to the Brandaris 128 ultra-high-speed camera. The microbubble oscillation was then recorded at approximately 17 Mfps during ultrasound insonification. Once this recording was completed, the light path was switched back towards the confocal scanning head to visualize the cellular response. Since insonification occurred within the first minute, the cellular response upon microbubble vibration was monitored for at least 3 min (Fig. 10.1B).

The area to be imaged was chosen based on the following inclusion criteria: (i) the FOV showed fully confluent cells, such that there were no empty spaces in which an extra cell could have grown and all cells were at least partially attached to neighboring cells; (ii) there was a single targeted microbubble in the FOV; (iii) this targeted microbubble was located on a cell that was completely in the FOV; (iv) this cell had a single nucleus; and (v) this nucleus did not overlap with that of any neighboring cells. Per CLINIcell, a maximum of 15 locations uniformly distributed and spaced by at least 1 cm to avoid overlapping insonification were imaged within 120 min. Additional CLINIcells were used for two types of control experiments: (i) sham, i.e. without microbubbles or ultrasound; and (ii) ultrasound only, i.e. without microbubbles.

Analysis of microbubble oscillation

Microbubble oscillation recorded by the Brandaris 128 ultra-high-speed camera was quantified using custom-designed image analysis software to determine the change in radius as a function of time[243]. The initial radius (R_0) was determined from the first 10 frames without ultrasound. Microbubble excursion amplitude was defined as the difference between the maximum radius (R_{max}) and R_0. The excursion amplitude threshold for sonoporation was determined by linear discriminant analysis and defined as the average over the full microbubble size range[224].

Nonlinear microbubble behavior was studied by assessing the harmonic response. To do so, the frequency spectrum of the radius-time curve was determined using a Fast Fourier Transformation (FFT). Amplitudes were determined within a ±300 kHz bandwidth centered at the subharmonic (1 MHz) and second harmonic (4 MHz) frequencies. The noise levels were defined as the mean amplitude within those bandwidths from the FFT of the radius-time curve before and after oscillation. When the maximum amplitude of the FFT from the radius-time curve during oscillation was at least 6 dB above the mean noise level of all recordings, a microbubble was classified as responsive[238,247].

Finally, the asymmetry of microbubble oscillation was investigated. This was quantified by the amount of expansion (E) relative to the amount of compression (C). As previously done by others[56,247,419,429,510], the E/C ratio was defined as $E/C = (R_{max} - R_0) / (R_0 - R_{min})$. Compression-only behavior is defined by an $E/C < 0.5$, symmetric oscillation ranges from $0.5 \leq E/C \leq 2$, and expansion-only behavior as an $E/C > 2$.

Analysis of confocal time-lapse images

The image analysis aimed at studying the microbubble-mediated drug delivery pathways induced in the "cell of interest", i.e. the cell with a single bound targeted microbubble, which from now on will be referred to as *the cell*. From the time-lapse confocal microscopy before insonification, the cell was classified based on the initial state of its contact with adjacent cells. When the cell edge was fully adjacent to the neighboring cells, it was classified as having *full junctions*, and when partially adjacent it was classified as having *partial junctions*. For the controls without ultrasound, the initial cell state was

determined from the first 30 s of time-lapse confocal microscopy. After ultrasound, the cellular response was evaluated by studying two different drug delivery pathways. Sonoporation was assessed based on PI uptake within the cell as described in detail below. Opening of cell-cell contacts was assessed by changes in the cell border integrity to adjacent cells based on CellMask. When a gap, or gaps, formed between the cell and its neighbor(s), the cell was classified as *retracting*. Manual classification was performed by two individual users (M.V. and I.B.) for alternating ultrasound settings and experiment days.

To determine the surface area of the cell and the microbubble location, the cell was delineated and the microbubble location was registered. The delineation and registration were performed manually using a custom-built MATLAB (The Mathworks Inc., Natick, MA, USA) routine. After cell delineation, another MATLAB routine was used to automatically segment the corresponding nucleus based on the Hoechst images. The microbubble location was quantified as the distance from the microbubble to the closest cell edge or, alternatively, to the center of the nucleus. The 4 min confocal microscopy time-lapse recording was split between before and after insonification by finding the period of time when the light path was switched towards the Brandaris 128 camera. The resulting sudden loss of CellMask signal in the confocal time-lapse recording was automatically detected using MATLAB. The first confocal frame after ultrasound was defined as $t = 0$.

During time-lapse imaging slight vertical displacements of the CLINIcell can occur within the water tank, caused by, for instance, thermal expansion of the heating element. These small displacements changed the imaging plane, and although the cell was still in the FOV, the focus drift could alter the detected fluorescent intensity. Therefore, the PI intensity in a sonoporated cell can appear to fluctuate. To correct for PI intensity variations caused by focus drift, the CellMask fluorescent intensity was used as a reference. Although CellMask stains the membrane while PI is present in the cytoplasm, it is a valid reference since endothelial cells are very thin, with a mean height of 0.9 µm at the periphery and up to 1.6 µm at the nucleus[511]. Hence, when the membrane is in focus, the cytoplasm is also within the same focal plane (600 nm). For each confocal time-lapse recording, a correction factor was determined as the ratio between the time-dependent CellMask signal and its initial value, both within the delineated cell. Next, the PI intensity detected upon sonoporation was corrected by this correction factor.

Analysis of PI uptake profiles

Upon sonoporation, the size of the pore created in the cellular membrane is closely related to the amount of PI uptake. Fan et al.[228] mathematically described this by

$$F(t) = \frac{\alpha \pi D C_0 r_0}{\beta}\left(1 - e^{-\beta t}\right) \tag{10.1}$$

The amount of fluorescent intensity $F(t)$ detected in a cell as a function of time is related to the initial pore radius (r_0), for a known diffusion coefficient of the PI fluorescent molecule (D), extracellular PI concentration (C_0), and imaging system dependent calibration coefficient (α). The pore size coefficient ($\alpha\pi DC_0r_0$) is a measure for the initial pore size, defined by the initial slope of the PI uptake profile and independent of cell size. The stabilization of the fluorescent intensity is quantified by the pore resealing coefficient (β). Since PI molecules bind to both RNA and DNA in the cell cytoplasm and nucleus[465], we were interested in the amount of PI fluorescence within the delineated cell area. The fluorescent intensity $F(t)$ was defined as the sum over the pixels within the cell area after ultrasound minus the mean before ultrasound. Thereby, we corrected for any initial background noise signal (the mean 12-bit pixel intensity, ranging from 0 to 4095, before ultrasound was 150 and increased by an order of magnitude upon sonoporation).

Since the light path towards the confocal microscope was temporarily intercepted during insonification, PI uptake could already have started before t = 0, i.e. before the confocal light path was restored. In other words, $F(0)$ might not be zero. Therefore, Eq. 10.1 was adapted such that PI uptake started at $t = t_0$ and $F(t_0) = 0$. This changes Eq. 10.1 into

$$F(t) = \frac{\alpha \pi D C_0 r_0}{\beta}\left(1 - e^{-\beta (t - t_0)}\right) \tag{10.2}$$

Confocal time-lapse imaging was restored within ~2 s after ultrasound insonification, hence t_0 ranged from −2 to 0 s. The influx of PI upon pore formation was monitored as a function of time and the determined $F(t)$ was fit to Eq. 10.2 using a non-linear least squares approach in MATLAB to determine the pore size coefficient ($\alpha\pi DC_0r_0$), the pore resealing coefficient (β), and the starting time of pore formation (t_0).

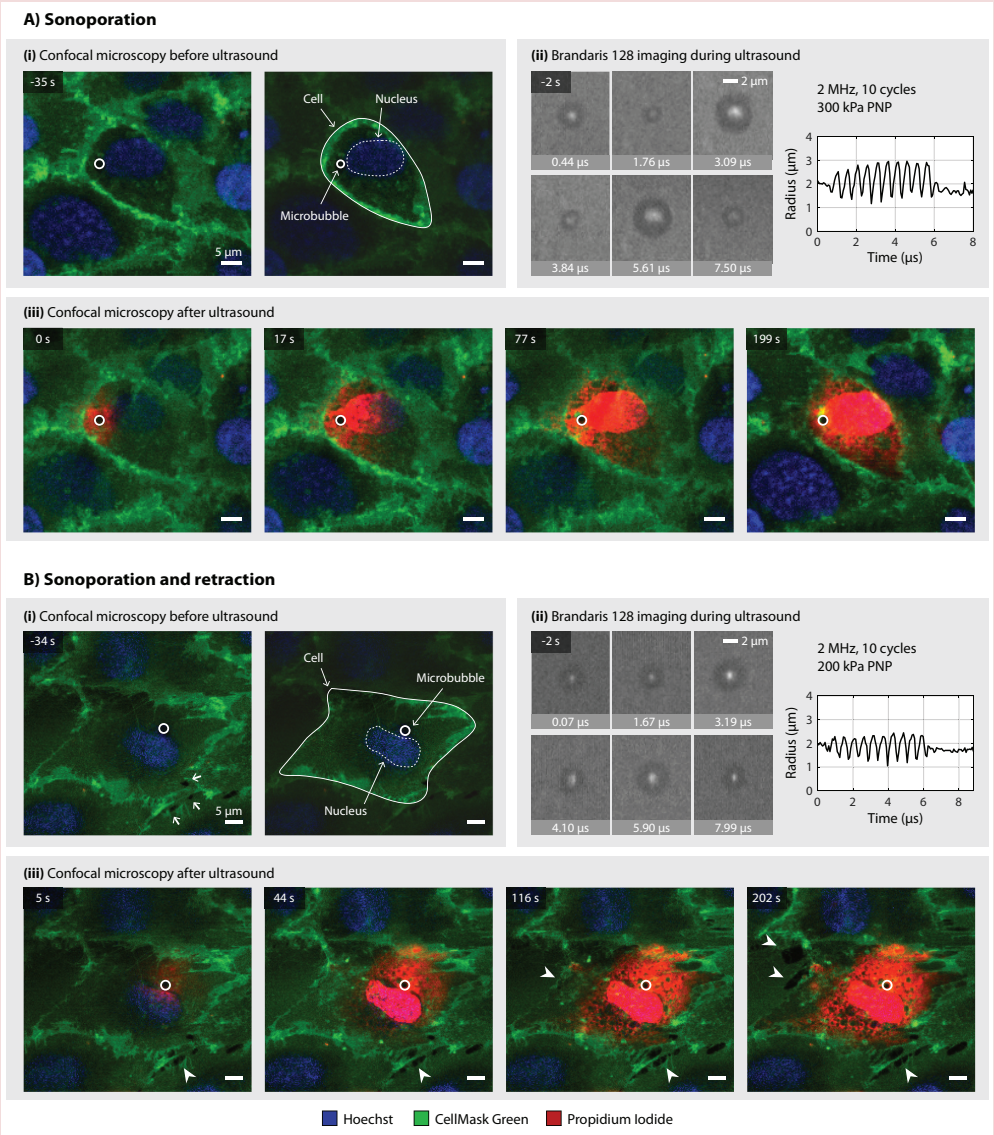

Figure 10.2. Cellular response upon ultrasound insonification of a targeted microbubble imaged with combined confocal microscopy and Brandaris 128 ultra-high-speed imaging. Selected frames are shown of (i) the initial cellular state with cell delineation and segmentation, (ii) the Brandaris 128 recording with the determined microbubble radius as a function of time, and (iii) of the cellular response. (A) Sonoporation of a cell that initially had full junctions and remained intact. (B) Sonoporation and retraction of a cell that initially had partial junctions. Partial junctions are indicated by the arrows in (i), and retraction is indicated by the arrowheads in (iii).

The time t_{90} at which 90% of the asymptotic value, $F(\infty) = \alpha\pi DC_0r_0/\beta$, was reached is

$$t_{90} = \frac{-\ln(1-0.9)}{\beta} + t_0 = \frac{2.30}{\beta} + t_0 \tag{10.3}$$

When t_{90} < 120 s it means PI uptake stabilizes, presumably caused by pore resealing[245]. However, in the case of high PI uptake, the detected fluorescent intensity can also stabilize due to image saturation or DNA/RNA saturation. Although more PI might be entering the cell, this increase can no longer be detected when the pixels are already saturated (i.e. when the 12-bit pixels are at their maximum value of 4095) or when there is no free DNA or RNA left for PI to bind to. In this study, the imaging settings were chosen such that high PI uptake results in image saturation before DNA/RNA saturation. The optimal settings were determined such that the pixels in the nucleus were image saturated when adding 0.1% Triton X-100 (X100, Sigma-Aldrich), which causes non-resealing membrane disruptions leading to DNA/RNA saturation. By doing so, we could easily identify when the fluorescent intensity of PI stabilized by image saturation, since pixels reached their maximum 4095 value, and we avoided the otherwise indiscernible DNA/RNA saturation. Image saturation starts in the cell nucleus, since there the fluorescent intensity is highest because there is more DNA for PI to bind to. Therefore, when 90% of the pixels in the segmented nucleus reached the 12-bit value, the cell was classified as saturated. Based on the pore resealing coefficient and signal saturation, the PI uptake curves were classified in the following three categories: (i) *resealing* < 120 s, i.e. when PI uptake stabilized with t_{90} < 120 s without saturation; (ii) *non-resealing*, i.e. when PI uptake did not stabilize within 120 s (i.e. t_{90}>120 s); and (iii) *saturated*, i.e. when PI uptake stabilized with t_{90} < 120 s due to image saturation.

Statistical analyses

The occurrence of a cellular pathway was presented in relative frequencies (%). This categorical data was tested for significant differences among groups using a χ^2 test. Quantitative data were assumed to be not normally distributed, and therefore presented in median and interquartile ranges and tested for significance using the Mann-Whitney U test. Statistically significant differences were indicated in the graphs with asterisks by

using * for $p < .05$, ** for $p < .01$, and *** for $p < .001$. A Spearman's rank-order correlation was performed to determine the relationship between the microbubble excursion amplitude and the pore size coefficient. All statistical analyses were performed using MATLAB.

Results

Drug delivery pathways

We evaluated the cellular response of 152 cells to a single targeted microbubble upon ultrasound insonification, in 21 different CLINIcells. Additionally, the response of 44 cells was monitored without microbubbles to assess the effect of ultrasound only experiments in four CLINIcells. To control for the experimental procedure, we also evaluated the response of 32 cells during sham experiments in three CLINIcells.

Table 10.1. Occurrence of cellular effects for sham (i.e. control without microbubbles and ultrasound), ultrasound only, and upon treatment with ultrasound and a targeted microbubble. Values reported as percentage (%) of the total amount of cells evaluated for each setting.

	Sham	**Ultrasound only**					**Ultrasound and targeted microbubble**				
Cellular Response (%)	0 kPa n=32	100 kPa n=8	200 kPa n=8	250 kPa n=9	300 kPa n=9	400 kPa n=10	100 kPa n=18	200 kPa n=43	250 kPa n=47	300 kPa n=31	400 kPa n=13
No effect	93.8	100	87.5	88.9	100	90	83.3	62.8	23.4	32.3	0
Retraction	6.3	0	12.5	11.1	0	10	16.7	2.3	21.3	3.2	0
Sonoporation	0	0	0	0	0	0	0	27.9	10.6	41.9	61.5
Sonoporation and retraction	0	0	0	0	0	0	0	7.0	44.7	22.6	38.5

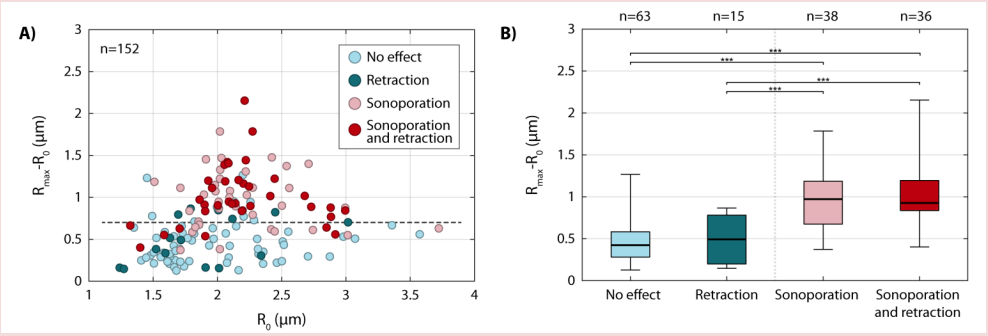

Figure 10.3. Microbubble excursion amplitude (R_{max}-R_0) inducing no cellular effect (light blue), retraction (dark blue), sonoporation (pink), or both sonoporation and retraction (red). (A) R_{max}-R_0 as a function of the initial microbubble radius (R_0) for each cellular response. The dashed line indicates the 0.7 μm threshold for sonoporation. (B) Median and interquartile range of excursion amplitude for each cellular response. The whiskers range from the minimum to maximum value and statistical significance was indicated with ***p < .001.

Four distinct cellular responses were observed: no effect, retraction, sonoporation, or sonoporation and retraction. A typical example of a sonoporated cell is shown in Fig. 10.2A, where selected frames of confocal microscopy and Brandaris 128 imaging are depicted. The corresponding confocal microscopy recording is shown in Video 1. Before ultrasound, in Fig. 10.2A(i) a single microbubble (R_0 = 2.00 μm) was located next to the nucleus, no PI was observed in the cell, and the cell-cell contacts were fully adjacent to the neighboring cells. During ultrasound, the microbubble excursion amplitude was determined from the Brandaris 128 recording to be R_{max} - R_0 = 0.95 μm (Fig. 10.2A(ii)). After ultrasound, PI uptake was observed at the location of the microbubble and spread throughout the cell over time, meanwhile the cell-cell contacts remained intact (no retraction), as shown in Fig. 10.2A(iii). In Fig. 10.2B, a typical example of sonoporation and retraction induced by the oscillating microbubble is shown. The corresponding confocal microscopy recording is shown in Video 2. Before ultrasound, there was no PI observed in the cell and the single microbubble (R_0 = 1.91 μm) was located next to the nucleus (Fig. 10.2B(i)). The white arrows show the initial cell-cell contacts that were classified as partial junctions. During ultrasound, the microbubble excursion amplitude was R_{max}- R_0 = 0.54 μm, as shown in Fig. 10.2B(ii). After ultrasound (Fig. 10.2B(iii)), PI uptake was observed locally around the microbubble and then diffused throughout the

cell. After 5 s the cell had already started to retract (white arrowheads in Fig. 10.2B(iii)). Retraction became more severe over the following 3 min. After 202 s, retraction was even observed on the other side of the cell, although it was fully adjacent at that location before ultrasound. In both examples, the PI intensity was brighter in the nucleus than in the cytoplasm, since there is more DNA for PI to bind to in the nucleus.

The occurrence of the four different cellular responses is reported in Table 10.1. The sham and ultrasound only experiments never induced sonoporation. The vast majority (93.4%) of these cells showed no cellular effect at all, independent of acoustic pressure. Retraction was only observed in 6.6% of all cells treated without microbubbles (5 out of 76 cells for both sham and ultrasound only). When treatment consisted of ultrasound insonification of targeted microbubbles, pressure dependence was observed. At 100 kPa PNP, there was no sonoporation induced and still only a small subgroup (3 out of 18 cells) showed retraction. However, for higher pressures the amount of sonoporated cells increased. At 400 kPa PNP, an oscillating microbubble always induced sonoporation. There was no clear correlation between retraction and acoustic pressure.

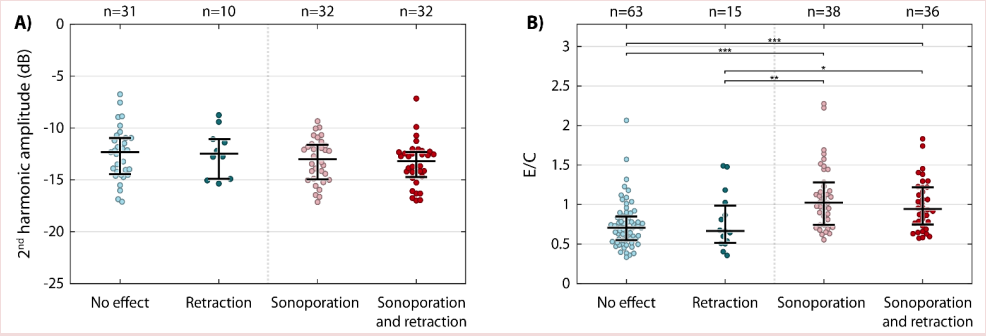

Figure 10.4. Nonlinear microbubble oscillation behavior. (A) Second harmonic amplitude normalized to the fundamental for each cellular response. (B) Asymmetry of microbubble oscillation quantified as the ratio of expansion over compression (E/C) for each cellular response. The medians and interquartile ranges are overlaid. Statistical significance is indicated with *p < .05, **p < .01, and ***p < .001.

Microbubble oscillation behavior

The microbubble studied had a mean R_0 of 2.1 µm, ranging from 1.2 µm to 3.7 µm. Insonifying these microbubbles from 100 kPa to 400 kPa PNP resulted in excursion amplitudes ranging from 0.1 µm to 2.2 µm (Fig. 10.3A; see Supplementary Fig. 10.1 for a separate excursion amplitude graph for each studied PNP). The highest excursion amplitudes were observed at R_0 of 2.2 µm and corresponded to the expected resonance size for DSPC-based microbubbles at 2 MHz[419]. All microbubbles were still targeted to the cell after insonification, and the median shrinkage (with IQR, interquartile range, between brackets) of the microbubbles was 92.1% (87.2%–97.3%), defined as the ratio between the final and initial radius. The excursion amplitudes inducing sonoporation (pink and red) were significantly larger than those where no sonoporation was induced (Fig. 10.3B). Using a linear discriminant analysis, the mean threshold for sonoporation was found to be $R_{max} - R_0 > 0.7$ µm (Fig. 10.3A). However, there was no distinct microbubble excursion amplitude associated with retraction. Since microbubble excursion can also be quantified by considering the minimum radius during oscillation (R_{min}) or relative to R_0, the statistical comparisons between the different cellular responses were also performed for $(R_{max} - R_{min})/R_0$, $R_0 - R_{min}$, and $R_{max} - R_{min}$. The same statistical differences ($p < .001$) were found between sonoporated and non-sonoporated cells, and the non-significant differences between retracting and nonretracting cells remained.

To evaluate the effect of nonlinear microbubble behavior on drug delivery, we determined if microbubbles exhibited a subharmonic or second harmonic frequency response. The FFT amplitude (mean ± standard deviation) of the subharmonic noise level was 21 ± 13 nm (−18 dB below average fundamental) and that of the second harmonic noise level was 11 ± 6 nm (−23 dB below average fundamental). Only 6 out of 152 microbubbles (4%) had a subharmonic response. The presence of subharmonics did not correlate with a higher occurrence of sonoporation and/or retraction. On the other hand, 105 out of 152 microbubbles (69%) exhibited a second harmonic response, as shown in Fig. 10.4A. Significantly ($p < .01$) more microbubbles responded at the second harmonic frequency when sonoporation was induced (49% no effect, 67% retraction only, 84% sonoporation only, 89% sonoporation and retraction). However, the second harmonic amplitude normalized to the fundamental was not higher for microbubbles inducing sonoporation and a second harmonic response was not associated with retraction (Fig. 10.4A).

The asymmetry of microbubble oscillation quantified as E/C is shown in Fig. 10.4B. The recorded microbubbles presented with a full range of E/C ratios, from compression-only behavior (E/C = 0.13) to expansion-only behavior (E/C = 2.15). The E/C resulting in sonoporation was significantly larger than that of microbubbles that did not induce sonoporation (Fig. 10.4B). However, no significant differences were found in E/C for retraction.

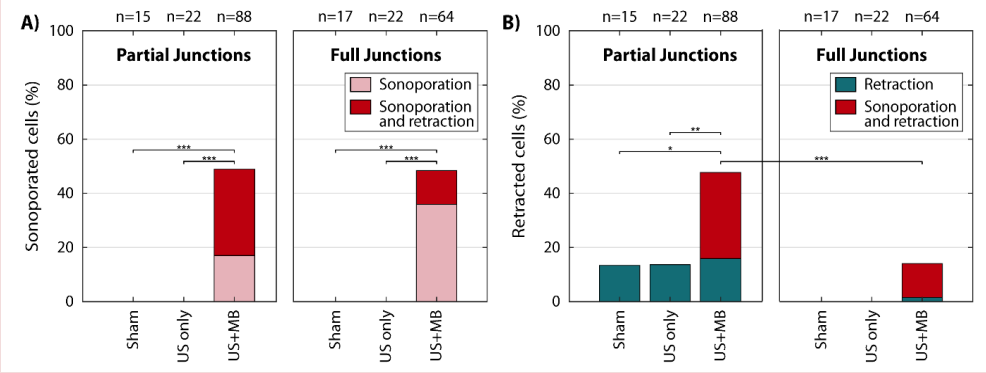

Figure 10.5. The cellular response of cells with partial or full junctions, classified based on the initial integrity of cell-cell contacts. (A) Occurrence of sonoporation, with or without retraction. (B) Occurrence of retraction, with or without sonoporation. Statistical significance indicated with *p < .05, **p < .01, ***p < .001; US = ultrasound; MB = microbubble.

Initial integrity of cell–cell contacts

As described in Section *Analysis of confocal time-lapse images*, the cells were classified into two subcategories based on the integrity of cell-cell contacts before ultrasound: partial junctions (n = 88, Fig. 10.2B) and full junctions (n = 64, Fig. 10.2A). The median (with IQR between brackets) excursion amplitude of microbubbles attached to a cell with partial junctions was 0.65 (0.38–0.94) µm and with full junctions 0.65 (0.42–1.05) µm. The cells in the control experiments were also classified using the same criteria.

When treated with ultrasound and microbubbles, the occurrence of sonoporation was the same for both cells with partial junctions (48.9%) and with full junctions (48.4%), as shown in Fig. 10.5A. In the case of partial junctions, 65.1% of the sonoporated cells

also retracted, while this was only 25.8% of the sonoporated cells with full junctions. For both cell junction subcategories, the sham and ultrasound only treatments never induced sonoporation. In contrast to sonoporation, retraction occurrence was affected by the initial integrity of the cell-cell contacts (Fig. 10.5B). After treatment with ultrasound and microbubbles, retraction occurred significantly ($p < .001$) more often when cells initially had partial junctions (47.73%) than when they had full junctions (14.1%) (Fig. 10.5B, US+MB). Sonoporation was only observed in 66.7% of cells with partial junctions that retracted (28 out of 42 cells), whereas almost all cells with full junctions that retracted were also sonoporated (88.9%, 8 out of 9 cells). Retraction without sonoporation in cells with partial junctions was similar for sham (13.3%), ultrasound only (13.6%), and treatment with ultrasound and microbubbles (15.91%). Retraction of cells with full junctions was never observed for the sham and ultrasound only treatments.

Cell size and microbubble location

The median (with IQR between brackets) cell area was 908 (725–1093) μm². There was no significant difference in cell area between the four distinct cell responses, as shown in Fig. 10.6A. Additionally, there was no significant difference in the location of the targeted microbubble on the cell, quantified as the distance from the microbubble to the closest cell edge (Fig.10.6B) or, alternatively, as the distance from the microbubble to the nucleus. Cells with partial junctions had a median area of 1021 (817–1215) μm²,

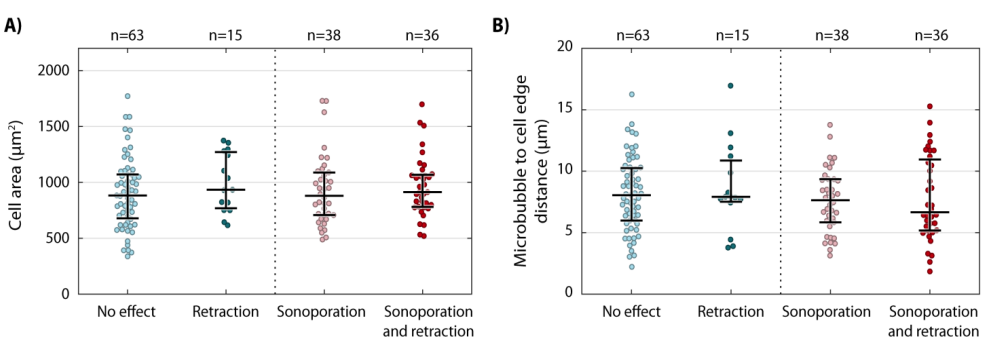

Figure 10.6. Effect of (A) cell area and (B) microbubble location on the cellular response. The medians and interquartile ranges are overlaid.

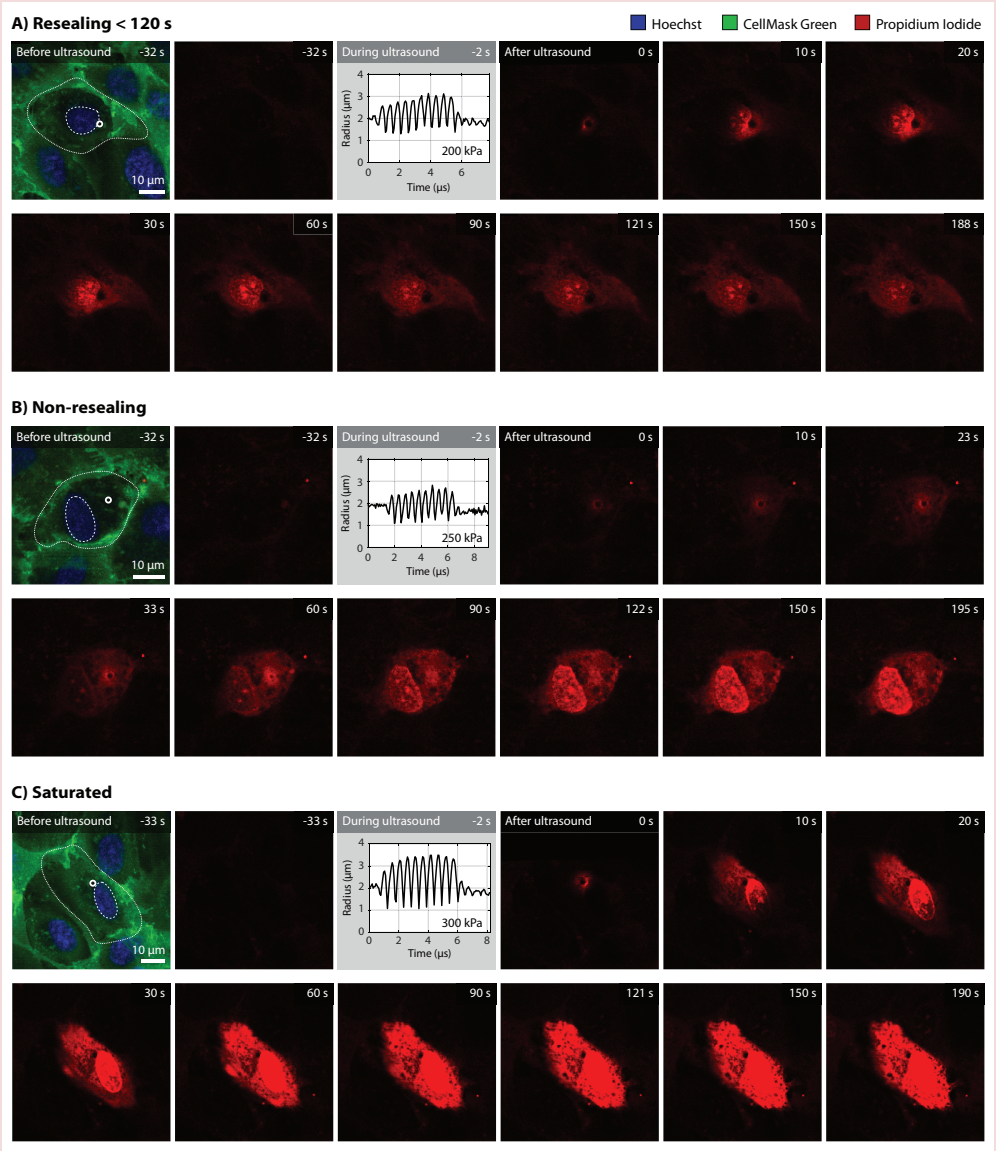

Figure 10.7. Different PI uptake categories upon sonoporation imaged with confocal microscopy. The initial cellular state is shown (composite image of CellMask Green, Hoechst, and PI) with the cell delineation (solid line), nucleus segmentation (dashed line), and microbubble location (white circle). During ultrasound insonification, the change in microbubble radius is shown as a function of time. All other frames show the PI imaging channel only, before and after ultrasound. (A) PI uptake classified as resealing <120 s. (B) PI uptake classified as non-resealing. (C) PI uptake classified as saturated. The resulting PI uptake curves of each example are shown in Fig. 10.8.

and therefore were significantly ($p < .001$) larger than cells with full junctions, at 794 (621–928) μm². Also, the median distance of the targeted microbubble to the cell edge was significantly ($p < .001$) larger for cells with partial junctions [8.4 (6.4–11.1) μm], than for cells with full junctions [6.7 (4.7–8.5) μm]. Within these junction subcategories, there was still no significant difference in cell area or distance from the microbubble to the edge between the four cellular responses.

Three typical examples of PI uptake profiles upon sonoporation are shown in Fig. 10.7. In the first example (Fig. 10.7A), the sonoporated cell had a PI uptake profile (Fig. 10.8, blue) that stabilized within 120 s, since 90% of the asymptotic value was reached after 25 s (i.e. $t_{90} = 25$ s). Signal saturation occurred in only 9.9% of the pixels in the nucleus. Therefore, this cell was classified as resealing < 120 s. In the second example (Fig. 10.7B), the PI uptake curve (Fig. 10.8, gray) did not stabilize within 120 s, since $t_{90} =$ 170 s. Signal saturation occurred in 16% of the pixels in the nucleus. Therefore, this cell was classified as non-resealing. In the third example (Fig. 10.7C), the PI uptake curve (Fig. 10.8, red) stabilized within 120 s, since $t_{90} = 81$ s. However, 97% of the pixels in the nucleus were saturated, so this cell was classified as saturated.

The pore size coefficient ($\alpha\pi DC_0r_0$) and pore resealing coefficient (β) of all sonoporated cells are shown in Fig. 10.9A. The classification based on the resealing time of the pore and the signal saturation in the nucleus separates the cells into three groups. Additionally, the pore size coefficients (median and IQR between brackets) of the saturated class [0.97 (0.68–1.73)×106] were significantly ($p<.001$) larger than that of the cells classified as resealing <120 s [0.30 (0.14–0.45) × 106] or non-resealing [0.18 (0.11–0.25) × 106]. As shown in Fig. 10.9B, larger microbubble excursion amplitudes correlated with larger pore size coefficients upon sonoporation (Spearman correlation coefficient $\rho = 0.53$, $p < .001$). Moreover, the excursion amplitudes (median and IQR between brackets) of the saturated class [1.22 (1.03–1.45) μm] were significantly ($p < .001$) larger than that of cells classified as resealing <120 s [0.88 (0.77–1.13) μm] or non-resealing [0.89 (0.62–1.00) μm]. The microbubble excursion amplitude did not distinguish between resealing or non-resealing pores.

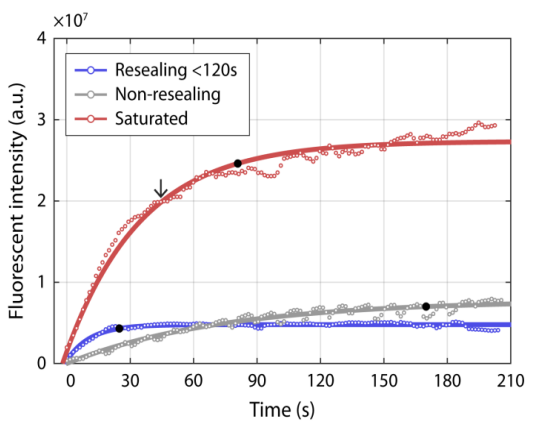

Figure 10.8. Cellular PI uptake curves shown as the fluorescent intensity as a function of time ($F(t)$, circles) and the corresponding fit to the mathematical model of Eq. (10.2) (solid lines). The three examples correspond to those in Fig. 10.7 for each category: resealing <120 s (blue, Fig. 10.7A), non-resealing (gray, Fig. 10.7B), and saturated (red, Fig. 10.7C). The black dots indicate the time t_{90} at which 90% of the asymptotic value was reached (Eq. (10.3)). The arrow marks the time at which 90% of the pixels in the nucleus were saturated; a.u. = arbitrary unit.

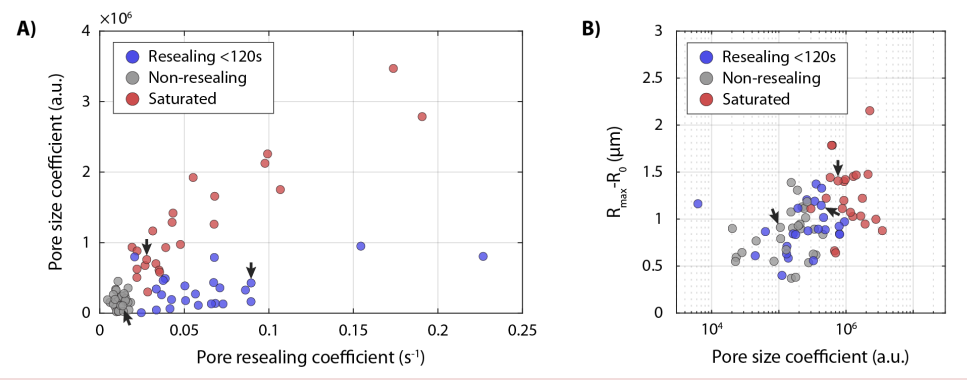

Figure 10.9. Quantification of PI uptake upon sonoporation (n = 74) and the resulting classification as resealing <120 s (blue), non-resealing (gray), and saturated (red). The arrows indicate the data points corresponding to the examples in Figs. 10.7 and 10.8. (A) The pore size coefficient as a function of the pore resealing coefficient. (B) The microbubble excursion amplitude (R_{max}-R_0) as a function of the pore size coefficient; a.u.=arbitrary unit.

Discussion

Sonoporation and the opening of cell-cell contacts upon ultrasound insonification of a single targeted microbubble were evaluated. Using high temporal and spatial resolution, we resolved both the microbubble oscillation and the cellular response. Susceptibility to sonoporation and opening of cell-cell contacts clearly depended on microbubble oscillation behavior and the initial state of the endothelial cell. Furthermore, quantification of sonoporation based on cellular PI uptake correlated with microbubble behavior and was used to assess reversibility of sonoporation.

Microbubble oscillation behavior

The ultra-high-speed recordings of microbubble oscillation revealed that sonoporation correlated with large excursion amplitudes, while there was no direct relationship between microbubble excursion and the opening of cell-cell contacts (Fig. 10.3). Sonoporation was induced for absolute excursion amplitudes R_{max} - R_0 > 0.7 µm, similar to the previously found thresholds at 2 MHz of R_{max} - R_0 > 0.72 µm (using 16 cycles) or R_{max} - R_0 > 1.02 µm (using 8 cycles) by Helfield et al.[224]. A relative vibration threshold of 0.5 at 1 MHz (with 6× 10 cycles) was reported by Kooiman et al.[454], which corresponds to an absolute threshold of R_{max} - R_0 > 0.65 µm (for a mean R_0 of 2.2 µm and symmetric oscillation), similar to our findings.

Microbubbles that induced sonoporation exhibited a second harmonic response more often than those that did not result in sonoporation. Since nonlinear behavior increases with microbubble excursion amplitude[512], this could be inherent to the larger excursions that result in sonoporation. We found no differences in the cellular response when the second harmonic amplitude was normalized to the fundamental (Fig. 10.4A). The E/C ratio was also higher in the case of sonoporation (Fig. 10.4B) only because the expansion phase becomes more dominant with increasing acoustic pressures, and thus excursion amplitudes[434,515]. Van Wamel et al.[227] hypothesized that cells can better withstand compression than elongation forces, thereby suggesting that compression-only (E/C < 0.5) could be more effective in sonoporation. However, in this study we found that nonlinear or asymmetric microbubble behavior itself did not affect the cellular response. The occurrence of sonoporation or opening of cell-cell contacts was found to be independent of the initial microbubble size for R_0 ranging from 1.24 to 3.72 µm, as previously found by others who studied similar size distributions[224,454]. However, to achieve high enough excursion amplitudes while insonifying at relatively low acoustic pressures, the microbubble size distribution should match the ultrasound frequency such that microbubbles are insonified at resonance. In this study, microbubbles were insonified at their mean resonance frequency of 2 MHz[419]. We limited our study to a single frequency, since Helfied et al.[224] only showed subtle differences between 0.5, 1, and 2 MHz. The excursion amplitude, i.e. acoustic pressure, plays a more important role than the frequency of oscillation, i.e. the ultrasound frequency (within the clinically relevant range 0.5 to 4 MHz). However, the microbubble–cell interaction upon insonification with longer bursts or repeated treatment remains open for investigation.

For instance, when using low acoustic pressures ≤200 kPa for longer treatment duration, the stimulation of the mechanosensory channels could possibly induce different drug delivery pathways, such as stimulated endocytosis[221].

The susceptibility to sonoporation or opening of cell-cell contacts was independent of the microbubble's location on the cell (Fig. 10.6B). This is favorable for the clinical applicability, since in vivo it would be impossible to control exact microbubble location on the cell membrane. Kooiman et al.[454] also found sonoporation to be independent of microbubble location, albeit based on a manual classification of microbubble positioning for 31 cells. Additionally, drug delivery was also independent of cell area (Fig. 10.6A), and thus all cell sizes seem to be equally susceptible to therapy.

Opening of cell–cell contacts due to sonoporation

Retraction of non-sonoporated cells was observed as often for both the control and ultrasound and microbubble experiments, while the enhanced retraction upon ultrasound and microbubbles only occurred upon sonoporation (Fig. 5B). From this we deduce that microbubble-mediated opening of cell-cell contacts only occurred due to sonoporation. Additionally, to open cell-cell contacts the targeted microbubble did not have to be near the cell edge (Fig. 10.6B), although that is often hypothesized[36,221]. Therefore, our results suggest that the opening of cell-cell contacts is a biological response triggered upon sonoporation, instead of an independent drug delivery pathway mechanically induced by microbubble oscillation. The retraction did not directly correlate to microbubble oscillation behavior (Fig. 10.3) and was strongly affected by the initial cell state (Fig. 10.5B), in contrast to the mechanical induced effect of sonoporation. This reinforces our conclusion that opening of cell-cell contacts is a cellular response mechanism and not directly caused by a microbubble mechanically rupturing the junctions. To the best of our knowledge, this is the first study that investigated the relationship between these two microbubble-mediated vascular drug delivery pathways in real-time and in the same field of view. Live cell imaging showing opening of endothelial cell-cell contacts had only been reported for a single example and without studying its correlation with sonoporation[224].

The initial cell integrity affected the susceptibility to opening of cell-cell contacts, because it occurred significantly more often when cells initially had partial junctions

(Fig. 10.5B). About 14% of cells with partial junctions even suffered from retraction in sham and in ultrasound only experiments, independent of the acoustic pressures. This retraction without treatment could be attributed to, for example, the imaging procedure (phototoxicity), the exposure of the CLINIcell to the open air after cutting out the top membrane, or the absence of 5% CO_2. The different susceptibility to microbubble-mediated treatment between partial and full junctions could mean that under physiological conditions that result in intercellular gaps, ranging from 0.3 to 4.7 µm in tumor vasculature[514,515] or during inflammation[516,517], the drug delivery pathway of opening cell-cell contacts is induced more often. At the same time, it emphasizes the importance of a realistic model to study the opening of cell-cell contacts. In previous studies, endothelial cell confluency varied from ~70% to full confluency so not all cells were completely adjacent to their neighbors. Additionally, the integrity of the cell-cell contacts before treatment was not assessed in these previous studies[224,245,518]. The only example in literature reporting the opening of endothelial cell-cell contacts was on a not fully confluent monolayer of endothelial cells having partial junctions[224]. In our study, the initial cell integrity was assessed using a CellMask cell membrane dye. However, this dye does not specifically stain for intercellular junctions and can eventually internalize, leading to a poorer co-localization with the plasma membrane. In the current study the plasma membrane remained well stained throughout the entire 120 min. Now that we observed the importance of the initial integrity of cell-cell contacts, in future studies the integrity of intercellular junctions could be more precisely assessed using specific fluorescent dyes.

A limitation of our study is that cellular response was only monitored up to 4 min after ultrasound insonification. Within that time frame it was not possible to study the recovery of cell-cell contacts, since Helfield et al.[224] showed that cell-cell contacts can remain open for tens of minutes. For long-term effects and recovery studies, the experimental conditions would need to be further optimized to reduce spontaneous retraction. Finally, when translating to in vivo studies often extravasation is assessed as a measure for the opening of intercellular junctions[519,520], without monitoring sonoporation. If extravasation of a fluorescent compound would also be monitored in vitro using a different set-up than the CLINIcell, allowing for measurements on the basolateral side of the monolayer, both intracellular delivery by sonoporation and extravascular delivery by opening of intercellular junctions could be quantified.

Additionally, since we found that retraction only occurred upon sonoporation, assessing cell membrane permeability and the possible resulting cell death in vivo is of great importance.

Transient pore formation

Based on cellular PI uptake upon sonoporation, the transient behavior of pore formation was quantified with the pore size and resealing coefficients, which resulted in three distinct classifications. Cells with pores that resealed within 120 s were assumed to be reversibly sonoporated, while irreversible sonoporation occurred when there was no resealing within 120 s[245]. We found that microbubble excursion amplitudes above 0.7 µm induced sonoporation, and the larger the excursion amplitude the bigger the pore that was created (Fig. 10.9B). This has never been observed before, since it was not possible to image both the microbubble oscillation behavior and detailed cellular response. Although intuitively there should be a higher chance for a small pore to reseal within 120 s, there was no clear correlation between pores resealing <120 s and the pore size coefficient or microbubble excursion amplitude (Fig. 10.9B). Van Rooij et al.[245] also did not find a correlation between smaller pore size and resealing within 120 s. The intrinsic variability among cells seems to influence membrane resealing more than the microbubble behavior and pore size. Therefore, cellular recovery mechanisms should be further unraveled by studying the underlying resealing mechanisms.

The mathematical model described by Fan et al.[228] considers any PI uptake plateau to be caused by pore resealing. However, we observed that many of the cells that plateau within <120 s, thus appearing to reseal, actually suffered from a saturated PI signal (Figs. 10.8 and 10.9). Saturation occurred when the pore size was largest. Reversibility of sonoporation cannot be assessed for the saturation class since the pore might remain open while the corresponding PI increase can no longer be detected. It is unclear if previous studies accounted for PI stabilization due to either image saturation or DNA/RNA saturation[228,245,466]. Therefore, it is possible that cells were assumed to be reversibly sonoporated when PI uptake plateaued due to PI saturation. Another difference with a previous study is that we monitored the PI uptake within the entire cell, while van Rooij et al.[245] determined the PI uptake profiles only within the nucleus. Therefore, small pores that quickly resealed might be missed if their PI uptake profiles started in the cytoplasm. In future sonoporation studies the limited dynamic range of an

imaging system should be considered. On the one hand, when interested in low uptake, i.e. small pores that quickly reseal, PI signal saturation for the larger pores is often inevitable. On the other hand, when interested in the high uptake, i.e. larger pores that do not or slowly reseal, the imaging settings can be adjusted such that image saturation is avoided while missing the initial and lower PI changes. However, in that case the fluorescent intensity could reach an equilibrium when there is no free DNA or RNA remaining for PI to bind to. Therefore, when avoiding image saturation, one should properly account for DNA/RNA saturation.

In this study we chose to have the cells on the bottom membrane of the CLINIcell to ensure that a targeted microbubble that did not bind would float up. Since the targeted microbubble was located between the objective and the cells, the microbubble gas core caused shadowing, impeding the laser to image directly underneath it (see Fig. 10.7A for an example). With this orientation it was not possible to directly image the created pore. Moreover, the imaging dependent calibration coefficient α (Eqs. (10.1) and (10.2)) was not determined in this study. Nevertheless, the pore size coefficient provides us with relative sizes because all imaging was performed under the same fluorescent imaging conditions, i.e. with the same α, and using the same extracellular PI concentration (C_0). Another limitation of this study is that reversibility could only be derived from the PI uptake profile. Literature has used two separate experiments to demonstrate the correlation between the occurrence of pore resealing within 120 s and cell viability[245]. However, if both the pore resealing timeline and cell viability were to be studied simultaneously with live cell microscopy, the underlying biological mechanisms leading to cell death could be further unraveled.

Conclusion

Using a state-of-the-art optical imaging system allowed for microbubble-mediated drug delivery to be studied with high sensitivity at short timescales, while also achieving the nanosecond resolution needed to resolve microbubble oscillation. Sonoporation and opening of cell-cell contacts by ultrasound insonification of targeted microbubbles were investigated. We found that larger microbubble excursion amplitudes(R_{max} - R_0>0.7 μm) correlated with the occurrence and amount of sonoporation, while the opening of cell-cell contacts could not be predicted from microbubble behavior. Microbubble-mediated opening of cell-cell contacts only occurred upon sonoporation and was influenced significantly by the initial cell state. Therefore, our results suggest that opening of cell-cell contacts is a biological response as a consequence of sonoporation, instead of an independent drug delivery pathway. These novel insights will aid the development of safe and efficient microbubble-mediated drug delivery.

Acknowledgements

This work was supported by the Applied and Engineering Sciences TTW (Veni-project 13669), part of NWO. The authors would like to thank Phoei Ying Tang from the Department of Biomedical Engineering for assistance during experiments and cell culture, and Michiel Manten and Geert Springeling from the Department of Experimental Medical Instrumentation for technical assistance, all from the Erasmus Medical Center, the Netherlands.

Supplemental Information

Supplemental videos of time-lapse confocal microscopy can be found online at: https://doi.org/10.1016/j.jconrel.2020.03.038

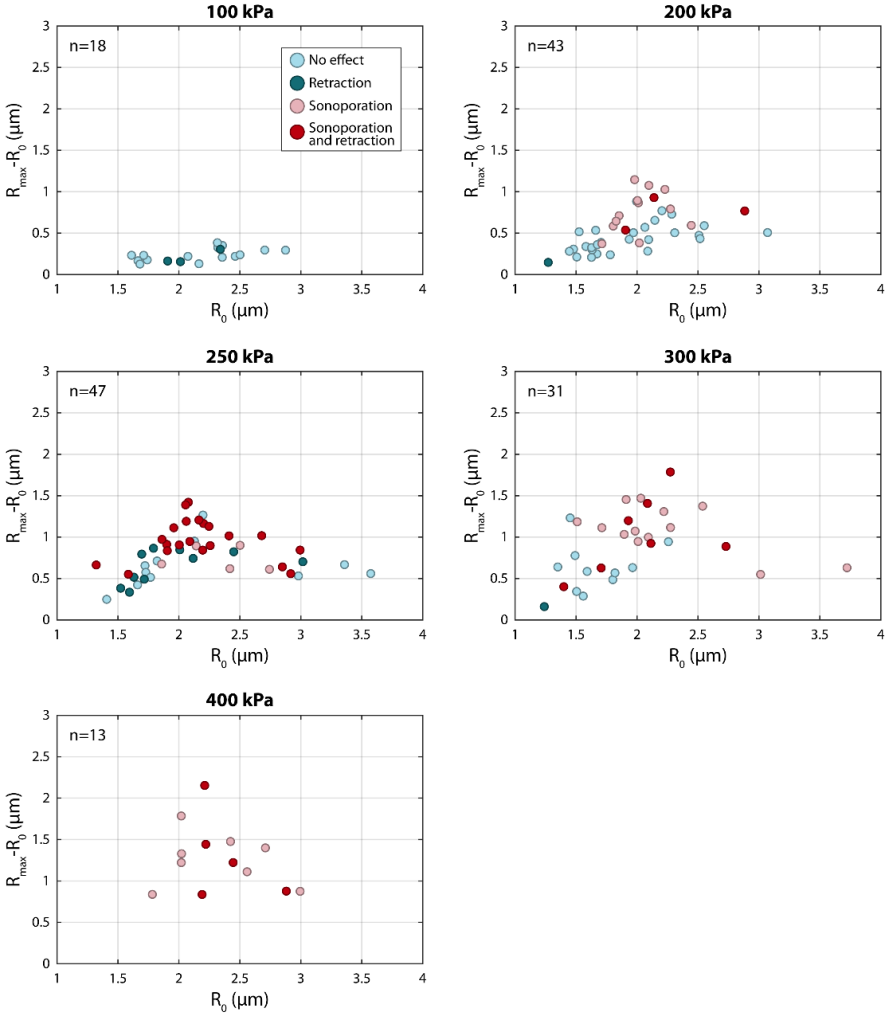

Supplemental Figure 10.1. Microbubble excursion amplitude (R_{max} - R_0) for each acoustic peak negative pressure (100 to 400 kPa), inducing no cellular effect (light blue), retraction (dark blue), sonoporation (pink), or both sonoporation and retraction (red).

“You can,
you should,
and if you're
brave enough
to start,
you will.

- Stephen King

What would you do if you weren't afraid?

11

Vancomycin-decorated microbubbles as a theranostic tool for Staphylococcus aureus biofilms

Joop J.P. Kouijzer, Kirby R. Lattwein, Inés Beekers, Simone A.G. Langeveld, Mariël Leon-Grooters, Jean-Marc Strub, Estefania Oliva, Gaëtan L.A. Mislin, Nico de Jong, Antonius F.W. van der Steen, Alexander L. Klibanov, Willem J.B. van Wamel, and Klazina Kooiman

Submitted

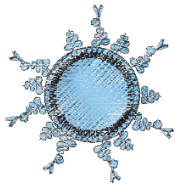

Abstract

Bacterial biofilms are a huge burden on our healthcare systems worldwide. The lack of specificity in diagnostic and treatment possibilities result in difficult-to-treat and persistent infections. The aim of this *in vitro* study was to develop and produce microbubbles that target specifically to bacteria in biofilms and demonstrate their theranostic potential for biofilm infection management. The antibiotic vancomycin was chemically coupled to the lipid shell of microbubbles and validated using mass spectrometry and high-axial resolution 4Pi confocal microscopy. Theranostic proof-of-principle was investigated by demonstrating the specific binding of vancomycin-decorated microbubbles (vMBs) to statically and flow grown *Staphylococcus aureus* biofilms with and without shear stress flow conditions (0-12 dyn/cm^2), as well as confirmation of microbubble oscillation and biofilm disruption upon ultrasound exposure (2 MHz, 250 kPa, and 5,000 or 10,000 cycles) using time-lapse confocal microscopy combined with the Brandaris 128 ultra-high-speed camera. Vancomycin was successfully incorporated into the microbubble lipid shell. vMBs bound significantly more than control microbubbles to biofilms in the presence of free vancomycin (0-1000 μg/mL) and remained bound under increasing shear stress flow conditions. Upon ultrasound insonification, Brandaris 128 recordings of vMB oscillation revealed stable cavitation and confocal microscopy showed a biofilm area reduction of up to 27.6%. Altogether, our results confirm the successful production of vMBs and support their potential as a new theranostic tool for *S. aureus* biofilm infections by allowing for specific bacterial detection and biofilm disruption.

Introduction

Approximately 80% of all bacterial infections are associated with biofilm formation[6], where bacteria encase themselves in a protective matrix hindering antibiotic effectiveness up to 1000-fold compared to free-floating (i.e., planktonic) bacteria and facilitating antibiotic resistance development[521]. This increased resistance is largely due to the reduced metabolic activity of biofilm-embedded bacteria and the limited penetration of antibiotics throughout the biofilm[73,75,302]. These life-threatening infections are challenging to diagnosis and treat, and are increasing in prevalence alongside the vulnerable aging population and surging use of implantable life-saving/enhancing technologies that create niches primed for colonization[522]. Furthermore, biofilm infections are difficult to cure, often requiring high-risk, costly, invasive procedures and can still become persistent, necessitating lifelong antibiotic use and/or repeated medical interventions. Biofilm infections can occur anywhere in all organ systems and can carry a high mortality rate depending on the location and infecting microbe. For example, infective endocarditis is an infection of the heart valves and/or endocardial surface with an in-hospital mortality of 18-47.5%[335,337] and a 5-year mortality of 40-69%[339,340,341]. Accurate diagnosis of biofilm infections at an early stage is critical because delayed diagnosis is associated with increased mortality[341,523], which for infective endocarditis this delay is often the case[43]. Currently there is no theranostic tool available in the clinic which combines the detection of biofilms with treatment possibilities. A novel theranostic agent to detect early biofilm formation and subsequently treat or be used as an adjunct would be a major breakthrough.

Microbubbles (1 – 10 µm) are ultrasound contrast agents that consist of an inert-gas core encapsulated by a protein, phospholipid, or biocompatible polymer shell[36,524] and used in daily clinical practice for several decades to aid in the ultrasound diagnosis of cardiovascular diseases and cancer[34,36,525,526]. Their therapeutic potential, however, has only begun being substantiated with clinical trials over the past years[519,520,527,528]. Microbubbles correspondingly respond volumetrically, i.e., oscillate, to the increase and decrease of pressure from ultrasonic waves[36,524], and it is these ultrasound-activated responses that enable them to be detected as well as induce various bioeffects for potential therapeutic applications. Promising pre-clinical investigations have only recently begun to determine if microbubble-mediated effects can be used to treat bacterial

infections, which is referred to as sonobactericide[304]. Until now, biofilms both grown and then treated under flow with sonobactericide have yet to be investigated, which would be relevant for infections situated in flow environments.

Targeted microbubbles are microbubbles that have a ligand incorporated into their coating so they can specifically bind to biomarkers, and have been extensively studied for their theranostic potential in regards to mammalian cells[529]. Preclinically, targeted microbubble binding under flow conditions has been used for the diagnosis of atherosclerosis[530], while clinical studies have shown the potential of ultrasound molecular imaging of cancer[190,191]. Treatment was more effective with targeted than with non-targeted microbubbles in preclinical studies, including *in vivo* studies[34,35]. To the best of our knowledge, targeted microbubbles for biofilms have been investigated only once before, which was for the detection of *Staphylococcus aureus* biofilms using a monoclonal immunoglobulin antibody to protein A (*S. aureus* bacterial cell wall surface protein) or a *Pseudomonas aeruginosa* lectin[45]. Although these microbubbles successfully bound to the biofilms, the clinical translation is poor because the antibody to protein A must compete with host antibodies that already bind to protein A for immune surveillance/clearance and the *P. aeruginosa* lectin causes red blood cell agglutination[192,193].

The purpose of this proof-of-principle study was to develop a clinically translatable novel theranostic using vancomycin-decorated microbubbles (vMBs) for the detection and treatment of *S. aureus* biofilms. The antibiotic vancomycin was chosen as the ligand for its 1) binding ability to the D-Ala-D-Ala moiety present in most gram-positive bacteria cell walls, 2) potential for clinical application, and 3) possibility to covalently couple this compound to the lipid shell of the microbubble without losing its functionality[531]. Vancomycin was chemically coupled to the microbubble coating via the functionalized polyethylene-glycol (PEG) conjugated lipid (DSPE-PEG(3400)) and confirmed with matrix-assisted laser desorption/ionization - time-of-flight mass spectrometry (MALDI-TOF MS), thin-layer chromatography (TLC), and 4Pi microscopy imaging. To mimic physiological conditions, a biofilm flow model was grown and treated under physiological shear stress conditions using an Ibidi microchannel flow set-up. We investigated the capability of the vMBs to remain bound to bacterial biofilms under static and shear stress conditions, and to evaluate their theranostic potential using confocal microscopy combined with ultra-high-speed imaging using the Brandaris 128.

Materials and Methods

Vancomycin coupling to lipid DSPE-PEG(3400)-N-hydroxysuccinimide

Thirty milligrams of DSPE-PEG(3400)-N-hydroxysuccinimide (DSPE-PEG(3400)-NHS; Sunbright DSPE-034GS; NOF America Corporation, New York, USA or NOF Europe GmbH, Frankfurt am Main, Germany) was dissolved in 1280 μL dimethyl sulfoxide (276855; Sigma-Aldrich, Saint. Louis, Missouri, USA) for a final concentration of 23.4 mg/mL. The covalent coupling of vancomycin to DSPE-PEG-NHS was performed as previously described for coupling of the cyclic RGD peptide[532], where the NHS ester of DSPE-PEG reacts with the primary amino group of the peptide. The reaction mixture was made by adding the DSPE-PEG(3400)-NHS solution to a 20% molar excess of vancomycin hydrochloride hydrate (V0045000, Sigma-Aldrich) in dimethyl sulfoxide. A 2-fold molar excess of N,N-diisopropylethylamine (496219, Sigma-Aldrich) relative to the vancomycin hydrochloride hydrate was also added. The reaction mixture was incubated on a rocker (15 rpm, PTR-35, Grant Instruments Ltd, Shepreth, United Kingdom) overnight at room temperature. N-hydroxy succinimide, unreacted vancomycin, and byproducts were removed by dialysis (Spectra/Por 1 Dialysis Membrane 6-8 kD; Spectrum, New Jersey, USA) in a 0.9% saline solution (Baxter International Inc., Deerfield, Illinois, USA) at 4 °C for 24 h. Then the saline solution was replaced with 4 °C demi water every 24 h for two days. On the fourth day, the demi water was replaced twice with 4 h in between to reach a microSiemens value of demi water, i.e. 1-3 μS. The final product (Fig. 11.1) was then freeze-dried (Alpha 1-2 LD plus; Mertin Christ GmbH, Osterode am Harz, Germany) and stored at -20 °C. Depending on the supplier of the DSPE-PEG(3400)-NHS, the produced DSPE-PEG(3400)-vancomycin conjugate is referred to as 'lipid conjugate batch USA', i.e. made from the DSPE-PEG(3400)-NHS supplied by NOF America Corporation or 'lipid conjugate batch EU', i.e. made from DSPE-PEG(3400)-NHS supplied by NOF Europe.

Mass spectrometry

Electrospray ionization mass spectrometry experiments were performed on an Agilent Accurate Mass QToF 6520 quadrupole time-of-flight instrument (Agilent Technologies, Santa Clara, CA, USA). The electrospray ionization source was performed in the positive

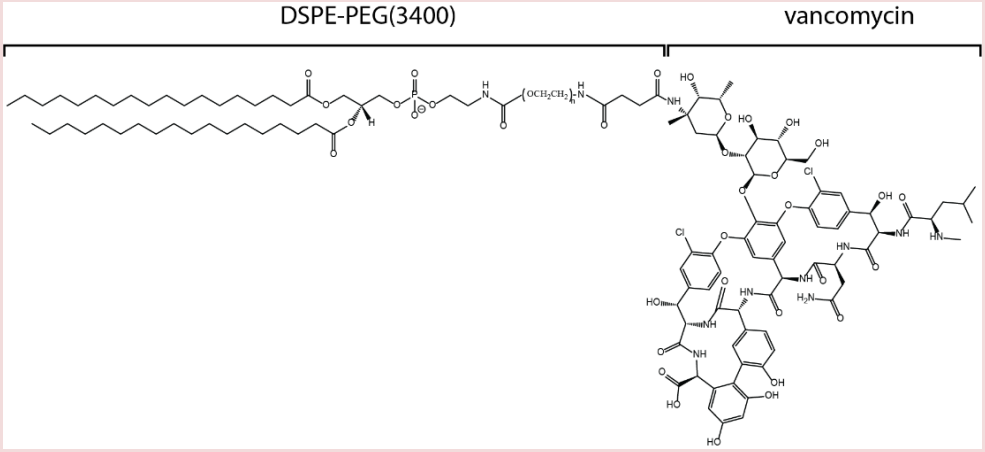

Figure 11.1. Molecular structure of the functionalized polyethylene-glycol (PEG) conjugated lipid (DSPE-PEG(3400)) coupled to the antibiotic molecule vancomycin.

ionization mode using a capillary voltage of 4500 V and the following conditions: nebulizer nitrogen gas pressure, 10 psig; drying gas flow rate, 5 L/min; and drying temperature, 340 °C. The scan range was m/z 50–3200 at 1 s/scan. Data acquisition was performed using MassHunter Qualitative Analysis software (B.07.00, Agilent). Direct introduction conditions: Samples were prepared at a concentration of 1 mg/mL (in chloroform for the commercial lipid and the conjugate, and in water for vancomycin) and 1 μL was injected. Injections were done using acetonitrile as the mobile phase with a flow rate of 0.1 mL/min. MALDI-TOF Mass measurements were carried out on an AutoflexTM MALDI-TOF mass spectrometer (Bruker Daltonics GmbH, Bremen, Germany). This instrument was used at a maximum accelerating potential of 20 kV in positive mode and was operated in linear mode. The delay extraction was fixed at 560 ns and the frequency of the laser (nitrogen 337 nm) was set at 5 Hz. The acquisition mass range was set to 2000-8000 m/z with a matrix suppression deflection (cut off) set to 1500 m/z. The equipment was externally calibrated with the single charge and double ion of insulin. Each raw spectrum was opened with flexAnalysis 2.4 build 11 (Bruker Daltonics GmbH, Bremen, Germany) software and processed using the following parameters: Savitzky-Golay algorithm for smoothing (width 5 and cycles 2), and sum algorithm for peak detection and labelling. The matrix solution was prepared from a saturated solution of α-cyano-4-hydroxycinnamic acid in water/acetonitrile 50/50. The

sample (less than 0.1 mg) was suspended in 1 mL of chloroform, and then 1 μL of the sample was added to 10 μL of saturated matrix solution. The mixture (1 μL) was loaded on the target and dried at room temperature.

Thin-layer chromatography

TLC sheets (TLC Silica gel 60 F_{254} Aluminum sheets; EMD Millipore Corporation, Burlington, Massachusetts, USA) were used as a stationary phase. A mixture of chloroform and methanol in a 9:1 ratio was used as the mobile phase. DSPE-PEG(3400)-NHS and DSPE-PEG(3400)-vancomycin were dissolved in chloroform to a concentration of 25 mg/mL and vancomycin was dissolved in methanol to a concentration of 25 mg/mL. Dissolved compounds were then spotted onto the TLC sheet using capillaries. Sheets were inspected for compounds under UV light (VL-6M, Vilber Lourmat, Collégien, France) after exposure to iodine vapors (207772; Thermo Fisher Scientific, Waltham, Massachusetts, USA).

Microbubble production

To produce vMBs, 1,2-distearoyl-sn-glycero-3-phosphocholine (DSPC, 12.5 mg/mL, 86.4 mol%; Sigma-Aldrich), custom-made DSPE-PEG(3400)-vancomycin conjugate (2.9 mg/mL, 5.3 mol%), and PEG-40 stearate (12.5 mg/mL, 8.3 mol%; Sigma-Aldrich), were first dissolved in phosphate buffered saline (PBS; 14200083; Thermo Fisher Scientific) saturated with perfluorobutane (C_4F_{10}; 355-25-9, F2 Chemicals Ltd, Preston, Lancashire, UK) using a sonicator bath for 10 min followed by probe sonication (Sonicator Ultrasonic Processor XL2020, Heat Systems, Farmingdale, New York, USA) at 20 kHz at power level 3 for 3 min. To fluorescently label the microbubble coating, the lipid dye DiD (1,1'-dioctadecyl-3,3,3',3'-tetramethylindodicarbocyanine perchlorate; D307; Thermo Fisher Scientific) or DiI (1,1'-Dioctadecyl-3,3,3',3'-Tetramethylindocarbocyanine Perchlorate; D282; Thermo Fisher Scientific) was added. This was followed by probe sonication for 60 s at power level 8 under continuous C_4F_{10} gas flow. The microbubbles were then stored in sealed vials under C_4F_{10} atmosphere at 4 °C and used within three days. To produce non-targeted control microbubbles (cMBs), DSPE-PEG(3400)-vancomycin was substituted for DSPE-PEG(3400) (2142-3400; Nanosoft Polymers, New York, USA). Before experiments, microbubbles were washed three times with C_4F_{10}-saturated PBS by centrifugation at 400 *g* for 1 min (Heraeus Biofuge Primo, Waltham,

Massachusetts, USA). The microbubble size distributions and concentrations were measured using a Coulter Counter Multisizer 3 (Beckman Coulter, Brea, California, USA). Particles (1 - 30 µm) were quantified using a 50 µm aperture tube.

4Pi microscopy imaging

vMBs containing DiD and cMBs containing DiI were incubated with anti-vancomycin IgG rabbit antibody coupled to a FITC-molecule (1 μg/1×10^8 MBs; LS-C540056; LifeSpan BioSciences, Seattle, Washington, USA) on ice for 30 min. To remove excess antibody, microbubbles were washed with C_4F_{10}-saturated PBS as described above. Microbubbles were then placed in 87% glycerol (v/v in PBS) to reduce Brownian motion. Y-stacked xz-scans were acquired using a Leica TCS 4Pi confocal laser-scanning microscope with two aligned opposing objectives for high axial resolution (90 nm step size, 100× glycerol HCX PL APO objective lens, numerical aperture 1.35). The FITC antibody was excited using a 488 nm laser and detected at 500-550 nm. For lipid shell visualization, DiI and DiD were excited with a 561 nm laser and detected at 580-640 nm and 647-703 nm, respectively. The 'voltex' function in AMIRA software (Version 2020.1, FEI, Mérignac Cedex, France) was used for rendering volume projections of the acquired y-stacked xz-scans.

Static biofilm formation

An IE patient-derived *S. aureus* bacterial strain, associated with cardiovascular infections (ST398), was used for this study. This strain was collected by the department of Medical Microbiology and Infectious Diseases, Erasmus MC, Rotterdam, the Netherlands, and anonymized and de-identified according to institutional policy. Frozen stock samples were streaked onto tryptic soy agar containing 5% sheep blood (BD, Trypticase™, Thermo Fisher Scientific) and allowed to grow overnight at 37 °C. Bacterial colonies were suspended in Iscove's Modified Dulbecco's Media (IMDM; Gibco, Thermo Fisher Scientific) until an optical density of 0.5 (± 0.05) was reached at 600 nm (Ultraspec 10, Amersham Biosciences, Little Chalfont, United Kingdom). IbiTreat polymer μ-Slides (80196; 0.8 mm channel height; I Luer; Ibidi GmbH, Gräfelfing, Germany) were inoculated with 200 μL of diluted bacterial suspension consisting of 1×10^4 colony forming units per mL (CFU/mL). In- and outlet-reservoirs were filled with 60 μL of IMDM. Slides were then incubated at 37 °C for 24 h in a humidified incubator under

constant agitation (150 rpm; Rotamax 120, Heidolph Instruments, Schwabach, Germany).

Biofilm formation under flow

IbiTreat μ-Slides were incubated with 320 μL of type O human plasma (citrate phosphate double dextrose as an anti-coagulant; pooled from five donors to minimize donor variability; Sanquin, Rotterdam, the Netherlands) to aid bacterial attachment under flow. After incubation at 37 °C for 24 h in a humidified incubator, plasma was removed and the slides were rinsed three times with 200 μL 0.9% saline solution (Baxter International). Then, an IMDM diluted *S. aureus* bacterial suspension of 200 μL containing 1×10^6 CFU/mL was pipetted into the slide. Bacteria were allowed to attach to the surface of the μ-Slide for 3 h and then the μ-Slide was connected to an Ibidi fluidic unit using corresponding perfusion sets (Perfusion set red, 10962; Ibidi) and a computer-controlled air pressure pump (Ibidi pump system; Ibidi). In order to later on inject microbubbles and dyes, an in-line Luer injection port (10820; Ibidi) was placed in the perfusion set 3.5 cm before the μ-Slide inlet. Biofilms were grown under laminar flow at 5 dyn/cm^2 (14.39 mL/min, corresponding to a Reynolds number of 32) for 24 h.

Experimental set-up

The μ-Slides were inserted into a custom-built water tank, that was maintained at 37 °C and situated underneath a custom-built Nikon A1R+ confocal microscope[273] (Nikon Instruments, Amsterdam, the Netherlands) (Fig. 11.2A, C). The orientation of the μ-Slide was either upright or flipped 180° depending on the experiment performed (Fig. 11.2). The transducer (2.25 MHz center frequency; 76.2 mm focal length; -6 dB beam width of 3 mm at 2 MHz; V305; Panametrics-NDT, Olympus, Waltham, MA, USA) was placed underneath the sample at a 45° angle to minimize ultrasound reflection and standing wave formation. Both the optical and ultrasound foci were aligned using a pulse-echo approach and a needle tip located at the optical focal plane[223], hereby the microbubbles and biofilm could both be simultaneously imaged and insonified. An arbitrary waveform generator (33220A; Agilent), in combination with a broadband amplifier (ENI A-500; Electronics & Innovation, Rochester, NY, USA), was connected to the transducer. The transducer output was calibrated in a separate experiment using a needle hydrophone (1 mm diameter; PA2293; Precision Acoustics, Dorchester, UK).

As a live/dead staining, SYTO 9 (S34854; Thermo Fisher Scientific) was excited at 488 nm and detected at 525/50 nm (center wavelength/bandwidth) and propidium iodide (PI; P4864-10ML; Sigma-Aldrich) was excited at 561 nm and detected at 595/50 nm. For experiments with DiI incorporated into the cMBs, the 561 nm laser with the same detection was also used for optical imaging. A third channel was used for the visualization of DiD incorporated into vMBs with an excitation at 640 nm and fluorescence detected at 700/75 nm.

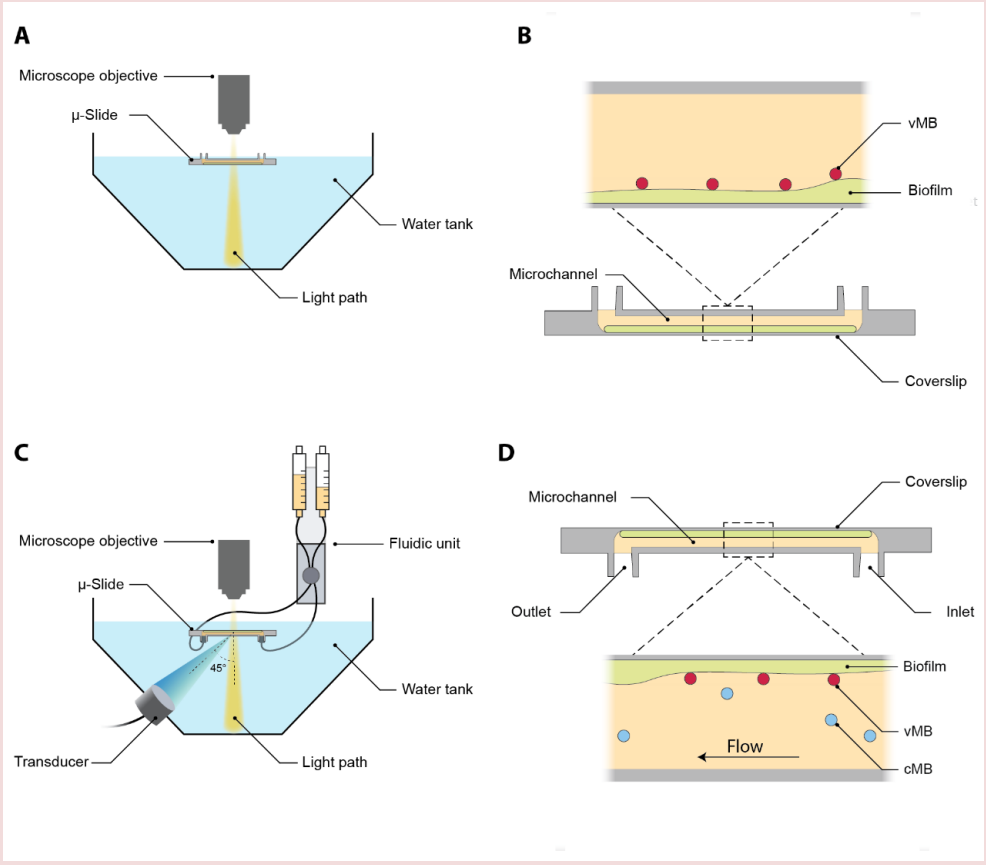

Figure 11.2. Schematic representation (not drawn-to-scale) of the experimental set-ups for (A, B) the static competitive microbubble binding assay and (C, D) the flow experiments. (B) Zoomed-in cross-section of the Ibidi μ-Slide in A and (D) of the μ-Slide in C, both indicating the placement of the biofilm within the microchannel containing vancomycin-decorated microbubbles (vMB, red) and/or control microbubbles (cMB, blue).

Competitive binding assay

To study the competitive binding of vMBs, statically grown biofilms were pre-incubated for 5 min with vancomycin concentrations of 0, 10, 20, 100 or 1000 μg/mL dissolved in IMDM. This includes the maximal recommended clinical blood level concentration of vancomycin, i.e., 20 μg/mL[533,534]. A final vancomycin concentration of 1000 μg/mL was used in the μ-Slides for cMBs. After this, the dyes (0.4 μL of 5 mM SYTO 9, 5 μL of 1.5 mM PI) and fluorescent DiD microbubbles (7.0×10^5 vMBs or cMBs) were added to IMDM containing the same pre-incubation vancomycin concentration to a total of 200 μL, and then added to the μ-Slide replacing the pre-incubation IMDM. Slides were flipped 180° for 5 min to allow the microbubbles to float up towards the biofilm for binding and then flipped back to their original position, such that any unbound microbubbles would rise to the top of the channel (Fig. 11.2B). At least three binding assays were performed for each vancomycin concentration. Slides were systematically imaged with a 100× water-dipping objective (CFI Plan 100XC W, Nikon Instruments) of which each field-of-view consisted of 512 × 512 pixels (128 × 128 μm^2). The number of microbubbles attached to bacterial biofilms was manually determined for 20 different fields-of-view distributed over each μ-Slide using Fiji software[535].

Additionally, nonspecific binding of the vMB was examined. For this, μ-Slides with and without statically grown biofilms were treated similarly. Before the binding assay all slides were first rinsed with 200 μL IMDM and incubated for 5 minutes. IMDM containing the dyes (0.4 μL of 5 mM SYTO 9, 5 μL of 1.5 mM PI), fluorescent DiD vMBs (7.0×10^5 vMBs), and either 0, 0.1, or 1% of bovine serum albumin (BSA; A9418-50G; Sigma-Aldrich) or casein (37582; Thermo Fisher Scientific). Slides were then flipped 180° for 5 min to allow the microbubbles to float up towards the biofilm for binding and then flipped back to their original position. Three binding assays were performed for each condition. Slides were systematically imaged with a 100× water-dipping objective of which each field-of-view consisted of 512 × 512 pixels. The number of vMBs attached to the bottom and top of the slide were manually determined using Fiji in 20 locations distributed over the whole microchannel.

Microbubble binding under increasing shear stress

To exclude differences in results due to biofilm heterogeneity and possible variable biofilm erosion under flow conditions, vMBs and cMBs were simultaneously added to biofilms grown under flow at 5 dyn/cm^2 at a ratio of 1:1. A solution of 200 μL IMDM containing 0.4 μL of 5 mM SYTO 9 and 1.2×10^7 microbubbles was injected into the in-line Luer injection port with a 1 mL Luer Solo syringe (Omnifix-F, B Braun, Melsungen, Germany) and 19G needle (Sterican, B Braun) while the flow was turned off and the Ibidi μ-Slide was oriented upside down (Fig. 11.2D). To introduce microbubbles and SYTO 9 into the μ-Slide, a shear stress of 1.3 dyn/cm^2 (3.74 mL/min) was applied for 17 s. The vMBs and cMBs were then incubated with the biofilm for 5 min without flow. Flow was started and increased every 60 s, with an initial increase of 0.5 dyn/cm^2, from 1.5 (4.33 mL/min) to 2 dyn/cm^2 (5.76 mL/min), and then each subsequent step was increased by 1 dyn/cm^2 until 12 dyn/cm^2 (34.53 mL/min, Reynolds number: 74.2) was achieved. The number of microbubbles remaining attached to the biofilm while applying increasing flows was monitored with confocal time-lapse microscopy (0.77 fps) using a 60× water-immersion objective (Plan Apo 60XA WI, Nikon Instruments). The binding percentage was defined by the following formula:

$$\text{Binding percentage} = \frac{\text{MBs bound after 60 s shear stress}}{\text{total amount MBs before flow}} \text{ x } 100\%$$

Sonobactericide experimental protocol

A solution of 200 μL containing 0.4 μL of 5 mM SYTO 9, 5 μL of 1.5 mM PI and 1.2×10^7 vMB containing DiD in IMDM was added to biofilms grown under flow at 5 dyn/cm^2. After this, a continuous laminar flow of 5 dyn/cm^2 was applied to the biofilm. For sonobactericide, the clinically used transthoracic echocardiography frequency of 2 MHz was chosen[409]. Biofilms were insonified with ultrasound after a minimum of 50 s of continuous flow exposure. A single 5,000- or 10,000-cycle burst at 250 kPa peak negative pressure was given, resulting in a treatment time of 2.5 or 5 ms. For the ultrasound only control, a single 10,000-cycle burst at 250 kPa peak negative pressure was given. All experiments were monitored for bacterial and vMBs responses with time-lapse confocal microscopy (0.77 fps) using a 60× water-immersion objective.

The biofilm reduction was quantified based on the SYTO 9 signal using a custom-built image analysis code in MATLAB (The MathWorks, Natick, MA, USA). The area without biofilm was determined in a frame before and within 15 s after ultrasound insonification, both selected based on minimal signal variability due to focus drift. Images were first converted to binary by thresholding at 300 (image intensity ranging from 0-4095). Next, all connected components were identified through the *bwconncomp* function in MATLAB. All connected components with an area larger than 200 pixels (33.5 μm^2) were classified as areas without biofilm and normalized to the size of the field-of-view (512×512 pixels; 210 × 210 μm^2). The biofilm reduction was defined as the change in normalized area without biofilm before and after ultrasound insonification.

Brandaris 128 ultra-high-speed recordings

To resolve the oscillation pattern made by the vMBs while bound to the bacterial biofilm under flow with simultaneous ultrasound exposure, the Brandaris 128 was used as previously described[273]. Briefly, the ultra-high-speed camera (up to 25 million fps) was coupled to the custom-built Nikon A1R+ confocal microscope, which made it possible to visualize both the microbubble behavior on a nanosecond time-scale and sonobactericide treatment effect after ultrasound exposure. A 100× water dipping objective was used for scanning a field-of-view of 128 × 128 µm (512 × 512 pixels). Time-lapse confocal imaging started during continuous flow (5 dyn/cm^2), capturing first the initial state of the biofilm and bound vMB. For the Brandaris 128 ultra-high-speed camera recording, the light path was automatically switched from the confocal scan head to the Brandaris 128. During ultrasound exposure (2 MHz, 250 kPa, 5,000 cycles), the microbubble oscillation was recorded at a framerate of 16.4 million fps. After obtaining all 128 frames, the light path was automatically switched back to the original position to continue confocal time-lapse imaging. The microbubble diameter as a function of time could be subtracted from the Brandaris 128 recording using custom-designed software[243].

Statistical analysis

All data were statistically analyzed using IBM SPSS Statistics 27 (IBM Corporation, Armonk, New York, USA), and a p-value of < 0.05 was used as the significance level. Data distribution was assessed using the Shapiro-Wilk test. Non-normal distributions were compared by performing a Mann-Whitney U test. When the equality of variance

was significant a Welch's t-test was performed instead. Normally distributed data was compared using an unpaired t-test or one-way ANOVA with post-hoc Tukey HSD test for multiple groups. The Spearman's rank-order correlation was used in MATLAB to further analyze the competitive microbubble binding assay data.

Results

Targeted microbubble preparation

The freeze-dried crude material obtained after dialysis was analyzed by mass spectrometry in order to assess the formation of the expected DSPE-PEG(3400)-vancomycin conjugate. Electrospray experiments emphasized the complexity of the crude material containing both the lipid and the expected conjugate. However, the multiplicity of PEG units in the lipid and the presence of the chlorine isotopes in vancomycin led to intricated spectra where the average molecular weight (MW) determination of our conjugate was not possible. Based on mass spectrometry analysis reported for similar compounds[536], MALDI-TOF experiments were performed on the crude and on the starting lipid used as a control. According to mass spectrometry experiments, the starting lipid was found to have a MW ca. 4260 (Fig. 11.3A). After lipid conjugation with vancomycin, the MW of the expected conjugate should be ca. 5700. MALDI-TOF experiments confirmed the presence of the starting lipid and a second compound with an average MW of 5691, matching with the expected conjugate (Fig. 11.3B).

Before producing the vMBs, successful conjugation between the DSPE-PEG(3400)-NHS and vancomycin was further confirmed by TLC (Fig. S11.1). This TLC visualized the main components of the conjugation before the chemical reaction. Vancomycin did not migrate, while DSPE-PEG(3400)-NHS did migrate and separated into two components: an unreacted part (Lipid-NHS) and a hydrolyzed part (Lipid-OH). The TLC on the right in Fig. S11.1 reveals the chemically coupled end product after dialysis and freeze-drying. The hydrolyzed unreacted Lipid-OH remains visible while the Lipid-NHS has reacted with the vancomycin and is not present anymore.

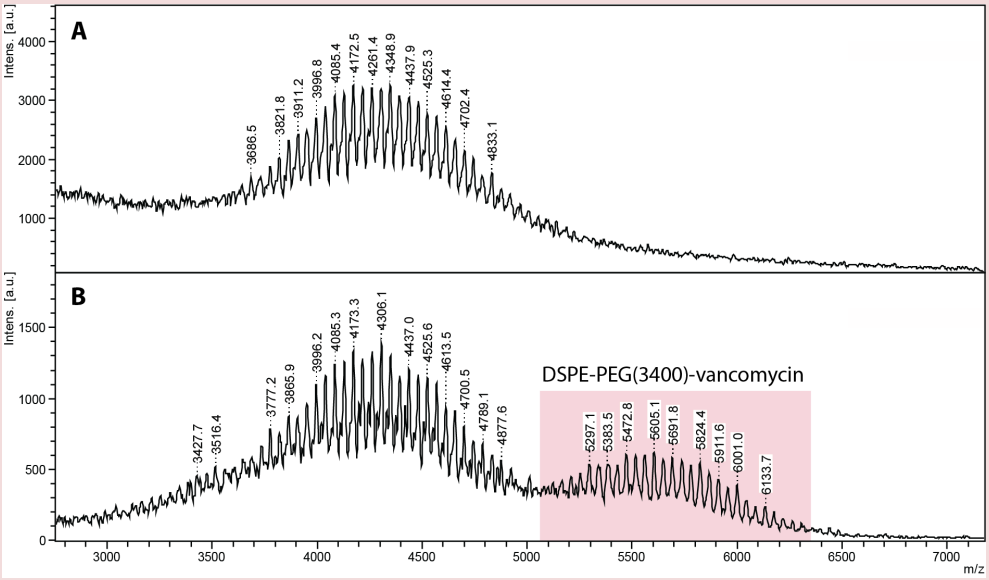

Figure 11.3. Matrix-assisted laser desorption/ionization - time-of-flight mass spectra of (A) the starting lipid (DSPE-PEG(3400) and (B) the reaction mixture after dialysis with the red shaded region confirming the vancomycin coupled to the polyethylene-glycol (PEG) conjugated lipid.

The number-weighted mean diameter of the microbubbles used for all experiments is shown in Fig. 11.4A. The mean diameter of the vMBs produced with lipid conjugate batch USA or lipid batch conjugate EU did not show a significant difference between batches (p = 0.669). Although the vMBs showed a little more spread between microbubble diameters (3.0 – 4.4 μm; 18 batches) than cMBs (3.6 – 4.4 μm; 10 batches), there was no significant difference between the two microbubble types (p = 0.759; vMB 3.9 ± 0.08 and cMB 3.9 ± 0.09 (mean ± SD)). Fig. 11.4B shows similar polydisperse microbubble size distributions for vMBs and cMBs.

High-axial resolution 4Pi microscopy

Incubation of vMBs with a FITC-labeled anti-vancomycin antibody confirmed the presence of vancomycin as a ligand on the phospholipid coating of the vMBs using high-axial resolution 4Pi confocal microscopy. The patch-like FITC-signal within the three-dimensional reconstruction of the vMBs, as seen in Fig. 11.5A, indicates that vancomycin

is heterogeneously distributed over the vMB coating. The absence of any FITC-signal in the cMBs (Fig. 11.5D) indicates that there was no nonspecific binding of the FITC-labeled anti-vancomycin antibody.

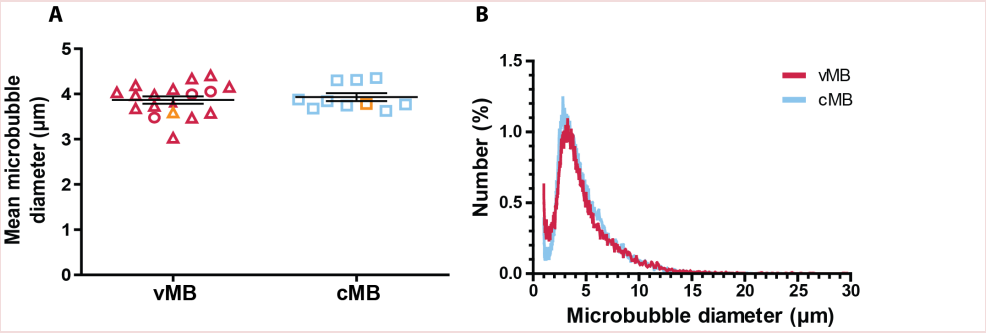

Figure 11.4. Microbubble number-weighted mean diameter and size distribution. (A) The mean diameter of vancomycin-decorated microbubbles (vMB, red, n=18 batches) and control microbubbles (cMB, blue, n=10 batches) used in all experiments. The vMB were produced with either the conjugate purchased in the United States of America (red circles) or European Union (red triangles). The mean and standard deviations are overlaid. Orange-colored symbols indicate the MB batches corresponding to B. (B) Representative size distribution of vMB and cMB batches.

Competitive microbubble binding assay

The ability of vMBs and cMBs to bind to statically grown biofilms was assessed with a competitive microbubble binding assay (Fig. 11.6). Significantly more vMBs bound to the bacterial biofilms compared to cMBs, regardless of the concentration of free vancomycin present. For vMBs, increasing the concentration of free vancomycin up to 20 μg/mL prior to the incubation with vMBs did not result in a significant decrease in the amount of bound vMBs. Only the preincubation of biofilms with a free vancomycin concentration greatly exceeding the maximal clinical dose of 20 μg/mL, namely 100 and 1000 μg/mL, reduced the number of bound vMB ($p = 0.02$). No significant difference was found between the binding of vMB produced with either the USA or EU conjugated lipid. Microbubble binding between the cMB preincubated without or with 1000 μg/mL of vancomycin was not significantly different ($p = 0.065$). The number of microbubbles was found to be mostly unaffected by location within the μ-Slides (Fig. S11.2). At most a moderate negative

correlation (i.e., number of microbubbles moderately decreases as the distance from the inlet increases) was observed for two conditions, both with vMBs and biofilm, with a free vancomycin concentration of 10 μg/mL (r = -0.53, p =0.00) and 1000 μg/mL (r = -0.54, p =0.00). All other conditions had coefficient values less than 0.4 (r values ranging from -0.33 - 0.13), which indicate little to no relationship between the two variables.

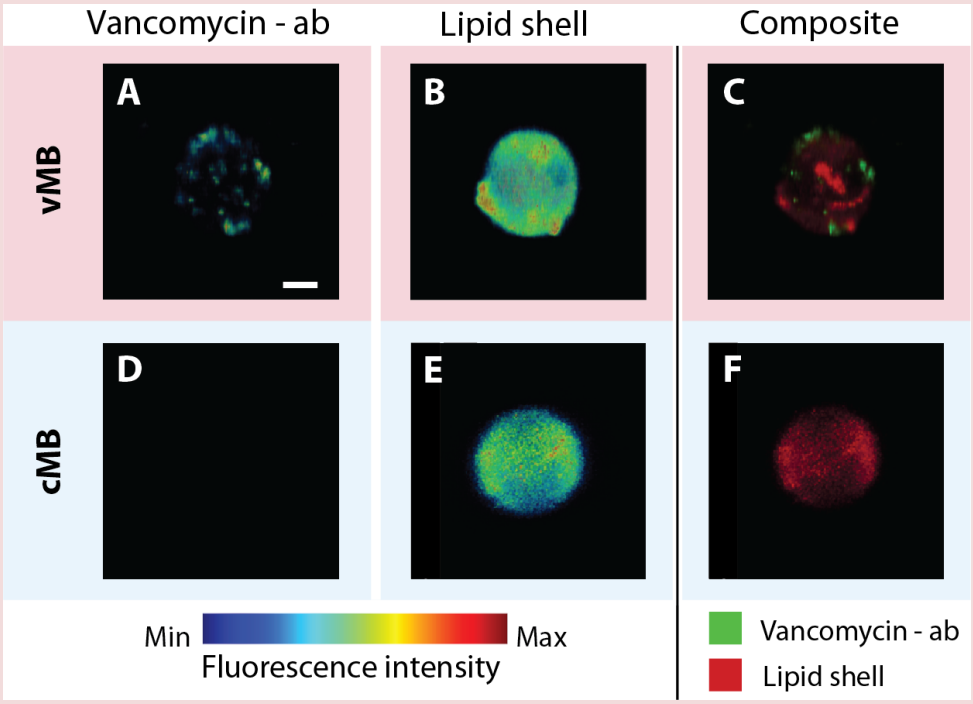

Figure 11.5. Representative 3D reconstructed images of high-axial resolution 4Pi confocal microscopy y-stacks of (A-C) a vancomycin-decorated microbubble (vMB, diameter = 4.2 μm) and (D-F) a control microbubble (cMB, diameter = 4.3 μm). (A, D) Images of the FITC-labeled anti-vancomycin antibody (vancomycin-ab). (B, E) The phospholipid shells visualized with the lipid dye DiD for vMB and DiI for cMB. (C, F) Composite view of the FITC-labeled anti-vancomycin antibody (green) and lipid dye (red). Scale bar is 1 μm and applies to all images.

Furthermore, nonspecific binding of vMBs to the Ibidi μ-Slides themselves, i.e. not the biofilm, was investigated. Figure 11.7 shows the percentage of vMBs bound to biofilms is on average 64.9%, while binding to an Ibidi μ-Slide without biofilm is 40.3%. When 0.1%

BSA was added, the average amount of observed microbubbles bound to the biofilms only slightly decreased to 57.6%. However, the average percentage of vMBs bound to the empty slide drastically dropped to 8.4%. When the BSA concentration is increased to 1%, the same trend is visible; the Ibidi μ-Slide with biofilm had 43.5% of bound vMB on average, whereas the nonspecific binding for this condition without biofilm decreased significantly to 3.2%. Similar results were obtained when BSA was substituted for casein (Fig. S11.3).

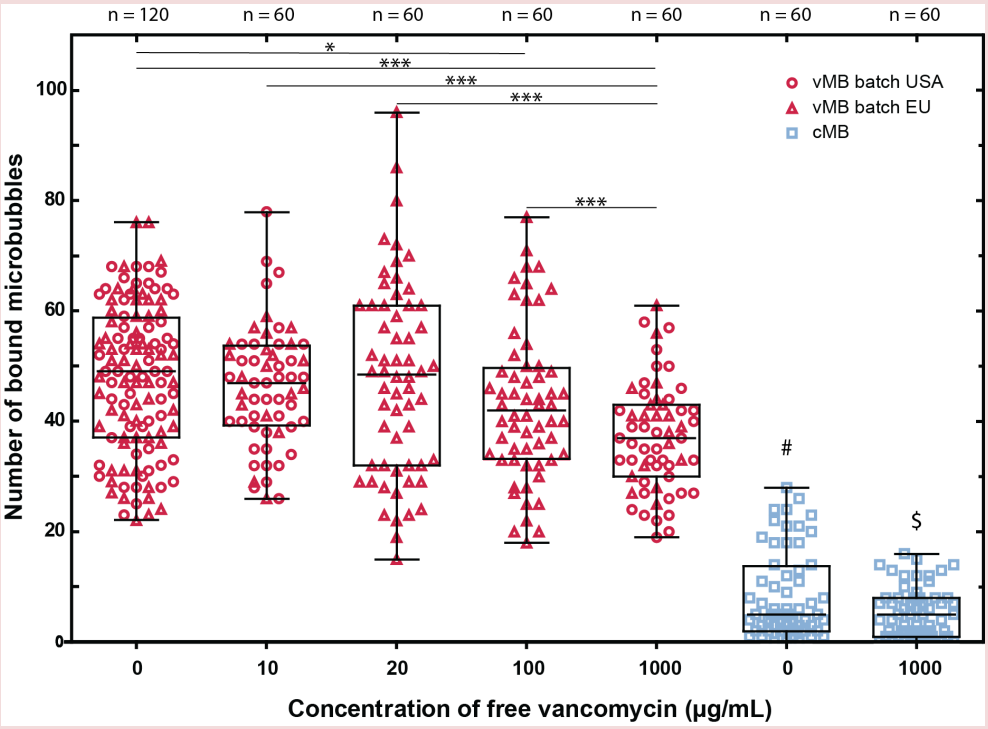

Figure 11.6. Competitive vancomycin binding assay for vancomycin-decorated (vMB, red symbols) and control (cMB, blue squares) microbubbles with statically grown biofilms. The vMBs were produced with either the United States of America (USA, red circles) or European Union (EU, red triangles) DSPE-PEG(3400) conjugated lipid. Each symbol represents the number of microbubbles counted in one field-of-view. The overlaid boxplots show the median, interquartile range, and the minimum to maximum values. Statistical significance is indicated with * ($p < 0.05$) or *** ($p < 0.001$) between the different vMB free vancomycin concentrations, # ($p < 0.001$) between cMBs without vancomycin and all vMB free vancomycin conditions, and $ ($p < 0.001$) between cMBs with 1000 μg/mL and all vMB free vancomycin conditions.

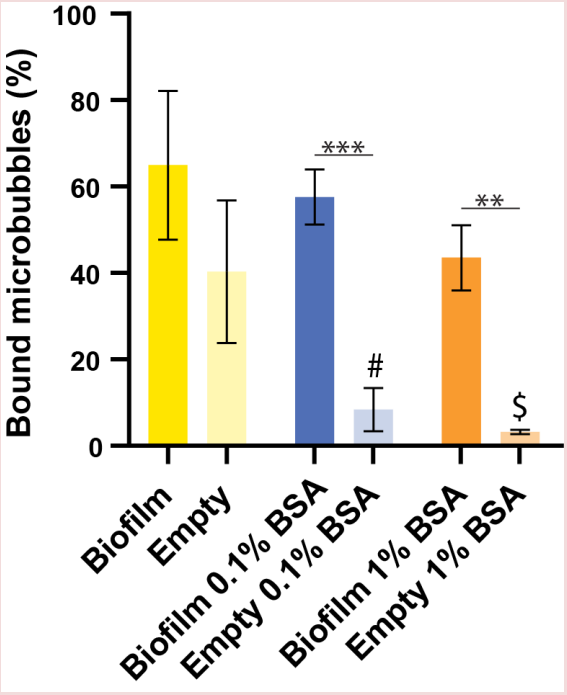

Figure 11.7. Nonspecific binding testing of vancomycin-decorated microbubbles. Ibidi µ-Slides with and without biofilms were blocked with either 0, 0.1 % or 1% bovine serum albumin protein (BSA) to bind to non-specific binding sites. Each bar represents mean with standard deviation overlaid with an n=60 locations. Statistical significance is indicated with ** ($p < 0.01$) or *** ($p < 0.001$), # ($p < 0.05$) between Empty 0.1% BSA and all other conditions except for Empty 1% BSA, and $ ($p < 0.05$) between Empty and all other conditions except for Empty 0.1% BSA. Empty = no biofilm.

Microbubble binding under flow

To determine the number of microbubbles that remained bound under flow, the vMBs and cMBs were distinguished by the different lipid dyes incorporated into their coating as shown in Fig. 11.8B-C and E-F, respectively. The average number of vMBs present before flow was 51 ± 37 and for cMBs 61 ± 44 (mean ± SD; n = 8) per a field-of-view, and the ratio of vMBs/cMBs was 0.87 ± 0.16. Time-lapse imaging while increasing flow from 1.5 to 12 dyn/cm^2 was performed to distinguish bound from unbound microbubbles and revealed that vMBs had a significantly higher binding percentage in comparison to cMBs at all shear stress values, except fromm 7 to 9 dyn/cm^2 (Fig. 11.8G). The biofilm remained attached to the bottom of the microchannel throughout the duration of flow binding experiments (Fig. 11.8A,D).

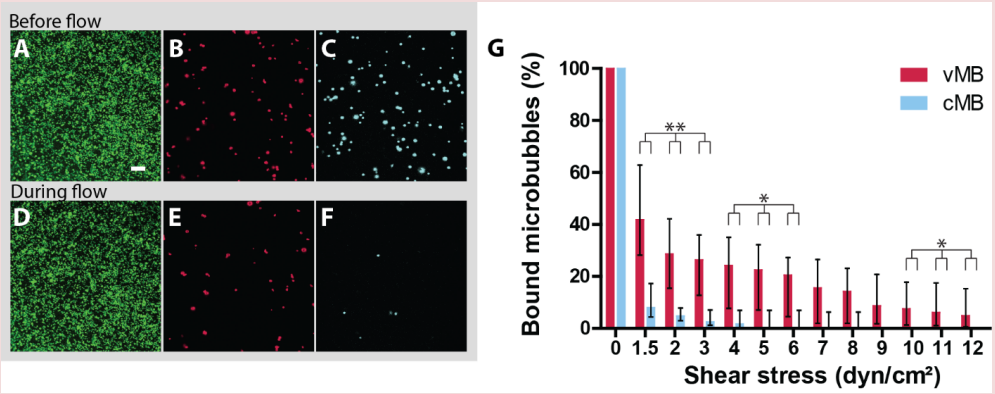

Figure 11.8. Bound microbubbles under increasing shear stress. Confocal microscopy images of (A-C) the initial state before flow and (D-F) after 60 s of 1.5 dyn/cm² shear stress flow at 60× magnification. Both sets of images are the same biofilm with (A, D) bacteria stained with SYTO 9 (green), (B, E) vancomycin-decorated microbubbles (vMB) stained with DiD (red), and (C, F) control microbubbles (cMB) stained with DiI (blue). Scale bar is 20 μm and applies to all images. (G) Bars represent median percentage with interquartile range of microbubbles in the field-of-view remaining bound to the bacterial biofilm during increasing shear stress (n = 8). Statistical significance between bound vMB percentage and bound cMB percentage is indicated with * ($p < 0.05$) or ** ($p < 0.01$).

Sonobactericide with vancomycin-targeted microbubbles

Biofilms grown under flow had a field-of-view coverage of 89.7% ± 10.7% (mean ± SD) (n=22 fields-of-view in 11 different μ-Slides). A typical example of a biofilm treated with sonobactericide using vMBs is shown in Fig. 11.9, where five vMBs remained attached to the biofilm (Fig. 11.9A) under flow (5 dyn/cm²) before treatment. Upon ultrasound insonification (2 MHz, 250 kPa, 5,000 cycles), all vMBs displaced resulting in a 24.0% reduction in biofilm area localized along the microbubble displacement trajectories (Fig. 11.9B). No noticeable increase in PI positive cells was observed following all treatments. Overall, biofilms treated with vMBs and a single ultrasound burst of 2 MHz, 250 kPa, and 5,000 cycles resulted in a median reduction of 19.6% (interquartile range 11.5%; Fig. 11.9C). When vMBs were exposed to 10,000 cycles (2 MHz, 250 kPa), a more consistent biofilm reduction amount was observed, with the highest being 27.6% and a median of 20.8% (interquartile range 6.3%; Fig. 11.9C), albeit not significantly different from 5,000 cycles. Both ultrasound settings in combination with vMBs resulted in significantly higher

biofilm area reduction than any of the control treatments (imaging under flow only, vMBs only, and ultrasound only). Similar low percentages (<6.3%) of biofilm area reduction occurred for all control treatments partly due to focus drift during the confocal microscopy recordings.

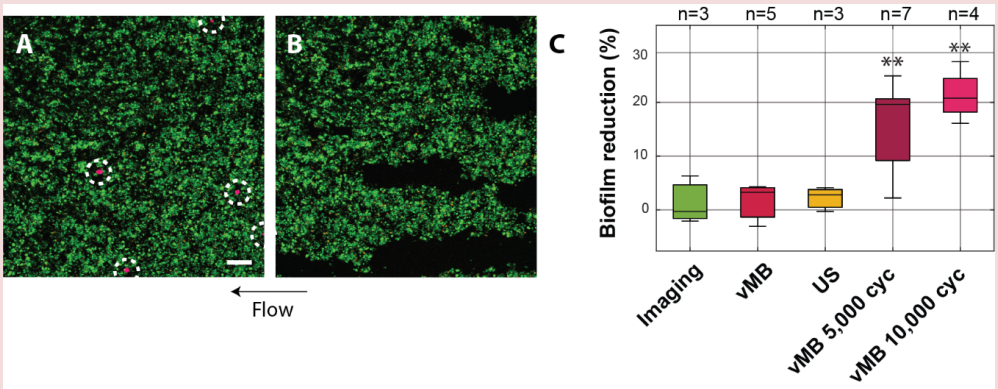

Figure 11.9. Biofilms treated under flow at 5 dyn/cm² with vancomycin-decorated microbubbles (vMB) and ultrasound. Confocal microscopy images of (A) before and (B) after sonobactericide treatment (2 MHz, 250 kPa, 5,000 cycles at 60× magnification. Live bacteria were stained with SYTO 9 (green), dead bacteria with propidium iodide (orange), and vMB with DiD (red; indicated by white dashed circles). Scale bar is 20 μm and applies to all confocal images. (C) Percentage of biofilm reduction upon treatment. Boxplots show the median, interquartile range, and the minimum to maximum values. The ultrasound (US) setting of 2 MHz, 250 kPa,10,000 cycles was used for US alone. Statistical significances between vMB in combination with US and the control treatment groups are indicated with ** ($p < 0.01$); cyc = cycles.

To visualize the effect of the sonobactericide treatment on a nanosecond time scale, Brandaris 128 ultra-high-speed camera recording was combined with time-lapse confocal microscopy. Fig. 11.10A shows an example of a selected confocal microscopy frame of a biofilm with a vMB (diameter 5.3 μm) attached under flow and before ultrasound insonification. During continuous flow, the vMB was simultaneously insonified and recorded at an ultra-high-speed (15 Mfps), where selected frames of this video can be seen in Fig. 11.10B. After ultrasound insonification, the effect of the single oscillating vMB on the biofilm was clearly visible (Fig. 11.10C), where approximately 606.1 μm² was removed, corresponding to a 3.7% total reduction in the field-of-view and 13.8% when normalized to only the areas covered with biofilm. The microbubble

oscillation amplitude was determined by tracking the microbubble excursion in each frame of the Brandaris 128 recording, resulting in a diameter range from 4.7 μm to 7.8 μm upon insonification (2 MHz, 250 kPa, 5,000 cycles). Visualizing the microbubble diameter as a function of time indicated an asymmetrical response under these acoustical parameters (Fig. 11.10E).

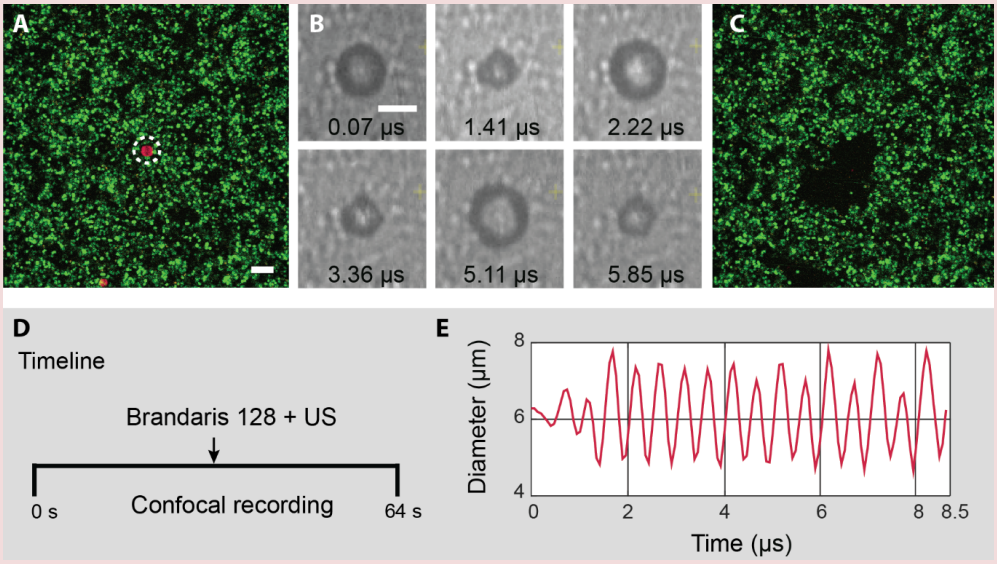

Figure 11.10. Theranostic potential of vancomycin-decorated microbubble (vMB) upon ultrasound under constant laminar flow (14.39 mL/min; 5 dyn/cm^2). (A) Initial state confocal microscopy image of a vMB (red, DiD stained; indicated by white dashed circles) bound to bacteria (green, SYTO 9 stained) before ultrasound exposure at 100× magnification. Dead bacteria were stained with propidium iodide (orange). Scale bar is 10 μm and also applies to C. (B) Selected frames of Brandaris 128 ultra-high-speed camera recordings showing the microbubble oscillating in response to a single burst of ultrasound (US; 2 MHz, 250 kPa, 5,000 cycles). Scale bar is 5 μm. (C) Corresponding confocal image after ultrasound exposure showing biofilm disruption. (D) Imaging timeline during recordings. (E) Microbubble diameter as a function of time visualizing the oscillation behavior of the microbubble during ultrasound insonification.

Discussion

In this study, a novel targeted microbubble was successfully developed based on the NHS ester chemical reaction that resulted in the coupling of the antibiotic vancomycin to the microbubble coating. Conjugation was evaluated with MALDI-TOF MS, 4Pi fluorescence microscopy, and TLC. Microbubble targeting efficiency was determined using a static binding competition assay with free vancomycin, while flow was used to examine the ability of vMBs to remain bound while exposed to increasing fluid shear stress. Furthermore, using clinically relevant bacteria-associated biofilms, ultrasound parameters, and flow, the theranostic proof-of-principle was demonstrated for the first time using a targeted microbubble and ultra-high-speed recording of the microbubble oscillation behavior under flow. Targeting microbubbles directly to biofilms has the potential to further enhance therapy and provide a diagnostic component at the same time, both of which are desperately needed.

Successful conjugation and incorporation of vancomycin

The coupling of vancomycin to the microbubble phospholipid component DSPE-PEG(3400) was done via the NHS ester functional group of the lipid and primary amine of the vancomycin. MALDI-TOF mass spectrometry confirmed successful conjugation, where the starting material only shows a peak at around 4260 Da and all conjugated samples had a second peak at ca. 5700 Da indicating the conjugate (Fig. 11.3). However, due to different isotopes of vancomycin and multiplicity of the lipid's PEG-tail, it is not possible to determine the exact ratio between starting materials and final conjugate. Nonetheless, the 4Pi microscopy data shows that the vancomycin was heterogeneously distributed over the microbubble coating after production (Fig. 11.5). Due to this heterogeneous ligand distribution, not every part of the microbubble coating can bind to bacteria. Heterogeneous ligand distributions have previously been reported for DSPC-based microbubbles[241,537]. Lipid handling prior to microbubble production[538] or different heating-cooling protocols after microbubble production[537] have been shown to alter ligand distribution to become homogeneous in DSPC-based microbubbles, but these require organic solvents or high temperatures which may compromise vancomycin functionality.

The antimicrobial property of vancomycin coupled to a microbubble coating should still be present since the binding site used to inhibit cell wall synthesis remains intact after conjugation. The overall therapeutic effect of the conjugated vancomycin alone is then only limited by the amount that is coupled and how many bacteria can bind to each microbubble. By taking into account the physical properties of both a molecule of vancomycin and a 4 μm diameter microbubble, the theoretical yield of a clinical dose of microbubbles (1×10^9)[428] with 100% labeling is 57.9 μg, and at 50% is 28.7 μg. This is extremely low when considering the clinical target serum concentration of vancomycin is 15-20 μg/mL[533,534]. Although microbubble coating coverage is crucial when considering it may increase chances of microbubble binding *in vivo,* the therapeutic enhancement effects that vMBs can provide lies more on the ultrasound-mediated microbubble behavior. This includes the potential to decrease the current dosage of vancomycin necessary for patients, which could lower the incidence of antibiotic-induced nephrotoxicity.

Successful binding of targeted microbubbles to bacteria in biofilms

vMBs successfully bound to bacteria statically (Fig. 11.6) and remained bound through increasing shear stresses of up to 12 dyn/cm^2 (Fig. 11.8). A factor that could affect vMB success is that patients are started on antibiotic therapy the moment infection is suspected, which means that the available binding sites could already be occupied before vMBs could be administered. Therefore, competition was assessed using free vancomycin concentrations ranging from 0 to 1000 μg/ml, and no significant differences were observed between 0 and 20 μg/ml, which is the clinical dose. This lends support that vMBs can still be used as a theranostic whether or not the patient is already on high-concentration antibiotic therapy. Variability was seen in the number of bound vMBs (Fig. 11.6), which partly could be explained by the heterogenous nature of biofilms and partly due to electrostatic nonspecific binding to the microchannel of the Ibidi μ-Slide (Fig.11.7). Regardless, the bound vMB groups were all significantly higher than the cMB groups. cMBs did exhibit some nonspecific binding (Fig.11.6), however this was minor. Nonspecific binding has been reported previously with non-targeted microbubbles for mammalian cells[508,539,540]. Some of this observed nonspecific binding, for example at 1.5 dyn/cm^2, could in fact be due to the natural rough, irregular surface of biofilms preventing microbubbles from moving away and requiring a certain level of flow to overcome this. cMBs binding results were different than vMBs, both in number

of microbubbles bound statically and in their ability to withstand flow. To minimize the effect heterogenous biofilms could have on the binding efficiency, both vMBs and cMBs were tested together in the experiments at a 1:1 ratio, however the ratio in the fields-of-view was found to be 0.87:1. It is possible that vMBs could have bound to bacteria potentially growing within the tubing set or inlet, and/or planktonic bacteria in the media before reaching the field-of-view within the μ-Slides resulting in the lower amount of vMBs in comparison to cMBs.

Theranostic proof-of-principle of vancomycin-decorated microbubbles

This study provides diagnostic and therapeutic proof-of-principle by showing microbubble response after ultrasound insonification. The binding of vMBs to biofilms could be used to detect early biofilm development, for which up till now no single suitable detection method is available. Using the Brandaris 128 ultra-high-speed camera, vMBs under flow were shown to exhibit nonlinear oscillation upon insonification (Fig. 11.10). This demonstrates the ability of vMBs to generate an echogenic signal that could be detected by clinical diagnostic scanners, which also utilize nonlinear behavior to differentiate ultrasound contrast agents (i.e. microbubbles) from tissue. Concerning therapeutic potential, vMBs bound to bacteria were able to significantly disrupt biofilms when exposed to ultrasound (Fig. 11.8). This conforms to other reports from sonobactericide papers where non-targeted microbubbles combined with ultrasound can have a therapeutic effect on *in vitro* and *in vivo* biofilms[304]. However, some differences in biofilm reduction exist which might be contributed to targeted microbubbles and flow. Specifically, the streak pattern and large amount of reduction caused by singular microbubbles and one pulse of ultrasound versus the craters and holes that others report by concentrated non-targeted microbubbles and different insonification schemes. Biofilm reduction was most likely caused by the microbubble oscillatory mechanical effects (Fig. 11.10), such as microstreaming in combination with flow. Regardless of the mechanism, damaged biofilms are known to become more sensitive to antibiotics[328], which could translate to shorter duration and lower dosage of antibiotics needed to achieve biofilm eradication.

Direct bacterial killing could potentially also occur and in a manner of two avenues. Firstly, the vancomycin on vMBs bound to bacteria still has the ability to kill via the same

mechanisms as free vancomycin. Secondly, ultrasound-induced microbubble behavior could enhance membrane permeabilization ultimately leading to cell death, as observed in mammalian cells[245]. The PI fluorescence stain is commonly used as a marker of cell death, as used in this study to assess the initial state of bacteria within biofilms, but also as a permeabilization marker since it is cell impermeable to intact membranes. Direct PI uptake after sonobactericide treatment was not observed in this study, supporting the minimal PI uptake also observed in Chapter 5, which suggests dispersion as the more dominant therapeutic effect. However, this could be due to bacterial cells requiring more time to die following membrane damage, than both these studies allowed, unlike mammalian cells. This is supported by other studies that report higher PI positive cell numbers but only seen by optical imaging up to hours and days after insonification[304], and dispersed cells that could have died or became more vulnerable to antibiotics cannot be tracked outside of the field-of-view. The therapeutic impact of one bound vMB is probably multifaceted, with direct and indirect consequences on both the bacteria and biofilm structure.

Limitations, considerations, and future studies

Blood flow velocities in the human body can vary depending on the vessel, condition of the heart, and many other variables. Although the maximal flow used in this *in vitro* model of 12 dyn/cm^2 is on the lower spectrum in healthy human arteries (10-70 dyn/cm^2), it is above the flow found in healthy veins (1-6 dyn/cm^2)[541]. Binding of targeted microbubbles under high shear stress conditions can be challenging. The velocity of which the microbubble is traveling along the region where it should bind might be too fast to facilitate binding. To bypass this problem, one could make use of primary acoustic radiation forces. *Dayton et al.* showed that this phenomenon could displace microbubbles towards the desired binding area *in vitro* and *in vivo*, while also significantly reducing the flow speed of these microbubbles[542]. Theoretically, this approach can increase the number of targeted microbubbles binding to biofilms and help them to remain bound. Another consideration is that the circulatory system experiences pulsatile flow with each heartbeat. The lull between each cyclical increase and decrease in flow and the forwards and backwards motion of fluid, both due to pulsatile flow, could provide enough time for vMBs to bind compared to a continuous flow state. It therefore is of interest for future studies to investigate binding under flow using ultrasound and pulsatile flow, potentially providing an even better binding profile of vMBs.

Almost all sonobactericide studies use static biofilm cultivation. For some research questions and target diseases, static biofilms are adequate. Here, static biofilms were used to test whether the vMB had more affinity to *S. aureus* biofilms in comparison with the cMB (Fig. 11.6). It was shown that vMBs bound significantly more to the biofilms. However, to also include flow-related biofilm-mediated diseases, the addition of multiple flow shear stresses to the biofilm model was pivotal. This addition, in combination with the human plasma coating, resulted in differently grown biofilms which often had a more three-dimensional structure to it than statically grown biofilms. As the flow fluid for growing and conducting experiments, a mammalian cell culture medium was used. To better estimate the full potential of vMBs, blood or other fluid per the infection disease model should also be used in future studies to understand how and if this impacts theranostic potential. One factor could be that blood viscosity dampens the microbubble response to ultrasound[36,543], which would then need to be adjusted to overcome this effect. Another factor which can also affect efficiency is plasma protein binding. For free vancomycin, this has been reported as approximately 26%[544], which could also be the case for vMBs. It is also possible that if vancomycin is administered to the patient before vMBs are infused, it could minimize the off-target binding to plasma proteins and other potential non-desired attachment. Nonetheless, experiments need to be performed in order to make this determination.

While this new approach shows promise to improve biofilm infection patient outcomes, the safety profile of vMBs should be investigated in the future to ensure do not contribute to more problems. This is specific per the location of the biofilm, for instance, bacterial dispersal and/or biofilm fragments being released into the circulation could potentially result in infarctions downstream, spread infection to distal locations, or trigger sepsis. Bacteria that are dispersed or dislodged from biofilms due to vMBs should be characterized to understand and be able to address the potential risks to be viable as a therapeutic[328]. For vMBs as a diagnostic, less risk is envisioned since the ultrasound settings used would remain on the lower spectrum not intended to induce major bioeffects, and microbubbles as contrast agents and vancomycin as an antibiotic are both already governmentally approved and used in the clinic with minimal side-effects.

Conclusion

In this study, for the first time, vMBs were produced and characterized which showed successful incorporation of the antibiotic vancomycin to the microbubble's lipid shell. Confocal microscopy revealed that vMBs were able to bind to *S. aureus* biofilms and remain attached under increasing physiological flow conditions. Significant biofilm reduction was seen upon ultrasound-activation of vMBs. The oscillation of vMBs under flow was visualized on a nanosecond time-scale using the Brandaris 128 ultra-high-speed camera. The ability of vMBs to bind to biofilms combined with the mechanical effects induced upon ultrasound insonification have promising potential to both enhance treatment and provide early diagnosis of biofilm-mediated diseases.

Acknowledgements

This work was supported by the European Research Council (ERC) under the European Union's Horizon 2020 research and innovation program (grant agreement No. 805308). The authors would like to thank Robert Beurskens and Frits Mastik from the Department of Biomedical Engineering, Michiel Manten from the Department of Experimental Medical Instrumentation, and Andi R. Sultan from the Department of Medical Microbiology and Infectious Diseases, all from the Erasmus University Medical Center Rotterdam, for their skillful technical assistance. The authors also thank the members of the Therapeutic Ultrasound Contrast Agent group (Biomedical Engineering Dept.) and the *S. aureus* working group (Medical Microbiology and Infectious Diseases Dept.) for their useful discussions.

Supplemental Information

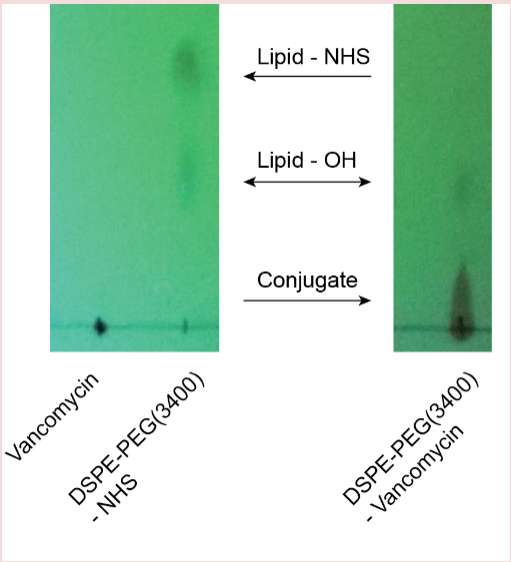

Supplemental Figure 11.1. Vancomycin coupling to the DSPE-PEG(3400)-NHS lipid. Thin-layer chromatography of compounds before coupling (left), and after coupling, dialysis, and freeze-drying (right). Lipid-NHS is DSPE-PEG(3400)-NHS; Lipid-OH is hydrolyzed DSPE-PEG(3400); conjugate is DSPE-PEG(3400)-vancomycin.

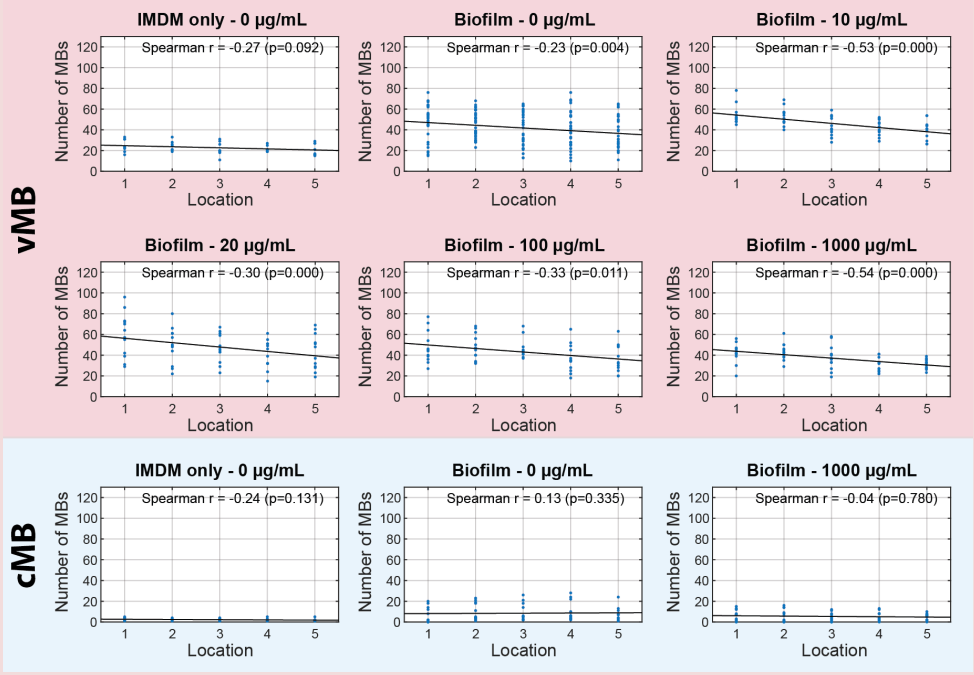

Supplemental Figure 11.2. Scatter plots visualizing the relationship between bound vancomycin-decorated microbubbles (vMB) or control microbubbles (cMB) and their location within Ibidi μ-Slides with and without biofilm and free vancomycin (0 – 1000 μg/mL). The blue circles are the experimental data points and the line representing best fit, with correlation assessed using the Spearman's correlation coefficient (r). Location 1 – 5 were equally spaced, with 1 representing near the inlet and 5 near the outlet.

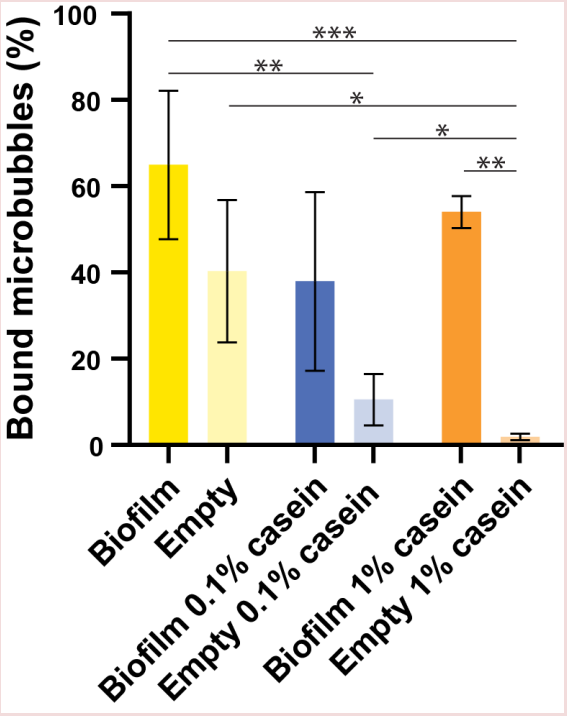

Supplemental Figure 11.3. Nonspecific binding testing of vancomycin-decorated microbubbles. Ibidi µ-Slides with and without biofilms were blocked with either 0, 0.1 % or 1% casein to bind to non-specific binding sites. Each bar represents mean with standard deviation overlaid with an n=60 locations. Statistical significance is indicated with * ($p < 0.05$), ** ($p < 0.01$) or *** ($p < 0.001$). Empty = no biofilm.

"Chance favors the prepared mind.

- Louis Pasteur

12

Summary, discussion, and contribution to science

Summary

Bacterial infections are becoming progressively more challenging to manage as we stand at the threshold of the antibiotic era. Untreatable infections threaten us again, and are only projected to increase with the vulnerable aging population and surging use of implantable life-saving technologies that create niches primed for colonization. Despite the defenses and unrelenting assaults that antibiotics and our immune system can provide, bacteria are able to successfully resist and persist when they form communities encased in a protective matrix called a biofilm. Even with the multitude of medical advancements over the last decades, mortality rates of biofilm-associated infections have barely improved and traditional antibiotic development has largely stagnated. It is therefore important to investigate alternative and adjunct therapeutic and theranostic approaches to successfully overcome life-threatening infections associated with biofilm formation, especially for those with higher risk caused by *Staphylococcus aureus* and involving the inner part of the heart called infective endocarditis. One potential approach is what we termed ***Sonobactericide***, which is the combination of ultrasound and microbubbles, with or without other therapeutics, for the treatment of bacterial infections. Microscopic gas bubbles, which are about the size of a red blood cell and coated in a layer of lipids, expand and contract (i.e. oscillate) when exposed to ultrasonic pressure waves. These oscillations can induce various well-studied mammalian cellular responses, e.g. enhanced endocytosis, membrane pore formation, and cell death, however little is known concerning bacteria/biofilm. **The primary aim of this thesis was to investigate the potential of sonobactericide as a therapeutic approach for biofilm-associated infections.**

Chapter 1 begins this thesis by setting the stage for sonobactericide by providing background interspersed with historical details on bacterial (biofilm) infection, ultrasound, and then leading into microbubbles. Sonobactericide is then extensively reviewed (27 publications) and discussed in **Chapter 2**. It highlights that a large heterogeneity and dynamic conditions exist among all aspects of sonobactericide, to include bacteria morphology, biofilm structure and inner milieu, ultrasound field in relation to disease location, and microbubble composition and behavioral responses. All of these, and more, should be taken into consideration as this new research field continues towards hopeful clinical translation.

In order to reveal the microscopic world of oscillating microbubbles and ensuing cellular effects in the same field-of-view, a novel optical imaging platform was developed, described, and demonstrated in **Chapter 3**. The coupling of the Brandaris 128 ultra-high-speed camera to a custom-built confocal microscope, used either together or separately throughout this thesis, allowed for the high spatial and temporal resolution necessary to visualize ultrasound-mediated microbubble responses. **Chapter 4** focuses on biofilm pathogenesis, demonstrating the potential of commonly used over-the-counter medications, like paracetamol in this study, to induce more resilient biofilm formation. Further genetic background appears to play a role. This highlights yet more variability that should be taken into consideration when performing biofilm research for clinical translation of not only sonobactericide, but also other therapeutic approaches.

In **Chapters 5-7**, ultrasound-activated non-targeted microbubbles were used to determine their sonobactericidal potential on biofilms grown from *S. aureus* isolated from infective endocarditis patients. **Chapter 5** studied the oscillating microbubble-induced effects of dispersion (displacement) and cell membrane permeabilization (i.e. sonoporation) on bacteria within biofilms grown in mammalian culture medium. Bacterial dispersion was the predominate phenomenon observed, with minimal sonoporation overall, and both effects enhanced by increasing the ultrasound pressure or cycles. Adding an antibiotic significantly influenced some treatment groups, with membrane compromised cells relative to all cells and dispersion increasing, and a less variable dispersal response at the highest cycle and pressure settings. In **Chapter 6,** a more cardiovascular representative biofilm with a fibrin mesh was developed by using 100% human plasma as the culture medium. Both fibrin strand bending and bacterial dispersal were observed in the ultrasound with microbubble arms, and were often accentuated and more frequent when microbubble clustering occurred. A thrombolytic combined with oscillating microbubbles led to observable fibrin strand breaking, and a different and faster fibrin dissolution pattern. To better emulate infective endocarditis pathophysiology *in vitro*, an infected human blood clot model was developed in **Chapter 7** and treated under flow. The addition of a thrombolytic and/or antibiotic to microbubbles and ultrasound resulted in almost complete clot loss after 30 minutes, and more cavitation was detected in these two groups. The majority of effluent particles were small enough to infer low potential for causing a downstream embolism.

Often, the presence of an infection is difficult to confirm until it has grown substantially. Targeting microbubbles directly and selectively to biofilms could enhance sonobactericide by providing (early-stage) infection detection capability and improving effectiveness beyond that of non-targeted bubbles, especially in challenging conditions like turbulent blood flow. **Chapters 8-9** compared non-targeted and targeted microbubbles to better understand their differences. Using various acoustical parameters in **Chapter 8,** distinguishable differences in acoustic stability and oscillatory behavior were found between bound and non-bound microbubbles. Further, these differing responses also varied depending on the main lipid in the microbubble coating. **Chapter 9** then examined targeted and non-targeted microbubble responses in relation to their influence on endothelial cells. Displacement was a large determinant of cell fate for targeted microbubbles, in that displacing resulted in reversible sonoporation and non-displacing in irreversible sonoporation, and thus death. Overall, non-targeted microbubbles induced more drug uptake than targeted microbubbles, however this trend is thought to reverse with flow conditions.

Chapters 10-11 focused solely on targeted microbubbles. Endothelial cell responses to ultrasound-activated $\alpha_V\beta_3$-targeted microbbubles were examined in **Chapter 10**. A minimum excursion amplitude for inducing sonoporation was determined, and larger amplitudes resulted in larger membrane pores. Membrane resealing was found to be independent of microbubble behavior and cell-cell contact opening occurred as a consequence of sonoporation and not mechanical microbubble effects. In **Chapter 11**, a new targeted MB was developed using the antibiotic vancomycin. It successfully bound to *S. aureus* biofilms and continued to under flow. Theranostic potential with ultrasound was demonstrated with therapeutic bacterial dispersal.

In the next part of **Chapter 12,** the main findings central to this thesis are placed into a larger context with discussion on several key topics relevant for the future perspectives of potential microbubble-mediated clinical applications.

Discussion

This thesis expands upon the limited knowledge that existed on sonobactericide at the beginning of my PhD to help pave the way for its clinical translation as an effective treatment, diagnostic, or theranostic strategy employed in infectious disease care. What becomes quickly apparent is the large heterogenicity in this line of research, both on the cellular side and acoustical side. Although a wealth of information already exists concerning mammalian cell responses to ultrasound-medicated microbubble behavior which can provide an investigative roadmap, it unfortunately cannot all be simply translated directly to bacteria and biofilms. This is partly due to the many unknowns that still exist regardless of cell type, such as controlling the microbubble responses to ultrasound or the complete cellular pathways involved once exposed to insonification and cavitating nuclei-induced effects. Nonetheless, the ensuing paragraphs will contemplate on future perspectives while touching upon broad cellular perspectives, ultrasound-induced microbubble responses, and potential concerns that may need to be addressed before clinical approval can be attained. Following this, the contributions this thesis provides towards the field of microbubble-mediated therapies is presented, thus marking the culmination of my PhD journey entitled, "Sonobactericide".

All cellular responses, whether mammalian or bacterial, are naturally intricate and complex as they strive towards the overall goal of maintaining the delicate balance for optimal functioning and survival. Thus, it is already not an easy feat to understand the operating pathways for a content cell at rest, nonetheless the ones activated when this balance is disrupted, such as by oscillating microbubbles. The development of the powerful optical-acoustical imaging system developed in **Chapter 3** afforded us the opportunity to get one step closer to unraveling these mechanistic minute cellular details in the context of responses to microbubbles. Since microbubbles are considered a blood pool agent and most commonly used for vascular applications, parts of this thesis studied the effects of ultrasound-induced microbubble behavior using the cell type that lines the entire circulatory system – the endothelial cell (**Chapters 9 and 10**). These cells are not just simply the gate keepers of the contents within the vasculature, but are critically involved in several other important multifaceted processes, such as blood flow regulation, angio- and atherogenesis, thrombosis, thrombolysis, and leukocyte involvement[545]. The other parts of this thesis used a non-mammalian cell – the

bacterium *Staphylococcus aureus* (*S.aureus*) (**Chapters 4-7**, and **Chapter 11**). *S.aureus* is a colonizer of the human skin, where approximately 20% of the population are persistent carriers, and 60% intermittently, within their anterior nasal passages[546]. *S.aureus* can become pathogenic and readily form life-threatening biofilms throughout the body (overall mortality rate ~25%)[7]. These bacteria possess an abundance of different virulent factors, physical and chemical, that aid in tissue attachment and immune system evasion, such as coagulases to convert fibrinogen into fibrin for additional protection, hemolysins to lysis red blood cells for their nutrients, and proteases that break down intercellular junctions. In this thesis, these two cells types were investigated separately allowing for moderate comparison. Combining the two, though potentially challenging, would provide an even better replicate of cardiovascular biofilms and insight into how these different cell types together respond.

The understanding of bacterial cell responses to ultrasound-mediated therapies is in its infancy when compared to mammalian cells. Even though the number of *in vitro* studies on sonobactericide is limited, already promising *in vivo* studies have been performed for several intended applications as reviewed in **Chapter 2**. This can perhaps be attributed to the knowledge that already exists on microbubble behavior from studies with mammalian cells present, and also without cells. However, bacteria are extremely different creatures, as well as also considering the vast diversity that exists within their own respective Kingdoms. Comparing just the cells in this thesis, the endothelial cell is thin/flat outside the central nucleus area and generally elongated; dimensions differ, depending on their bodily location, from 30-50 µm in length, 10-30 µm in width, and 0.1-10 µm in thickness; structure consists of a phospholipid-bilayer membrane (~10 nm thick) and strengthened by an internal microfilament network, junctions to other endothelial cells, and anchoring to a basal membrane[547]. *S. aureus* are spherical-shaped with a 0.5-1 µm diameter and can divide in two planes forming grape-like clusters; layers of peptidoglycan make-up the compact, rigid cell wall that is 20-40 nm thick and increases (> 50 nm) with antibiotic resistance[548,549]; and has a cytosolic turgor (internal osmotic pressure) of ~20 atm (2,027 kPa)[550]. It would be of interest to investigate if and how bacterial cell wall thickening and internal cellular pressure impacts sonobactericide efficiency.

The cellular differences between the two cell types can be seen within this thesis. For example, in **Chapter 10** microbubbles were insonified with a single ultrasound pulse of 2 MHz, 400 kPa (peak negative pressure) and 10 cycles which resulted in 100% sonoporation of endothelial cells, whereas in **Chapter 5** using the same transducer, frequency, and pressure but with 100 cycles and 30 pulses (repeated 10 times) only led to sonoporation of around 3% of bacteria overall. Of course this is not a perfect comparison because **Chapter 10** used targeted microbubbles, and in **Chapter 9** non-displacing microbubbles were associated with more endothelial sonoporation which was also irreversible, albeit at different settings. However, even if we look at **Chapter 11,** which used targeted microbubbles for bacteria in biofilms, minimal sonoporation was observed, although this cannot be definitively certain for all cells as the used settings (2 MHz, 250 kPa, 5,000 and 10,000 cycles) led to cell displacement. Bacteria are much more easily dispersed as clearly observed in **Chapters 5-7 and Chapter 11,** where in **Chapter 9 and 10** this was not observed, even at the highest setting of 500 kPa, 50,000 cycles. Although these comparisons are imperfect, they provide support and allude that the ultrasound parameters and microbubble behavior that induce cellular effects in endothelial cells cannot be directly translated to *S. aureus,* and most likely other bacteria. It is possible though that bacteria having a different morphology may respond more similarly to endothelial cells, such as the rod-shape, larger size (2 µm length; up to 1 µm width), thinner cell wall structure (4 nm; monolayered peptidoglycan) of a *Escherichia coli* bacterium with a lower cytosolic turgor of ~5-6 atm (506 - 608 kPa)[551,552]. Regardless, this highlights that further investigations, from modeling to *in vivo* studies, are necessary to determine the best settings for optimal microbubble-mediated therapy per the given cellular circumstances.

When developing a novel targeted microbubble, such as the vancomycin-decorated microbubbles for binding to bacteria in **Chapter 11**, many design aspects need to be considered in order to obtain the optimal product to best achieve the desired goal. One such consideration is the lipid used in the coating, which two were investigated for their impact on the vibrational responses of microbubbles in **Chapter 8**. The main finding were that DSPC-based microbubbles were acoustically more stable than DPPC-based bubbles, including with increasing acoustic pressure. This supported the choice to use DSPC for all studies using in-house produced microbubbles in this thesis. In the study of Kooiman *et al.* (2014), the DPPC-based coating was favored for targeting because

of the increased binding area, homogenous ligand distribution, and the dome-shape that is thought to better withstand flow shear over spherical-shaped microbubbles[241]. Unfortunately this means choosing for either lipid is a compromise, and it could be that different lipid-coatings may be better suited for some applications than others, such as ones involving flow. It is possible that the vancomycin-decorated microbubbles developed in Chapter 11, which are DSPC-based but use DSPE-PEG(3400) instead of the DSPE-PEG(2000) and have a different ligand-biomarker pair than **Chapter 8** and Kooiman *et al.* (2014)[241], may have different acoustical responses and binding efficiency. Further investigations, such as with acoustical spectroscopy, could help determine if there is a more optimal formulation while keeping the intended application in mind, as this may already be the most suitable. If using DPPC is found to produce less acoustically stable bacteria-targeted microbubbles and ligand distribution is the crucial element for binding and sonobactericide efficiency, which may be different for environments with and without flow, it is possible other production methods could be incorporated that have been shown to induce a more homogeneous distribution, such as with lipid handling[538] or temperature[537] before and/or after microbubble production. However, these methods may need to be adjusted to ensure vancomycin, or other targeting ligand, is not inactivated in the process. Another investigative avenue that may enhance functionality of these and other targeted-microbubbles designed for sonobactericide could be found in a dual-targeting approach, which has been shown to be favorable over a single-targeted approach for microbubbles targeted to mammalian cells[553].

Endothelial cell work involving the mechanistic study of responses to contrast agents largely involves healthy endothelium, including this thesis. While this is important, a large cohort exists world-wide with some sort of cardiovascular disease, and this is only projected to increase with an aging population and growing prevalence in obesity. Many cardiovascular diseases, as well as cancer and bacterial infections, are related to endothelial dysfunction, either as the causative agent or a byproduct[545]. Further, this dysfunction also varies depending on the disease, with one or more of the normal healthy functions affected. **Chapter 10** hints toward cellular response differences, since the initial state of cells already leads to variability in susceptibility to ultrasound-induced microbubble treatment. The endothelial cells used in this thesis that exhibited partial junctions better represent the endothelium encased in biofilm than those with full

junctions due to the cellular dysfunction caused by biofilm presence and the bacterial proteases secreted that degrade cell-cell contact integrity. Based on **Chapter 10,** these endothelial cells connected to infection would be more likely to sonoporate and/or retract due to ultrasound and microbubbles. Further, endothelial cells exhibiting dysfunction may respond to targeted and non-targeted microbubbles contrarily or at varying degrees to the healthy cell responses seen in **Chapter 9**. Future work should include investigations using diseased endothelial cells, and in different diseased states, to understand how these physiological abnormalities impact cellular and cavitation nuclei responses in an ultrasound field down to the intracellular pathway level. Furthermore, using bacteria to induce the disease state per the desired infection model would be beneficial Unraveling these unknowns would allow for the most efficient utilization of microbubble-mediated therapy tailored to the intended application and patient profile, regardless of whether the goal is drug delivery, biofilm disruption, or direct cell (e.g., bacteria or tumor) killing.

For sonobactericide to be a viable theranostic tool for the clinic, assessing safety is a critical step for future success. Though different infected areas of the body will have varying risks to assess, the therapeutic promise of sonobactericide via bacteria dispersed out of biofilms also has the potential to hinder overall success for several infected organ systems[328]. **Chapters 5-7** and **Chapter 11** show sonobactericide-induced disruption of different types of biofilm all leading to dispersal, which has also been observed post-treatment by others groups as reviewed in **Chapter 2**. It should be noted that chemical and physical bacterial dispersion/biofilm detachment occurs naturally, such as by changes in the micro-environment of a biofilm progressing in maturity that prompts the releasement of matrix degrading enzymes or erosion/sloughing due to fluid shear stress as observed with endovascular biofilms[328,554]. For some infection locations, for example superficially on the skin and in the urinary tract, biofilm disruption may be less of a danger than for others, such as within the cardiovascular system that grants access to the entire body. Here biofilm detachment could with seemingly relative ease lead to metastatic infections and/or down-stream emboli. Another concern, not only for the cardiovascular system, is the triggering of sepsis, which is a severe dysregulated bodily response that can lead to multiorgan failure and has a clinical mortality of 28-43%[555-557]. Septicemia has been reported in an *in vivo* wound infection mouse model after administration of a chemical

dispersal agent[558], but not for physical biofilm disruption studies as of yet[328]. Currently, none of the three negative post-treatment outcomes mentioned have been reported in *in vivo* sonobactericide studies[304]. Though this is promising, the differences in outcome compared to chemical dispersal could potentially be due to a range of factors, such as the degree and/or rate of bacterial dispersal, antibiotic susceptibility of liberated bacteria, or length of post-treatment follow-up, and should be further investigated. There already exist several strategies/technologies that could be used to prevent and/or combat these concerns if proven viable, which some are touched upon in **Chapter 2.** In the case of the septicemia induced by chemical-induced dispersion, a co-administration of an antibiotic was able to prevent this outcome and even led to infection resolution[558]. However, Wille and Coenye (2020) point out that although antibiotic addition was successful for this model, other studies show that this may not be the case for all situations and the method of dispersal and corresponding antibiotic will be critical determinants on whether septicemia can be prevented or not[328].

Outside of these dispersal induced concerns, is also the potential deleterious issue of lethal mammalian cell toxicity in target cells containing intercellular bacteria or near-by healthy cells, as an unintended off-target problem for sonobactericide. This most likely would be caused by the ultrasound-induced microbubble effects leading to synergistic drug responses and/or increases in cell membrane permeability exposing these non-intended cell targets to lethal doses which would otherwise not be toxic. This was observed in a sonobactericide study using an intracellularly infected human bladder cell organoid model of urinary tract infection, where ultrasound-activated microbubbles alone (dose-dependent) had an approximate two-fold higher cytotoxic effect in bladder cells than a free antibiotic therapeutic dose alone, and for microbubbles coated with liposomes containing an almost 100-fold less antibiotic dose resulted in a three-fold cytotoxicity increase[70]. For infective endocarditis, depending on (pre-existing) physiological circumstances and the infecting microbe, bacteria not only adhere to, but can also be internalized by or invade endothelial cells[43]. If cytotoxicity is properly evaluated per the specific infection to treat, potential off-target lethal side-effects can be properly addressed by choosing parameters that are within acceptable safe levels preserving tissue, as the urinary tract infection sonobactericide study went on to do.

I envision sonobactericide in the clinic to be a non-invasive theranostic strategy, where patients suspected of a bacterial infection can receive a definitive diagnosis using broad-spectrum biofilm/bacteria-targeted microbubbles, and then in the same setting receive treatment with ultrasound-activated cavitation nuclei. The larger aim of sonobactericide is to reduce, if not eliminate, the uncertainty that currently exists with bacterial infection diagnosis and management. Less uncertainty should translate to earlier diagnosis requiring less diagnostic modalities and enhance antimicrobial success with lower therapeutic dosages to eliminate side-effects and lower mortality for overall patient life improvement. To be an effective strategy, sonobactericide may still require some complements, such as blood culture and antimicrobials, or open the door to currently contraindicated therapeutics, e.g., thrombolytics for adults with infective endocarditis, by local delivery via microbubbles and/or reduced dosages due to sonobactericide synergistic effects.

Sonobactericide, in theory, could be applied anywhere in the body an infection exists. That means to move towards clinical trials, safety will need to be evaluated and best strategy determined per the specific application, such as initial dosages and types(s) of cavitation nuclei, complements, and acoustical parameters. In the face of those challenges that are already present and the ones yet to reveal themselves, it is not to say that sonobactericide may already be a viable option. Drugs and diagnostics often still have many unknowns when entering clinical trials, and even remain that way through and after approval because their net positive improvement overrides the "black box" effect. Even if this would be the case for sonobactericide, it is still of the utmost importance that research continues not only for maximizing diagnostic and therapeutic outcome which is tailored to each disease and pathogen, but also to predict and overcome every potential challenge face-on with the best possible solution. This approach is aligned with the viewpoint of Louis Pasteur, the world-renowned French microbiologist who forever changed how we approach infection by definitively proving that pathogenic microorganisms (germs) cause disease (and not spontaneous generation or bad air), who said, "Chance favors the prepared mind".

Contribution to science

The contribution to science provided by the work within this thesis is severalfold. The extensive review of the current literature provides the scaffold on which future sonobactericide investigations can be built upon. With the development of a powerful new system by coupling two state-of-the-art, custom-built technologies, nanometer spatial and nanosecond temporal resolution imaging can now be accomplished in the same field-of-view of a single sample; this has expanded, and will continue to do so, our knowledge on how ultrasound-mediated microbubble behavior directly impacts both cells and their surroundings. Commonly used over-the-counter medicines may alter biofilm development, as paracetamol was seen to enhance virulence in this thesis, which highlights an important consideration for future research because this may affect theranostic capabilities and outcomes.

For the first time, microbubble behavior was observed in real-time and at high-resolution to directly lead to several anti-biofilm effects. Sonobactericide potential was demonstrated on four different *in vitro* biofilm models, three of which were developed in this thesis with two designed to replicate intravascular biofilms and one replicating biofilms grown in flow environments. Observed sonobactericide effects that could enhance therapy includes biofilm disruption with bacterial dispersal, sonoporation (membrane permeabilization), fibrin strand manipulation (bending, recovery, and breaking), and synergistic responses when a thrombolytic and/or antibiotic were present, all lending support for continued research. Through comparing targeted and non-targeted microbubbles, several acoustical and binding differences/advantages of two lipid-based microbubble coatings were observed that can aid decision making in new microbubble design. Additionally, certain microbubble responses corresponding with cell viability were found to occur more frequently within a given set of acoustic parameters, which provides valuable insight towards optimizing microbubble-mediated therapies per the goal of either viable drug delivery or direct mammalian cell death.

The investigation of microbubbles targeted to endothelial cells using high-sensitivity imaging revealed initial cell integrity affecting treatment outcomes. Since various diseases can affect cellular status to different degrees, this highlights the importance of

future experimental designs needing to use cells that are in the appropriate disease-state per the intended therapeutic application. Additionally, this study also discovered that cell-cell contact opening is not a separate drug-delivery pathway from sonoporation, but is a consequence of it and not directly related to specific microbubble behavior. A novel targeted microbubble for gram-positive biofilm infections, that is non-immunogenic by using the antibiotic vancomycin, was successfully developed, and observed to remain bound under flow and lead to biofilm disruption upon ultrasound insonification. This not only provides support of the true potential of sonobactericide to definitively detect these often difficult to diagnose infections and with the same microbubble be able to produce therapeutic effects, but may also inspire others to develop novel targeted microbubbles for infectious diseases.

The impressive potential of something so small, the microbubble, combined with the power of sound to solve a truly vast dynamic range of challenges and improve upon and beyond the current existing technologies and therapies for the betterment of all life on earth, speaks to its extraordinary versatility and strength that will indubitably echo well into the future. Therefore, it is clear, as is the hallmark of investigative science, that as knowledge is expanded upon more questions arise, and the adventure should surely continue beyond the work presented here upon these pages.

"If you talk to a man in a language he understands, that goes to his head. If you talk to him in his language, that goes to his heart.

- Nelson Mandela

Nederlandse Samenvatting

Het behandelen van bacteriële infecties wordt steeds uitdagender, aangezien we bijna het plafond van onze antibiotische mogelijkheden bereikt hebben. Onbehandelbare infecties bedreigen ons opnieuw en zullen naar verwachting alleen maar toenemen door de kwetsbare vergrijzende bevolking en het stijgende gebruik van implanteerbare levensreddende technologieën, die niches creëren die gevoelig zijn voor kolonisatie. Ondanks de afweer en de niet aflatende aanvallen die antibiotica en ons immuunsysteem kunnen bieden, zijn bacteriën in staat om met succes weerstand te bieden en te volharden wanneer ze groepen vormen die zijn ingekapseld in een beschermende matrix, genaamd biofilm. Zelfs met de grote medische vooruitgang in de afgelopen decennia zijn de sterftecijfers van biofilm-gerelateerde infecties nauwelijks verbeterd en de ontwikkeling van traditionele antibiotica is grotendeels gestagneerd. Het is daarom belangrijk alternatieve en aanvullende therapeutische en theragnostische aanpakken te onderzoeken om met succes levensbedreigende infecties, geassocieerd met de vorming van een biofilm, te overwinnen. Dit is vooral belangrijk voor mensen met een verhoogd risico veroorzaakt door *Staphylococcus aureus* en waarbij het binnenste deel van het hart betrokken is, infectieuze endocarditis genaamd. Een mogelijke aanpak is wat we ***Sonobactericide*** hebben genoemd. Dat is de combinatie van ultrageluid en microbellen, met of zonder andere medicijnen, voor de behandeling van bacteriële infecties. Microscopische gasbellen, die ongeveer zo groot zijn als een rode bloedcel en een vetlaag als schil hebben, zetten uit en trekken samen (d.w.z. oscilleren) wanneer ze worden blootgesteld aan ultrageluid drukgolven. Deze oscillaties kunnen verschillende goed bestudeerde reacties in cellen van zoogdieren induceren, b.v. verbeterde endocytose, vorming van membraanporiën en celdood, maar er is weinig bekend over het effect op bacteriën/biofilm. **Het hoofddoel van dit proefschrift was het onderzoeken van de mogelijkheid om van Sonobactericide een therapeutische behandeling voor biofilm-gerelateerde infecties te maken.**

Dit proefschrift begint met **Hoofdstuk 1** waarin Sonobactericide geïntroduceerd wordt door achtergrondinformatie af te wisselen met historische details over bacteriële (biofilm) infecties en ultrageluid, om vervolgens uit te komen bij microbellen. Sonobactericide wordt vervolgens uitgebreid gereviewd (27 publicaties) en besproken in **Hoofdstuk 2.** Daarin komt naar voren dat er een grote dynamische verscheidenheid bestaat tussen alle aspecten van Sonobactericide, waaronder bacteriemorfologie,

biofilmstructuur en inwendige omstandigheden, echografisch veld in relatie tot ziektelocatie en microbelcompositie en microbelgedrag. Met al deze factoren en meer moet rekening worden gehouden in de ontwikkeling van dit nieuwe onderzoeksveld tot een veelbelovende nieuwe behandelmethode voor patiënten.

Om de microscopische wereld van oscillerende microbellen en de daaropvolgende effecten op de cellen in hetzelfde gezichtsveld in beeld te brengen, werd er een nieuw optisch beeldvormingsplatform ontwikkeld, beschreven en gedemonstreerd in **Hoofdstuk 3**. De koppeling van de Brandaris 128 ultrahogesnelheidscamera aan een op maat gemaakte confocale microscoop, die samen of afzonderlijk werden gebruikt in dit proefschrift, zorgde voor de hoge ruimtelijke en temporele resolutie die nodig is om door ultrageluid gemedieerde microbelreacties te visualiseren. **Hoofdstuk 4** richt zich op de biofilmpathogenese en toont het potentieel van veelgebruikte, vrij verkrijgbare medicijnen, zoals paracetamol in deze studie, om een meer veerkrachtige biofilmvorming mogelijk te maken. Ook lijkt de genetische achtergrond een rol te spelen. Dit benadrukt dat er nog meer verschillen zijn waarmee rekening moet worden gehouden bij het uitvoeren van biofilmonderzoek voor klinische toepassingen. Dit geldt zowel voor Sonobactericide, als ook voor andere therapeutische aanpakken.

In de **hoofdstukken 5-7** werden met ultrageluid geactiveerde niet-getargete microbellen gebruikt om hun Sonobactericide potentieel te bepalen op biofilms van *S. aureus*, geïsoleerd uit patiënten met infectieuze endocarditis. **Hoofdstuk 5** bestudeerde de door oscillerende microbellen veroorzaakte effecten van dispersie (verplaatsing) en permeabilisatie van celmembranen (d.w.z. sonoporatie) op bacteriën in biofilms die werden gekweekt in kweekmedium voor zoogdiercellen. Bacteriële dispersie was het belangrijkste waargenomen fenomeen, met in het algemeen minimale sonoporatie. Beide effecten werden versterkt door het verhogen van de druk of het aantal cycli van het ultrageluid. Het toevoegen van een antibioticum beïnvloedde sommige behandelingsgroepen significant, met een verhoogde dispersie en membraan-aangetaste cellen ten opzichte van alle cellen, en een minder variabele dispersierespons bij de hoogste cyclus- en drukinstellingen. In **Hoofdstuk 6** werd een meer cardiovasculair representatieve biofilm met een fibrinenetwerk ontwikkeld door 100% menselijk plasma

te gebruiken als kweekmedium. Zowel buiging van fibrinestrengen als bacteriële verspreiding werden waargenomen in de 'ultrageluid met microbellen' groepen. Dit werd vaak geaccentueerd en kwam vaker voor wanneer clustering van microbellen optrad. Een trombolyticum gecombineerd met oscillerende microbellen leidde tot zichtbare breuk van de fibrinestreng en een ander en sneller oplossingspatroon van fibrine. Om de pathofysiologie van infectieuze endocarditis in het laboratorium beter na te bootsen, werd in **Hoofdstuk 7** een geïnfecteerd menselijk bloedstolselmodel ontwikkeld en onder stroming behandeld. De toevoeging van een trombolyticum en/of antibioticum aan microbellen en ultrageluid resulteerde in een bijna volledig verdwijnen van het stolsel na 30 minuten, en meer cavitatie werd gedetecteerd in deze twee groepen. De meeste van de weggevoerde deeltjes waren klein genoeg om maar weinig risico op een bloedstroomafwaartse embolie te veroorzaken.

Vaak is de aanwezigheid van een infectie moeilijk te bevestigen totdat deze aanzienlijk is gegroeid. Door microbellen direct en selectief op biofilms te richten (d.w.z. te targeten), zou Sonobactericide kunnen worden verbeterd, doordat ze hierdoor mogelijk infecties (in een vroeg stadium) kunnen opsporen. Ze zouden effectiever zijn dan niet-getargete microbellen, vooral in uitdagende omstandigheden zoals een turbulente bloedstroom. In de **hoofdstukken 8-9** werden niet-getargete en getargete microbellen vergeleken om hun verschillen beter te kunnen begrijpen. Met behulp van verschillende akoestische parameters werden in **Hoofdstuk 8** duidelijke verschillen in akoestische stabiliteit en oscillerend gedrag gevonden tussen gebonden en niet-gebonden microbellen. Verder varieerden deze verschillende reacties ook afhankelijk van het belangrijkste lipide in de schil van de microbellen. **Hoofdstuk 9** onderzocht vervolgens de reacties van getargete en niet-getargete microbellen in relatie tot hun invloed op endotheelcellen. Verplaatsing was een grote bepalende factor van het lot van de cel bij getargete microbellen, in die zin dat verplaatsing resulteerde in omkeerbare sonoporatie en niet-verplaatsing in onomkeerbare sonoporatie, en dus celdood. Over het algemeen bewerkstelligden niet-getargete microbellen meer medicijnopname dan getargete microbellen, maar er wordt verwacht dat dit andersom is onder stroming.

Hoofdstukken 10-11 concentreerden zich uitsluitend op getargete microbellen. Endotheelcelreacties op door ultrageluid geactiveerde $\alpha_v\beta_3$-getargete microbellen

werden onderzocht in **Hoofdstuk 10**. Een minimale excursie-amplitude voor het veroorzaken van sonoporatie werd bepaald, en grotere amplituden resulteerden in grotere membraanporiën. Het hersluiten van membranen bleek onafhankelijk te zijn van het gedrag van microbellen en het openen van cel-celcontact trad op als gevolg van sonoporatie en niet als gevolg van het mechanische effect van microbellen. In **Hoofdstuk 11** werd een nieuwe getargete microbel ontwikkeld met het antibioticum vancomycine. De microbel bond met succes aan *S. aureus* biofilms en bleef gebonden onder stroming. Theragnostische mogelijkheden werd aangetoond met therapeutische bacteriële dispersie. Ten slotte worden in **Hoofdstuk 12** de belangrijkste bevindingen die centraal staan bij Sonobactericide in een grotere context geplaatst. Besproken worden verschillende belangrijke onderwerpen met betrekking tot toekomstige klinische mogelijkheden.

Dit proefschrift bouwt voort op de beperkte kennis die bestond over Sonobactericide om de weg vrij te maken voor de klinische vertaling ervan als een effectieve behandelings-, diagnostische of theragnostische strategie die wordt gebruikt in de zorg voor infectieziekten. Toch is het duidelijk, en dat is het kenmerk van de onderzoeks-wetenschap, dat naarmate veelbelovende kennis wordt verworven, er meer vragen rijzen, en het avontuur zou zeker verder moeten gaan dan het werk dat hier op deze pagina's wordt gepresenteerd.

References

[1] R. Sender, S. Fuchs, and R. Milo, "Revised estimates for the number of human and bacteria cells in the body," bioRxiv, p. 036103, 2016.

[2] T. Yingchoncharoen, "Infective Endocarditis," in an atlas of mitral valve imaging, M. Desai, C. Jellis, and T. Yingchoncharoen, Eds. London: Springer London, pp. 147-170, 2015.

[3] M. Lobanovska and G. Pilla, "Penicillin's discovery and antibiotic resistance: lessons for the future?," The Yale Journal of Biology and Medicine, vol. 90, no. 1, pp. 135-145, 2017.

[4] H.F. Chambers, "The changing epidemiology of *Staphylococcus aureus*?," Emerg Infect Dis, vol. 7, no. 2, pp. 178-182, 2001.

[5] G.D. Wright, "Q&A: Antibiotic resistance: where does it come from and what can we do about it?," BMC Biology, vol. 8, pp. 123-123, 2010.

[6] National Institutes of Health. NIH research on microbial biofilms. Available: http://grants.nih.gov/grants/guide/pa-files/PA-03–047.html.

[7] N.K. Archer, M.J. Mazaitis, J.W. Costerton, J.G. Leid, M.E. Powers, and M.E. Shirtliff, "*Staphylococcus aureus* biofilms: properties, regulation, and roles in human disease," Virulence, vol. 2, no. 5, pp. 445-459, 2011.

[8] A. Leewenhoeck, "An abstract of a letter from Mr. Anthony Leevvenhoeck at Delft, dated Sep. 17. 1683. Containing some microscopical observations, about animals in the scurf of the teeth, the substance call'd worms in the nose, the cuticula consisting of scales," Philosophical Transactions of the Royal Society of London, vol. 14, no. 159, pp. 568-574, 1683.

[9] J.C. Nickel, I. Ruseska, J.B. Wright, and J.W. Costerton, "Tobramycin resistance of *Pseudomonas aeruginosa* cells growing as a biofilm on urinary catheter material," Antimicrob Agents Chemother, vol. 27, no. 4, pp. 619-624, 1985.

[10] N. Lane, "The unseen world: reflections on Leeuwenhoek (1677) 'Concerning little animals'," Philosophical transactions of the Royal Society of London. Series B, Biological Sciences, vol. 370, no. 1666, p. 20140344, 2015.

[11] J. Penterman et al., "Rapid evolution of culture-impaired bacteria during adaptation to biofilm growth," Cell Reports, vol. 6, no. 2, pp. 293-300, 2014.

[12] J.F. González, M.M. Hahn, and J.S. Gunn, "Chronic biofilm-based infections: skewing of the immune response," Pathog Dis, vol. 76, no. 3, p. fty023, 2018.

[13] L. Jackson, O. Kroukamp, and G. Wolfaardt, "Effect of carbon on whole-biofilm metabolic response to high doses of streptomycin," Front Microbiol, vol. 6, no. 953, 2015.

[14] N. Cerca et al., "Comparative assessment of antibiotic susceptibility of coagulase-negative staphylococci in biofilm versus planktonic culture as assessed by bacterial enumeration or rapid XTT colorimetry," J Antimicrob Chemother, vol. 56, no. 2, pp. 331-336, 2005.

[15] T. Bjarnsholt, "The role of bacterial biofilms in chronic infections," APMIS Suppl, no. 136, pp. 1-51, 2013.

[16] V.J. Savage, I. Chopra, and A.J. O'Neill, "*Staphylococcus aureus* biofilms promote horizontal transfer of antibiotic resistance," Antimicrob Agents Chemother, vol. 57, no. 4, pp. 1968-1970, 2013.

[17] X. Zhao, Z. Yu, and T. Ding, "Quorum-sensing regulation of antimicrobial resistance in bacteria," Microorganisms, vol. 8, no. 3, p. 425, 2020.

[18] M. McFall-Ngai, "Care for the community," Nature, vol. 445, no. 7124, pp. 153-153, 2007.

[19] S.Y. Tong, J.S. Davis, E. Eichenberger, T.L. Holland, and V.G. Fowler, Jr., "*Staphylococcus aureus* infections: epidemiology, pathophysiology, clinical manifestations, and management," Clin Microbiol Rev, vol. 28, no. 3, pp. 603-61, 2015.

[20] M. Peetermans, P. Verhamme, and T. Vanassche, "Coagulase activity by *Staphylococcus aureus*: a potential target for therapy?," Semin Thromb Hemost, vol. 41, no. 4, pp. 433-44, 2015.

[21] T.J. Cahill and B.D. Prendergast, "Infective endocarditis," The Lancet, vol. 387, no. 10021, pp. 882-893, 2016.

[22] R.M. Donlan, "Biofilms on Central Venous Catheters: Is Eradication Possible?," in Bacterial Biofilms, T. Romeo, Ed. Berlin, Heidelberg: Springer Berlin Heidelberg, pp. 133-161, 2008.

[23] M.L. Gaynor, Sounds of healing: A physician reveals the therapeutic power of sound, voice, and music. New York: Broadway Books, 1999.

[24] D. Neumann and E. Kollorz, "Ultrasound," in Medical Imaging Systems: An Introductory Guide, A. Maier, S. Steidl, V. Christlein, and J. Hornegger, Eds. Cham (CH), pp. 237-249, 2018.
[25] K.B. Bader, E. Vlaisavljevich, and A.D. Maxwell, "For whom the bubble grows: physical principles of bubble nucleation and dynamics in histotripsy ultrasound therapy," Ultrasound Med Biol, vol. 45, no. 5, pp. 1056-1080, 2019.
[26] M.C. Fyfe and M.I. Bullock, "Therapeutic ultrasound: some historical background and development in knowledge of its effect on healing," Aust J Physiother, vol. 31, no. 6, pp. 220-224, 1985.
[27] R.W. Wood and A.L. Loomis, "The physical and biological effects of high-frequency sound waves of great intensity," The Philosophical Magazine and Journal of Science, vol. 4, pp. 417-436, 1927.
[28] M. Dyson, "Non-thermal cellular effects of ultrasound," Br J Cancer, vol. 5, pp. 165-171, 1982.
[29] J. Li et al., "Ultrasound-induced *Escherichia coli* O157:H7 cell death exhibits physical disruption and biochemical apoptosis," Front Microbiol, vol. 9, p. 2486, 2018.
[30] M. Erriu et al., "Microbial biofilm modulation by ultrasound: current concepts and controversies," Ultrason Sonochem, vol. 21, no. 1, pp. 15-22, 2014.
[31] Y. Cai, J. Wang, X. Liu, R. Wang, and L. Xia, "A review of the combination therapy of low frequency ultrasound with antibiotics," Biomed Res Int, p. 2317846, 2017.
[32] H. Yu, S. Chen, and P. Cao, "Synergistic bactericidal effects and mechanisms of low intensity ultrasound and antibiotics against bacteria: a review," Ultrason Sonochem, vol. 19, no. 3, pp. 377-82, 2012.
[33] W.G. Pitt, M.O. McBride, J.K. Lunceford, R.J. Roper, and R.D. Sagers, "Ultrasonic enhancement of antibiotic action on gram-negative bacteria," Antimicrob Agents Chemother, vol. 38, no. 11, pp. 2577-82, 1994.
[34] K. Kooiman et al., "Ultrasound-responsive cavitation nuclei for therapy and drug delivery," Ultrasound Med Biol, vol. 46, no. 6, pp. 1296-1325, 2020.
[35] T. van Rooij, V. Daeichin, I. Skachkov, N. de Jong, and K. Kooiman, "Targeted ultrasound contrast agents for ultrasound molecular imaging and therapy," Int J Hyperth, vol. 31, no. 2, pp. 90-106, 2015.
[36] K. Kooiman, H.J. Vos, M. Versluis, and N. de Jong, "Acoustic behavior of microbubbles and implications for drug delivery," Adv Drug Deliv Rev, vol. 72, pp. 28-48, 2014.
[37] J.T. Sutton, K.J. Haworth, G. Pyne-Geithman, and C.K. Holland, "Ultrasound-mediated drug delivery for cardiovascular disease," Expert Opin Drug Deliv, vol. 10, no. 5, pp. 573-92, 2013.
[38] S. Wang, J.A. Hossack, and A.L. Klibanov, "Targeting of microbubbles: contrast agents for ultrasound molecular imaging," J Drug Target, vol. 26, no. 5-6, pp. 420-434, 2018.
[39] J.J. Black, F.T.H. Yu, R.G. Schnatz, X. Chen, F.S. Villanueva, and J.J. Pacella, "Effect of thrombus composition and viscosity on sonoreperfusion efficacy in a model of micro-vascular obstruction," Ultrasound Med Biol, vol. 42, no. 9, pp. 2220-2231, 2016.
[40] I. Rosenthal, J.Z. Sostaric, and P.Riesz, "Sonodynamic therapy—a review of the synergistic effects of drugs and ultrasound," Ultrason Sonochem, vol. 11, no. 6, pp. 349-363, 2004.
[41] A. Algburi, N. Comito, D. Kashtanov, L.M.T. Dicks, and M.L. Chikindas, "Control of biofilm formation: antibiotics and beyond," Appl Environ Microbiol, vol. 83, no. 3, pp. e02508-16, 2017.
[42] S.S. Grant and D.T. Hung, "Persistent bacterial infections, antibiotic tolerance, and the oxidative stress response," Virulence, vol. 4, no. 4, pp. 273-283, 2013.
[43] K. Werdan et al., "Mechanisms of infective endocarditis: pathogen–host interaction and risk states," Nat Rev Cardiol, vol. 11, no. 1, pp. 35-50, 2014.
[44] N. Vyas et al., "Which parameters affect biofilm removal with acoustic cavitation? A review," Ultrasound Med Biol, vol. 45, no. 5, pp. 1044-1055, 2019.
[45] P. Anastasiadis, K.D.A. Mojica, J.S. Allen, and M.L. Matter, "Detection and quantification of bacterial biofilms combining high-frequency acoustic microscopy and targeted lipid microparticles," J Nanobiotechnology, vol. 12, no. 1, p. 24, 2014.
[46] F. Cavalieri, M. Ashokkumar, F. Grieser, and F. Caruso, "Ultrasonic synthesis of stable, functional lysozyme microbubbles," Langmuir, vol. 24, no. 18, pp. 10078-10083, 2008.
[47] F. Cavalieri et al., "Antimicrobial and biosensing ultrasound-responsive lysozyme-shelled microbubbles," ACS Appl Mater Interfaces, vol. 5, no. 2, pp. 464-471, 2013.

[48] M. Zhou, F. Cavalieri, and M. Ashokkumar, "Modification of the size distribution of lysozyme microbubbles using a post-sonication technique," Instrum Sci Tech, vol. 40, no. 1, pp. 51-60, 2012.

[49] S. Mahalingam, Z. Xu, and M. Edirisinghe, "Antibacterial activity and biosensing of pva-lysozyme microbubbles formed by pressurized gyration," Langmuir, vol. 31, no. 36, pp. 9771-9780, 2015.

[50] M. Argenziano et al., "Vancomycin-loaded nanobubbles: A new platform for controlled antibiotic delivery against methicillin-resistant *Staphylococcus aureus* infections," Int J Pharm, vol. 523, no. 1, pp. 176-188, 2017.

[51] F. Cavalieri, M. Zhou, M. Tortora, B. Lucilla, and M. Ashokkumar, "Methods of preparation of multifunctional microbubbles and their *in vitro / in vivo* assessment of stability, functional and structural properties," Curr Pharm Des, vol. 18, no. 15, pp. 2135-51, 2012.

[52] D.T. Kysela, A.M. Randich, P.D. Caccamo, and Y.V. Brun, "Diversity takes shape: Understanding the mechanistic and adaptive basis of bacterial morphology," PloS Biol, vol. 14, no. 10, p. e1002565, 2016.

[53] B.H.T. Goh et al., "High-speed imaging of ultrasound-mediated bacterial biofilm disruption," in 6th European Conference of the International Federation for Medical and Biological Engineering, Cham, 2015, pp. 533-536: Springer International Publishing.

[54] M. Wang, Y. Zhang, C. Cai, J. Tu, X. Guo, and D. Zhang, "Sonoporation-induced cell membrane permeabilization and cytoskeleton disassembly at varied acoustic and microbubble-cell parameters," Sci Rep, vol. 8, no. 1, p. 3885, 2018.

[55] M. Overvelde, V. Garbin, B. Dollet, N. de Jong, D. Lohse, and M. Versluis, "Dynamics of coated microbubbles adherent to a wall," Ultrasound Med Biol, vol. 37, no. 9, pp. 1500-1508, 2011.

[56] T. van Rooij, I. Beekers, K.R. Lattwein, A.F.W. van der Steen, N. de Jong, and K. Kooiman, "Vibrational responses of bound and nonbound targeted lipid-coated single microbubbles," IEEE Trans Ultrason Ferroelectr Freq Control, vol. 64, no. 5, pp. 785-797, 2017.

[57] T.J. Silhavy, D. Kahne, and S. Walker, "The bacterial cell envelope," Cold Spring Harbor Perspectives in Biology, vol. 2, no. 5, pp. a000414-a000414, 2010.

[58] A. Mai-Prochnow, M. Clauson, J. Hong, and A.B. Murphy, "Gram positive and Gram negative bacteria differ in their sensitivity to cold plasma," Sci Rep, vol. 6, no. 1, p. 38610, 2016.

[59] W.G. Pitt, M.O. McBride, J.K. Lunceford, R.J. Roper, and R.D. Sagers, "Ultrasonic enhancement of antibiotic action on gram-negative bacteria," Antimicrob Agents Chemother, vol. 38, no. 11, p. 2577, 1994.

[60] X. Liao et al., "Multiple action sites of ultrasound on *Escherichia coli* and *Staphylococcus aureus*," Food Sci Hum Well, vol. 7, no. 1, pp. 102-109, 2018.

[61] J.M. Escoffre, J. Piron, A. Novell, and A. Bouakaz, "Doxorubicin delivery into tumor cells with ultrasound and microbubbles," Mol Pharm, vol. 8, no. 3, pp. 799-806, 2011.

[62] E. Ronan, N. Edjiu, O. Kroukamp, G. Wolfaardt, and R. Karshafian, "USMB-induced synergistic enhancement of aminoglycoside antibiotics in biofilms," Ultrasonics, vol. 69, pp. 182-190, 2016.

[63] T. Tandiono et al., "Sonolysis of *Escherichia coli* and *Pichia pastoris* in microfluidics," Lab Chip, 10.1039/C2LC20861J vol. 12, no. 4, pp. 780-786, 2012.

[64] A. Agarwal, W. Jern Ng, and Y. Liu, "Removal of biofilms by intermittent low-intensity ultrasonication triggered bursting of microbubbles," Biofouling, vol. 30, no. 3, pp. 359-365, 2014.

[65] C. Zhu et al., "Ultrasound-targeted microbubble destruction enhances human β-defensin 3 activity against antibiotic-resistant staphylococcus biofilms," Inflammation, vol. 36, no. 5, pp. 983-996, 2013.

[66] S. Li et al., "Ultrasound microbubbles enhance human β-defensin 3 against biofilms," J Surg Res, vol. 199, no. 2, pp. 458-469, 2015.

[67] J. Hu et al., "The synergistic bactericidal effect of vancomycin on UTMD treated biofilm involves damage to bacterial cells and enhancement of metabolic activities," Sci Rep, vol. 8, no. 1, p. 192, 2018.

[68] K.R. Lattwein et al., "An *in vitro* proof-of-principle study of sonobactericide," Sci Rep, vol. 8, no. 1, p. 3411, 2018.

[69] Y.Y. Fu et al., "Synergistic antibacterial effect of ultrasound microbubbles combined with chitosan-modified polymyxin B-loaded liposomes on biofilm-producing *Acinetobacter baumannii*," Int J Nanomedicine, vol. 14, pp. 1805-1815, 2019.

[70] H. Horsley et al., "Ultrasound-activated microbubbles as a novel intracellular drug delivery system for urinary tract infection," J Control Release, vol. 301, pp. 166-175, 2019.
[71] K.T. Bæk et al., "Genetic variation in the *Staphylococcus aureus* 8325 strain lineage revealed by whole-genome sequencing," PLOS ONE, vol. 8, no. 9, p. e77122, 2013.
[72] H.A. Crosby, J. Kwiecinski, and A.R. Horswill, "Chapter One - *Staphylococcus aureus* aggregation and coagulation mechanisms, and their function in host–pathogen interactions," in Advances in Applied Microbiology, vol. 96, S. Sariaslani and G. M. Gadd, Eds.: Academic Press, 2016, pp. 1-41.
[73] P.S. Stewart and J.W. Costerton, "Antibiotic resistance of bacteria in biofilms," The Lancet, vol. 358, no. 9276, pp. 135-138, 2001.
[74] R.A. Brady, C.P. Mocca, R.D. Plaut, K. Takeda, and D.L. Burns, "Comparison of the immune response during acute and chronic *Staphylococcus aureus* infection," PLOS ONE, vol. 13, no. 3, p. e0195342, 2018.
[75] K. Lewis, "Persister cells and the riddle of biofilm survival," Biochem (Mosc), vol. 70, no. 2, pp. 267-274, 2005.
[76] J.W. Costerton, P.S. Stewart, and E.P. Greenberg, "Bacterial biofilms: A common cause of persistent infections," Science, vol. 284, no. 5418, p. 1318, 1999.
[77] C.A. Fux, P. Stoodley, L. Hall-Stoodley, and J.W. Costerton, "Bacterial biofilms: a diagnostic and therapeutic challenge," Expert Rev Anti Infect Ther, vol. 1, no. 4, pp. 667-683, 2003.
[78] D. Lebeaux, J.M. Ghigo, and C. Beloin, "Biofilm-related infections: bridging the gap between clinical management and fundamental aspects of recalcitrance toward antibiotics," Microbiol Mol Biol Rev, vol. 78, no. 3, p. 510, 2014.
[79] M. Zapotoczna, E. O'Neill, and J.P. O'Gara, "Untangling the diverse and redundant mechanisms of *Staphylococcus aureus* biofilm formation," PloS Pathogens, vol. 12, no. 7, p. e1005671, 2016.
[80] N.M. Maurice, B. Bedi, and R.T. Sadikot, "*Pseudomonas aeruginosa* biofilms: Host Response and clinical implications in lung infections," Am J Respir Cell Mol Biol, vol. 58, no. 4, pp. 428-439, 2018.
[81] C. Delcaru et al., "Microbial biofilms in urinary tract infections and prostatitis: Etiology, pathogenicity, and combating strategies," Pathogens, vol. 5, no. 4, 2016.
[82] M. Magana et al., "Options and limitations in clinical investigation of bacterial biofilms," Clin Microbiol Rev, vol. 31, no. 3, pp. e00084-16, 2018.
[83] F.L. Short, S.L. Murdoch, and R.P. Ryan, "Polybacterial human disease: the ills of social networking," Trends Microbiol, vol. 22, no. 9, pp. 508-516, 2014.
[84] T. Bjarnsholt et al., "The *in vivo* biofilm," Trends Microbiol, vol. 21, no. 9, pp. 466-474, 2013.
[85] A.E.L. Roberts, K.N. Kragh, T. Bjarnsholt, and S.P. Diggle, "The limitations of *in vitro* experimentation in understanding biofilms and chronic infection," J Mol Biol, vol. 427, no. 23, pp. 3646-3661, 2015.
[86] A.C. Vollmer, S. Kwakye, M. Halpern, and E.C. Everbach, "Bacterial stress responses to 1-megahertz pulsed ultrasound in the presence of microbubbles," Appl Environ Microbiol, vol. 64, no. 10, pp. 3927-3931, 1998.
[87] M. Otto, "Staphylococcal biofilms," Curr Top Microbiol Immunol, vol. 322, pp. 207-228, 2008.
[88] S.L. Chua et al., "Dispersed cells represent a distinct stage in the transition from bacterial biofilm to planktonic lifestyles," Nat Commun, vol. 5, no. 1, p. 4462, 2014.
[89] K.L. Connolly, A.L. Roberts, R.C. Holder, and S.D. Reid, "Dispersal of Group A streptococcal biofilms by the cysteine protease SpeB leads to increased disease severity in a murine model," PLOS ONE, vol. 6, no. 4, p. e18984, 2011.
[90] L.R. Marks, B.A. Davidson, P.R. Knight, and A.P. Hakansson, "Interkingdom signaling induces Streptococcus pneumoniae biofilm dispersion and transition from asymptomatic colonization to disease," mBio, vol. 4, no. 4, pp. e00438-13, 2013.
[91] S.W. Lee, H. Gu, J.B. Kilberg, and D. Ren, "Sensitizing bacterial cells to antibiotics by shape recovery triggered biofilm dispersion," Acta Biomaterialia, vol. 81, pp. 93-102, 2018.
[92] Y. Ikeda-Dantsuji et al., "Synergistic effect of ultrasound and antibiotics against Chlamydia trachomatis-infected human epithelial cells *in vitro*," Ultrason Sonochem, vol. 18, no. 1, pp. 425-430, 2011.

[93] A. Halford, C.D. Ohl, A. Azarpazhooh, B. Basrani, S. Friedman, and A. Kishen, "Synergistic effect of microbubble emulsion and sonic or ultrasonic agitation on endodontic biofilm *in vitro*," J Endod, vol. 38, no. 11, pp. 1530-1534, 2012.

[94] A.H. Liao, C.R. Hung, C.F. Lin, Y.C. Lin, and H.K. Chen, "Treatment effects of lysozyme-shelled microbubbles and ultrasound in inflammatory skin disease," Sci Rep, vol. 7, no. 1, p. 41325, 2017.

[95] H. Zhou et al., "Effect of low frequency ultrasound plus fluorescent composite carrier in the diagnosis and treatment of methicillin-resistant *Staphylococcus aureus* biofilm infection of bone joint implant," Int J Clin Exp Med, vol. 11, no. 2, pp. 799-805, 2018.

[96] C. Estrela, C. R.A. Estrela, E.L. Barbin, J.C.E. Spanó, M.A. Marchesan, and J.D. Pécora, "Mechanism of action of sodium hypochlorite," Braz Dent J, vol. 13, pp. 113-117, 2002.

[97] V. Dhople, A. Krukemeyer, and A. Ramamoorthy, "The human beta-defensin-3, an antibacterial peptide with multiple biological functions," Biochim Biophys Acta Biomembr, vol. 1758, no. 9, pp. 1499-1512, 2006.

[98] L.A. Mermel et al., "Clinical practice guidelines for the diagnosis and management of intravascular catheter-related infection: 2009 Update by the Infectious Diseases Society of America," Clin Infect Dis, vol. 49, no. 1, pp. 1-45, 2009.

[99] L.A. Mandell, T.J. Marrie, R.F. Grossman, A.W. Chow, R.H. Hyland, and a.t.C.C.A.P.W. Group, "Canadian guidelines for the initial management of community-acquired pneumonia: An Evidence-Based Update by the Canadian Infectious Diseases Society and the Canadian Thoracic Society," Clin Infect Dis, vol. 31, no. 2, pp. 383-421, 2000.

[100] D.R. Osmon et al., "Diagnosis and management of prosthetic joint infection: Clinical Practice Guidelines by the Infectious Diseases Society of Americaa," Clin Infect Dis, vol. 56, no. 1, pp. e1-e25, 2012.

[101] L.M. Baddour et al., "Infective endocarditis in adults: Diagnosis, antimicrobial therapy, and management of complications," Circulation, vol. 132, no. 15, pp. 1435-1486, 2015.

[102] G. Habib et al., "2015 ESC Guidelines for the management of infective endocarditis: The Task Force for the Management of Infective Endocarditis of the European Society of Cardiology," Eur Heart J, vol. 36, no. 44, pp. 3075-3128, 2015.

[103] E. Lanjouw, S. Ouburg, H. de Vries, A. Stary, K. Radcliffe, and M. Unemo, "2015 European guideline on the management of *Chlamydia trachomatis* infections," Int J STD AIDS, vol. 27, no. 5, pp. 333-348, 2016.

[104] T. Lin et al., "*In vitro* and *in vivo* evaluation of vancomycin-loaded pmma cement in combination with ultrasound and microbubbles-mediated ultrasound," BioMed Res Int, vol. 2015, p. 309739, 2015.

[105] M.G. Sugiyama et al., "Lung ultrasound and microbubbles enhance aminoglycoside efficacy and delivery to the lung in *Escherichia coli*–induced pneumonia and acute respiratory distress syndrome," Am J Respir and Crit Care Med, vol. 198, no. 3, pp. 404-408, 2018.

[106] F. Hu, D. Zhu, F. Wang, and M. Wang, "Current status and trends of antibacterial resistance in China," Clin Infect Dis, vol. 67, no. suppl_2, pp. S128-S134, 2018.

[107] Y.W. Han, A. Ikegami, P. Chung, L. Zhang, and C.X. Deng, "Sonoporation is an efficient tool for intracellular fluorescent dextran delivery and one-step double-crossover mutant construction in Fusobactenum nucleatum," Appl Environ Microbiol, Article vol. 73, no. 11, pp. 3677-3683, 2007.

[108] Y.W. Han et al., "Identification and characterization of a novel adhesin unique to oral Fusobacteria," J Bacteriol, vol. 187, no. 15, p. 5330, 2005.

[109] S. Yi et al., "Microbubble-mediated ultrasound promotes accumulation of bone marrow mesenchymal stem cell to the prostate for treating chronic bacterial prostatitis in rats," Sci Rep, vol. 6, no. 1, p. 19745, 2016.

[110] T. Nishikawa et al., "A study of the efficacy of ultrasonic waves in removing biofilms," Gerodontology, vol. 27, no. 3, pp. 199-206, 2010.

[111] H. Guo, Z. Wang, Q. Du, P. Li, Z. Wang, and A. Wang, "Stimulated phase-shift acoustic nanodroplets enhance vancomycin efficacy against methicillin-resistant *Staphylococcus aureus* biofilms," Int J Nanomedicine, vol. 12, pp. 4679-4690, 2017.

[112] N. He et al., "Enhancement of vancomycin activity against biofilms by using ultrasound-targeted microbubble destruction," Antimicrob Agents Chemother, vol. 55, no. 11, p. 5331, 2011.

[113] W.T. Coakley, D.W. Bardsley, M.A. Grundy, F. Zamani, and D.J. Clarke, "Cell manipulation in ultrasonic standing wave fields," J Chem Technol Biotechnol, vol. 44, no. 1, pp. 43-62, 1989.
[114] M.A. O'Reilly, Y. Huang, and K. Hynynen, "The impact of standing wave effects on transcranial focused ultrasound disruption of the blood–brain barrier in a rat model," Phys Med Biol, vol. 55, no. 18, pp. 5251-5267, 2010.
[115] A. Shi, Y. Min, and M. Wan, "Flowing microbubble manipulation in blood vessel phantom using ultrasonic standing wave with stepwise frequency," Appl Phys Lett, vol. 103, no. 17, p. 174105, 2013.
[116] T. Azuma et al., "Bubble generation by standing wave in water surrounded by cranium with transcranial ultrasonic beam," Jpn J Appl Phys, vol. 44, no. 6B, pp. 4625-4630, 2005.
[117] T. Deffieux and E.E. Konofagou, "Numerical study of a simple transcranial focused ultrasound system applied to blood-brain barrier opening," IEEE Trans Ultrason Ferroelectr Freq Control, vol. 57, no. 12, pp. 2637-2653, 2010.
[118] T.M. Huber, N.M. Beaver, and J.R. Helps, "Elimination of standing wave effects in ultrasound radiation force excitation in air using random carrier frequency packets," J Acoust Soc Am, vol. 130, no. 4, pp. 1838-1843, 2011.
[119] R.T. Kleven et al., "The effect of 220 kHz insonation scheme on rt-PA thrombolytic efficacy *in vitro*," Phys Med Biol, vol. 64, no. 16, p. 165015, 2019.
[120] L.E. Kinsler, A.R. Frey, A.B. Coppens, and J.V. Sanders, Fundamentals of Acoustics, 4th Ed. 1999, p. 560.
[121] K. Hensel, M.P. Mienkina, and G. Schmitz, "Analysis of ultrasound fields in cell culture wells for *in vitro* ultrasound therapy experiments," Ultrasound Med Biol, vol. 37, no. 12, pp. 2105-2115, 2011.
[122] G. ter Haar et al., "Guidance on reporting ultrasound exposure conditions for bio-effects studies," Ultrasound Med Biol, vol. 37, no. 2, pp. 177-183, 2011.
[123] C. Mannaris and M.A. Averkiou, "Investigation of microbubble response to long pulses used in ultrasound-enhanced drug delivery," Ultrasound Med Biol, vol. 38, no. 4, pp. 681-691, 2012.
[124] Y. Dong, S. Chen, Z. Wang, N. Peng, and J. Yu, "Synergy of ultrasound microbubbles and vancomycin against *Staphylococcus epidermidis* biofilm," J Antimicrob Chemother, vol. 68, no. 4, pp. 816-826, 2012.
[125] Y. Dong, Y. Xu, P. Li, C. Wang, Y. Cao, and J. Yu, "Antibiofilm effect of ultrasound combined with microbubbles against *Staphylococcus epidermidis* biofilm," Int J Med Microbiol, vol. 307, no. 6, pp. 321-328, 2017.
[126] P. Thomen, J. Robert, A. Monmeyran, A.F. Bitbol, C. Douarche, and N. Henry, "Bacterial biofilm under flow: First a physical struggle to stay, then a matter of breathing," PLOS ONE, vol. 12, no. 4, p. e0175197, 2017.
[127] D. Carugo, J. Owen, C. Crake, J.Y. Lee, and E. Stride, "Biologically and acoustically compatible chamber for studying ultrasound-mediated delivery of therapeutic compounds," Ultrasound Med Biol, vol. 41, no. 7, pp. 1927-1937, 2015.
[128] H.X. Zhu, X.Z. Cai, Z.L. Shi, B. Hu, and S.G. Yan, "Microbubble-mediated ultrasound enhances the lethal effect of gentamicin on planktonic *Escherichia coli*," BioMed Res Int, vol. 2014, p. 142168, 2014.
[129] Y. Dong, J. Li, P. Li, and J. Yu, "Ultrasound microbubbles enhance the activity of vancomycin against *Staphylococcus epidermidis* biofilms *in vivo*," J Ultrasound Med, vol. 37, no. 6, pp. 1379-1387, 2018.
[130] M. Okshevsky and R.L. Meyer, "Evaluation of fluorescent stains for visualizing extracellular DNA in biofilms," J Microbiol Methods, vol. 105, pp. 102-104, 2014.
[131] L. Yu, M. Zhong, and Y. Wei, "Direct fluorescence polarization assay for the detection of glycopeptide antibiotics," Anal Chem, vol. 82, no. 16, pp. 7044-7048, 2010.
[132] J.C.E. Odekerken, D.M.W. Logister, L. Assabre, J.J.C. Arts, G.H.I.M. Walenkamp, and T.J.M. Welting, "ELISA-based detection of gentamicin and vancomycin in protein-containing samples," SpringerPlus, vol. 4, no. 1, p. 614, 2015.
[133] M. Schneider et al., "BR1: a new ultrasonographic contrast agent based on sulfur hexafluoride-filled microbubbles," Invest Radiol, vol. 30, no. 8, pp. 451-457, 1995.
[134] C.P. Nolsøe and T. Lorentzen, "International guidelines for contrast-enhanced ultrasonography: ultrasound imaging in the new millennium," Ultrasonography (Seoul, Korea), vol. 35, no. 2, pp. 89-103, 2016.

[135] P.C. Sontum, "Physicochemical characteristics of Sonazoid™, a new contrast agent for ultrasound imaging," Ultrasound Med Biol, vol. 34, no. 5, pp. 824-833, 2008.
[136] S.B. Feinstein, "New Developments in ultrasonic contrast techniques: transpulmonary passage of contrast agents and diagnostic implications," Echocardiography, vol. 6, no. 1, pp. 27-33, 1989.
[137] S. Mayer and P.A. Grayburn, "Myocardial contrast agents: Recent advances and future directions," Prog Cardiovasc Dis, vol. 44, no. 1, pp. 33-44, 2001.
[138] F. Forsberg, Y. Wu, I.R.S. Makin, W. Wang, and M.A. Wheatley, "Quantitative acoustic characterization of a new surfactant-based ultrasound contrast agent," Ultrasound Med Biol, vol. 23, no. 8, pp. 1201-1208, 1997.
[139] J.M. Gorce, M. Arditi, and M. Schneider, "Influence of bubble size distribution on the echogenicity of ultrasound contrast agents: a study of SonoVue™," Invest Radiol, vol. 35, no. 11, 2000.
[140] C.M. Moran, R.J. Watson, K.A.A. Fox, and W.N. McDicken, "*In vitro* acoustic characterisation of four intravenous ultrasonic contrast agents at 30 MHz," Ultrasound Med Biol, vol. 28, no. 6, pp. 785-791, 2002.
[141] W.S. Chen, T. J. Matula, A.A. Brayman, and L.A. Crum, "A comparison of the fragmentation thresholds and inertial cavitation doses of different ultrasound contrast agents," J Acoust Soc Am, vol. 113, no. 1, pp. 643-651, 2003.
[142] K. Chetty, E. Stride, C.A. Sennoga, J.V. Hajnal, and R.J. Eckersley, "High-speed optical observations and simulation results of SonoVue microbubbles at low-pressure insonation," IEEE Trans Ultrason Ferroelectr Freq Control, vol. 55, no. 6, pp. 1333-1342, 2008.
[143] F. Guidi, H. J. Vos, R. Mori, N. D. Jong, and P. Tortoli, "Microbubble characterization through acoustically induced deflation," IEEE Trans Ultrason Ferroelectr Freq Control, vol. 57, no. 1, pp. 193-202, 2010.
[144] T. Faez, D. Goertz, and N. De Jong, "Characterization of Definity™ ultrasound contrast agent at frequency range of 5–15 MHz," Ultrasound Med Biol, vol. 37, no. 2, pp. 338-342, 2011.
[145] B.L. Helfield and D.E. Goertz, "Nonlinear resonance behavior and linear shell estimates for Definity™ and MicroMarker™ assessed with acoustic microbubble spectroscopy," J Acoust Soc Am, vol. 133, no. 2, pp. 1158-1168, 2013.
[146] O.D. Kripfgans, J.B. Fowlkes, D.L. Miller, O.P. Eldevik, and P.L. Carson, "Acoustic droplet vaporization for therapeutic and diagnostic applications," Ultrasound Med Biol, vol. 26, no. 7, pp. 1177-1189, 2000.
[147] C.Y. Lin and W.G. Pitt, "Acoustic droplet vaporization in biology and medicine," BioMed Res Int, vol. 2013, p. 404361, 2013.
[148] P. Liu, X. Wang, S. Zhou, X. Hua, Z. Liu, and Y. Gao, "Effects of a novel ultrasound contrast agent with long persistence on right ventricular pressure: Comparison with SonoVue," Ultrasonics, vol. 51, no. 2, pp. 210-214, 2011.
[149] T. Leighton, The acoustic bubble. Academic press, 2012.
[150] K. Hettiarachchi, E. Talu, M.L. Longo, P.A. Dayton, and A.P. Lee, "On-chip generation of microbubbles as a practical technology for manufacturing contrast agents for ultrasonic imaging," Lab Chip, vol. 7, no. 4, pp. 463-468, 2007.
[151] M. Postema, A. Bouakaz, C.T. Chin, and N. de Jong, "Optically observed microbubble coalescence and collapse," in 2002 IEEE Ultrasonics Symposium Proceedings, vol. 2, pp. 1949-1952, 2002.
[152] K.B. Bader, M.J. Gruber, and C.K. Holland, "Shaken and stirred: mechanisms of ultrasound-enhanced thrombolysis," Ultrasound Med Biol, vol. 41, no. 1, pp. 187-96, 2015.
[153] G. ter Haar, "Ultrasound bioeffects and safety," Proc Inst Mech Eng H, vol. 224, no. 2, pp. 363-373, 2009.
[154] W.L. Nyborg, "Acoustic streaming due to attenuated plane waves," J Acoust Soc Am, vol. 25, no. 1, pp. 68-75, 1953.
[155] D. Dalecki, "Mechanical bioeffects of ultrasound," Annu Rev Biomed Eng, vol. 6, pp. 229-248, 2004.
[156] G. ter Haar, "Safety and bio-effects of ultrasound contrast agents," Med Biol Eng Comput vol. 47, no. 8, pp. 893-900, 2009.
[157] S. Hajdu, J. Holinka, S. Reichmann, A.M. Hirschl, W. Graninger, and E. Presterl, "Increased temperature enhances the antimicrobial effects of daptomycin, vancomycin, tigecycline, fosfomycin, and cefamandole on staphylococcal biofilms," Antimicrob Agents Chemother, vol. 54, no. 10, pp. 4078-4084, 2010.

[158] L. Juffermans, P.A. Dijkmans, R. Musters, C.A. Visser, and O. Kamp, "Transient permeabilization of cell membranes by ultrasound-exposed microbubbles is related to formation of hydrogen peroxide," Am J Physiol Heart Circ Physiol, vol. 291, no. 4, pp. H1595-H1601, 2006.
[159] K.B. Bader and C.K. Holland, "Gauging the likelihood of stable cavitation from ultrasound contrast agents," Phys Med Biol, vol. 58, no. 1, p. 127, 2012.
[160] C.K. Holland and R.E. Apfel, "An improved theory for the prediction of microcavitation thresholds," IEEE Trans Ultrason Ferroelectr Freq Control, vol. 36, no. 2, pp. 204-8, 1989.
[161] R.E. Apfel, "Sonic effervescence: A tutorial on acoustic cavitation," J Acoust Soc Am, vol. 101, no. 3, pp. 1227-1237, 1997.
[162] S.A. Elder, "Cavitation microstreaming," J Acoust Soc Am, vol. 31, no. 1, pp. 54-64, 1959.
[163] J. Collis et al., "Cavitation microstreaming and stress fields created by microbubbles," Ultrasonics, vol. 50, no. 2, pp. 273-279, 2010.
[164] J.E. Chomas, P. Dayton, J. Allen, K. Morgan, and K.W. Ferrara, "Mechanisms of contrast agent destruction," IEEE Trans Ultrason Ferroelectr Freq Control, vol. 48, no. 1, pp. 232-248, 2001.
[165] W.T. Shi, F. Forsberg, A. Tornes, J. Østensen, and B.B. Goldberg, "Destruction of contrast microbubbles and the association with inertial cavitation," Ultrasound Med Biol, vol. 26, no. 6, pp. 1009-1019, 2000.
[166] S.W. Ohl, E. Klaseboer, and B. C. Khoo, "Bubbles with shock waves and ultrasound: a review," Interface Focus, vol. 5, no. 5, p. 20150019, 2015.
[167] H. Chen, W. Kreider, A.A. Brayman, M.R. Bailey, and T.J. Matula, "Blood vessel deformations on microsecond time scales by ultrasonic cavitation," Phys Rev Lett, vol. 106, no. 3, p. 034301, 2011.
[168] H. Chen, A.A. Brayman, A.P. Evan, and T.J. Matula, "Preliminary observations on the spatial correlation between short-burst microbubble oscillations and vascular bioeffects," Ultrasound Med Biol, vol. 38, no. 12, pp. 2151-2162, 2012.
[169] M.E. Olson, H. Ceri, D.W. Morck, A.G. Buret, and R. R. Read, "Biofilm bacteria: formation and comparative susceptibility to antibiotics," Can J Vet Res, vol. 66, no. 2, p. 86, 2002.
[170] T. Conner-Kerr et al., "The effects of low-frequency ultrasound (35 kHz) on methicillin-resistant *Staphylococcus aureus* (MRSA) *in vitro*," Ostomy Wound Manage, vol. 56 5, pp. 32-43, 2010.
[171] M. Ward, J. Wu, and J.F. Chiu, "Experimental study of the effects of optison® concentration on sonoporation *in vitro*," Ultrasound Med Biol, vol. 26, no. 7, pp. 1169-1175, 2000.
[172] K.H. Song, A.C. Fan, J.J. Hinkle, J. Newman, M.A. Borden, and B.K. Harvey, "Microbubble gas volume: A unifying dose parameter in blood-brain barrier opening by focused ultrasound," Theranostics, vol. 7, no. 1, p. 144, 2017.
[173] C. Christiansen, H. Kryvi, P. Sontum, and T. Skotland, "Physical and biochemical characterization of Albunex, a new ultrasound contrast agent consisting of air-filled albumin microspheres suspended in a solution of human albumin," Biotechnol Appl Biochem, vol. 19, no. 3, pp. 307-320, 1994.
[174] P.K. Sharma, M.J. Gibcus, H.C. van der Mei, and H.J. Busscher, "Influence of fluid shear and microbubbles on bacterial detachment from a surface," Appl Environ Microbiol, vol. 71, no. 7, pp. 3668-3673, 2005.
[175] M.R. Parini and W.G. Pitt, "Dynamic removal of oral biofilms by bubbles," Colloids Surf B: Biointerfaces, vol. 52, no. 1, pp. 39-46, 2006.
[176] H.H.T. Madsen and F. Rasmussen, "Contrast-enhanced ultrasound in oncology," Cancer Imaging, vol. 11, no. 1A, p. S167, 2011.
[177] K. Wei, "Contrast echocardiography: Applications and limitations," Cardiol Rev, vol. 20, no. 1, pp. 025-032, 2012.
[178] A. Alzaraa et al., "Contrast-enhanced ultrasound in the preoperative, intraoperative and postoperative assessment of liver lesions," Hepatol Res, vol. 43, no. 8, pp. 809-819, 2013.
[179] G. Menozzi, V. Maccabruni, and E. Gabbi, "Left kidney infarction in a patient with native aortic valve infective endocarditis: diagnosis with contrast-enhanced ultrasound," J Ultrasound, vol. 16, no. 4, p. 145, 2013.
[180] G. Menozzi, V. Maccabruni, E. Gabbi, N. Leone, and M. Calzolari, "Contrast-enhanced ultrasound evaluation of splenic embolization in patients with definite left-sided infective endocarditis," Ultrasound Med Biol, vol. 39, no. 11, pp. 2205-2210, 2013.

[181] K. Jahan, S. Balzer, and P. Mosto, "Toxicity of nonionic surfactants," WIT Trans Ecol Environ, vol. 110, pp. 281-290, 2008.
[182] D. Koley and A. J. Bard, "Triton X-100 concentration effects on membrane permeability of a single HeLa cell by scanning electrochemical microscopy (SECM)," Proc Natl Acad Sci USA, vol. 107, no. 39, pp. 16783-16787, 2010.
[183] K. Lewis, "Platforms for antibiotic discovery," Nat Rev Drug Discov, vol. 12, no. 5, pp. 371-387, 2013.
[184] M. Gajdács, "The concept of an ideal antibiotic: implications for drug design," Molecules, vol. 24, no. 5, p. 892, 2019.
[185] A.V. Carli, F.P. Ross, S.J. Bhimani, S.R. Nodzo, and M.P. Bostrom, "Developing a clinically representative model of periprosthetic joint infection," J Bone Joint Surg Am, vol. 98, no. 19, pp. 1666-1676, 2016.
[186] C.A. Owens, "Ultrasound-enhanced thrombolysis: EKOS EndoWave infusion catheter system," Semin Intervent Radiol, vol. 25, no. 1, p. 37, 2008.
[187] J. Kim et al., "Intravascular forward-looking ultrasound transducers for microbubble-mediated sonothrombolysis," Sci Rep, vol. 7, no. 1, pp. 1-10, 2017.
[188] B.B. Goldberg, J.-B. Liu, and F. Forsberg, "Ultrasound contrast agents: A review," Ultrasound Med Biol, vol. 20, no. 4, pp. 319-333, 1994.
[189] S.J. McConoughey et al., "Biofilms in periprosthetic orthopedic infections," Future Microbiol, vol. 9, no. 8, pp. 987-1007, 2014.
[190] M. Smeenge et al., "First-in-human ultrasound molecular imaging with a VEGFR2-specific ultrasound molecular contrast agent (BR55) in prostate cancer: a safety and feasibility pilot study," Invest Radiol, vol. 52, no. 7, pp. 419-427, 2017.
[191] J.K. Willmann et al., "Ultrasound molecular imaging with BR55 in patients with breast and ovarian lesions: first-in-human results," J Clin Oncol, vol. 35, no. 19, p. 2133, 2017.
[192] N. Gilboa-Garber and D. Sudakevitz, "The hemagglutinating activities of *Pseudomonas aeruginosa* lectins PA-IL and PA-IIL exhibit opposite temperature profiles due to different receptor types," FEMS Immunol Med Microbiol, vol. 25, no. 4, pp. 365-369, 999.
[193] B.M. Bröker, S. Holtfreter, and I. Bekeredjian-Ding, "Immune control of *Staphylococcus aureus* – Regulation and counter-regulation of the adaptive immune response," Int J Med Microbiol, vol. 304, no. 2, pp. 204-214, 2014.
[194] M. van Oosten et al., "Targeted imaging of bacterial infections: advances, hurdles and hopes," FEMS Microbiol Rev, vol. 39, no. 6, pp. 892-916, 2015.
[195] H. Koo, R.N. Allan, R.P. Howlin, P. Stoodley, and L. Hall-Stoodley, "Targeting microbial biofilms: current and prospective therapeutic strategies," Nat Rev Microbiol, vol. 15, no. 12, p. 740, 2017.
[196] Y. Shen, S. Stojicic, W. Qian, I. Olsen, and M. Haapasalo, "The synergistic antimicrobial effect by mechanical agitation and two chlorhexidine preparations on biofilm bacteria," J Endod, vol. 36, no. 1, pp. 100-104, 2010.
[197] J.C. Carmen et al., "Ultrasonic-enhanced gentamicin transport through colony biofilms of *Pseudomonas aeruginosa* and *Escherichia coli*," J Infect Chemother, vol. 10, no. 4, pp. 193-199, 2004.
[198] A. Oberbach et al., "New insights into valve-related intramural and intracellular bacterial diversity in infective endocarditis," PLOS ONE, vol. 12, no. 4, p. e0175569, 2017.
[199] T. Coenye and H.J. Nelis, "*In vitro* and *in vivo* model systems to study microbial biofilm formation," J Microbiol Methods, vol. 83, no. 2, pp. 89-105, 2010.
[200] M. Malone, D.M. Goeres, I. Gosbell, K. Vickery, S. Jensen, and P. Stoodley, "Approaches to biofilm-associated infections: the need for standardized and relevant biofilm methods for clinical applications," Expert Rev Anti Infect Ther, vol. 15, no. 2, pp. 147-156, 2017.
[201] J.J. Kwan et al., "Ultrasound-propelled nanocups for drug delivery," Small, vol. 11, no. 39, pp. 5305-5314, 2015.
[202] C.C. Chen, P.S. Sheeran, S.Y. Wu, O.O. Olumolade, P.A. Dayton, and E.E. Konofagou, "Targeted drug delivery with focused ultrasound-induced blood-brain barrier opening using acoustically-activated nanodroplets," J Control Release, vol. 172, no. 3, pp. 795-804, 2013.

[203] K.B. Bader et al., "Efficacy of histotripsy combined with rt-PA *in vitro*," Phys Med Biol, vol. 61, no. 14, p. 5253, 2016.
[204] D.P. Gnanadhas et al., "Successful treatment of biofilm infections using shock waves combined with antibiotic therapy," Sci Rep, vol. 5, p. 17440, 2015.
[205] X. Qi et al., "Increased effects of extracorporeal shock waves combined with gentamicin against *Staphylococcus aureus* biofilms *in vitro* and *in vivo*," Ultrasound Med Biol, vol. 42, no. 9, pp. 2245-2252, 2016.
[206] J. Xu, T.A. Bigelow, L.J. Halverson, J.M. Middendorf, and B. Rusk, "Minimization of treatment time for *in vitro* 1.1MHz destruction of *Pseudomonas aeruginosa* biofilms by high-intensity focused ultrasound," Ultrasonics, vol. 52, no. 5, pp. 668-675, 2012.
[207] T.A. Bigelow, C.L. Thomas, H. Wu, and K.M. Itani, "Histotripsy treatment of *S. aureus* biofilms on surgical mesh samples under varying pulse durations," IEEE Trans Ultrason Ferroelectr Freq Control, vol. 64, no. 10, pp. 1420-1428, 2017.
[208] N. Vakil and E.C. Everbach, "Transient acoustic cavitation in gallstone fragmentation: A study of gallstones fragmented *in vivo*," Ultrasound Med Biol, vol. 19, no. 4, pp. 331-342, 1993.
[209] E. Vlaisavljevich, Y.Y. Durmaz, A. Maxwell, M. ElSayed, and Z. Xu, "Nanodroplet-mediated histotripsy for image-guided targeted ultrasound cell ablation," Theranostics, vol. 3, no. 11, p. 851, 2013.
[210] P. Birkin et al., "Cold water cleaning of brain proteins, biofilm and bone–harnessing an ultrasonically activated stream," Phys Chem Chem Phys, vol. 17, no. 32, pp. 20574-20579, 2015.
[211] J.B. Kaplan, "Biofilm Dispersal: Mechanisms, Clinical Implications, and Potential Therapeutic Uses," J Dent Res, vol. 89, no. 3, pp. 205-218, 2010.
[212] K.B. Bader, G. Bouchoux, and C.K. Holland, "Sonothrombolysis," in Therapeutic Ultrasound: Springer, 2016, pp. 339-362.
[213] M. Whiteley, S.P. Diggle, and E.P. Greenberg, "Progress in and promise of bacterial quorum sensing research," Nature, vol. 551, no. 7680, pp. 313-320, 2017.
[214] O. Fleitas Martínez et al., "Interference with quorum-sensing signal biosynthesis as a promising therapeutic strategy against multidrug-resistant pathogens," Front Cell Infect Microbiol, vol. 8, p. 444, 2019.
[215] R.M. Miller, X. Zhang, A.D. Maxwell, C.A. Cain, and Z. Xu, "Bubble-induced color Doppler feedback for histotripsy tissue fractionation," IEEE Trans Ultrason Ferroelectr Freq Control, vol. 63, no. 3, pp. 408-419, 2016.
[216] K.J. Haworth, K.B. Bader, K.T. Rich, C.K. Holland, and T.D. Mast, "Quantitative frequency-domain passive cavitation imaging," IEEE Trans Ultrason Ferroelectr Freq Control, vol. 64, no. 1, pp. 177-191, 2016.
[217] T. Sun et al., "Closed-loop control of targeted ultrasound drug delivery across the blood–brain/tumor barriers in a rat glioma model," Proc Natl Acad Sci USA, vol. 114, no. 48, pp. E10281-E10290, 2017.
[218] Z.M. Binsalamah, A. Paul, S. Prakash, and D. Shum-Tim, "Nanomedicine in cardiovascular therapy: recent advancements," Expert Rev Cardiovasc Ther, vol. 10, no. 6, pp. 805-815, 2012.
[219] E. Westein, U. Flierl, C.E. Hagemeyer, and K. Peter, "Destination known: targeted drug delivery in atherosclerosis and thrombosis," Drug Dev Res, vol. 74, no. 7, pp. 460-471, 2013.
[220] I. Lentacker, I. De Cock, R. Deckers, S.C. De Smedt, and C.T.W. Moonen, "Understanding ultrasound induced sonoporation: Definitions and underlying mechanisms," Adv Drug Deliv Rev, vol. 72, pp. 49-64, 2014.
[221] P. Qin, T. Han, A.C.H. Yu, and L. Xu, "Mechanistic understanding the bioeffects of ultrasound-driven microbubbles to enhance macromolecule delivery," J Control Release, vol. 272, pp. 169-181, 2018.
[222] C.T. Chin et al., "Brandaris 128: A digital 25 million frames per second camera with 128 highly sensitive frames," Rev Sci Instrum, vol. 74, no. 12, pp. 5026-5034, 2003.
[223] X. Chen, J. Wang, M. Versluis, N. de Jong, and F.S. Villanueva, "Ultra-fast bright field and fluorescence imaging of the dynamics of micrometer-sized objects," Rev Sci Instrum, vol. 84, no. 6, p. 063701, 2013.
[224] B.L. Helfield, X. Chen, S.C. Watkins, and F.S. Villanueva, "Biophysical insight into mechanisms of sonoporation," Proc Natl Acad Sci USA, vol. 113, no. 36, pp. 9983-9988, 2016.
[225] B.L. Helfield, X. Chen, B. Qin, S.C. Watkins, and F.S. Villanueva, "Mechanistic Insight into sonoporation with ultrasound-stimulated polymer microbubbles," Ultrasound Med Biol, vol. 43, no. 11, pp. 2678-2689, 2017.

[226] K. Kooiman, M. Foppen-Harteveld, A.F.W. van der Steen, and N. de Jong, "Sonoporation of endothelial cells by vibrating targeted microbubbles," J Control Release, vol. 154, no. 1, pp. 35-41, 2011.
[227] A. van Wamel et al., "Vibrating microbubbles poking individual cells: Drug transfer into cells via sonoporation," J Control Release, vol. 112, no. 2, pp. 149-155, 2006.
[228] Z. Fan, H. Liu, M. Mayer, and C.X. Deng, "Spatiotemporally controlled single cell sonoporation," Proc Natl Acad Sci USA, vol. 109, no. 41, pp. 16486-16491, 2012.
[229] Y. Hu, J.M.F. Wan, and A.C.H. Yu, "Membrane perforation and recovery dynamics in microbubble-mediated sonoporation," Ultrasound Med Biol, vol. 39, no. 12, pp. 2393-2405, 2013.
[230] I. De Cock et al., "Ultrasound and microbubble mediated drug delivery: Acoustic pressure as determinant for uptake via membrane pores or endocytosis," J Control Release, vol. 197, pp. 20-28, 2015.
[231] I. Lentacker, N. Wang, R.E. Vandenbroucke, J. Demeester, S.C. De Smedt, and N.N. Sanders, "Ultrasound exposure of lipoplex loaded microbubbles facilitates direct cytoplasmic entry of the lipoplexes," Mol Pharm, vol. 6, no. 2, pp. 457-467, 2009.
[232] I. Lentacker, B. Geers, J. Demeester, S.C. De Smedt, and N.N. Sanders, "Design and evaluation of doxorubicin-containing microbubbles for ultrasound-triggered doxorubicin delivery: Cytotoxicity and mechanisms involved," Mol Ther, vol. 18, no. 1, pp. 101-108, 2010.
[233] C. Jia, L. Xu, T. Han, P. Cai, A.C.H. Yu, and P. Qin, "Generation of reactive oxygen species in heterogeneously sonoporated cells by microbubbles with single-pulse ultrasound," Ultrasound Med Biol, vol. 44, no. 5, pp. 1074-1085, 2018.
[234] I. De Cock, G. Lajoinie, M. Versluis, S.C. De Smedt, and I. Lentacker, "Sonoprinting and the importance of microbubble loading for the ultrasound mediated cellular delivery of nanoparticles," Biomaterials, vol. 83, pp. 294-307, 2016.
[235] X. Chen, R.S. Leow, Y. Hu, J.M. Wan, and A.C. Yu, "Single-site sonoporation disrupts actin cytoskeleton organization," J R Soc Interface, vol. 11, no. 95, p. 20140071, 2014.
[236] B. Lammertink et al., "Dynamic fluorescence microscopy of cellular uptake of intercalating model drugs by ultrasound-activated microbubbles," Mol Imaging Biol, vol. 19, no. 5, pp. 683-693, 2017.
[237] M. Emmer, H.J. Vos, M. Versluis, and N. De Jong, "Radial modulation of single microbubbles," IEEE Trans Ultrason Ferroelectr Freq Control, vol. 56, no. 11, pp. 2370-2379, 2009.
[238] B.L. Helfield, E. Cherin, F.S. Foster, and D.E. Goertz, "Investigating the subharmonic response of individual phospholipid encapsulated microbubbles at high frequencies: A comparative study of five agents," Ultrasound Med Biol, vol. 38, no. 5, pp. 846-863, 2012.
[239] D. Maresca et al., "Acoustic Sizing of an Ultrasound Contrast Agent," Ultrasound Med Biol, vol. 36, no. 10, pp. 1713-1721, 2010.
[240] J.J. Kwan and M.A. Borden, "Lipid monolayer collapse and microbubble stability," Adv Colloid Interface Sci, vol. 183-184, pp. 82-99, 2012.
[241] K. Kooiman et al., "DSPC or DPPC as main shell component influences ligand distribution and binding area of lipid-coated targeted microbubbles," Eur J Lipid Sci Technol, vol. 116, no. 9, pp. 1217-1227, 2014.
[242] E.C. Gelderblom et al., "Brandaris 128 ultra-high-speed imaging facility: 10 years of operation, updates, and enhanced features," Rev Sci Instrum, vol. 83, no. 10, p. 103706, 2012.
[243] S.M. van der Meer et al., "Microbubble spectroscopy of ultrasound contrast agents," J Acoust Soc Am, vol. 121, no. 1, pp. 648-656, 2007.
[244] T. Baumgart, G. Hunt, E.R. Farkas, W.W. Webb, and G.W. Feigenson, "Fluorescence probe partitioning between Lo/Ld phases in lipid membranes," Biochim Biophys Acta Biomembr, vol. 1768, no. 9, pp. 2182-2194, 2007.
[245] T. van Rooij et al., "Viability of endothelial cells after ultrasound-mediated sonoporation: Influence of targeting, oscillation, and displacement of microbubbles," J Control Release, vol. 238, pp. 197-211, 2016.
[246] Y. Luan et al., "Lipid shedding from single oscillating microbubbles," Ultrasound Med Biol, vol. 40, no. 8, pp. 1834-1846, 2014.
[247] K. Kooiman et al., "Focal areas of increased lipid concentration on the coating of microbubbles during short tone-burst ultrasound insonification," PLOS ONE, vol. 12, no. 7, p. e0180747, 2017.
[248] J.M. Yarwood and P.M. Schlievert, "Quorum sensing in Staphylococcus infections," J Clin Investig, vol. 112, no. 11, pp. 1620-1625, 2003.

[249] M.K. Luther et al., "Clinical and genetic risk factors for biofilm-forming *Staphylococcus aureus*," Antimicrob Agents Chemother, vol. 62, no. 5, pp. e02252-17, 2018.
[250] A.E. Barsoumian et al., "Clinical infectious outcomes associated with biofilm-related bacterial infections: a retrospective chart review," BMC infectious diseases, vol. 15, pp. 223-223, 2015.
[251] S.Y.C. Tong, J.S. Davis, E. Eichenberger, T.L. Holland, and V.G. Fowler, Jr., "*Staphylococcus aureus* infections: epidemiology, pathophysiology, clinical manifestations, and management," Clin Microbiol Rev, vol. 28, no. 3, pp. 603-661, 2015.
[252] J.B. Kaplan, "Antibiotic-Induced Biofilm Formation," Int J Artif Organs, vol. 34, no. 9, pp. 737-751, 2011.
[253] J.B. Kaplan et al., "Low levels of β-lactam antibiotics induce extracellular DNA release and biofilm formation in *Staphylococcus aureus*," mBio, vol. 3, no. 4, p. e00198, 2012.
[254] Z.A. Mirani and N. Jamil, "Effect of sub-lethal doses of vancomycin and oxacillin on biofilm formation by vancomycin intermediate resistant *Staphylococcus aureus*," J Basic Microbiol, vol. 51, no. 2, pp. 191-195, 2011.
[255] H.S. Joo, J.L. Chan, G.Y.C. Cheung, and M. Otto, "Subinhibitory concentrations of protein synthesis-inhibiting antibiotics promote increased expression of the agr virulence regulator and production of phenol-soluble modulin cytolysins in community-associated methicillin-resistant *Staphylococcus aureus*," Antimicrob Agents Chemother, vol. 54, no. 11, pp. 4942-4944, 2010.
[256] A. Resch, R. Rosenstein, C. Nerz, and F. Götz, "Differential gene expression profiling of *Staphylococcus aureus* cultivated under biofilm and planktonic conditions," Appl Environ Microbiol, vol. 71, no. 5, pp. 2663-2676, 2005.
[257] A.R. Sultan et al., "Production of staphylococcal complement inhibitor (SCIN) and other immune modulators during the early stages of *Staphylococcus aureus* biofilm formation in a mammalian cell culture medium," Infect Immun, vol. 86, no. 8, pp. e00352-18, 2018.
[258] A.R. Sultan et al., "During the early stages of *Staphylococcus aureus* biofilm formation, induced neutrophil extracellular traps are degraded by autologous thermonuclease," Infect Immun, vol. 87, no. 12, pp. e00605-19, 2019.
[259] S. Croes, R.H. Deurenberg, M.L.L. Boumans, P.S. Beisser, C. Neef, and E.E. Stobberingh, "*Staphylococcus aureus* biofilm formation at the physiologic glucose concentration depends on the S. aureus lineage," BMC Microbiol, vol. 9, pp. 229-229, 2009.
[260] P.M. den Reijer et al., "Detection of alpha-toxin and other virulence factors in biofilms of *Staphylococcus aureus* on polystyrene and a human epidermal model," PLOS ONE, vol. 11, no. 1, p. e0145722, 2016.
[261] C.A. Kennedy and J.P. O'Gara, "Contribution of culture media and chemical properties of polystyrene tissue culture plates to biofilm development by *Staphylococcus aureus*," J Med Microbiol, vol. 53, no. Pt 11, pp. 1171-1173, 2004.
[262] P. Chen, J.J. Abercrombie, N.R. Jeffrey, and K.P. Leung, "An improved medium for growing *Staphylococcus aureus* biofilm," J Microbiol Methods, vol. 90, no. 2, pp. 115-118, 2012.
[263] C.T. Price, F.G. O'Brien, B.P. Shelton, J.R. Warmington, W.B. Grubb, and J.E. Gustafson, "Effects of salicylate and related compounds on fusidic acid MICs in *Staphylococcus aureus*," J Antimicrob Chemother, vol. 44, no. 1, pp. 57-64, 1999.
[264] C. Dotto et al., "The active component of aspirin, salicylic acid, promotes *Staphylococcus aureus* biofilm formation in a pia-dependent manner," Front Microbiol, vol. 8, p. 4, 2017.
[265] L.P. Alvarez, M.S. Barbagelata, A.L. Cheung, D.O. Sordelli, and F.R. Buzzola, "Salicylic acid enhances *Staphylococcus aureus* extracellular adhesin protein expression," Microbes Infect, vol. 13, no. 12-13, pp. 1073-80, 2011.
[266] J.R. Bowers et al., "Improved subtyping of *Staphylococcus aureus* clonal complex 8 strains based on whole-genome phylogenetic analysis," mSphere, vol. 3, no. 3, 2018.
[267] L. Tan, S.R. Li, B. Jiang, X.M. Hu, and S. Li, "Therapeutic targeting of the *Staphylococcus aureus* accessory gene regulator (agr) system," Front Microbiol, vol. 9, p. 55, 2018.
[268] K.Y. Le and M. Otto, "Quorum-sensing regulation in staphylococci-an overview," Front Microbiol, vol. 6, p. 1174, 2015.
[269] K.H. Rand, H.J. Houck, P. Brown, and D. Bennett, "Reproducibility of the microdilution checkerboard method for antibiotic synergy," Antimicrob Agents Chemother, vol. 37, no. 3, pp. 613-5, 1993.

[270] M.P. Weinstein, Methods for dilution antimicrobial susceptibility tests for bacteria that grow aerobically, 11th ed. Clinical and Laboratory Standards Institute, 2018, p. 112.
[271] G.D. Christensen et al., "Adherence of coagulase-negative staphylococci to plastic tissue culture plates: a quantitative model for the adherence of staphylococci to medical devices," J Clin Microbiol, vol. 22, no. 6, pp. 996-1006, 1985.
[272] J.M. Yarwood, D.J. Bartels, E.M. Volper, and E.P. Greenberg, "Quorum sensing in *Staphylococcus aureus* biofilms," J Bacteriol, vol. 186, no. 6, pp. 1838-1850, 2004.
[273] I. Beekers et al., "Combined confocal microscope and Brandaris 128 ultra-high-speed camera," Ultrasound Med Biol, vol. 45, no. 9, pp. 2575-2582, Sep 2019.
[274] S.H. Rooijakkers, W.J. van Wamel, M. Ruyken, K.P. van Kessel, and J.A. van Strijp, "Anti-opsonic properties of staphylokinase," Microbes Infect, vol. 7, no. 3, pp. 476-84, Mar 2005.
[275] T. Ueno, A. Tanaka, Y. Hamanaka, and T. Suzuki, "Serum drug concentrations after oral administration of paracetamol to patients with surgical resection of the gastrointestinal tract," Br J Clin Pharmacol, vol. 39, no. 3, pp. 330-2, 1995.
[276] N. Buckley and M. Eddleston, "Paracetamol (acetaminophen) poisoning," BMJ Clin Evid, 2007.
[277] R.M. Donlan and J.W. Costerton, "Biofilms: survival mechanisms of clinically relevant microorganisms," Clin Microbiol Rev, vol. 15, no. 2, pp. 167-193, 2002.
[278] L. Montanaro et al., "Extracellular DNA in biofilms," Int J Artif Organs, vol. 34, no. 9, pp. 824-831, 2011.
[279] C.B. Whitchurch, T. Tolker-Nielsen, P.C. Ragas, and J.S. Mattick, "Extracellular DNA required for bacterial biofilm formation," Science, vol. 295, no. 5559, p. 1487, 2002.
[280] A.E. Paharik and A.R. Horswill, "The staphylococcal biofilm: Adhesins, regulation, and host response," Microbiol Spectr, vol. 4, no. 2, pp. 10.1128, 2016.
[281] C.R. Arciola, D. Campoccia, S. Ravaioli, and L. Montanaro, "Polysaccharide intercellular adhesin in biofilm: structural and regulatory aspects," Front Cell Infect Microbiol, vol. 5, no. 7, 2015.
[282] H.S. Joo and M. Otto, "Mechanisms of resistance to antimicrobial peptides in staphylococci," Biochim Biophys Acta, vol. 1848, no. 11, pp. 3055-61, 2015.
[283] C. Vuong et al., "Polysaccharide intercellular adhesin (PIA) protects *Staphylococcus epidermidis* against major components of the human innate immune system," Cell Microbiol, vol. 6, no. 3, pp. 269-275, 2004.
[284] C.T. Price, I.R. Lee, and J.E. Gustafson, "The effects of salicylate on bacteria," Int J Biochem Cell Biol, vol. 32, no. 10, pp. 1029-43, Oct 2000.
[285] I. Jongerius, M. Puister, J. Wu, M. Ruyken, J.A. van Strijp, and S.H. Rooijakkers, "Staphylococcal complement inhibitor modulates phagocyte responses by dimerization of convertases," J Immunol, vol. 184, no. 1, pp. 420-5, 2010.
[286] S.H. Rooijakkers et al., "Structural and functional implications of the alternative complement pathway C3 convertase stabilized by a staphylococcal inhibitor," Nat Immunol, vol. 10, no. 7, pp. 721-7, 2009.
[287] R.P. van Swelm et al., "Acute acetaminophen intoxication leads to hepatic iron loading by decreased hepcidin synthesis," Toxicol Sci, vol. 129, no. 1, pp. 225-33, 2012.
[288] M. Johnson, A. Cockayne, and J.A. Morrissey, "Iron-regulated biofilm formation in *Staphylococcus aureus* Newman requires ica and the secreted protein Emp," Infect Immun, vol. 76, no. 4, pp. 1756-65, 2008.
[289] E.M. Walker, Jr. et al., "Acetaminophen protects against iron-induced cardiac damage in gerbils," Ann Clin Lab Sci, vol. 37, no. 1, pp. 22-33, 2007.
[290] M. Johnson, A. Cockayne, P.H. Williams, and J.A. Morrissey, "Iron-responsive regulation of biofilm formation in *Staphylococcus aureus* involves fur-dependent and fur-independent mechanisms," J Bacteriol, vol. 187, no. 23, pp. 8211-5, 2005.
[291] H.F. Wertheim et al., "Associations between *Staphylococcus aureus* genotype, infection, and in-hospital mortality: A nested case-control study," J Infect Dis, vol. 192, no. 7, pp. 1196-200, 2005.
[292] H. Ghasemzadeh-Moghaddam, W. van Wamel, A. van Belkum, R. A. Hamat, M. Tavakol, and V. K. Neela, "Humoral immune consequences of *Staphylococcus aureus* ST239-associated bacteremia," Eur J Clin Microbiol Infect Dis, vol. 37, no. 2, pp. 255-263, 2018.
[293] N. Lemmens, W.J.B. van Wamel, S. Snijders, A.J. Lesse, H. Faden, and A. van Belkum, "Genomic comparisons of USA300 *Staphylococcus aureus* colonizating the nose and rectum of children with skin abscesses," Microb Pathog, vol. 50, no. 3-4, pp. 192-9, 2011.

[294] R. Novick, "Properties of a cryptic high-frequency transducing phage in *Staphylococcus aureus*," Virology, vol. 33, no. 1, pp. 155-66, 1967.
[295] R.P. Novick, H.F. Ross, S.J. Projan, J. Kornblum, B. Kreiswirth, and S. Moghazeh, "Synthesis of staphylococcal virulence factors is controlled by a regulatory RNA molecule," Embo Journal, vol. 12, no. 10, pp. 3967-3975, 1993.
[296] E.S. Duthie and L.L. Lorenz, "Staphylococcal coagulase; mode of action and antigenicity," J Gen Microbiol, vol. 6, no. 1-2, pp. 95-107, 1952.
[297] S.H. Rooijakkers, M. Ruyken, J. van Roon, K.P. van Kessel, J.A. van Strijp, and W.J.B. van Wamel, "Early expression of SCIN and CHIPS drives instant immune evasion by *Staphylococcus aureus*," Cell Microbiol, vol. 8, no. 8, pp. 1282-93, 2006.
[298] P. Stoodley et al., "Orthopaedic biofilm infections," Curr Orthop Pract, vol. 22, no. 6, pp. 558-563, 2011.
[299] R.P. Wenzel, "Health care–associated infections: major issues in the early years of the 21st century," Clin Infect Dis, vol. 45, no. Supplement_1, pp. S85-S88, 2007.
[300] M. Jamal et al., "Bacterial biofilm and associated infections," J Chin Med Assoc, vol. 81, no. 1, pp. 7-11, 2018.
[301] K. Lewis, "Persister cells, dormancy and infectious disease," Nat Rev Microbiol, vol. 5, no. 1, pp. 48-56, 2007.
[302] A. Ito, A. Taniuchi, T. May, K. Kawata, and S. Okabe, "Increased antibiotic resistance of *Escherichia coli* in mature biofilms," Appl Environ Microbiol, vol. 75, no. 12, pp. 4093-4100, 2009.
[303] D. Lebeaux, J.M. Ghigo, and C. Beloin, "Biofilm-related infections: bridging the gap between clinical management and fundamental aspects of recalcitrance toward antibiotics," Microbiol Mol Biol Rev, vol. 78, no. 3, pp. 510-543, 2014.
[304] K.R. Lattwein, H. Shekhar, J.J.P. Kouijzer, W.J.B. van Wamel, C.K. Holland, and K. Kooiman, "Sonobactericide: An emerging treatment strategy for bacterial infections," Ultrasound Med Biol, vol. 46, no. 2, pp. 193-215, 2020.
[305] Z. Fan, R.E. Kumon, and C.X. Deng, "Mechanisms of microbubble-facilitated sonoporation for drug and gene delivery," Ther Deliv, vol. 5, no. 4, pp. 467-486, 2014.
[306] K. Kooiman et al., "Ultrasound-responsive cavitation nuclei for therapy and drug delivery," Ultrasound Med Biol, vol. 46, no. 6, pp. 1296-1325, 2020.
[307] S. Roovers et al., "The role of ultrasound-driven microbubble dynamics in drug delivery: From microbubble fundamentals to clinical translation," Langmuir, vol. 35, no. 31, pp. 10173-10191, 2019.
[308] B. Slingerland et al., "Whole-genome sequencing to explore nosocomial transmission and virulence in neonatal methicillin-susceptible *Staphylococcus aureus* bacteremia," Antimicrob Resist Infect Control, vol. 9, no. 1, p. 39, 2020.
[309] D. Harmsen et al., "Typing of methicillin-resistant *Staphylococcus aureus* in a university hospital setting by using novel software for spa repeat determination and database management," J Clin Microbiol, vol. 41, no. 12, p. 5442, 2003.
[310] S.K. Shukla and T.S. Rao, "An Improved crystal violet assay for biofilm quantification in 96-well microtitre plate," bioRxiv, p. 100214, 2017.
[311] L. Corte, D. Casagrande Pierantoni, C. Tascini, L. Roscini, and G. Cardinali, "Biofilm specific activity: a measure to quantify microbial biofilm," Microorganisms, vol. 7, no. 3, 2019.
[312] L. Boulos, M. Prévost, B. Barbeau, J. Coallier, and R. Desjardins, "LIVE/DEAD® BacLight™: application of a new rapid staining method for direct enumeration of viable and total bacteria in drinking water," J Microbiol Methods, vol. 37, no. 1, pp. 77-86, 1999.
[313] J.B. Cornett and G.D. Shockman, "Cellular lysis of *Streptococcus faecalis* induced with triton X-100," J Bacteriol, vol. 135, no. 1, pp. 153-160, 1978.
[314] A.L. Klibanov et al., "Detection of individual microbubbles of ultrasound contrast agents: imaging of free-floating and targeted bubbles," Investig Radiol, vol. 39, no. 3, pp. 187-195, 2004.
[315] FDA/Center for Drug Evaluation and Research (2015). Oxacillin Injection, USP, data safety label
[316] A. Kashif et al., "*Staphylococcus aureus* ST398 virulence is associated with factors carried on prophage ϕSa3,", Front Microbiol, vol. 10, no. 2219, 2019.
[317] K. Bouiller, H. Gbaguidi-Haore, D. Hocquet, P. Cholley, X. Bertrand, and C. Chirouze, "Clonal complex 398 methicillin-susceptible *Staphylococcus aureus* bloodstream infections are associated with high mortality," Clin Microbiol Infect, vol. 22, no. 5, pp. 451-455, 2016.

[318] A.S. Brunel et al., "Methicillin-sensitive *Staphylococcus aureus* CC398 in intensive care unit, France," Emerg Infect Dis, vol. 20, no. 9, pp. 1511-1515, 2014.

[319] I. Bonnet et al., "High prevalence of spa type t571 among methicillin-susceptible *Staphylococcus aureus* from bacteremic patients in a French University Hospital," PLOS ONE, vol. 13, no. 10, pp. e0204977-e0204977, 2018.

[320] L.B. Price et al., "*Staphylococcus aureus* CC398: host adaptation and emergence of methicillin resistance in livestock," mBio, vol. 3, no. 1, 2012.

[321] A.C. Uhlemann et al., "Identification of a highly transmissible animal-independent *Staphylococcus aureus* ST398 clone with distinct genomic and cell adhesion properties," mBio, vol. 3, no. 2, 2012.

[322] A.S. Valentin-Domelier et al., "Methicillin-susceptible ST398 *Staphylococcus aureus* responsible for bloodstream infections: an emerging human-adapted subclone?," PLOS ONE, vol. 6, no. 12, pp. e28369-e28369, 2011.

[323] N. van der Mee-Marquet et al., "Emergence of unusual bloodstream infections associated with pig-borne-like *Staphylococcus aureus* ST398 in France," Clin Infect Dis, vol. 52, no. 1, pp. 152-3, 2011.

[324] I. Beekers et al., "Opening of endothelial cell–cell contacts due to sonoporation," J Control Release, vol. 322, pp. 426-438, 2020.

[325] L. Schermelleh, R. Heintzmann, and H. Leonhardt, "A guide to super-resolution fluorescence microscopy," J Cell Biol, vol. 190, no. 2, pp. 165-175, 2010.

[326] P. Cheng, W. Ingrid, and E.P. Robert, "Femtosecond near-infrared opto-injection of single living cells: pore size in dependence of laser intensity," in Proc SPIE, vol. 6084, 2006.

[327] C.E.M. Krämer, W. Wiechert, and D. Kohlheyer, "Time-resolved, single-cell analysis of induced and programmed cell death via non-invasive propidium iodide and counterstain perfusion," Sci Rep, vol. 6, pp. 32104-32104, 2016.

[328] J. Wille and T. Coenye, "Biofilm dispersion: The key to biofilm eradication or opening Pandora's box?," Biofilm, vol. 2, p. 100027, 2020.

[329] Y.S. Tung, F. Vlachos, J.A. Feshitan, M.A. Borden, and E.E. Konofagou, "The mechanism of interaction between focused ultrasound and microbubbles in blood-brain barrier opening in mice," J Acoust Soc Am, vol. 130, no. 5, pp. 3059-3067, 2011.

[330] S. Michelin, E. Guérin, and E. Lauga, "Collective dissolution of microbubbles," Phys Rev Fluids, vol. 3, no. 4, p. 043601, 2018.

[331] C. Lazarus, A.N. Pouliopoulos, M. Tinguely, V. Garbin, and J. J. Choi, "Clustering dynamics of microbubbles exposed to low-pressure 1-MHz ultrasound," J Acoust Soc Am, vol. 142, no. 5, pp. 3135-3146, 2017.

[332] C. Ohl et al., "Sonoporation from jetting cavitation bubbles," Biophys J, vol. 91 11, pp. 4285-95, 2006.

[333] H.C. Flemming and J. Wingender, "The biofilm matrix," Nat Rev Microbiol, vol. 8, no. 9, pp. 623-33, 2010.

[334] G. Thiene and C. Basso, "Pathology and pathogenesis of infective endocarditis in native heart valves," Cardiovasc Pathol, vol. 15, no. 5, pp. 256-263, 2006.

[335] D.R. Murdoch et al., "Clinical presentation, etiology, and outcome of infective endocarditis in the 21st century: the International Collaboration on Endocarditis-Prospective Cohort Study," Arch Intern Med, vol. 169, no. 5, pp. 463-73, 2009.

[336] A. Wang et al., "Contemporary clinical profile and outcome of prosthetic valve endocarditis," JAMA, vol. 297, no. 12, pp. 1354-61, 2007.

[337] C. Chirouze et al., "Prognostic factors in 61 cases of *Staphylococcus aureus* prosthetic valve infective endocarditis from the International Collaboration on Endocarditis merged database," Clin Infect Dis, vol. 38, no. 9, pp. 1323-7, 2004.

[338] C. Selton-Suty et al., "Preeminence of *Staphylococcus aureus* in infective endocarditis: a 1-year population-based survey," Clin Infect Dis, vol. 54, no. 9, pp. 1230-9, 2012.

[339] A. Bannay et al., "The impact of valve surgery on short- and long-term mortality in left-sided infective endocarditis: do differences in methodological approaches explain previous conflicting results?," Eur Heart J, vol. 32, no. 16, pp. 2003-2015, 2009.

[340] A.A. Bin Abdulhak et al., "Global and regional burden of infective endocarditis, 1990-2010: a systematic review of the literature," Glob Heart, vol. 9, no. 1, pp. 131-43, 2014.

[341] M. Mirabel et al., "Long-term outcomes and cardiac surgery in critically ill patients with infective endocarditis," Eur Heart J, vol. 35, no. 18, pp. 1195-204, 2014.
[342] B. Hoen and X. Duval, "Clinical practice. Infective endocarditis," N Engl J Med, vol. 368, no. 15, pp. 1425-33, 2013.
[343] L. Slipczuk et al., "Infective endocarditis epidemiology over five decades: a systematic review," PLOS ONE, vol. 8, no. 12, p. e82665, 2013.
[344] L. Kritharides and R.W. Sy, "Health care exposure and age in infective endocarditis: results of a contemporary population-based profile of 1536 patients in Australia," Eur Heart J, vol. 31, no. 15, pp. 1890-1897, 2010.
[345] M.L. Fernández Guerrero, B. Álvarez, F. Manzarbeitia, and G. Renedo, "Infective endocarditis at autopsy: A review of pathologic manifestations and clinical correlates," Medicine, vol. 91, no. 3, pp. 152-164, 2012.
[346] L. Liesenborghs, S. Meyers, T. Vanassche, and P. Verhamme, "Coagulation: At the heart of infective endocarditis," J Thromb Haemost, vol. 18, no. 5, pp. 995-1008, 2020.
[347] C.A. Schneider, W.S. Rasband, and K.W. Eliceiri, "NIH Image to ImageJ: 25 years of image analysis," Nat Methods, vol. 9, no. 7, pp. 671-675, 2012.
[348] D.T. Durack, "Experimental bacterial endocarditis. IV. Structure and evolution of very early lesions," J Pathol, vol. 115, no. 2, pp. 81-89, 1975.
[349] P. Moreillon et al., "Role of *Staphylococcus aureus* coagulase and clumping factor in pathogenesis of experimental endocarditis," Infect Immun, vol. 63, no. 12, pp. 4738-43, 1995.
[350] H.J. Rogers, "The rate of formation of hyaluronidase, coagulase and total extracellular protein by strains of *Staphylococcus aureus*," Microbiology, vol. 10, no. 2, pp. 209-220, 1954.
[351] T.J. Foster and M. Hook, "Surface protein adhesins of *Staphylococcus aureus*," Trends Microbiol, vol. 6, no. 12, pp. 484-8, 1998.
[352] P.M. Sullam, T.A. Drake, and M.A. Sande, "Pathogenesis of endocarditis," Am J Med, vol. 78, no. 6B, pp. 110-5, 1985.
[353] A. Ito, A. Taniuchi, T. May, K. Kawata, and S. Okabe, "Increased antibiotic resistance of *Escherichia coli* in mature biofilms," Appl Environ Microbiol, vol. 75, no. 12, pp. 4093-100, 2009.
[354] J.C. Carmen et al., "Treatment of biofilm infections on implants with low-frequency ultrasound and antibiotics," Am J Infect Control, vol. 33, no. 2, pp. 78-82, 2005.
[355] A.K. Seth et al., "Noncontact, low-frequency ultrasound as an effective therapy against *Pseudomonas aeruginosa*-infected biofilm wounds," Wound Repair Regen, vol. 21, no. 2, pp. 266-74, 2013.
[356] X. Liu, H. Yin, C.X. Weng, and Y. Cai, "Low-frequency ultrasound enhances antimicrobial activity of colistin-vancomycin combination against pan-resistant biofilm of *Acinetobacter baumannii*," Ultrasound Med Biol, vol. 42, no. 8, pp. 1968-75, 2016.
[357] T. Karosi, I. Sziklai, and P. Csomor, "Low-frequency ultrasound for biofilm disruption in chronic rhinosinusitis with nasal polyposis: *in vitro* pilot study," Laryngoscope, vol. 123, no. 1, pp. 17-23, 2013.
[358] D.L. Miller, "Overview of experimental studies of biological effects of medical ultrasound caused by gas body activation and inertial cavitation," Prog Biophys Mol Biol, vol. 93, no. 1-3, pp. 314-30, 2007.
[359] E.C. Unger, E. Hersh, M. Vannan, T.O. Matsunaga, and T. McCreery, "Local drug and gene delivery through microbubbles," Prog Cardiovasc Dis, vol. 44, no. 1, pp. 45-54, 2001.
[360] S. Datta et al., "Correlation of cavitation with ultrasound enhancement of thrombolysis," Ultrasound Med Biol, vol. 32, no. 8, pp. 1257-67, 2006.
[361] A. Levitas, N. Zucker, E. Zalzstein, S. Sofer, J. Kapelushnik, and K.A. Marks, "Successful treatment of infective endocarditis with recombinant tissue plasminogen activator," J Pediatr, vol. 143, no. 5, pp. 649-52, 2003.
[362] R.E. Fleming, S.J. Barenkamp, and S.B. Jureidini, "Successful treatment of a staphylococcal endocarditis vegetation with tissue plasminogen activator," J Pediatr, vol. 132, no. 3 Pt 1, pp. 535-7, 1998.
[363] A.M. Gunes, O.M. Bostan, B. Baytan, and E. Semizel, "Treatment of infective endocarditis with recombinant tissue plasminogen activator," Pediatr Blood Cancer, vol. 50, no. 1, pp. 132-4, 2008.

[364] A. Levitas, H. Krymko, J. Richardson, E. Zalzstein, and V. Ioffe, "Recombinant tissue plasminogen activator as a novel treatment option for infective endocarditis: a retrospective clinical study in 32 children," Cardiol Young, vol. 26, no. 1, pp. 110-5, 2016.

[365] J.Y. Cheng, G.J. Shaw, and C.K. Holland, "*In vitro* microscopic imaging of enhanced thrombolysis with 120-kHz ultrasound in a human clot model," Acoust Res Lett Online, vol. 6, no. 1, pp. 25-29, 2005.

[366] J.H.K. Chen et al., "The use of high-resolution melting analysis for rapid spa typing on methicillin-resistant *Staphylococcus aureus* clinical isolates," J Microbiol Methods, vol. 92, no. 2, pp. 99-102, 2013.

[367] D. Harmsen et al., "Typing of methicillin-resistant *Staphylococcus aureus* in a university hospital setting by using novel software for spa repeat determination and database management," J Clin Microbiol, vol. 41, no. 12, pp. 5442-5448, 2003.

[368] B. Shopsin et al., "Evaluation of protein A gene polymorphic region DNA sequencing for typing of *Staphylococcus aureus* strains," J Clin Microbiol, vol. 37, no. 11, pp. 3556-3563, 1999.

[369] National Committee for Clinical Laboratory Standards, "Methods for dilution antimicrobial susceptibility tests for bacteria that grow aerobically," in M07-A9 vol. 9: 32(2), ed, 2012.

[370] L.G. Harris, S.J. Foster, and R.G. Richards, "An introduction to *Staphylococcus aureus*, and techniques for identifying and quantifying *S. aureus* adhesins in relation to adhesion to biomaterials: review," Eur Cell Mater, vol. 4, pp. 39-60, 2002.

[371] R.J. Gordon and F.D. Lowy, "Pathogenesis of methicillin-resistant *Staphylococcus aureus* infection," Clin Infect Dis, vol. 46 Suppl 5, pp. S350-9, 2008.

[372] J.M. Meunier, C.K. Holland, C.J. Lindsell, and G.J. Shaw, "Duty cycle dependence of ultrasound enhanced thrombolysis in a human clot model," Ultrasound Med Biol, vol. 33, no. 4, pp. 576-83, 2007.

[373] S. Rodbard, "Blood velocity and endocarditis," Circulation, vol. 27, pp. 18-28, 1963.

[374] L. Hatle, "Assessment of aortic blood flow velocities with continuous wave Doppler ultrasound in the neonate and young child," J Am Coll Cardiol, vol. 5, no. 1, pp. 113S-119S, 1985.

[375] G.J. Shaw, J.M. Meunier, C.J. Lindsell, and C.K. Holland, "Tissue plasminogen activator concentration dependence of 120 kHz ultrasound-enhanced thrombolysis," Ultrasound Med Biol, vol. 34, no. 11, pp. 1783-92, 2008.

[376] Oxacillin Injection, USP in Plastic Container For Intravenous Use Only GALAXY Container (PL 2040)

[377] H. Shekhar et al., "*In vitro* thrombolytic efficacy of echogenic liposomes loaded with tissue plasminogen activator and octafluoropropane gas," Phys Med Biol, vol. 62, no. 2, pp. 517-538, 2017.

[378] L.M. Imaging, "Definity Safety Label," in "U.S. Food and Drug Administration," FDA/Center for Drug Evaluation and Research, Silver Spring, USA,2011.

[379] J.E. Bennett, M.J. Blaser, Mandell, Douglas, and Bennett's Infectious Disease Essentials, 1 ed. Elsevier, 2016, p. 560.

[380] P.S. McKinnon and S.L. Davis, "Pharmacokinetic and pharmacodynamic issues in the treatment of bacterial infectious diseases," Eur J Clin Microbiol Infect Dis, vol. 23, no. 4, pp. 271-88, 2004.

[381] P. Tanswell, E. Seifried, E. Stang, and J. Krause, "Pharmacokinetics and hepatic catabolism of tissue-type plasminogen activator," Arzneimittelforschung, vol. 41, no. 12, pp. 1310-9, Dec 1991.

[382] E. Seifried, P. Tanswell, D. Ellbruck, W. Haerer, and A. Schmidt, "Pharmacokinetics and haemostatic status during consecutive infusions of recombinant tissue-type plasminogen activator in patients with acute myocardial infarction," Thromb Haemost, vol. 61, no. 3, pp. 497-501, 1989.

[383] W.M. Scheld, R.W. Strunk, G. Balian, and R.A. Calderone, "Microbial adhesion to fibronectin *in vitro* correlates with production of endocarditis in rabbits," Proc Soc Exp Biol Med, vol. 180, no. 3, pp. 474-82, 1985.

[384] Y.H. An and R.J. Friedman, "Concise review of mechanisms of bacterial adhesion to biomaterial surfaces," J Biomed Mater Res, vol. 43, no. 3, pp. 338-48,1998.

[385] C. Nethercott et al., "Molecular characterization of endocarditis-associated *Staphylococcus aureus*," J Clin Microbiol, vol. 51, no. 7, pp. 2131-8, 2013.

[386] G. Rasmussen, S. Monecke, R. Ehricht, and B. Soderquist, "Prevalence of clonal complexes and virulence genes among commensal and invasive *Staphylococcus aureus* isolates in Sweden," PLOS ONE, vol. 8, no. 10, p. e77477, 2013.

[387] C. Bouchiat et al., "*Staphylococcus aureus* infective endocarditis versus bacteremia strains: Subtle genetic differences at stake," Infect Genet Evol, vol. 36, pp. 524-530, 2015.
[388] A. Sabat, D.C. Melles, G. Martirosian, H. Grundmann, A. van Belkum, and W. Hryniewicz, "Distribution of the serine-aspartate repeat protein-encoding sdr genes among nasal-carriage and invasive *Staphylococcus aureus* strains," J Clin Microbiol, vol. 44, no. 3, pp. 1135-8, 2006.
[389] D.T. Durack and P.B. Beeson, "Experimental bacterial endocarditis. II. Survival of a bacteria in endocardial vegetations," Br J Exp Pathol, vol. 53, no. 1, pp. 50-3, 1972.
[390] D.T. Durack and P.B. Beeson, "Experimental bacterial endocarditis. I. Colonization of a sterile vegetation," Br J Exp Pathol, vol. 53, no. 1, pp. 44-9, 1972.
[391] G.W. Gibson et al., "Development of a mouse model of induced *Staphylococcus aureus* infective endocarditis," Comp Med, vol. 57, no. 6, pp. 563-9, 2007.
[392] L.R. Freedman and J. Valone, Jr., "Experimental infective endocarditis," Prog Cardiovasc Dis, vol. 22, no. 3, pp. 169-80, 1979.
[393] W.M. Scheld, R.J. Whitley, and C.M. Marra, Infections of the central nervous system, Fourth edition. ed. Philadelphia: Wolters Kluwer Health, 2014.
[394] B.J. McGrath, S.L. Kang, G.W. Kaatz, and M.J. Rybak, "Bactericidal activities of teicoplanin, vancomycin, and gentamicin alone and in combination against *Staphylococcus aureus* in an *in vitro* pharmacodynamic model of endocarditis," Antimicrob Agents Chemother, vol. 38, no. 9, pp. 2034-40, 1994.
[395] S.M. Palmer and M.J. Rybak, "Pharmacodynamics of once- or twice-daily levofloxacin versus vancomycin, with or without rifampin, against *Staphylococcus aureus* in an *in vitro* model with infected platelet-fibrin clots," Antimicrob Agents Chemother, vol. 40, no. 3, pp. 701-5, 1996.
[396] V.J. Torres, G. Pishchany, M. Humayun, O. Schneewind, and E.P. Skaar, "*Staphylococcus aureus* IsdB is a hemoglobin receptor required for heme iron utilization," J Bacteriol, vol. 188, no. 24, pp. 8421-9, 2006.
[397] C. Dias Kde, P.A. Barbugli, and C.E. Vergani, "Influence of different buffers (HEPES/MOPS) on keratinocyte cell viability and microbial growth," J Microbiol Methods, vol. 125, pp. 40-2, 2016.
[398] K.P. Haley and E.P. Skaar, "A battle for iron: host sequestration and *Staphylococcus aureus* acquisition," Microbes Infect, vol. 14, no. 3, pp. 217-27, 2012.
[399] R.T. Scheife, "Protein binding: what does it mean?," DICP, vol. 23, no. 7-8 Suppl, pp. S27-31, 1989.
[400] N.J. Mutch, L. Thomas, N.R. Moore, K.M. Lisiak, and N.A. Booth, "TAFIa, PAI-1 and alpha-antiplasmin: complementary roles in regulating lysis of thrombi and plasma clots," J Thromb Haemost, vol. 5, no. 4, pp. 812-7, 2007.
[401] D.B. Khismatullin, "Resonance frequency of microbubbles: effect of viscosity," J Acoust Soc Am, vol. 116, no. 3, pp. 1463-73, 2004.
[402] W.Y. Kim et al., "Left ventricular blood flow patterns in normal subjects: a quantitative analysis by three-dimensional magnetic resonance velocity mapping," J Am Coll Cardiol, vol. 26, no. 1, pp. 224-38, 1995.
[403] F. Bajd, J. Vidmar, A. Blinc, and I. Sersa, "Microscopic clot fragment evidence of biochemo-mechanical degradation effects in thrombolysis," Thromb Res, vol. 126, no. 2, pp. 137-43, 2010.
[404] F. Bajd and I. Sersa, "A concept of thrombolysis as a corrosion-erosion process verified by optical microscopy," Microcirculation, vol. 19, no. 7, pp. 632-41, 2012.
[405] F. Bajd and I. Sersa, "Mathematical modeling of blood clot fragmentation during flow-mediated thrombolysis," Biophys J, vol. 104, no. 5, pp. 1181-90, 2013.
[406] D.A. Gabriel, K. Muga, and E.M. Boothroyd, "The effect of fibrin structure on fibrinolysis," J Biol Chem, vol. 267, no. 34, pp. 24259-63, 1992.
[407] D. Collen, "On the regulation and control of fibrinolysis. Edward Kowalski Memorial Lecture," Thromb Haemost, vol. 43, no. 2, pp. 77-89, 1980.
[408] A.A. Fassa, D. Himbert, and A. Vahanian, "Mechanisms and management of TAVR-related complications," Nat Rev Cardiol, vol. 10, no. 12, pp. 685-95, 2013.
[409] F.W. Kremkau, "General principles of echocardiography," In: ASE's comprehensive echocardiography: Elsevier, 2015.
[410] S. Rodbard and C. Yamamoto, "Effect of stream velocity on bacterial deposition and growth," Cardiovasc Res, vol. 3, no. 1, pp. 68-74,1969.

[411] E. Hershberger, E.A. Coyle, G.W. Kaatz, M.J. Zervos, and M.J. Rybak, "Comparison of a rabbit model of bacterial endocarditis and an *in vitro* infection model with simulated endocardial vegetations," Antimicrob Agents Chemother, vol. 44, no. 7, pp. 1921-4, 2000.

[412] A. Alzaraa et al., "Targeted microbubbles in the experimental and clinical setting," Am J Surg, Review vol. 204, no. 3, pp. 355-66, 2012.

[413] J.S. Yeh et al., "Quantitative ultrasound molecular imaging," Ultrasound Med Biol, 2015.

[414] L. Abou-Elkacem, S.V. Bachawal, and J.K. Willmann, "Ultrasound molecular imaging: Moving toward clinical translation," Eur J Radiol, 2015.

[415] F. Kiessling, S. Fokong, J. Bzyl, W. Lederle, M. Palmowski, and T. Lammers, "Recent advances in molecular, multimodal and theranostic ultrasound imaging," Adv Drug Deliv Rev, vol. 72, pp. 15-27, 2014.

[416] A.L. Klibanov, "Ultrasound contrast materials in cardiovascular medicine: from perfusion assessment to molecular imaging," J Cardiovasc Transl Res, 2013.

[417] Y. Luan et al., "Acoustical properties of individual liposome-loaded microbubbles," Ultrasound Med Biol, vol. 38, no. 12, pp. 2174-85, 2012.

[418] T. Faez, M. Emmer, M. Docter, J. Sijl, M. Versluis, and N. de Jong, "Characterizing the subharmonic response of phospholipid-coated microbubbles for carotid imaging," Ultrasound Med Biol, vol. 37, no. 6, pp. 958-70, 2011.

[419] T. van Rooij et al., "Non-linear response and viscoelastic properties of lipid-coated microbubbles: DSPC versus DPPC," Ultrasound Med Biol, vol. 41, no. 5, pp. 1432-45, 2015.

[420] S. Zhao, D.E. Kruse, K.W. Ferrara, and P.A. Dayton, "Acoustic response from adherent targeted contrast agents," J Acoust Soc Am, Letter, vol. 120, no. 6, pp. EL63-9, 2006.

[421] B.L. Helfield, E. Cherin, F.S. Foster, and D.E. Goertz, "The effect of binding on the subharmonic emissions from individual lipid-encapsulated microbubbles at transmit frequencies of 11 and 25 MHz," Ultrasound Med Biol, vol. 39, no. 2, pp. 345-59, 2013.

[422] S. Zhao, K.W. Ferrara, and P.A. Dayton, "Asymmetric oscillation of adherent targeted ultrasound contrast agents," Appl Phys Lett, vol. 87, no. 13, pp. 1341031-1341033, 2005.

[423] J. Casey, C. Sennoga, H. Mulvana, J.V. Hajnal, M.X. Tang, and R.J. Eckersley, "Single bubble acoustic characterization and stability measurement of adherent microbubbles," Ultrasound Med Biol, vol. 39, no. 5, pp. 903-14, 2013.

[424] K. Kooiman et al., "Surface contact of bound targeted microbubbles," in IEEE Ultrasonics Symposium Proceedings, Dresden, Germany, 2012.

[425] R.H. Abou-Saleh, S.A. Peyman, K. Critchley, S.D. Evans, and N.H. Thomson, "Nanomechanics of lipid encapsulated microbubbles with functional coatings," Langmuir, vol. 29, no. 12, pp. 4096-103, 2013.

[426] J.E.G. McKendry, C.A. Johnson, B.R.G. Coletta, P.L. Evans, J.A. Evans, S.D., "Force spectroscopy of streptavidin conjugated lipid coated microbubbles," Bubble Sci Eng Technol, vol. 2, no. 2, 2010.

[427] M. Schneider et al., "Gray-scale liver enhancement in VX2 tumor-bearing rabbits using BR14, a new ultrasonographic contrast agent," Invest Radiol, vol. 32, no. 7, pp. 410-7, 1997.

[428] B. D. Inc., "Lumason Safety Label," in "U.S. Food and Drug Administration," FDA/Center for Drug Evaluation and Research, Silver Spring, USA, 2016.

[429] N. de Jong et al., "Compression-only" behavior of phospholipid-coated contrast bubbles," Ultrasound Med Biol, vol. 33, no. 4, pp. 653-6, 2007.

[430] J. Chomas, P. Dayton, D. May, and K. Ferrara, "Nondestructive subharmonic imaging," IEEE Trans Ultrason Ferroelectr Freq Control, vol. 49, no. 7, pp. 883-92, 2002.

[431] J. Sijl et al., "Subharmonic behavior of phospholipid-coated ultrasound contrast agent microbubbles," J Acoust Soc Am, vol. 128, no. 5, pp. 3239-52, 2010.

[432] P.L. van Neer, G. Matte, M.G. Danilouchkine, C. Prins, F. van den Adel, and N. de Jong, "Super-harmonic imaging: development of an interleaved phased-array transducer," IEEE Trans Ultrason Ferroelectr Freq Control, vol. 57, no. 2, pp. 455-68, 2010.

[433] D.H. Kim, M.J. Costello, P.B. Duncan, and D. Needham, "Mechanical properties and microstructure of polycrystalline phospholipid monolayer shells: Novel solid microparticles," Langmuir, vol. 19, no. 20, pp. 8455-8466, 2003.

[434] P. Marmottant et al., "A model for large amplitude oscillations of coated bubbles accounting for buckling and rupture," J Acoust Soc Am, vol. 118, no. 6, pp. 3499-3505, 2005.
[435] M. Minnaert, "XVI. On musical air-bubbles and the sounds of running water," The Philosophical Magazine and Journal of Science, vol. 16, no. 104, pp. 235-248, 1933.
[436] A. Needles et al., "Nonlinear contrast imaging with an array-based micro-ultrasound system," Ultrasound Med Biol, vol. 36, no. 12, pp. 2097-106, 2010.
[437] S. Zhao, M. Borden, S.H. Bloch, D. Kruse, K.W. Ferrara, and P.A. Dayton, "Radiation-force assisted targeting facilitates ultrasonic molecular imaging," Mol Imaging, vol. 3, no. 3, pp. 135-48, 2004.
[438] P.A. Dayton, K.E. Morgan, A.L. Klibanov, G.H. Brandenburger, and K.W. Ferrara, "Optical and acoustical observations of the effects of ultrasound on contrast agents," IEEE Trans Ultrason Ferroelectr Freq Control, vol. 46, no. 1, pp. 220-32, 1999.
[439] T. van Rooij, A.F.W. van der Steen, N. de Jong, and K. Kooiman, "Influence of binding on the vibrational responses of targeted lipid-coated microbubbles," in IEEE Ultrasonics Symposium Proceedings, Chicago, USA, 2014.
[440] P.M. Shankar, P.D. Krishna, and V.L. Newhouse, "Subharmonic backscattering from ultrasound contrast agents," J Acoust Soc Am, vol. 106, no. 4 Pt 1, pp. 2104-10, 1999.
[441] P.M. Shankar, P.D. Krishna, and V.L. Newhouse, "Advantages of subharmonic over second harmonic backscatter for contrast-to-tissue echo enhancement," Ultrasound Med Biol, vol. 24, no. 3, pp. 395-9, 1998.
[442] M. Kaya, S. Feingold, K. Hettiarachchi, A.P. Lee, and P.A. Dayton, "Acoustic responses of monodisperse lipid-encapsulated microbubble contrast agents produced by flow focusing," Bubble Sci Eng Technol, vol. 2, no. 2, pp. 33-40, 2010.
[443] E. Talu, K. Hettiarachchi, R.L. Powell, A.P. Lee, P.A. Dayton, and M.L. Longo, "Maintaining monodispersity in a microbubble population formed by flow-focusing," Langmuir, vol. 24, no. 5, pp. 1745-9, 2008.
[444] E. Talu et al., "Tailoring the size distribution of ultrasound contrast agents: possible method for improving sensitivity in molecular imaging," Mol Imaging, vol. 6, no. 6, pp. 384-92, 2007.
[445] T. Segers and M. Versluis, "Acoustic bubble sorting for ultrasound contrast agent enrichment," Lab Chip, vol. 14, no. 10, pp. 1705-14, 2014.
[446] T. Faez, I. Skachkov, M. Versluis, K. Kooiman, and N. de Jong, "*In vivo* characterization of ultrasound contrast agents: microbubble spectroscopy in a chicken embryo," Ultrasound Med Biol, vol. 38, no. 9, pp. 1608-17, 2012.
[447] I. Skachkov, Y. Luan, A.F.W. van der Steen, N. de Jong, and K. Kooiman, "Targeted microbubble mediated sonoporation of endothelial cells *in vivo*," IEEE Trans Ultrason Ferroelectr Freq Control, vol. 61, no. 10, pp. 1661-7, 2014.
[448] T.J. Kokhuis et al., "Secondary bjerknes forces deform targeted microbubbles," Ultrasound Med Biol, vol. 39, no. 3, pp. 490-506, 2013.
[449] V. Garbin, D. Cojoc, E. Ferrari, and E. Di Fabrizio, "Changes in microbubble dynamics near a boundary revealed by combined optical micromanipulation and high-speed imaging," App Phys Lett, 2007.
[450] D. Cosgrove and C. Harvey, "Clinical uses of microbubbles in diagnosis and treatment," Med Biol Eng Comput, vol. 47, no. 8, pp. 813-26, 2009.
[451] S.B. Feinstein et al., "Contrast enhanced ultrasound imaging," J Nucl Cardiol, Review vol. 17, no. 1, pp. 106-15, 2010.
[452] L. Abou-Elkacem, S.V. Bachawal, and J.K. Willmann, "Ultrasound molecular imaging: Moving toward clinical translation," Eur J Radiol, vol. 84, no. 9, pp. 1685-1693, 2015.
[453] E.C. Pua and P. Zhong, "Ultrasound-mediated drug delivery," IEEE Eng Med Biol Mag, vol. 28, no. 1, pp. 64-75, 2009.
[454] K. Kooiman, M. Foppen-Harteveld, A.F.W. van der Steen, and N. de Jong, "Sonoporation of endothelial cells by vibrating targeted microbubbles," J Control Release, vol. 154, no. 1, pp. 35-41, 2011.
[455] F. Yan et al., "Therapeutic ultrasonic microbubbles carrying paclitaxel and LyP-1 peptide: preparation, characterization and application to ultrasound-assisted chemotherapy in breast cancer cells." Ultrasound Med Biol, vol. 37, no. 5, pp. 768-79, 2011.

[456] L.C. Phillips, A.L. Klibanov, B.R. Wamhoff, and J.A. Hossack, "Intravascular ultrasound detection and delivery of molecularly targeted microbubbles for gene delivery," IEEE Trans Ultrason Ferroelectr Freq Control, vol. 59, no. 7, pp. 1596-1601, 2012.

[457] S. Chang et al., "Targeted microbubbles for ultrasound mediated gene transfection and apoptosis induction in ovarian cancer cells," Ultrason Sonochem, no. 1, pp. 171-9, 2013.

[458] J. McLaughlan et al., "Increasing the sonoporation efficiency of targeted polydisperse microbubble populations using chirp excitation," IEEE Trans Ultrason Ferroelectr Freq Control, vol. 60, no. 12, pp. 2511-20, 2013.

[459] H. Liu et al., "Ultrasound-mediated destruction of LHRHa-targeted and paclitaxel-loaded lipid microbubbles induces proliferation inhibition and apoptosis in ovarian cancer cells," Mol Pharm, vol. 11, no. 1, pp. 40-8, 2014.

[460] A. Xie et al., "Ultrasound-Mediated vascular gene transfection by cavitation of endothelial-targeted cationic microbubbles," Jacc-Cardiovasc Imag, vol. 5, no. 12, pp. 1253-1262, 2012.

[461] J.L. Tlaxca et al., "Ultrasound-based molecular imaging and specific gene delivery to mesenteric vasculature by endothelial adhesion molecule targeted microbubbles in a mouse model of Crohn's disease," J Control Release, vol. 165, no. 3, pp. 216-25, 2013.

[462] C. Pu et al., "Ultrasound-mediated destruction of LHRHa-targeted and paclitaxel-loaded lipid microbubbles for the treatment of intraperitoneal ovarian cancer xenografts," Mol Pharm, vol. 11, no. 1, pp. 49-58, 2014.

[463] C.H. Fan et al., "Antiangiogenic-targeting drug-loaded microbubbles combined with focused ultrasound for glioma treatment," Biomaterials, vol. 34, no. 8, pp. 2142-55, 2013.

[464] F.E. Shamout et al., "Enhancement of non-invasive trans-membrane drug delivery using ultrasound and microbubbles during physiologically relevant flow," Ultrasound Med Biol, vol. 41, no. 9, pp. 2435-48, 2015.

[465] M. Edidin, "A rapid, quantitative fluorescence assay for cell damage by cytotoxic antibodies," J Immunol, vol. 104, no. 5, pp. 1303-6, 1970.

[466] Z. Fan, D. Chen, and C.X. Deng, "Improving ultrasound gene transfection efficiency by controlling ultrasound excitation of microbubbles," J Control Release, vol. 170, no. 3, pp. 401-13, 2013.

[467] C. E. Shannon, "Communication in the presence of noise (Reprinted from the Proceedings of the IRE, vol 37, pg 10-21, 1949)," Proceedings of the IEEE, vol. 86, no. 2, pp. 447-457, 1998.

[468] Z. Fan, D. Chen, and C.X. Deng, "Characterization of the dynamic activities of a population of microbubbles driven by pulsed ultrasound exposure in sonoporation," Ultrasound Med Biol, vol. 40, no. 6, pp. 1260-72, 2014.

[469] T.J. Kokhuis et al., "Intravital microscopy of localized stem cell delivery using microbubbles and acoustic radiation force," Biotechnol Bioeng, vol. 112, no. 1, pp. 220-7, 2015.

[470] J.R. Doherty, G.E. Trahey, K.R. Nightingale, and M.L. Palmeri, "Acoustic radiation force elasticity imaging in diagnostic ultrasound," IEEE Trans Ultrason Ferroelectr Freq Control, vol. 60, no. 4, pp. 685-701, 2013.

[471] D.L. Miller and J. Song, "Tumor growth reduction and DNA transfer by cavitation-enhanced high-intensity focused ultrasound *in vivo*," Ultrasound Med Biol, vol. 29, no. 6, pp. 887-93, 2003.

[472] A. Ghanem et al., "Focused ultrasound-induced stimulation of microbubbles augments site-targeted engraftment of mesenchymal stem cells after acute myocardial infarction," Journal of Molecular And Cellular Cardiology, vol. 47, no. 3, pp. 411-8, 2009.

[473] B.D.M. Meijering et al., "Ultrasound and microbubble-targeted delivery of macromolecules is regulated by induction of endocytosis and pore formation," Circ Res, vol. 104, no. 5, pp. 679-87, 2009.

[474] B.D.M. Meijering, R. H. Henning, W. H. Van Gilst, I. Gavrilovic, A. Van Wamel, and L. E. Deelman, "Optimization of ultrasound and microbubbles targeted gene delivery to cultured primary endothelial cells," J Drug Target, vol. 15, no. 10, pp. 664-671, 2007.

[475] J.R. Lindner, J. Song, J. Christiansen, A.L. Klibanov, F. Xu, and K. Ley, "Ultrasound assessment of inflammation and renal tissue injury with microbubbles targeted to P-selectin," Circulation, vol. 104, no. 17, pp. 2107-12, 2001.

[476] D. Bratosin, L. Mitrofan, C. Palii, J. Estaquier, and J. Montreuil, "Novel fluorescence assay using calcein-AM for the determination of human erythrocyte viability and aging," Cytometry A, vol. 66, no. 1, pp. 78-84, 2005.
[477] K.A. Smith, S.A. Hill, A.C. Begg, and J. Denekamp, "Validation of the fluorescent dye Hoechst 33342 as a vascular space marker in tumours," Br J Cancer, vol. 57, no. 3, pp. 247-53, 1988.
[478] M. Sriram, G.A. van der Marel, H.L. Roelen, J.H. van Boom, and A.H. Wang, "Conformation of B-DNA containing O6-ethyl-G-C base pairs stabilized by minor groove binding drugs: molecular structure of d(CGC[e6G]AATTCGCG complexed with Hoechst 33258 or Hoechst 33342," EMBO J, vol. 11, no. 1, pp. 225-32, 1992.
[479] W.D. Wilson, C.R. Krishnamoorthy, Y.H. Wang, and J.C. Smith, "Mechanism of intercalation: ion effects on the equilibrium and kinetic constants for the interaction of propidium and ethidium with DNA," Biopolymers, vol. 24, no. 10, pp. 1941-61, 1985.
[480] W.S. Rasband, "ImageJ," ed. Bethesda, Maryland, USA: U. S. National Institutes of Health, 1997-2016.
[481] N. Otsu, "Threshold Selection Method from Gray-Level Histograms," IEEE Trans Syst Man Cybern, vol. 9, no. 1, pp. 62-66, 1979.
[482] T.R. Jones, A. Carpenter, and P. Golland, "Voronoi-based segmentation of cells on image manifolds," Computer Vision for Biomedical Image Applications, Proceedings, vol. 3765, pp. 535-543, 2005.
[483] S. Wold, K. Esbensen, and P. Geladi, "Principal Component Analysis," Chemom Intell Lab Syst, vol. 2, no. 1-3, pp. 37-52, 1987.
[484] R.L. Tatusov et al., "The COG database: new developments in phylogenetic classification of proteins from complete genomes," Nucleic Acids Res, vol. 29, no. 1, pp. 22-8, 2001.
[485] Z. Zivkovic and F. van der Heijden, "Efficient adaptive density estimation per image pixel for the task of background subtraction," Pattern Recognit Lett, vol. 27, no. 7, pp. 773-780, 2006.
[486] D. Allan, N. Keim, T. Caswell, and C. van der Wel. (2015, March 9). trackpy: Trackpy v0.3.0. Available: http://zenodo.org/record/34028
[487] S. van der Walt et al. (2014, March 30). Blob detection, scikit-image: Image Processing in Python. Available: http://scikit-image.org/docs/dev/auto_examples/plot_blob.html
[488] Y. Zhou, K. Yang, J. Cui, J.Y. Ye, and C.X. Deng, "Controlled permeation of cell membrane by single bubble acoustic cavitation," J Control Release, vol. 157, no. 1, pp. 103-11, 2012.
[489] B. Lammertink, R. Deckers, G. Storm, C.T. Moonen, and C. Bos, "Duration of ultrasound-mediated enhanced plasma membrane permeability," Int J Pharm, vol. 482, no. 1-2, pp. 92-8, 2015.
[490] A. Yudina, M. Lepetit-Coiffe, and C.T. Moonen, "Evaluation of the temporal window for drug delivery following ultrasound-mediated membrane permeability enhancement," Mol Imaging Biol, vol. 13, no. 2, pp. 239-49, 2011.
[491] P. Wu and L. Brand, "Resonance energy transfer: methods and applications," Anal Biochem, vol. 218, no. 1, pp. 1-13, 1994.
[492] T. Frey, "Detection of bromodeoxyuridine incorporation by alteration of the fluorescence emission from nucleic acid binding dyes using only an argon ion laser," Cytometry, vol. 17, no. 4, pp. 310-8, 1994.
[493] X. Chen, J. Wang, J.J. Pacella, and F.S. Villanueva, "Dynamic behavior of microbubbles during long ultrasound tone-burst excitation: mechanistic insights into ultrasound-microbubble mediated therapeutics using high-speed imaging and cavitation detection," Ultrasound Med Biol, 2015.
[494] H.M. DeLisser, P. J. Newman, and S.M. Albelda, "Molecular and functional aspects of PECAM-1/CD31," Immunol Today, vol. 15, no. 10, pp. 490-5, 1994.
[495] L.M. Kornmann, K.D. Reesink, R.S. Reneman, and A.P. Hoeks, "Critical appraisal of targeted ultrasound contrast agents for molecular imaging in large arteries," Ultrasound Med Biol, vol. 36, no. 2, pp. 181-91, 2010.
[496] M. de Saint Victor, C. Crake, C.C. Coussios, and E. Stride, "Properties, characteristics and applications of microbubbles for sonothrombolysis," Expert Opin Drug Deliv, vol. 11, no. 2, pp. 187-209, 2014.
[497] Z. Fan, R.E. Kumon, J. Park, and C.X. Deng, "Intracellular delivery and calcium transients generated in sonoporation facilitated by microbubbles," J Control Release, vol. 142, no. 1, pp. 31-9, 2010.

[498] S.A.G. Langeveld, I. Beekers, G. Collado-Lara, A.F.W. van der Steen, N. de Jong, and K. Kooiman, "The impact of lipid handling and phase distribution on the acoustic behavior of microbubbles," Pharmaceutics, vol. 13, no. 1, p. 119, 2021.

[499] A. Carovac, F. Smajlovic, and D. Junuzovic, "Application of ultrasound in medicine," Acta Inform Med, vol. 19, no. 3, pp. 168-171, 2011.

[500] A. A. Doinikov, J. F. Haac, and P. A. Dayton, "Resonance frequencies of lipid-shelled microbubbles in the regime of nonlinear oscillations," Ultrasonics, vol. 49, no. 2, pp. 263-268, 2009.

[501] S. Roovers et al., "Sonoprinting of nanoparticle-loaded microbubbles: Unraveling the multi-timescale mechanism," Biomaterials, vol. 217, p. 119250, 2019.

[502] N. Kudo, K. Okada, and K. Yamamoto, "Sonoporation by single-shot pulsed ultrasound with microbubbles adjacent to cells," Biophys J, vol. 96, no. 12, pp. 4866-4876, 2009.

[503] K. Hynynen, "Ultrasound for drug and gene delivery to the brain," Adv Drug Deliv Rev, vol. 60, no. 10, pp. 1209-1217, 2008.

[504] E.E. Konofagou, "Optimization of the ultrasound-induced blood-brain barrier opening," Theranostics, vol. 2, no. 12, pp. 1223-1237, 2012.

[505] P.C. Brooks, R.A. Clark, and D.A. Cheresh, "Requirement of vascular integrin alpha v beta 3 for angiogenesis," Science, vol. 264, no. 5158, p. 569, 1994.

[506] I. Beekers, T. van Rooij, A.F.W. van der Steen, N. de Jong, M.D. Verweij, and K. Kooiman, "Acoustic characterization of the CLINIcell for ultrasound contrast agent studies," IEEE Trans Ultrason Ferroelectr Freq Control, vol. 66, no. 1, pp. 244-246, 2019.

[507] P.A. Dayton et al., "Ultrasonic analysis of peptide- and antibody-targeted microbubble contrast agents for molecular imaging of $\alpha_v\beta_3$-expressing cells," Mol Imaging, vol. 3, no. 2, pp. 125-134, 2004.

[508] V. Daeichin et al., "Quantification of endothelial $\alpha_v\beta_3$ expression with high-frequency ultrasound and targeted microbubbles: *in vitro* and *in vivo* studies," Ultrasound Med Biol, vol. 42, no. 9, pp. 2283-2293, 2016.

[509] D.B. Ellegala et al., "Imaging tumor angiogenesis with contrast ultrasound and microbubbles targeted to $\alpha_v\beta_3$," Circulation, vol. 108, no. 3, pp. 336-341, 2003.

[510] M. Emmer, A. van Wamel, D. E. Goertz, and N. de Jong, "The onset of microbubble vibration," Ultrasound Med Biol, vol. 33, no. 6, pp. 941-949, 2007.

[511] D. Tsvirkun, A. Grichine, A. Duperray, C. Misbah, and L. Bureau, "Microvasculature on a chip: study of the endothelial surface layer and the flow structure of red blood cells," Sci Rep, vol. 7, no. 1, p. 45036, 2017.

[512] N. de Jong, M. Emmer, A. van Wamel, and M. Versluis, "Ultrasonic characterization of ultrasound contrast agents," Med Biol Eng Comput, vol. 47, no. 8, pp. 861-873, 2009.

[513] J. Sijl et al., ""Compression-only" behavior: a second-order nonlinear response of ultrasound contrast agent microbubbles," J Acoust Soc Am, vol. 129, no. 4, pp. 1729-1739, 2011.

[514] H. Maeda, "Macromolecular therapeutics in cancer treatment: the EPR effect and beyond," J Control Release, vol. 164, no. 2, pp. 138-144, 2012.

[515] H. Hashizume et al., "Openings between defective endothelial cells explain tumor vessel leakiness," Am J Pathol, vol. 156, no. 4, pp. 1363-1380, 2000.

[516] G.P. van Nieuw Amerongen and V.W.M. van Hinsbergh, "Targets for pharmacological intervention of endothelial hyperpermeability and barrier function," Vasc Pharmacol, vol. 39, no. 4, pp. 257-272, 2002.

[517] D.M. McDonald, G. Thurston, and P. Baluk, "Endothelial gaps as sites for plasma leakage in inflammation," Microcirculation, vol. 6, no. 1, pp. 7-22, 1999.

[518] R.E. Kumon et al., "Spatiotemporal effects of sonoporation measured by real-time calcium imaging," Ultrasound Med Biol, vol. 35, no. 3, pp. 494-506, 2009.

[519] N. Lipsman et al., "Blood–brain barrier opening in Alzheimer's disease using MR-guided focused ultrasound," Nat Commun, vol. 9, no. 1, p. 2336, 2018.

[520] T. Mainprize et al., "Blood-brain barrier opening in primary brain tumors with non-invasive MR-guided focused ultrasound: a clinical safety and feasibility study," Sci Rep, vol. 9, no. 1, p. 321, 2019.

[521] T.F.C. Mah and G. A. O'Toole, "Mechanisms of biofilm resistance to antimicrobial agents," Trends Microbiol, vol. 9, no. 1, pp. 34-39, 2001.

[522] A. Cassini *et al.*, "Attributable deaths and disability-adjusted life-years caused by infections with antibiotic-resistant bacteria in the EU and the European Economic Area in 2015: a population-level modelling analysis," Lancet Infect Dis, vol. 19, no. 1, pp. 56-66, 2019.
[523] D.C. DeSimone and M.R. Sohail, "Management of bacteremia in patients living with cardiovascular implantable electronic devices," Heart Rhythm, vol. 13, no. 11, pp. 2247-2252, 2016.
[524] V. Daeichin *et al.*, "Microbubble composition and preparation for high-frequency contrast-enhanced ultrasound imaging: *in vitro* and *in vivo* evaluation," IEEE Trans Ultrason Ferroelectr Freq Control, vol. 64, no. 3, pp. 555-567, 2017.
[525] C. A. Sennoga *et al.*, "Microbubble-mediated ultrasound drug-delivery and therapeutic monitoring," Expert Opinion on Drug Delivery, vol. 14, no. 9, pp. 1031-1043, 2017.
[526] A.F.L. Schinkel, J.G. Bosch, D. Staub, D. Adam, and S.B. Feinstein, "Contrast-enhanced ultrasound to assess carotid intraplaque neovascularization," Ultrasound Med Biol, vol. 46, no. 3, pp. 466-478, 2020.
[527] G. Dimcevski *et al.*, "A human clinical trial using ultrasound and microbubbles to enhance gemcitabine treatment of inoperable pancreatic cancer," J Control Release, vol. 243, pp. 172-181, 2016.
[528] S. Kotopoulis, G. Dimcevski, O. Helge Gilja, D. Hoem, and M. Postema, "Treatment of human pancreatic cancer using combined ultrasound, microbubbles, and gemcitabine: A clinical case study," Med Phys, vol. 40, no. 7, p. 072902, 2013.
[529] A. Kosareva, L. Abou-Elkacem, S. Chowdhury, R. Lindner Jonathan, and B.A. Kaufman, "Seeing the invisible - Ultrasound molecular imaging," Ultrasound Med Biol, vol. 46, no. 3, p. 479, 2020.
[530] F. Moccetti et al., "Ultrasound molecular imaging of atherosclerosis using small-peptide targeting ligands against endothelial markers of inflammation and oxidative stress," Ultrasound Med Biol, vol. 44, no. 6, pp. 1155-1163, 2018.
[531] W.A. McGuinness, N. Malachowa, and F.R. DeLeo, "Vancomycin resistance in *Staphylococcus aureus*," The Yale Journal of Biology and Medicine, vol. 90, no. 2, pp. 269-281, 2017.
[532] S. Unnikrishnan, Z. Du, G.B. Diakova, and A.L. Klibanov, "Formation of microbubbles for targeted ultrasound contrast imaging: practical translation considerations," Langmuir, vol. 35, no. 31, pp. 10034-10041, 2019.
[533] L. Pritchard, C. Baker, J. Leggett, P. Sehdev, A. Brown, and K.B. Bayley, "Increasing vancomycin serum trough concentrations and incidence of nephrotoxicity," Am J Med, vol. 123, no. 12, pp. 1143-1149, 2010.
[534] S. Tongsai and P. Koomanachai, "The safety and efficacy of high versus low vancomycin trough levels in the treatment of patients with infections caused by methicillin-resistant *Staphylococcus aureus*: a meta-analysis," BMC Res Notes, vol. 9, no. 1, pp. 455-455, 2016.
[535] J. Schindelin et al., "Fiji: an open-source platform for biological-image analysis," Nat Methods, vol. 9, no. 7, pp. 676-682, 2012.
[536] E. Dauty, J.S. Remy, G. Zuber, and J.P. Behr, "Intracellular Delivery of nanometric DNA Particles via the folate receptor," Bioconjug Chem, vol. 13, no. 4, pp. 831-839, 2002.
[537] M. A. Borden et al., "Lateral phase separation in lipid-coated microbubbles," Langmuir, vol. 22, no. 9, pp. 4291-4297, 2006.
[538] S. A. G. Langeveld et al., "Ligand distribution and lipid phase behavior in phospholipid-coated microbubbles and monolayers," Langmuir, vol. 36, no. 12, pp. 3221-3233, 2020.
[539] T. Bettinger et al., "Ultrasound molecular imaging contrast agent binding to both E- and P-selectin in different species," Invest Radiol, vol. 47, no. 9, pp. 516-523, 2012.
[540] S. Wang, E.B. Herbst, F.W. Mauldin, Jr., G.B. Diakova, A.L. Klibanov, and J.A. Hossack, "Ultra-low-dose ultrasound molecular imaging for the detection of angiogenesis in a mouse murine tumor model: how little can we see?," Invest Radiol, vol. 51, no. 12, pp. 758-766, 2016.
[541] A.M. Malek, S. L. Alper, and S. Izumo, "Hemodynamic shear stress and its role in atherosclerosis," JAMA, vol. 282, no. 21, pp. 2035-2042, 1999.
[542] P. Dayton, A.L. Klibanov, G.H. Brandenburger, and K.W. Ferrara, "Acoustic radiation force *in vivo*: a mechanism to assist targeting of microbubbles," Ultrasound Med Biol, vol. 25, no. 8, pp. 1195-1201, 1999.
[543] B. Helfield, X. Chen, B. Qin, and F.S. Villanueva, "Individual lipid encapsulated microbubble radial oscillations: effects of fluid viscosity," J Acoust Soc Am, vol. 139, no. 1, pp. 204-214, 2016.

[544] V. Stove, L. Coene, M. Carlier, J.J. De Waele, T. Fiers, and A.G. Verstraete, "Measuring unbound versus total vancomycin concentrations in serum and plasma: methodological issues and relevance," Ther Drug Monit, vol. 37, no. 2, 2015.

[545] P. Rajendran et al., "The vascular endothelium and human diseases," Int J Biol Sci, vol. 9, no. 10, pp. 1057-1069, 2013.

[546] J. Kluytmans, A. van Belkum, and H. Verbrugh, "Nasal carriage of *Staphylococcus aureus*: epidemiology, underlying mechanisms, and associated risks," Clin Microbiol Rev, vol. 10, no. 3, pp. 505-520, 1997.

[547] A. Krüger-Genge, A. Blocki, R.P. Franke, and F. Jung, "Vascular endothelial cell biology: an update," Int J Mol Sci, vol. 20, no. 18, p. 4411, 2019.

[548] A.B. García, J.M. Viñuela-Prieto, L. López-González, and F.J. Candel, "Correlation between resistance mechanisms in *Staphylococcus aureus* and cell wall and septum thickening," Infect Drug Resist, vol. 10, pp. 353-356, 2017.

[549] L. Cui et al., "Cell wall thickening is a common feature of vancomycin resistance in *Staphylococcus aureus*," J Clin Microbiol, vol. 41, no. 1, p. 5, 2003.

[550] P. Giesbrecht, T. Kersten, H. Maidhof, and J. Wecke, "Staphylococcal cell wall: morphogenesis and fatal variations in the presence of penicillin," Microbiol Mol Biol Rev, vol. 62, no. 4, pp. 1371-1414, 1998.

[551] N. W. Nanne, C.L., Cell growth, genome duplication, and cell division. In Molecular Cytology of *Escherichia coli*. London; Orlando, Fla.: Academic Press, 1985.

[552] A.L. Koch and M.F. Pinette, "Nephelometric determination of turgor pressure in growing gram-negative bacteria," J Bacteriol, vol. 169, no. 8, pp. 3654-3663, 1987.

[553] E.A. Ferrante, J.E. Pickard, J. Rychak, A. Klibanov, and K. Ley, "Dual targeting improves microbubble contrast agent adhesion to VCAM-1 and P-selectin under flow," J Control Release, vol. 140, no. 2, pp. 100-107, 2009.

[554] C.J. Rupp, C.A. Fux, and P. Stoodley, "Viscoelasticity of *Staphylococcus aureus* biofilms in response to fluid shear allows resistance to detachment and facilitates rolling migration," Appl Environ Microbiol, vol. 71, no. 4, p. 2175, 2005.

[555] M. Singer et al., "The third international consensus definitions for sepsis and septic shock (Sepsis-3)," JAMA, vol. 315, no. 8, pp. 801-810, 2016.

[556] S. M. Opal et al., "Effect of eritoran, an antagonist of MD2-TLR4, on mortality in patients with severe sepsis: the ACCESS randomized trial," JAMA, vol. 309, no. 11, pp. 1154-1162, 2013.

[557] M. M. Levy et al., "Outcomes of the Surviving Sepsis Campaign in intensive care units in the USA and Europe: a prospective cohort study," Lancet Infect Dis, vol. 12, no. 12, pp. 919-924, 2012.

[558] D. Fleming and K. Rumbaugh, "The consequences of biofilm dispersal on the host," Scientific Reports, vol. 8, no. 1, p. 10738, 2018.

Publications

Publications in this thesis

Kirby R. Lattwein*, Andi R. Sultan*, Nicole A. Lemmens-den Toom, Susan V. Snijders, Klazina Kooiman, Annelies Verbon, and Willem J.B. van Wamel
*Both authors contributed equally
Paracetamol Modulates Biofilm Formation in Staphylococcus aureus Clonal Complex 8 Strains
Scientific Reports, vol.11, 5114, 2021

Inés Beekers, Merel Vegter, **Kirby R. Lattwein**, Frits Mastik, Robert Beurskens, Antonius F.W. van der Steen, Nico de Jong, Martin D. Verweij, and Klazina Kooiman
Opening of endothelial cell–cell contacts due to sonoporation
Journal of Controlled Release, vol. 322, pp. 426-38, 2020

Kirby R. Lattwein, Himanshu Shekhar, Joop J.P.Kouijzer, Willem J.B. van Wamel, Christy K. Holland, and Klazina Kooiman
Sonobactericide: An Emerging Treatment Strategy for Bacterial Infections
Ultrasound in Medicine & Biology, vol. 46, no. 2, pp. 193-215, 2020

Inés Beekers, **Kirby R. Lattwein**, Joop J.P. Kouijzer, Simone A.G. Langeveld, Merel Vegter, Robert Beurskens, Frits Mastik, Rogier Verduyn Lunel, Emma Verver, Antonius F.W. van der Steen, Nico de Jong, and Klazina Kooiman
Combined Confocal Microscope and Brandaris 128 Ultra-High-Speed Camera
Ultrasound in Medicine & Biology, vol. 45, no. 9, pp. 2575-82, 2019

Kirby R. Lattwein, Himanshu Shekhar, Willem J.B. van Wamel, Tammy Gonzalez, Andrew B. Herr, Christy K. Holland, and Klazina Kooiman
An in vitro proof-of-principle study of sonobactericide
Scientific Reports, vol. 8, 3411, 2018

Tom van Rooij, Inés Beekers, **Kirby R. Lattwein**, Antonius F.W. van der Steen, Nico de Jong, and Klazina Kooiman
Vibrational Responses of Bound and Nonbound Targeted Lipid-Coated Single Microbubbles
IEEE Transactions on Ultrasonics, Ferroelectrics, and Frequency Control, vol. 64, no. 5, pp. 785-97, 2017

Tom van Rooij, Ilya Skachkov, Inés Beekers, **Kirby R. Lattwein**, Jason D. Voorneveld, Tom J.A. Kokhuis, Deep Bera, Ying Luan, Antonius F.W. van der Steen, Nico de Jong, and Klazina Kooiman
Viability of endothelial cells after ultrasound-mediated sonoporation: Influence of targeting, oscillation, and displacement of microbubbles
Journal of Controlled Release, vol. 238, pp. 197-211, 2016

Manuscripts submitted or in preparation

Joop J.P. Kouijzer, **Kirby R. Lattwein**, Inés Beekers, Mariël Leon-Grooters, Nico de Jong, Antonius F.W. van der Steen, Alexander L. Klibanov, Willem J.B. van Wamel, and Klazina Kooiman
Vancomycin-decorated microbubbles as a theranostic tool for Staphylococcus aureus biofilms

Kirby R. Lattwein, Inés Beekers, Joop J.P. Kouijzer, Tom van Rooij, Mariël Leon-Grooters, Antonius F.W. van der Steen, Nico de Jong, Willem J.B. van Wamel, and Klazina Kooiman
Dispersing and sonoporating biofilm-associated bacteria with sonobactericide

Kirby R. Lattwein, Margot E. Starrenburg, Joop J.P. Kouijzer, Simone A.G. Langeveld, Mariël Leon-Grooters, Antonius F. W. van der Steen, Nico de Jong, Moniek P.M. de Maat, Willem J.B. van Wamel, and Klazina Kooiman
Ultrasound-activated microbubble effects on fibrin-based biofilms

Supervised academic reports

Margot E. Starrenburg, "*Developing fibrin-targeted microbubbles for the treatment of Staphylococcus aureus biofilms*", MSc Infection and Immunity internship report, Erasmus University Medical Center Rotterdam, the Netherlands, 2020

Joop J.P. Kouijzer, "*Targeted microbubbles as a novel therapy for Staphylococcus aureus biofilms*", MSc Bio-Pharmaceutical Sciences thesis report, Leiden University, the Netherlands, 2018

Publication not in this thesis

Arpit Saxena, Alexander Chumanevich, Emma Fletcher, Bianca Larsen, **Kirby R. Lattwein**, Kamaljeet Kaur, and Raja Fayad

Adiponectin deficiency: Role in chronic inflammation induced colon cancer

Biochimica et Biophysica Acta - Molecular Basis of Disease, vol. 1822, no.4, pp. 527-536, 2012

PhD Portfolio

Project Title	Sonobactericide
Supervisors	Prof. dr. ir. N. de Jong Prof. dr. ir. A.F.W. van der Steen Dr. K. Kooiman Dr. W.J.B. van Wamel
Department	Biomedical Engineering, Thorax Center
Research School	Cardiovascular Research School (COEUR)
PhD period	2016-2020

Courses	**Year**	**ECTS**
Congenital Heart Disease	2017	0.5
Zeiss Confocal Microscopy	2017	0.2
Endovascular Thrombectomy in Acute Ischemic Stroke	2017	0.4
Therapeutic Ultrasound Winter School (*Les Houches, France*)	2017	3
Nikon Confocal Microscopy	2018	0.5
Career Development for PhD Candidates	2019	0.15
Microbubbles and Nanodroplets for Biomedical Ultrasound Applications (*IEEE IUS, Glasgow, Scotland*)	2019	0.15

Teaching

Translational Imaging Workshop AMIE - From mouse to man	2017	0.2
Supervision MSc student Bio-Pharmaceutical Sciences (Leiden U)	2018	1
Lecture Biomedical Research Techniques Course	2018	0.2
Supervision MSc student Infection and Immunity (Erasmus MC)	2019	1.5
Lecture Therapeutic Ultrasound Course (University of Chicago)	2020	0.2

Scientific Presentations and Meetings

22nd European Symposium on Ultrasound Contrast Imaging *Rotterdam, the Netherlands* (poster presentation)	2017	1.1
6th Dutch Bio-medical Engineering Conference *Egmond aan Zee, the Netherlands* (oral presentation)	2017	1.6
Innovation for Health *Rotterdam, the Netherlands* (poster and pitch)	2017	0.8
21st Molecular Medicine Day *Rotterdam, the Netherlands* (oral presentation)	2017	1.3
Cardiovascular Research School PhD Day *Rotterdam, the Netherlands* (oral presentation)	2017	1.3
173rd Meeting of the Acoustical Society of America *Boston, Massachusetts, USA* (poster and oral presentation)	2017	2.9
Erasmus MC PhD Day *Rotterdam, the Netherlands*	2017	0.2
23rd European Symposium on Ultrasound Contrast Imaging *Rotterdam, the Netherlands*	2018	0.3
24th European Symposium on Ultrasound Contrast Imaging *Rotterdam, the Netherlands*	2019	0.6
Department of Cardiothoracic Surgery Research Meeting *Erasmus MC, Rotterdam, the Netherlands* (oral presentation)	2019	0.2
Cardiovascular Research School PhD Day *Rotterdam, the Netherlands* (organized)	2019	0.3
IEEE International Ultrasonics Symposium *Glasgow, Scotland, UK* (oral presentation)	2019	2.1

Scientific Presentations and Meetings continued	**Year**	**ECTS**
Department of Hematology Research Meeting *Erasmus MC, Rotterdam, the Netherlands* (oral presentation)	2019	0.2
Emergent Technologies to deliver Antibacterial Drugs into Biofilms Workshop - *Ghent, Belgium*	2019	0.6
25th European Symposium on Ultrasound Contrast Imaging *Rotterdam, the Netherlands* (oral presentation)	2020	1.6
IEEE International Ultrasonics Symposium *Las Vegas, Nevada, USA – Digital* (oral poster presentation)	2020	1.7
Department of Biomedical Engineering Research Meetings *Erasmus MC, Rotterdam, the Netherlands* (4 oral presentations)	2016-2020	0.8
Department of Medical Microbiology and Infectious Diseases – *Staphylococcus aureus* Working Group Research Meetings *Erasmus MC, Rotterdam, the Netherlands* (4 oral presentations)	2016-2020	0.8

Other Activities		
Erasmus MC Cardiovascular Research School PhD Committee *Communications chair*	2017-2019	1
ExCOEURsion Philips Healthcare *Best, the Netherlands*	2017	0.3
Organization of 'lab-day-out', Department of Biomedical Engineering – *Utrecht, the Netherlands*	2017	0.3
TV Program De Kennis van NU Appearance 'De ongekende kracht van belletjes'	2017	4
	Total:	**32.0**

Awards

2nd Best Oral Presentation 2017
6th Dutch Bio-medical Engineering Conference

2nd Best Oral Presentation 2017
Therapeutic Ultrasound Winter School

Travel award 2017
173rd Meeting of the Acoustical Society of America – Boston

Travel award 2019
IEEE International Ultrasonics Symposium – Glasgow

Young Investigator Award 2021 nominee 2020
European Federation of Societies for Ultrasound in Medicine and Biology – nominated by the Dutch Society for Medical Ultrasound

About the author

Kirby Lattwein's path has seemingly not been straight, but she believes an invisible running thread has been there all along stitched from her sincere passion for medicine and science.

Educationally, her initial focus was towards a career in medicine and spanned attendance at three higher education institutions: the United States Naval Academy, the University of South Carolina, and Maastricht University. Alongside her curriculum, she was awarded two undergraduate research grants for *in vivo* investigations into chronic inflammation-induced colon cancer, a cancer her grandfather had recently passed away from. That experience, and others, helped lead her towards a research master's in Infection and Immunity at Erasmus University Medical Center, during which she joined Dr. Klazina Kooiman at the Department of Biomedical Engineering. Klazina had an inspiring idea of using ultrasound-activated microbubbles against pathogenic bacteria, and since meeting, they have been investigating *sonobactericide* as a potential treatment strategy for life-threatening infections closely with Kirby's other co-promotor, Dr. Willem van Wamel (Medical Microbiology). Kirby received the Dutch Heart Foundation and I&I Fund grants during her master's to travel as a student researcher to Professor Christy Holland's lab at the University of Cincinnati, during which a model of infective endocarditis was developed and treated with sonobactericide. The multi-disciplinary nature of sonobactericide has enabled Kirby to connect and learn from experts of several other fields, to include hematology, thoracic surgery, and pathology, and will continue to work with them as she continues developing sonobactericide towards clinical application as a postdoctoral researcher.

Kirby has had many life-enriching experiences, such as an intelligence analyst in the US Marine Corps, an Iraq deployment, attendance at a premiere military university, sports competitions (sailing and triathlon) at the national and collegiate level, volunteer medical outreach and surgical assistance in Cambodia, expatriation to the Netherlands, teaching university students, assisting in the internalization of a university, and Dutch healthcare witnessed from both a clinical and patient standpoint. She considers all of her experiences, in academia and life, to have played a significant role in leading her to this moment. On a personal note, Kirby believes that life is about the people you meet and things you create with them, including personal and professional connections. She may not know where her future path will go, but she is confident that it won't be alone and is sincerely appreciative to the connections she has made along the way and the ones yet to come.

Someday when the pages of my life end,
I know that you will be one of its most beautiful chapters

-unknown

Acknowledgements

"I've learned that people will forget what you said, people will forget what you did, but people will *never forget how you made them feel*." – Maya Angelou

For myself, I find this quote is aligned to what I want to capture in this section. I may not remember all the kind words and helpful acts from over the years in exact detail, but each of them has impacted me in a positive way. Not only have these kind moments helped me to attain this achievement, but they also shape me as a person. I purposely made the word 'shape' not past tense despite grammatical rules, because I do believe the impact of each kindness, both verbal and physical acts, are equally endless (Proposition #9). When I think back over the years, although they have had their fair share of hardship, all I can feel when I write this section is overwhelming gratitude and warmth. My eyes fill with happy tears, and my mind with wonder at how fortunate I am to have had all your kindnesses bestowed on me. So whether your name is mentioned here or not, for all who helped along the way, please know this achievement is not mine alone, but it shared with you as well. Words will not be able to aptly capture what I feel, but thank you, truly, for being a part of my village.

Klazina, this book is as much mine as it is yours. You have been with me every step of the way, since that fateful day during the biomedical research techniques course where we first met. You opened my eyes to the amazing power of ultrasound contrast agents, and took a chance with your idea of bubbles and bacteria on a student who approached you with very limited acoustical knowledge. I couldn't have asked for a better supervisor. You gave me the independence I craved as well as the guidance I needed throughout this amazing and challenging journey. Your caring and supportive nature is remarkable, and I'm so appreciative to that because it helped me through tough times. The way you've fostered my development throughout the years is truly touching, and thank you for providing me continually with access to tools to become my best self and helping me to believe in myself. You gave me a safe space to express myself, while inspiring and pushing me to grow. I've thoroughly enjoyed all of our laughs and travels together along the way, especially our time in Cincinnati together in close quarters. Thank you for your coaching, discussions, support, thoughts…for truly, truly everything. I hope you feel my sincerest gratitude, not only from these words which only display a small grain of it, but from everything over the years and beyond.

Willem, I have thoroughly enjoyed all of our discussions over the years and your enthusiasm for sonobactericide. Thank you for allowing me to intellectually spar with you over science and life. You allowed it to feel safe to do just that. This thesis is better because of it, and I thoroughly enjoyed each one as well as your guidance…I have learned so much from them. Please never lose your interest for the non-sheep and the allowance of people less experienced to debate on the subject at hand. I'm truly appreciative of all your support in my endeavors, both professional and personal, since my master's period and am happy to call you my co-promotor.

Nico, you have pushed me to do more than I thought I was capable of from the beginning and I'm better because of it. From giving me the opportunity to write a first draft of a manuscript early on after joining the department to the deadline set for my thesis which I felt was overly ambitious, you did this because you believed in me when I didn't and I can't thank you enough for that. You were correct each time, which speaks to your wisdom in guiding people. I am so fortunate to have been able to work with several people who have pushed the frontier of ultrasound and contrast agents, you one of the most noteworthy, and even though you were highly sought by many people, you always made the time for me. Thank you for your guidance and thoughtful discussions. I hope this next chapter in your life is a fantastic journey filled with plenty of moments for dancing.

Ton, thank you for allowing me to drop by your office quite frequently for your words of wisdom and guidance. Thank you for listening, and checking in during the tough times. Also for being open about things that were on your mind. I'm unsure if you're aware of it, but they provided nice mentoring moments. You've fostered not only a team atmosphere at the department, but a family one. I've been fortunate to have had the opportunity to work in many different environments and witness as many different styles of leadership. The horizontal structure and inclusive atmosphere you embody and inspire in others is one I hope to emulate, if my future allows for such a path. Thank you for providing me with many opportunities to learn as well as shine. You've been instrumental in my growth process then and now, and feel honored to have had you as my promotor. I hope you get to travel again soon. Proost (over good wine and food to thank you all one day soon)!

Christy, you not only warmly welcomed me into your lab, but also your home for which I am truly thankful and grateful to you and **Scott**. You taught me so much during that time, both scientifically and personally. I'll never forget you guiding us to the drawing board to figure out a blood clotting problem, which quickly led to a solution. I was astounded by its helpfulness and

pay homage to that teachable moment with Proposition #2. Your ability to balance your social life while blending your interests and admirable thoughtfulness of others, with the large demands that leading a lab and being an editor of a journal place on you is nothing short of impressive. I am truly appreciative to all those great mentoring moments in and out of the lab, including while tending to the garden, learning about the bees, discussions over a glass of wine after a long day's work, and listening to Aretha Franklin live from a boat. Thank you for continuing to support me with being on my doctoral committee. Heel erg bedankt voor alles!

Moniek, thank you for all the discussions and guidance over the past years. Your sincerity, warm personality, and passion for science is inspiring, and I am truly honored that you are a part of this journey. Although I did not succeed in getting your quote, "Life of a scientist is always challenging" into my propositions, which was part of response to some experimental challenges I had been facing, I have not forgotten how this made me feel…a sense of encouragement and understanding. Thank you so much for taking the time and your interest in sonobactericide and in me. I am honored and I wish you all the best! I look forward to our future encounters and bringing the fibrin biofilm research to a more sound state.

Tom Coenye, thank you for taking the time to read my thesis as a small committee member. I was happy to learn you had accepted the invitation, as I find your biofilm research intriguing and the insights valuable. Thank you also for the recent enjoyable conversation and guidance in setting up our dispersion experiments. It is always uplifting when people are open to share knowledge and work together and thus, I am excited to when we have results to share soon.

Eleanor Stride, I am honored you are a part of my doctoral committee. Since attending my first European symposium on ultrasound contrast imaging in 2015, I have admired your research and its wide range from microbubble behavior to clinical application. Thank you for your time and providing your perspective on sonobactericide.

Peter Verhamme, your interest in science and willingness to continue to be on my doctoral committee despite the new date falling during your holidays was moving. Thank you sincerely for that. I have read your infective endocarditis research with interest, and with also your clinical expertise, I look forward to the future discussion.

Inés, I could not have asked for a better partner-in-crime and work sister. So many wonderful memories of navigating this topsy-turvy journey…you made the tops even higher and the turvy parts less turvy. You were the missing bubble of the three bubbles and having

you to tease tom with me was so much fun. I don't think he expected that, and perhaps neither did I when we first met you briefly while busy with Brandaris. So you were an unexpected yet very pleasant surprise, who became one of my best friends. I felt honored to be your paranymph and so happy you're mine. You've been my rock over these years and I'm so incredibly lucky. From the late work nights/early mornings with comfort food to the adventuring in Boston, the after conference, work, any day drinks, the games, the venting sessions, the talks around the grocery store you had in your desk, are/contain just some of the moments of many that you filled my PhD chapter with happiness. Among those moments also includes **Rogier.** Thank you for all the many snacks during the alignment days, joining in the games even though it might not always be your thing, and your big heart that cares dearly for Inés, but also the people who are important to her. I wish you both a beautiful future, and am thankful to have been a part of it thus far.

Nora, I am so fortunate to have you as my rollercoaster buddy of life, from our "rere" experience, to fun cycling treks together, to so many other moments. My dear paranymph, you are my sister from another mother and it's been so nice to share life with you over the last years. I loved our daily talks when I was pregnant and all of our spontaneous meet-ups, including the surprise candle light one. You are such a caring person and the most empathetic person I know. It makes you vulnerable, but also it's a great strength and thank you for using it to help me through all the loops on the coaster track. You embody the sun and vitamin "sea", and I'm so happy you are getting to live by the sea now. I'm not exactly sure why, but I still feel your spirit animal is a giraffe, and one never too far from the water. Thank you for always being there for me, and I'll never forget the feeling of comfort you gave me from stroking my hair while I felt so ill with a stomach bug. Thank you **Luuk** for sharing Nora with me. I'm so happy for you guys and to have been a part of the special moments, and look forward to the future ones. I wish you both the best in your future adventures, whether it be in the camper exploring distant lands or long walks on a foreign beach. I look forward to future nature adventures together Nora and much love, laughs, smiles, and big hugs liefie!

My dear fellow bubblers, thank you for being such great company. I've enjoyed all the many laughs, and smiles, and hugs, and pick me-ups. **Tom (van Rooij)**, I had so much fun having a work brother to tease and be teased back, as well as to work with and learn from in a very new field to me. Thank you for instantly making me feel like home in the trench, the many laughs, and letting me tag along during the conference adventures. You're my first bubble friend and part of the three bubbles. I'm glad we've still stayed in touch and look forward to enjoying more bubbles (most likely the drinking kind) together in the near future. **Ying**, although

you were exiting when I was starting, it was great to get to know you for that bit and to continue to over the years at conferences. You're a really sweet person and congratulations to you and Jason on your second mini person! **Sara**, grazie mille for being a great trench mate and teaching us the important Italian hand gestures. I wish you the best and look forward to meeting up one day in your beautiful country. **Merel**, you really made such a great addition to team bubble. Thank you for often thinking of me and being the cheerful cheerleader for all of us. Your excitement for the research you were a part of was contagious. It was nice getting to be a paranymph together and please keep that positive energy. **Joop**, I'm glad you decided to stay after your internship and be my first mate in the sonobactericide team. It's been quite the adventure with lots of fun times and laughs. I enjoyed your playful spirit, from the many games to the tree climbing adventure, and escpeially our spontaneous starbucks coffee bets, which also provided a good reason to get some fresh air and re-caffeinate our brains. Thanks for letting me help you grow and in turn what you taught me. I'm sure we will still have more times to come as we continue investigating sonobactericide together.

Simone, thanks for the many chats and your listening ear. I enjoyed the many games, the beers in the picnic, and getting to know you over the last years. We've both had our trials and I'm glad we had each other to get them off our minds. Thank you for being my photographer for my big day and the familiar warm face in the room. Your support is always comforting and I enjoy your fur baby Nala stories. This is a big year for you and having watched you grow over these last years, I'm sure you will rock it! Thanks **Niels** for having me over for games and letting me join your picnic dates. **Margot**, it was so much fun having you in the lab. Your enthusiasm and support for sonobactericide and experimenting was refreshing and I loved all the jokes and smiles. Thank you for the "I'm sorry" jar and adding your impeccable style to Julia's wardrobe. Let's go cycling together one day soon! Wish you all the best for your internships and hope you find a place in the specialty of your dreams. **Mariël**, you have been such a big help not only in your support in the lab, but also personally and as a friend. You're a fantastic listener and your desire to do more and be more involved is motivating. Thank you, truly for always being there and providing mental support, whether during a long experimental day or just a tough day. I love the dresses you've added to Julia closet and I hope we can do a playdate soon with the warmer weather - can't wait to meet your little ones. You're incredibly sweet and I look forward to continued adventures in and out of the lab. **Bram**, I've enjoyed having you as a desk neighbor and thanks for all the treats. Though our research doesn't overlap, it's always nice to hear your stories (personal ones also) and to see someone doing the chicken embryos again. I wish you success for the rest of your PhD adventure!

Reza, I think you're next. Nice that you joined the bubble group. I'm glad you've been able to finally navigate your way through the sometimes murky waters of your research experience to getting your PhD. Thank you your support and listening. I've enjoyed our discussions and good luck in your future trajectory wherever it may lead you. **Gert-Jan**, thank you for being incredibly thoughtful. Your desk allowed us a view into your interests while also adding laughter and light to the office along with your bright personality. Good luck at your next internship! **Hongchen**, though we have not had much time together because of corona, it has been nice to get to know you both digitally and physically. I hope the future will allow for more discussions in person and look forward to experimenting together with bubbles and bacteria, as I have no doubt you'll get the shimadzus running. I wish you much success in your PhD journey. **Jiyeon**, though you only just joined the sonobactericide adventure I believe we have fun times ahead pushing the fibrin biofilms to the next level together, and looking forward to it. Never lose expressing your enthusiasm for the things that interest you, it is a great trait to have. And thank you for your patience while I have had to redirect my focus at times towards my thesis and defense. Welcome to the bubble team **Yuchen**.

Dear **Robert(a)**, I don't know where I would be without all your help. It was instrumental to not only to the progress of sonobactericide but also just to me. Your support whether it be a listening ear, sending an interesting link, or advice, or one of your hallmark Robert jokes, you were always there with a smile and encouraging words. Not just for me, but for all of us. You are a crucial cog for the department, and though you down play that because you're modest, I hope you know it's true. I think you embody the quote, "life's too short to not laugh" and I like that so much about you, including the jokes that are an acquired taste. I don't know how to thank you enough. Thank you for being my friend and being there for me. I'm really happy you have Hanneke, you two seem like a great fit and wish you lots of love and laughs in your new house and beyond.

Frits, the Brandaris guru as Inés call you which are true words. Thank you for all the advice and help over the years, and a special thank you for your time and help when my external hard drive died. I enjoyed all our discussions and enjoyed listening to your stories. I hope you are able to go on new adventures soon. **Gerard**, thanks for all your support, despite I was one of the few apple users. I always enjoyed seeing your new year's card showing images of your latest travels and hope that this summer you're able to do that again. As a fellow cycler, it was also fun to see the impact cycling can have on someone. Thank you for all the technical support **Michiel** and **Geert**. You helped us to achieve the best results we could with optimal design whenever we sought you out.

Sharon, you're not just the administrative rock of the department, but also a friend. You're always there when I need you, or anyone needs you, whether that be for help with something or a listening ear. I think sometimes you are an unsung hero, and these words are not enough to thank you. Nonetheless, thank you for all the chats and advice and stories and laughs and support and encouragement. I can't wait to enjoy yummy pisco sours together. Thank you for all the clothes and interest in Julia. It's been fun to share stories about our children together and see them grow. You're real and you set your boundaries and go above and beyond which makes you special. And thank you to your sister **Blossom**. Thank you for your time, trying, and understanding. I hope you can see I kept some elements and wish you the best in your future career.

Lana, I'm so happy to have met you. All our desk trench talks in dutch (and English) and adventures together whether traveling, including to Glasgow or driving to Leuven. Your excitement for games is so much fun. Glad to have had many moments to play them over the years together and I hope many more in the future. You have brought happy tears to my eyes on many occasions because of your thoughtfulness and I can't thank you enough.

Jason, thank you for all the laughs (including the Granny sticker for my computer although I'm only a year older) and conversations along the way. I hope one day we get to have our projects overlap to one day work together. You're a fellow game lover and always keen for a game if the time allows for it, which always puts a smile on my face. Dear **Jenna**, you are a warm soul and so thoughtful. Thank you for thinking of me for walks and playdates for our darling daughters. It has been wonderful to share our parenting adventures together and to see the bond between Julia and your adorable **Juni** grow, as well as with her uncle and aunt. I look forward to the future playdates, both for the little ones and for us, and hope for a game night soon on the horizon. It was a pleasure to meet you **Ann**, and hope you have a smooth transition to the UK.

Rik, thank you for all the advice both scientifically and personally over the years, as well as checking in from time to time. You are always wearing a smile no matter how busy you are, which rubs off on the people around you. Perhaps one day we will make it to go cycling and wish you the best both scientifically and personally. **Hans**, thanks for the words of wisdom and listening to me over the years whenever I dropped in the office, often on the search for Nico. I hope you can experience more rock climbing adventures in beautiful locations soon!

Gonzalo, thank you for opening up your home to me when I needed it most. I've enjoyed the fun adventures together, from the early morning beers in Glasgow with Jason to the many

game nights. I'll never forget all the fun and laughing, especially during the climbing adventure with Joop at the highest level in the trees at the klimbos during the PhD weekend. **Jorinde**, it was fun planning the first PhD weekend together, for which you were instrumental for with your ideas and house hunting. Over the years it has been nice getting to know you, and also sharing our PhD juggling experiences with pregnancy and baby life. I know you'll produce a beautiful dissertation. Enjoy the precious moments with your darling Isabel. **Sophie Heijmans**, thanks for the chats and I hope you're able to stay in science and investigate everything that interests you. **Luxi**, **Geraldi**, **Annette Caenen**, **Sander**, **Fox**, **Mihai**, and **Deep,** thank you for the nice conversations over the years.

To the biomechanics group, thank you for letting me often drop by whether for a break with conversation or help, as well as joining in the game nights from time to time. **Eric**, I was honored to be your paranymph and look forward to see where your career takes you. I enjoyed our many discussions and musings about life. Your social interaction and presenting skills are truly a strength and hope you get to use them effectively in your next professional step. **Eline**, it was fun twining with you over the years, as well as the drinks, the many laughs, the desk-side chats, and walks. You're inclusive and social, which I really liked and hope your path to specialization is smooth and leads you to exactly where you want to be. **Ayla**, thanks for tagging me from the beginning with organizing the PhD labuitje and then a place on the coeur PhD committee. Both lead to memorable experiences and hope your adventure down under was great. **Ruoyu**, although we never pursued it further, I enjoyed our discussions and brainstorming about potential avenues of entrepreneurship. **Astrid**, I have fond memories from bowling to beach walks with you, Ruoyu, and Inés at the Dutch Biomedical engineering conference at Egmond aan Zee to also sharing our mini people experiences. Congratulations on your second mini and your wedding. **Annette**, **Hilary**, and **Ali**, thanks for the discussions and chats about life and science. **Su**, from the first time I met you at the PhD weekend in Bergen op Zoom, I found you to be very sweet and indeed with each interaction, that has only been further confirmed. Good luck with finishing your PhD and hope you'll be able to spend more time in the lab. **Kim van Gaalen**, thank you for thinking of me and always being open to share about life and your babes. Thanks for all the hallway chats and I look forward to more of them in the future.

Frank, I'll never forget how you rescued me from a moment of extreme stress when I was surprisingly nominated to pitch my research in a min or two for an oral presentation award. That second place is because of you and your quick help in formulating a pitch in just a few

minutes, “we want to see them, we want to kill them”. Thank you also for the many warm conversations, scientific help, and general guidance. **Kim van der Heiden**, thank you for your words of support over the years and your texts checking in to see how I was doing. It was nice to share experiences and really happy for you that it worked out with the Vidi, yay! Thank you also for the items for Julia. Also **Jolanda**, thank you too for the maxi-cosi and cover. It was really thoughtful and touching how even though I was unable to attend the labuitje because of the illness around my pregnancy, on your own time you and your daughter painted the activity of me for me – thank you!

To the optics group, thanks for all the many discussions and support. **Gijs**, I still remember your warm welcome to the department. I’ve enjoyed all the conversations, whether over science or life with a beer. Congratulations on making it to full professor and I wish you much success with Kaminari Medical. Happy cycling! **Sophinese**, you are such a sweetheart. It’s been a pleasure to get to know you birthday twin. Thanks for the warm chats and always listening. Much success in Delft, and perhaps we can figure out a way to work together one day. **Jovana**, thanks for all the warm memories, whether while moving Jason and Jenna, or planning the labuitje together, or over breakfast, or visiting Julia. **Mirjam**, thank you for providing some much needed mental breaks when you dropped by the trench, or from bumping into each other in the hall, or over drinks or breakfasts. It’s funny only found out at the end of our tenure that you also swim and cycle. Maybe one day we can still do that together. Hope all is settled and enjoying your new house and job. **Nuria**, it was nice to learn you also live on the “silver lining” of the south of Rotterdam as well as see your strava activity. Thanks for the chats and hope the mass spec treats you nicer than it did in the beginning. Good luck with finishing your PhD! **Ingeborg**, thanks for letting me drop in the trench often, you make a great neighbor for Robert. It has been fun to follow you on strava. Thanks for all the kudos and I look forward to seeing all your future runs. **Leonardo**, nice that you were always open to always joined social events thanks for your kind words and hope you’re doing well in Italy. **Aaron**, **Antonio**, **Shengnan**, **Martin**, and **Tianshi,** thanks for all the nice conversations and good luck and fortune for the future.

Verya, your question for a thermo-meter is a language example I often use when talking about language quirks, because it took me a minute too long to realize you were asking for a thermometer. Thanks for the invites to join you at the climbing wall, maybe one day will become a today. Good luck with your new adventure at Kaminari Medical. **Pieter**, thanks for all the fun and interesting discussions over life and science as well as your kind words over the

years. Congrats again on your little one. I look forward to seeing you push the frontiers of ultrasound in the neurological world. **Pim**, thanks for the nice lunch discussion for when I did join.

To all the **BME family members** whether from the past or the future, whether explicitly mentioned here or not, whether still in science or far away from it, I wish you all the best. To the **current and future PhDs**, persistence through the times when the science seems to not work and everything seems to not go as planned will get you through. Don't forget to celebrate every small thing that went well, because altogether they amount to something big.

To the Medical Microbiology and Infectious Diseases department, thank you for welcoming me into your space and for all the support over the years. To the staphylococcus working group, thanks for all the great discussions and feedback on sonobactericide. **Andi**, thanks for all that you taught me on biofilms and to bounce experimental design ideas with. I enjoyed our many talks whether in the lab or walking from or to Erasmus since we were nearby neighbors. Wish you all the best in Indonesia and hopefully soon we will be celebrating your defense. **Nicole**, no matter the question or help I needed over the years, you were always there with the answer, direction, or feedback. Thank you so much for that. **Corné**, thanks for all your help along the way. It's been nice to get to know you and work more together since working on fibrin biofilms together. Look forward to hopefully continuing to together in the future. Enjoy your new-ish little one. **Valérie**, I enjoyed the conversations in the lab and discussions about our projects even though we didn't end up working together in the end. Looking forward to seeing your future work and also celebrating your thesis. **Mehri**, you are really sweet and I enjoyed the many conversations in the lab whether over science or Julia or your daughter and grandchild. Thanks for the help. **Michèle**, thanks for the feedback on sonobactericide and I hope one day we can collaborate with your phage work. Good luck as you continue your PhD work. **Jannette**, thanks for all the discussions. **Susan** and **Deborah**, thanks for all the practical work and helping me in the lab whenever I was in search for assistance. **Carla** and **Ger**, thank you for always being available to help whether it's looking for supplies, equipment, or making plates. **Annelies**, thank you for taking an interest in sonobactericide and all your support and positive responses as well as **Karin** and **Nelianne**, also for your help and guidance with the isolates. **Wendy**, thanks for helping with sonobactericide in the early stages and all the chats following. **Astrid and Michel**, I also enjoyed our lab and hallway conversations and discussion about life and science.

To the pizza club members, thank you for warmly welcoming me into your tribe when I arrived at Cincinnati. I enjoyed all the laughs and discussions over the many different pizzas

deriving from a multitude of pizza parlors. I hope one day we can all get together one day for an adventure, maybe with all our kids too. **Kevin**, I cannot thank you enough for letting me join your early morning commute every morning to the lab. Those conversations musing about life are some of the best memories from that time. They not only expanded my perspective on many topics, but through them you also became a dear friend. Thanks for all the laughs and guidance over the years, as well as putting up the lights in my new house, the fun adventures at ASA Boston with Inés and Ken among others, as well as when you and **Tricia** came over to Rotterdam together. It's been great to get to know you both better over the years and see your beautiful daughters Clara and Hailey grow. **Himanshu**, I have so many fond memories of working on sonobactericide together and of outside the lab. Thanks for all the support and your words of wisdom then and over the years. I learned a lot from you along way, not only professionally. Hope the situation allows for a visit to Rotterdam soon so I can take you around. Was also great to see you and **Karla** (and growing Karuna) in Boston, and hope I can visit you all in India soon. It was nice to have you stay over **Karla** when you were doing some work with Rik. I enjoyed doing some Dutch adventuring together with nice Amsterdam memories. Thank you also for teaching me how to properly make rice. **Ken**, thank you for sharing your uniqueness, which provided many opportunities for laughter - especially your past life as a rodeo clown. Thanks also for the help and chats in and out of the lab. I'm happy I got to meet you and **Kara** before moving to Chicago. And was so nice to see you both in Glasgow and learn you also have an interest in Outlander. Congrats to you both on your new mini and enjoy the new adventure.

To the departments of Experimental Cardiology and Experimental Anesthesiology, a warm thank you for all the friendly support and hallway conversations. **Harold**, thanks for all the warm chats and asking how I am doing whenever in passing. **Patricia**, it was always nice to share stories about our children and I hope you're able to have animal experiments soon. **Marielle**, I enjoyed our chats in the lab as well and congratulations on your new little one. **Dirk-Jan**, thanks for the nice elevator and hallway conversations, whether about science, life, or the US. Hope there will be more in the future. **Maarten**, thanks for all the insight whether into parenthood, PhD-ing, Postdocing, or sharing your grant application experience. I hope it all works out with many grants in your future! **Jarno**, it was nice getting to know you a bit better during the meetings and activities while being on the Coeur PhD committee together. Good luck in your future endeavors. Thank you **Lau**, **and Ester**, for all your friendly help with the practical things and always available whenever I had a question.

For the people I have and haven't mentioned yet but were involved in the Sonobac and Bubblecure tissue studies, thank you for your help either in getting this up and running or your continued support as patients are included and we move forward with the *ex vivo* investigations, to include resisdents as well as: **Ad Bogers**, **Ali Wahadat**, **Corstiaan den Uil**, **Jos Bekkers**, **Wouter van Leeuwen**, **Frans Oei**, **Tomas Szili Torok**, **Peter Riegman**, **Cindy Groenendijk-Kok**, **Marianne Bout**, **Jeanette Duys-Huizinga**, **Monica Jongenotter**, **Mark Hoogendijk**, **Steffanie Klosinski**, **Sing Yap**, **Yvonne Schotting**, **Mattie Lenzen**, **Rob Levens**. **Mostafa Mokhles**, thanks for your help from the very beginning and the beautiful tissue over the years. Good luck in your new adventure at UMC Utrecht. **Margreet Bekker**, I've enjoyed our conversations over the years and thank you for thinking of us for every potential patient. Also thank you for helping me with the clinical trials program application and your support. I hope you're able to go on great adventures like the one to the Galápagos islands soon. **Jan von der Thüsen**, I appreciate the warm and informative conversations over the years and thank you your help and time with the pathology side of things.

Felix Zijlstra, thank you truly for everything, much of this research within this thesis would not have been possible without your support. I also appreciate your help with my clinical trials application and the female top talent program. **Wilma Verhoek**, thank you for your quick assistance whenever I've needed it.

Shirley Uitte de Willige, thanks for all the nice lunch breaks together, and for the nice chats over the years whether personal or over Coeur items. Also for the hematological assistance near the start of the project when initially looking into fibrin clots. Hope it is a smooth transition over to the graduate school.

Michel Versluis, **Guillaume Lajoinie**, **Tim Segers**, **Ine Lentacker**, **Ine de Cock**, **Heleen Dewitte**, and **Silke Roovers**, thanks for always welcoming from the start to join the drinks and chats at the conferences. Thank you for the fond memories, support, and making it feel like a reunion to see all your smiles with each conference. Wish you all the best wherever your research or paths may lead you.

Ruud van Sloon, it's been nice to get to know more with each conference over the years. I always enjoyed the drinks Inés and I had with you and your Eindhoven group each time. Thanks for all the fun and I'm really happy for you with all your success thus far and I have no doubt you will continue to soar. Rock on!

To the **Infection & Immunity program**, thank you for all the opportunities you afforded me. It is because of the design of the program that I met Klazina and all of this happened. **Jan Nouwen**, thank you for the friendly conversation, support, and suggesting to pair up with Willem. **Frank van Vliet**, you have provided so much encouragement and belief in me over the years. Thank you for always willing to help whenever I needed it. I am so appreciative to it all, from the military funding, the applications, the tissues, to the coffee and conversations.

My dear, dear celebration time friends, **Agustin**, **Arthur**, **Denise**, **Jasper**, and **Nora**, you have all been my strength, my support, and my foundation through it all. You have always been there for me, whether with laughs or hugs or kind words or encouragement or celebrations or a place to rest my head. How lucky am I to have met you all and to call you all my dear friends. I loved all our adventures, even the gruelling study days because having you there made them doable and fun. From our drinks and house warmings, to game nights and glühwein, to birthday wishes and parties, to dinners out in the town, to Christmas markets and walks and runs, to dancing and Nora's wedding, to abroad calls and spinning classes, and to so much more. You all have added so much joy to these years and I can't thank you enough which words only fall short. I so wished you could all share this day with me, but alas it wasn't so. I hope in the near future we can all celebrate together again soon everything we've missed! Much, much love my dear loves. Thank you **Frank** and **Irene** to sharing your plus ones with me as well as joining in some of the adventures.

JD, thank you for all the beautiful moments and laughs and smiles as well as all the words of support and encouragement along the way. The leafe is real and I hope one day stella works. Remember to be true to yourself, for in that is where I think happiness lies. And please don't ever feel bad for being so thoughtful. Enjoy all the precious moments with your kids and I wish you all the best no matter where your journey leads you.

Simone, thank you for all your support over the years and being there when I needed you. I especially enjoyed all our wine and prosecco dates in the park and by the water in the harbour under the sun. It's been great to get to know you better over the last years, including on travels outside the Netherlands and the many events we've shard together. Thank you for always listening. Enjoy your new home and many cheers into the future!

To my wonderful neighbors, **Xamara**, **Guido**, **Mika**, **Kai**; **Lieke**, **Said**, **Kenza**, **Lemoon**; **Diewertje** and others that have I gotten to know over the last couple years, thank you for always checking in, your support, and the Dutch practice. I've enjoyed getting to know you all better and the many playdates.

Jessie, oh we had so many memories and fun times. You are an amazing friend, a fantastic writer, and just an all-around sweet person with a big heart. If I could have taken you over the pond I would have. Thank you for always being there for me in every way during my young adulthood. Much love to you and your family. **Diana**, my dear dear friend, I loved all our adventures in Columbia together, the jazz nights, the drinks, the late evenings, the many many coffee dates. I still have my necklace with a K. You have two beautiful kids and I'm so happy for you guys. I wish you much love amiga – te quiero.

Stefan, thank you for everything you've done as a friend, including the time you gave during work. You're a kind and thoughtful person, and a great friend to Johan. I appreciate all the times we've spent together, accepting my american hugs, and support. Also to your family as well.

Ylske, I cannot thank you enough for helping me find peace during a time when I felt pulled in so many directions that at times it felt crushing. You allowed me a safe space to just talk about everything freely and without judgement, and through that it helped me process, find comfort, and take in everything at a healthy pace. You were my self-care during a time I needed it most, when that is the thing I drop when I feel time is overwhelming limited. Although I still did that, you were not persistent or pushing and I really appreciate that. I admire how well you put your boundaries out and stick to them. I only hope I can be as balanced as you one day. I wish you the best in all your future journey. Thank you for always understanding and helping me grow into a stronger person and broadening my perspective.

What is family…I know it isn't defined by blood, but by the people who want you in their life and accept you for who you are…it's love…it's who you love and who loves you… and so I don't believe I have just one family, but multiple families and people, that I am so, so fortunate have. Thank you for loving me and being there for me no matter what, even when time and distance and the busyness of life gets in the way. I hope you know I love you all dearly. You have all provided so much support and love over the years, especially when I needed it so, especially on my not straight path. Thank you for all the wonderful memories and celebrations and travels and so much more over the years. To **Dixie**, **Mike**, **Sydney**, **Casey**, **Carol** (Maw-maw), and **Ken** (Paw-paw) and to all the extended family members, thank you for accepting me as me with all my faults into your family as your family even though we are not blood. To **Pam** (mom), **Tim**, **Alex**, **Samantha**, **Rachel**, **Ben**, **Caleb**, **Degan**, **Killian** and **mini Rachel/Ben.** To **Grandpa**, **Grandma**, **Paula**, **Barry**, **Peggy**, **PJ**, **George** (godfather), **Kalyn**, **Georgie**, **James** (little bear), **Brian**, **Michelle**, **Madison**, **Ella**, **Pierrette**, **Kristen**, **Alex**, and **Austin**. To the **Lattwein** family, **Birgit** (godmother) and extended family members. To **Ana Maria**, **Han**, **Chela**, **Maarten**, **Kirki**, **Georgie**, **Sophia**, and **Philip**. **Johan**, we have an amazing, beautiful daughter together and you played a huge role in the making of this thesis over the years. Thank you for both of those and for the many adventures we took together and the good times. **Julia**, I love you more with each passing day, even when I thought I was already at the maximum possible. You constantly remind me to appreciate the smallest things and watching you grow and develop is amazing. You are so caring and your cuddles mean the world. I love you up to the sky and down again, around the world and back again…unconditionally forever….high five, box, buzz, mwah, hug.